NASA-CP-2368-PT-2 19850015529

NASA Conference Publication 2368
Part 2

Large Space Antenna Systems Technology 1984

Proceedings of a conference
held in Hampton, Virginia
December 4-6, 1984

NASA

NASA Conference Publication 2368
Part 2

Large Space Antenna Systems Technology 1984

Compiled by
William J. Boyer
Langley Research Center

Proceedings of a conference sponsored jointly by the NASA Office of Aeronautics and Space Technology and NASA Langley Research Center and held in Hampton, Virginia
December 4–6, 1984

NASA
National Aeronautics and Space Administration
Scientific and Technical Information Branch
1985

Page intentionally left blank

PREFACE

This publication is a compilation of the papers presented at the NASA Conference on Large Space Antenna Systems Technology, held at the Langley Research Center, Hampton, Virginia, December 4-6, 1984. The conference was sponsored jointly by the NASA Office of Aeronautics and Space Technology (OAST) and the NASA Langley Research Center. The conference was organized into seven sessions: Mission Applications for Large Space Antenna Systems, Large Space Antenna Structural Systems, Materials and Structures Technology, Structural Dynamics and Control Technology, Electromagnetics Technology, Large Space Antenna Systems and the Space Station, and Flight Test and Evaluation. All speakers and topics were selected by the session co-chairmen and included representation from industry, universities, and government. The program was organized to provide a comprehensive review of space missions requiring large antenna systems and of the status of key technologies required to enable these missions.

The general co-chairmen for the conference were Dr. Leonard A. Harris, Director for Space, NASA Office of Aeronautics and Space Technology, and Paul F. Holloway, Deputy Director, Langley Research Center. The program chairmen were Dr. Earle K. Huckins III, Head, Large Space Antenna Systems Technology, Langley Research Center, and William J. Boyer, Head, Office of Space Flight Experiment Definition and Integration, Langley Research Center. The conference committee wishes to express its appreciation to the session chairmen, authors, and conference administrative assistants for their outstanding contributions to the meeting.

This publication was expedited and enhanced through the efforts of the staff of the Research Information and Applications Division, Langley Research Center.

Page intentionally left blank

CONTENTS

*Part 1 is presented under separate cover.

PART 2

SESSION 4: STRUCTURAL DYNAMICS AND CONTROL TECHNOLOGY

SESSION 5: ELECTROMAGNETICS TECHNOLOGY

Page intentionally left blank

LSAST-1984 CONFERENCE ATTENDEE LIST

ABOIM, DR. CARLOS A.	ANCO ENGINEERS
ACHARD, ROBERT T.	U.S. AIR FORCE
ADAMS, RICHARD R.	NASA LANGLEY RESEARCH CENTER
ADELMAN, HOWARD M.	NASA LANGLEY RESEARCH CENTER
AGNEW, DONALD L. (DON)	EASTMAN KODAK COMPANY
AKIN, DR. D. L.	MASSACHUSETTS INSTITUTE OF TECHNOLOGY
AKLE, W.	TRW INCORPORATED
ALFF, WILLIAM	LOCKHEED MISSILES & SPACE COMPANY
ALLEN, BIBB B.	HARRIS CORPORATION, GASD
ALLEN, JR., JOHN L.	NASA LANGLEY RESEARCH CENTER
AMOS, DR. ANTHONY K.	AIR FORCE OFFICE OF SCIENTIFIC RES.
ANDERSON, DR. MELVIN S.	NASA LANGLEY RESEARCH CENTER
ANDERSON, DR. WILLARD W.	NASA LANGLEY RESEARCH CENTER
ANDREAS, ROBERT J.	HARRIS CORPORATION, GASD
ARAYA, ROBERTO	UCLA
ARCHER, DR. JOHN S.	TRW INCORPORATED
ARMSTRONG, ERNEST	NASA LANGLEY RESEARCH CENTER
ASHLEY, PROFESSOR HOLT	STANFORD UNIVERSITY
ASWANI, MOHAN	AEROSPACE CORPORATION
BAILEY, DR. MARION C.	NASA LANGLEY RESEARCH CENTER
BAINUM, PETER M.	HOWARD UNIVERSITY
BALDWIN, C. A.	NASA LANGLEY RESEARCH CENTER
BARNARD, MICHAEL J.	TRW INCORPORATED
BARRETT, MICHAEL F.	HONEYWELL, SYSTEMS & RESEARCH CENTER
BARTLETT, WAYNE M.	NASA LEWIS RESEARCH CENTER
BASU, J. P.	PERKIN-ELMER
BAYARD, DAVID S.	JET PROPULSION LABORATORY
BEASLEY, GARY P.	NASA LANGLEY RESEARCH CENTER
BEATTY, MARVIN	NASA LANGLEY RESEARCH CENTER
BECK, FRED B.	NASA LANGLEY RESEARCH CENTER
BECOUVARAKIS, TIM G.	NASA LANGLEY RESEARCH CENTER
BEHUN, VAUGHAN	KENTRON
BELVIN, W. KEITH	NASA LANGLEY RESEARCH CENTER
BENNETT, WILLIAM	SYSTEMS ENGINEERING FOR POWER, INC.
BENTON, MAX D.	AEC-ABLE ENGINEERING COMPANY, INC.
BERMAN, DR. FRED	GEORGIA INSTITUTE OF TECHNOLOGY
BLANKENSHIP, CHARLES P.	NASA LANGLEY RESEARCH CENTER
BLUME, DR. H. J. C.	NASA LANGLEY RESEARCH CENTER
BOENSCH, FRANK D.	U.S. AIR FORCE
BOUNDY, ROBERT A.	JET PROPULSION LABORATORY
BOYER, WILLIAM J.	NASA LANGLEY RESEARCH CENTER
BRACALENTE, EMEDIO M.	NASA LANGLEY RESEARCH CENTER
BREAKWELL, JOHN	LOCKHEED MISSILES & SPACE COMPANY
BRITT, C. L.	RESEARCH TRIANGLE INSTITUTE
BROWN, LARRY J.	HONEYWELL, SSAVD
BRUMFIELD, M. L. (LARRY)	NASA LANGLEY RESEARCH CENTER
BURMEISTER, GEORGE J.	BOEING AEROSPACE CORPORATION
BUTLER, DAVID H.	NASA LANGLEY RESEARCH CENTER

LSAST-1984 CONFERENCE ATTENDEE LIST - CONTINUED

CAMARDA, CHARLIE	NASA LANGLEY RESEARCH CENTER
CAMARET, TIM	ROCKWELL INTERNATIONAL-ROCKETDYNE DIV.
CAMPBELL, BRUCE	ASTRO RESEARCH CORPORATION
CAMPBELL, THOMAS G.	NASA LANGLEY RESEARCH CENTER
CARD, DR. MICHAEL F.	NASA LANGLEY RESEARCH CENTER
CHEN, DR. JAY-CHUNG	JET PROPULSION LABORATORY
CLAYTON, MICHAEL J.	EASTMAN KODAK COMPANY
COCKRELL, DR. CAPERS R.	NASA LANGLEY RESEARCH CENTER
COFFEE, JR., CLAUDE W.	NASA LANGLEY RESEARCH CENTER
COON, KENNETH C.	JET PROPULSION LABORATORY
COPPA, ANTHONY	GENERAL ELECTRIC
COUCH, LANA M.	NATIONAL AERONAUTICS & SPACE ADMINISTRATION
COUGHLIN, THOMAS B.	JOHNS HOPKINS UNIVERSITY
COYNER, JR., J. V.	MARTIN MARIETTA CORPORATION
CROOP, HAROLD C.	U.S. AIR FORCE
CROWE, DAVID A.	EASTMAN KODAK COMPANY
CRUMBLY, K. H. (KEN)	NASA LANGLEY RESEARCH CENTER
CUCHANSKI, MICHAEL	RCA ASTRO ELECTRONICS
CUDNEY, JR., HARLEY H.	STATE UNIVERSITY OF NEW YORK AT BUFFALO
DARRAH, JOHN H.	HQ SPACE COMMAND/XPN
DAUKAS, ANTHONY (TONY)	ASTRO RESEARCH CORPORATION
DAVIS, LARRY D.	HARRIS CORPORATION, GASD
DE LAFONTAINE, JEAN	DEFENCE RESEARCH ESTABLISHMENT OTTAWA
DEAN, ED	NASA LANGLEY RESEARCH CENTER
DEAVER, JOSEPH	NRL, BENDIX AEROSPACE
DI BATTISTA, JOHN D.	NATIONAL AERONAUTICS & SPACE ADMINISTRATION
DIARRA, C. MODIBO	HOWARD UNIVERSITY
DIGLIO, JOHN	GRUMMAN AEROSPACE CORPORATION
DORSEY, JOHN T.	NASA LANGLEY RESEARCH CENTER
DUSTIN, MILES O.	NASA LEWIS RESEARCH CENTER
EDIGHOFFER, HAROLD	EDIGHOFFER INCORPORATED
EVANS, RON	SPERRY
FADDOUL, JAMES R.	NASA LEWIS RESEARCH CENTER
FARMER, JEFFERY T.	NASA LANGLEY RESEARCH CENTER
FENG, G. C.	LOCKHEED-EMSCO
FICHTER, W. B.	NASA LANGLEY RESEARCH CENTER
FIGGE, I. E. (WARD)	ATLANTIC RESEARCH CORPORATION
FOLDES, PETER	FOLDES INCORPORATED
FONTANA, ANTHONY	NASA LANGLEY RESEARCH CENTER
FREELAND, ROBERT E.	JET PROPULSION LABORATORY
FREEMAN, JR., W. T.	NASA LANGLEY RESEARCH CENTER
FULTON, DR. ROBERT E.	GEORGE WASHINGTON UNIVERSITY
GANSSLE, EUGENE R.	RCA ASTRO-ELECTRONICS
GARCIA, NICHOLAS F.	LOCKHEED MISSILES & SPACE COMPANY
GARIBOTTI, JOSEPH F.	HR TEXTRON INCORPORATED

LSAST-1984 CONFERENCE ATTENDEE LIST - CONTINUED

GARRETT, DR. L. BERNARD	NASA LANGLEY RESEARCH CENTER
GATES, RICHARD M.	BOEING AEROSPACE COMPANY
GIESY, D. P.	KENTRON INTERNATIONAL, INC.
GOGINENI, DR. S. P.	UNIVERSITY OF KANSAS
GOSLEE, JOHN W. (BILL)	NASA LANGLEY RESEARCH CENTER
GRANTHAM, WILLIAM L.	NASA LANGLEY RESEARCH CENTER
GYNTHER, DANIEL E.	MRJ, INCORPORATED
HADAEGH, FRED	JET PROPULSION LABORATORY
HAGAMAN, JANE A.	NASA LANGLEY RESEARCH CENTER
HAGEN, HOWARD G.	LOCKHEED MISSILES & SPACE COMPANY
HAIGHT, R. W.	LOCKHEED MISSILES & SPACE COMPANY
HALE, DR. ARTHUR L.	GENERAL DYNAMICS CONVAIR
HALL, JR., JOHN B. (JACK)	NASA LANGLEY RESEARCH CENTER
HAM, FRED M.	HARRIS CORPORATION, GASD
HAMIDI, MASSIH	JET PROPULSION LABORATORY
HAMILTON, EDWARD C.	NASA MARSHALL SPACE FLIGHT CENTER
HAMMELL, ALLAN K.	HONEYWELL INCORPORATED
HANKS, BRANTLEY R.	NASA LANGLEY RESEARCH CENTER
HANNAN, GENE J.	LOCKHEED MISSILES AND SPACE COMPANY
HARCROW, HARRY	MARTIN MARIETTA DENVER AEROSPACE
HARRINGTON, DR. RICHARD F.	NASA LANGLEY RESEARCH CENTER
HARRIS, JACK E.	NASA LANGLEY RESEARCH CENTER
HARRISON, DENNIS C.	HARRIS CORPORATION
HEARD, JR., WALTER L. (DOUG)	NASA LANGLEY RESEARCH CENTER
HEDGEPETH, DR. J. M.	ASTRO RESEARCH CORPORATION
HERSTROM, CATHERINE L.	NASA LANGLEY RESEARCH CENTER
HILL, HENRY C.	MARSHALL SPACE FLIGHT CENTER
HILL, J. E.	LOCKHEED MISSILES & SPACE COMPANY
HILL, THOMAS E.	GENERAL ELECTRIC-SPACE SYSTEMS DIV.
HIRSCHBEIN, MURRAY	NATIONAL AERONAUTICS & SPACE ADMINISTRATION
HOEHNE, VERNON	AIR FORCE WRIGHT AERONAUTICAL LABS.
HOLCOMB, DR. LEE B.	NATIONAL AERONAUTICS & SPACE ADMINISTRATION
HOLLOWAY, PAUL F.	NASA LANGLEY RESEARCH CENTER
HOLLOWAY, III, S. E. (CHIP)	NASA LANGLEY RESEARCH CENTER
HOOK, W. RAY	NASA LANGLEY RESEARCH CENTER
HORNER, DR. GARNETT C.	NASA LANGLEY RESEARCH CENTER
HORTA, LUCAS G.	NASA LANGLEY RESEARCH CENTER
HORTON, JOHN B.	TRW INCORPORATED
HOUSNER, DR. JERROLD M.	NASA LANGLEY RESEARCH CENTER
HOWLAND, RAY	THE HOWLAND CO., INC.
HSING, JOHN C.	COMSAT
HUANG, FELIX	ITEK OPTICAL SYSTEMS
HUDSON, WAYNE R.	NATIONAL AERONAUTICS & SPACE ADMINISTRATION
HYLAND, DR. DAVID C.	HARRIS CORPORATION, GASD
IRVINE, THOMAS B.	NASA LEWIS RESEARCH CENTER
IWAMOTO, HENRY H.	LOCKHEED MISSILES & SPACE COMPANY

LSAST-1984 CONFERENCE ATTENDEE LIST - CONTINUED

JACOBS, ERNEST	AEROSPACE CORPORATION
JACOCKS, JR., MILTON L.	NASA LANGLEY RESEARCH CENTER
JAMNEJAD-DAILAMI, DR. VAHRAZ	JET PROPULSION LABORATORY
JEANS, J. R.	U.S. GOVERNMENT
JOHNSON, JAMES W.	NASA LANGLEY RESEARCH CENTER
JONES, PETER A.	EASTMAN KODAK COMPANY
JONES, WILLIAM R.	NASA LANGLEY RESEARCH CENTER
JORDAN, DR. JAMES F.	JET PROPULSION LABORATORY
JOSHI, SURESH M.	NASA LANGLEY RESEARCH CENTER
JUANG, DR. JER-NAN	NASA LANGLEY RESEARCH CENTER
KADER, JAC	KADER ROBOTICS CORPORATION
KAMINSKAS, RIM A.	TRW INCORPORATED
KECKLER, CLAUDE R.	NASA LANGLEY RESEARCH CENTER
KELLERMEIER, HANS	MBB COMPANY, SPACE DIVISION
KENDALL, BRUCE	NASA LANGLEY RESEARCH CENTER
KEY, RICHARD	JET PROPULSION LABORATORY
KIDD, ALAN	SPAR AEROSPACE LIMITED
KINGSBURY, MICHAEL G.	BRUNSWICK CORPORATION-DEFENSE DIV.
KLICH, PHILLIP J.	NASA LANGLEY RESEARCH CENTER
KOPRIVER, FRANK	JL ASSOCIATES
KROEN, MARIAN L.	NASA LANGLEY RESEARCH CENTER
KULICK, SHEL	GENERAL DYNAMICS
KYSER, ALBERT C.	INSTRUMECH
LAKE, MARK S.	NASA LANGLEY RESEARCH CENTER
LAMBERTY, BERNARD J.	BOEING AEROSPACE COMPANY
LAWRENCE, ROLAND W.	NASA LANGLEY RESEARCH CENTER
LE ROY, BRUCE E.	NASA LEWIS RESEARCH CENTER
LEVY, GERALD S.	JET PROPULSION LABORATORY
LIGHTNER, E. BURTON	NASA LANGLEY RESEARCH CENTER
LIN, DR. YU-HWAN	JET PROPULSION LABORATORY
LIN, J. GENE	CONTROL RESEARCH CORPORATION
LINDBERG , ROBERT	NAVAL RESEARCH LABORATORY
LIPS, KENNETH W.	DEPT. OF COMMUNICATIONS
LOPRIORE, MARIO	ESA-ESTEC
LOVELACE, U. M. (WOODY)	NASA LANGLEY RESEARCH CENTER
LYON, JUD	HOWLAND COMPANY, INCORPORATED
LYONS, M.G.	INTEGRATED SYSTEMS INC.
MALLETTE, MICHAEL F.	UNIVERSITY OF VIRGINIA
MALONE, JOHN E.	NASA JOHN F. KENNEDY SPACE CENTER
MANSOUR, WAGDY A.	GEORGE WASHINGTON UNIVERSITY
MANTUS, MORTON	GRUMMAN AEROSPACE CORPORATION
MC DONALD, K. D.	FEDERAL AVIATION ADMINISTRATION
MC GOWAN, PAUL	NASA LANGLEY RESEARCH CENTER
MECK, DR. ULRICH	MBB COMPANY
MIKULAS, JR., DR. MARTIN M.	NASA LANGLEY RESEARCH CENTER

LSAST-1984 CONFERENCE ATTENDEE LIST - CONTINUED

MILLER, CHRISTOPHER C.	MARTIN MARIETTA CORPORATION
MILLER, JAMES B.	NASA LANGLEY RESEARCH CENTER
MISERENTINO, ROBERT	NASA LANGLEY RESEARCH CENTER
MOBLEY, TOM	MARTIN MARIETTA CORPORATION
MONTEITH, JAMES H.	NASA LANGLEY RESEARCH CENTER
MONTGOMERY, DR. RAYMOND C.	NASA LANGLEY RESEARCH CENTER
MONTGOMERY, JOHN	MARTIN MARIETTA DENVER
MOORMAN, JOSEPH C.	NASA LANGLEY RESEARCH CENTER
MORRIS, DAVID P.	HONEYWELL, SSAVD
MOULTON, RICH	HEXCEL
NARKIS, YAHLI	UNIVERSITY OF VIRGINIA
NEWTON, ROBERT B.	MARTIN MARIETTA AERO.-MICHOUD DIV.
NEWTON, RON	AEROJET TECHSYSTEMS COMPANY
NICHOLS, STEPHEN A.	NAVAL ELECTRONIC SYSTEMS COMMAND
NIMMO, NANCY	NASA LANGLEY RESEARCH CENTER
NOBLITT, B. G.	TELEDYNE BROWN ENGINEERING
NOOR, AHMED K.	GEORGE WASHINGTON UNIVERSITY
NYGREN, EVERT C.	FORD AEROSPACE & COMMUNICATIONS CORP.
OAKES, THOMAS J.	GOODYEAR AEROSPACE CORPORATION
OSBORNE, ERIC P.	NASA GODDARD SPACE FLIGHT CENTER
PALUSZEK, MICHAEL	C.S. DRAPER LABORATORY
PAPPA, RICHARD S.	NASA LANGLEY RESEARCH CENTER
PATTERSON, L. ROY	ORI, INCORPORATED
PINSON, DR. LARRY D.	NASA LANGLEY RESEARCH CENTER
PITCAIRN, IAN	UNITED TECHNOLOGIES RES. CENTER-OATL
PITTMAN, R. BRUCE	NASA AMES RESEARCH CENTER
POHLEN, L. J. (LARRY)	HQ USAF SPACE DIVISION, SD/YOM
POLLOCK, SAMUEL J.	AFWAL/FIBAC
PORTER, AL	HEATH TECHNA
QUARTARARO, RICHARD	HR TEXTRON INCORPORATED
RAHMAT-SAMII, DR. YAHYA	JET PROPULSION LABORATORY
RANEY, J. P.	NASA LANGLEY RESEARCH CENTER
RANSOM, JAMES	AEROSPACE CORPORATION
RAO, S. K.	SPAR AEROSPACE LIMITED
REDDY, A. S. S. R.	HOWARD UNIVERSITY
REICHHARDT, TONY	SPACE WORLD MAGAZINE
RHODES, MARVIN D.	NASA LANGLEY RESEARCH CENTER
RICE, ROBERT B.	MARTIN MARIETTA CORPORATION
ROBERTSON, ANDREW	GENERAL DYNAMICS-CONVAIR
ROBERTSON, BRENT	UNIVERSITY OF VIRGINIA
RODGERS, FREDERICK C.	ATLANTIC RESEARCH CORPORATION
ROGERS, DR. L. C.	AF WRIGHT AERONAUTICAL LABS./FIBA

LSAST-1984 CONFERENCE ATTENDEE LIST - CONTINUED

ROMERO, JAMES M.	NATIONAL AERONAUTICS & SPACE ADMINISTRATION
ROWELL, L. F. (LARRY)	NASA LANGLEY RESEARCH CENTER
RUDDUCK, DR. R. C.	OHIO STATE UNIVERSITY
RUNGE, FRITZ C.	MCDONNELL DOUGLAS ASTRONAUTICS COMPANY
SANTOS-MASON, BEATRICE	NASA LANGLEY RESEARCH CENTER
SATTER, CELESTE M.	CAMBRIDGE RESEARCH ASSOCIATES
SAUNDERS, CHARLES G.	NASA LANGLEY RESEARCH CENTER
SCHILLING, DR. RALPH F.	TRW FEDERAL SYSTEMS DIVISION
SCHMID, PAUL E.	U.S. GOVERNMENT
SCHNEIDER, DR. WILLIAM C.	NASA JOHNSON SPACE CENTER
SCHOCK, RICHARD W.	NASA MARSHALL SPACE FLIGHT CENTER
SCHOEN, NEIL C.	TRW INCORPORATED
SCHRADER, JAMES H.	RESEARCH TRIANGLE INSTITUTE
SCHROEDER, LYLE C.	NASA LANGLEY RESEARCH CENTER
SCHY, ALBERT A.	NASA LANGLEY RESEARCH CENTER
SHARP, G. RICHARD	NASA LEWIS RESEARCH CENTER
SHIEH, RONG C.	MRJ, INCORPORATED
SHIELDS, DAVID	U.S. GOVERNMENT
SHIUE, DR. JAMES C.	NASA GODDARD SPACE FLIGHT CENTER
SHORE, CHARLES P.	NASA LANGLEY RESEARCH CENTER
SIGNORELLI, JOEL	AFRPL/DYSS
SINGH, SAHJENDRA N.	VIGYAN RESEARCH ASSOCIATES, INC.
SMITH, DAVEY L.	AFWAL/FIBG
SNYDER, E. GLENN	ROCKWELL SPACE
SOKOL, SAMUEL	NASA LANGLEY RESEARCH CENTER
SOOSAAR, DR. KETO	CAMBRIDGE RESEARCH ASSOCIATES
SOROCKY, STEPHEN J.	SPAR AEROSPACE LIMITED
STEIN, BLAND A.	NASA LANGLEY RESEARCH CENTER
STEIN, PETER A.	NASA LANGLEY RESEARCH CENTER
STEVENSON, DONALD L.	E.I. DU PONT DE NEMOURS & CO., INC.
STIEBER, MICHAEL E.	COMMUNICATIONS RESEARCH CENTRE
SUNDARARAJAN, NARASIMHAN	OLD DOMINION UNIV. RES. FOUNDATION
SUSSMAN, JERRY	U.S. GOVERNMENT
SYKES, GEORGE F.	NASA LANGLEY RESEARCH CENTER
TALBOT, JOE	NASA LANGLEY RESEARCH CENTER
TANKERSLEY, DR. B. C.	HARRIS CORPORATION, GASD
TAYLOR, JR., L. W. (LARRY)	NASA LANGLEY RESEARCH CENTER
TENNEY, DR. DARREL R.	NASA LANGLEY RESEARCH CENTER
THOMAS, MITCHELL	L'GARDE, INC.
THOMPSON, CHARLES CLARK	UNITED TECHNOLOGIES RESEARCH CENTER
TILSON, JR., PAUL E.	U.S. AIR FORCE
TOLIVAR, FERNANDO	JET PROPULSION LABORATORY
TOLLISON, DANNY K.	CONTROL DYNAMICS COMPANY
TOLSON, ROBERT	NASA LANGLEY RESEARCH CENTER
TOMPKINS, STEPHEN S.	NASA LANGLEY RESEARCH CENTER

LSAST-1984 CONFERENCE ATTENDEE LIST - CONCLUDED

TRACY, DANIEL J.	BOEING AEROSPACE COMPANY
TSENG, G. T.	AEROSPACE CORPORATION
TUMULTY, WILLIAM T.	NATIONAL AERONAUTICS & SPACE ADMINISTRATION
VAN VOOREN, ROBERT H.	TRW INCORPORATED
VANDER VELDE, WALLACE E.	MASSACHUSETTS INSTITUTE OF TECHNOLOGY
VENKAYYA, VIPPERLA B.	AIR FORCE WRIGHT AERONAUTICAL LABS.
VICTER, IRA	ROCKWELL INTERNATIONAL
WADA, BEN K.	JET PROPULSION LABORATORY
WALL, JOE	HONEYWELL SYSTEMS AND RESEARCH CENTER
WALLSOM, RICHARD E.	KENTRON
WALZ, JOSEPH E.	NASA LANGLEY RESEARCH CENTER
WANG, HARRY S. C.	AEROSPACE CORPORATION
WARD, JR., JAMES C.	NASA LANGLEY RESEARCH CENTER
WATSON, JUDITH J.	NASA LANGLEY RESEARCH CENTER
WEBER, III, DR. WILLIAM J.	JET PROPULSION LABORATORY
WEGROWICZ, L. A.	SPAR AEROSPACE LIMITED
WEIDLER, DARRYL	MIT LINCOLN LABORATORY
WEIDMAN, DR. DEENE J.	NASA LANGLEY RESEARCH CENTER
WEISS, MICHAEL A.	FAIRCHILD SPACE COMPANY
WEISSMAN, DR. DAVID E.	HOFSTRA UNIVERSITY
WELIK, GEORGE	LOCKHEED MISSILES & SPACE COMPANY
WELLING, REBECCA L.	LOCKHEED RESEARCH & DEVELOPMENT DIV.
WENDEL, W. R.	SPACE STRUCTURES INTERNATIONAL
WILLIAMS, JAMES L.	NASA LANGLEY RESEARCH CENTER
WILLIAMS, JEFFREY P.	NASA LANGLEY RESEARCH CENTER
WISSINGER, ALAN B.	PERKIN-ELMER
WITT, WILLIAM P.	AIR FORCE WEAPONS LABORATORY
WOO, KENNETH	JET PROPULSION LABORATORY
WOODS, JR., ARTHUR A.	LOCKHEED MISSILES & SPACE COMPANY
WRENN, G. A.	KENTRON INTERNATIONAL
WRIGHT, HOWARD T.	NASA LANGLEY RESEARCH CENTER
WRIGHT, ROBERT L.	NASA LANGLEY RESEARCH CENTER
YOUNG, JOHN W.	NASA LANGLEY RESEARCH CENTER
ZAGHLOUL, AMIR	COMSAT LABORATORIES
ZIMCIK, DR. D. G.	COMMUNICATIONS RESEARCH CENTRE

ON-ORBIT SYSTEMS IDENTIFICATION OF FLEXIBLE SPACECRAFT

Larry Taylor and Larry D. Pinson
NASA Langley Research Center
Hampton, Virginia

Large Space Antenna Systems Technology - 1984
December 4-6, 1984

SPACECRAFT CONTROL

Future spacecraft include configurations which are too flexible to be adequately tested prior to flight and which will require on-orbit systems identification to ensure safe operation of the flight control systems.

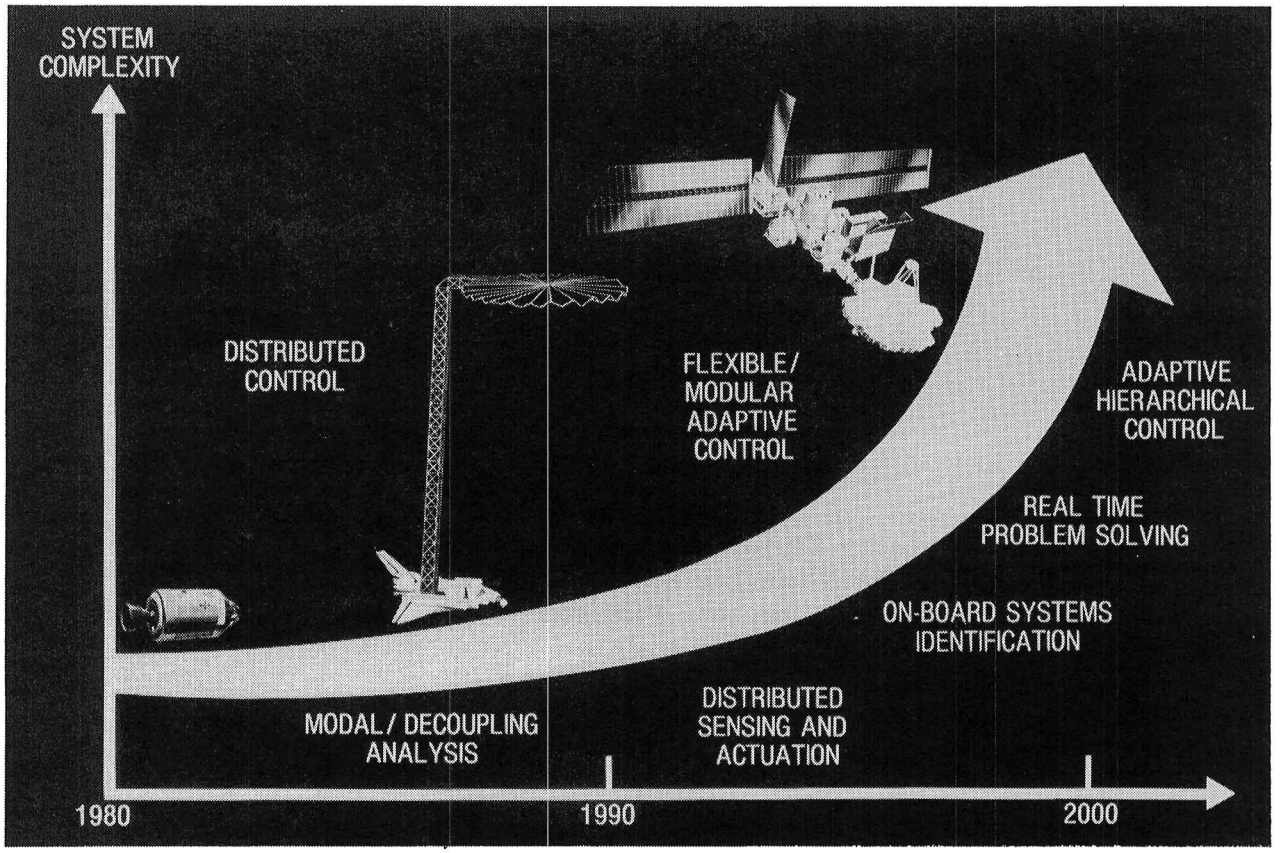

STABILITY LIMITS OF CONTROL TYPES

As the relative sizes of flexible appendages and the control bandwidth approach the structural frequencies, the point is reached at which an accurate representation of the structural dynamics is necessary for designing the flight control system.

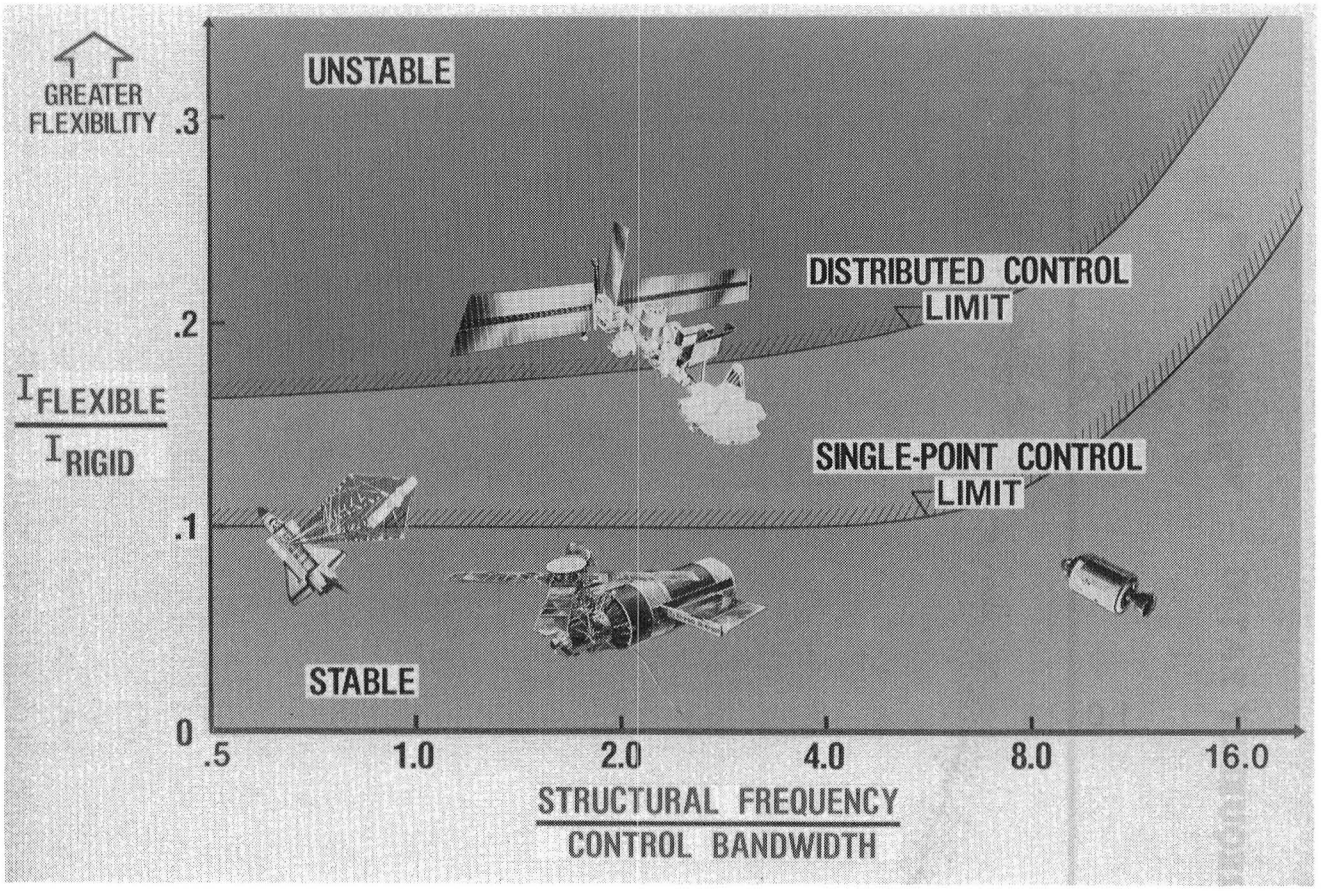

EFFECT OF UNCERTAINTY IN STRUCTURAL DYNAMICS
ON SYSTEM PERFORMANCE

The performance of flight control systems is adversely affected by uncertainty in the structural dynamics because it is necessary to accommodate for a range of characteristics.

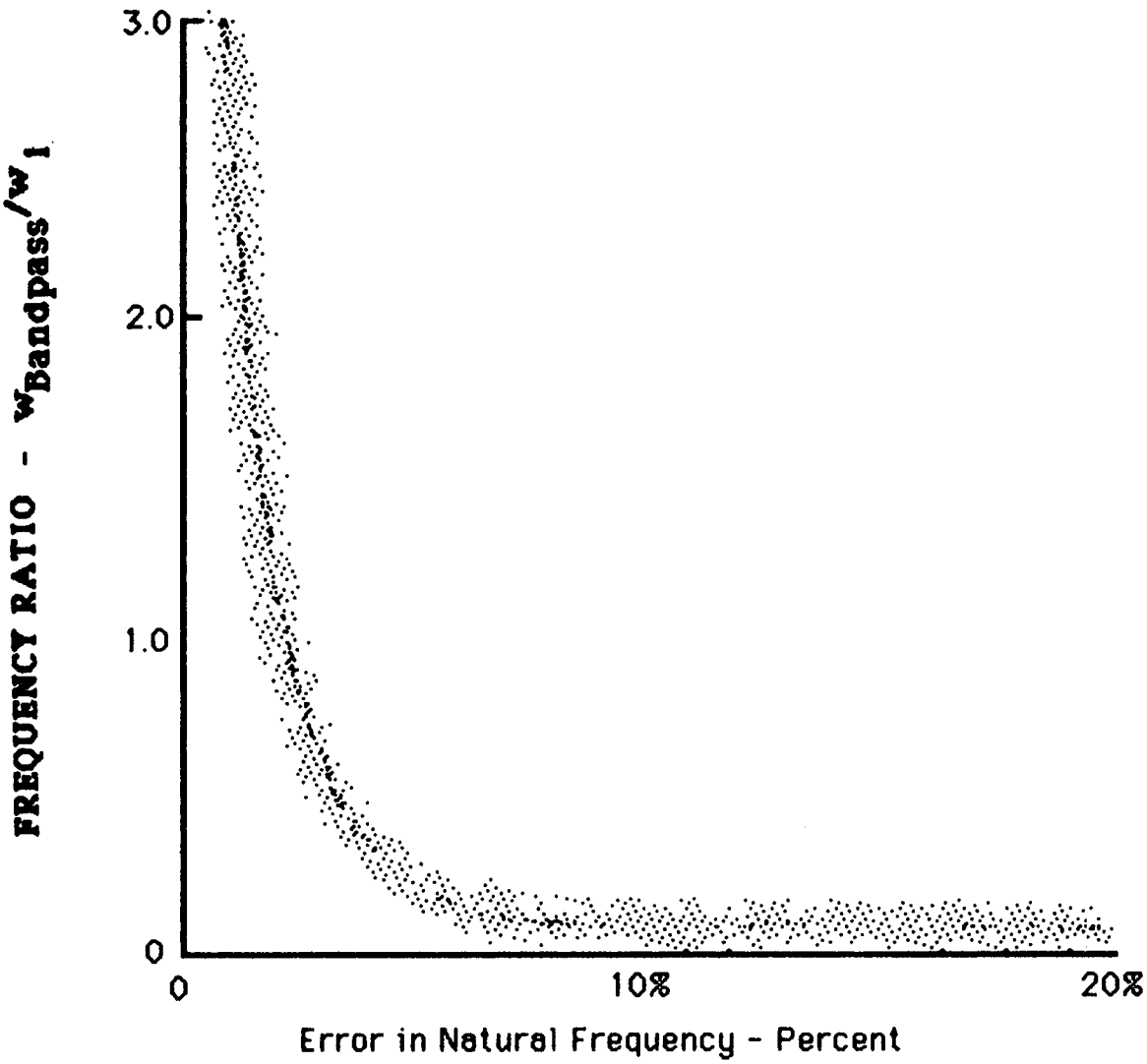

MAST DESIGN CONSIDERATIONS

Design considerations for the Mast, or COFS-1, Flight Experiment show how the structural frequencies decrease as size increases and point to sensor concerns. It is also evident that ground test results will be severely impacted by gravity for large space structures, thereby making on-orbit systems identification mandatory.

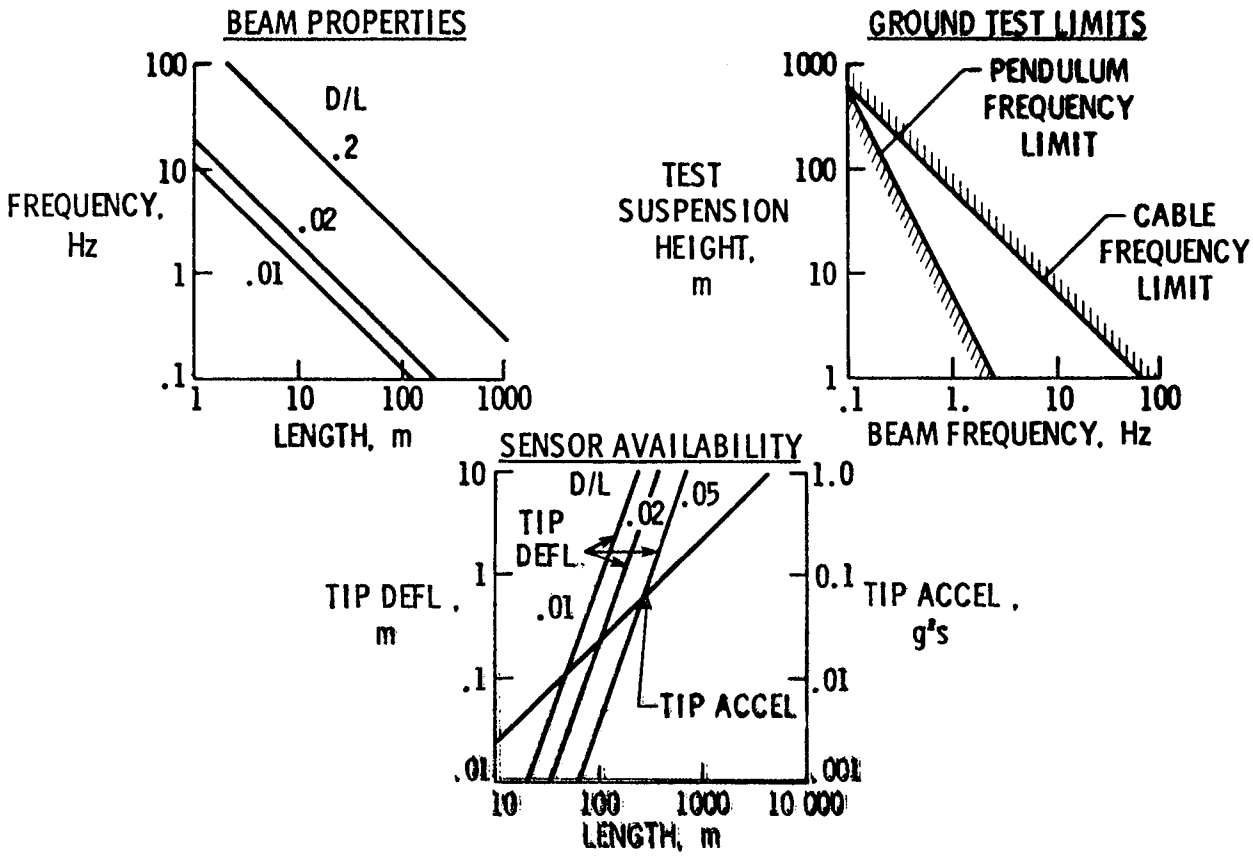

APPLICATION OF THE ITD ALGORITHM TO LANDSAT TRANSIENT RESPONSES

The Landsat satellite offered a unique opportunity to employ systems identification to determine on-orbit structural characteristics. Structural frequencies typically differed from the expected values by 1.0 percent. Damping differed by about 20 percent.

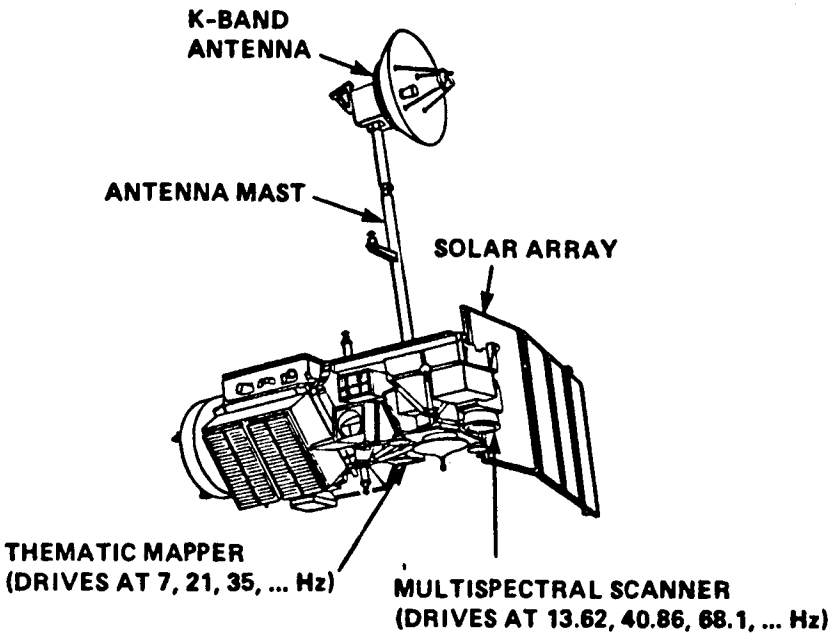

Comparison of analytical and ITD modal parameters
NDOF = 60 case * MSS ⊖-X excitation**

ANALYTIC MODE NUMBER	ANALYTIC FREQ. (Hz)	ANALYTIC DAMPING (% C/C)	ITD FREQ. (Hz)	% Δ	ITD DAMPING (% C/C_0)	% Δ	MODE SHAPE DOT PRODUCTS
11	1.615	1.0	1.336	-17.28	19.016	1801.60	-.993
12	2.145	1.0	2.166	.98	1.313	31.30	-.940
24	14.076	1.0	14.102	.18	.980	-2.00	-.918
27	16.771	1.0	16.758	-.08	.724	-27.60	1.000
30	20.066	1.0	20.081	.07	1.103	10.30	1.000
39	28.881	1.0	28.892	.04	1.104	10.40	.999
41	32.893	1.0	32.869	-.07	.981	-1.90	-.999
45	35.112	1.0	35.053	-.17	.941	-5.90	.999
49	38.186	1.0	37.959	-.59	2.238	123.80	.828
50	38.238	1.0	38.214	-.06	.779	-22.10	.996
58	42.144	1.0	41.964	-.43	1.177	-17.70	-.924
67	48.578	1.0	48.583	.01	1.151	15.10	-1.000
92	65.967	1.0	65.949	-.03	.852	-14.80	-.997
108	78.513	1.0	78.407	-.14	1.163	16.30	1.000

From R. R. Kauffman, Application of the ITD Algorithm to Landsat Transient Responses, 55th Shock and Vibration Symposium, Dayton, Ohio, 1984.

SOLAR ARRAY EXPERIMENT

The Solar Array Experiment offers the best opportunity to date for employing on-orbit systems identification for modeling a highly flexible space structure. The data are being analyzed and will be baseline data for several studies in which actual structural dynamic characteristics are compared with expected values.

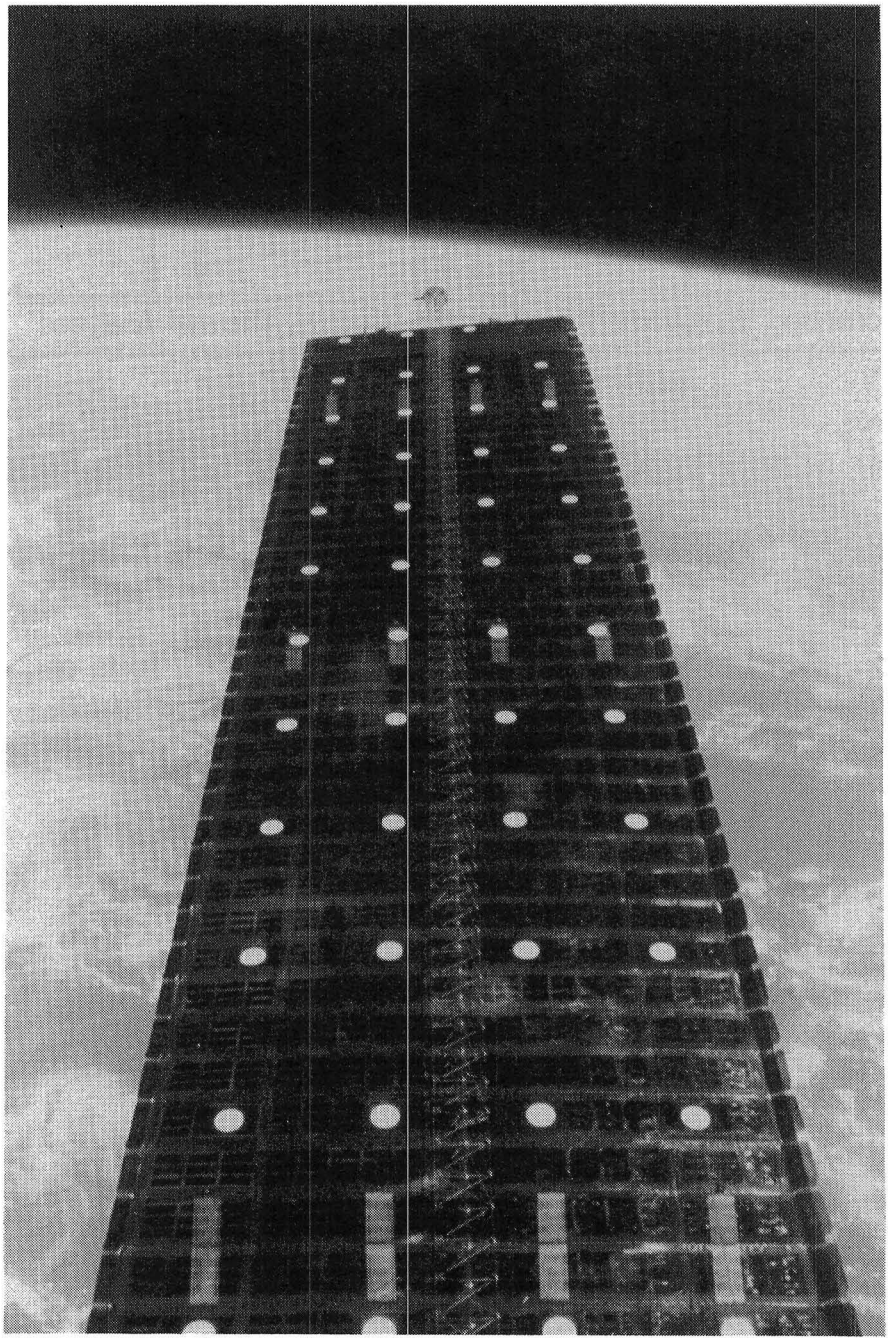

APPROACH FOR OBTAINING QUALIFICATION OF MATH MODELS

The sturctural dynamics model of a large flexible space structure will evolve and its accuracy will improve in stages as ground tests of full-scale components and replica-scale models are performed. Finally, on-orbit systems identification will further enhance the accuracy by building on the model that had evolved prior to flight.

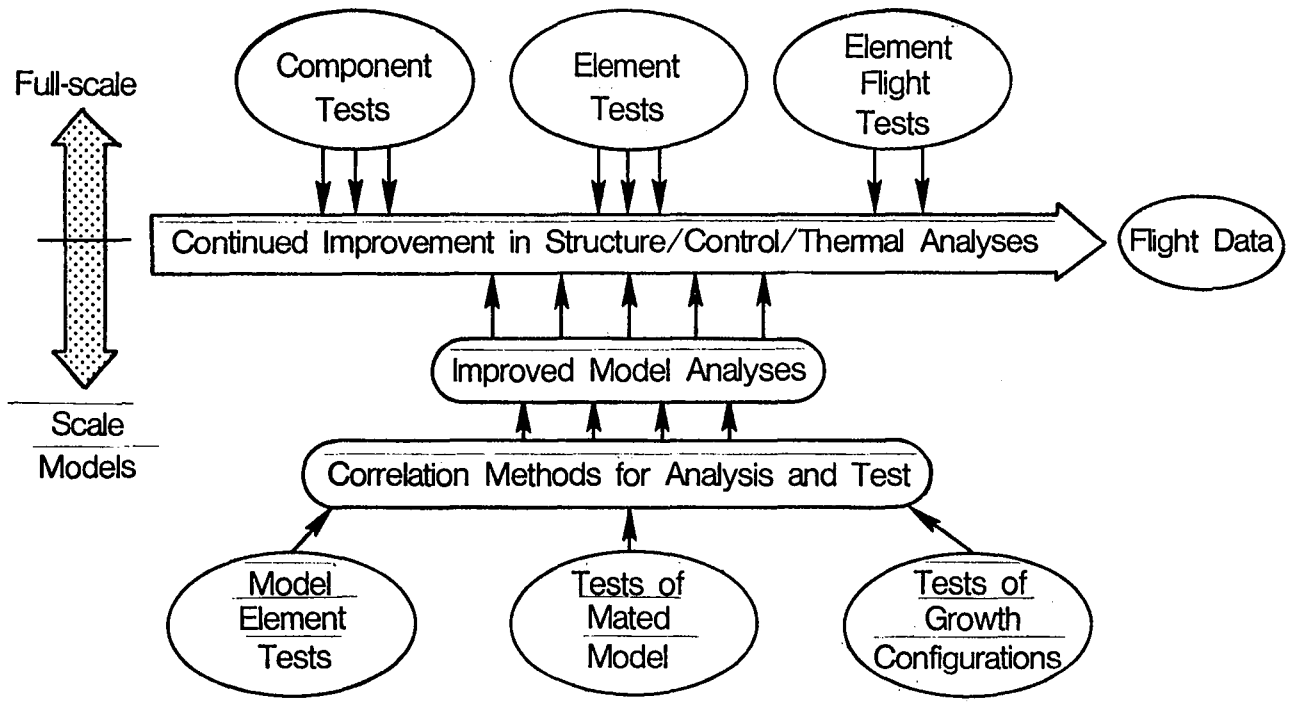

A PRIORI, PRE-ORBIT INFORMATION

State Space Modeling and Conditional Maximum Likelihood Parameter Estimation methodology can provide the formal probability-based framework for the process of upgrading a model as additional test results are obtained. Both ground test and on-orbit test results can be handled in this manner.

$\dot{X} = AX + BU$ — State Equations

$y = Cx + n$ — Sensor Noise

$E\begin{bmatrix} a \\ b \\ c \end{bmatrix} = (\ldots)$ — Parameter Values

$E(nn^T) = (\ldots)$ — Noise Covariance

$E\begin{bmatrix} a \\ b \\ c \end{bmatrix}\begin{bmatrix} a \\ b \\ c \end{bmatrix} = (\ldots)$ — Parameter Error Covariance

CONDITIONAL MAXIMUM LIKELIHOOD EXTIMATE
MODIFIED NEWTON-RAPHSON TECHNIQUE

It can be seen in the recursive equation for the model parameter estimates how the a priori or previous parameter values, c_o, and their corresponding error covariance enter into the estimation process.

$$C_{k+1}=C_k+\left[\sum_{i=1}^{N}\nabla_c y_{i_k}^T M_1^{-1}\nabla_c y_{i_k}+M_2^{-1}\right]^{-1}\left[\sum_{i=1}^{N}\nabla_c y_{i_k}^T M^{-1}(z_i-y_{i_k})-M_2^{-1}(c_k-c_o)\right]$$

Where:

C = Unknown Model Parameter

y = Response Variable

z = Measured Response

k = Iteration Index

M_1 = Measurement Error Covariance

M_2 = Apriori Parameter Error Covariance

MODAL FREQUENCY DENSITY

The modal frequency density is dependent on the type of structure. For example, plate-like structures have a greater number of modes in a frequency interval than do beam-like structures. The IOC Reference Configuration for the Manned Space Station has a particularly high modal frequency density because of the eight similar appendages.

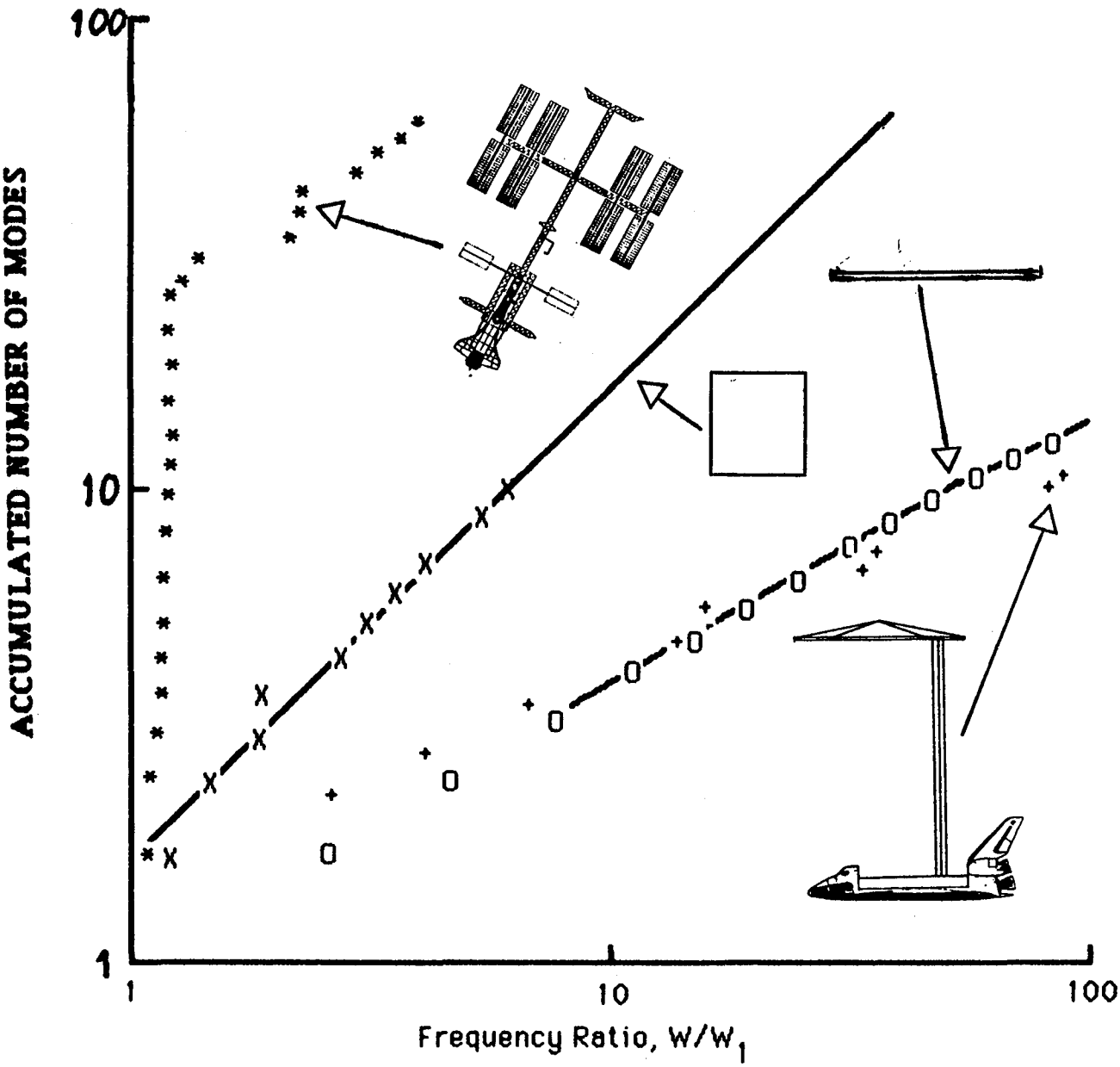

NUMBER OF MODES VS CONTROL BANDPASS

As the bandpass of the flight control system increases, the number of modes that must be included in the model used for design increases. For beam-like configurations the modeling problem can be handled. For the Space Station, the large number of modes will require special consideration.

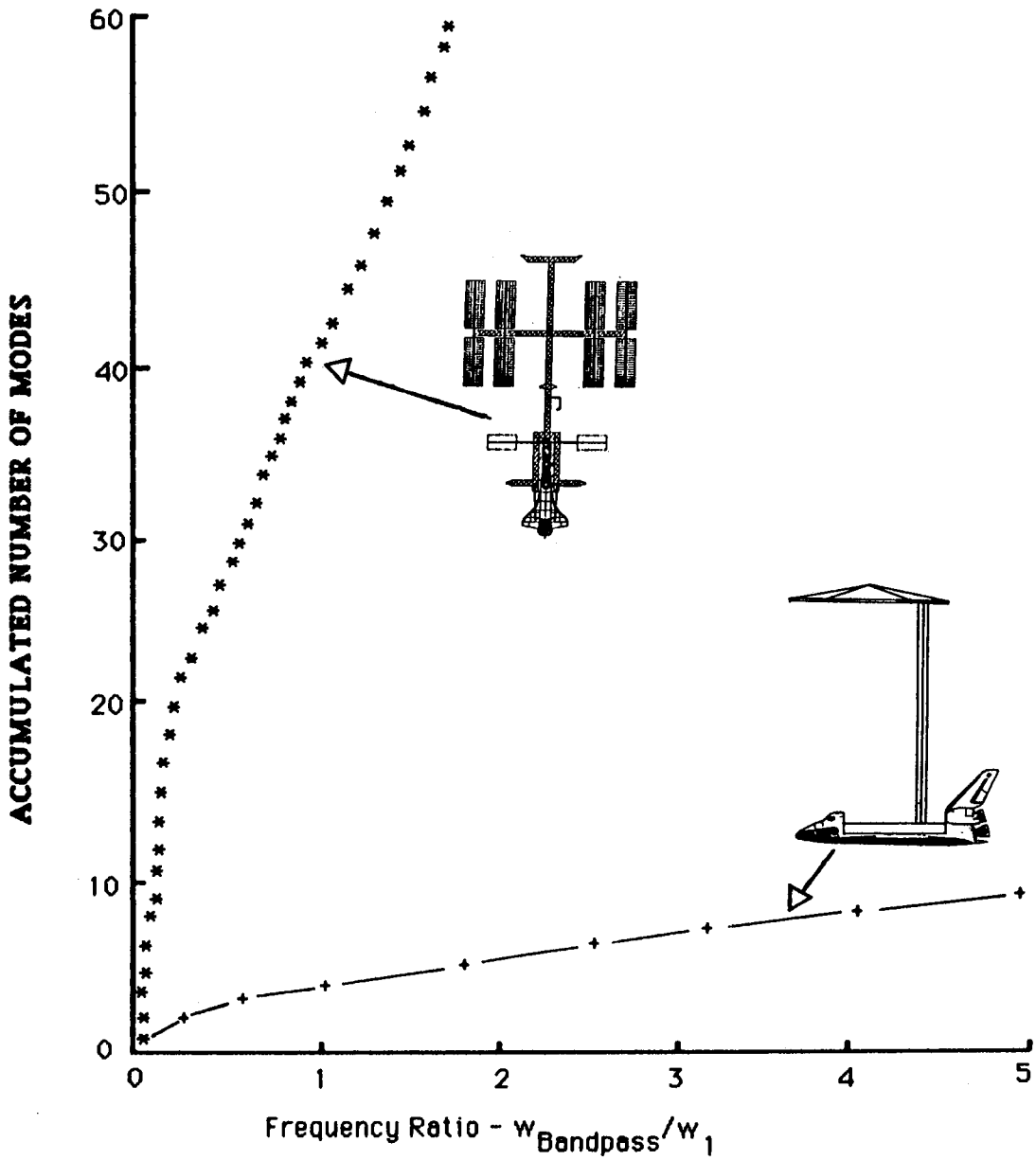

NUMBER OF MODES REQUIRED

NUMBER OF UNKNOWN PARAMETERS VS CONTROL BANDPASS

Although the number of unknown parameters can be reduced by the use of canonical forms for the stability matrix, the number of unknown model parameters quickly becomes unmanageable unless advantage is taken of the relationship of a much fewer number of global model parameters. Examples of such global parameters include the stiffness of the truss-beam and the stiffness of the solar array attachment structure.

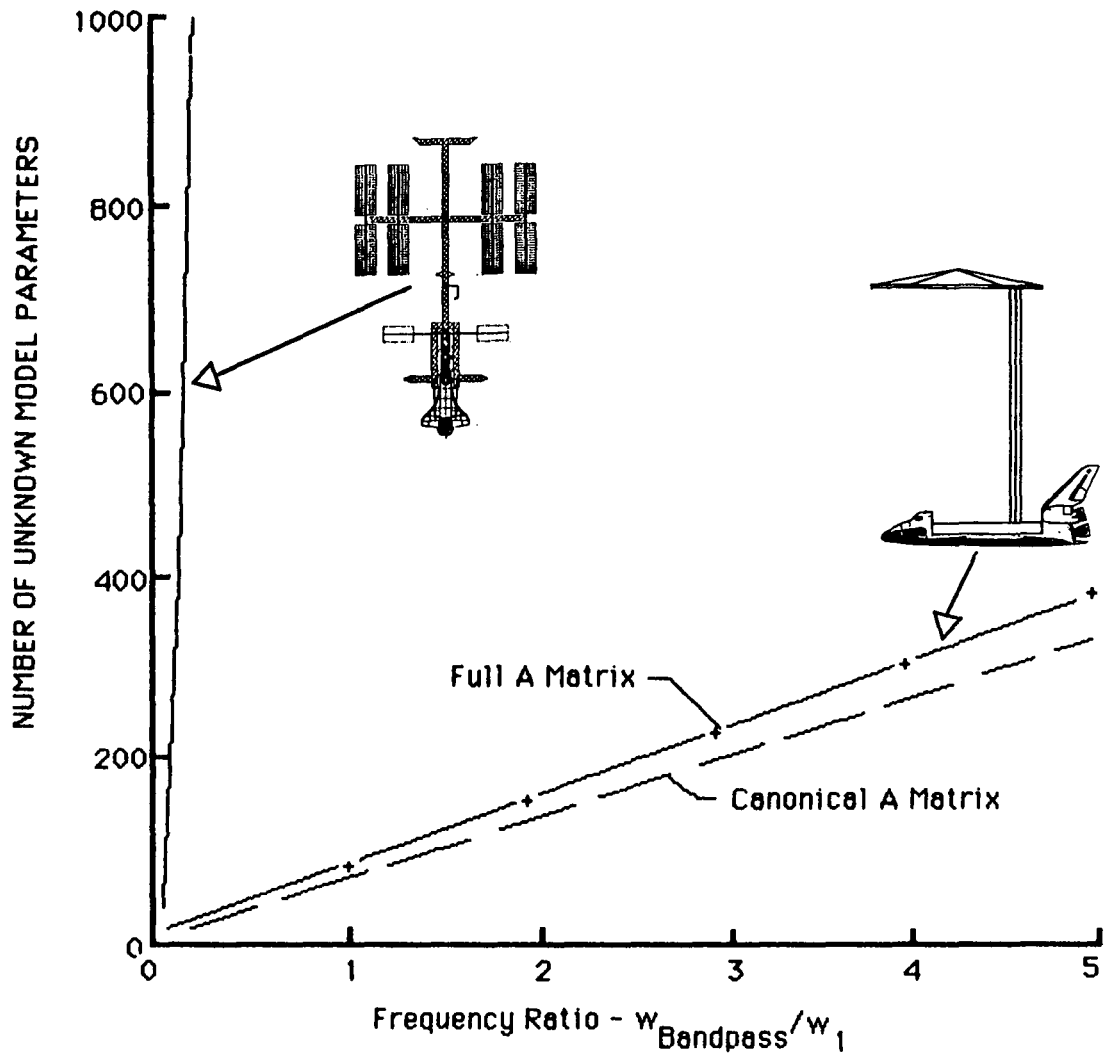

SYSTEMS IDENTIFICATION FOR DISTRIBUTED PARAMETER SYSTEMS

Distributed parameter systems or partial differential equation models are one way to take advantage of such global parameters to reduce the number of unknown model parameters. The Unconditional Maximum Likelihood Parameter Estimation methodology applies to these continuous parameter models as it does for the lumped case.

$$M\frac{d}{dt}\begin{vmatrix}\dot{y}\\ y\end{vmatrix} = A\begin{vmatrix}\dot{y}\\ y\end{vmatrix} + Bu \qquad \text{State Equation}$$

$$M\frac{d}{dt}\begin{vmatrix}\dot{\frac{dy}{dc}}\\ \frac{dy}{dc}\end{vmatrix} = A\begin{vmatrix}\dot{\frac{dy}{dc}}\\ \frac{dy}{dc}\end{vmatrix} + \frac{dB}{dc}u \qquad \text{Sensitivity Equation}$$

Where:

$$A = \left[\begin{array}{c|c} CE\frac{d^4}{ds^4} & EI\frac{d^4}{ds^4} \\ \hline I & 0 \end{array}\right] \qquad \text{Stability Matrix}$$

M = Mass Matrix

y = Deflection

u = Control Input

TEST INPUT FOR ON-ORBIT SYSTEMS IDENTIFICATION

Operational considerations such as the time required for a test impact the selection of test inputs for on-orbit systems identification. Other considerations include frequency spectra and signal/noise.

- Control actuators will be primary source of input.
- Time constraints will preclude steady-state response to sine-wave inputs.
- Input must contain suitable frequency spectrum.
  - Continuous spectrum excites all modes.
  - Discrete spectrum gives best signal/noise.
- Test input should result in typical response amplitudes but be safe under conditions of uncertainty.
- Use of feedback for critical gain test is particularly useful in detecting critical modes.

SAMPLE FREQUENCY REQUIRED FOR SYSTEMS IDENTIFICATION

The sample frequency required for on-orbit systems identification would seem to be reasonable although the rate might exceed that required for the flight control system operation.

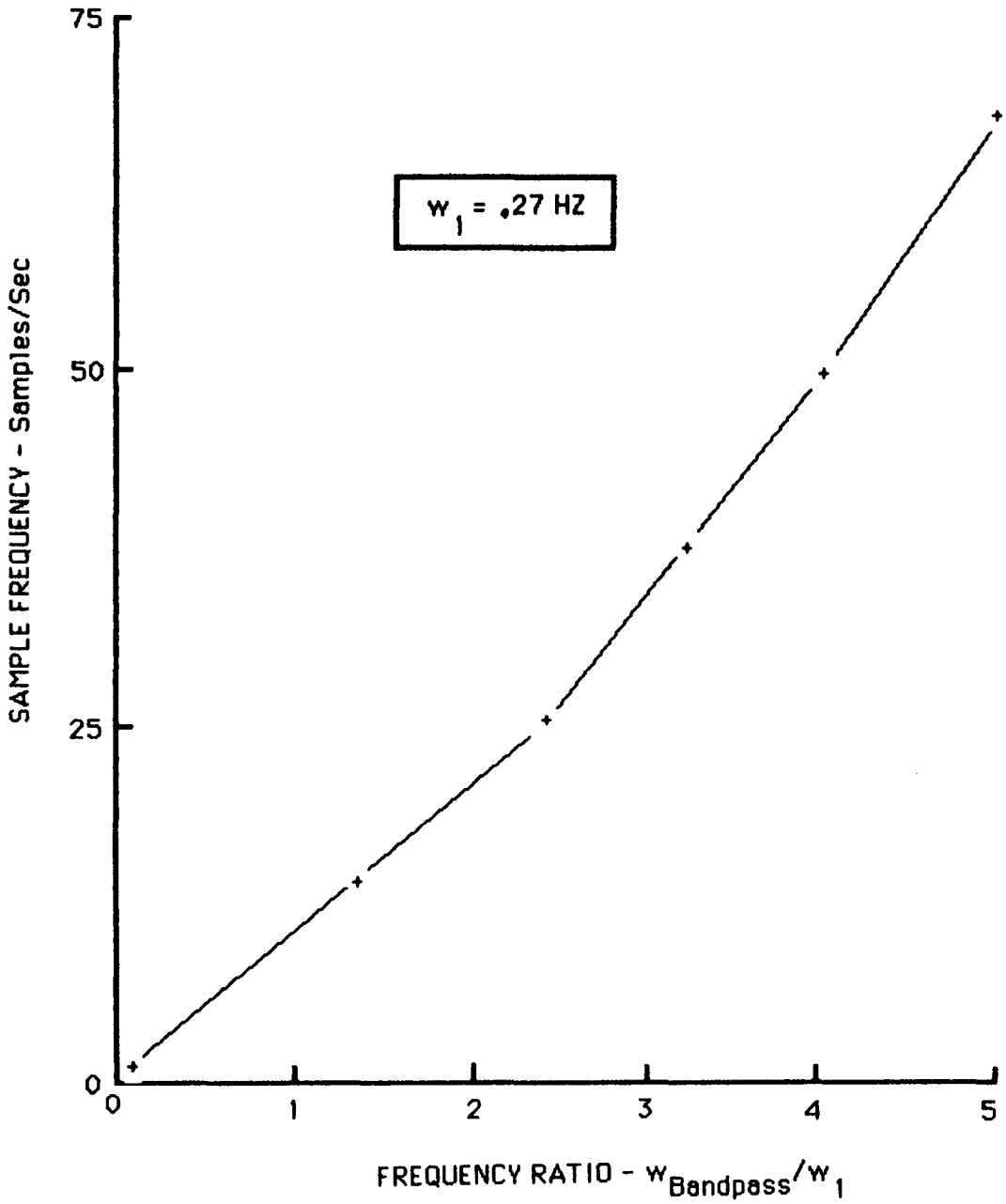

CONCLUDING REMARKS

- On-orbit systems identification will be required for spacecraft too flexible to ground test.
- The model complexity required to guarantee system stability and performance can be unmanageable.
- A priori information from theory and ground tests must be an integral part of on-orbit systems identification.
- It will be necessary to temper control system performance objectives due to remaining model uncertainties.
- Use of input/output and distributed parameter models may be beneficial.

Page intentionally left blank

AN EIGENSYSTEM REALIZATION ALGORITHM FOR APPLICATION TO MODAL TESTING

Jer-Nan Juang
NASA Langley Research Center
Hampton, Virginia

Large Space Antenna Systems Technology - 1984

December 4-6, 1984

SYSTEM IDENTIFICATION

The purpose of parameter estimation from modal testing, a subset of system identification (realization), is to estimate the eigenparameters including frequencies, mode shapes and mode participation factors from sampled dynamic response measurements. The field of system identification of structures is characterized by a growing body of knowledge and a large number of researchers, methods, ad hoc approaches and heuristic reasoning from structure and control areas. As a result, the literature on system identification is extensive, diverse, and sometimes confusing. Many people regard the area to be a "bag of tricks" rather than a theory, and it is called a "fiddler's paradise" in the survey by Astrom and Eykhoff (ref. 1).

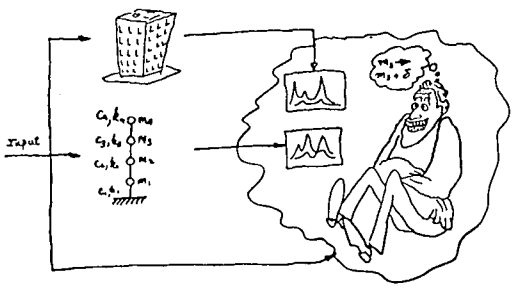

FUNDAMENTAL PROBLEM
IN SYSTEM IDENTIFICATION

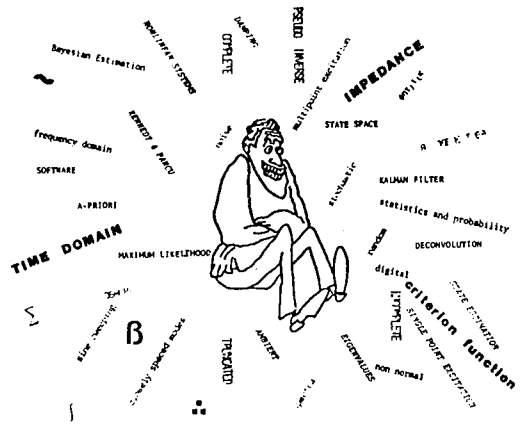

FUNDAMENTAL PROBLEM
IN USING SYSTEM IDENTIFICATION

Reproduced from Ibanez, P.: Review of Analytical and Experimental Techniques For Improving Structural Dynamic Models. Welding Research Council Bulletin, No. 249, June 1979, pp. 1-44.

WHY SO MANY DIFFERENT MODAL TESTING TECHNIQUES?

There are several reasons why so many different modal testing techniques are developed. Technical communications among different disciplines such as structures and controls are not quite established. New techniques require investment in specialized training and software. Slight modification and improvement of others become economically efficient to minimize the cost of investment. Different approximations and tricks for performance improvement lead to a myriad of algorithms that in fact are closely related. Close modes and nonlinearities in structures affect techniques differently.

- Classical vs. modern approaches
- Infrequency of modal tests/little experience with more than one method
- New techniques require investment in specialized training, software
- Limited test time & computer resources
- Close modes & nonlinearities affect techniques differently
- Difficult to quantify accuracy and accuracy requirements

BASIC MODAL IDENTIFICATION OPTIONS

In the structural testing area, the tuned-multiexciter sinusoidal dwell is the classical method of modal testing first developed by Lewis and Wrisley (ref. 2). The method involves manual variation of excitation frequency and forces to accentuate the response of a single mode while suppressing all others. Modal parameters are directly observed and estimated from measurements of tuned responses. Among the multimode methods, a widely used modal testing method is often referred to as the single-point random method. This technique involves exciting the structure at a single point with a broadband input and computing the frequency response function by Fast Fourier Transformation (FFT). The modal parameters are then determined by curvefitting analytical expressions to those measured functions. To overcome some of the difficulties of the FFT, such as close modes and damping estimation, time domain algorithms have been developed. The basic development of the time domain concept is attributed to Ho and Kalman (ref. 3), introducing the important principles of minimum realization theory. The procedure utilizes a sequence of real matrices known as Markov parameters (free decay response functions) to construct a state space representation of a linear system. Among follow-up developments along similar lines on minimum realization theory, Juang and Pappa (ref. 4) derive an Eigensystem Realization Algorithm (ERA) for modal parameter identification and system model reduction.

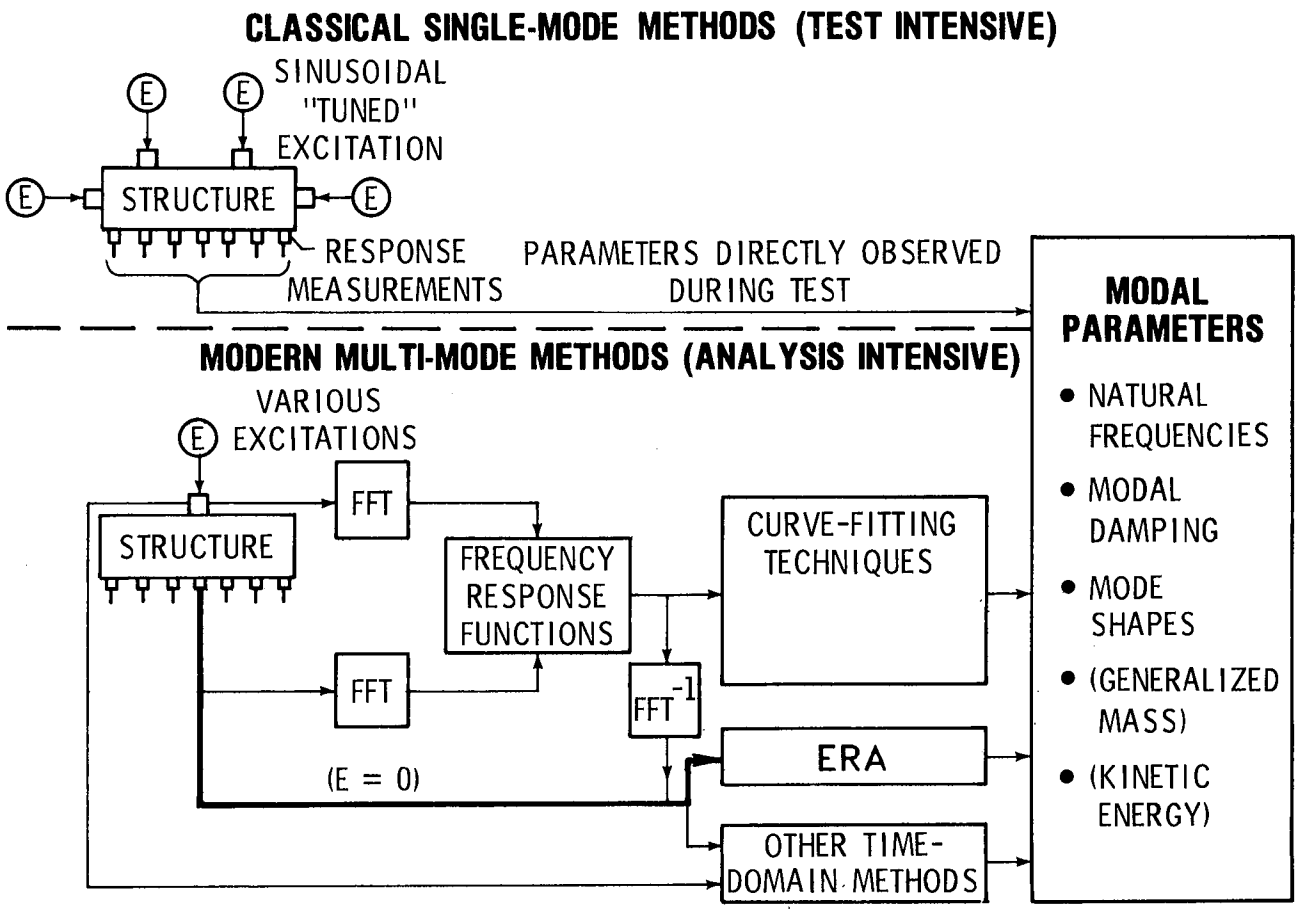

WHAT IS THE EIGENSYSTEM REALIZATION ALGORITHM (ERA)?

Under the interaction of structure and control disciplines, the Eigensystem Realization Algorithm (ERA) is developed. The algorithm consists of two major parts, namely, basic formulation of the minimum order realization and modal parameter identification. In the basic formulation, the Hankel matrix which represents the data structure for the Ho-Kalman algorithm is generalized to allow random distribution of Markov parameters generated by free decay responses. A unique approach based on this generalized Hankel matrix is developed to extend the Ho-Kalman algorithm in combination with the singular value decomposition technique (ref. 5). Through the use of the generalized Hankel matrix, a linear model is realized for dynamical systems matching the input and output relationship. The realized system model is then transformed into modal space for modal parameter identifications. As part of ERA, two accuracy indicators, namely, the modal amplitude coherence and the modal phase collinearity, are developed to quantify the system modes and noise modes. The degree of modal excitation and observation is evaluated. The ERA method thus forms the basis for a rational choice of model size determined by the singular values and accuracy indicators.

- An extended version of Ho-Kalman system realization algorithm
- Developed at LaRC under interdisciplinary structural dynamics/ controls research
- Various accuracy indicators used to assess effects of noise and nonlinearities
- Realization used for:
  - controller design
  - simulation
  - parameter identification

CONTRIBUTION:

EIGENSYSTEM REALIZATION ALGORITHM

Two developments are given in the ERA method. First, a new approach is developed to derive the basic ERA formulation of minimum realization for dynamical systems. This approach provides a new idea in efficiently managing the measurement data. For example, the generalized Hankel matrix can be formed by selecting only good measurement data and disregarding the rest of the data to reduce the size of the matrix and the cost of computations and to minimize the distortion of the identified system parameters. Second, accuracy indicators are developed to quantify the participation of system modes and noise modes in the realized system model. In other words, degree of controllability and observability for each participating mode is determined. A model reduction can then be made for controller design, which is very important for flexible structures in real-time control.

- New approach to extend the Ho-Kalman algorithm for better treatment of noisy data
- Accuracy indicators for modal parameter identification for structures
- Amplitude of modal excitation (degree of controllability)
- Amplitude of modal observation (degree of observability)
- To obtain reduced model for controller design

SECOND-ORDER MECHANICAL SYSTEM

Identification is a link between the mathematical-model world and the real world. It is necessary to have a model of a system in order to derive the procedure of an identification technique. For many purposes, the model need not be very sophisticated, and most problems are probably solved using only simplified models. For structures, one problem concerns approximations in modeling stiffness, mass, damping and boundary conditions. Let M, D, and K be mass, damping and stiffness matrices, respectively, W, $\dot{W}$ and $\ddot{W}$ the vectors of acceleration, velocity and displacement, and f(t) the forcing function over the time of interest. The structural system can then be described by a set of second-order differential equations of motion and measurement equations. For convenience, the set of second-order differential equations of motion is converted into a set of first-order differential equations in terms of three matrices A, B, and C.

Equation of Motion:

$M\ddot{w}(t) + D\dot{w}(t) + Kw = f(t)$ Is equivalent to

$$\begin{bmatrix} \dot{w}(t) \\ \ddot{w}(t) \end{bmatrix} = \begin{bmatrix} O & I \\ -M^{-1}K & -M^{-1}D \end{bmatrix} \begin{bmatrix} w(t) \\ \dot{w}(t) \end{bmatrix} + \begin{bmatrix} O \\ M^{-1} \end{bmatrix} f(t) \longrightarrow \dot{x} = Ax + Bu$$

n States
m Inputs

Measurement Equation:

$$y(t) = C \begin{bmatrix} w(t) \\ \dot{w}(t) \end{bmatrix} \longrightarrow y = Cx, \text{ p Outputs}$$

Note that the number of measurements (outputs) is, in general, independent of the number of states.

SYSTEM REALIZATION

The process of constructing a state space representation from experimental data is called system realization. The problem of system realization is then the following. Given the measurement functions y(k), construct constant matrices [A, B, C] such that the functions y(k) are reproduced by the state-variable equations. The method presented here will not only furnish a linear model but will also develop a so-called minimal order, that is, the linear model consisting of a minimum number of system parameters (i.e. modal parameters in modal space) necessary to reproduce the pulse response data within a specified degree of accuracy. If a realization is completely controllable and completely observable, then it is of minimum dimension (minimum realization). This necessary and sufficient condition was presented and proved by Kalman (ref. 6) and has been an important axiom in several algorithms devised to obtain realizations of minimum dimensions.

Definition

A realization is a triplet [A,B,C] for which the state equations are satisfied for sets of input and output data:

Discrete Time	**Continuous Time**
$x(k+1) = Ax(k) + Bu(k)$	$\dot{x}(t) = \bar{A}x(t) + \bar{B}u(t)$
$y(k) = Cx(k)$	$y(t) = \bar{C}x(t)$
x(k) - n States	A - State Matrix
u(k) - m Inputs	B - Input Matrix
y(k) - p Outputs	C - Output Matrix

Solution of discrete-time state equations:

$$y(k) = Cx(k) = C[\underbrace{A^k x_0}_{\text{Transient response}} + \underbrace{\sum_{i=0}^{k-1} A^{k-i-1} Bu(i)}_{\text{Forced response}}]$$

DATA OPTIONS FOR ERA

A state-space model consists of a matrix triple (A, B, C) parameterizing a set of differential equations. The dimension of the matrix A is said to be the order of the state-space model. The products CA^iB, i=0, 1, 2,... are called the Markov parameters. An input-output representation often takes the form of a transfer function (frequency-domain characterization) or an impulse response function (time-domain characterization). The transfer function can be computed by a Fast Fourier Transformation (FFT). The impulse response of a system can be obtained by actually measuring the response to an impulse input or by estimating the correlation between the system output and a white-noise input. The impulse response of a discrete-time system is related to the state-space parameters (A, B, C) in a simple form of the Markov parameter.

- Impulse responses:

  $Y(k) = CA^{k-1} B$

  [ith column of Y(k) is free response from ith impulse]

- Initial condition responses:

  $Y(k) = CA^{k} X_0$

  [ith column of Y(k) is free response from ith initial condition]

- Forced responses:

DATA STRUCTURE FOR ERA

Since the pulse response functions Y(k), k=1,2,... have the simple form of Markov parameters, the question arises whether there exists a special matrix consisting of the response functions Y(k) such that the state-space parameters (A, B, C) can be extracted. The answer is positive, that is how the Hankel matrix is generated (ref. 3). The Hankel matrix is a popular and powerful tool for system identification. The reason for its popularity is the well-known Kronecker's Theorem (refs. 3 and 7), which states that the rank of the Hankel matrix is equal to the order of the sytem, i.e. equal to the dimension of the state matrix of minimal realization. In addition, the singular values of a Hankel matrix have an intimate relation with the so-called controllability and observability Gramians (ref. 7). In contrast to the conventional system realization methods, the generalized Hankel matrix defined for the ERA method allows to include only good and strong measurement signals to minimize the distortion of the identified system parameters. This is a considerable improvement, particularly for a complex structure which requires a large number of measurements to accurately identify the modal parameters.

- Generalized Hankel matrix

$$H_{rs}(k-1) = \begin{bmatrix} Y(k) & Y(k+t_1) & \cdots & Y(k+t_{s-1}) \\ Y(j_1+k) & Y(j_1+k+t_1) & \cdots & Y(j_1+k+t_{s-1}) \\ \vdots & \vdots & & \vdots \\ Y(j_{r-1}+k) & Y(j_{r-1}+k+t_1) & \cdots & Y(j_{r-1}+k+t_{s-1}) \end{bmatrix}$$

where $j_i (i = 1,2,\ldots,r-1)$ and $t_i (i = 1,2,\ldots,s-1)$ are arbitrary integers

k is the sample time integer

- For the case where $k=1$, $j_i = t_i = i (i=1,2,\ldots)$

$$H_{rs}(0) = \begin{bmatrix} Y(1) & Y(2) & \cdots & Y(s) \\ Y(2) & Y(3) & \cdots & Y(s+1) \\ \vdots & \vdots & & \vdots \\ Y(r) & Y(r+1) & \cdots & Y(r+s-1) \end{bmatrix}$$

- For the case where $k = 2$, $j_i = t_i = i (i = 1, 2, \ldots)$

$$H_{rs}(1) = \begin{bmatrix} Y(2) & Y(3) & \cdots & Y(s+1) \\ Y(3) & Y(4) & \cdots & Y(s+2) \\ \vdots & \vdots & & \vdots \\ Y(r+1) & Y(r+2) & \cdots & Y(r+s) \end{bmatrix}$$

BASIC FORMULATION FOR ERA

Examination of the relations $Y(k) = CA^{k-1}B$, $k = 1,2,\ldots$, between the pulse response functions and the Markov parameters reveals that $Y(k)$ is composed by the three matrices C, A^{k-1} and B. This observation thus suggests that the generalized Hankel matrix should accordingly be decomposed into three matrices, which can determine the rank of the Hankel matrix and form the basis for the construction of considered state space. The best choice for the decomposition is the singular value decomposition (SVD) which provides the right and left orthogonal components, and the singular values. By singular values is meant the square root of the eigenvalues of the Hankel matrix multiplied by its transpose. The components associated with small singular values are then removed to obtain a reasonable lower order approximation of the Hankel matrix. The singular value decomposition technique (ref. 5) has been widely recognized as being very effective and numerically stable. The state-space parameters (A, B, C) can then be obtained from a simple formulation (ref. 4) involving a shift generalized Hankel matrix $H_{rs}(1)$, and orthogonal components and singular values of the initial Hankel matrix $H_{rs}(0)$.

- Singular value decomposition

$$H_{rs}(0) = P\ D\ Q^T$$

where P and Q^T are isometric matrices and D is a diagonal matrix with positive elements $d_1 \geq d_2 \geq \ldots \geq d_n$

- Minimum-order realization

$$Y(k+1) = [E_p^T P D]\,[D^{-1} P^T H_{rs}(1) Q]^k\,[Q^T E_m] = C\,A^k\,B;$$

pulse response where $E_p = [I_p, 0]$ and $E_m = [I_m, 0]$

Let ψ be any nonsingular square matrix. The triple $[\ \psi^{-1}A\ \psi\ ,\ \psi^{-1}B,\ C\ \psi\ ]$ will also be a realization and the predicted responses using this realization will be identical to those predicted by [A, B, C]. Since there are an infinite number of nonsingular matrices ψ, there are an infinite number of such realizations. This is equivalent to modeling a structure by using different coordinate systems. However, the eigenvalues of the state matrix A remain unchanged under this similarity transformation. In other words, modal parameters such as frequencies and damping factor should be unique for a linear flexible structure.

- Transformation to modal coordinates

$$[A,B,C] = [\psi^{-1}A\psi\ ,\ \psi^{-1}B\ ,\ C\psi] = [z\ ,\ \psi^{-1}B\ ,\ C\psi\ ]$$

- System eigenvalues

$$s = (\ln z)/\Delta\tau = (\ln[\psi^{-1}D^{-1}P^{T}H_{rs}(1)Q\psi])/\Delta\tau$$

- Initial condition

$$\psi^{-1}B = \psi^{-1}Q^{T}E_{m}$$

- Mode shape

$$C\psi = E_{p}^{T}P\,D$$

FLOWCHART OF ERA

A flowchart of the procedure followed by ERA in system model identification is presented in this figure. The computational steps are summarized as follows (ref. 4): 1) construct a block-Hankel matrix $H_{rs}(0)$ by arranging the measurement data into its rows; 2) decompose $H_{rs}(0)$ using singular value decomposition; 3) determine the order of the system by examining the singular values of the Hankel matrix $H_{rs}(0)$; 4) construct a minimum-order realization (A, B, C) using a shifted block-Hankel matrix, where A is the state matrix, B is the control influence matrix and C is the measurement influence matrix; 5) find eigensolutions of the realized state matrix and compute the modal damping rates and frequencies; 6) calculate the coherence parameter and the collinearity parameter to quantify system modes and noise modes; 7) determine the reduced system model based on accuracy indicators, reconstruct the functions Y(k) and compare with measurement data.

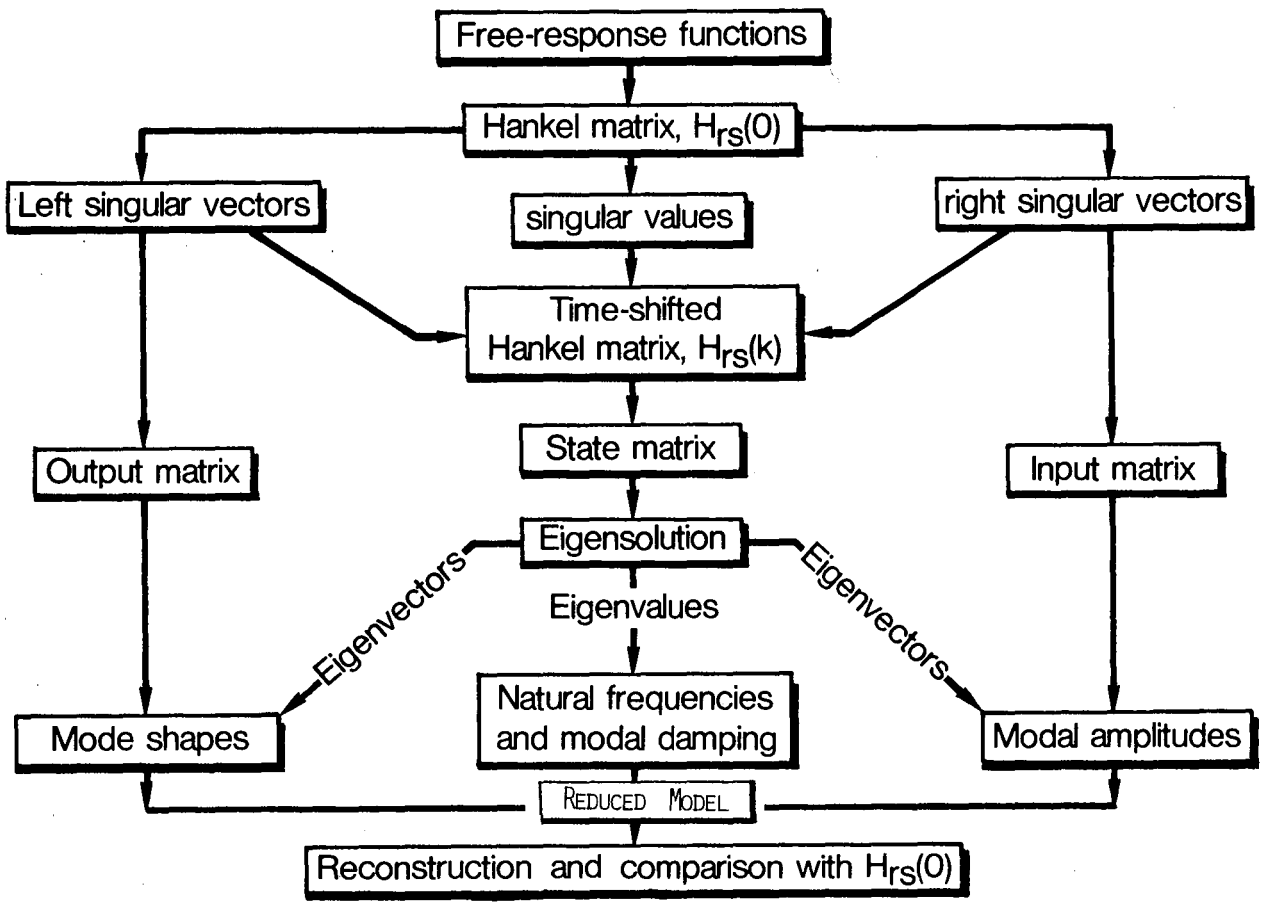

ACCURACY INDICATORS

In modal parameter identification, the indicator referred to as modal amplitude coherence is developed to quantitatively distinguish the system and noise modes. Based on the accuracy parameter, the degree of the modal excitation (controllability) is estimated. The modal amplitude coherence is determined by calculating the coherence between each modal amplitude history and an ideal one formed by extrapolating the initial value of the history to latter points using the identified eigenvalue. For lightly damped structures, normal mode behavior should be observed. An indicator referred to as the modal phase collinearity is developed to measure the strength of linear functional relationships between the real part and the imaginary part of the sensor modal displacement (mode shape) for each mode. Based on the accuracy indicator, the degree of the modal observation is estimated.

- Modal amplitude coherence
  - Correlation factor between the identified modal amplitude history and an ideal one
  - Degree of controllability (amplitude of modal excitation)
- Modal phase collinearity
  - The deviation from 0^0 - 180^0 behavior among identified mode shape components
  - Degree of observability (amplitude of modal observation)

NUMERICAL SIMULATIONS

It is known from control theory that a system with repeated eigenvalues and independent mode shapes is not identifiable by single input and/or single output. Methods which allow only one initial condition (input) at a time will miss repeated eigenvalues. Also, if the realized system is not of a minimum order and matrix inversion is used for constructing an oversized state matrix, numerical errors may become dominant. To illustrate the ERA method satisfying the control theory, numerical simulations are studied for an assumed structure with distinct and repeated frequencies. Results are summarized as follows:

- Single input (test) and single output (sensor) can be used to identify modal parameters for a system with the absence of repeated eigenvalues, if the actuator and sensor locations are properly located.
- Multiple inputs (tests) and multiple outputs (sensors) are required to identify modal parameters for a system with repeated eigenvalues and independent eigenvectors.
- All results satisfy the theory of controllability and observability derived from control field.

EXPERIMENTAL RESULTS ON GALILEO SPACECRAFT

To illustrate the ability of the ERA method, experimental results for a complex structure - the Galileo spacecraft - are given (ref. 8). The Galileo spacecraft is an interplanetary vehicle to be launched in 1986 for a detailed investigation of the planet Jupiter and its moons. It consists of a planetary orbiter and an atmospheric entry probe that will be deployed towards the planet. Improved instrumentation, combined with satellite flybys more than 20 times closer than achieved by Voyager, promises exceptional data on the chemical composition and structure of the Jovian system. In the design of the spacecraft, finite-element analytical models of the structure are used to assess dynamic launch loads and interaction effects with the attitude control system. As a final check of the accuracy of these models, modal survey tests (ref. 9) were conducted on a completely assembled twin of the flight vehicle--the so-called Development Test Model (DTM). These tests were performed at the Jet Propulsion Laboratory (JPL) in the summer of 1983. The DTM is a replica of the flight unit except that all electronics and scientific instruments are replaced by rigid mass simulations. It was built to mission specifications and will later be refurbished to become the backup flight vehicle.

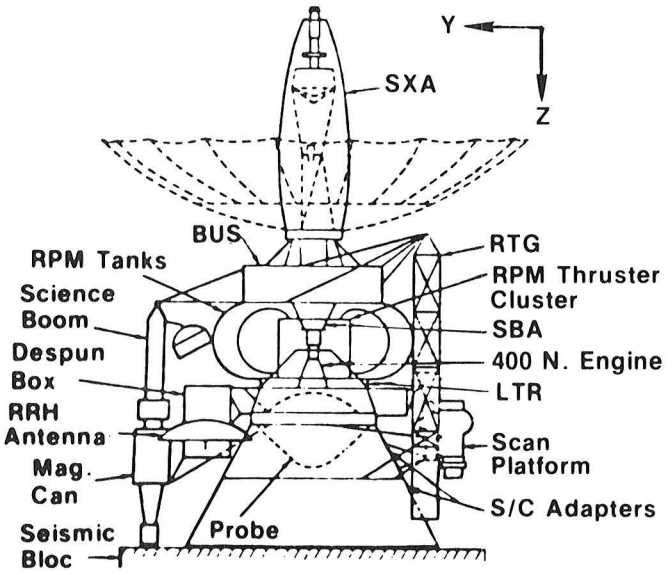

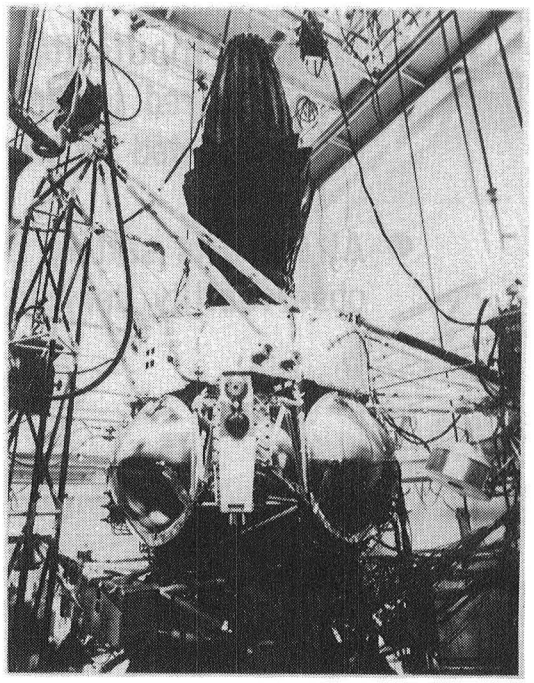

TYPICAL MODAL AMPLITUDE

Typical examples of modal amplitude results from the Galileo analysis are shown in the following figure. These data were selected to illustrate the variation in the purity of the modal amplitude histories for a mode which was strongly excited in only one of the two ERA tests. The figure can be used to clarify the definition of Modal Amplitude Coherence, mentioned earlier. Note that although these ERA-identified modal amplitudes are similar in form to traditional decay plots obtained following sine-dwell modal tuning, they are the result of digital processing of random response data. The mode shown in this figure at approximately 38 Hz is the fundamental z-direction "bounce mode" of the structure. As would be expected, the modal amplitude plots illustrate that the mode was more strongly excited in the z-direction test than in the x-direction test. This conclusion is made by comparing the purity and amplitude of the time history shown at the top with that at the bottom. To better see how well the exponential decay persists at small amplitudes, the right-hand plots in the figure show the data from the left-hand side on a logarithmic scale. In this form, exponential decay corresponds to a linearly decreasing envelope.

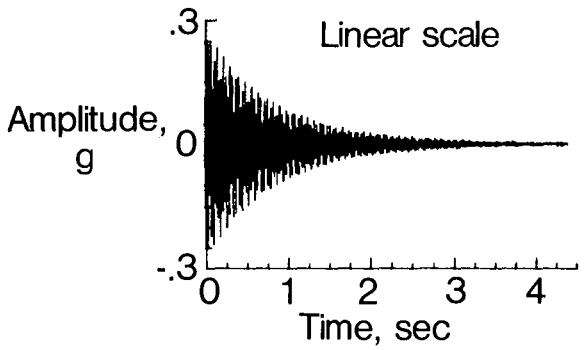

38.037 Hz mode from Z-direction test.

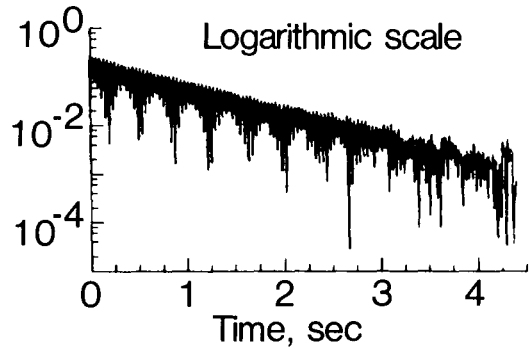

Modal amplitude coherence = 99.8%

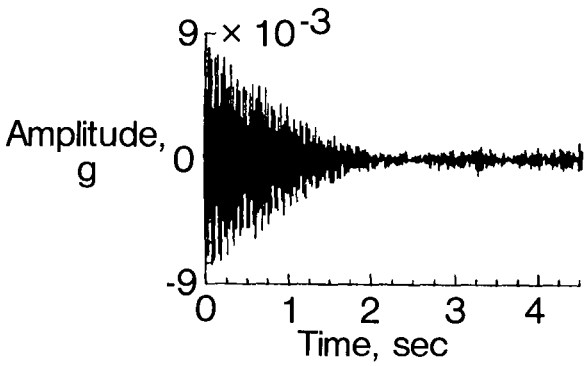

38.019 Hz mode from X-direction test.

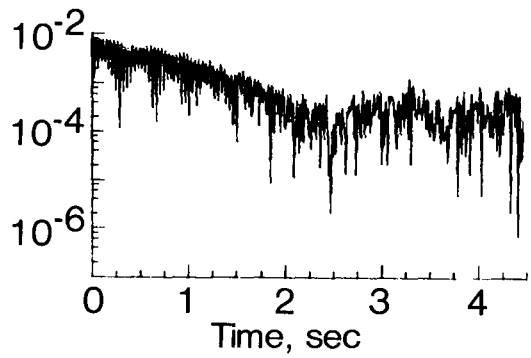

Modal amplitude coherence = 94.1%

THE ERA DATA RECONSTRUCTION

One aspect of the ERA method available for assessing identification accuracy is the process of data reconstruction. This procedure consists of comparing the original free-response time histories (and their frequency spectra) with ones calculated using the set of identified modal parameters. If the ERA modal decomposition process is performed accurately, the reconstruction results will closely match the original data. This figure shows a typical comparison from the Galileo data analysis. The two time histories are compared at the left side of the figure, and their Fourier transforms (FFT), in both amplitude and phase, in the right-hand side plots. The reconstruction result, the smoother of the two lines in the FFT plots, is seen to closely follow the original data in both amplitude and phase. The increase in amplitude of the test data below 2 Hz is due to residual motion of the shaker on its soft suspension. These response characteristics, well below the first flexural mode of the spacecraft, do not affect the modal results and were not retained in the identified parameter set.

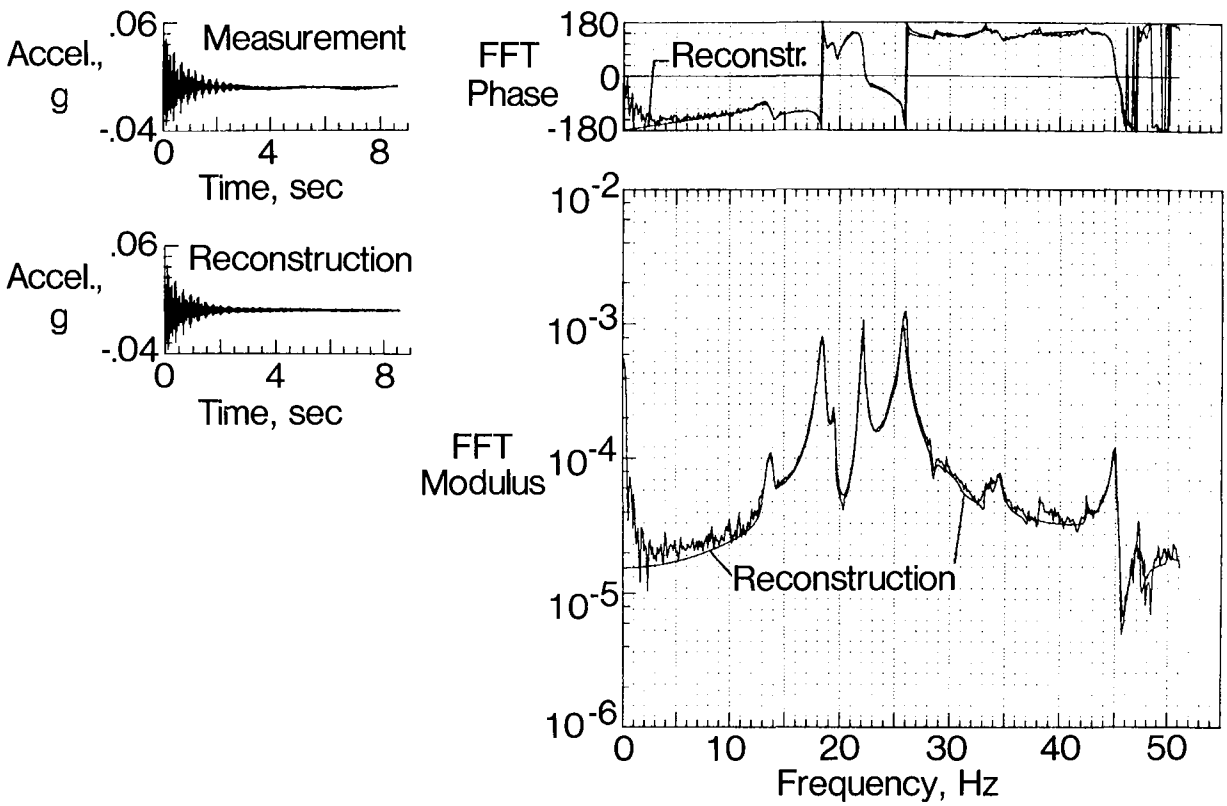

THE ERA FEATURES

Important features of the ERA algorithm are summarized as follows: (1) from the computational standpoint, the algorithm is attractive, since only simple numerical operations are needed; (2) the computational procedure is numerically stable; (3) the structural dynamics requirements for modal parameter identification and the control design requirements for a reduced-state space model are satisfied; (4) data from more than one test can be used simultaneously to efficiently identify the closely spaced eigenvalues; (5) no restrictions on number of measurments are imposed.

- The ERA method is an adaptation of system realization theory from the controls field
- ERA can be used successfully for modal parameter identification of complex structures
- A reduced-state space model can be generated for controller design of flexible structures
- Only simple numerical operations are needed
- The computational procedure is numerically stable
- The effects of noise and nonlinearities on the results need further attention

REFERENCES

1. Astrom, K. J.; and Eykhoff, P.: System Identification - A Survey. Automation, Vol. 7, pp. 123-167.

2. Lewis, R. C.; and Wrisley, D. L.: A System for the Excitation of Pure Natural Modes of Complex Structures. Journal of Aeronautical Sciences, Vol. 17, No. 11, pp. 705-722, 1950.

3. Ho, B. L.; and Kalman, R. E.: Effective Construction of Linear State-variable Models From Input/Output Data. Proc. 3rd Annual Allerton Conf. Circuit and System Theory, 1965, pp. 449-459.

4. Juang, J. N.; and Pappa, R. S.: An Eigensystem Realization Algorithm (ERA) For Modal Parameter Identification and Modal Reduction. Presented at NASA/JPL Workshop on Identification and Control of Flexible Space Structures, San Diego, California, June 4-6, 1984.

5. Klema, V. C; and Laub, A. J.: The Singular Value Decomposition: Its Computation and Some Application. IEEE Transactions on Automatic Control, Vol. AC-25, No. 2, April 1980, pp. 164-176.

6. Kalman, R. E.: Mathematical Description of Linear Dynamical Systems. SIAM J. Control 1, 52 (1963).

7. Kailath, T.: Linear Systems, Englewood Cliffs, New Jersey: Prentice-Hall, 1980.

8. Pappa, R. S.; and Juang, J. N.: Galileo Spacecraft Modal Identification Using an Eigensystem Realization Algorithm. AIAA Paper 84-1070-CP. Presented at the AIAA Dynamics Specialists Conference, Palm Springs, CA, May 1984.

9. Chen, J. C.; and Trubert, M.: Galileo Modal Test and Pre-Test Analysis. Proc. of the 2nd International Modal Analysis Conference. Orlando, FL February 1984, pp. 796-802.

SUMMARY OF GALILEO MODAL TESTS*

J. Chen
Jet Propulsion Laboratory
Pasadena, California

Large Space Antenna Systems Technology - 1984
December 4-6, 1984

*Paper unavailable at time of publication.

Page intentionally left blank

MSFC DATA ANALYSIS OF THE SAFE/DAE EXPERIMENT

R. W. Schock, T. E. Nesman, and D. K. Reed
Marshall Space Flight Center
Huntsville, Alabama

Large Space Antenna Systems Technology - 1984
December 4-6, 1984

SOLAR ARRAY LSS CHARACTERISTICS

The Solar Array Flight Experiment (SAFE) on-orbit experiment for measurement of large structures dynamics consists of a dynamic sensing system designed to record and analyse the dynamic characteristics of the SAFE.

The early availability of the SAFE and its basic large space structure characteristics made it a logical candidate for verification of the sensing system and evaluation technique.

The characteristics of the solar array which place it well within the generic class of large space structures are:

1. Large size
2. Low natural frequencies
3. Mechanical complexity of its extendable/retractable mast
4. The inability to dynamic test in earth atmosphere and one g

The fourth characteristic is due to its size, air damping dominance of the blanket, and structural instability in one g.

The specific characteristics of the solar array are shown in Figure 1 and illustrate the applicability to large space structures.

Figure 2 illustrates the extendable mast which erects the array.

- ARRAY WT -- 225 Kg
  - BLANKET – 132 Kg
  - MAST – 40 Kg
  - CONTAINER – 40 Kg
  - COVER ASSY – 14 Kg
- FREQUENCY – .033 – .4 Hz
- ARRAY LENGTH – 3101 CM
- ARRAY WIDTH – 400 CM
- MAX. ALLOWABLE BM ~ 120.9 N–m

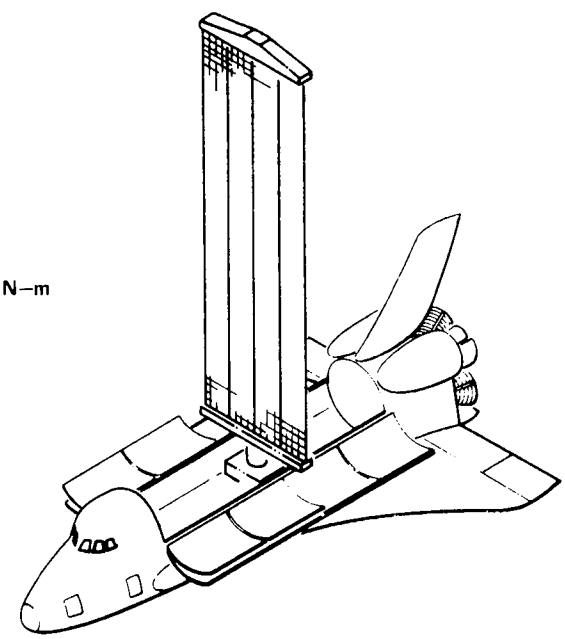

Figure 1

SOLAR ARRAY EXTENSION MAST

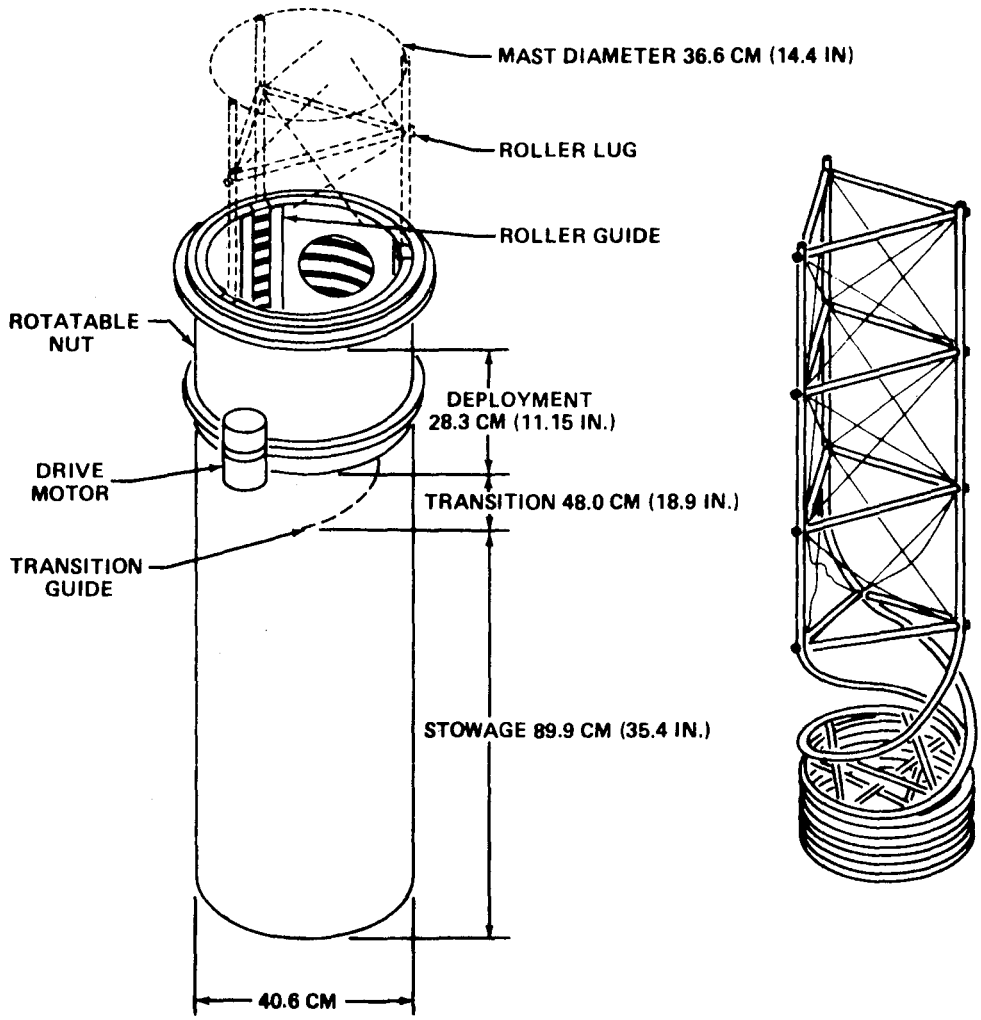

Figure 2

SAFE DYNAMICS AUGMENTATION EXPERIMENT

The basic objectives of the SAFE Dynamics Augmentation Experiment are:

1. Demonstrate the technology readiness of hardware and a technique for on-orbit test definition of large space structural systems dynamic characteristics

2. Demonstrate success by test definition of SAFE dynamic characteristics

To accomplish these objectives, a remote sensing system was developed by MSFC. The sensing system is an adaptation of a multi-field star tracker. The technique is illustrated in Figure 3. The emitter, positioned at the base of the solar array, illuminates the array of 23 retroreflectors. The retroreflectors return the emitted energy to the receiver. The receiver focuses the reflector images on a solid state sensor. The sensor characteristics are shown in Figure 4. The sensor transmits angular displacement data to a microprocessor. The microprocessor computes the dynamic array displacement from the initial or rest position and provides a digital output through a multiplexer to a digital tape recorder. The recorded data is returned for ground processing. Excitation is provided by the orbiter VRCS system, defined to maximize response without approaching structural limits.

Ground processing defines the dynamic characteristics of the array frequencies, mode shapes, and damping. These characteristics will be used to verify math models, provide test defined inputs for control software, and provide zero g correlation to one g ground test data.

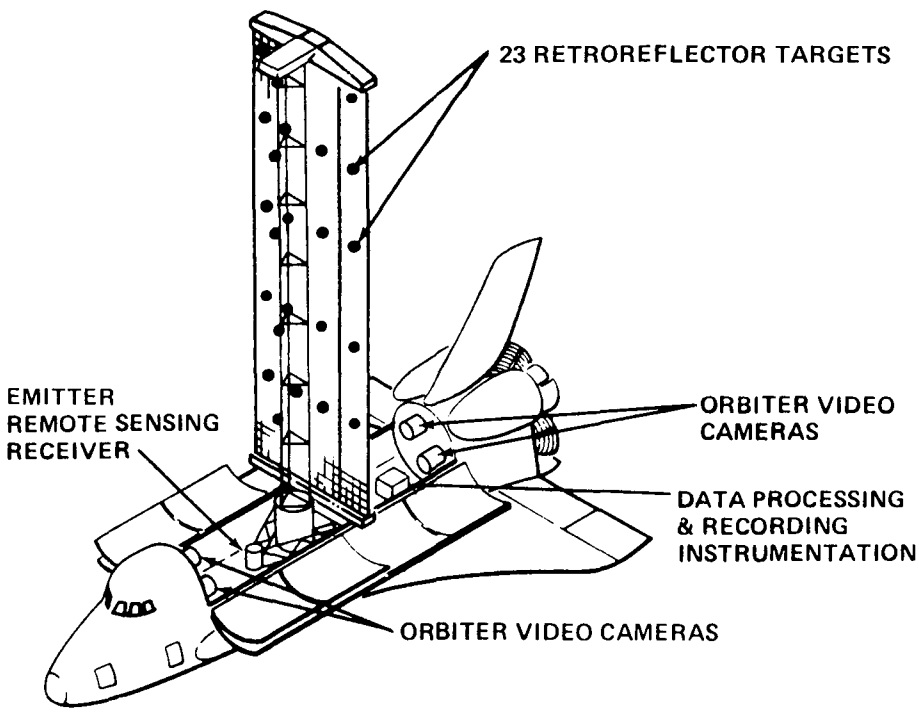

Figure 3

- SENSOR SYSTEM CHARACTERISTICS
  - TRACKS 23 RETROREFLECTING TARGETS ON SAFE SOLAR ARRAY
  - GE ST-256 CHARGE INJECTION DEVICE DETECTOR WITH 256 x 256 PIXEL PATTERN
  - 5, 30 MW LASER DIODES ILLUMINATE ARRAY AT 820 NANOMETERS
  - ILLUMINATOR/SENSOR SEPARATELY PACKAGED FROM MICROPROCESSOR
  - 19 ARC SECONDS RESOLUTION
  - 2 HZ SAMPLE RATE, 6 HZ TRACK RATE
  - 6.20 CM/SEC TARGET RATE LIMIT
  - TRACK MAST TIP MOTION UP TO ± 45 CM
  - MULTIPLEX AND RECORD DATA ON DIGITAL TAPE

Figure 4

OAST-1 PAYLOAD AND DYNAMICS AUGMENTATION
EXPERIMENT FLOW DIAGRAM

The OAST-1 experiment with DAE attached is shown in Figure 5 along with a flow diagram of the sensor system in Figure 6. Although both the solar array dynamic augmentation experiment and the systems are mounted to the mission peculiar equipment support structures (MPESS), the only interaction between is optical. The retroreflector field tracker illuminates the solar array reflectors with five 800 nm laser diodes. The retroreflected energy is imaged on a charge injection device solid state tracker. The tracker is scanned by sensor electronics and the angular deviation from the reference position measured and converted by a microprocessor to engineering units. This data is digitized and fed through a multiplexer to a digital tape recorder. The power control and distribution assembly (PCDA) obtains power from the mission peculiar equipment (MPE) power control box (PCB) and distributes it to the DAE hardware. The PCDA also receives and distributes commands from the orbiter aft flight deck via the flexible multiplexer demultiplexer and returns housekeeping and indicator data. The scientific dynamic data recorded on the tape recorder is returned for ground data processing.

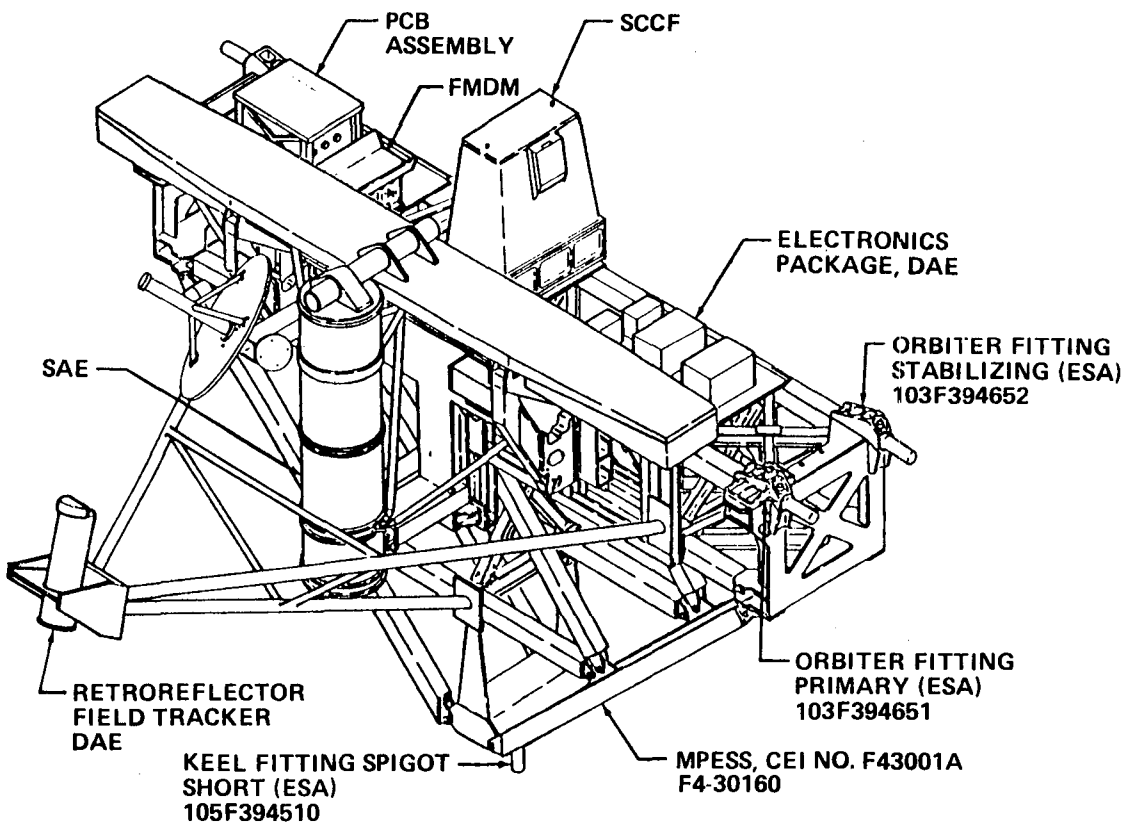

Figure 5

DYNAMICS AUGMENTATION EXPERIMENT

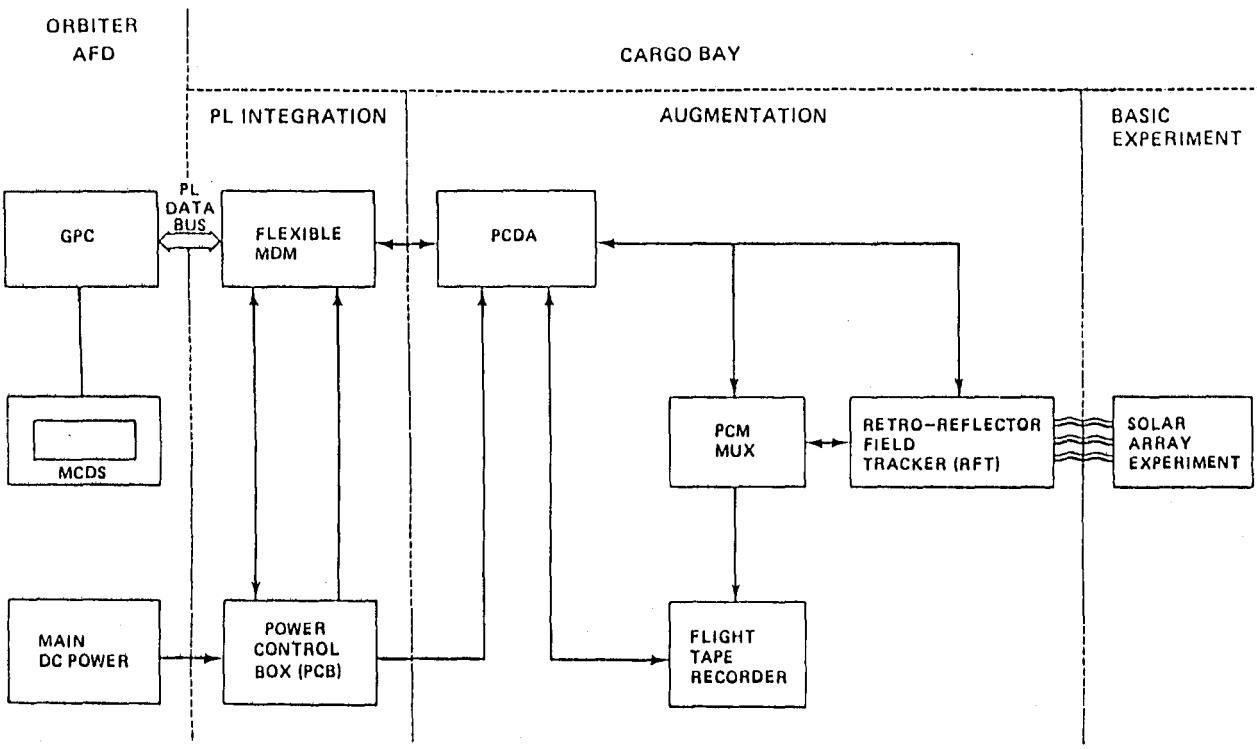

Figure 6

DYNAMIC AUGMENTATION EXPERIMENT
REFLECTOR INSTALLATION

The SAFE/DAE reflectors were pop out targets with retroreflective tape attached. The retroreflective tape ensures that the reflected light always returns to the source of illumination, no matter what the angle of incidence. Figure 7 shows the stand-up target above a photogrammetric target. Figure 8 shows how the array looked on-orbit to the sensors. The small intense dots are the retroreflective targets.

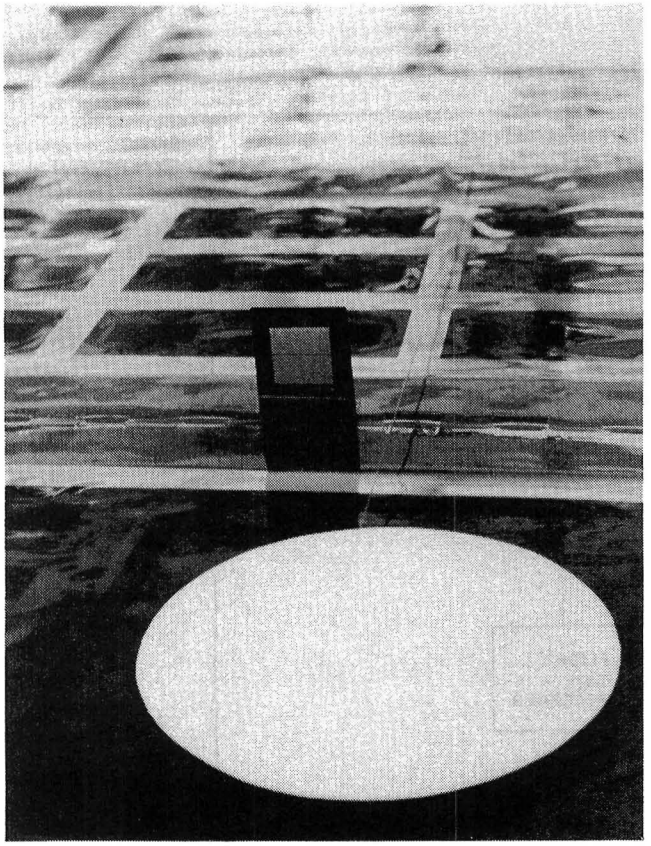

Figure 7

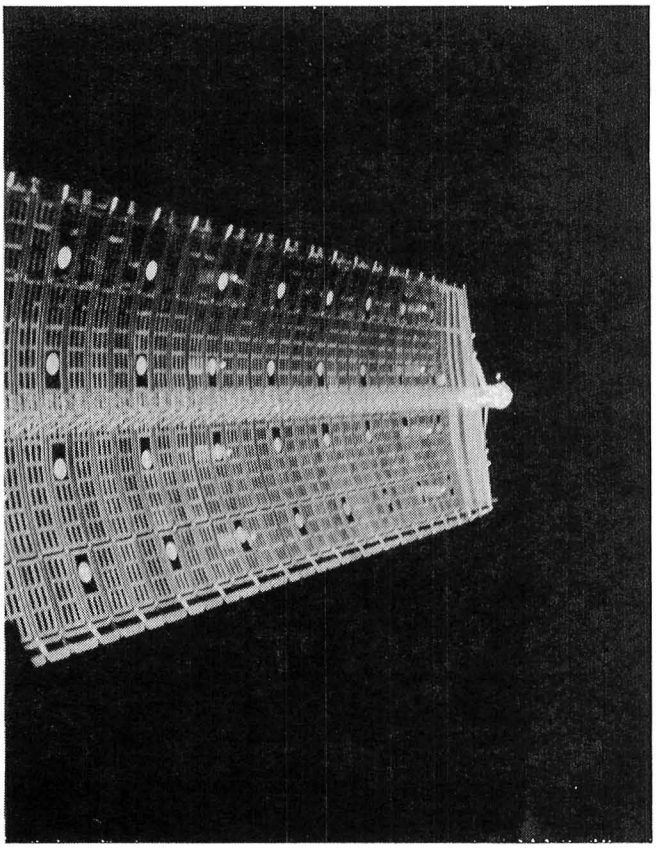

Figure 8

ANALYSIS METHODOLOGY

Figure 9 illustrates the X direction displacement/time signature of a reflector mounted on the solar array cover during multimodal excitation. An ensemble of 36 measurements similar to this example is analysed for each test to provide the solar array dynamic characteristics. As is apparent from this single measurement, the solar array is highly damped. The analysis methodology outline is shown in Figure 10. Both are free decay techniques.

The Complex Exponential parameter estimation technique utilizes a least squares technique to fit a series of damped complex exponentials to the impulse responses or free decay responses of a viscous damped mechanical structure. The method is limited to single input data and consequently can only determine parameters for modes excited by that input.

Poly-Reference is a complex exponential estimation technique that uses responses from several input locations. A consistent set of data is obtained by simultaneous analysis of all the measurements for all the inputs. The method can be applied to structures with closely spaced modes, repeated roots, and high damping.

Both techniques have been proven on simulations.

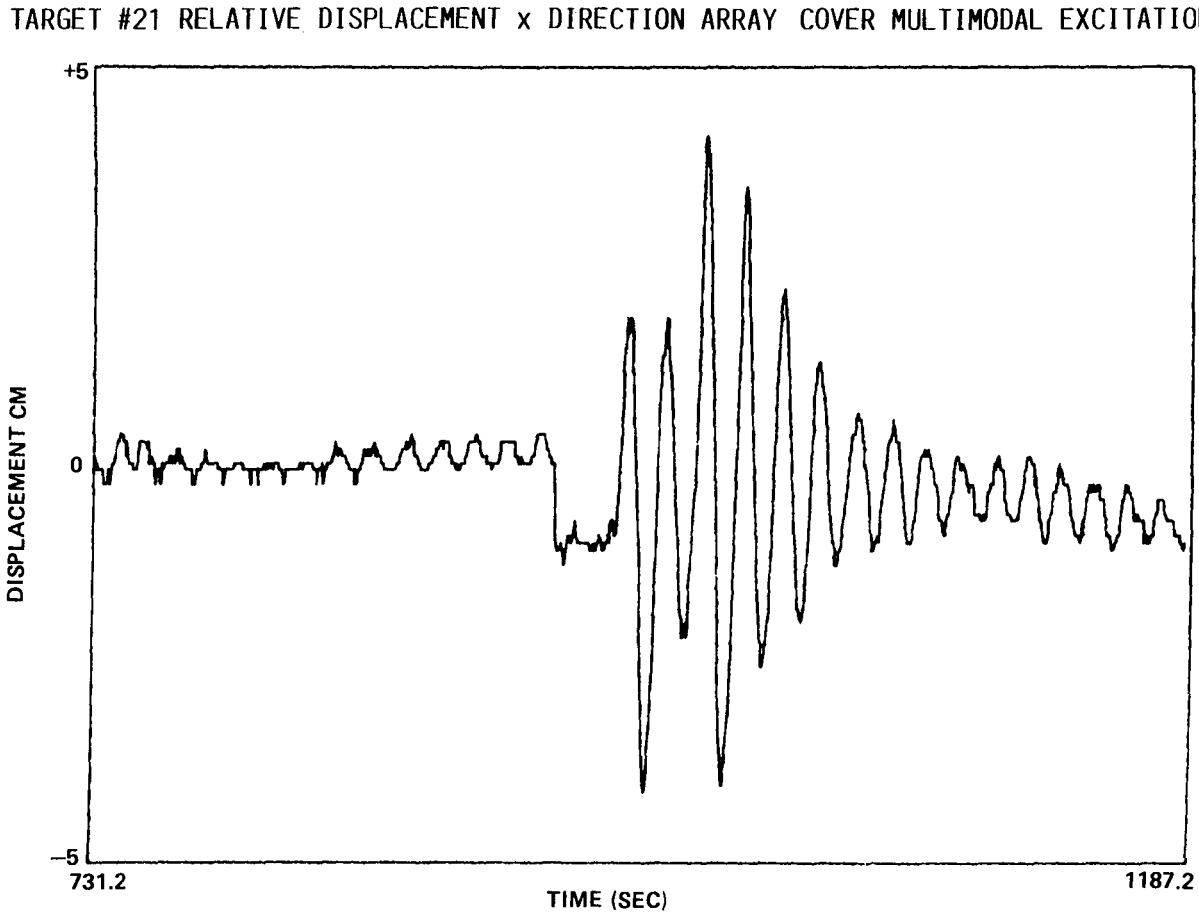

Figure 9

ANALYSIS METHODOLOGY

- 18 TARGETS DISPLACEMENT RECORDED ON DIGITAL TAPE
- TWO DATA ANALYSIS METHODOLOGIES TO BE USED
  - COMPLEX EXPONENTIAL TECHNIQUE
    - TIME DOMAIN CURVE FIT TO OBTAIN FREQUENCIES AND DAMPING
    - CURVE FIT OF RESPONSE SPECTRA FOR MODE SHAPES
  - POLY REFERENCE TECHNIQUE
    - TIME DOMAIN CURVE FIT FOR FREQUENCIES AND DAMPING
    - TIME DOMAIN CURVE FIT FOR MODE SHAPES
    - COMBINES MULTIPLE TESTS TO ENHANCE ACCURACY AND MODAL DEFINITION
- PROVEN BY OAST–1 ANALYSIS RESPONSE SIMULATION

Figure 10

One unusual solar array characteristic noted during flight was a static bowing of the wing. This phenomenon occurred during nighttime passes and appeared to be relieved during the daylight passes. The Dynamic Augmentation Experiment measured this bowing during each of 6 runs. The results were very consistent and are shown in Figure 11. The deflection values are X direction position from an arbitrary reference and show the array "bowed" a maximum of 35 cm and rotated counterclockwise approximately 7^{o}.

A summary of the current flight dynamics results is shown in Figure 12. The damping was high which significantly reduced the dynamic response. The array was a consistently different structure from daylight to dark. Based on tip accelerometer results, the first natural frequency (cantilever in pitch) varied between 0.052-0.055 Hz during the day and 0.060-0.068 Hz at night. The analyses essentially split the difference. The solar array response, suppressed as it was, never caused a margin of safety less than approx. 200%. The tracker system operated normally even in out of normal conditions. Preliminary modal analysis results confirm the first torsional mode of 0.09 Hz shown in Figure 13.

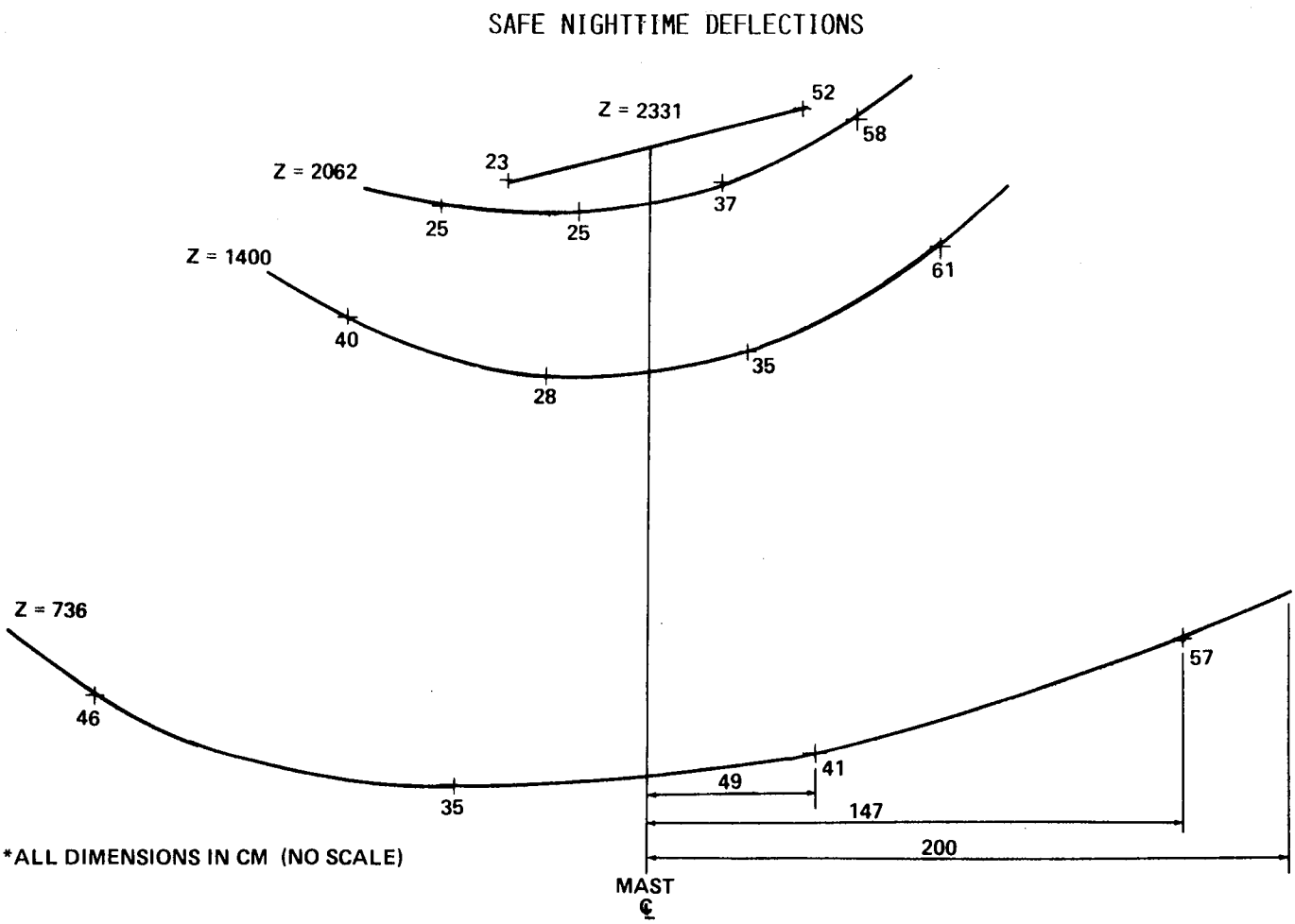

Figure 11

FLIGHT DYNAMICS SUMMARY

- SOLAR ARRAY HIGHLY DAMPED
  - 4–8% VRS TYPICAL STRUCTURES OF 0.5 – 1.0%
  - DYNAMIC RESPONSE VARIES FROM EXPECTED TO SIGNIFICANTLY LESS THAN EXPECTED (FACTORS OF 2–3)
- ANALYSES PREDICTED 1ST MODE FREQUENCIES WITHIN ± 15%
- SOLAR ARRAY 1ST MODE FREQUENCY VARIED FROM DAY TO NIGHT AND TEST CONDITION

	DAY	NIGHT
70% EXPECTED	0.059	0.059
70% MEASURED	0.052–0.055	0.060–0.068
100% EXPECTED	0.034	0.034
100% MEASURED	0.034–0.040	NA

- SOLAR ARRAY RESPONSE REMAINED VERY SAFE

Figure 12

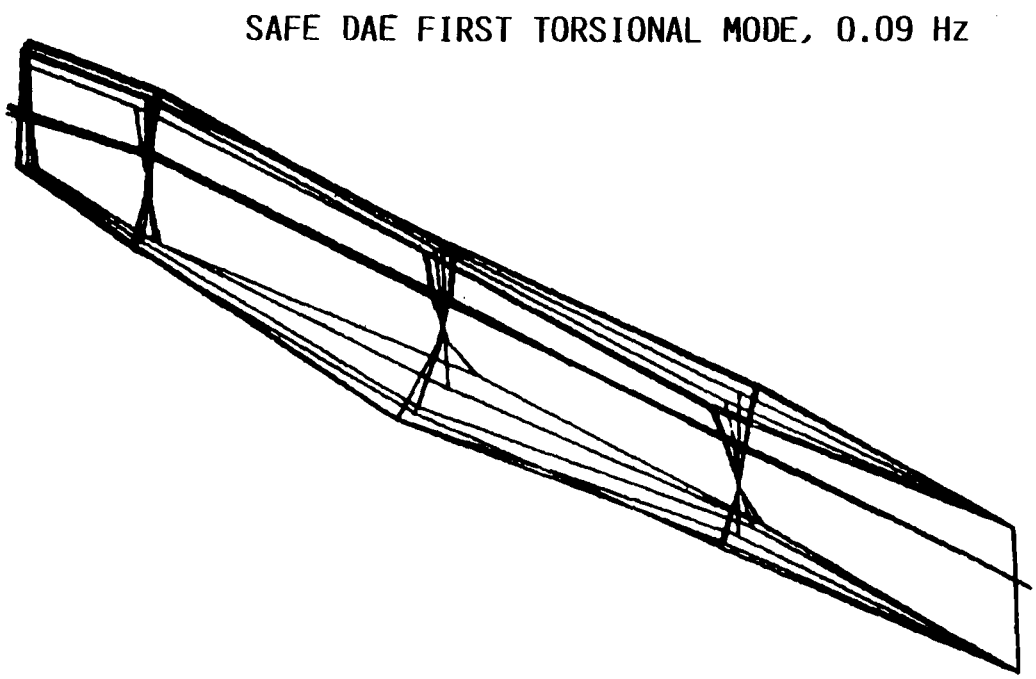

Figure 13

LANGLEY RESEARCH CENTER PHOTOGRAMMETRIC MEASUREMENTS OF SOLAR ARRAY DYNAMICS: PRELIMINARY RESULTS

M. Larry Brumfield, Richard S. Pappa,
James B. Miller, and Richard R. Adams

NASA Langley Research Center
Hampton, Virginia

LARGE SPACE ANTENNA SYSTEMS TECHNOLOGY - 1984
DECEMBER 4-6, 1984

On August 31, 1984, the OAST-1 Solar Array Experiment was launched on shuttle mission 41-D. Figure 1 is a photo of the array taken from the orbiter aft flight deck. The array was built by the Lockheed Missiles and Space Co., Sunnyvale, Calif., under contract to the NASA Marshall Space Flight Center. It is fabricated from 3-mil-thick Kapton and consists of 84 panels, each 15 inches wide by 13 feet long, joined edge-to-edge to form a 105-foot-tall array. For launch and reentry, the array is folded accordian like into a 3-inch-thick stack. A triangular-shaped, coilable longeron extension mast is used to deploy the solar array on orbit. Provision is made to deploy the array to both 70% and 100% of full length with tension applied to the array blanket once 70% deployment is reached.

Only two panels have active solar cells applied; the remainder have either aluminum or glass mass simulators. A flat, multi-conductor "ribbon" cable is attached to both edges of the array for power and signal paths.

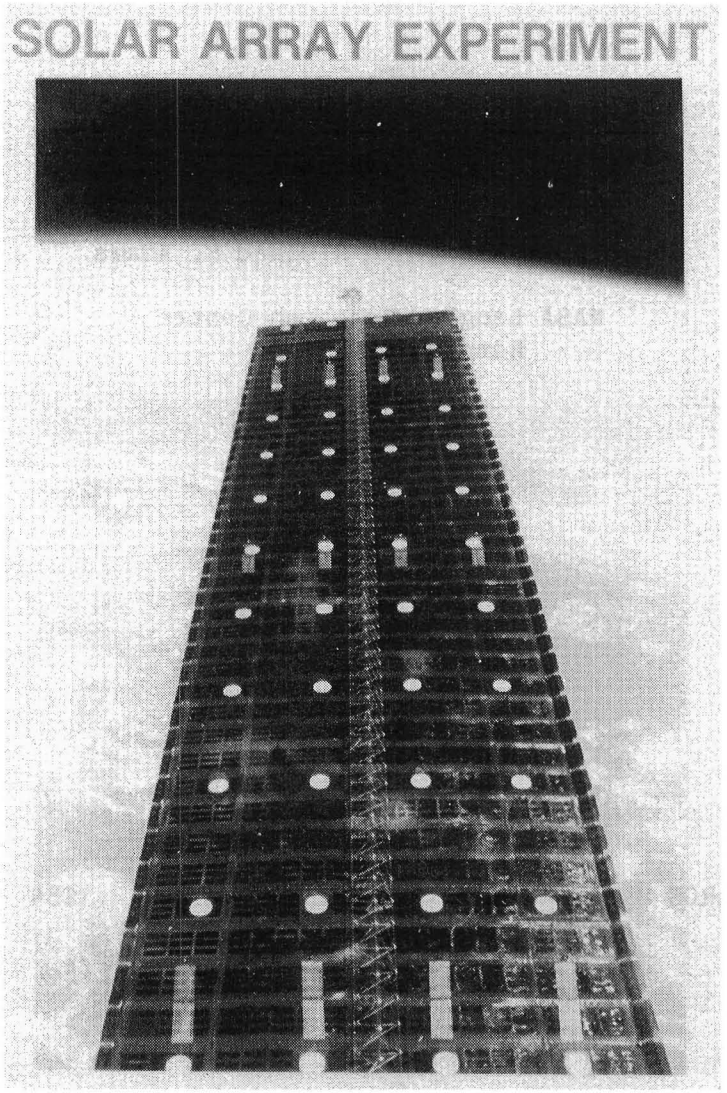

Figure 1.

The NASA Langley Research Center participated in the Solar Array Experiment with two primary objectives: 1) to study the structural and control dynamics of a new class of large, lighweight, low-frequency space structures, and 2) to develop technology for remote video measurement of structural motions. The shuttle orbiter's closed circuit television (CCTV) system was used to provide recorded video images of the solar array from four locations in the payload bay, two on the forward bulkhead and two on the aft bulkhead. Figure 2 illustrates schematically the experiment configuration with only two CCTV cameras shown for clarity. White reflective targets were placed on the array to provide discrete points at which to track array motion. A dynamic test consisted of a quiescent period in which orbiter operations were inhibited and crew motion restricted, an excitation period, and a free decay period. The orbiter was placed in free drift while in a gravity gradient orientation and dynamics tests were timed to occur at orbital noon so that the sun would illuminate one side of the array and earth albedo the other. The CCTV system was turned on during the quiescent period, approximately 3 minutes prior to excitation. Video from all four CCTV cameras was recorded continuously through the excitation and free-decay periods for a total test record of 8 to 10 minutes.

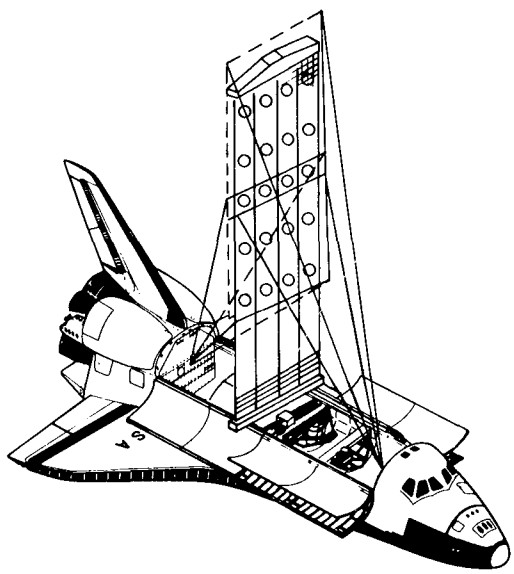

LaRC SOLAR ARRAY DYNAMICS EXPERIMENT

- Structural/control dynamics studies
- Remote video photogrammetric measurement technology

Figure 2.

Excitation for the dynamics experiment was provided by the shuttle orbiter's vernier reaction control jets. A predetermined set of commands was programmed into the orbiter digital autopilot and initiated by the crew to execute a planned set of pulses by the vernier control jets. The length and spacing of these pulses were keyed to selected frequencies of the predicted dynamic response of the solar array. In order to minimize the net orbiter angular accelerations and still excite the array, the pulses were designed to occur in pairs with opposing directions. Figure 3 illustrates the characteristics of typical pulses for two different tests. These are not time histories of any particular jet firings, nor do they represent energy inputs. Rather, they are meant to illustrate the spacing and opposing directions of jet firings required to input energy to the array at the appropriate point during its response while minimizing the net angular acceleration input to the shuttle orbiter.

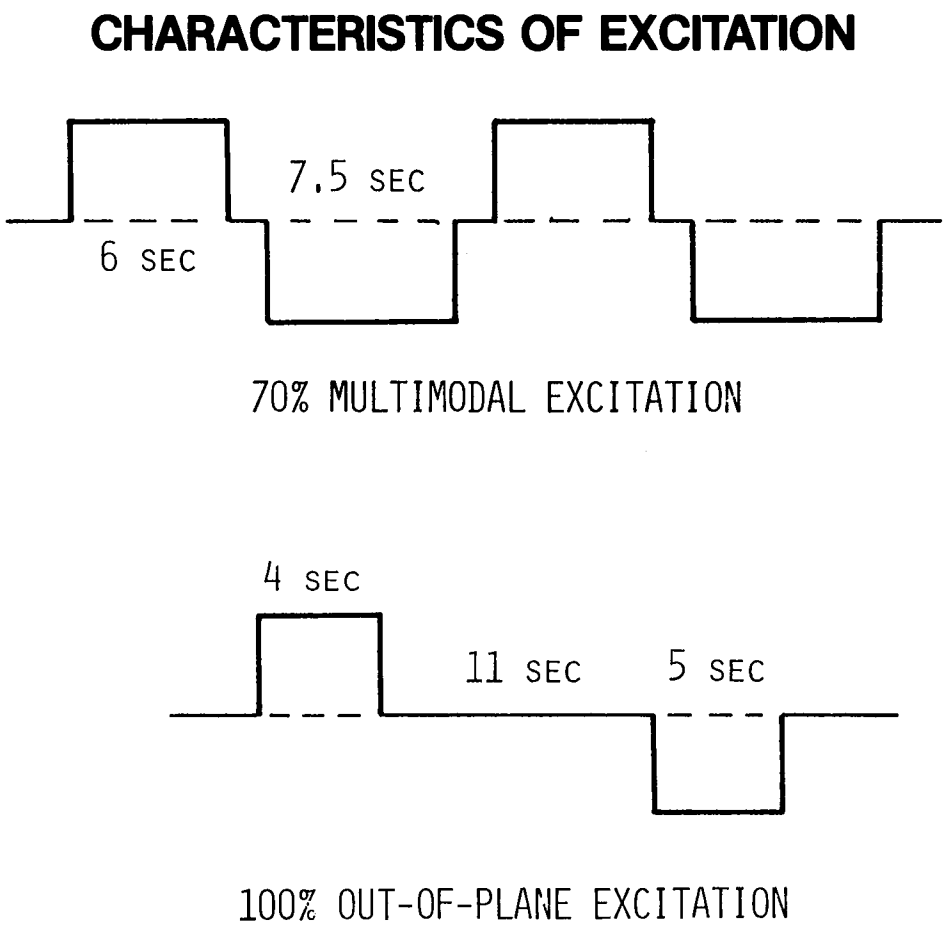

Figure 3.

Dynamic tests were conducted with the solar array extended to both the 70% and 100% positions. Excitations for different tests were tailored to excite different combinations of modes, with three general types of excitation being out-of-plane, in-plane, and multi-modal. Table 1 lists seven tests of the solar array that were done on orbit using the orbiter CCTV system for photogrammetric measurements of response. For some tests the CCTV was configured for high resolution and narrow field of view and in other tests for high coverage and wider field of view. The times shown for the tests were determined by reading the GMT time that was recorded on each videotape during the orbital test.

SOLAR ARRAY EXPERIMENT
LaRC PHOTOGRAMMETRY TESTS

	Extension	Excitation	Camera Configuration	Test Time
1.	70%	OP	HCOV	246:14:58:10
2.	70%	OP	HRES	245:19:23:19
3.	70%	IP	HRES	247:18:05:10
4.	70%	MM	HCOV #1	246:13:27:10
5.	70%	MM	HCOV #2	246:16:28:10
6.	100%	OP	HRES	246:18:05:40
7.	100%	MM	HCOV	246:19:29:05

OP: OUT–OF–PLANE
IP: IN–PLANE
MM: MULTI–MODAL

HCOV: HIGH COVERAGE
HRES: HIGH RESOLUTION

Table 1.

Analysis of the flight data is done post-flight on the ground and requires three major steps as indicated in Figure 4. First, each flight videotape is analyzed to determine motion of targets in the camera image plane. Then certain corrections are made for electronic and optical distortions. The next major step is merging all four camera views in in a photogrammetric triangulation process to determine the 3-D motion in the orbiter coordinate system. To accomplish this we used the Stereo Triangulation and Resection System (STARS) developed by Geodetic Services Incorporated. (See Reference 1 for a detailed description of STARS.) Once the 3-D time histories of target displacements are determined, the next major step in the process is application of system identification techniques to determine the dynamic response characteristics of the solar array. In addition to the standard FFT analysis we also use an Eigensystem Realization Algorithm (ERA) developed at Langley Research Center by Mr. Richard S. Pappa and Dr. Jer-Nan Juang. (See Reference 2 for a detailed description of the ERA technique.) This is a time domain analysis technique whose basic concepts originated in control theory. Out of this analysis come the desired frequencies, mode shapes and damping characteristics of the solar array.

OVERVIEW OF DYNAMIC DATA ANALYSIS

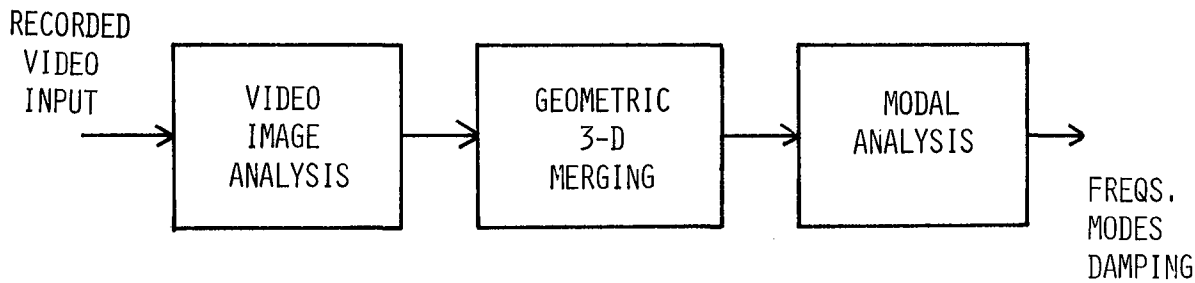

Figure 4.

As the first step in the analysis process, the flight videotapes are analyzed using a system illustrated schematically in Figure 5. This unique system combines commercial and Langley designed components with Langley developed operational software to extract information on target motion in the image plane of the CCTV camera. Tape analysis begins with an operator working interactively through a terminal to define initial conditions. A zero reference frame is digitized and stored by the frame storage unit and displayed on the monitor. The operator uses a cursor to define the initial target positions and size of search area for each target of interest. With a priori knowledge of the length of the dynamic test record, the operator selects the desired sample rate, analysis interval and total number of frames to be analyzed. Typically, we work with 3 frames per second (or every tenth frame) for solar array data but it can be up to 30 samples per second with the standard recorded video.

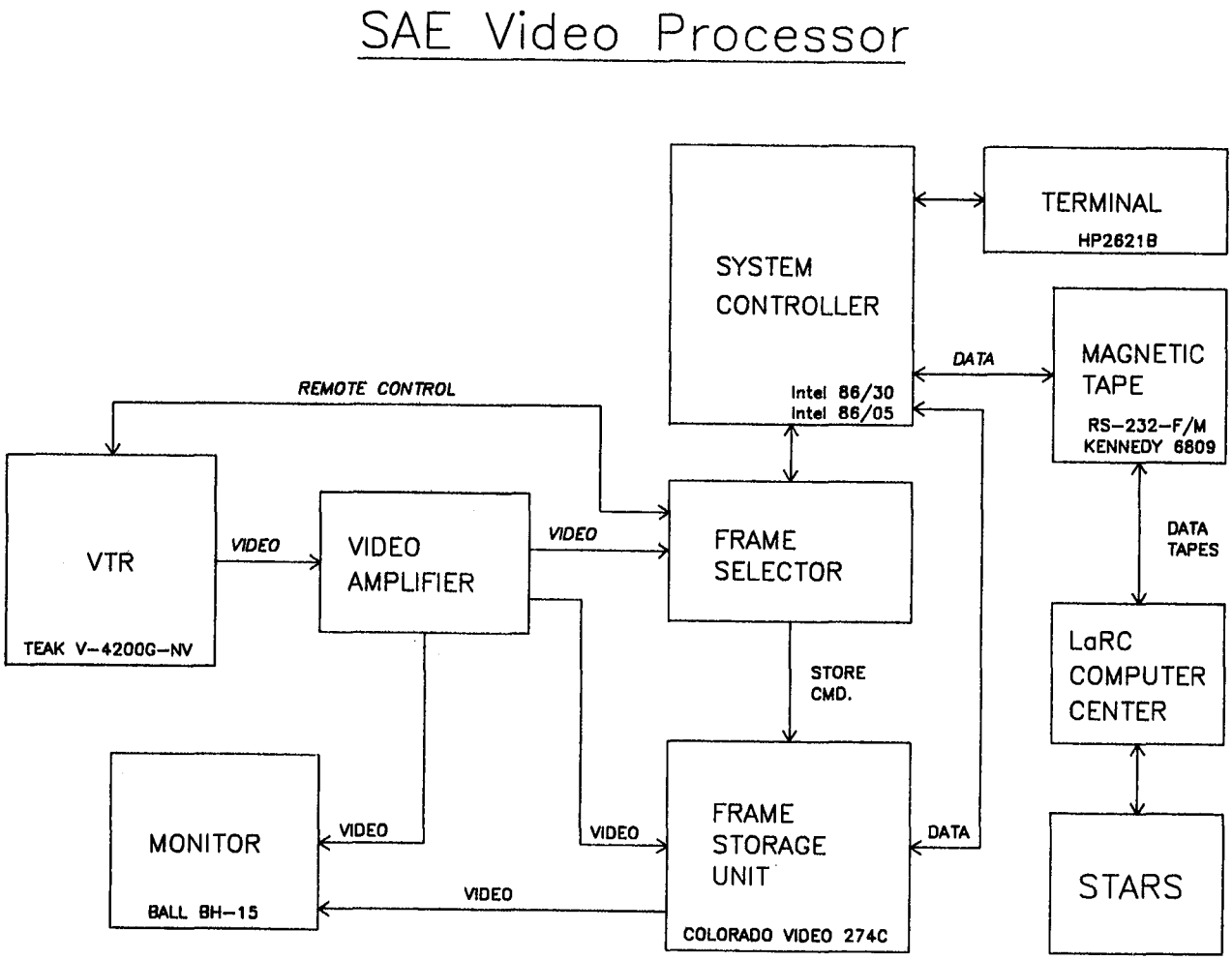

Figure 5.

Once initial conditions are defined, the system is commanded into an automatic mode that is completely software driven with no operator interaction. The frame selector reads the GMT time recorded on the tapes during the flight test and identifies the next frame in the sequence for analysis. The frame is digitized and stored for analysis. The system searches for each target at its previously defined location, calculates and stores the location of the center of brightness for each target, and repositions the search area to the new target location. This is repeated until the complete frame is analyzed. The information is then formatted, tagged with appropriate time and test information, and dumped to buffer memory. This frame-by-frame process is repeated until the end of the record is detected by the frame selector, at which time the videotape is rewound to the zero reference frame and a new pass through the tape is started. On the second pass, the first frame is selected one sample interval later in time than on the first pass. Additional passes will be made with analysis beginning one sample interval later on each successive pass until enough frames are interleaved to fill the analysis interval at the desired sample rate. For solar array data, we typically use a sample rate of three frames per second (or every tenth frame) and an analysis interval of 40 to 60 frames, which means the system will make four to six passes through the videotape to analyze all the desired frames. This analysis scheme was chosen to build flexibility into the system and reduce the cost of very high speed processing components.

During the processing of the video frames, the system begins to write data from the buffer memory to a digital magnetic tape. This is done on a time-available basis throughout the analysis process. After analysis is completed, all data still remaining in buffer is written to digital tape in preparation for being entered into a data base management system in the Langley central computer facility where processing continues.

Figure 6 shows an image frame taken from a flight videotape of a test with the solar array extended to the 70% position and CCTV system configured for high resolution. This is a typical image that an operator would work with in initializing the video processing. An area including the rightmost target in the top row has been expanded using the video processor to show the individual pixel intensities of the image. During analysis, each pixel intensity within a given target search area is evaluated on a 256-level gray scale and used in determining the center of brightness for that target.

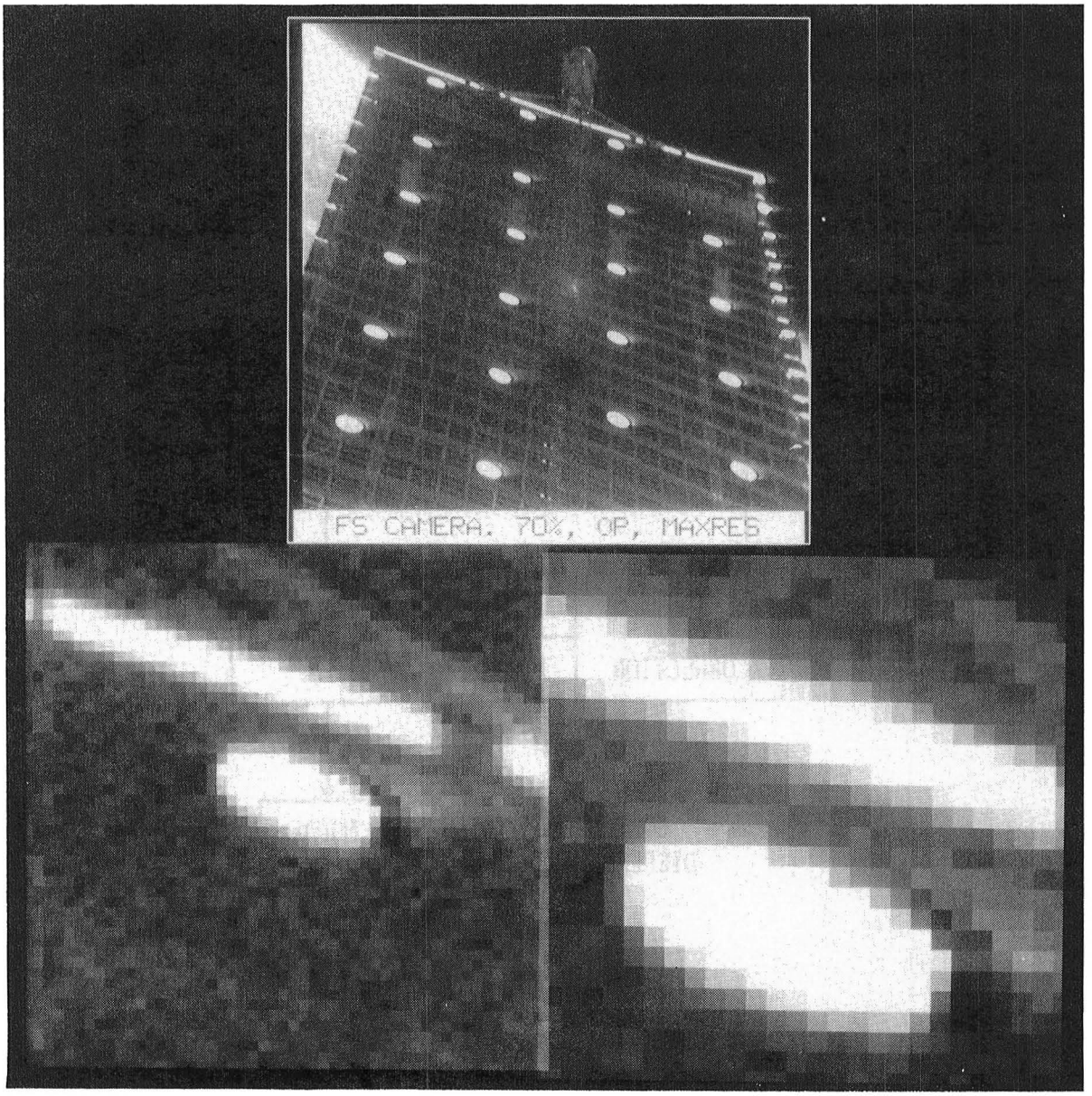

Figure 6.

The next major step in the analysis is the photogrammetric triangulation process in which data from all four CCTV cameras is merged to produce 3-D time histories of target motion in the orbiter coordinate system. This process is illustrated schematically in Figure 7. In preparation for the triangulation process, correction factors are applied to all the raw data coming out of the video analysis process to remove most of the optical and electronic distortions. These correction factors were obtained using post-flight video data taken in an optical laboratory at Kennedy Space Center with the flight CCTV cameras looking at a precision optical target. Once corrections have been made to raw data, then it is ready for the triangulation.

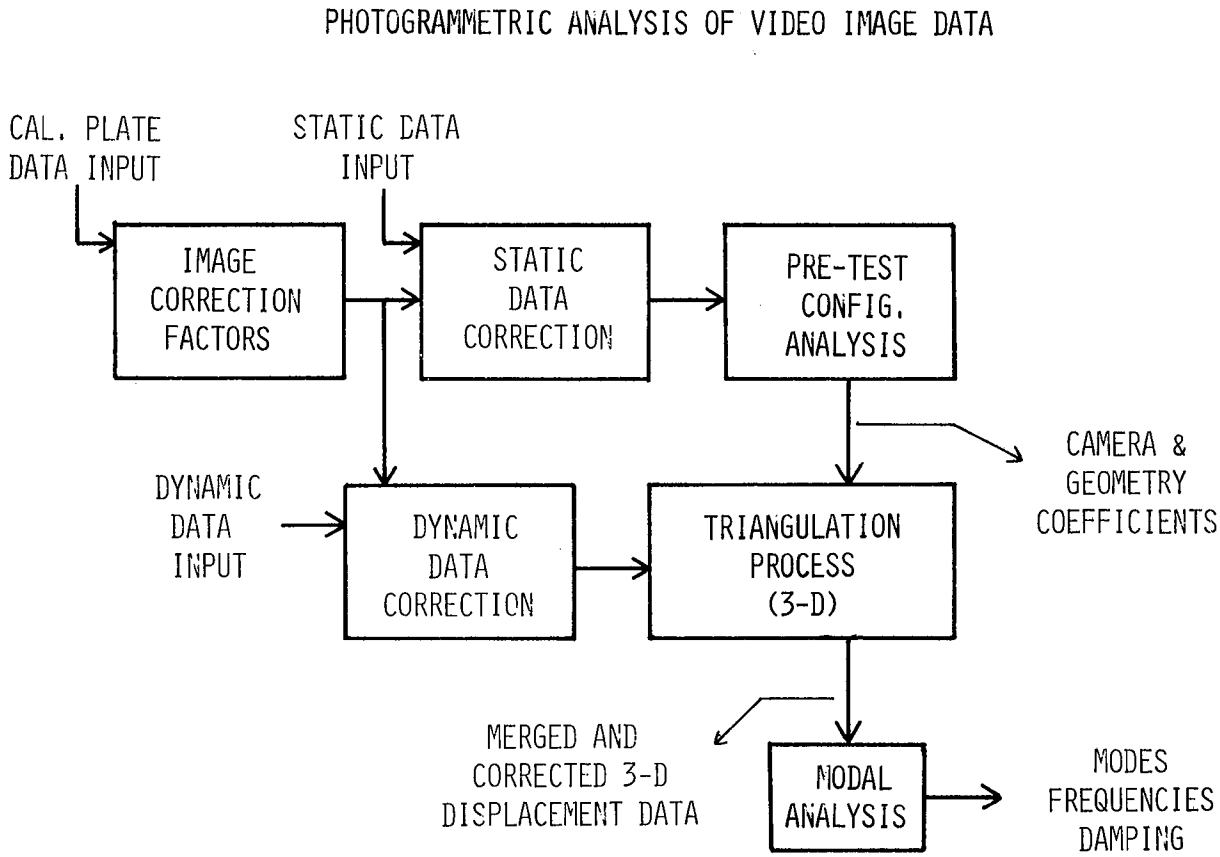

Figure 7.

The first step of the triangulation is a full least-squares bundle adjustment using the Simultaneous Triangulation and Resection System (STARS) developed by Geodetic Services Incorporated (Reference 1). This is essentially a self-calibration technique that looks at all targets seen by all four CCTV cameras during the pre-excitation or quiescent portion of the the test data to determine a set of coefficients that specify the CCTV configuration. Using an assumed set of parameters, STARS calculates locations of targets on the solar array and theoretical camera locations. Camera parameters are adjusted by incremental amounts and the process is repeated iteratively until convergence is achieved within a pre-established bound as determined by comparing calculated camera positions to actual positions and comparing calculated target positions relative to each other with ideal or undistorted design values. The resultant set of coefficients defines the CCTV configuration for that test only. Since the CCTV system is used for other operations between dynamic tests, a new set of coefficients must be calculated for each test using actual video data from the quiescent portion of that test.

The set of CCTV configuration coefficients obtained from the bundle adjustment is then used in a photogrammetric triangulation process. Data that comes out of the video analysis describes a target's motion in the image plane of the respective camera that sees that target. This data is in the coordinate system of the CCTV image plane. In the triangulation process, data from all four cameras is merged geometrically to produce 3-D time histories of the motion of targets in the coordinate system of the shuttle orbiter.

After 3-D time histories of targets are obtained, system identification techniques are applied to determine the dynamic response characteristics of the solar array. Traditional FFT techniques have been applied as well as newer techniques such as the Eigensystem Realization Algorithm developed at Langley Research Center by Mr. Richard S. Pappa and Dr. Jer-Nan Juang. The ERA is a time domain analysis technique for constructing an analytical model or realization of a structure from its dynamic responses. Reference 2 gives a thorough discussion of the ERA technique.

The remainder of this paper will present some typical results obtained in the different steps of the analysis process for two of the orbital tests.

Figure 8 is a photo of actual images selected by the frame storage device from videotapes of the out-of-plane test at 100% extension. A view as seen from each of the four CCTV cameras is included. These are some of the actual images analyzed by the video processing system for this test. The slight curvature noticed in the lower left or aft-port camera is real, not an optical illusion, and will be mentioned again later.

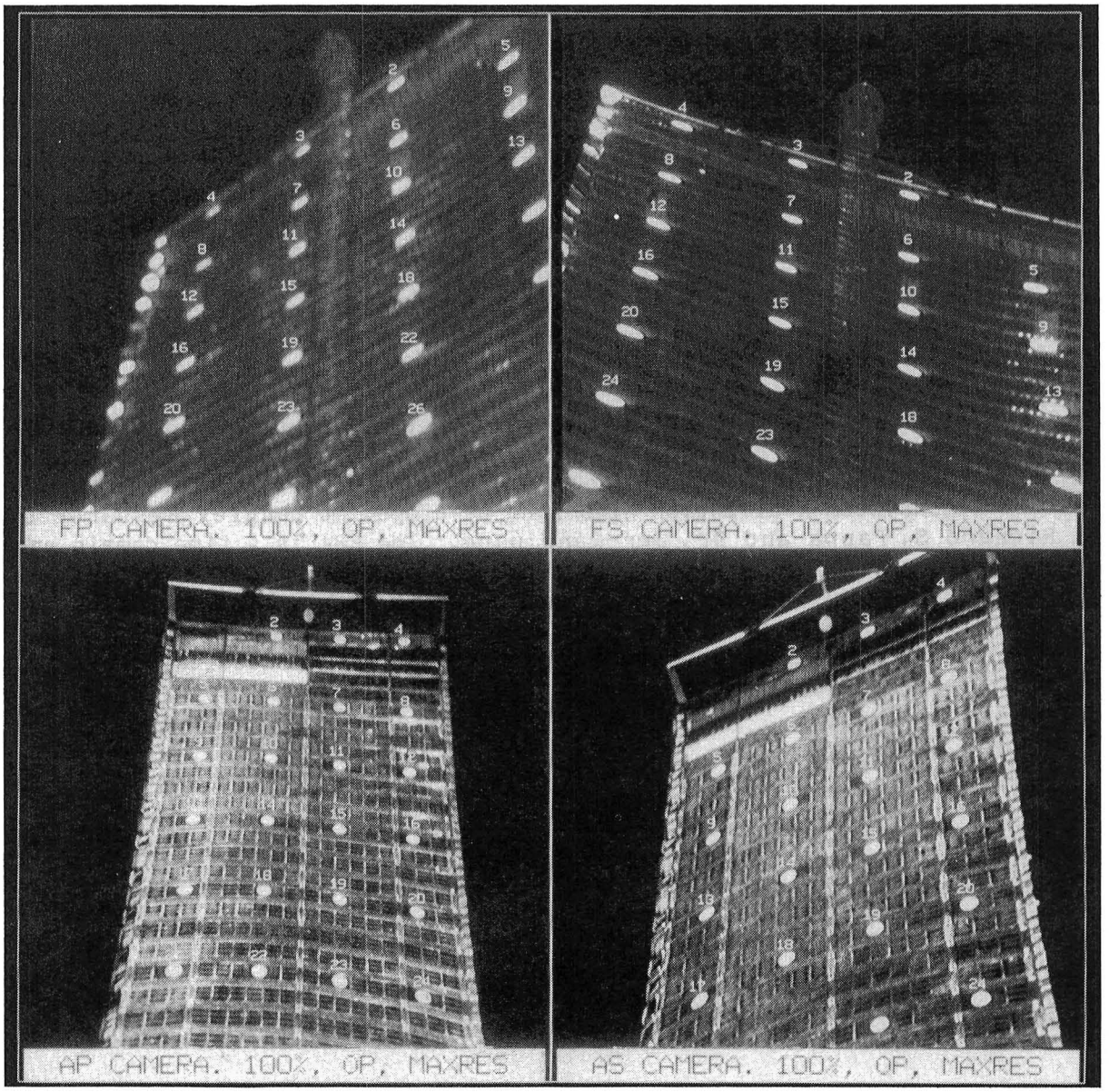

Figure 8.

Figure 9 shows plots of the data that comes out of the analysis of the flight videotapes by the video processor. These are raw data plots of the X and Y motion of a target in the image plane of the CCTV camera. The data covers a continuous period beginning in the pre-excitation or quiescent period and running through the free-decay period. Note that the video recording was not long enough to cover the complete decay to the initial or pre-excitation conditions. It should be noted that both the peak-to-peak displacements at the end of the test record and the steady state motions during quiescent periods were small enough that they were not detected by the crew.

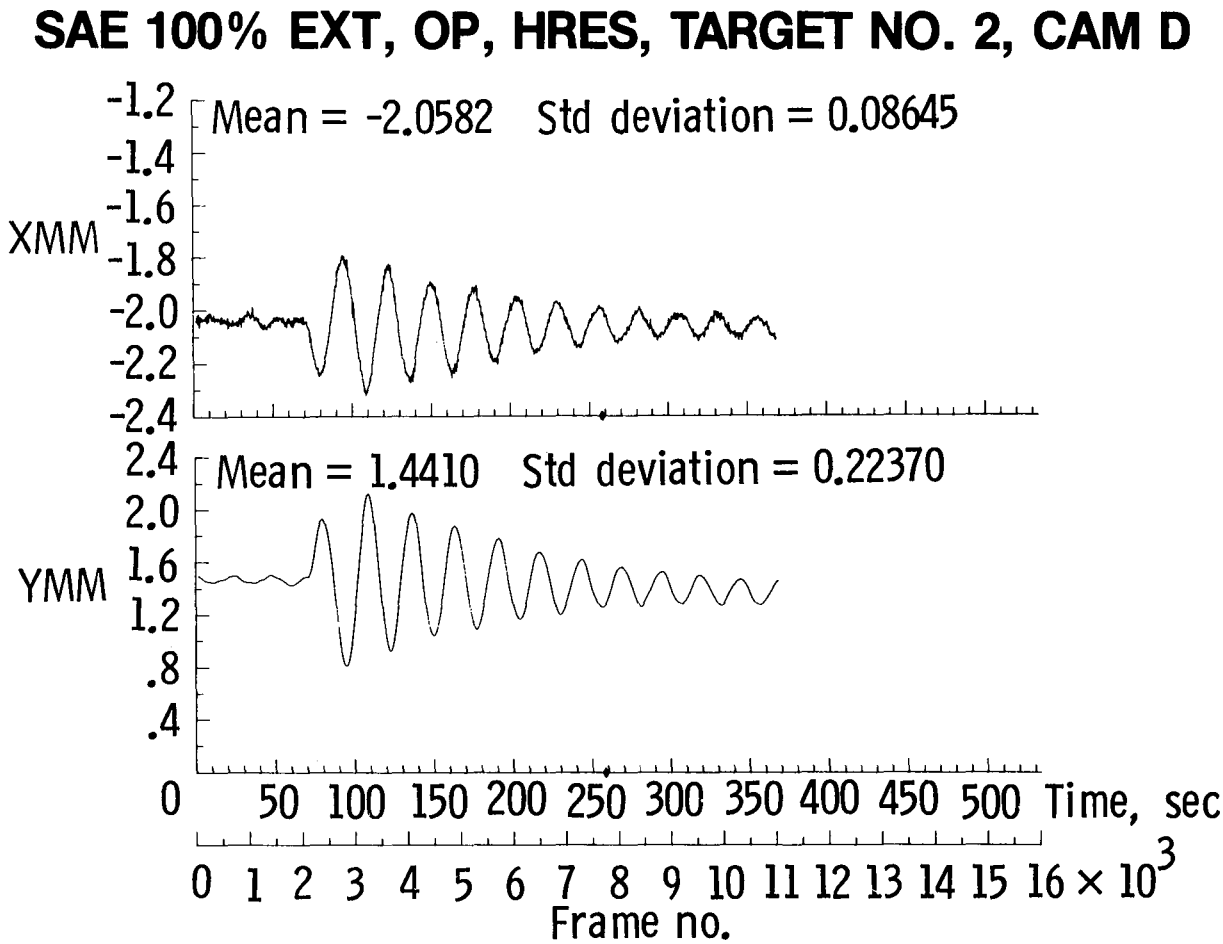

Figure 9.

Results of the STARS analysis are shown in Figure 10. Data from Figure 9 has been merged with corresponding data from the other 3 cameras and all appropriate corrections and triangulations have been applied to produce the X,Y,Z plots shown. This is the final form of a 3-D time history of the motion of target #2 in the shuttle orbiter coordinate system and is ready for application of system identification techniques. Even cursory examination of these plots reveals that the motion is dominated by displacements in the X direction, which is the out-of-plane bending direction.

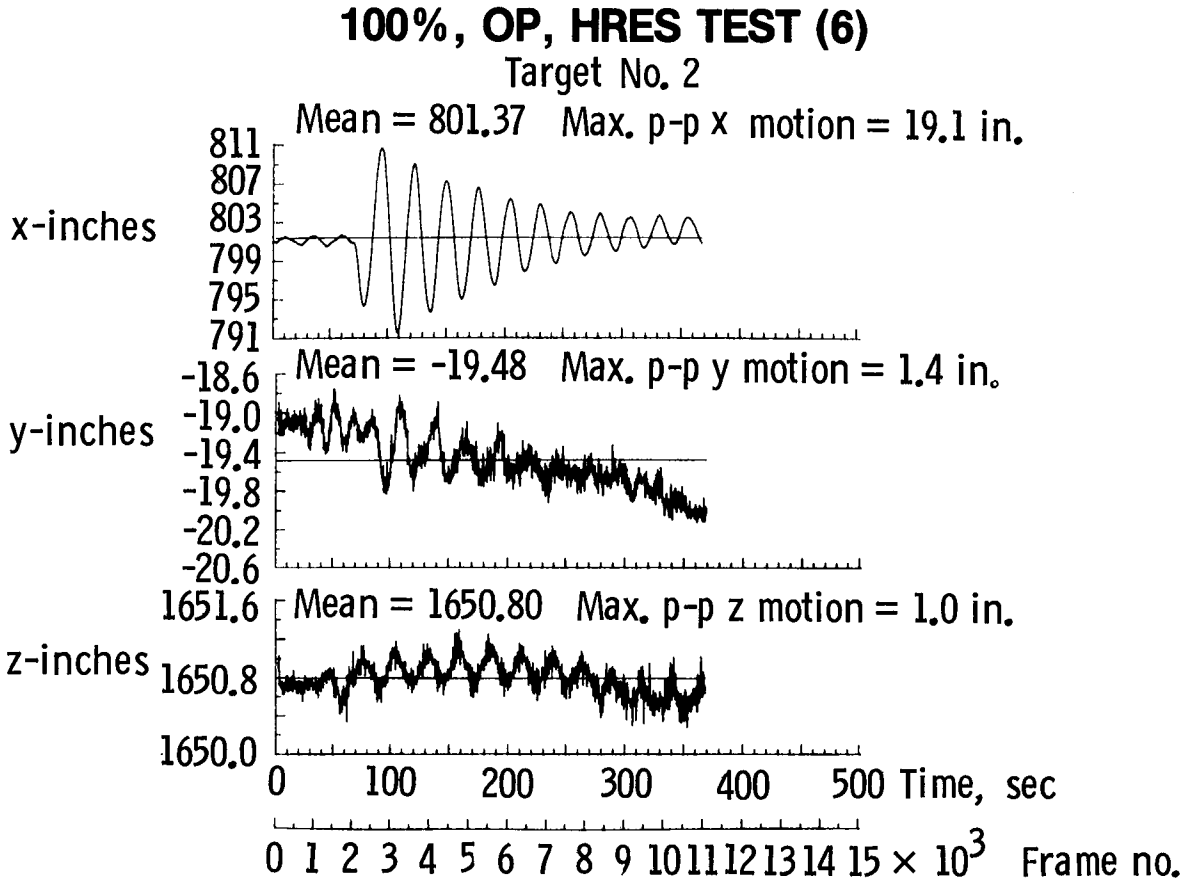

Figure 10.

Table 2 lists the maximum peak-to-peak motions in the X direction for 15 targets seen by all cameras in the images from Figure 8. The numbering of targets begins with the row at the top of the array and proceeds toward the lower rows with the lowest targets having the largest numbers. The targets are grouped by rows. Examination of the average X position indicates that the array is twisted about its longitudinal axis.

100%, OP, HRES TEST

TARGET NO.	AVG. X POSITION (ORBITER COORD.)	MAX. P-P X MOTION INCHES
2	801.367	19.1
3	807.481	19.1
4	813.562	18.9
5	795.091	18.8
6	802.130	18.8
7	807.094	18.8
8	812.322	18.8
9	795.260	18.4
10	802.284	18.5
11	806.756	18.5
12	811.544	18.5
13	795.119	17.9
14	802.637	18.1
15	806.721	18.2
16	810.388	18.2

Table 2.

Figure 11 is a frequency plot obtained by applying FFT analysis to the X displacement data for target 2 which was plotted in Figure 10. Again, this is data from a dynamic test at 100% extension with excitation designed to stimulate out-of-plane bending. Two frequencies are clearly identified and both agree very closely with predicted frequencies for this test.

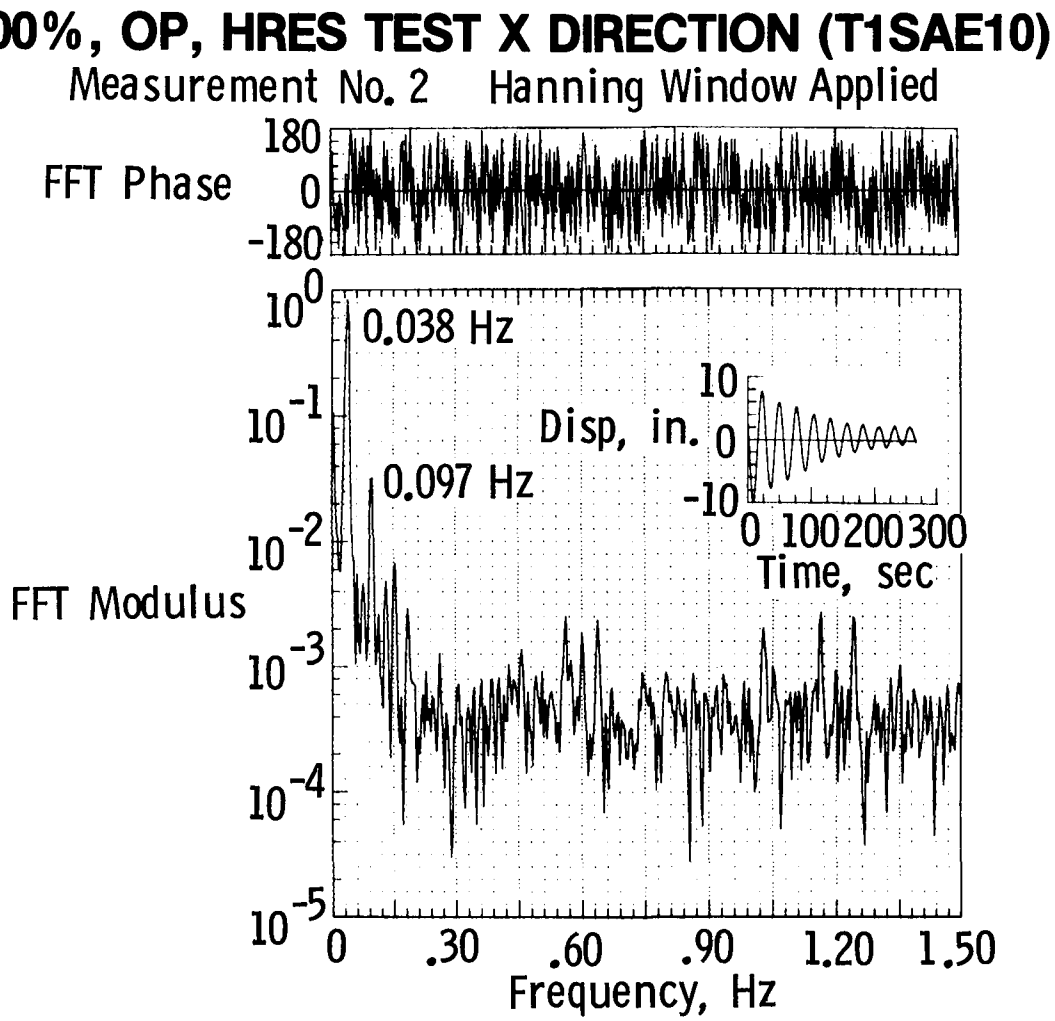

Figure 11.

The ERA technique was used to calculate damping for this same test. Results show that the overall damping for this test was approximately 3.3%. In Figure 12 we have plotted the X displacement curve that was shown in Figure 10 and fitted curves representing various damping estimates to it. In this figure, the displacement plot seems to fit the 4.0% damping curve better than the 3.3% ERA result. This can be explained by the fact that ERA considers all the frequencies present and the true 3-D motion in determining damping whereas the displacement plot is only for the X displacement. The thing that is most obvious is that the damping is much higher than the 0.5% that was assumed for pre-flight predictions.

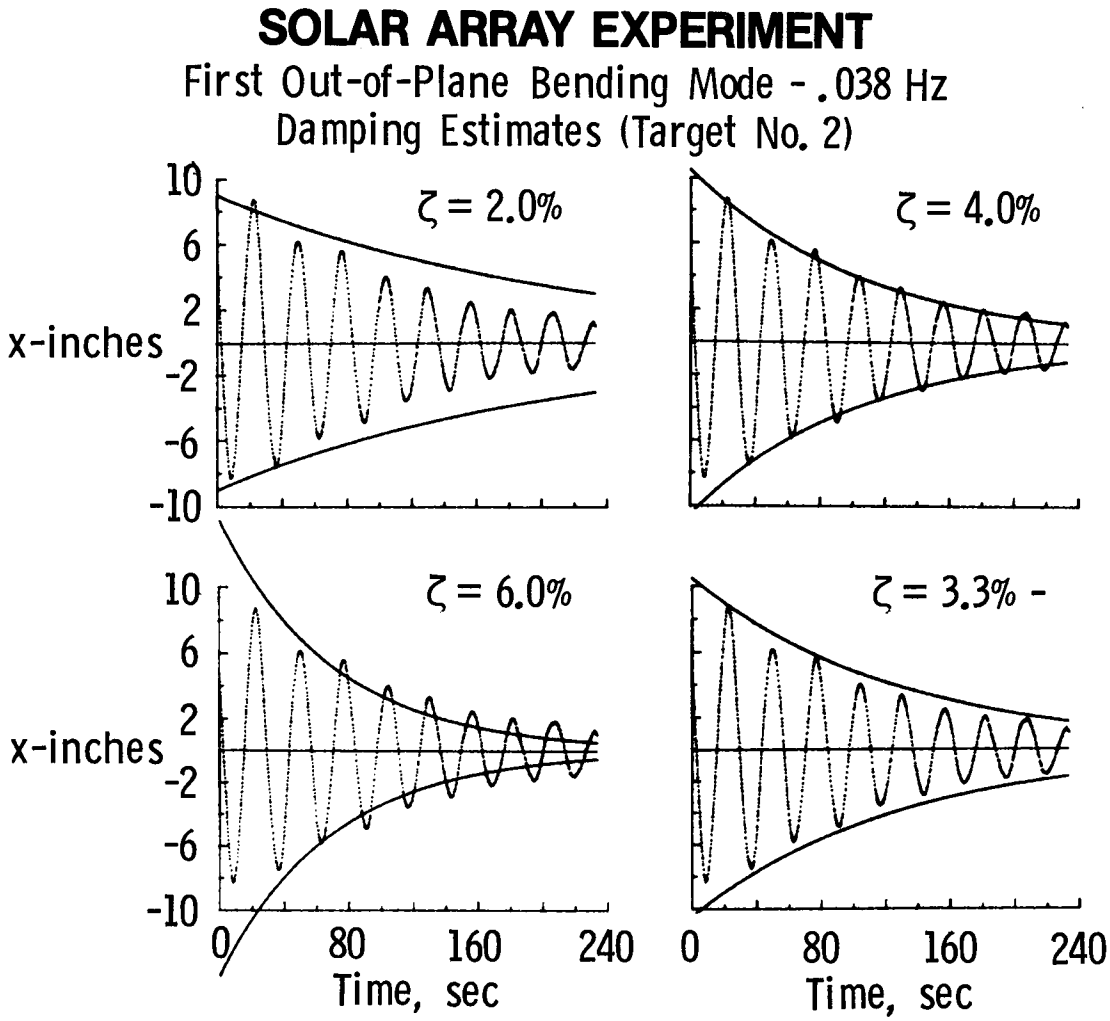

Figure 12.

Figure 13 is a photo of actual video images taken from all four cameras during a dynamic test at 70% extension. For this test, the CCTV cameras were configured for higher coverage than in the previous test shown in Figure 8. The wider field of view covers approximately 50% of the array from the top down and allows a better determination of mode shape.

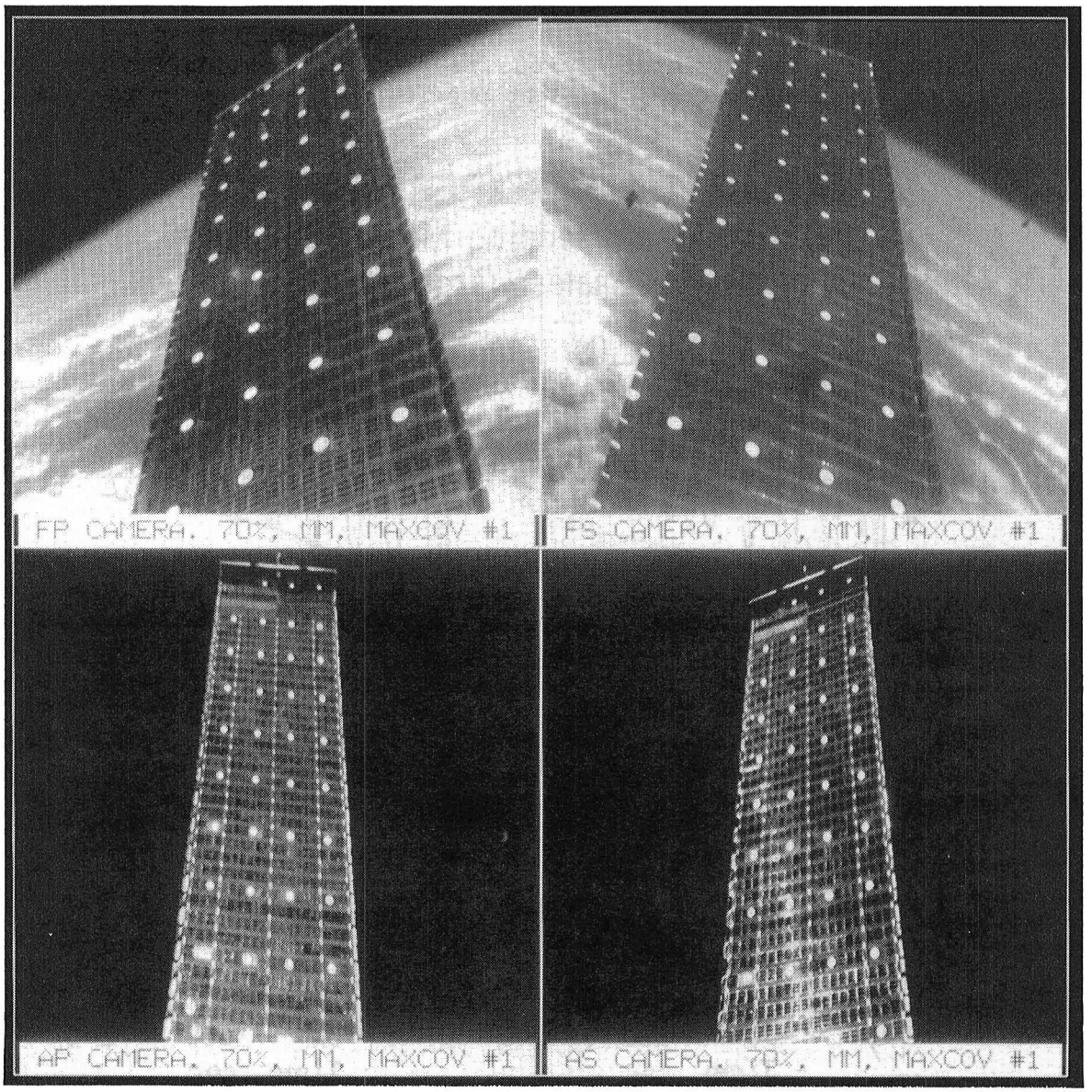

Figure 13.

The dynamic test illustrated here is a test at 70% extension in which the input was designed to excite multiple modes. Figure 14 is a plot of raw data out of the video processing system for a selected target from one camera. One can readily see from the obvious beat frequency that there is more than one mode active in the solar array response. Note that this is two-dimensional data only and the coordinates shown are in the image plane of the CCTV camera and not in orbiter coordinates. Again, the data record runs continuously from the pre-excitation quiescent period, through excitation, into the free-decay period.

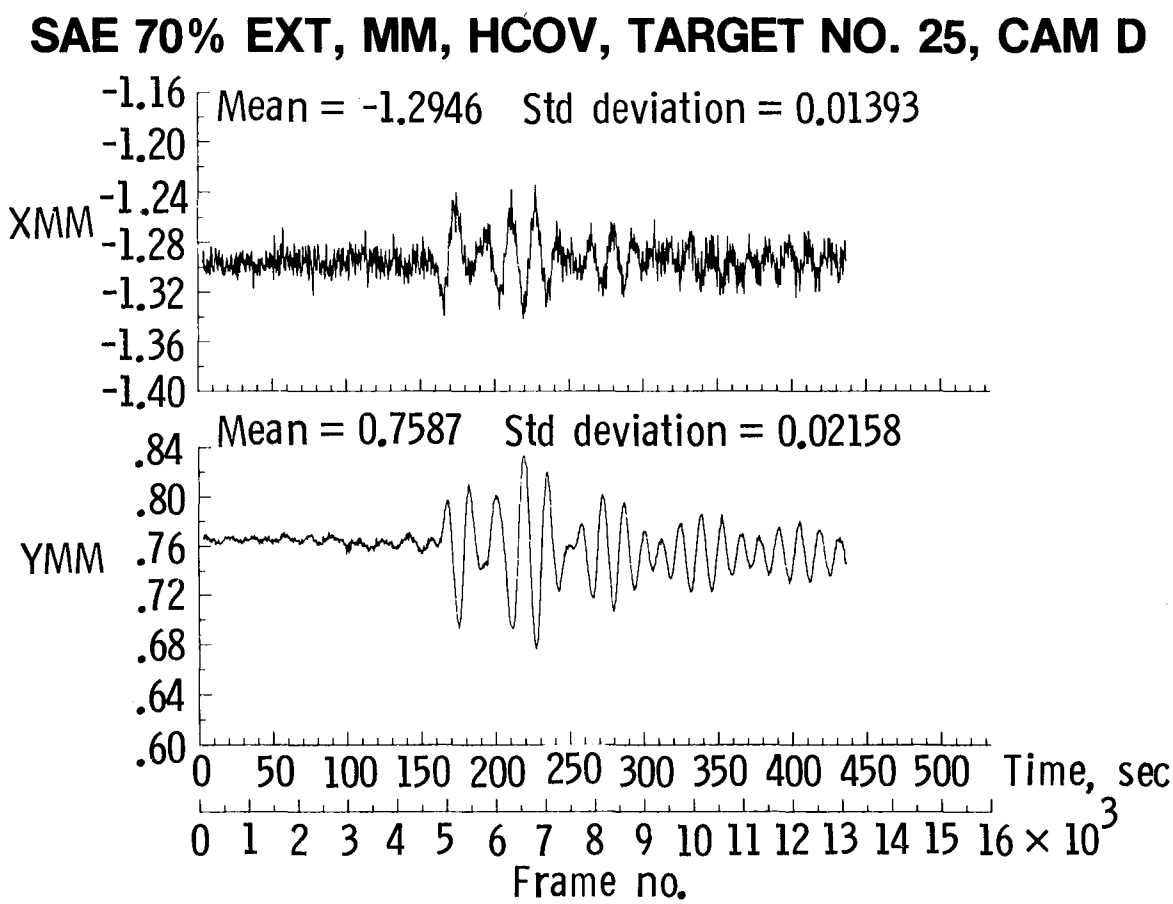

Figure 14.

After the triangulations were done, standard FFT analysis was applied resulting in the frequency plot shown in Figure 15. Indeed, more than one frequency has been identified, and again they are very close to the predicted frequencies. ERA techniques are still being applied to this data to determine mode shapes and damping factors for each mode.

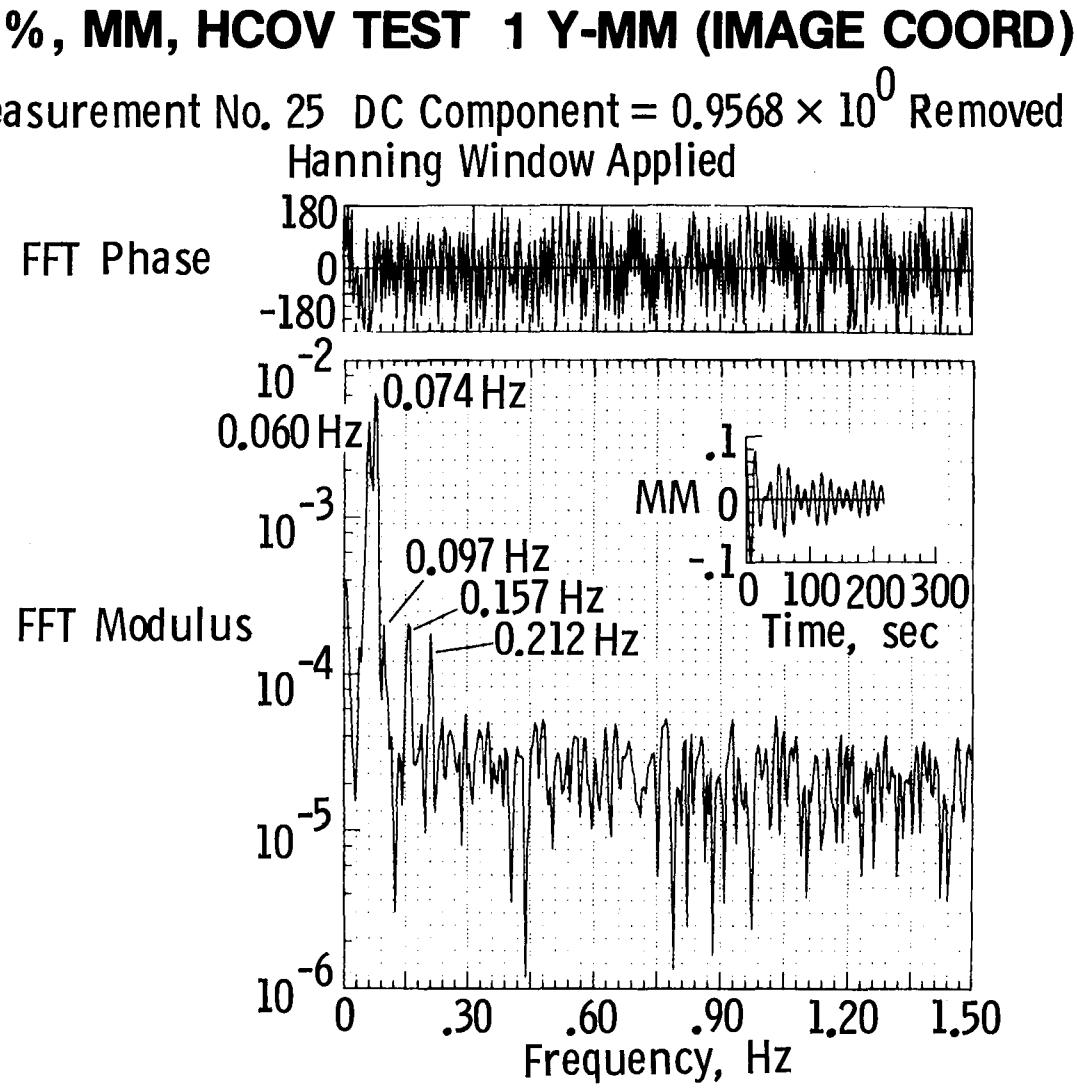

Figure 15.

Figure 16 is a plot of raw data from the video analysis of another test at 70% extension. For this test the inputs were chosen to excite primarily out-of-plane bending. Again, this plot shows target motion in the image plane of the CCTV camera. Triangulations have not yet been done of this data, but if the motion indicated on the camera image plane is compared with that shown in Figure 9 for a similar test at 100% extension, it is obvious that the displacements at 70% extension are significantly less.

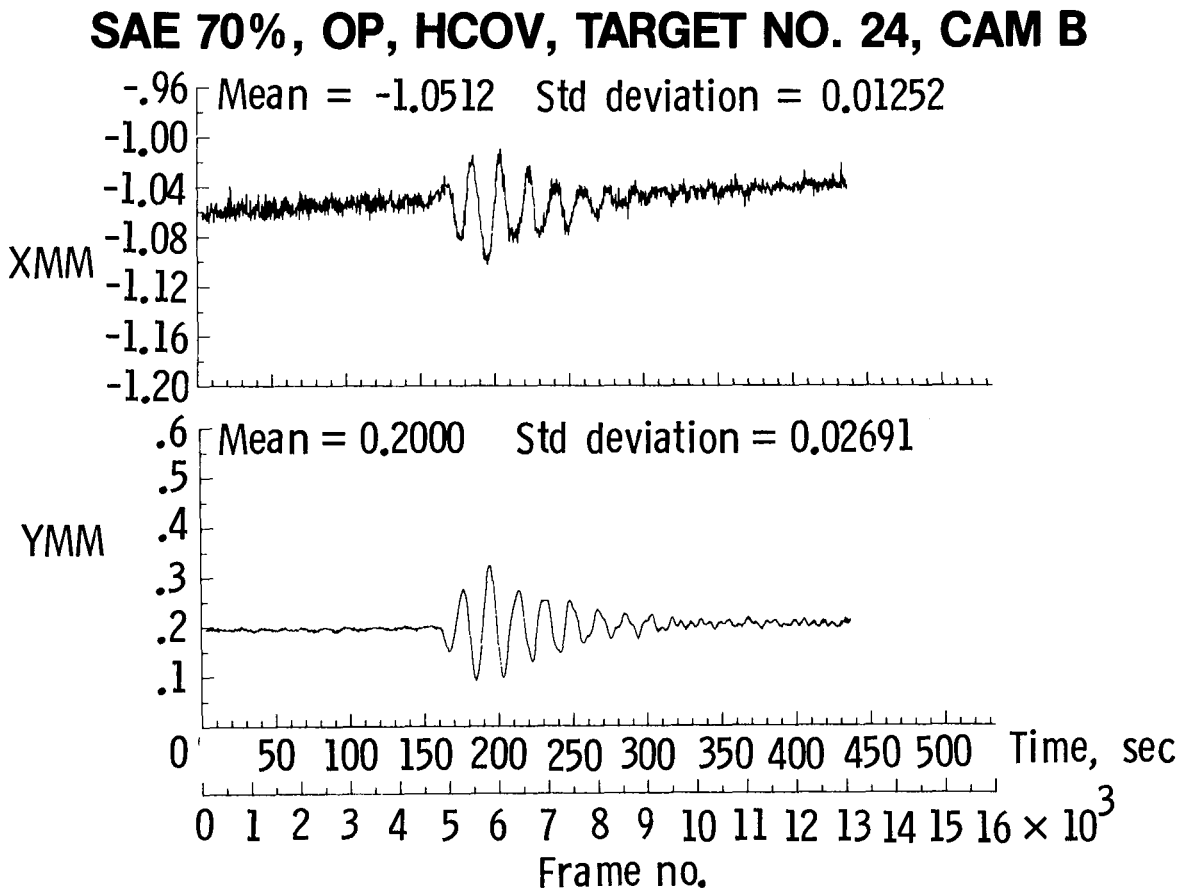

Figure 16.

Figure 17 is another raw data plot, this time from a test at 70% extension with inputs chosen for in-plane excitation. The apparent larger displacements are due to an automatic change in scale by the plotting machine and not to actual increases in motion.

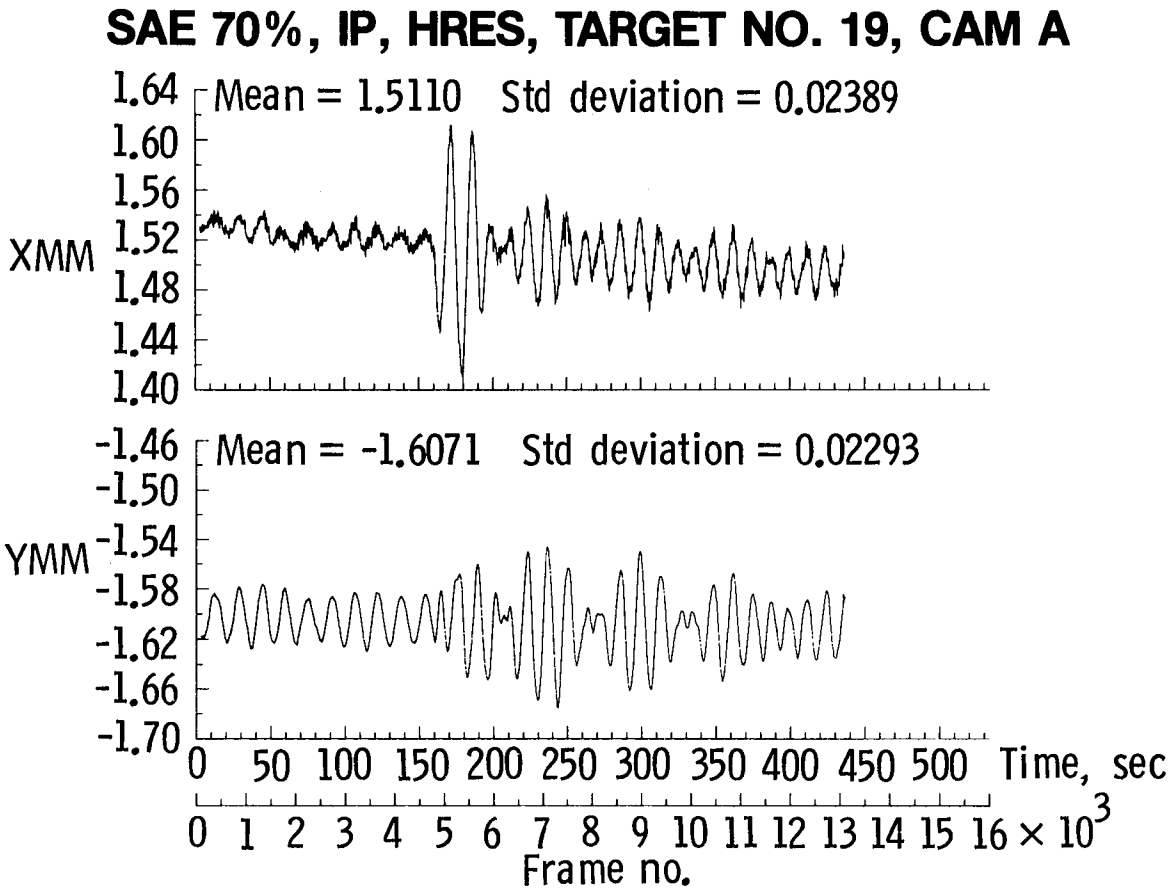

Figure 17.

Figure 18 is a raw data sample from a test at 100% extension with inputs selected to excite multiple modes. While it is not as obvious as some previous tests illustrated, there is more than one mode present. Note that this data happens to be shown in pixel dimensions instead of millimeters. This is merely an option of the video analysis routines and has no particular significance other than to indicate that the motion plotted is in the image plane of the CCTV camera. This figure and the preceding two figures have been presented to illustrate the varied nature of responses recorded from different dynamic tests. Data reduction and analysis from these are still in process.

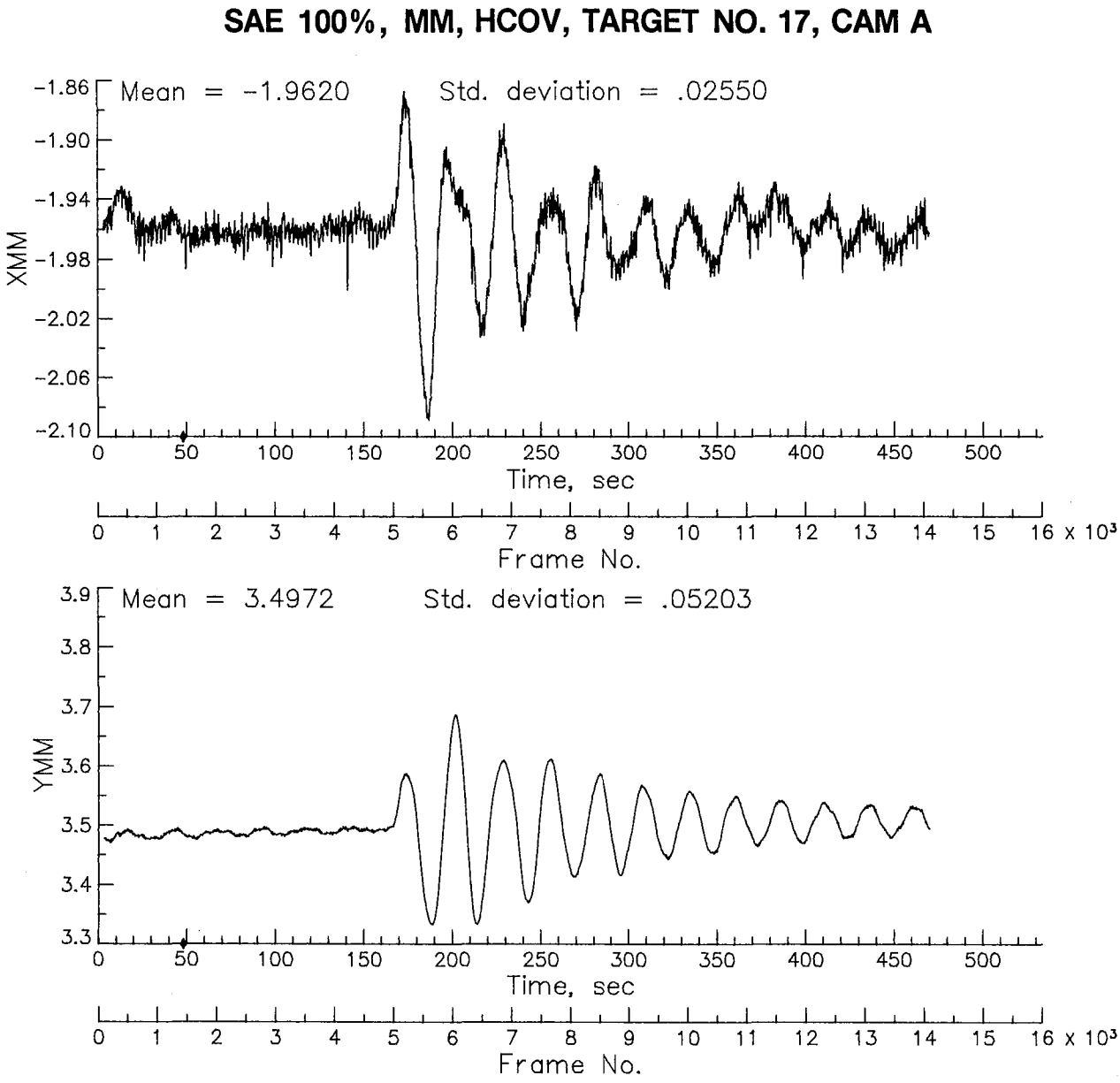

Figure 18.

There are some difficulties encountered when using natural lighting in continuously operating optical measuring devices. Illustrated in Figure 19 are extraneous reflections from other objects or areas. The two images shown are from different portions of the same video record of a test at 70% extension. In the image on the left there is good contrast and distinct targets can be seen in most cases. This image is relatively easy to analyze. The image on the right occurs later in the same videotape and has numerous extraneous reflections which, in some cases, almost obscure a target. This image presents more of an analysis problem. Because of the orbital geometry and the shuttle's movement along the orbital path, the angles of incidence of sunlight and earth albedo continually change. This causes the extraneous reflections to move across the array as time progresses. Each camera will see the same extraneous reflection at a different image location at the same time. In the video recordings analyzed thus far, only the aft cameras have had any noticeable problem with these extraneous reflections.

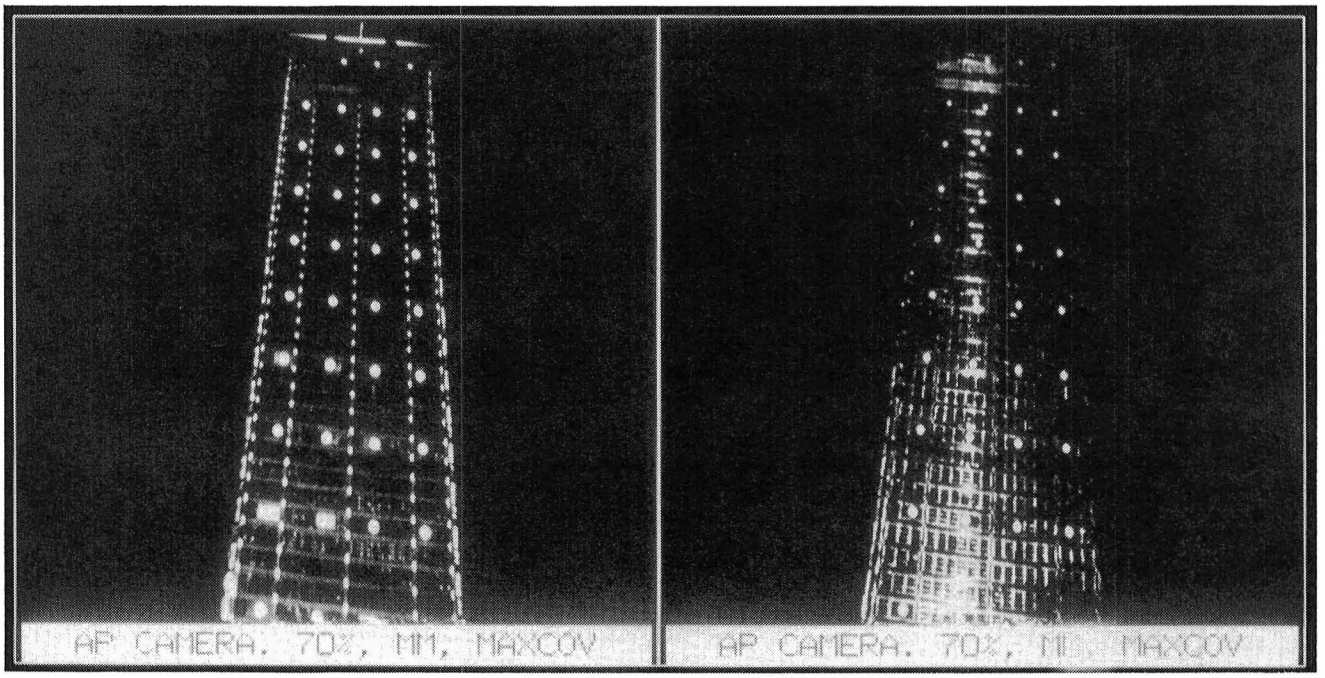

Figure 19.

Figure 20 is a raw data plot from the same video data tape the previous images were extracted from, and in fact includes those two images. Notice the anomalies that occur at about 350 seconds. These anomalies are caused by an extraneous reflection that moves within the target search area and causes an offset in the calculated target location. There are several ways in which to handle this situation. Probably the easiest is simply to examine each data plot and delete those data points that are obvious anomalies. Since all four cameras see the targets from different angles, the anomaly does not occur at the same time in each video recording. This means that short segments can be deleted from one camera, and three cameras still provide coverage. Such deletions of short segments result in somewhat lower resolution, but even the reduced resolution is adequate for the analysis. Another possibility is to exercise an option in the triangulation software for automatic rejection of data based on a priori assumptions. The net effect of this option is also to slightly reduce resolutions. A third option, which has not been attempted yet, is to operate the video processing system in a manual mode and manually determine (via cursor operation) the centroids of targets temporarily affected adversely by extraneous reflections. The preliminary analysis has been performed with satisfactory results by having the triangulation routines automatically reject anomalous data points.

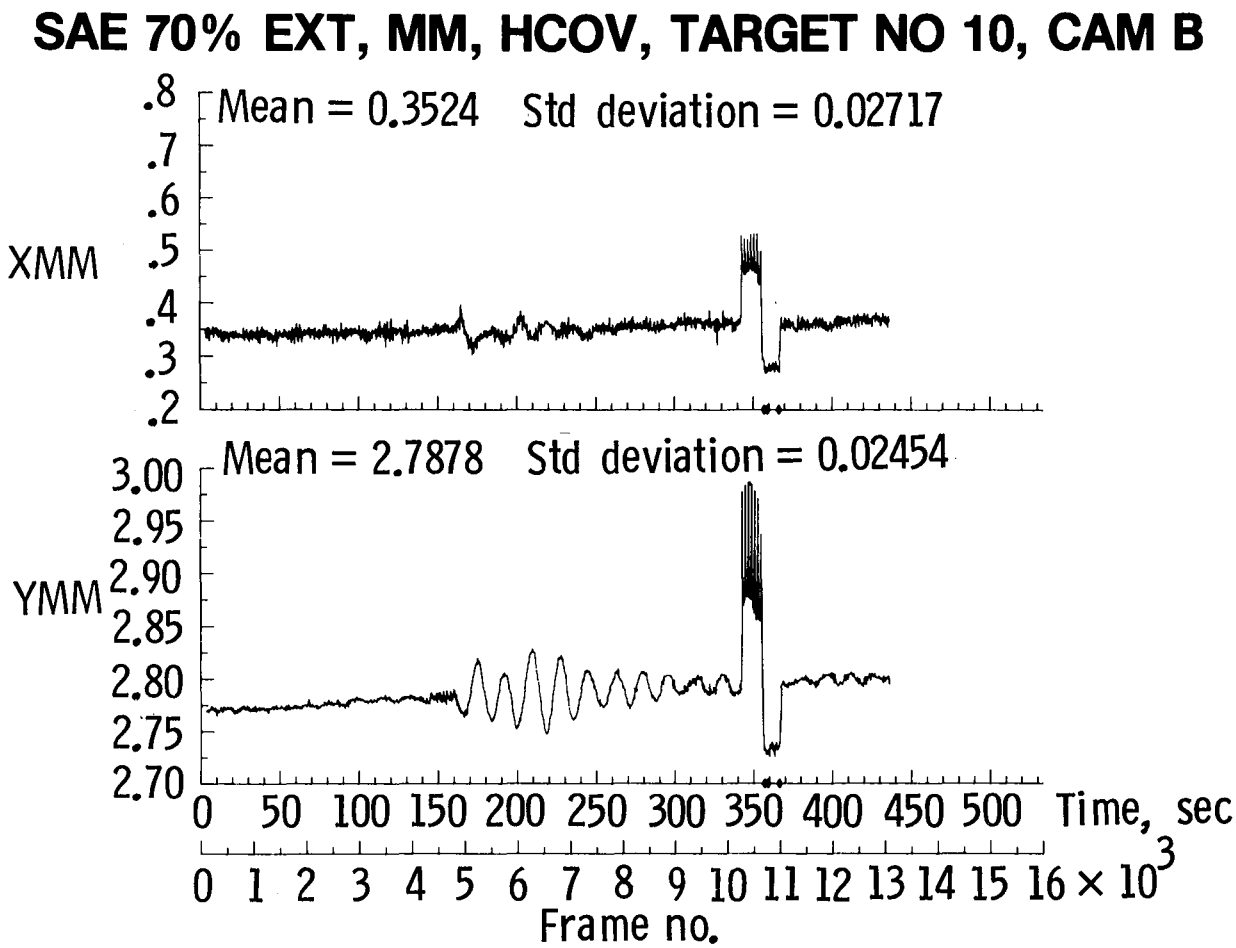

Figure 20.

Some comments on accuracies are appropriate at this point. It should be pointed out that there are no fixed reference targets in the field of view of any camera for these orbital tests. Therefore, the standard calibrations cannot be done as they are when photogrammetric techniques have been used in static measurements on the ground. What we are measuring is the relative displacements of targets in three-dimensional space, and it is not necessary to relate each measurement point to some absolute reference point. Table 3 presents RMS accuracies for displacement measurements from the out-of-plane test at 100% extension illustrated in Figure 10. These numbers are determined by the STARS system from the statistical scatter of the triangulated data. They represent the resolution capability of the video photogrammetric measurement technique as indicated from the statistics of the data itself. For measurements in the X and Y directions, the resolution capability is less than 0.04 inches. The reduced resolution in the Z direction is because of the configuration geometry in which most of the Z displacement is along the optical axis of the cameras and therefore cannot be detected. In the solar array experiment, there is very little displacement along the Z axis so this does not present a problem. Note that the accuracies are presented in shuttle orbiter coordinates.

1-SIGMA RMS DISPLACEMENT MEASUREMENT ACCURACIES

100% EXTENSION - HIGH RESOLUTION - PRIOR TO OUT-OF-PLANE EXCITATION
20 TARGETS SEEN BY FOUR CAMERAS

SIGMA X (IN.)	SIGMA Y (IN.)	SIGMA Z (IN.)
0.039	0.038	0.128

Table 3.

To illustrate what the resolution capability means in terms of array motion, we extracted a portion of the video data from the quiescent period prior to the 100% test that was illustrated in Figure 10. This data is plotted in Figure 21. When analyzed using the STARS system the results were 0.59-inch peak-to-peak displacement in the orbiter X direction and 0.175-inch peak-to-peak in the Y direction. This analysis quantified what had been observed in the data plots in general; that is, the small, "steady-state" motions of the solar array during the so-called "quiescent" period. In the tests we have analyzed thus far, we have always seen some "steady-state" or residual motion of the array. No explanations are offered as to what causes this motion. We do plan to do some frequency and modal analyses of data from these quiescent periods at a later date with the hope of gaining insight into the possible causes of this motion.

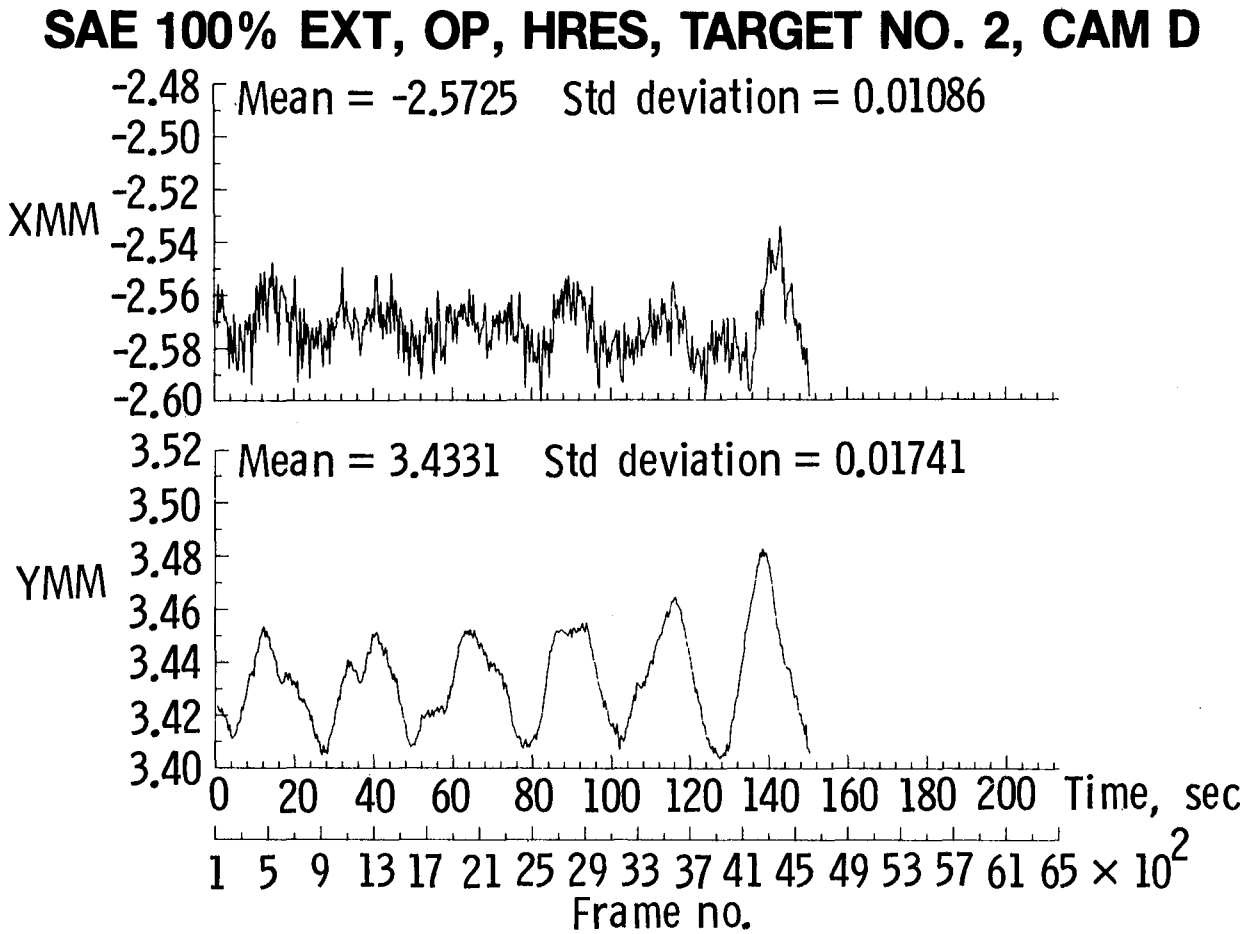

Figure 21.

SUMMARY OF PHOTOGRAMMETRY RESULTS

(AS OF DECEMBER 3, 1984)

THESE OBSERVATIONS ARE BASED ON PRELIMINARY ANALYSIS OF APPROX. 125 OUT OF OVER 900 TIME HISTORIES.

- WE SEE GOOD AGREEMENT WITH PREDICTED FREQUENCIES.
- DAMPING IS SIGNIFICANTLY HIGHER THAN WAS ASSUMED FOR PREDICTIONS.
- THERE IS A STATIC OFF-SET AND TWIST IN THE DEPLOYED ARRAY.
- THE ARRAY HAS NOT YET BEEN OBSERVED TO BE STATIONARY,BUT APPEARS TO HAVE A STEADY-STATE RESIDUAL MOTION.
- WE ARE GETTING SUB-PIXEL RESOLUTION OF TARGET CENTROIDS IN THE VIDEO ANALYSIS, APPROACHING 0.1 PIXEL.
- GOOD ACCURACIES FOR THE 1-SIGMA RMS DISPLACEMENT MEASUREMENTS; LESS THAN 0.04) INCH IN X- AND Y-DISPLACEMENTS.

REFERENCES

1. Brown, Duane C.: Application of Close-Range Photogrammetry to Measurements of Stuctures in Orbit, Vol. 1 and 2, Geodetic Services Inc. Technical Report Number 80-012, 1980.

2. Juang, Jer-Nan, and Pappa, Richard S.: An Eigensystem Realization Algorithm (ERA) for Modal Parameter Identification, JPL Workshop on Identification and Control of Flexible Space Structures, San Diego, CA, June 1984.

Page intentionally left blank

LARGE ANTENNA CONTROL METHODS: CURRENT STATUS AND FUTURE TRENDS

G. Rodriguez, Y. H. Lin, and M. H. Milman
Jet Propulsion Laboratory
Pasadena, California

Large Space Antenna Systems Technology - 1984
December 4-6, 1984

LARGE SPACE ANTENNA MISSIONS

Various antenna sizes have been considered for each of the missions shown in the chart below. Typically, the LMSS* and SSS require antennas of 50 to 120 meters in diameter. The VLBI QUASAT antenna is approximately 15 to 20 meters in diameter, and the LDR is about 20 meters in diameter. The highest operating frequency is about 1 GHz for LMSS or SSS, 20 GHz for the VLBI QUASAT, and 10,000 GHz for LDR.

MISSION	LMSS/SSS	VLBI	LDR
SIZE (M)	15-122	15-40	10-30
FREQUENCY	806-1090 MHz	1.7-22 GHz	300-10,000 GHz
TARGET YEAR	1995	1990-2000	2010

* LMSS - LAND MOBILE SATELLITE SYSTEM (COMMUNICATIONS)

SSS - SURVEILLANCE SATELLITE SYSTEM (AIRCRAFT SURVEILLANCE)

VLBI - VERY LONG BASELINE INTERFEROMETER (RADIO ASTRONOMY)

LDR - LARGE DEPLOYABLE REFLECTOR (IR, SUBMILLIMETER ASTRONOMY)

TARGET LARGE ANTENNA MISSIONS

This paper addresses, from a somewhat broad perspective, current methods for control of large antennas, as well as future trends required for improved performance. Some of the target missions in which these methods would be used are shown below: the Land Mobile Satellite System (LMSS) for communications; the Satellite Surveillance System (SSS) for aircraft traffic control; the orbiting Very Long Baseline Interferometer (VLBI), or QUASAT, for radio astronomy; and the Large Deployable Reflector (LDR) for IR and submillimeter astronomy.

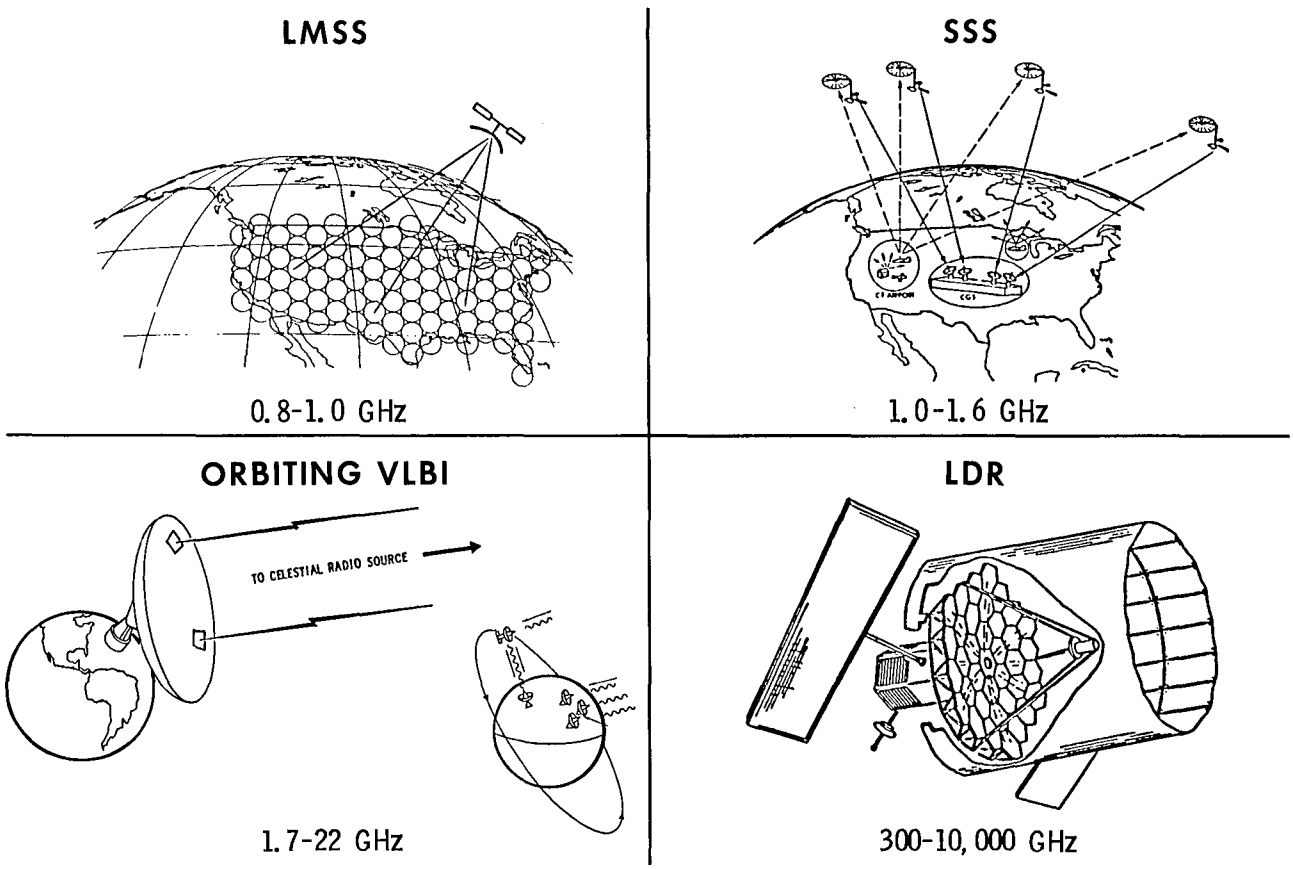

ANTENNA CONTROL REQUIREMENTS

Large antenna missions impose three principal requirements on the control system, i.e. pointing, surface accuracy, and feed/reflector relative stability. The first two requirements are illustrated below: the antenna pointing requirement for LMSS or SSS is about one tenth of a degree, and the surface accuracy required for these two missions is between 1 to 10 mm. For VLBI QUASAT, the pointing requirement is about 60 arc second, and the surface accuracy requirement is a fraction of a millimeter. The LDR has the most stringent requirements of them all, with pointing at a few hundredths of an arc second, and surface accuracy at a couple of microns.

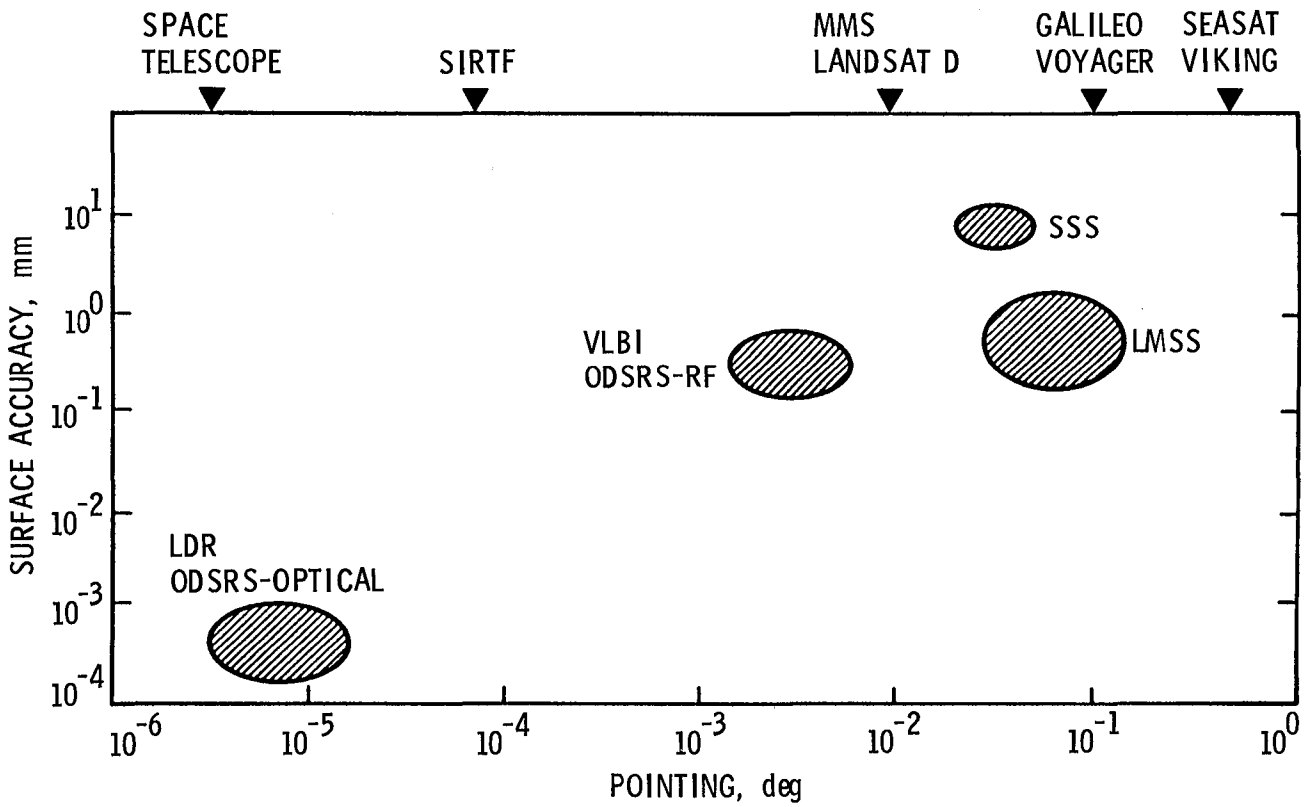

ANTENNA WITH RIGIDLY ATTACHED FEED

The third type of control requirement is illustrated below. The relative motion between the antenna feed and the reflector must be maintained or controlled so that the antenna electromagnetic performance is properly met.

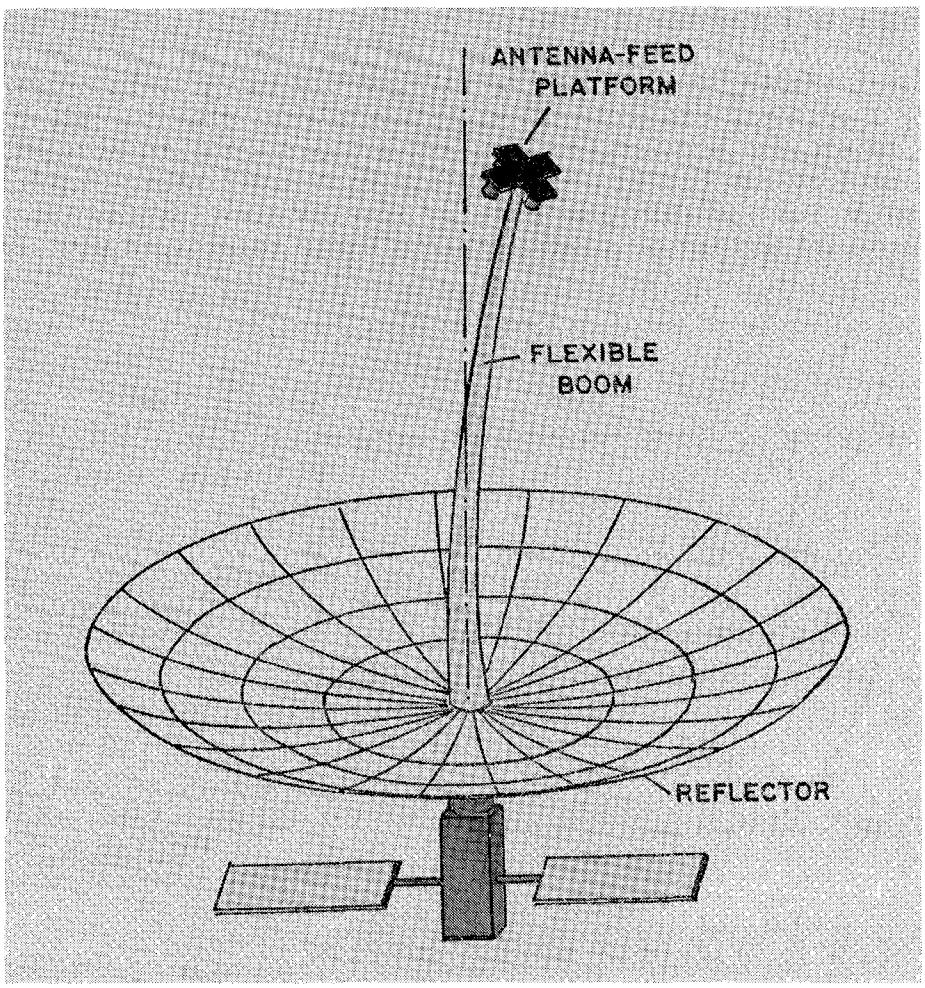

CONTROL SENSITIVITY SUBJECT TO PARAMETER ERRORS (WRAP-RIB)

To meet control requirements, three classes of control systems have been analyzed for control performance comparisons.

System 1 reflects current attitude control technology with control sensors and actuators located at the rigid spacecraft bus. The flexible dynamics associated with the L-shaped boom and the dish (reflector) can only be inferred from the pre-flight dynamic model loaded into the control computer. System 2 is System 1 plus an additional sensor to take measurements of dish vibrations at multiple locations. The distributed sensing of the dish will provide dynamic information about the dish and the L-shaped boom to the control computer. Control is also performed at the spacecraft bus. System 3 is System 2 plus an extra control authority at the hub of the reflector, realizing a control system with actuation at two locations which are not rigidly connected.

Typical corresponding performance is illustrated in the left portion of the figure. System 3 performs one order-of-magnitude better than the other 2 systems, signifying the importance of distributed sensing and control to large flexible space antennas. The performance curves also indicate that model errors will degrade control performance and possibly cause system instability. System identification is needed to reduce model errors or system uncertainties associated with large antennas.

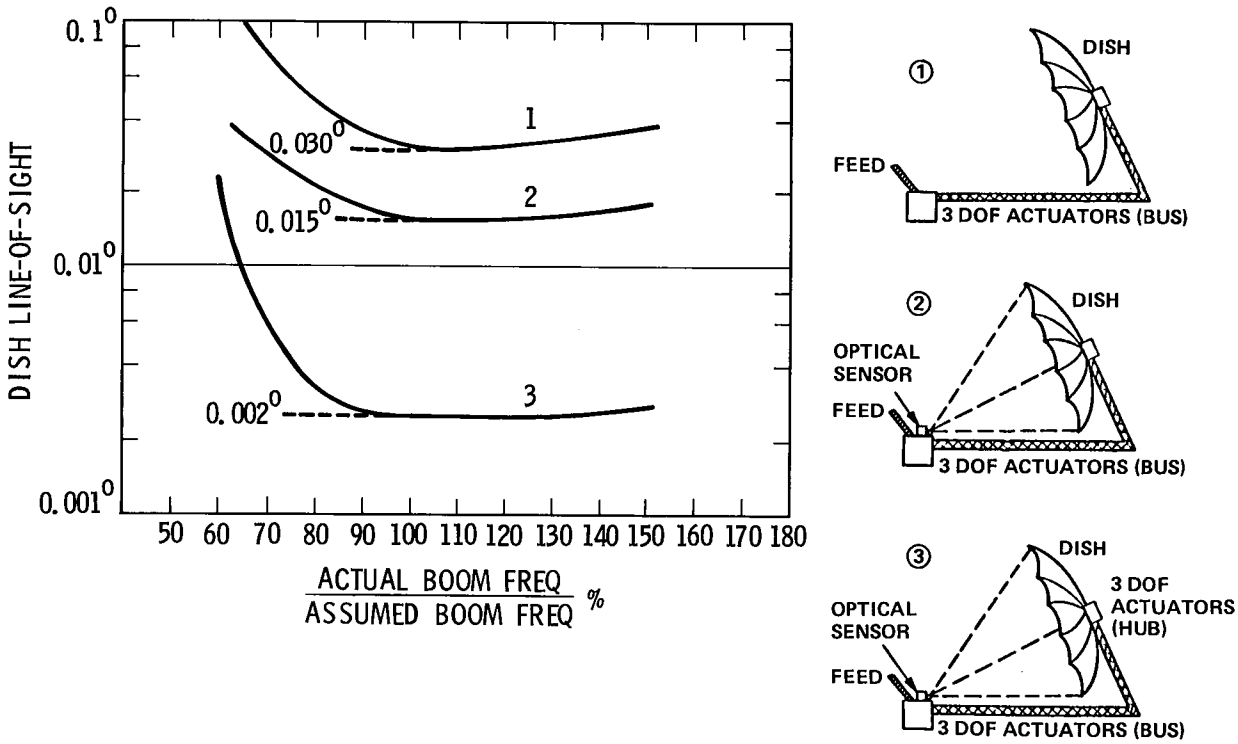

ANTENNA WITH DUAL DECOUPLER

The technology of distributed sensing and control can also be beneficial in maintaining the relative stability between the antenna feed implemented along the flexible column of the hoop/column antenna. The vibrations of the column would be isolated from the feed, leaving the relative feed/reflector motion small.

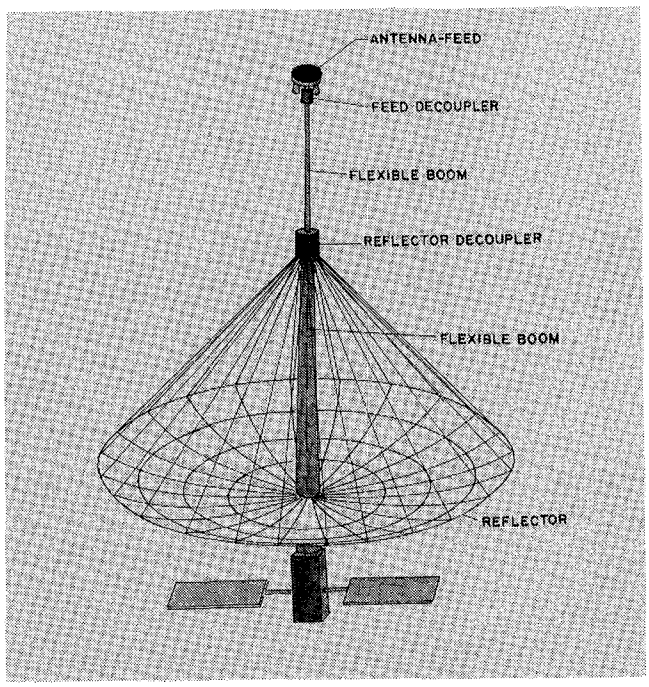

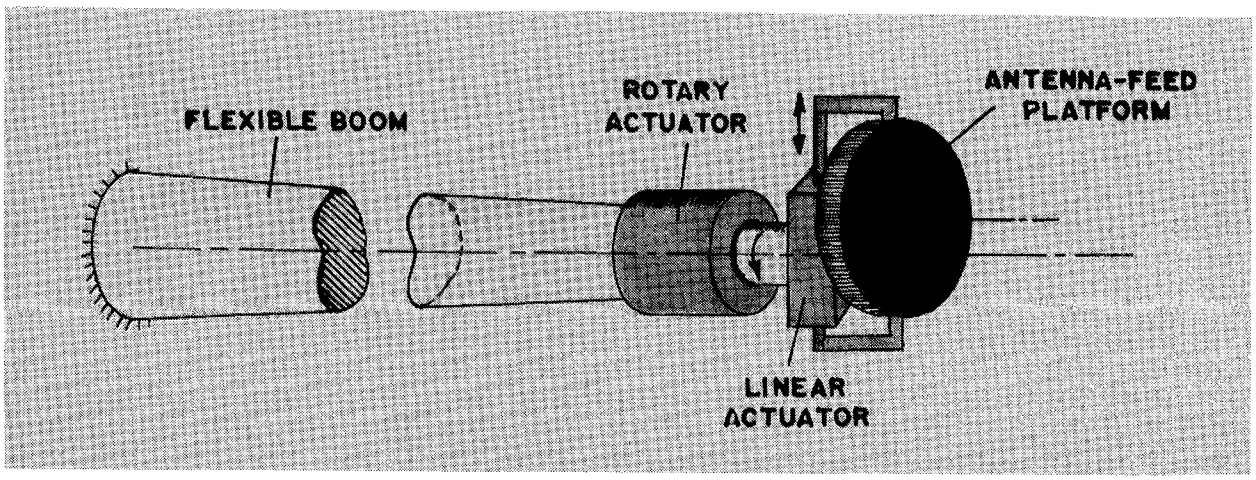

REDUCED FEED ROTATION CONTROLLED DECOUPLING

This chart shows that the column is divided by two decouplers into two segments of lengths ℓ_1 and ℓ_2 respectively. Even though the column rotation is about 0.02 radians for the period shown, the feed rotation is kept about two orders-of-magnitude smaller.

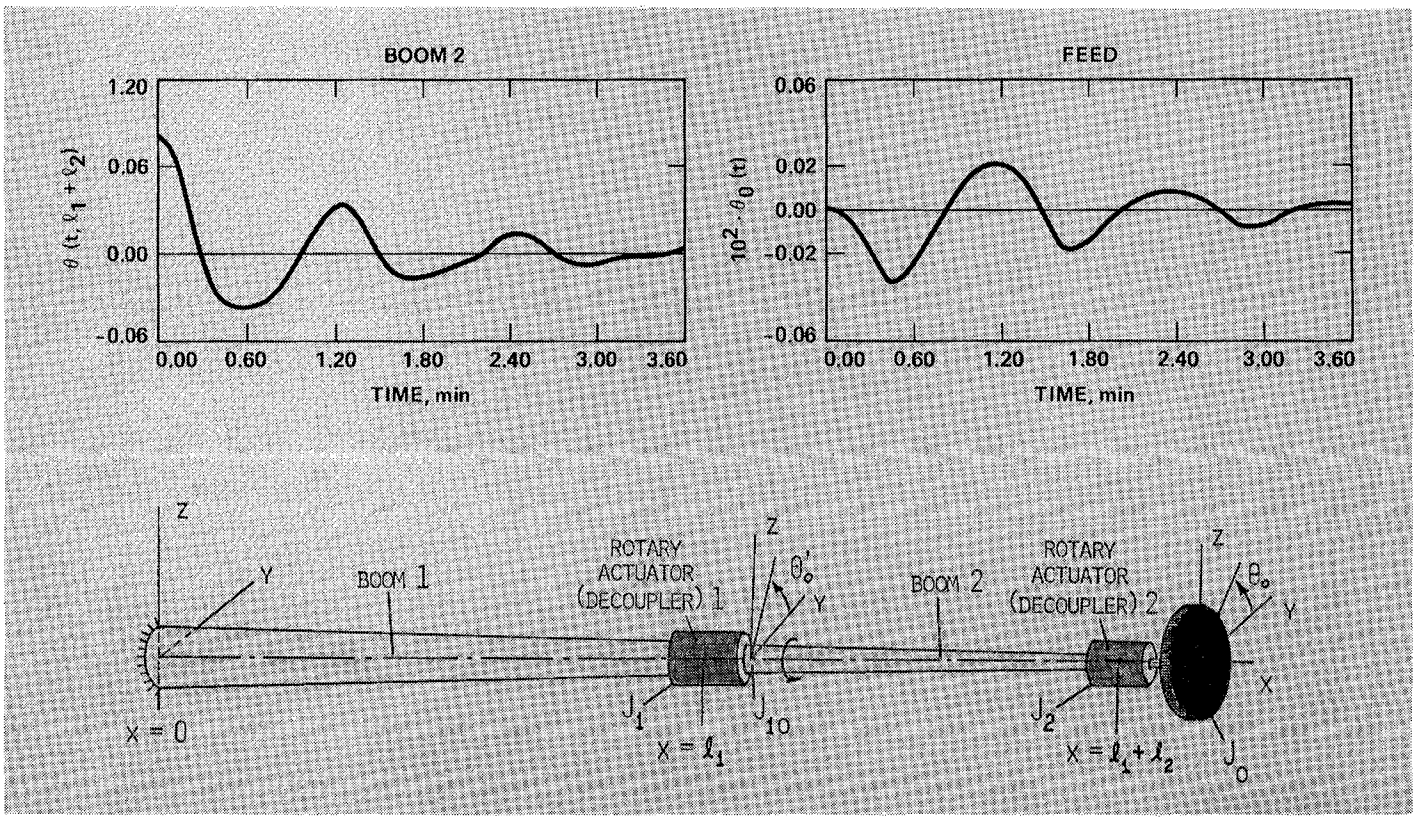

CURRENT DESIGN APPROACH

Currently, control design follows the procedure below: the large flexible antenna is modeled by high-order finite-dimensional equations, and, for practical reasons, the control law is developed based on a truncated low-order model. However, the control performance must be verified with the high-order model. Design iteration becomes inevitable and frustrating. The difficulties are mainly caused by the philosophy of the current approach, which is to truncate the model even before control design begins.

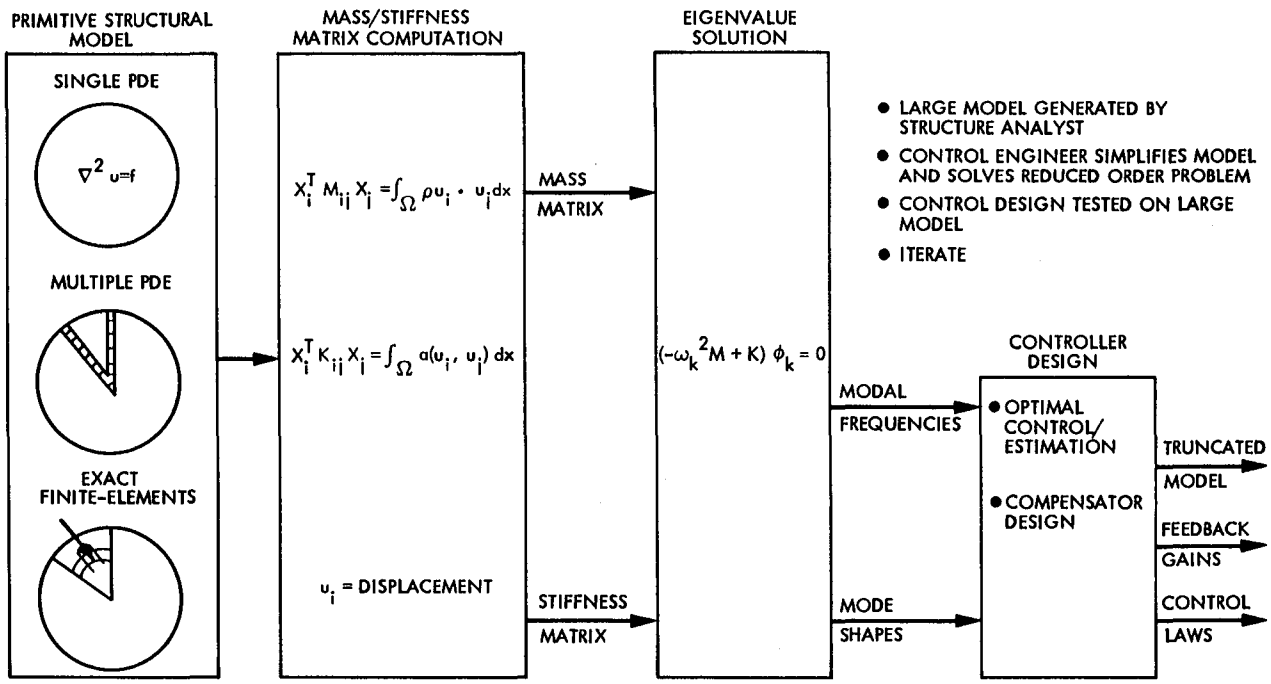

DRAWBACKS OF CURRENT METHOD

- STRUCTURE MODELING OBJECTIVES INDEPENDENT OF CONTROL OBJECTIVES
- MODEL ORDER SELECTION IS AN AD HOC PROCESS
- DIFFICULT TO OBTAIN APPROPRIATE SIMPLIFIED DESIGN MODELS
- NO STANDARD OF COMPARISON FOR CONTROLLERS DERIVED FROM DIFFERENT MODELS
- SYSTEM LEVEL CLOSED LOOP STUDIES BECOME PROHIBITIVE (MODEL-CONTROL DESIGN INTERACTIONS DIFFICULT TO ACCOUNT FOR)

- LARGE MODEL GENERATED BY STRUCTURE ANALYST
- CONTROL ENGINEER SIMPLIFIES MODEL AND SOLVES REDUCED ORDER PROBLEM
- CONTROL DESIGN TESTED ON LARGE MODEL
- ITERATE

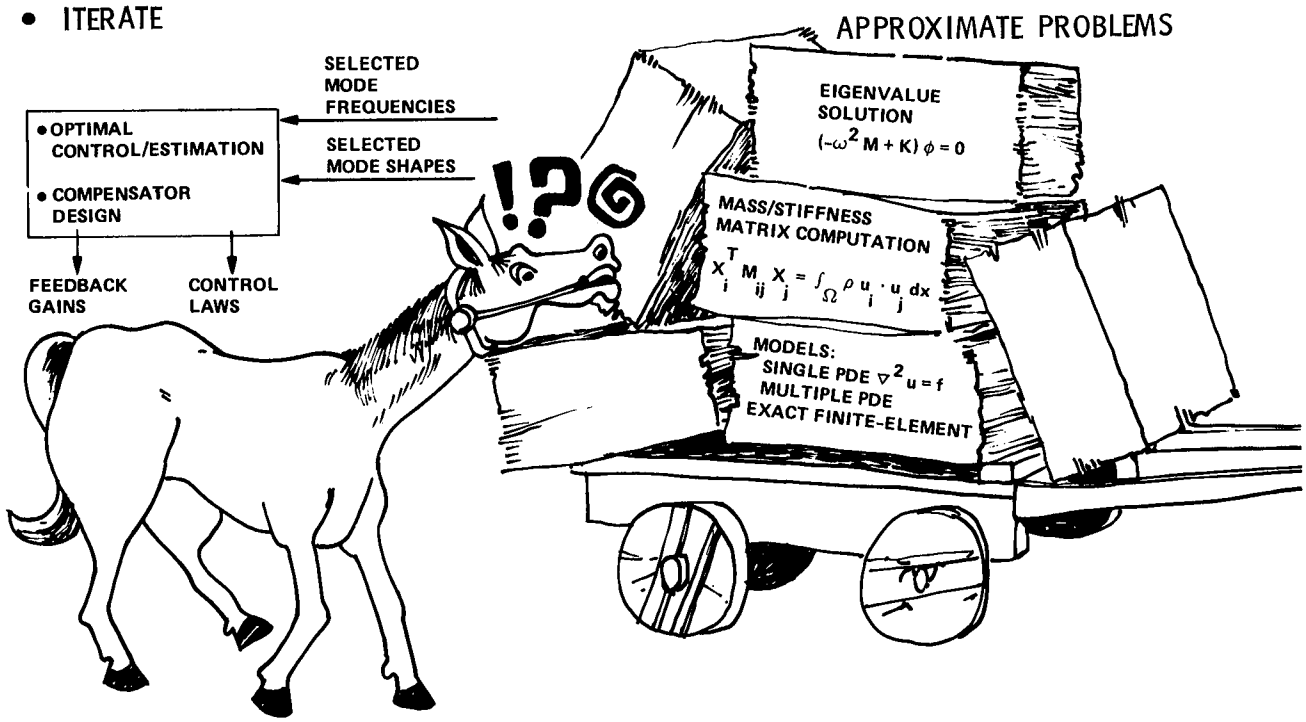

UNIFIED DESIGN APPROACH

A new philosophy for control design is embodied in the unified design approach outlined below and on the next page. The problems of structural modeling and of control modeling and design are combined and the corresponding solution is obtained analytically without truncation or approximation. Then, the complete solution is truncated or approximated for practical implementation.

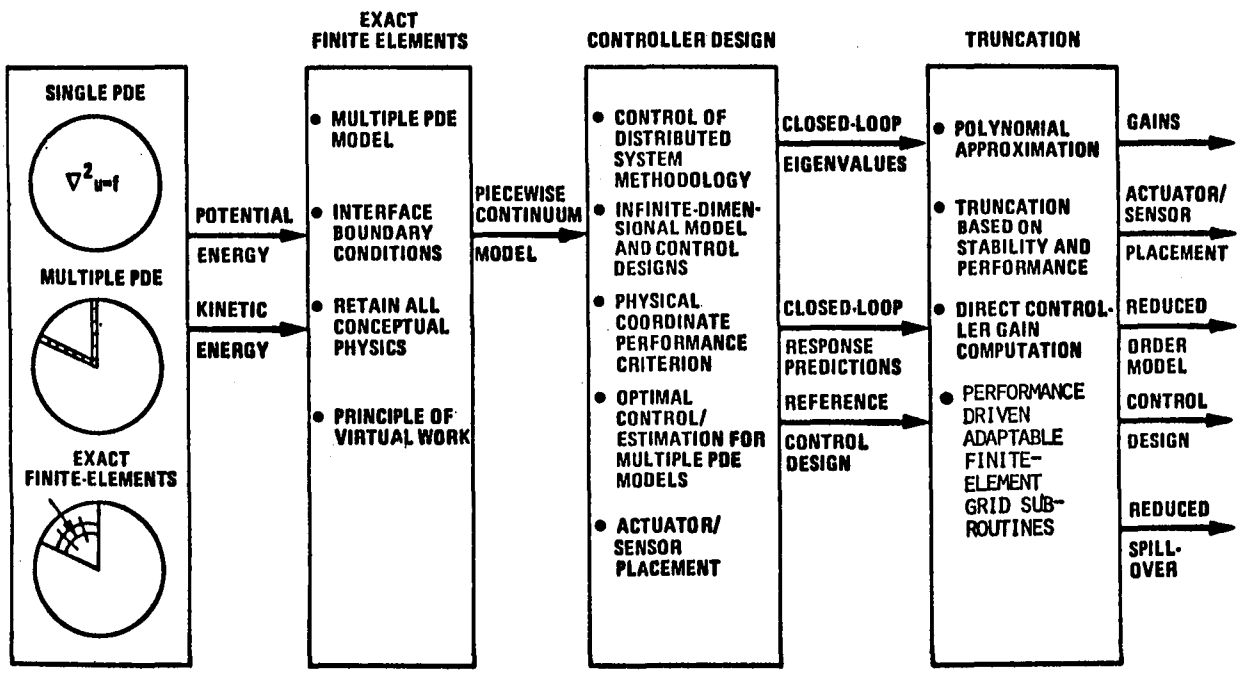

PROJECTED BENEFITS:

- FINITE-ELEMENT MODELS ARE DRIVEN BY CONTROL/STRUCTURE INTEGRATED REQUIREMENTS
- END-TO-END PARAMETRIC STUDIES READILY CONDUCTED
- MODEL TRUNCATION DETERMINED BY CLOSED-LOOP REQUIREMENTS
- POTENTIAL REDUCTION OF SPILLOVER INSTABILITIES
- SIMULTANEOUS OPTIMIZATION OF PARAMETERS

KEY CHALLENGES:

- SOFTWARE TO ASSEMBLE CONTROL-DRIVEN FINITE-ELEMENT MODELS FOR COMPLICATED STRUCTURES DOES NOT CURRENTLY EXIST
- BASIC RESEARCH IN UNIFIED MODELING AND DESIGN TO HANDLE COMPLICATED STRUCTURES

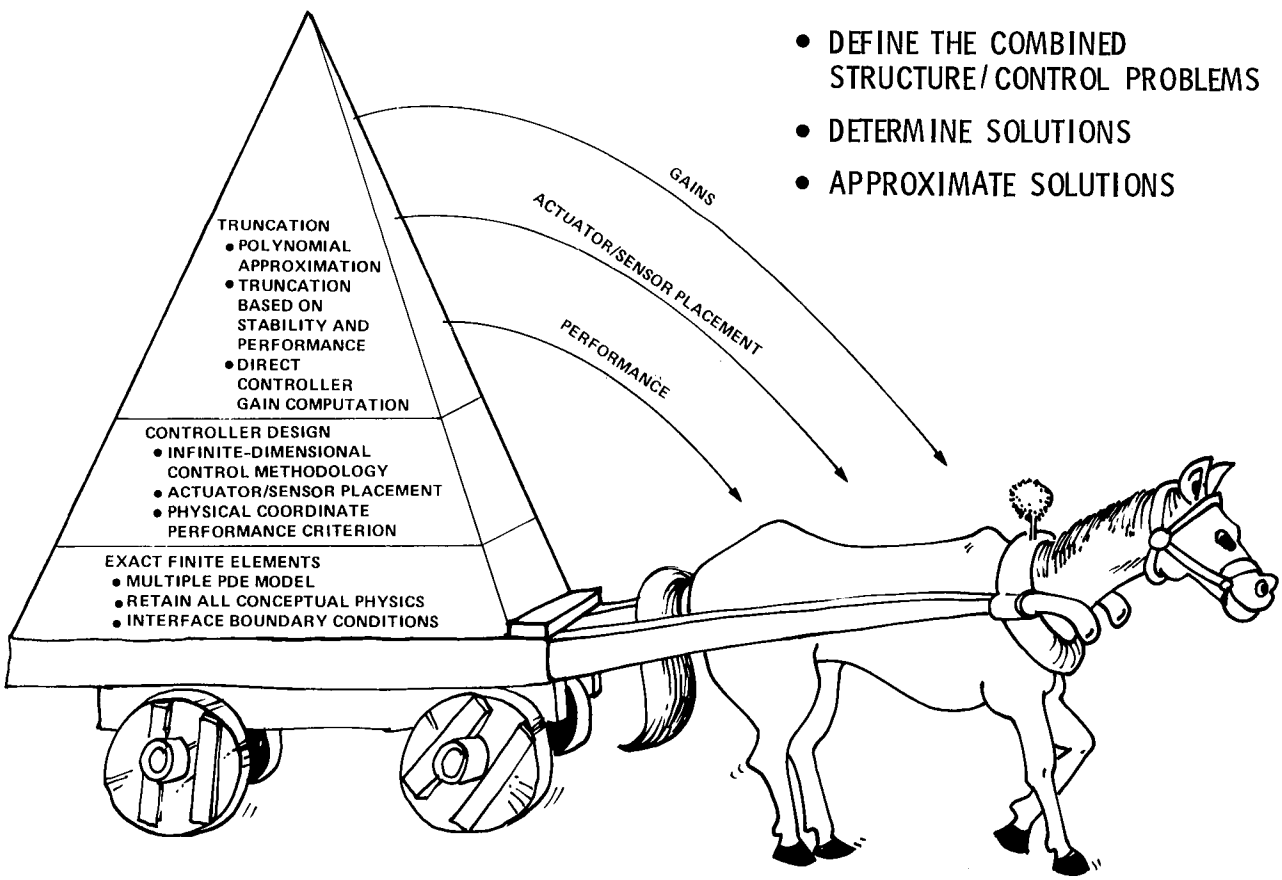

MODEL ORDER SELECTION BASED ON PERFORMANCE OBJECTIVES

The first step in the unified design approach is to determine a finite-element model that is tailored to the control performance objective. This model could be referred to as a control-driven finite-element model. The figure illustrates this idea by using selection of model order as an example. The model order selection can be achieved by taking two separate paths: the left path depicts the use of distributed parameter modeling and design to determine the control gain K without approximation, and the right path illustrates the state-space approximation to the same problem and yields control gain K_n, where n is the order of the model. Note that $K_n \to K$ as $n \to \infty$. Therefore, the model order n can be selected based on the size of the residual $|K_m - K_n|$.

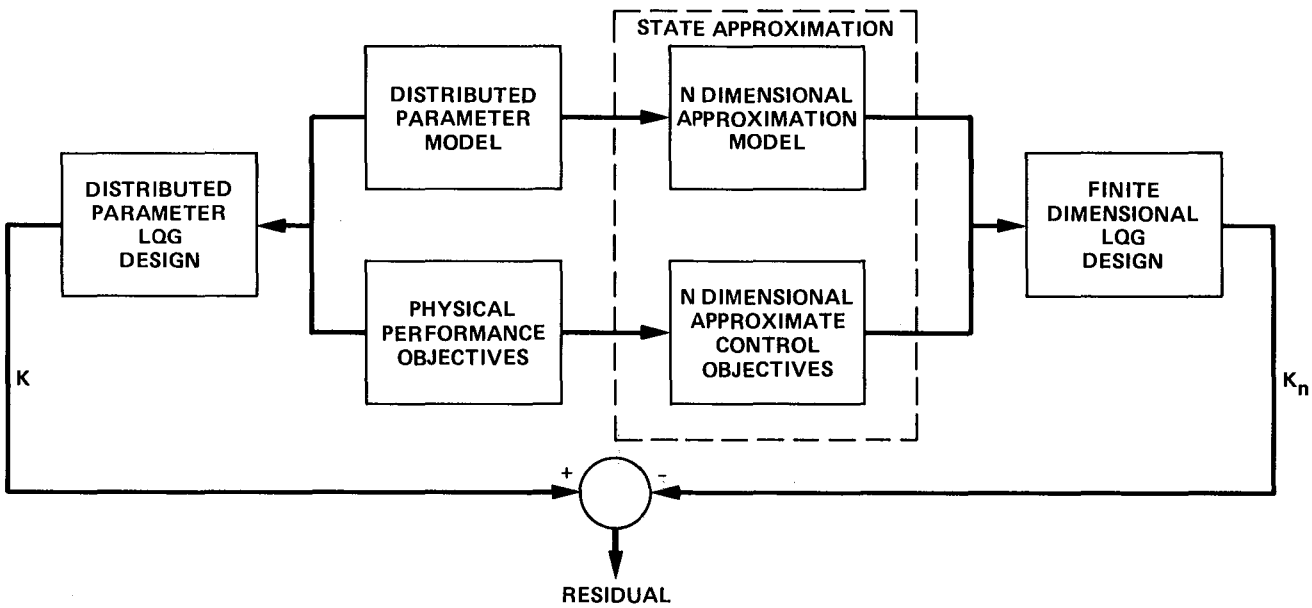

- K = IRRATIONAL TRANSFER FUNCTION
  K_n = RATIONAL APPROXIMATION
- RESIDUAL $\longrightarrow$ 0 AS $n \longrightarrow \infty$
- MODEL ORDER SELECTION BASED ON
  $| K_n - K_m |$

- CHANGING PERFORMANCE OBJECTIVES CHANGES MODEL ORDER SELECTION

COMPENSATION REDUCTION BASED ON PERFORMANCE OBJECTIVES - BALANCED REALIZATION

The large-order model selected from the previous viewgraph will be used to obtain the reduced-order compensator. The indirect reduction approach is given along the top path. This is typical of current methods in which model order is reduced and is followed by compensator design. The direct reduction shown in the lower path reflects the philosophy of the unified approach. The compensator is designed based on the large-order (evaluation) model and truncation is performed on the solution (i.e., the large-order compensator).

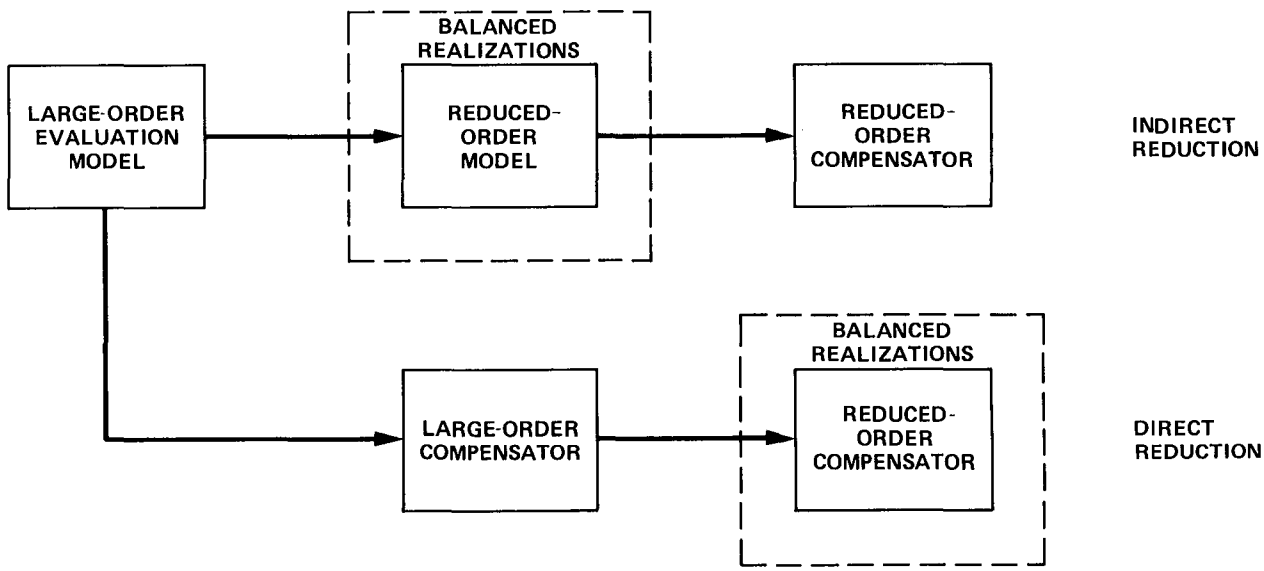

- BALANCED REALIZATIONS - ESTABLISHED AN ORDERING OF SYSTEM STATES WITH RESPECT TO THEIR CONTRIBUTION TO THE INPUT - OUTPUT PROPERTIES OF THE SYSTEM
- MODEL REDUCTION - BASED ON BALANCED REALIZATIONS; RETAINS THE MORE CONTROLLABLE AND OBSERVABLE STATES

ANTENNA MODELING AND CONTROL DESIGN EXAMPLE

The unified approach is applied to an antenna reflector with multiple sensors and actuators for control implementation. The control objective is to maintain antenna pointing and minimize system energy. A 42nd-order model is suitable for the problem based on the residual size of $|K_m - K_n|$.

- PROBLEM - MAINTAIN ANTENNA POINTING AND MINIMIZE SYSTEM ENERGY
- APPROACH - DISTRIBUTED PARAMETER MODELING AND LQG DESIGN

  INFINITE/FINITE DIMENSIONAL MODEL TRUNCATION AND REDUCTION METHODS

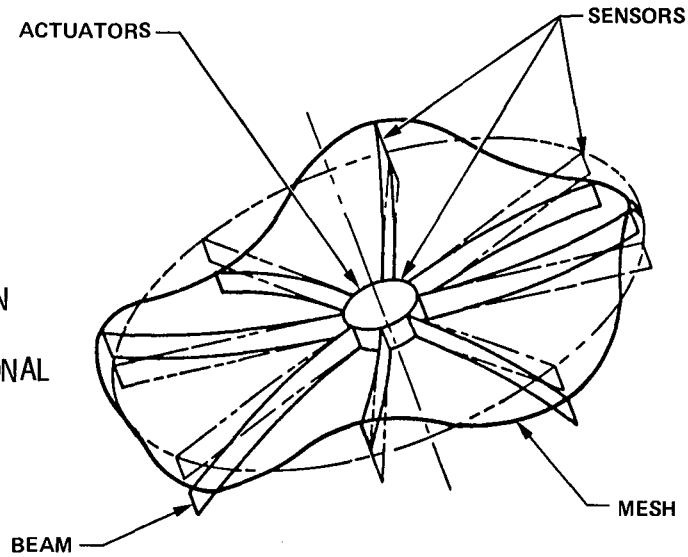

COMPENSATION DESIGN VIA UNIFIED APPROACH

The chart illustrates the benefits to be gained by using a unified approach in providing a systematic procedure for model truncation. If the unified approach is used, 34th- and even 22nd-order compensators will suffice to retain the most significant dynamics of the closed-loop antenna control system. Performance of the compensator designed with current approaches is significantly degraded for a 34th-order compensator.

- PERFORMANCE - DRIVEN CONTROL DESIGN
- COMPENSATOR DESIGN BASED ON LQG FORMULATION FOR PDE
- COMPENSATOR ORDER REDUCED BY BALANCED REALIZATION

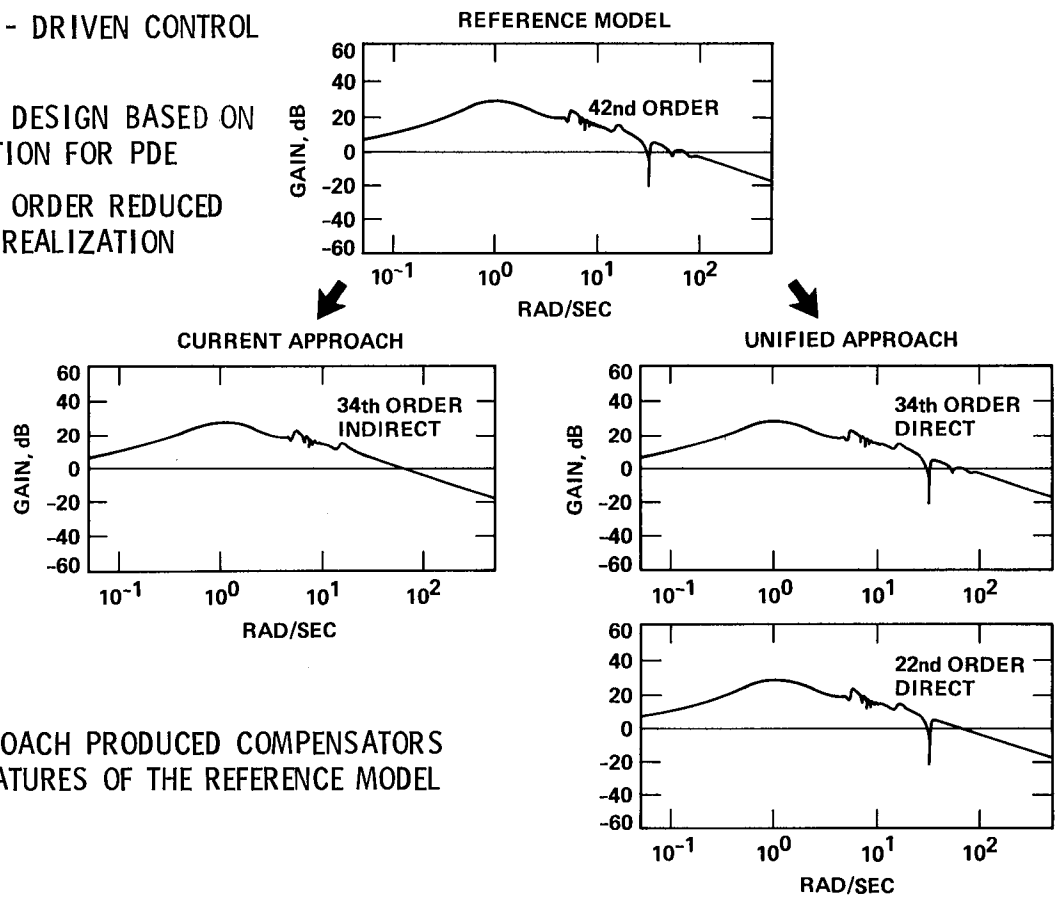

- UNIFIED APPROACH PRODUCED COMPENSATORS RETAINING FEATURES OF THE REFERENCE MODEL

CONTROLLER DESIGN BASED ON RF CONSIDERATIONS

Most current control designs are based on structural dynamic models. The electromagnetic model information associated with antennas has not been utilized. Work is being carried out to correct this deficiency. One approach taken is illustrated in this chart. The structural finite-element model is integrated with the RF model so that RF performance parameters can be determined as a result of antenna vibration or distortion. For example, the sensitivity of the antenna RF gain as a function of feed displacements or vibration mode shapes can be obtained, which in turn can be used for control design.

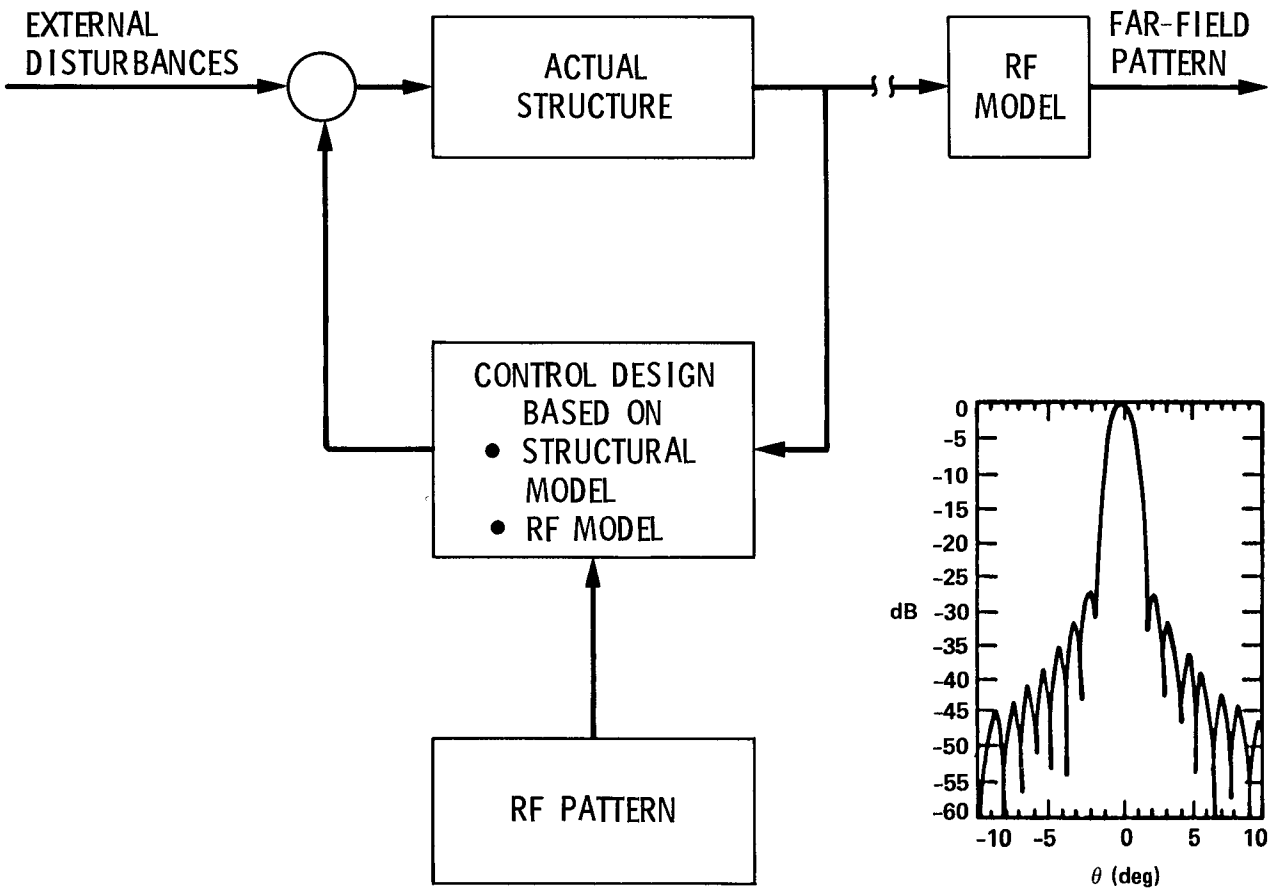

EFFECTS OF MODAL DISTORTION ON ANTENNA RF PATTERN

The figure shown in the upper right corner of this chart represents the undistorted antenna RF pattern for a perfect antenna shape. The figures shown in the lower half of the chart represent distorted patterns due to distortions of mode 1, mode 2 and mode 15, respectively. Based on the extent of these pattern distortions, the relative importance of modes 1, 2, and 15 can be determined. This information can be used in the control design to effectively utilize control energy in controlling each of the distorted antenna modes.

- RELATIVE IMPORTANCE OF MODES CAN BE DETERMINED FROM SENSITIVITY ANALYSIS
- SENSITIVITY ANALYSIS RESULTS ARE USED IN THE CONTROL DESIGN
- SYSTEM PERFORMANCE IMPROVED IF DESIGNED WITH ADDITIONAL INFO AS SHOWN BELOW

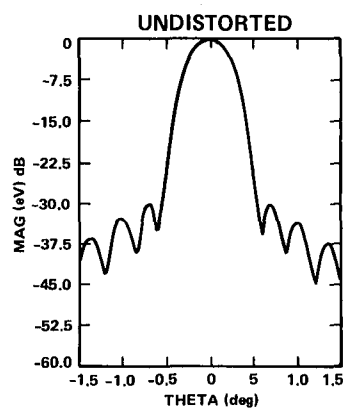

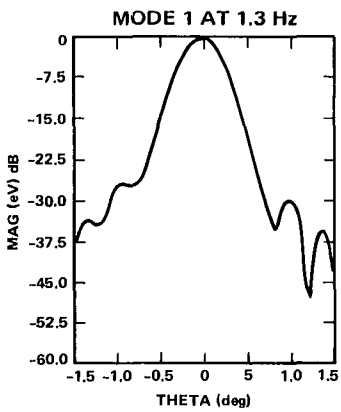

DISH ROTATION

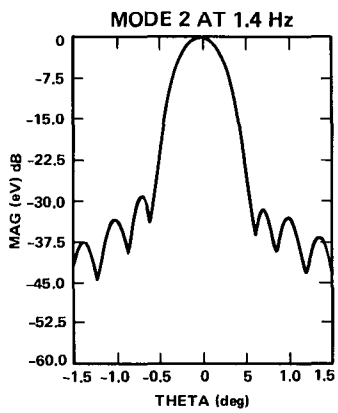

DISH CUPPING

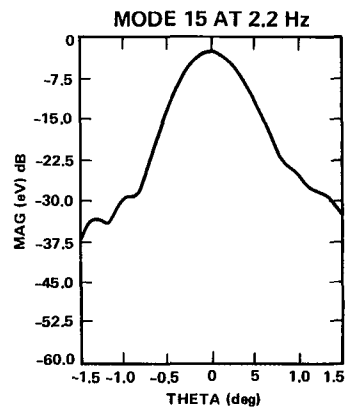

DISH CUPPING/ROTATION

SHAPE CONTROL TECHNOLOGY EVOLUTION

Another key problem in control of large antennas is that of shape estimation and control. A typical current approach for shape estimation is that of least-squares fit of surface deformation data to a perfect paraboloid. More advanced technology levels are: the use of a finite-element model to replace the paraboloid model; the use of electro-optical sensing for near-real-time application; and the use of microwave holographic measurements of the antenna fields, in cases where such measurements may be available. One of the areas of intense interest at JPL is the combination of holographic data, electro-optical sensing, and a high-resolution finite-element model to obtain a precise estimate of the shape of a deformable antenna. The most advanced level of technology would involve precise shape control of the full antenna systems, including the subreflector if appropriate. This level of technology would achieve the best antenna surface accuracy possible.

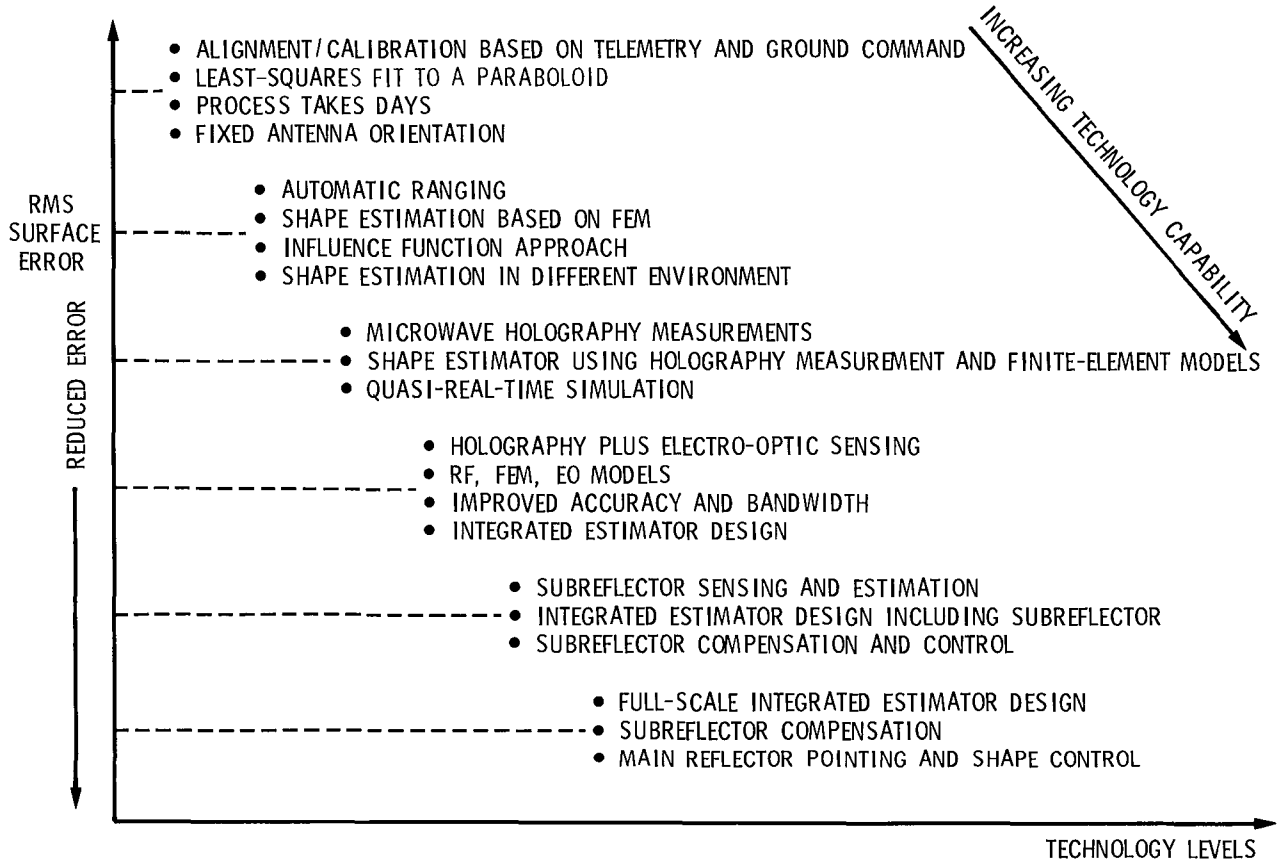

INTEGRATED ANTENNA MODEL

A large space antenna can be modeled with the finite-element method establishing the relationships between the antenna structural deflections and the external disturbances due to thermal, gravitational, and other random effects. The structural deflections can be determined by either of the two measurements: the upper path depicts the RF approach, and the lower path the electro-optic approach. In the RF approach, the structural deflections are related to the electromagnetic (EM) fields through the EM model. By measuring incremental (holographic) far-field patterns of the antenna, the antenna surface distortion can be estimated based on the EM model. In the electro-optical approach, an electro-optic sensor is used to take 3-dimensional displacement measurements of various locations distributed throughout the antenna surface. These displacement data can be processed to determine the antenna surface errors. The electro-optical data would be available on a near-real-time basis, whereas the RF data would be used as an update only at those times when such data are available.

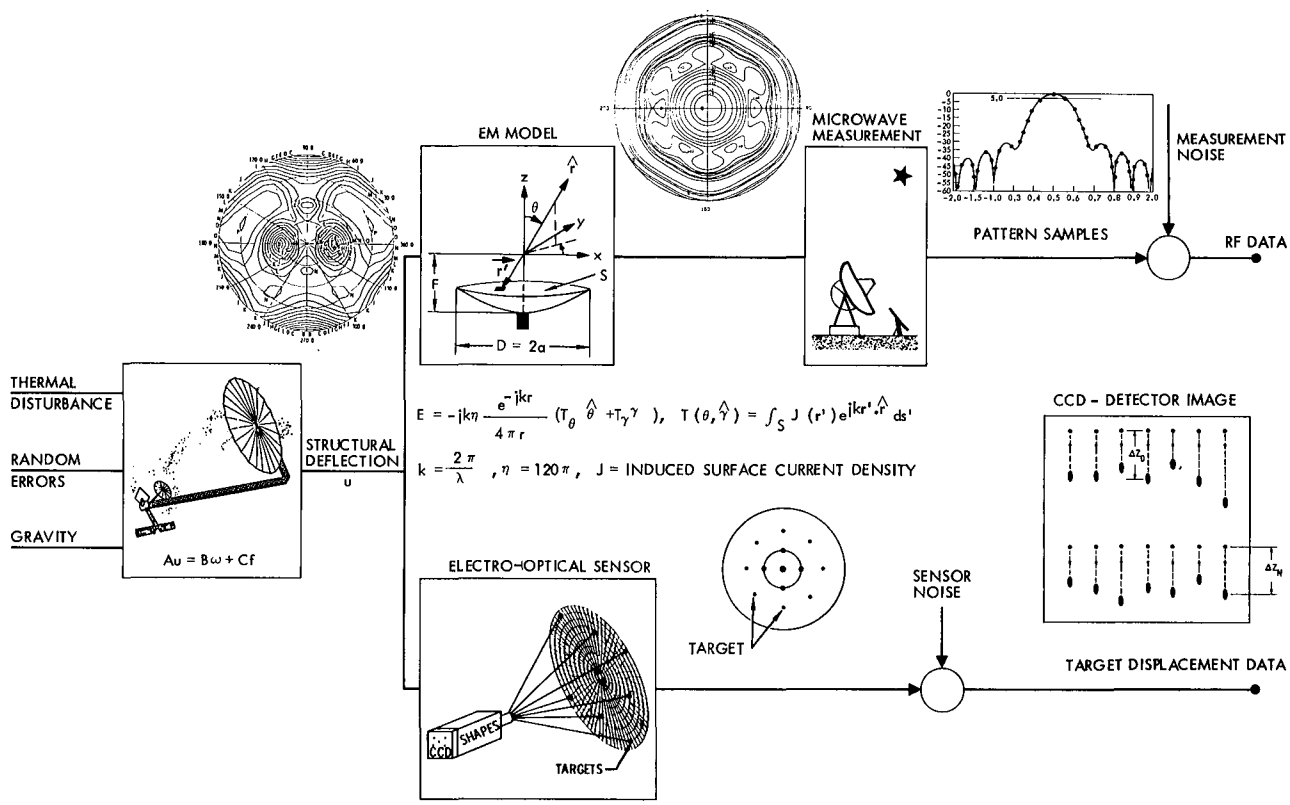

INTEGRATED SHAPE DETERMINATION APPROACH

A systematic method for shape determination that would make best use of combined structural/RF/control expertise is illustrated below. A finite-element model with external disturbance estimates is used to predict the antenna shape. This predicted estimate, along with the electro-optic sensor model, generates the predicted target displacement signals. These predicted signals are compared with the actual target displacement signals from the measurement and a residual signal is produced. The residual signal is multiplied by an optimal 3-dimensional spatial filter gain K_1 to improve the predicted shape estimate that was derived from the finite-element method and the electro-optical approach. To combine the data, the corrected estimate is used with the EM model to produce the predicted RF data. This is compared with the actual RF measurement data to generate pattern residual signals. These signals are multiplied by another optimal 3-dimensional spatial filter gain K_2 to further improve the corrected shape estimate. This results in the integrated shape estimate utilizing all information from the finite-element model, the electro-optic measurements, and the RF measurements.

The shape control problem can be treated as the dual problem of the shape estimation and can be solved in a similar manner.

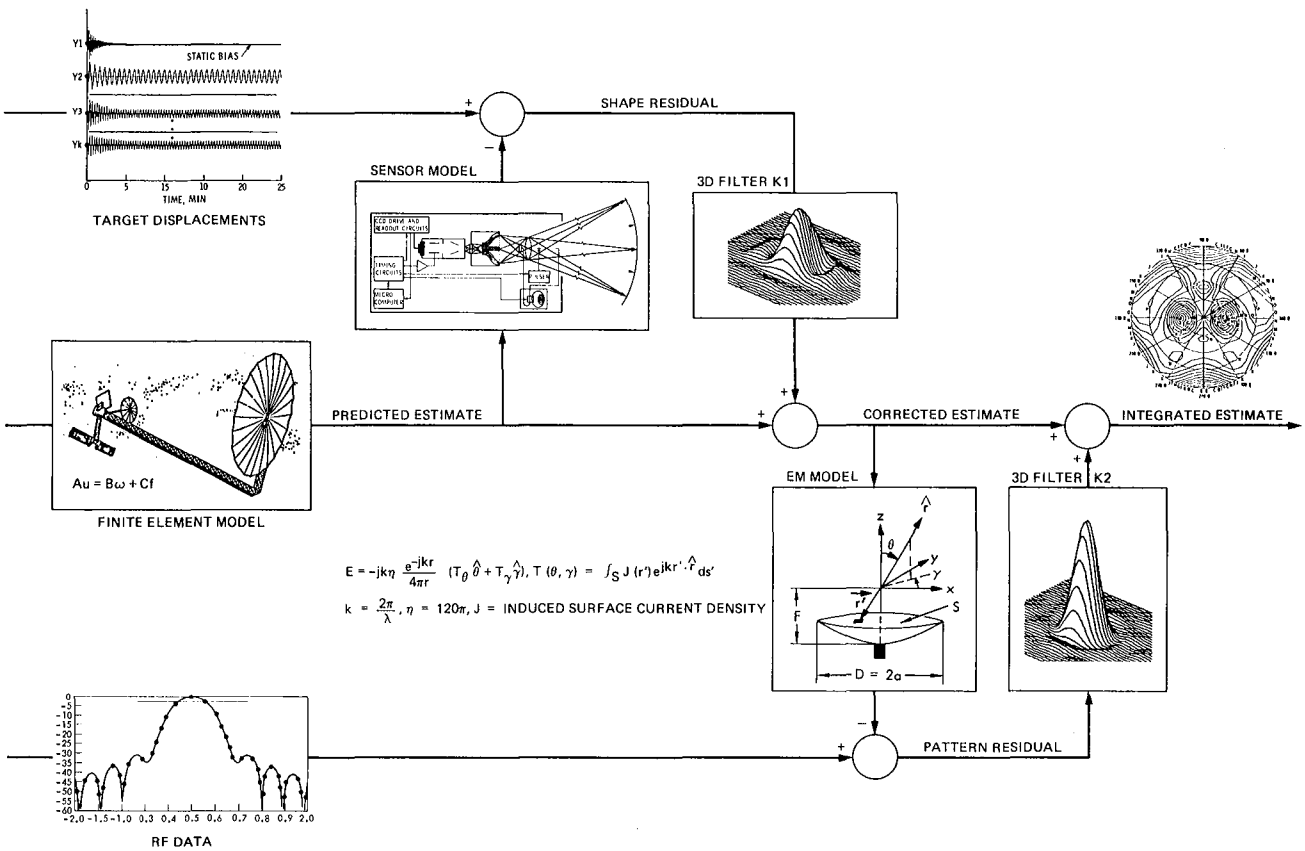

SUMMARY

In this paper, the rationale for a range of new control technology developments is presented. The current approaches fail because they do not integrate sufficiently the appropriate disciplines of structures, control and electromagnetics. The trends of new methods should be toward unification and integration. Methods for unified modeling, control design, and shape estimation and control currently under development will achieve better performance results.

- A RANGE OF NEW CONTROL TECHNOLOGIES ARE REQUIRED TO SUPPORT:
  - LAND MOBILE SATELLITE SYSTEM——— 0.9 GHz, 55-120 mD, 10 mm RMS, 0.1^{0}
  - FAA SURVEILLANCE SATELLITE SYSTEM— 1.6 GHz, 15-50 mD, 5 mm RMS, 0.2^{0}
  - VLBI/QUASAT——————————— 22 GHz, 15-40 mD, SUBMILLIMETER RMS, 60 arc sec
  - LDR——————————————— 10,000 GHz, 10-30 mD, SUBMICRON RMS, SUB arc sec

- NEW CONTROL TECHNOLOGIES
  - DISTRIBUTED SENSING AND CONTROL (LMSS, QUASAT, LDR)
  - SHAPE DETERMINATION AND CONTROL (QUASAT, LDR)
  - SYSTEM IDENTIFICATION (LMSS, SSS, LDR)
  - UNIFIED CONTROL/STRUCTURE MODELING AND DESIGN (ALL)
  - INTEGRATED CONTROL/STRUCTURE/RF DESIGN (ALL)

EXPERIMENTAL DEVELOPMENT OF A FAILURE DETECTION SCHEME FOR LARGE SPACE STRUCTURES

Raymond C. Montgomery and Jeffrey P. Williams
NASA Langley Research Center
Hampton, Virginia

Large Space Antenna Systems Technology - 1984
December 4-6, 1984

Large flexible spacecraft may require control sytems consisting of large numbers of sensors and actuators. To assure a viable mission, the control system should tolerate failures of some of the control components. Hence, it is desirable to automate the process of failure detection, identification, and control system reconfiguration (FDI&R). This paper briefly states some of the opportunities to accommodate failure in the spacecraft design. Some methods for FDI&R are presented in overview, and the method chosen for experimental testing is described. Finally, the experimental activities leading to the validation of the technique are presented.

* **Motivation for FDI&R**

* **Opportunities in Spacecraft Design**

* **Overview of methods for FDI&R**

* **FDI&R configuration selected for experimental work**

* **Experimental activities leadiing to FDI&R evaluation**

The need to consider component reliablity in space flight has long been recognized, but the problem becomes more serious as the size and complexity of the control system increase to improve the performance of the highly flexible structures. Although in-flight servicing may be available, it is desirable to make the service interval long compared to the total mission lifetime. Based on current component reliablity and projected flexible spacecraft missions, it can reasonably be expected that a significant number of components will fail during the service interval. Therefore, the control system must accommodate these failures to maintain mission performance at acceptable levels.

WHY DO WE NEED TO CONSIDER COMPONENT UNRELIABILITY?

- A LARGE, LIGHTWEIGHT STRUCTURE IN SPACE WILL DISPLAY MANY VIBRATORY MODES WHICH MAY HAVE TO BE ACTIVELY DAMPED TO ASSURE MISSION SUCCESS
- EFFECTIVE CONTROL OF THESE MANY MODES WILL REQUIRE USE OF A LARGE NUMBER OF SENSORS AND ACTUATORS--POSSIBLY HUNDREDS OF THEM
- EVEN IF THESE CONTROL SYSTEMS ARE SERVICED IN ORBIT, ONE WOULD LIKE THE SERVICE INTERVAL TO BE LONG--AT LEAST ONE YEAR
- WITH COMPONENT MEAN TIME BETWEEN FAILURES WHICH CAN REASONABLY BE ANTICIPATED, ONE MUST EXPECT MANY OF THE CONTROL SYSTEM COMPONENTS TO FAIL IN THE COURSE OF A YEAR

There are two basic opportunities to handle component failures. The first occurs during the design phase when the component type, number and placement are selected. A technique, to be discussed in the next slide, has been proposed whereby the component type and location are selected to minimize the cost of component failure over the service interval. The second opportunity is during the operational phase of the mission. This essentially requires the implementation of an FDI&R scheme such as the one described in this paper. Some schemes involve multiple or binary hypothesis testing and nearly all require a good model of the system for successful failure accommodation.

OPPORTUNITIES TO HANDLE FAILURES

* **Design Phase - Component type, number, and placement**
  - **select component type and location which minimizes the costs of component failures over the mission life**

* **Operational Phase - Automatic failure detection and control system reconfiguration**
  - **use multiple or binary hypothesis testing techniques**
  - **reqiures good design model**

This slide illustrates that the need to consider reliability in future spacecraft designs increases with the number of components in the system. Indeed, if a control system involves 50 components each with a mean time between failures of 100,000 hours (typical of actuator and sensor components) then each year one can expect about 4 failures. One is left with the fact that an enormous amount of reservicing is required or that the system must be able to operate in the presence of noncatastrophic failures. One can, however, place the actuators in such a way that the noncatastrophic failures in system components will have minimal impact on the system performance. A criterion has been used to incorporate reliability of system components in the performance criterion. A cost function is constructed by calculating the best achievable performance assuming a certain set of components is working, multiplying that by the probability of that configuration occuring in the design reservicing interval, and summing the result over all possible noncatastrophic failure cases. This is illustrated for two possible actuator locations for the grid experimental apparatus illustrated in the slide. There are five actuators to place and two candidate location sets. Considering the catastrophic failure modes to be the simultaneous failure of three componenets, the cost function is plotted versus the ratio of mission time (or reservicing time) to mean failure time. The graph shows that for a ratio less than 0.5, configuration 1 is superior to 2 whereas the opposite is true for ratios greater then 0.5.

SYSTEM RELIABILITY

NEED FOR CONSIDERING RELIABILITY

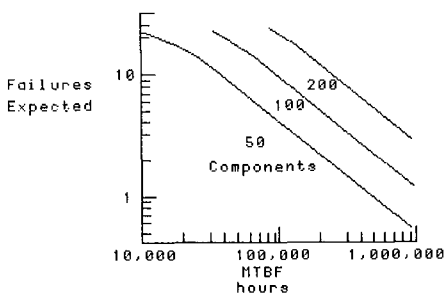

Component Location Sets

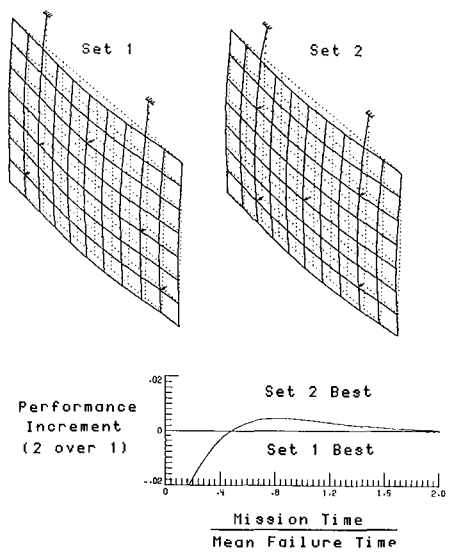

For the operational phase of a mission, real-time on-line detection, isolation, and recovery from noncatastrophic system failures are required. Since the results of the last slide were predicted on the assumption that the performance in each operational configuration will be the best achievable, the problem is to determine the configuration (i.e. which components are currently working properly) and to switch to the control system design for that configuration. Some techniques for determining the configuration are listed in this slide.

SOME FDI TECHNIQUES

* SIMPLE VOTING
* MIDPOINT SELECT WITH THRESHOLD TEST
* SIMPLE PARITY RELATIONS
* GENERALIZED PARITY RELATIONS
* MULTIPLE HYPOTHESIS TESTS
* BINARY HYPOTHESIS TESTS

The technique of multiple hypothesis testing is illustrated in this slide for the case of detecting sensor failures. Multiple hypothesis testing requires the design of a bank of optimal filters that assume a given set of functioning components and the selections of the most likely assumption using a decision law. Here, the filters are square-root realizations of Kalman filters and the failure detection logic is designed based on Bayesian decision theory. Once the most likely assumption is determined from on-line observations the Kalman filter estimate of the state conditioned under that assumption is selected for the feedback path.

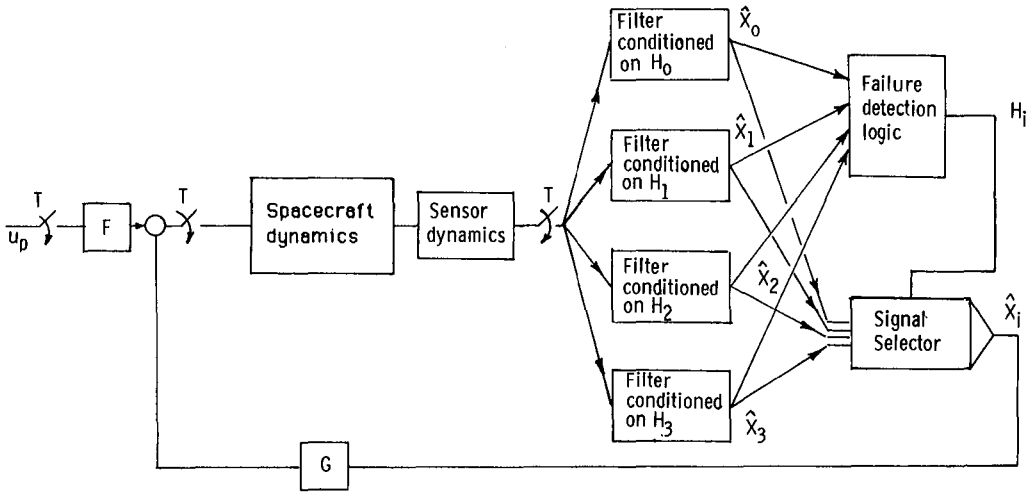

These are the basic steps to test and validate FDI&R. Select and assemble a suitable test apparatus, in this case a flexible grid structure. Then develop an analytic model of the test article which includes all constraints, gravity forces, and component masses. Having defined the model in this way, an appropriate FDI scheme may be selected. Then the scheme may be implemented and tested on the test structure using the analytic model. Although the performance based on the analytic model may be satisfactory, the FDI should also be tested with an empirical model of the structure. In this case a Least-Squares Lattice Filter is used to generate mode shapes and frequency and damping parameters. Next the FDI is re-evaluated using this empirical model. Finally, control reconfiguration schemes can be tested using the validated FDI technique. This last step is not addressed in this paper.

ACTIVITIES LEADING TO EXPERIMENTAL VALIDATION

* **Assemble suitable test apparatus**

* **Generate an analytic model of the apparatus**

* **Select FDI scheme compatible with apparatus**

* **Evaluate FDI scheme on apparatus using analytic model**

* **Use Least-Squares Lattice filter to generate an empirical model of the apparatus**

* **Evaluate the performance of the FDI design using the empirical model**

* **Evaluate reorganization schemes to yield FDI&R capability**

The test apparatus selected for this investigation consists of a 7- x 10-ft grid made of overlapping aluminum bars and is suspended by two 2-ft cables. The structure has ten modes below 5 Hz. Three modes are associated with the rigid-body pendulum and one flexible mode has a lower frequency than one of the "rigid-body" modes. This requires that the flexible modes be included in the rigid-body controller. The control system objective for the validation tests is to control all three rigid-body modes and suppress vibrations of two flexible modes. This control must be accomplished with up to two simultaneous failures of any physically distributed sensor or actuator. The limit of two failures is established by the fact that only five sensors and actuators are placed on the grid and three actuators are required to control the rigid-body modes.

TEST APPARATUS

PHYSICAL CHARACTERISTICS

7-X 10-FT GRID MADE OF OVERLAPPING ALUMINUM BARS

SUSPENSION - TWO CABLES ATTACHED TO HORIZONTAL BAR

DYNAMIC CHARACTERISTICS

THREE MODES ASSOCIATED WITH RIGID-BODY PENDULUM

ONE FLEXIBLE MODE WITH LOWER FREQUENCY THAN ONE OF THE RIGID-BODY MODES

CONTROL SYSTEM OBJECTIVE

CONTROL ALL THREE RIGID-BODY MODES AND SUPPRESS VIBRATIONS IN TWO FLEXIBLE MODES

ACCOUNTING FOR UP TO TWO SIMULTANEOUS FAILURES OF ANY PHYSICALLY DISTRIBUTED SENSOR OR ACTUATOR

This is a photograph of the grid experiment laboratory installation. Note the placement of the torque actuators on the front of the structure. The aluminum bars are .125-in thick and are glued at the intersections. The suspension cables are positioned at the third vertical bar from the edge. The power and signal wires are routed up the two cables. Maximum linear displacement is limited to +/- 1 inch.

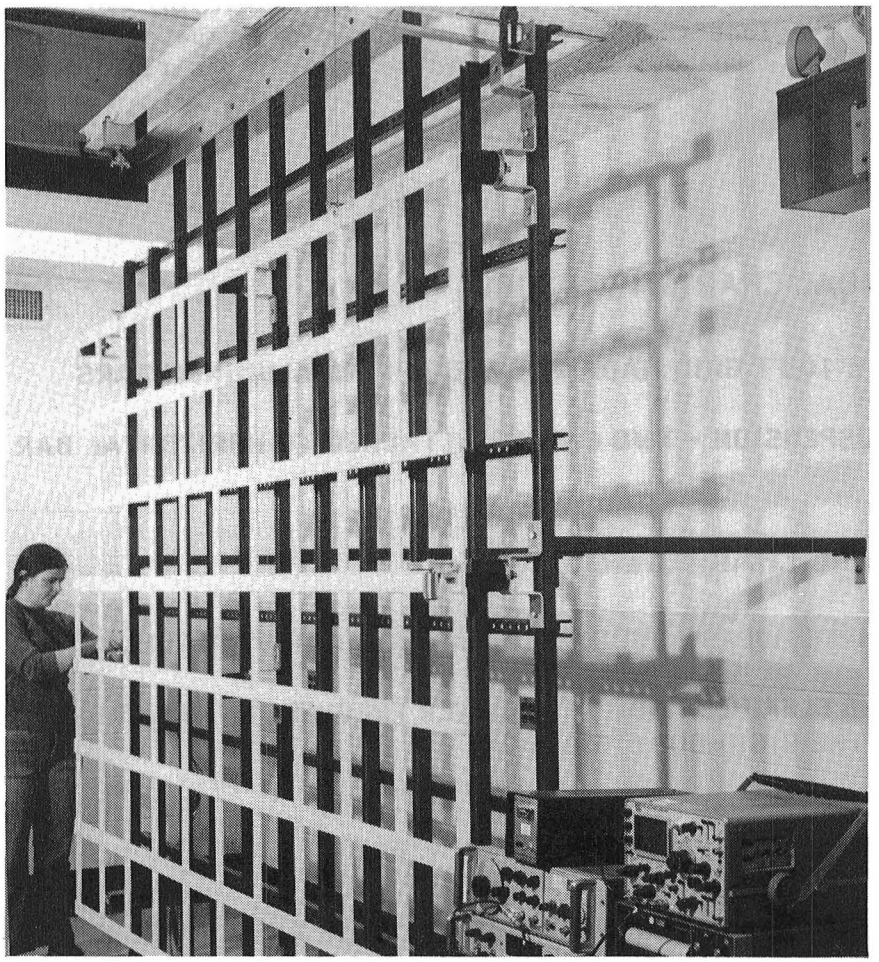

The finite-element model of the grid was generated using the SPAR computer program. The model consists of 88 nodes with bar elements for the grid. The suspension cables, gravity force and sensor and actuator mass are included in the model. The first six mode frequencies and a representative mode shape are shown.

FINITE-ELEMENT MODEL OF GRID

* 88 NODE, BAR ELEMENT

* 11 MODES BELOW 5 HZ:

.344 HZ

.504 HZ

.965 HZ

1.232 HZ

1.859 HZ

2.653 HZ

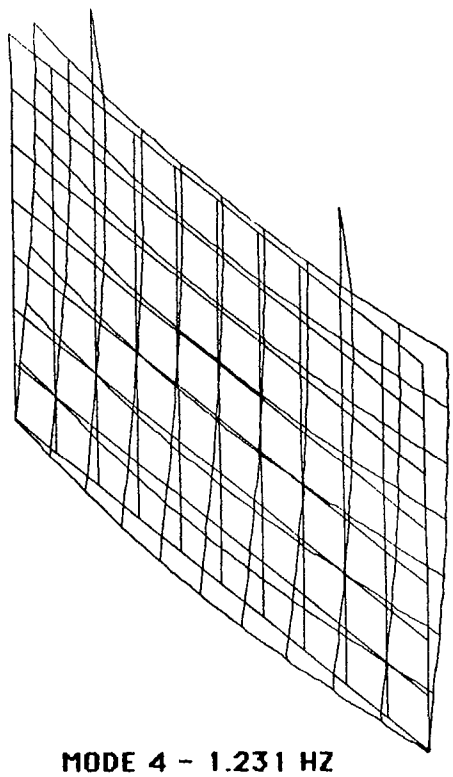

MODE 4 - 1.231 HZ

In order to address the issues of distributed smart components, smart actuators have been designed and will be operated in the configuration shown in the slide. The actuators are designed to produce torque output by reacting against the inertia of a wheel. The torque is produced by motors mounted to the grid. Current is provided by current amplifiers which receive inputs either from the microprocessor shown or from the central processor. Each smart actuator has a dedicated microprocessor to affect local closed-loop control. The optical sensor provides the required feedback signal in the form of a square-wave whose frequency is proportional to the angular speed of the wheel. Currently, processor communication is hierarchical with the processors communicating with only the central processor. Plans call for the processors to communicate with each other in a control network as well as with the central processor. This would leave the central processor with the functions of overall system planning, scheduling, and monitoring. The central processor is a Charles River Data Systems processor with a UNOS operating system. Sensors to be used include rate gyros and accelerometers that are grid mounted and interfaced to the central system through analog-to-digital converters. These sensors will be used for performance monitoring and for feedback control. Position sensors are also included in the configuration, interfacing to the central processor, but will be used only for performance evaluation.

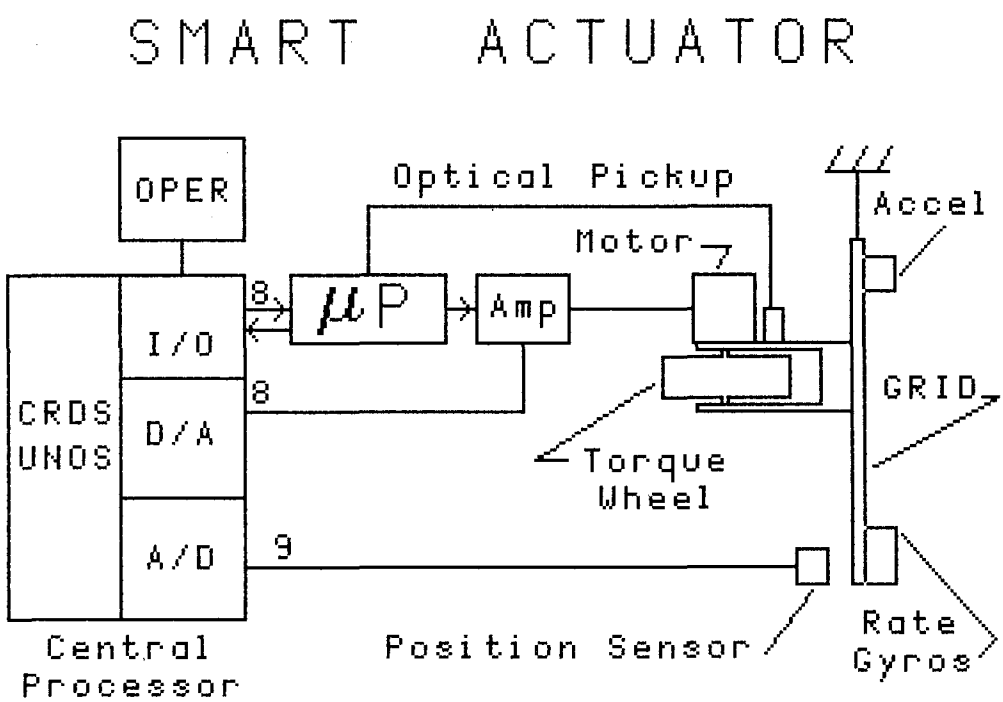

The five torque actuators are placed on the grid as shown. The axis of applied torque is indicated by the arrow. Note the two actuators position to have influence about two principal axes and the cancellation of angular momentum about the horizontal axis. These positions were selected based on a design phase analysis to optimize the performance over the mission life while considering failures. The actuators consist of a DC-torque motor rated at 20 oz-in peak torque with an inertia wheel attached to prevent rpm saturation at low frequencies.

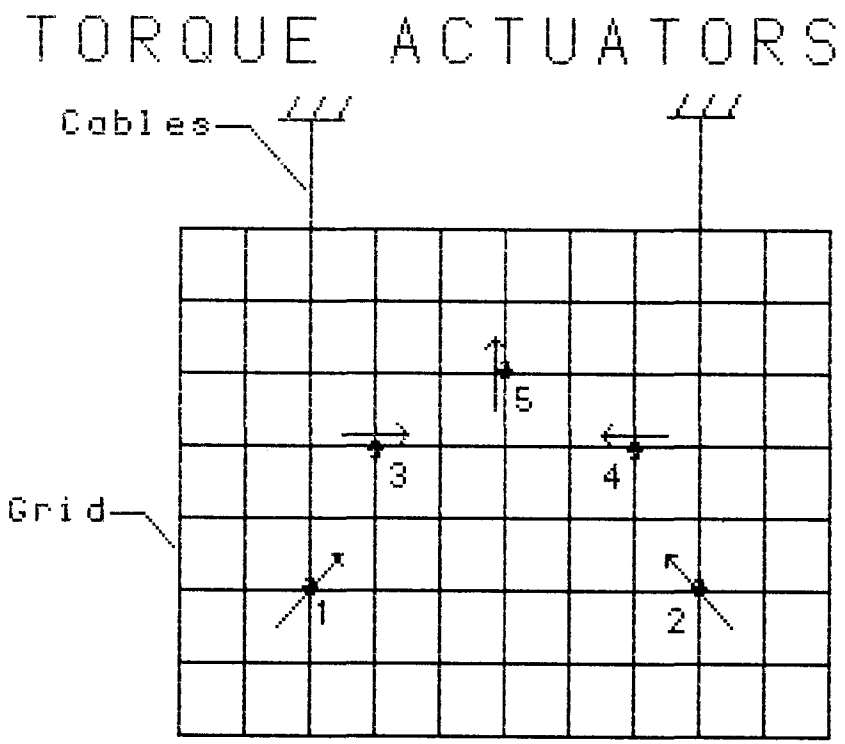

The rate gyros are positioned as shown. This provides collocation of 4 sensors and actuators and one noncollocated measurement axis.

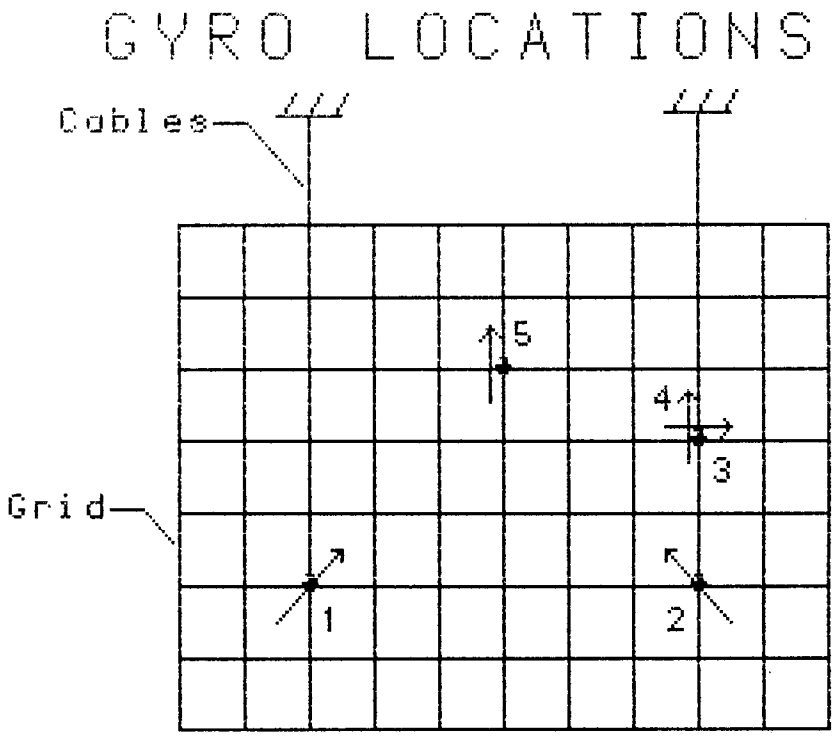

Preliminary testing of the SPRT-based failure detection scheme is under way. This consists of a tenth-order Kalman filter estimate of the 5-rate gyro signals. The residual process (which should be zero mean) is monitored to detect failure of a sensor. The scheme requires that each residual be checked with a Kalman filter conditioned on each failure hypothesis in order to identify the failed sensor. Having detected and identified the failure, the control may be reconfigured using a control model based on the failure hypothesis identified.

SPRT-BASED FAILURE DETECTION AND RECONFIGURATION

* 10-th ORDER KALMAN FILTER OF 5-RATE GYRO SIGNALS
* MONITOR RESIDUALS TO DETECT FAILURE OF THE SENSORS
* MUST CHECK EACH SENSOR CHANNEL ASSUMING EACH HYPOTHESIS
* RECONFIGURE CONTROL LAW TO ACCOMMODATE THE DETECTED FAILURE(S)

The sequential probability ratio test is a binary implementation of the multiple hypothesis tests referred to earlier. It was first used in the 1940's to detect radar returns. The test assumes two hypotheses: one, that the process is Gaussian with a known mean and covariance, and the other, that the process has zero mean with the same covariance. In order to make the best decision as to which hypothesis is most likely, the logarithm of the likelihood ratio is used.

Sequential Probability Ratio Test

H_1: Process is Gaussian with mean μ and variance V

H_2: Process is Gaussian with zero mean and variance V

Decision: use log likelihood ratio

The log likelihood ratio is defined as the ratio of the log of the probability density function conditioned under hypothesis one and that conditioned under hypothesis two. Since the processes are assumed Gaussian their probability density satisfies the proportionality shown in the slide.

Gaussian distribution:

$$P \sim \exp[-(y-\mu)'V^{-1}(y-\mu)]$$

Log likelihood ratio:

$$\lambda = \frac{\log P \text{ assuming } H_1}{\log P \text{ assuming } H_2}$$

Substitution of the Gaussian form of the density functions results in the simple formula shown for the log likelihood ratio given a sensor measurement, y. If several samples, say N, are used then the log likelihood ratio considering the entire data set is as shown.

$$\lambda = -(y-\mu)'V^{-1}(y-\mu) + y'V^{-1}y$$

$$= (\frac{\mu}{2} - y)'V^{-1}\mu$$

For N samples y_k

$$\lambda_N = \sum_{k=1}^{N} (\frac{\mu}{2} - y_k)'V^{-1}\mu$$

One interesting point is that the expected value of the log likelihood ratio has the same magnitude but the oppostie sign for the two hypotheses.

Note:

$$E(\lambda_N) = \frac{N}{2}\mu'V^{-1}\mu \qquad \text{Assuming } H_2$$

$$= -\frac{N}{2}\mu'V^{-1}\mu \qquad \text{Assuming } H_1$$

This slide indicates the expected behavior of the accumulated log likelihood ratio as measurement data are collected when there has been no failure. The ratio drifts positively toward boundary at level b. As long as the ratio is between boundary limits a and b then no failure is declared. If a and b are very small then a decision is made with few samples. On the other hand, if the values of a and b are large then many samples may be required before a decision can be reached. Obviously, there is an intimate relation between the declaration of false alarms, the number of missed failures, and the noise characteristics of the signal being monitored. Indeed, it is possible to calculate the levels of a and b appropriate to a given probability of false alarm and missed failure. This can be done either analytically or experimentally.

SPRT Mechanization

No failure case

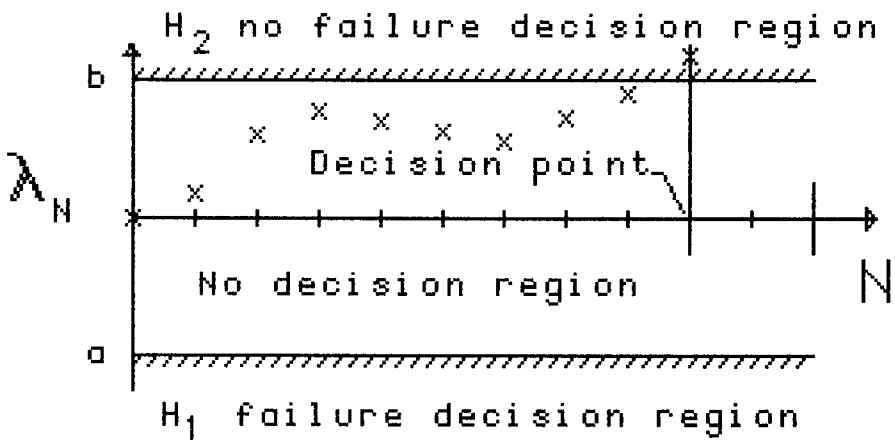

Results of an on-line test using the experimental apparatus described earlier are presented in these time histories. The top four traces are signals associated with rate gyro 1. The bottom trace indicates the sequential failure, one at a time, of the five rate gyros. The Kalman estimate shown is always based on the model which assumes no failures of the sensors. The first two traces are self explanatory. The third indicates that when rate gyro 1 fails at about 12 seconds, the filter can still generate an estimate, but the residual amplitude increases. This should be detected by the SPRT algorithm as a failure (but not identified). After twenty seconds, the failure of gyros 2, 3, and 4 does not affect the residual for this Kalman filter. This demonstrates the need to run filters conditioned on each failure hypothesis. The failure of gyro 5 results in a very large residual signal which may indicate a modeling error.

Future work will include implementation of the SPRT algorithm and simultaneously running the filters based on all hypotheses.

EXPERIMENTAL EVALUATION OF ANALYTIC MODEL

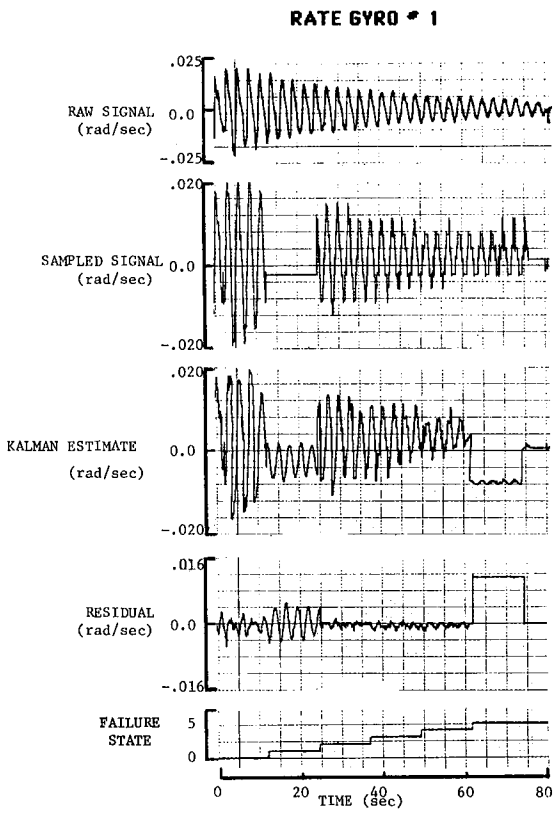

Page intentionally left blank

DYNAMIC VERIFICATION OF LARGE SPACE STRUCTURES

D. K. Tollison
Control Dynamics Company
Huntsville, Alabama

H. B. Waites
NASA Marshall Space Flight Center
Huntsville, Alabama

Large Space Antenna Systems Technology - 1984
December 4-6, 1984

NASA Marshall Space Flight Center has developed a facility in which closed-loop control of Large Space Structures (LSS) can be demonstrated and verified. The main objective of the facility is to verify LSS control system techniques so that on-orbit performance can be ensured. The facility consists of an LSS test article which is connected to a payload mounting system that provides control torque commands. It is attached to a base excitation system which will simulate disturbances most likely to occur for orbiter and DOD payloads. A control computer will contain the calibration software, the reference system, the alignment procedures, the telemetry software, and the control algorithms. The total system will be suspended in such a fashion that the LSS test article has the characteristics common to all LSS.

The first version of the LSS/ground test verification (GTV) facility is shown below. It consisted of an ASTROMAST beam mounted to the faceplate of the Angular Pointing System (APS). The APS, in turn, is mounted to the Base Excitation Table (BET). Six separately packaged inertial measurement assemblies comprise the control system sensors. The signals from these sensors are received and processed in the COSMEC-I data gathering and control system, which computes and transmits control actuator signals to the APS actuators. The COSMEC-I interfaces with a Hewlett Packard HP9845C desktop computer which stores data as they are collected during test runs; it then provides post-experiment data reduction and off-line displays.

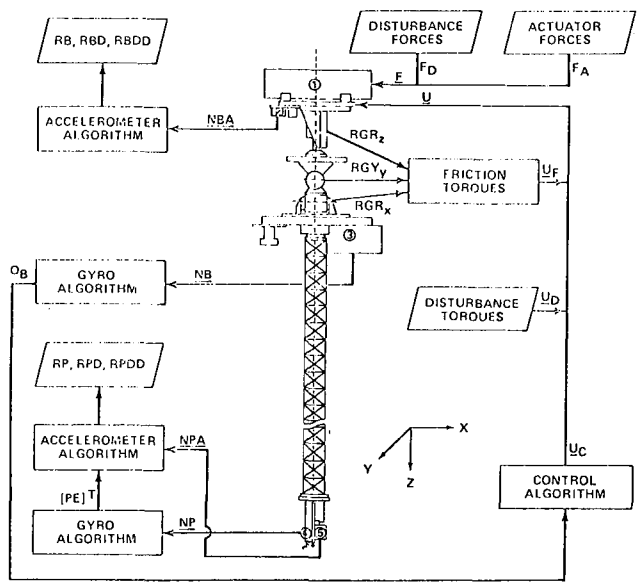

LSS SIMULATION – GTV ASSEMBLY INPUT/OUTPUT WITHOUT CRUCIFORM

1. SHAKE TABLE
2. 3-AXIS BASE ACCELEROMETERS
3. 3-AXIS BASE RATE GYROS
4. 3-AXIS TIP RATE GYROS
5. 3-AXIS TIP ACCELEROMETERS

The original test configuration had all the desired LSS characteristics except the densely packed vibrational modes. Several design configuration changes were considered so that this important missing structural constraint could be implemented. The configuration change which could effect the densely packed modes was the addition of a cruciform structure at the tip of the ASTROMAST. To a degree, the new configuration approximates an antenna or a radar system.

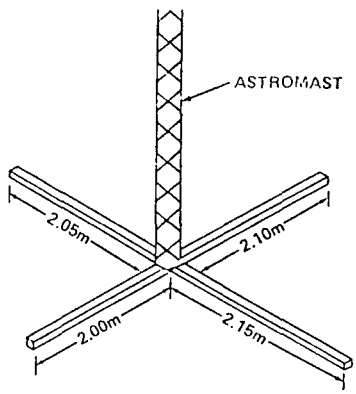

THE CRUCIFORM STRUCTURE

FOR SIMULATION PURPOSES, THE 4 ALUMINUM BARS WERE PLACED AT THE TIP OF THE BEAM; IN ACTUALITY, THEY ARE TO BE LOCATED AT THE END OF THE TIP BRACKET. THE RODS VARY IN LENGTH FROM 2.00m TO 2.15m. THEY ALL HAVE A CONSTANT CROSS–SECTION OF 1/4" x 1/4".

MODE #	FREQ. (Hz)
1–5	0.0 (RIGID BODY)
6	.382
7	1.052
8	1.149
9	1.154
10	1.157
11	1.219
12	1.254
13	1.266
14	1.287
15	1.409
16	2.973
17	3.520
18	3.870

MODES, MODAL, FREQUENCIES FOR COMBINED STRUCTURE

The test structure is mounted to the payload mounting plate of an Angular Pointing System (APS). The APS provides the control inputs for the initial configuration system and the cruciform-modified system. The APS actuators are the Advanced Gimbal System engineering model, produced by Sperry for the Spacelab program, and a third (roll) gimbal designed and built inhouse (as were the amplifiers used to drive the gimbal torquers). The roll gimbal, serving the vertical axis, is suspended by an air bearing which requires approximately 85 psi to operate. The roll gimbal provides a means of rotating the entire system to produce different test scenarios. The air bearing is connected to a Base Excitation Table (BET) which is free to translate in two directions. This actuator assembly setup, with its low friction torques, permits control in three angular directions. With the added roll gimbal, the test article can be rotated about its centerline so that different test setups can be achieved.

In the initial research and technology task, the effectors for the LSS/GTV control system are three torque motors which are capable of providing control torques about three axes. The bottom two gimbals can generate up to 51 N.m of torque, and the roll or azimuth gimbal can generate up to 10 N.m of torque. The bandwidth limitation for all three gimbals is 100 Hz. The APS amplifiers receive torque commands from the COSMEC-1 digital processor in the form of analog inputs over the range of -10 to +10 volts. This saturation represents the current limit of 27 amps which is built into the APS servo amplifiers. Because the APS servo amplifier outputs a current which is proportional to torque, the control law algorithm was designed to produce torque command signals. The gimbal torquers are shown below.

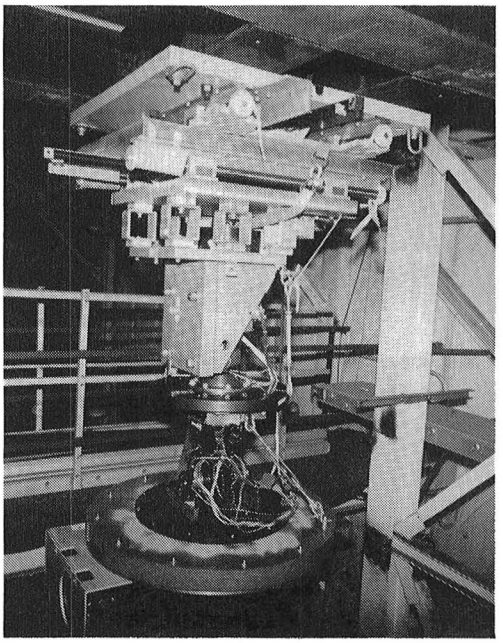

All of the GTV configurations need a device to excite the system in a consistent manner so that the effectiveness of the different control methodologies can be determined. Initially, these disturbances will represent either an astronaut pushoff, a reaction control system thruster firing, or a free-flyer disturbance. The Base Excitation Table (BET), which is attached to the building support structure, is shown below. It provides a means of producing such disturbance inputs. The BET is comprised of signal generators (deterministic or random noise), DC conditioning amplifiers, hydraulic servo controllers, and an oscillograph. The DC conditioning amplifiers are used to scale the signal generator while the signal conditioners are used to condition the electronic deflection indicator motion monitors for display. The oscillograph is used for recording the actual motion of the BET.

The precise motion of the BET is obtained by supplying a commanded voltage input to the BET servo control system. The BET movements are monitored by the directional feedback electronic deflection indicators which are fed back to the servo controllers. The servo controllers compare the commanded input voltage to the electronic deflection indicators and automatically adjust the position of the BET. The closed-loop controller allows any type of BET movement within the frequency limitations of the hydraulic system.

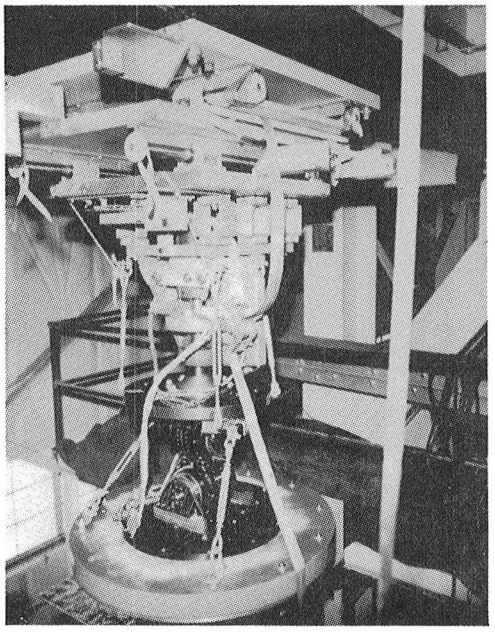

The first test article is a spare Voyager ASTROMAST built by ASTRO Research, Inc. It was supplied to MSFC by the Jet Propulsion Laboratory (JPL). The ASTROMAST is extremely lightweight (about five pounds) and approximately 45 feet in length. It is constructed almost entirely of S-GLASS. It is of the type flown on the Solar Array Flight Experiment-I (SAFE-I).

When fully developed, the ASTROMAST exhibits a longitudinal twist of about 280°. This twist contributes to the coupling between the torsional and bending modes.

As previously stated, the second test article consists of the ASTROMAST with a cruciform attached to the tip. The cruciform structure, which is made of aluminum, weighs eight pounds and is shown below. The cruciform rods vary in length from 2.00 m to 2.15 m. They all have constant cross sections of 1/4" x 1/4".

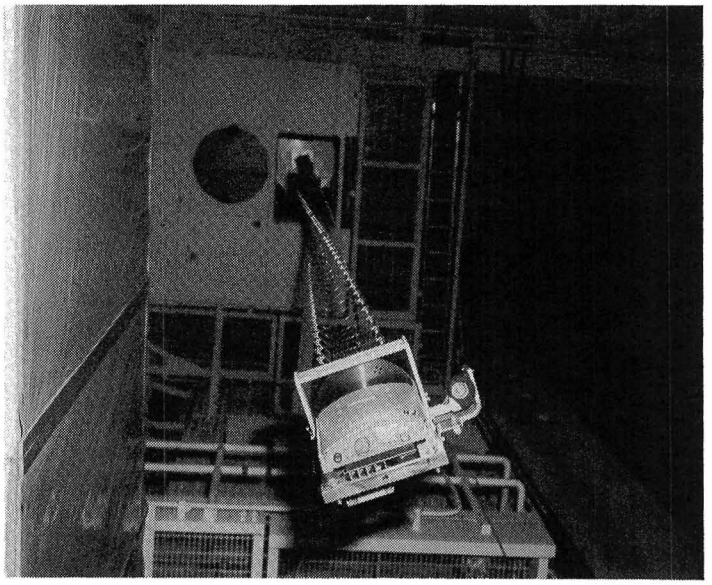

The signals from the sensors are utilized by the control computer and processed according to the control law under consideration. The COSMEC-I is the control computer which is used for data acquisition, reference identification, and feedback control for the first experiment configuration. The COSMEC-I is a highly modified AIM-65 microcomputer system. It was developed originally by MSFC for the solar heating and cooling program. As a result the development cost was not underwritten by the LSS/GTV facility.

The main purposes of the control computer are to process the sensor inputs, keep up with the laboratory coordinate system, provide torque commands for the APS, and off-load control and sensor data to the Hewlett Packard HP9845C desktop computer. The COSMEC-I performs these tasks with twelve sensor inputs and three torque outputs, while maintaining a 50-Hz sampling rate.

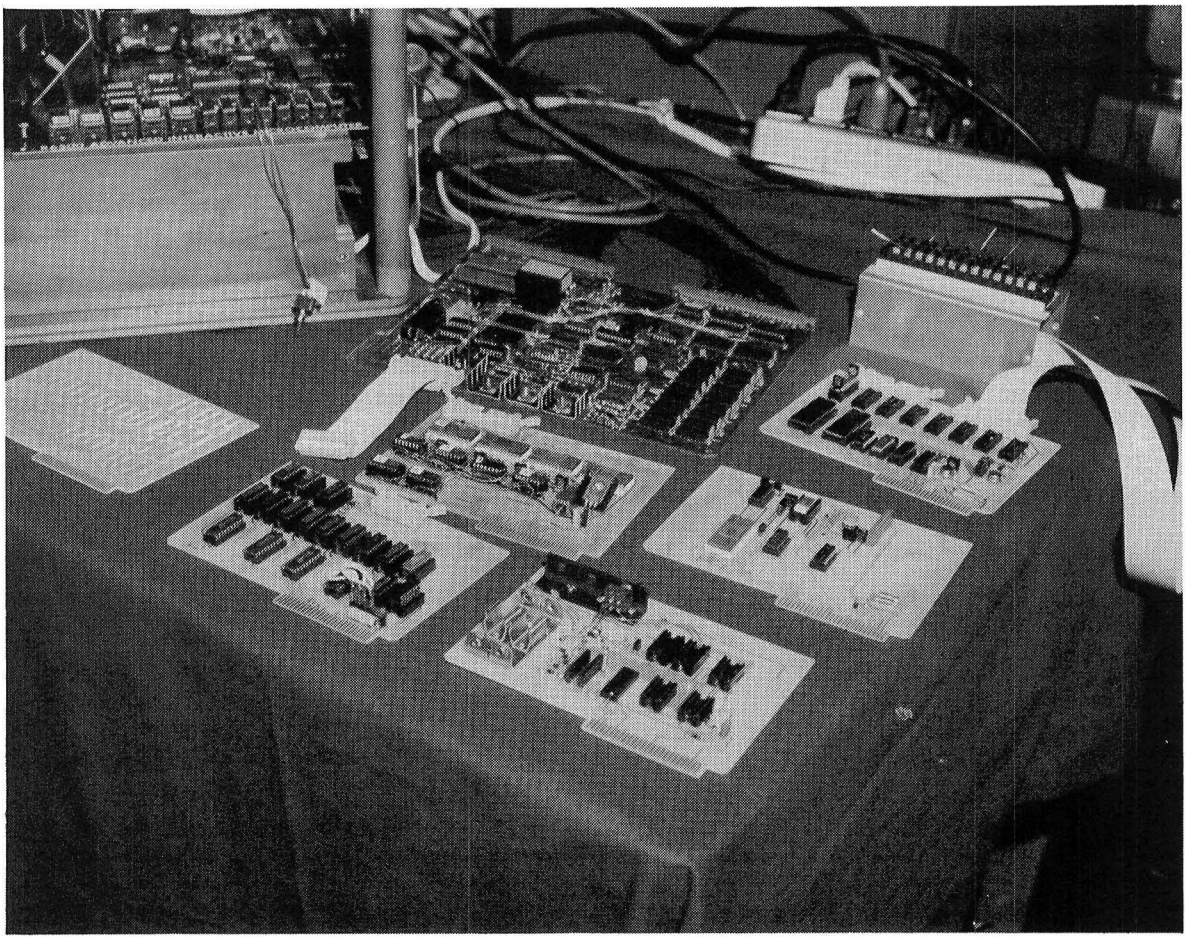

Six separately packaged inertial measurement assemblies comprise the control system sensors. Two of the packages, containing three-axis translational accelerometers, are identical. One is mounted on the mast tip and the other on the lower surface of the BET. Three other packages contain Skylab ATM (Apollo Telescope Mount) rate gyroscopes and are mounted on the APS faceplate (see left figure below). The sixth package, the Kearfott Attitude Reference System (KARS), is located on the mast tip along with the remaining accelerometer package.

The Kearfott Attitude Reference System (KARS) includes three rate gyros and three accelerometers. The KARS unit is mounted to the test article tip (see the right-hand figure below) so that the sensors provide information about the tip motion. The rate gyros have a resolution of approximately 50 arc-sec/sec about two axes and 90 arc-sec/sec about the third axis. The KARS rate gyro bandwidth is about 70 Hz.

The ATM rate gyros are mounted to the APS payload mounting plate. The minimum resolution for the ATM gyros is approximately 2 arc-sec/sec. The gyros operate in a fine mode, which has a bandwidth of 12 Hz, and a coarse mode, which has a bandwidth of 40 Hz.

The two three-axis accelerometer packages incorporate six Kearfott 2401 accelerometers. The minimum resolution for each of these units is 11 micro g's and their bandwidth is 25 Hz.

The signals from these instruments are read by the COSMEC-I data gathering and control system and processed according to the particular control strategy under scrutiny. The control actuator signals are then transmitted to the APS as inputs to the dynamical system.

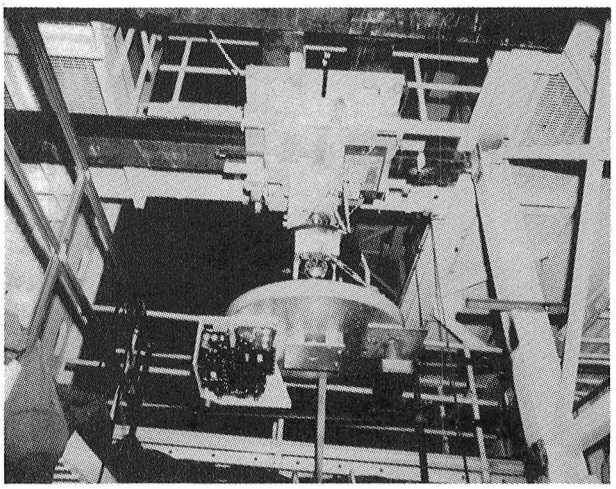

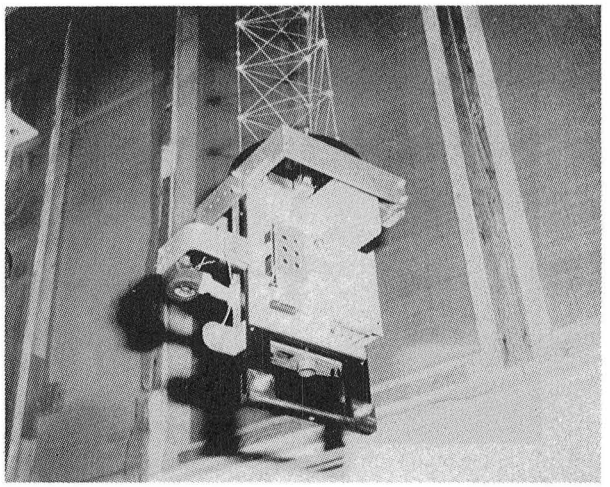

One of the important aspects of the LSS/GTV is to verify the analytical model of the test article. The procedure is to describe the structure mathematically as well as possible, then perform structural tests on the test article, and finally to factor these results into the mathematical model.

One of several modeling efforts included the APS, BET, and instrument packages. This model was used as an aid in conducting the modal test on the structure in this configuration. Again, the test data were used to refine the corresponding structural model. The upper table on the next page provides the corresponding synopsis of the modal frequencies as predicted pre-test, measured, and "tuned." Tuning was accomplished by varying the inertial properties, which were poorly known, and the bending and torsional stiffness, which change with the different gravity loading in this configuration. Examination of the percentage errors in the upper table shows the refinement of the model.

The modeling was then expanded to include the cruciform structure at the ASTROMAST tip which was added to obtain more LSS-like pathologies, i.e., closely spaced modal frequencies. The "model-test-tune" procedure described in the previous paragraph was carried out for this configuration in order to produce a high-fidelity model of the LSS/GTV experiment structure. The modal frequencies and damping for the two previous measured models are shown in the bottom table. The results described as "local modes" in this table primarily involve deformation of the cruciform arms.

The last modal test that was performed was to determine the effects of connecting cables to the various components on the test structure. All the cabling was stripped off the stiff external wrapping and sufficient length and coiling were provided to reduce any cabling effect on the structural dynamics. The acquired test data conclusion is that no significant modal shifts occurred when the cables were connected.

Structural Natural Frequencies Without Cruciform

MODE #	DESCRIPTION	ORIGINAL ANALYTICAL	MEASURED	Δ(%)	TUNED ANALYTICAL	Δ(%)
1	RB (xy-plane)	0.00				
2	RB (yz-plane)	0.00				
3	RB (torsion)	0.00				
4	1st Bend (yz-plane)	0.14	0.14	0.0	0.14	0
5	1st Bend (xz-plane)	0.15	0.15	0.0	0.15	0
6	1st Torsion	1.18	0.99	19.0	1.02	3
7	2d Bend (xz-plane)	1.27	1.33	4.5	1.29	3
8	2d Bend (yz-plane)	1.40	1.80	22.0	1.64	9
9	3d Bend (xz-plane)	3.02	3.30	8.5	3.34	1
10	3d Bend (yz-plane)	3.91	3.94	0.0	4.31	11
11	4th Bend (xz-plane)	6.69	8.06	17.0	8.10	0
12	4th Bend (yz-plane)	7.03	8.13	14.0	8.21	1
13	2d Torsion	8.42	9.60	12.0	9.61	0

Summary of LSS/GTV Modal Test Results

Description	W/o Cruciform			W/Cruciform		
System Mode	Freq Hz	% Damp	TSS	Freq Hz	% Damp	TSS
1st Bndg (x)	0.144	0.35	002	No Data	No Data	N/A
" (y)	No Data	No Data	N/A	No Data	No Data	N/A
2nd Bndg (x)	1.33	1.33	002B	1.36	1.9	005
" (y)	1.83	1.88	002A	1.83	1.9	004
3rd Bndg (x)	3.38	1.76	002B	3.24	1.7	005
" (y)	3.9	2.2	002A	3.74	2.0	004
4th Bndg (x)	8.06	2.9	003	6.36	1.1	005
" (y)	8.13	4.5	003	6.67	1.85	004
1st Torsion	0.991	0.44	001	0.377	0.56	006
2nd Torsion	9.6	1.1	001	3.02	0.34	007
Local Modes						
Y Bndg	N/A	N/A	N/A	0.38	0.53	008
"	"	"	"	1.149	0.53	008
"	"	"	"	6.418	0.70	008
"	"	"	"	6.876	0.44	008
"	"	"	"	7.326	0.415	008
"	"	"	"	7.706	0.156	008
Z Bndg	N/A	N/A	N/A	1.143	0.79	008
"	"	"	"	6.756	1.09	008
"	"	"	"	7.062	1.23	008

A future configuration change will be the addition of a three-meter offset antenna to the ASTROMAST tip and an antenna feed located on the payload mounting plate. This addition will facilitate both decentralized and distributive control methodologies. Also, a bi-directional linear thruster system is planned for location at the ASTROMAST tip so that active vibration suppression can be tested using these thrusters. The integration of the previously mentioned LSS/GTV modifications will provide adequate sensors, effectors, and LSS dynamic pathologies so that the test facility can encompass many facets of dynamics and control verification.

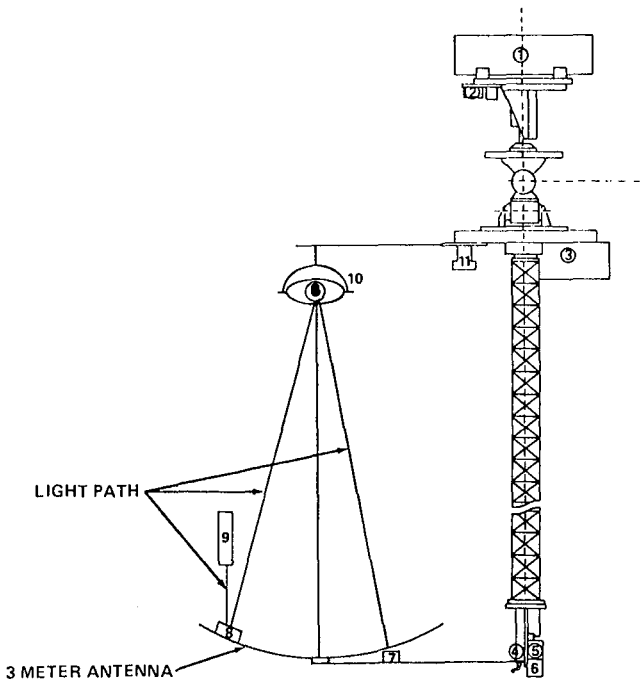

FIGURE FUTURE LSS/GTV SETUP

1. SHAKE TABLE
2. 3 AXIS BASE ACCELEROMETERS
3. 3 AXIS BASE RATE GYROS
4. 3 AXIS TIP RATE GYROS
5. 3 AXIS TIP ACCELEROMETERS
6. BIDIRECTIONAL THRUSTERS
7. OPTICAL DETECTOR
8. REFLECTORS
9. LASER
10. 2 GIMBAL SYSTEM
11. N_2 BOTTLES

Page intentionally left blank

PASSIVE AND ACTIVE CONTROL OF SPACE STRUCTURES (PACOSS)

G. Morosow and H. Harcrow
Martin Marietta Corporation
Denver, CO

and

L. Rogers
Air Force Wright Aeronautical Laboratories
Dayton, OH

Large Space Antenna Systems Technology - 1984
December 4-6, 1984

The PACOSS is a 5-year program designed to investigate highly-damped space structures in conjunction with active control systems.

PACOSS Program Description

Develop Technology That Integrates

Passive Damping and **Active Controls**

To Achieve Precise Pointing Control for

Large Space Systems

Major emphasis will be placed into two areas of investigation:

(a) Highly-damped parent material, and

(b) Ingenious damping devices.

It is hoped that the combination of these two will yield damping values in the order of 5% of critical in those modes which affect the pointing accuracy.

Major Areas of Research

- Metal Matrix Composites
- Viscoelastic Materials
- Ingenious Damping Devices
- Dynamic Test Article Design, Fabrication & Test
- Active Damping

The problem selected to be worked in this study pertains to Space Based Laser system. These two slides show a large, flexible gun trying to aim at a target after completing a retargeting maneuver.

PACOSS—The Problem

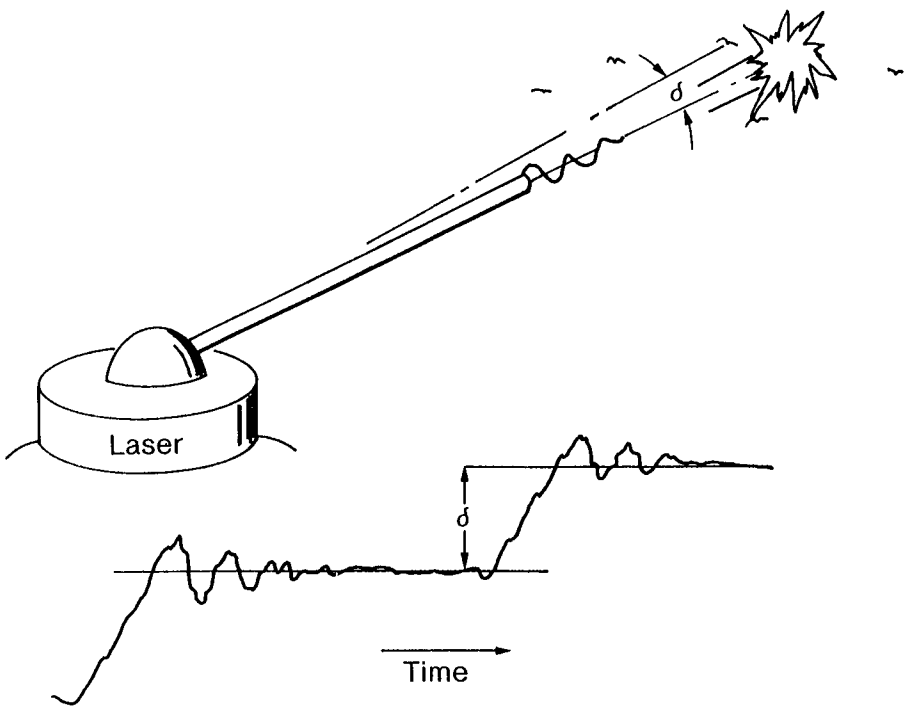

PACOSS PROGRAM REQUIREMENTS

INTEGRATE MSSTM TO A REPRESENTATIVE SYSTEM

DEVELOP PASSIVE DAMPING CONCEPTS

DESIGN OF DYNAMIC TEST ARTICLE

VERIFY PASSIVE AND ACTIVE DAMPING

FABRICATE FLIGHT QUALIFIABLE DTA

COMPLETE STRUCTURAL/DYNAMIC TESTING

CORRELATION OF TEST DATA

The PACOSS program plan starts with Air Force Mission definition (MSSTM). Likely candidates are analyzed, and a candidate for further investigation is selected. Potential structural elements suitable for damping treatment are defined and constructed. Then generic test articles are built. The only requirement in terms of selected configuration is that construction-wise it resemble some parts of the selected Dynamic Test Article (DTA).

After the generic test articles are tested and correlated with analysis, more research is performed into subsystems of the future DTA.

Finally, the entire DTA is constructed, tested, and compared to analysis.

PACOSS—Simplified Flow Diagram

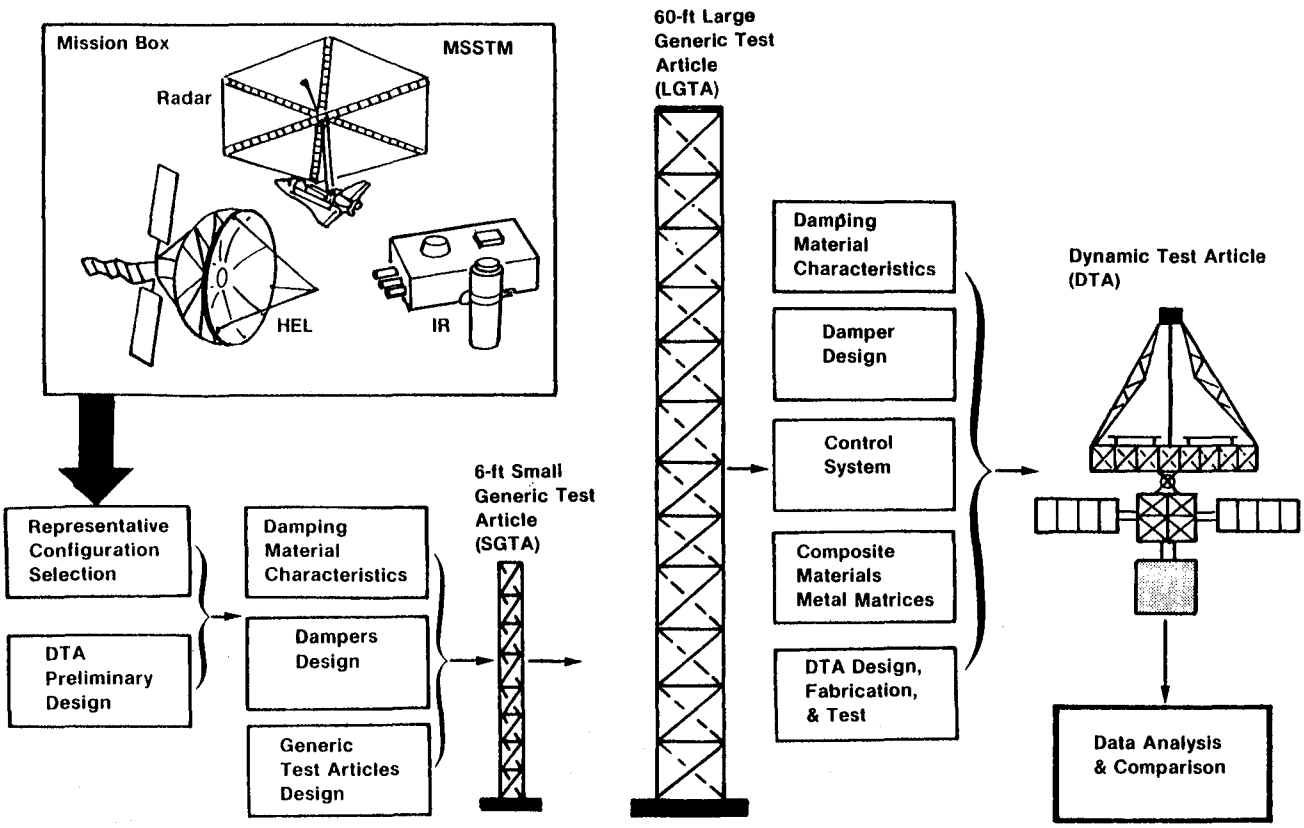

PACOSS POTENTIAL MISSION APPLICATION

MSSTM MISSION CONCEPTS	CONCEPT CHARACTERISTICS	DYNAMIC TECHNOLOGY ISSUES	PACOSS TECHNOLOGY APPLICATION	MISSION NEED DATE	PACOSS RESOLUTION DATE	OVERLAB RESOLUTION
6,7,8,10	Typified by large flexible and deployable structures. These missions present difficult dimensional precision problems. Surveillance/reconnaissance radars are in this category.	Deployment	Assist		TBD	1/90
		Jitter/Settling	Resolve		1/88	1/90
		Assembly	Assist		N/A	1/90
		Model Verif.	Resolve		TBD	1/90
		Struc. Interact.	Assist		1/88	1/90
		Limit Response	Resolve		1/88	1/90
24,26,27,28	Typified by large relatively flexible structures (except for Mission 24) whose space defense applications impose severe dimensional precision requirements.	Vib. Control	Resolve		TBD	1/90
		Model Verif.	Resolve		TBD	1/90
		Struc. Interact.	Assist		1/88	1/90
		Assembly	Assist		TBD	1/90
		Acoustic	N/A		N/A	N/A
		Jitter/Settling	Resolve		1/88	1/90
30,31,32,33,34	Large launch vehicles, orbital transfer vehicles, manned space station and space flight vehicle.	Berthing	Assist		N/A	1/90
		Acoustic	N/A		N/A	N/A
		Deployment	Assist		TBD	1/90
		Vib. Control	Resolve		TBD	1/90

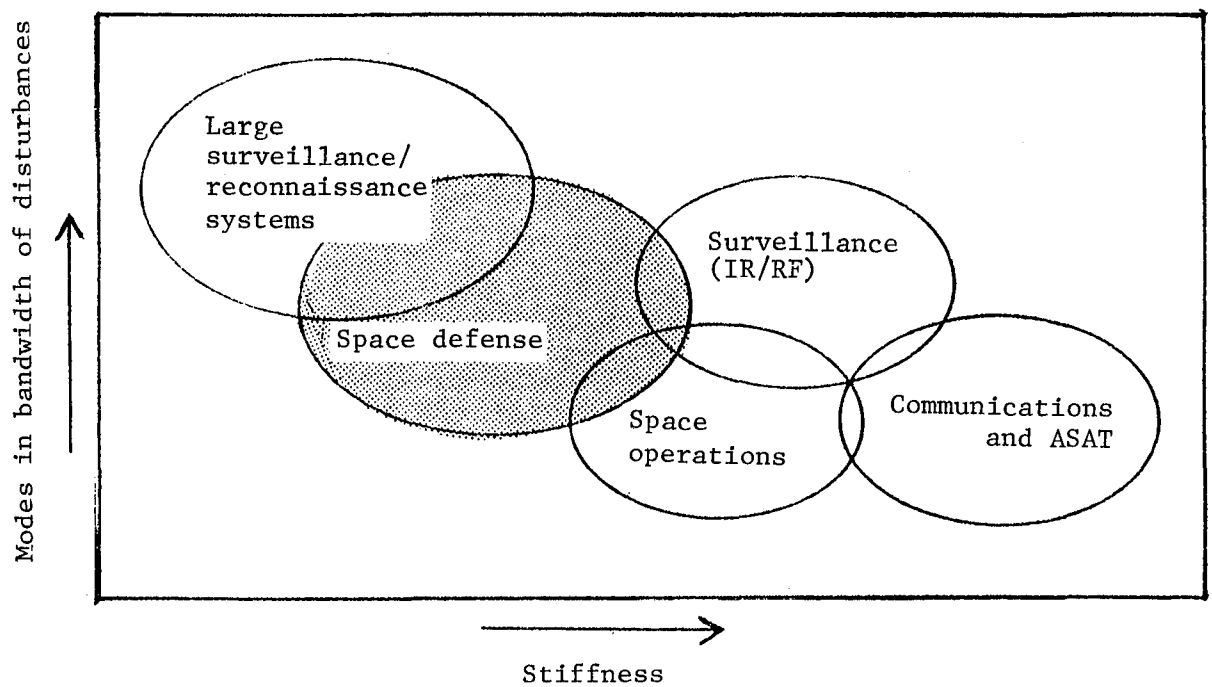

PACOSS—Goals and Objectives

Rapid Retargeting and Fine Pointing/Isolation Have Conflicting Requirements

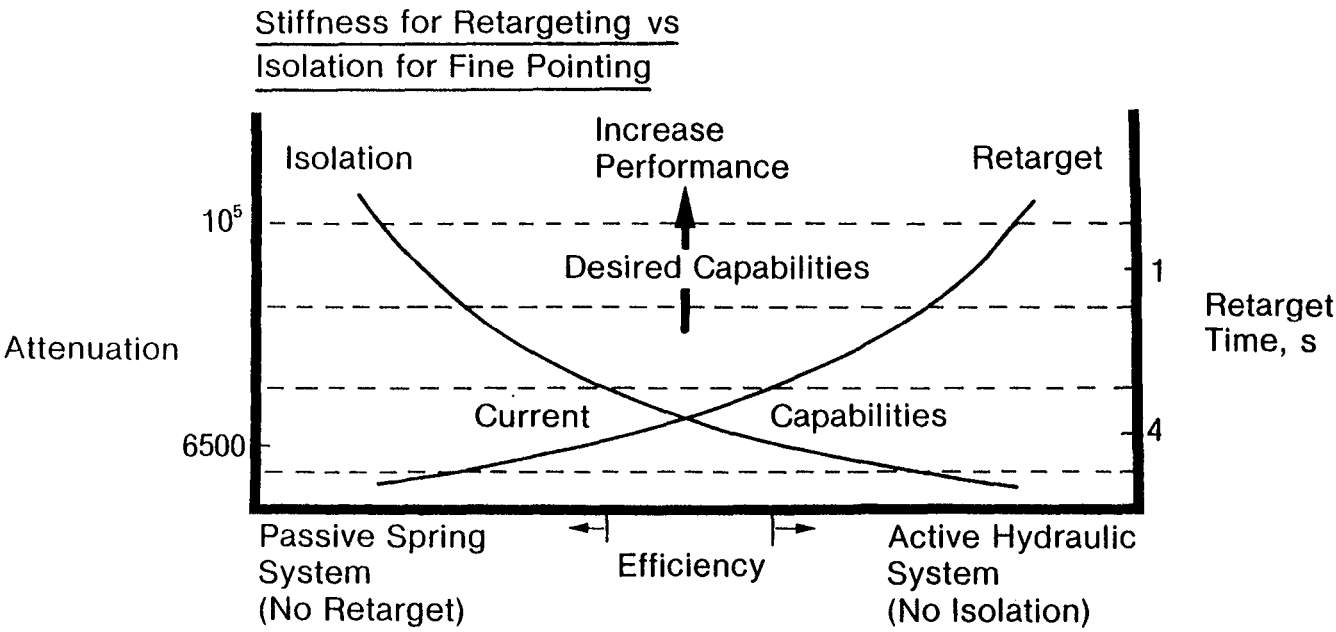

This slide shows graphically a difference in the time required to acquire a target, effect a kill, and retarget to another target.

SBL Performance

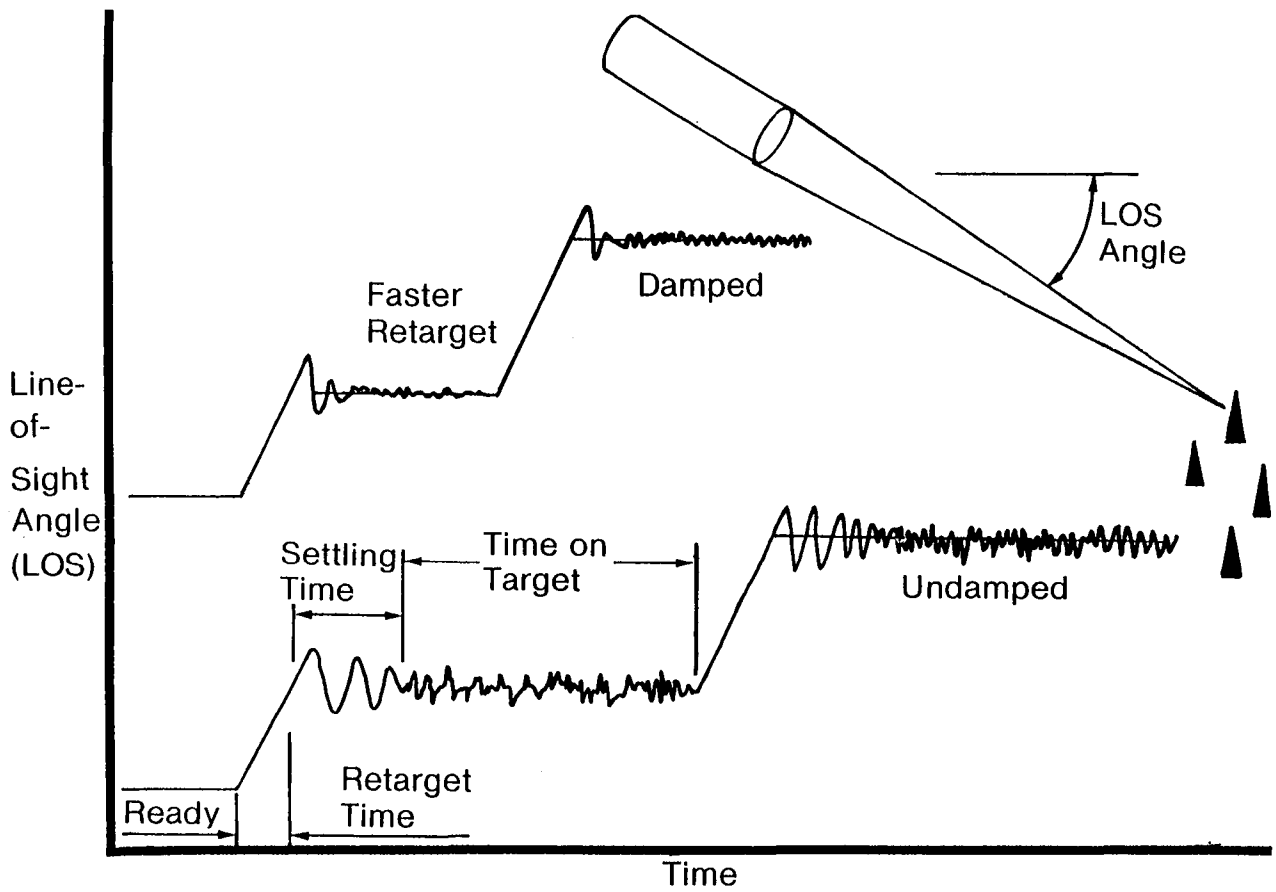

This slide presents Large Generic Test Articles. One of the articles is constructed out of Lexan (diagonals and horizontals), and the other out of Plexiglas. The corner posts are aluminum, in order to carry the dynamic load during the vibration. Plexiglas is a high-damped material, Lexan low. The difference is approximately one order of magnitude (0.3% vs. 3%). Both are not space qualifiable without some sort of surface treatment.

In addition, the articles have discrete dampers located in one plane. In this way shaking the article in two planes (one at a time) produces two sets of data, one with dampers, and one without.

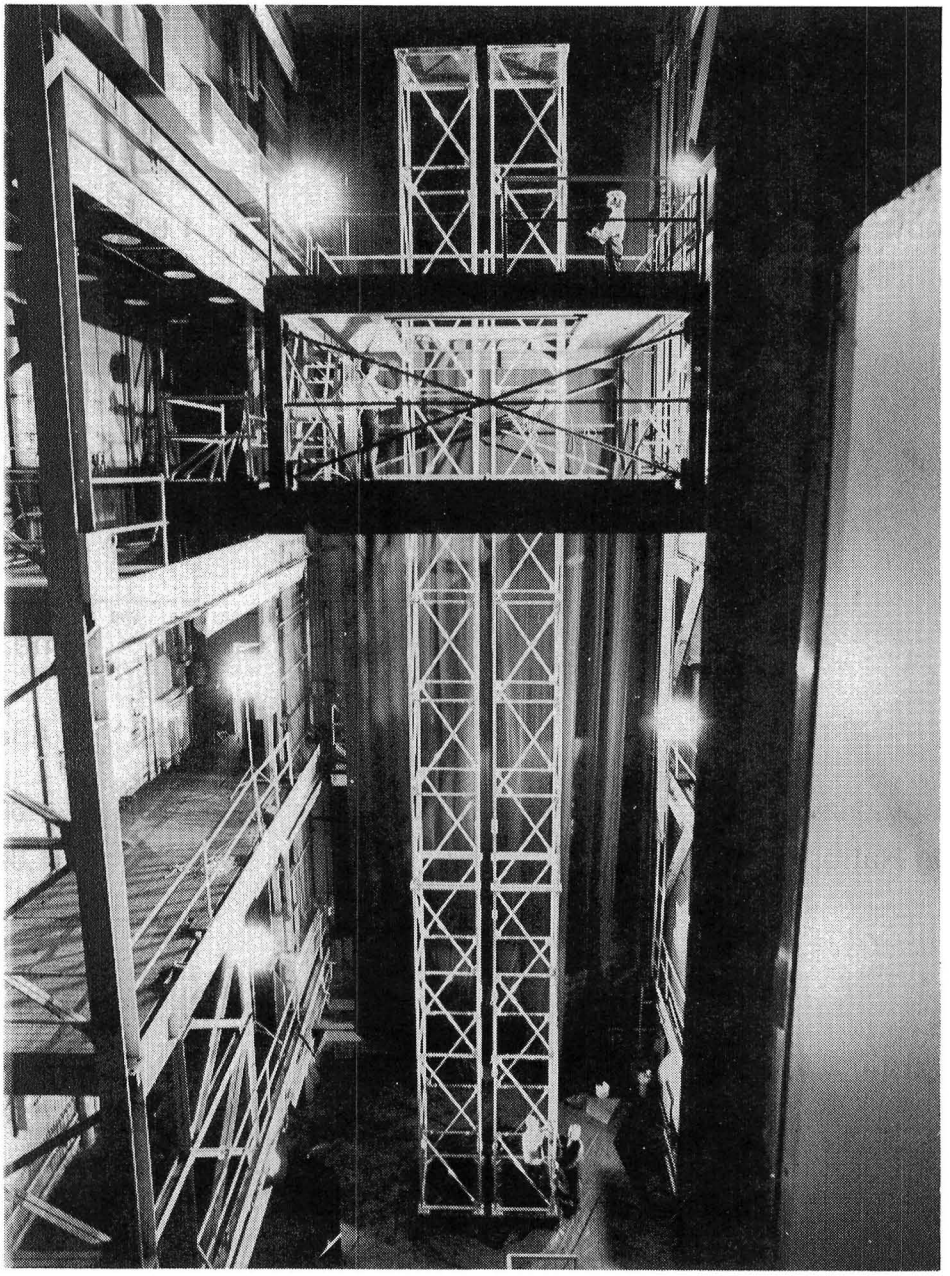

At the present time the Generic Test Articles have been constructed and tested. Preliminary analyses were performed and the results are presented in this slide. A significant point is that the fundamental bending frequencies compare within acceptable accuracy. The damping ratios do not. At the present time, it is postulated that the temperature gradient in the lab was greater than assumed from the available temperature data. Additional tests are in progress to resolve this problem.

Comparison of Test and Analysis

		Plexiglas		Lexan	
		Test	Analysis	Test	Analysis
Dampers	Frequency, Hz	1.67	1.59	1.60	1.60
	Damping Ratio, %	4.05	6.00	4.00	4.00

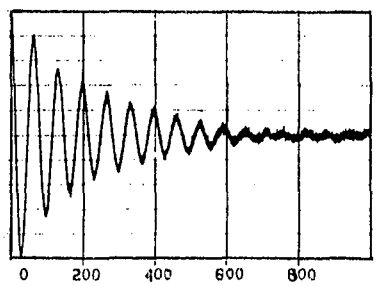

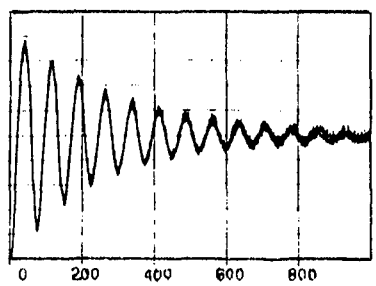

		Test	Analysis	Test	Analysis
No Dampers	Frequency, Hz	1.73	1.70	1.59	1.60
	Damping Ratio, %	1.55	1.00	0.30	1.00

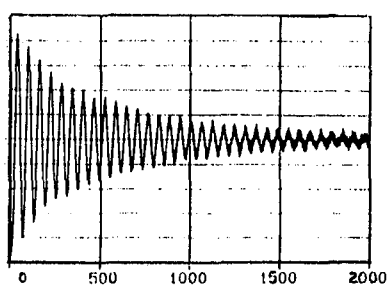

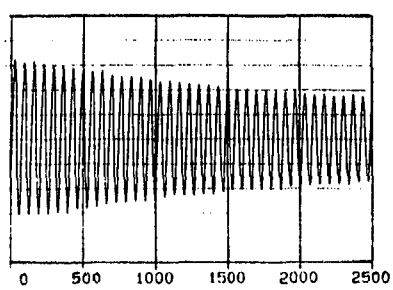

The graph on the right side reflects a relation between the system's damping ratio and the subsequent retarget time. In our example, an increase in damping from 1% to 2% produces approximately 1.9 seconds saving in retarget time.

Taking this number and applying it on the left plot, we obtain 16 SBLs saving, if a delay time of 90 seconds is chosen.

Improve Damping—Save Dollars

Cluster Attack

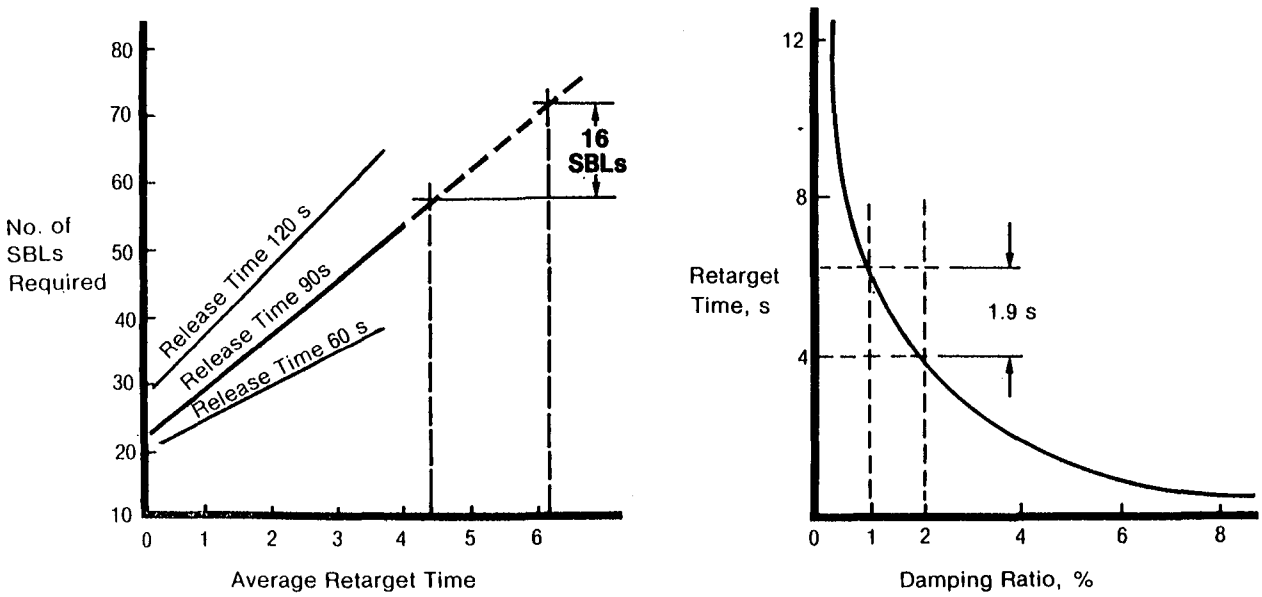

INITIAL RESULTS INDICATE SIGNIFICANT LSS SAVINGS

ENHANCE CURRENTLY PLANNED SYSTEMS

NEED FLIGHT DEMONSTRATION FOR VALIDATION

STRUCTURE/CONTROL INTERACTION CAUSES

- DEPLOYMENT
  - ERECTABLES
    - VARIABLE GEOMETRY STRUCTURE
    - SIGNIFICANT FREQUENCY VARIATION
    - GENERIC CONTROL
  - DEPLOYABLES
    - VARIABLE GEOMETRY STRUCTURE
    - DEPLOYMENT FORCES
- OPERATIONS
  - SURFACE CONTROL
    - OPTICAL SURFACE DISTORTION
  - STRUCTURAL CONTROL
    - SYSTEM DYNAMIC RESPONSE
  - SLEW CONTROL
    - SATELLITE REORIENTATION

STRUCTURAL/CONTROL INTERACTION SOLUTIONS

STRUCTURAL REVISION

INCREASE MASS, DIFFICULT DUE TO LAUNCH LIMITS
INHERENT DAMPING, POTENTIAL LIGHT-WEIGHT MATERIAL STRUCTURE

DISTURBANCE AVOIDANCE

FREQUENCY SEPARATION, DIFFICULT FOR FLEXIBLE STRUCTURE
ISOLATION, NON-SOLUTION FOR CONTROLLABLE STRUCTURE
ENERGY DISSIPATION, POTENTIAL STRUCTURAL/JOINT CONFIGURATIONS

DAMPED STRUCTURE

JOINT DESIGN, DIFFICULT TO MODEL/ANALYZE
VISCOELASTIC DAMPERS, 3 ORDERS OF MAGNITUDE
STRUCTURAL DESIGN, PACOSS DAMPING CONCEPTS

SOLUTION

SYNERGISTIC BEHAVIOR DAMPED STRUCTURES WITH ACTIVE CONTROL

Page intentionally left blank

APPLICATION OF THE MAXIMUM ENTROPY/OPTIMAL PROJECTION CONTROL DESIGN APPROACH FOR LARGE SPACE STRUCTURES

D. C. Hyland
Harris Corporation
Government Aerospace Systems Division
Melbourne, Florida

Large Space Antenna Systems Technology - 1984
December 4-6, 1984

INTRODUCTION: OPTIMAL PROJECTION/MAXIMUM ENTROPY DESIGN SYNTHESIS

In this presentation we (1) discuss the underlying philosophy and motivation of the optimal projection/maximum entropy (OP/ME) stochastic modelling and reduced order control design methodology for high order systems with parameter uncertainties, (2) review the OP/ME design equations for reduced-order dynamic compensation including the effect of parameter uncertainties, and (3) illustrate the application of the methodology to several Large Space Structure (LSS) problems of representative complexity. The basis for this paper is references [1-25] along with recently obtained results.

The OP/ME approach, as its name suggests, represents the synthesis of two distinct ideas: (1) reduced-order dynamic compensator design for a given high-order plant (i.e., optimal projection design) and (2) minimum-information stochastic modelling of parameter uncertainties (i.e., maximum entropy modelling). Maximum entropy modelling is discussed in [1-13,15] and optimal projection design is studied in [6,10,12,14,16-25].

Before attempting an overview of the OP/ME approach, it is important to discuss the class of problems that motivated this work, namely, control of large flexible space structures. A finite-element model of a large flexible space structure is, generally, an extremely high-order system. For example, a version of the widely studied CSDL Model #2 includes 150 modes and 6 disturbance states, i.e., a total of 306 states, along with 9 sensors and 9 actuators. The size of the model and the coupling between sensors and actuators render classical control-design methods useless and all but confound attempts to use LQG to obtain a controller of manageable order. Indeed, these difficulties were a prime motivation for the optimal projection approach. Besides the high order of these systems, finite element modelling is known to have poor accuracy, particularly for the high-order modes. Reasonable and not overly conservative uncertainty estimates predict 30-50 percent error in modal frequencies after the first 10 modes, with the situation considerably more complex (and pessimistic) for damping estimates. Otherwise-successful control-design methodologies widely promulgated in the aerospace community were severely strained in the face of such difficulties.

As indicated in Figure 1, maximum entropy modelling addresses the robustness problem by permitting direct inclusion of parameter uncertainties in the plant and disturbance models so that quadratically optimal system design plus maximum entropy modelling automatically yield system designs that trade performance off against modelling uncertainties. Furthermore, complexity and cost generally preclude implementation of very high dimension controllers (as in standard LQG techniques). Optimal projection design deals directly and rigorously with the question of system dimension by trading controller order off against performance.

OPTIMAL PROJECTION/MAXIMUM ENTROPY DESIGN SYNTHESIS

- **Parameter uncertainties are directly incorporated into the design process**
  - ⇨ **Optimal quantification of robustness/performance tradeoff**
- **Controller order fixed by implementation constraints**
  - ⇨ **Optimal quantification of order/performance tradeoff**

Figure 1

MAXIMUM ENTROPY MODELLING

Maximum entropy modelling is a form of stochastic modelling. Although external disturbances are traditionally modelled stochastically as random processes, the use of stochastic theory to model plant parameter uncertainty has seen relatively limited application. All objections to a stochastic parameter uncertainty model are dispelled by invoking the modern information-theoretic interpretation of probability theory. Rather than regarding the probability of an event as the limiting frequency of numerous repetitions (as, e.g., the number of heads in 1,000 coin tosses) we adopt the view that the probability of an event is a quantity which reflects the observer's certainty as to whether a particular event will or will not occur. This quantity is nothing more than a measure of the information (including, e.g., all theoretical analysis and empirical data) available to the observer. In this sense the validity of a stochastic model of a flexible space structure, for example, does not rely upon the existence of a fleet of such objects (substitute "ensemble" for "fleet" in the classical terminology) but rather resides in the interpretation that it expresses the engineer's certainty or uncertainty regarding the values of physical parameters such as stiffnesss of structural components. This view of probability theory has its roots in Shannon's information theory but was first articulated unambiguously by Jaynes (see [26-29]).

The preeminent problem in modelling the real world is thus the following: given limited (incomplete) a priori data, how can a well-defined (complete) probability model be constructed which is consistent with the available data but which avoids inventing data which does not exist? To this end we invoke Jaynes' Maximum Entropy Principle: First, define a measure of ignorance in terms of the information-theoretic entropy, and then determine the probability distribution which maximizes this measure subject to agreement with the available data. The smallest collection of data for which a well-defined probability model (called the minimum information model) can be constructed is known as the minimum data set.

The reasoning behind this principle is that the probability distribution which maximizes a priori ignorance must be the least presumptive (i.e., least likely to invent data) on the average since the amount of a posteriori learned information (should all uncertainty suddenly disappear) would necessarily be maximized. If, for some probability distribution, the a priori ignorance and hence the a posteriori learning were less than their maximum value then this distribution must be based upon invented and, hence, generally incorrect data. The Maximum Entropy Principle is clearly desirable for control-system design where the introduction of false data is to be assiduously avoided.

It is shown in [1] that the stochastic model induced by the Maximum Entropy Principle of Jaynes is a Stratonovich multiplicative white noise model. The earlier developments considered a relatively restricted class of parameter uncertainties. At present, however, the theory extends to the most general modelling uncertainties encountered in flexible mechanical systems. Moreover, the minimum data set presently used to induce the maximum entropy stochastic model consists of stipulated bounds on the deviations of physical parameters about their nominal values. This description is both convenient and deeply rooted in engineering tradition. As indicated in Figure 2, these parameter bounds are the basic data needed to implement maximum entropy modelling in practice.

MINIMUM-INFORMATION MODELLING

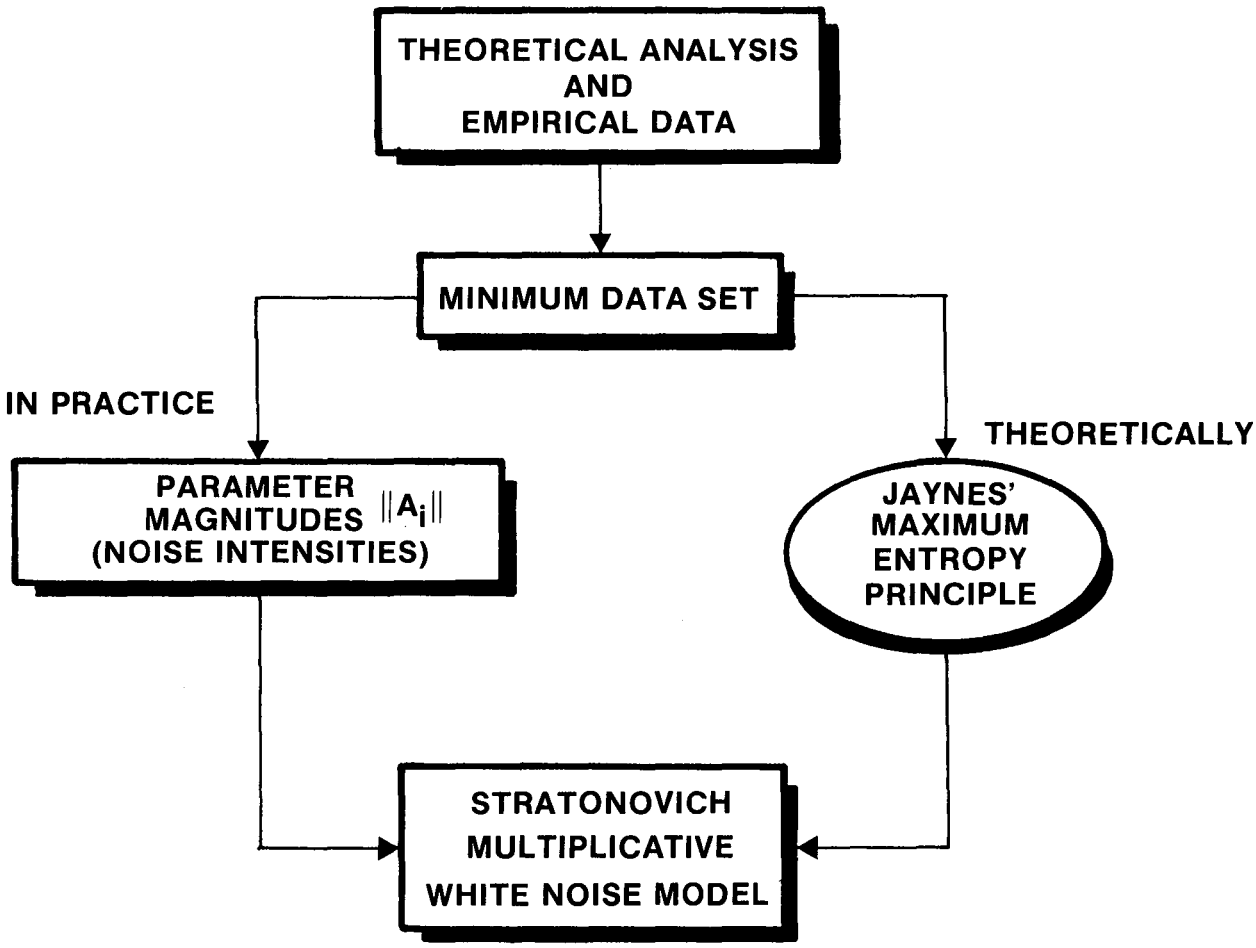

Figure 2

REPRESENTATION OF PARAMETER UNCERTAINTIES

Once significant types of parameter uncertainty have been identified and bounds on parameter variations established, the maximum entropy model can be placed in the general form shown in Figure 3. The set $\{A_i, i=1,\ldots,N\}$ of deterministic matrices defines the geometric pattern of the uncertain perturbation, ΔA, of the dynamics matrix. The norm $||A_i||$ defines the magnitude of uncertainty and is uniquely related to the originally stipulated parameter deviation bound. The stochastic model which follows in consequence of Jayne's Maximum Entropy Principle is a form of Stratonovich white noise. This model is extremely mathematically tractable since the second moment equation for the state can be closed. Moreover, the Stratonovich formulation allows crucial effects of uncertainty to be reproduced.

A = Nominal Dynamics Matrix

$A + \Delta A$ = Actual Dynamics Matrix (But ΔA Is Unknown)

WHITE NOISE REPRESENTATION

$$\Delta A = \sum_{i=1}^{p} \alpha_i(t) A_i$$

$\alpha_i(t)$ = Zero-Mean, Unit-Intensity, Uncorrelated White Noise Processes

A_i = Uncertainty Pattern

$||A_i||$ = Uncertainty Magnitude

MULTIPLICATIVE WHITE NOISE MODEL

$$\dot{x}(t) = (A + \sum_{i=1}^{p} \alpha_i(t) A_i) x(t)$$

Figure 3

STOCHASTIC DIFFERENTIAL EQUATIONS AND THE STRATONOVICH CORRECTION

Figure 4 displays the stochastic differential equation (second equation in the figure) arising from the Stratonovich model. To illustrate the crucial features of this model, a brief review of the literature on multiplicative white noise is absolutely essential. The theory of stochastic differential equations was placed on a firm mathematical foundation by Ito [30] and has been widely developed and applied to modelling, estimation and control problems [31-59]. The basic linear multiplicative white noise model is given by the Ito differential equation:

$$dx_t = (Adt + \sum_{i=1}^{p} d\alpha_{it} A_i) X_t$$

where the $d\alpha_{it}$ are Wiener processes. Although such models were studied extensively for estimator and control design [40-56], this approach fell into disrepute with the publication of [58,59] where it was shown for discrete-time systems that sufficiently high uncertainty levels (i.e., magnitudes $||A_i||$ above a threshold) led to the nonexistence of a steady state solution. Although it was purported in [58] that this "phenomenon" was an "obvious" consequence of high uncertainty levels, these conclusions failed to take into account (possibly because of the discrete-time setting) the subtle relationship between the ordinary differential equation (the first equation in Figure 4) and the stochastic differential equation. Indeed, it was shown in [31] that if a stochastic differential equation is regarded as the limit of a sequence of ordinary differential equations, then the above Ito equation is not correct. Instead, the ordinary differential equation with multiplicative white noise corresponds to the corrected Ito equation appearing as the second equation in Figure 4. It is seen that this differs from the "naive" equation by a systematic drift term (the Stratonovich correction). Although skepticism regarding this unusual result was admitted to in [31], the form of the second equation in Figure 4 was corroborated completely independently by Stratonovich in [32], whose results actually appeared in the Russian literature prior to 1965. His approach is based upon an alternative definition of stochastic integration which differs from Ito stochastic integration by a mathematical technicality. The Stratonovich approach, it should be noted, has the interesting feature that approximating sums involve future values of a Brownian motion process which, although physically unacceptable in the classical view of probability, is completely consistent with the information-theoretic interpretation.

In spite of the glaring technicality of the Stratonovich correction, almost all research on the estimation and control of such systems failed to perceive its physical significance. To the author's knowledge, the work of Gustafson and Speyer [56] was the only paper prior to the appearance of [1] which demonstrated the crucial feature: The Stratonovich correction neutralizes the threshold uncertainty principle. In particular for systems which are inherently stable under particular parameter variations (e.g., structures with uncertain stiffness matrices), the Stratonovich formulation correctly predicts unconditional second-moment stability - in contrast to the Ito formulation within which a stringent uncertainty threshold is encountered.

STRATONOVICH CORRECTION

Stratonovich, 1966 [31]; **Wong and Zakai, 1965** [32]

Ordinary Differential Equation: $\dot{x}(t) = (A + \sum_{i=1}^{p} \alpha_i(t) A_i) x(t)$

Itô Stochastic Differential Equation: $dx_t = (A_s dt + \sum_{i=1}^{p} d\alpha_{it} A_i) x_t$

$$A_s = A + \underbrace{\frac{1}{2} \sum_{i=1}^{p} A_i^2}_{\text{correction}}$$

Figure 4

MAXIMUM ENTROPY MODIFICATION OF THE STATE CONVARIANCE EQUATION

Note that when undertaking quadratic optimization within the maximum entropy model, one minimizes the mathematical expectation of the usual quadratic performance penalty taken over the maximum entropy statistics. Thus the feature of the stochastic model most utilized in practice is the second moment equation for the system state. The form of this equation that results from the Stratonovich white noise model is given explicitly in Figure 5. The "stochastic modification" term given by the bottom expression in Figure 5 distinguishes this stochastic Lyapunov equation from the ordinary Lyapunov equation that would result from a deterministically parametered model.

The importance of the stochastic modification term cannot be underrated. In particular, for most types of parameter uncertainty encountered in structural systems, the Stratonovich corrections in M[Q] imply progressive decorrelation between pairs of dynamical states. This informational or statistical damping phenomenon is a direct result of parameter uncertainties that is captured by the multiplicative white noise model. The Stratonovich correction, moreover, is crucial: By neutralizing the threshold uncertainty principle, it permits the consideration of long-term effects for arbitrary uncertainty levels.

$$\dot{Q}(t) = A_S Q(t) + Q(t)A_s^T + \sum_{i=1}^{p} A_i Q(t) A_i^T + V$$

$Q(t) = E[x(t)x(t)^T]$ (The quantity of interest in quadratic optimization)

E = Average over parameter uncertainties and disturbances

$$A_S = A + \frac{1}{2}\sum_{i=1}^{p} A_i^2 \qquad V = \text{Disturbance Intensity}$$

STOCHASTIC MODIFICATION

$$M[Q] = \frac{1}{2}\left(\sum_{i=1}^{p} A_i^2 Q + Q \sum_{i=1}^{p} A_i^{2T}\right) + \sum_{i=1}^{p} A_i Q A_i^T$$

Figure 5

RAMIFICATIONS FOR THE STRUCTURE OF THE STEADY STATE COVARIANCE

The far-reaching ramifications of the foregoing observations are explored extensively in [1-10]. As an example, assume (as is usually the case in practice) that uncertainties in modal frequency obtained from a finite-element analysis of a large flexible space structure increase with mode number. From the form of M[Q(t)] it is easy to deduce that the steady state covariance becomes increasingly diagonally dominant with increasing frequency and thus assumes the qualitative form given in Figure 6. The benefits of this sparse form are important: The computational effort required to determine the steady state covariance (and thus to design a closed-loop controller, for example) is directly proportional to the amount of information reposed in the model or, equivalently, inversely proportional to the level of modelled parameter uncertainty. This casts new light on the computational design burden vis-a-vis the modelling question: The computational burden depends only upon the information actually available. A simple control-design exercise involving full-state feedback for a simply supported beam presented in [4] illustrates this point. The gains for the higher-order modes of the beam, whose frequency uncertainties increase linearly with frequency, were obtained with modest computational effort in spite of 100 structural modes included in the model. Another important ramification of the qualitative form of Q is the automatic generation of a high/low-authority control law. Note that for the higher order and hence highly uncertain modes the control gains reported in [3,4] indicated an inherently stable, low performance rate-feedback control law, whereas for the lowest order modes the control law is high authority, i.e., "LQ" in character.

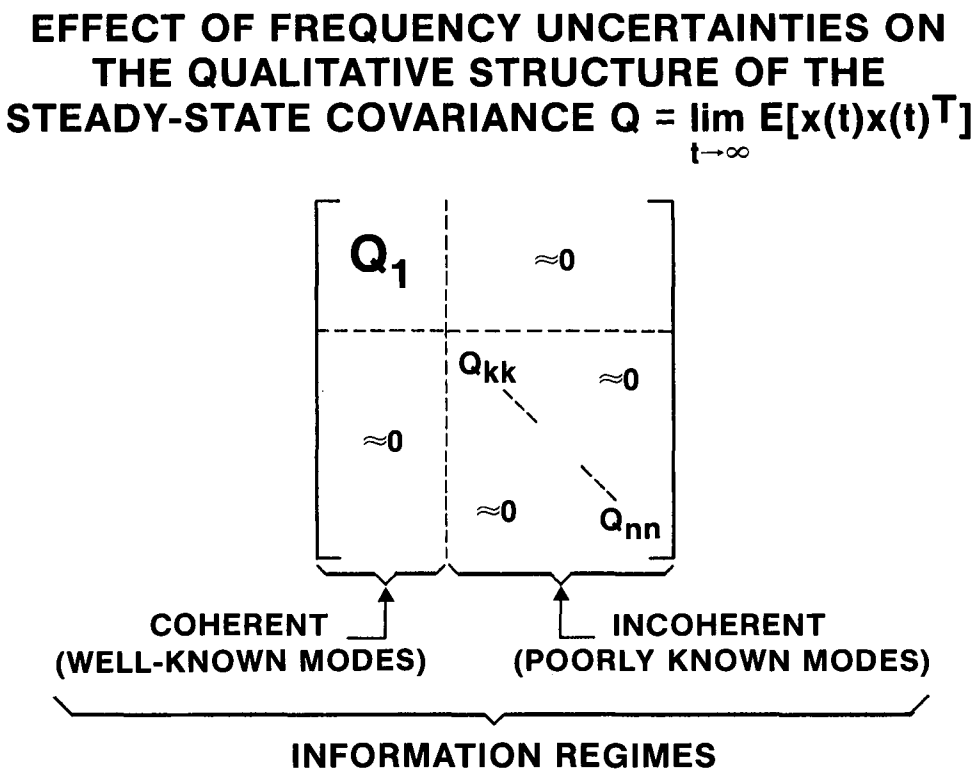

Figure 6

PERFORMANCE ROBUSTNESS

Figure 7 illustrates the basic concept of robustness with respect to performance that is so essential to adequate LSS control design. The curves shown sketch the variation of closed-loop performance (e.g., line-of-sight error) for particular control designs when system parameters deviate from their nominal values. As illustrated in one example below, standard LQG design provides a sharp minimum at the nominal parameter values but can be extremely sensitive to off-nominal variations. On the other hand, since the maximum entropy formulation includes the deleterious effects of uncertainty within the basic design model, it provides the mechanism to assure satisfaction of performance objectives not only for the nominal model but also over the likely range of parameter deviations. Note that the price paid for this is a degradation of performance (relative to a deterministic model, LQG design) whenever the system parameters happen to be near their nominal values. However, this tradeoff between nominal performance and robustness is widely recognized as an inescapable fact of life. The prime motivation for the maximum entropy development is to achieve a design methodology which sacrifices as little near-nominal performance as possible while securing performance insensitivity over the likely range of modelling errors.

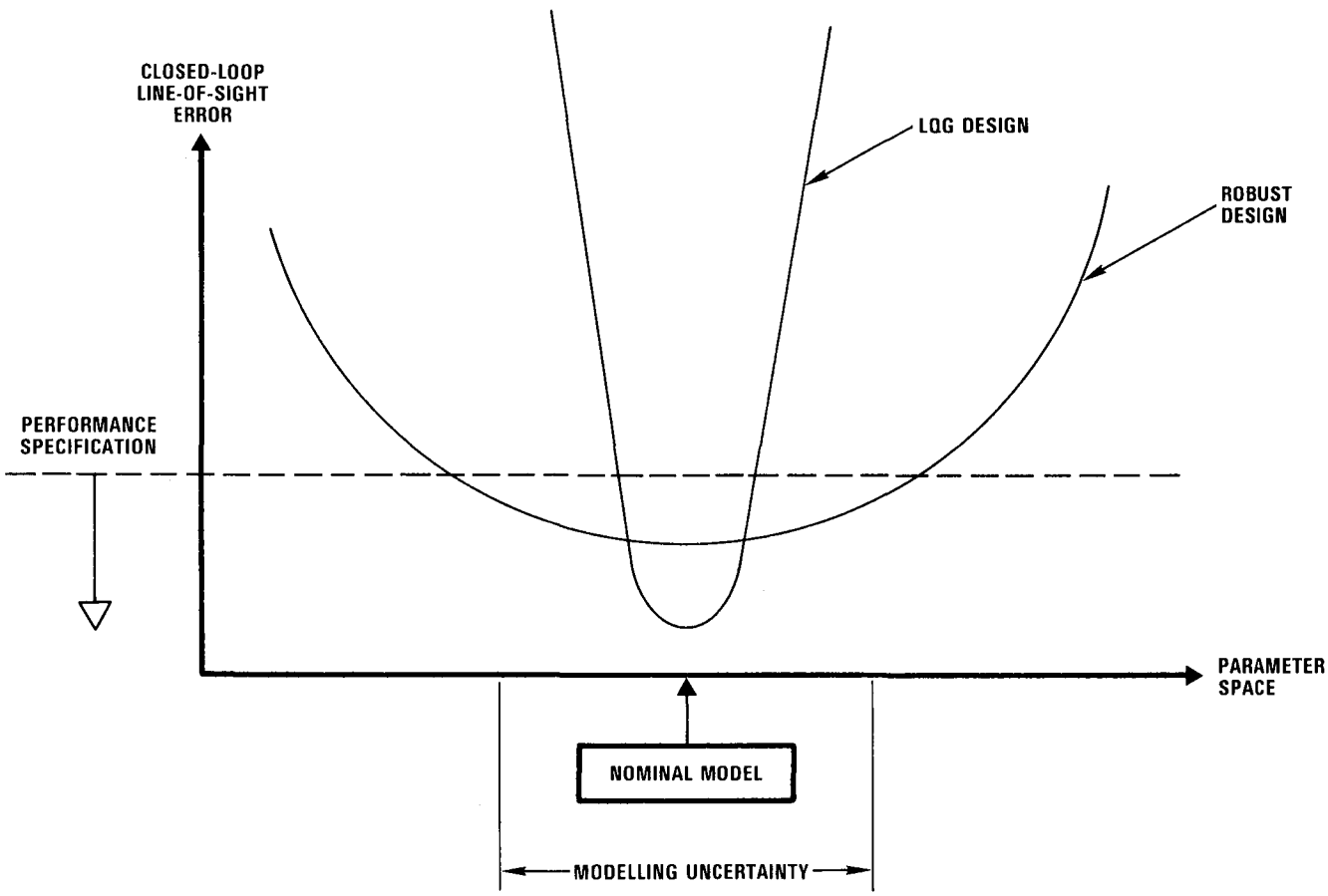

Figure 7

DEVELOPMENT OF THE OP/ME SYNTHESIS

At this point, we consider the optimal projection approach and its amalgamation with maximum entropy modelling. Figure 8 illustrates that the overall development proceeded along two distinct paths, starting from standard LQG theory. One path of development (the right branch) retained the LQG assumption that the dynamic controller to be designed is of the same dimension as the plant but extended the theory by including the effects of parameter uncertainty via stochastic modelling. The optimality conditions for full-order dynamic compensation under a maximum entropy model are the principal design results and consist of two modified Riccati equations coupled to two Lyapunov equations by the stochastic modification terms. These equations were presented in [5,15] and were also independently discovered by a Soviet researcher [57].

The second path of development from LQG retained the assumption of a deterministically parametered model but removed the restriction to full-order compensation - i.e., a quadratically optimal but fixed-order compensator is sought for a higher order plant in order to simplify implementation. This led to the optimal projection approach to fixed-order compensation.

The optimal projection approach is based entirely on a theorem which characterizes the quadratically optimal reduced-order dynamic compensator. Assuming a purely dynamic linear system structure for the desired compensator whose order is determined by implementation constraints (e.g., reliability, complexity or computing capability), a parameter optimization approach is taken. There is, of course, nothing novel about this approach per se and it has been widely studied in the control literature [60-73]. Clearly, the parameter optimization approach fell into disrepute because of the extreme complexity of the grossly unwieldy first-order necessary conditions which afforded little insight and engendered brute force gradient search techniques. The crucial discovery occurred in [6] where it was revealed that the necessary condition for the dynamic-compensation problem gives rise to the definition of an optimal projection as a rigorous, unassailable consequence of quadratic optimality without recourse to ad hoc methods as in [74-83]. Exploitation of this projection leads to immense simplification of the "primitive" form of the necessary conditions for this problem. The novel equations consist of two modified Riccati equations and two modified Lyapunov equations (analogous to the four optimality conditions for full-order compensation under maximum entropy models) coupled, in this instance, by a projection of rank equal to the desired controller dimension. This "optimal projection" essentially characterizes the geometric structure of a reduced-order plant model employed internally by the compensator.

OPTIMAL PROJECTION/MAXIMUM ENTROPY APPROACH TO LOW-ORDER, ROBUST CONTROLLER DESIGN

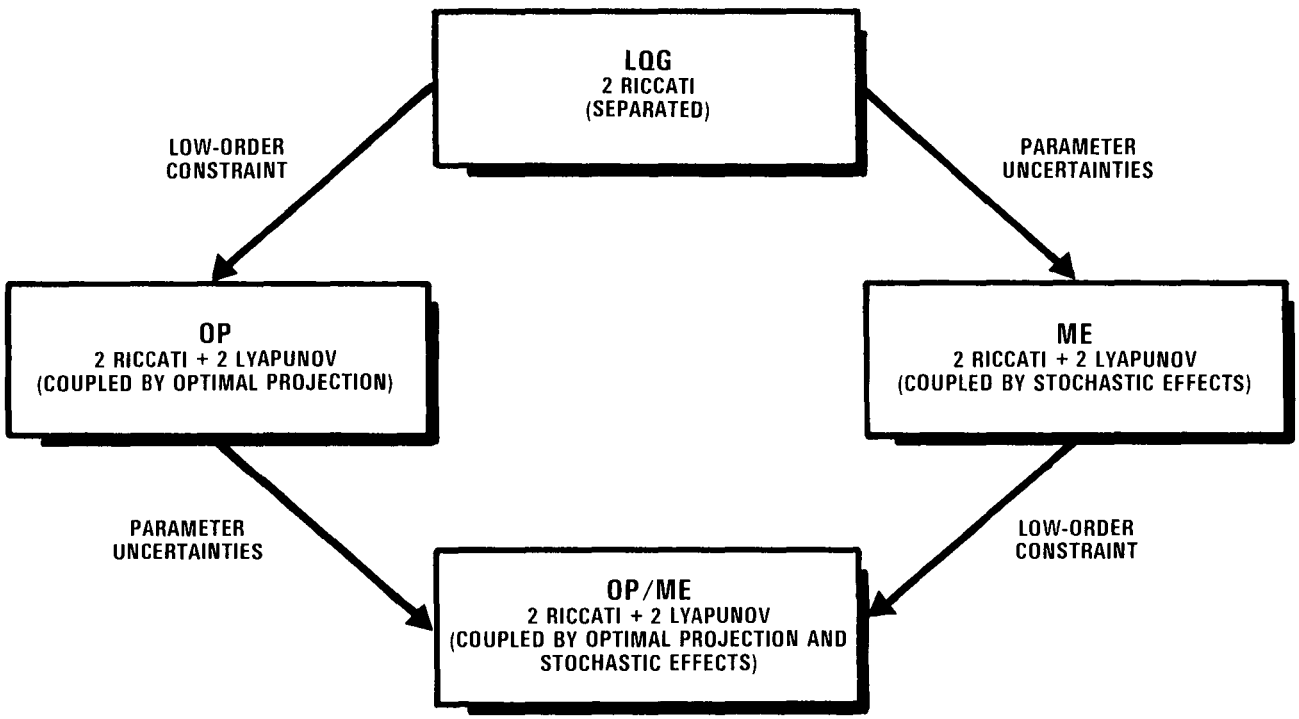

Figure 8

SURVEY OF APPROACHES TO FIXED-ORDER DYNAMIC COMPENSATOR DESIGN

Before describing the synthesis of the optimal projection (OP) and maximum entropy (ME) approaches, we sketch the relationship between optimal projection and previously proposed techniques for reduced-order compensator design. The general relationships among general categories of approaches are illustrated in Figure 9.

The basic premise is that the plant to be controlled is distributed parameter in character (as are structural systems). The usual engineering approach (the right branch in Figure 9) is to replace the distributed parameter system with a high-order finite-dimensional model. However, fundamental difficulties remain since application of LQG leads to a controller whose order is identical to that of the high-order approximate model. Attempts to remedy this problem usually rely upon some method of open-loop model reduction followed by LQG design or LQG design followed by closed-loop controller reduction (see, e.g., [74-83]). Most of these techniques are ad hoc in nature, however, and hence guarantees of optimality and stability are lacking.

A more direct approach that avoids both model and controller reduction is to fix the controller structure and optimize the performance criterion with respect to the controller parameters. This is the optimal projection formulation. As noted above, the new forms of optimality conditions discovered in [6] harbor the definition of an oblique projection (i.e., idempotent matrix) which is a consequence of optimality and not the result of an ad hoc assumption. By exploiting the presence of this "optimal projection," the originally very complex stationary conditions can be transformed without loss of generality into much simpler and more tractable forms. The resulting equations (see (2.10)-(2.17) of [22]) preserve the simple form of LQG relations for the gains in terms of covariance and cost matrices which, in turn, are determined by a coupled system of two modified Riccati equations and two modified Lyapunov equations. This coupling, by means of the optimal projection, represents a graphic portrayal of the demise of the classical separation principle for the reduced-order controller case. When, as a special case, the order of the compensator is required to be equal to the order of the plant, the modified Riccati equations immediately reduce to the standard LQG Riccati equations and the modified Lyapunov equations express the proviso that the compensator be minimal, i.e., controllable and observable. Since the LQG Riccati equations as such are nothing more than the necessary conditions for full-order compensation, the "optimal projection equations" appear to provide a clear and simple generalization of standard LQG theory.

On the other hand (see the left branch of Figure 9), the approach taken by the mathematical community accepts the distributed parameter model, extends LQG results to obtain a controller of similarly infinite dimensional nature and then resorts to discretization and truncation to achieve a suitably low-order (and finite dimensional) controller for implementation. However, the finite-dimensional approximation schemes that have been applied to optimal infinite-dimensional control laws [84-87] only guarantee optimality in the limit, i.e., as the order of the approximating controller increases without bound. Hence, there is no guarantee that a particular approximate (i.e., discretized) controller is actually optimal over the class of approximate controllers of a given order which may be dictated by implementation constraints. Moreover, even if an optimal approximate finite-dimensional controller could be obtained, it would almost certainly be suboptimal in the class of all controllers of the given order.

It should be mentioned that notable exceptions to the above-mentioned work on distributed parameter controllers are the contributions of Johnson [88] and Pearson [89,90] who suggest fixing the order of the finite-dimensional compensator while retaining the distributed parameter model. Progress in this direction, however, was impeded not only by the intractability of the optimality conditions that were available for the finite-dimensional problem, but also by the lack of a suitable generalization of these conditions to the infinite-dimensional case. Recent results [18,21,23] made significant progress in filling these gaps by deriving explicit optimality conditions which directly characterize the optimal finite-dimensional fixed-order dynamic compensator for an infinite-dimensional system and which are exactly analogous to the highly simplified optimal projection equations obtained in [6,12,14,16,22] for the finite-dimensional case. Specifically, instead of a system of four matrix equations we obtain a system of four operator equations whose solutions characterize the optimal finite-dimensional fixed-order dynamic compensator. Moreover, the optimal projection now becomes a bounded idempotent Hilbert-space operator whose rank is precisely equal to the order of the compensator.

As Figure 9 suggests, this represents the most direct approach yet taken to designing low-order controllers for infinite-dimensional systems. Computational techniques for solution of the operator equations remain the object of research, but success in the finite-dimensional case leads to confidence that existing solution techniques can be appropriately generalized.

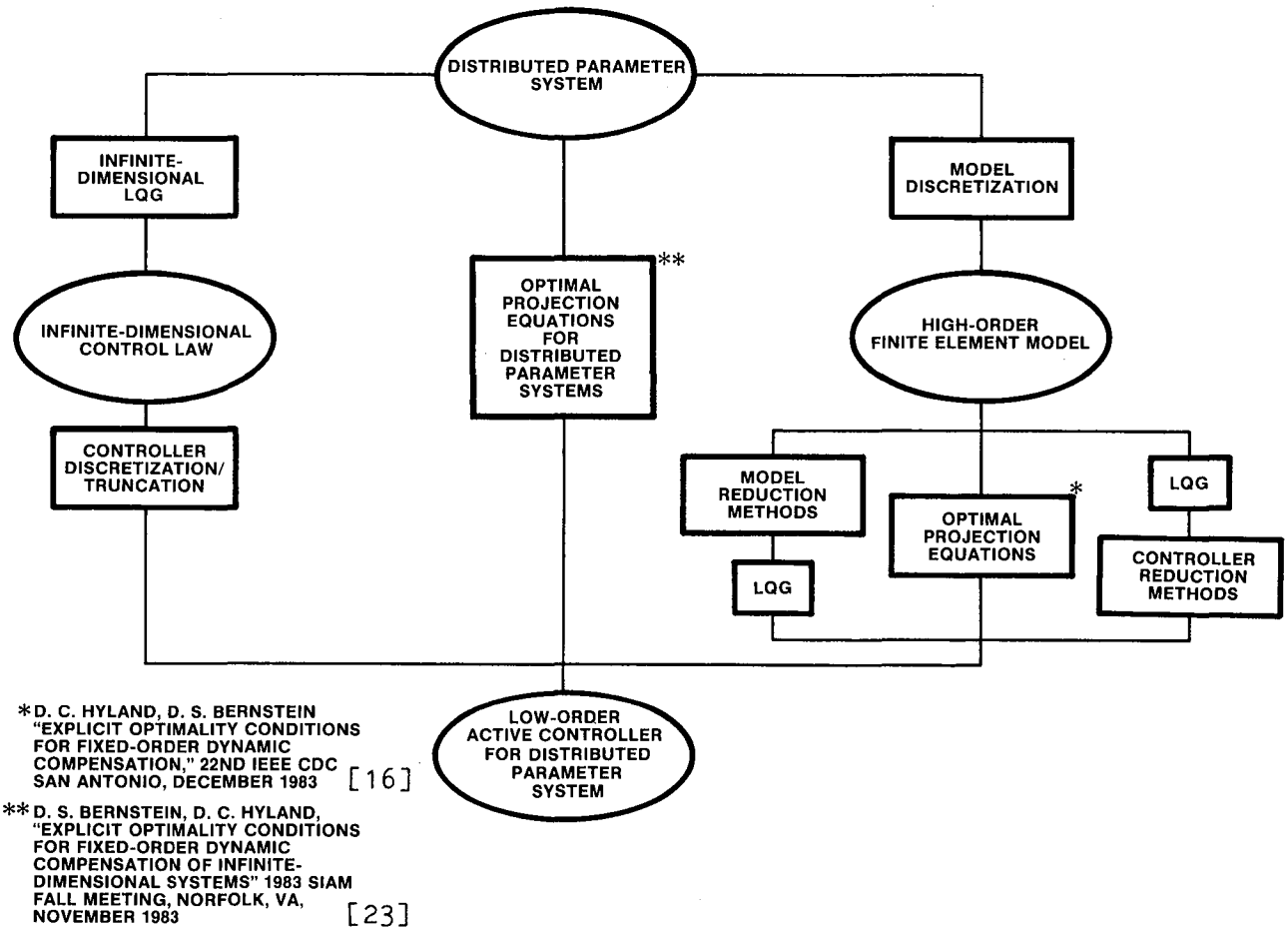

Figure 9

STEADY STATE REDUCED-ORDER DYNAMIC COMPENSATION
PROBLEM WITH PARAMETER UNCERTAINTIES

Now we explicitly present the combined OP/ME design equations. First, Figure 10 gives the problem statement. The high-order, uncertain plant has state $X \varepsilon \mathbb{R}^N$ where N is finite. As indicated using previous notation, uncertainties in the dynamics matrix, A, the control input matrix, B, and the sensor output matrix, C, are all modelled via the maximum entropy approach. Furthermore, the general formulation allows cross-correlation between the disturbance noise, w_1, and the observation noise, w_2.

The object is to design a lower order dynamic controller with state $X_c \varepsilon \mathbb{R}^{N_c}$ where $N_c < N$ by choosing the controller matrices A_c, B_c and C_c so as to minimize the indicated quadratic performance criterion. Note that the possibility of cross terms ($R_{12} \neq 0$) in the performance index is accounted for in this formulation.

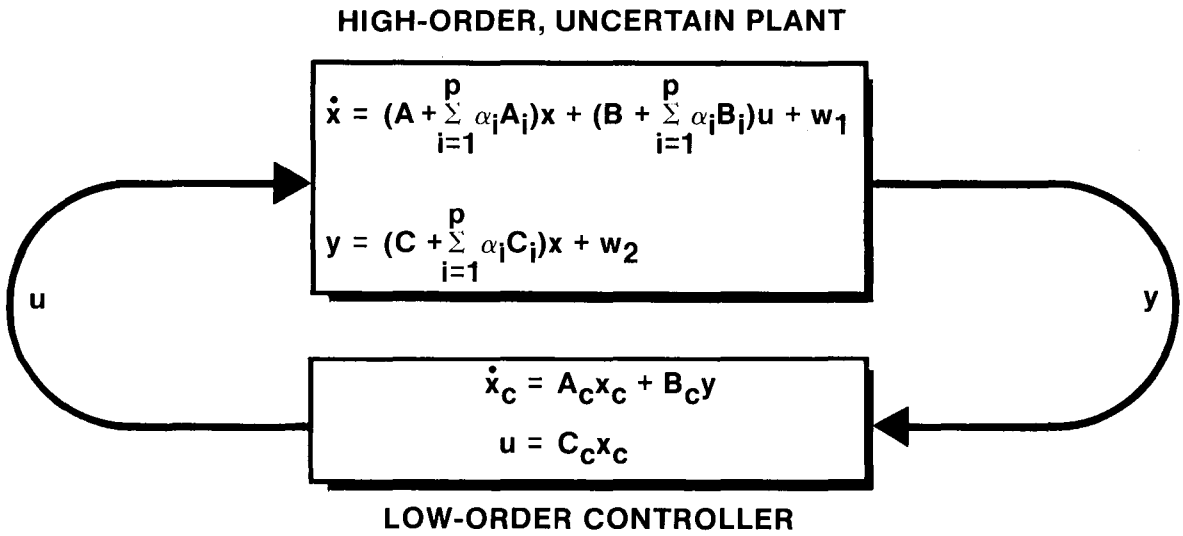

PERFORMANCE CRITERION

$$J(A_c, B_c, C_c) = \lim_{t \to \infty} E[x^T R_1 x + 2x^T R_{12} u + u^T R_2 u]$$

Technical Assumption: $B_i \neq 0 \Rightarrow C_i = 0$

Figure 10

MAIN THEOREM OF OP/ME: OPTIMAL COMPENSATOR GAINS

With the foregoing problem statement, the quadratically optimal gains are given by the first three expressions in Figure 11. These relationships are basically LQG in character - the major modification being brought about by the appearance of the matrices $\Gamma \varepsilon \mathbb{R}^{N_c \times N}$ and $G \varepsilon \mathbb{R}^{N_c \times N}$. A particular factorization of the optimal projection τ, i.e., $\Gamma G^T = I_{N_c}$, is represented by Γ and G so that $\tau = G^T\Gamma$ is idempotent. Note that any rank N_c projection can be factored in this way and, for given τ, any and all such factorizations yield the same closed-loop performance (see [22]).

Determination of A_c, B_c and C_c requires that we first solve the basic design equations (shown in Figure 12) for the quantities Q, P, and $\hat{Q}$, $\hat{P}$ and τ. The notational conventions given on the lower half of Figure 11 serve to define these design equations precisely.

CONTROLLER GAINS (Functions of Q, P, $\hat{Q}$, $\hat{P}$)

$$A_c = \Gamma(A_s - B_s R_{2s}^{-1} P_s - Q_s V_{2s}^{-1} C_s) G^T$$

$$B_c = \Gamma Q_s V_{2s}^{-1}$$

$$C_c = -R_{2s}^{-1} P_s G^T$$

NOTATION

$$\hat{Q}\hat{P} = G^T M \Gamma, \quad \Gamma G^T = I_{n_c} \; (\Rightarrow \tau = G^T\Gamma = \tau^2)$$

$$AQA^T = \sum_{i=1}^{p} A_i Q A_i^T, \quad AQB = \sum_{i=1}^{p} A_i Q B_i, \text{ etc.}$$

$$A_s = A + \frac{1}{2}A^2 \qquad B_s = B + \frac{1}{2}AB \qquad C_s = C + \frac{1}{2}CA$$

$$R_{2s} = R_2 + B^T(P+\hat{P})B \qquad V_{2s} = V_2 + C(Q+\hat{Q})C^T$$

$$Q_s = QC_s^T + V_{12} + A(Q+\hat{Q})C^T \qquad P_s = B_s^T P + R_{12}^T + B^T(P+\hat{P})A$$

Figure 11

OPTIMAL PROJECTION/MAXIMUM ENTROPY DESIGN EQUATIONS

Finally, Figure 12 shows the fundamental OP/ME design equations for determination of P, Q, $\hat{P}$, $\hat{Q}$ and τ. The nonnegative-definite matrices P and Q are analogous to the regulator and observer cost matrices of LQG and are determined by two modified Riccati equations. The two modified Lyapunov equations satisfied by matrices $\hat{Q}$ and $\hat{P}$ are analogous to the Lyapunov equations determining controllability and observability Grammians that are employed by many of the current, suboptimal, controller-order reduction schemes. Note that the optimal projection, τ, is given explicitly in terms of the group generalized inverse of the product $\hat{Q}\hat{P}$. Thus, the nonnegative-definite matrices $\hat{Q}$ and $\hat{P}$ largely serve to determine τ.

In contrast to LQG, all four equations are coupled both by the optimal projection and by the stochastic modification terms - indicating that the classical separation principle generally breaks down under restrictions on controller dimension and/or under the impact of parameter uncertainties.

The four equations in Figure 12 summarize a generalized LQG-type approach wherein robust controllers of low dimension follow as a direct consequence of the optimality criterion and a priori uncertainty levels. Moreover, the computational task is well-defined: solve a system of two Riccati and two Lyapunov equations coupled by the optimal projection and stochastic effects. A variety of computational procedures are presented in [1, 4, 14-15, 17, 19] and these are currently included in an automated design software package. We illustrate this automated design capability in the example problems that follow.

SOLVE FOR NONNEGATIVE-DEFINITE Q, P, $\hat{Q}$, $\hat{P}$

$$0 = A_s Q + Q A_s^T + A Q A^T + V_1 + (A - B R_{2s}^{-1} P_s)\hat{Q}(A - B R_{2s}^{-1} P_s)^T - Q_s V_{2s}^{-1} Q_s^T + \tau_\perp Q_s V_{2s}^{-1} Q_s^T \tau_\perp^T$$

$$0 = A_s^T P + P A_s + A^T P A + R_1 + (A - Q_s V_{2s}^{-1} C)^T \hat{P} (A - Q_s V_{2s}^{-1} C) - P_s^T R_{2s}^{-1} P_s + \tau_\perp^T P_s^T R_{2s}^{-1} P_s \tau_\perp$$

$$0 = (A_s - B_s R_{2s}^{-1} P_s)\hat{Q} + \hat{Q}(A_s - B_s R_{2s}^{-1} P_s)^T + Q_s V_{2s}^{-1} Q_s^T - \tau_\perp Q_s V_{2s}^{-1} Q_s^T \tau_\perp^T$$

$$0 = (A_s - Q_s V_{2s}^{-1} C_s)^T \hat{P} + \hat{P}(A_s - Q_s V_{2s}^{-1} C_s) + P_s^T R_{2s}^{-1} P_s - \tau_\perp^T P_s^T R_{2s}^{-1} P_s \tau_\perp$$

$$\text{RANK } \hat{Q} = \text{RANK } \hat{P} = \text{RANK } \hat{Q}\hat{P} = n_c$$

$$\tau = \hat{Q}\hat{P}(\hat{Q}\hat{P})^{\#} \qquad \tau_\perp = I_n - \tau$$

⇨ GROUP GENERALIZED INVERSE

Figure 12

EXAMPLE 1: CSDL MODEL #2

The first two examples considered here illustrate application of the optimal projection approach without inclusion of parameter uncertainty effects. The third and final example serves to illustrate the combined OP/ME design capability.

The first case was treated in [17] and is depicted in Figure 13. Specifically, it is a version of the CSDL, ACOSS Model 2 previously considered in [91]. The steady state performance index has the form

$$J = E\left[X^T R_1 X\right] + RE\left[U^T U\right]$$

where R_1 represents the state penalties on mean square line-of-sight errors and defocus and R is a positive scalar. Clearly, controller authority and bandwidth are both inversely proportional to R.

This example was used to compare both theoretically and numerically the optimal projection approach with a variety of suboptimal controller-order reduction methods. The theoretical comparison shows that all current suboptimal techniques essentially define a (suboptimal) projection characterizing the reduced-order compensator. In contrast, the optimal projection design equations define the needed projection by rigorous application of optimality principles. Moreover, all the approaches considered in [7] can be displayed in a common notation, and this graphically reveals the suboptimal design equations as special cases of or approximations to the optimal projection equations.

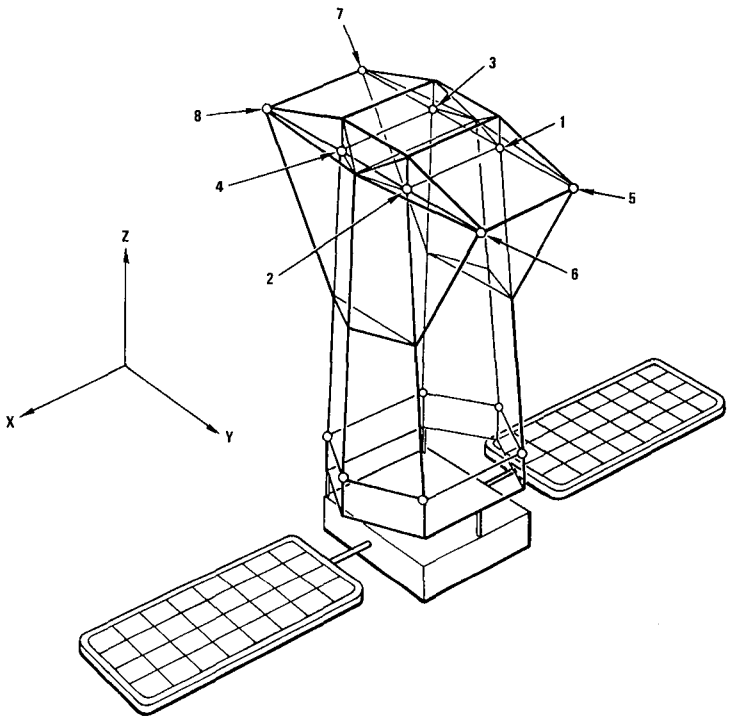

REFERENCE: [91]

R. E. Skelton and P. C. Hughes, "Modal Cost Analysis for Linear Matrix Second-Order Systems," J Dyn Syst Meas and Control Vol 102, September 1980, pp 151-180

Figure 13

NUMERICAL COMPARISON OF SUBOPTIMAL AND OPTIMAL PROJECTION APPROACHES

Now for the numerical comparisons. As is standard in the application of quadratic optimization, one characterizes each design for a fixed compensator order by plotting the "regulation cost" ($E[X^T R_1 X]$) as a function of the "control cost" ($E[U^T U]$). Results for these tradeoff curves are shown in Figure 14. The very bottom-most curve represents the full-order, LQG design. Since this is the best obtainable when there is no restriction on compensator order, the problem is obtaining a lower order design whose tradeoff curve is as close to the LQG results as possible.

The thin black lines in Figure 14 show the N_c = 10, 6, and 4 designs obtained via Component Cost Analysis [83], where N_c denotes the compensator dimension. This appears to be the most successful suboptimal method applied to the example problem considered here. Note that the 10th and 6th order compensator designs are quite good, but when compensator order is sufficiently low (N_c = 4) and controller bandwidth sufficiently large (R<5.0), the method fails to yield stable designs. This difficulty is characteristic of all suboptimal techniques surveyed, and, in fairness, it should be noted that most other suboptimal design methods fail to give stable designs for compensator orders below 10.

In contrast, the width of the grey line in Figure 14 encompasses all the optimal projection results for compensators of orders 10, 6, and 4.

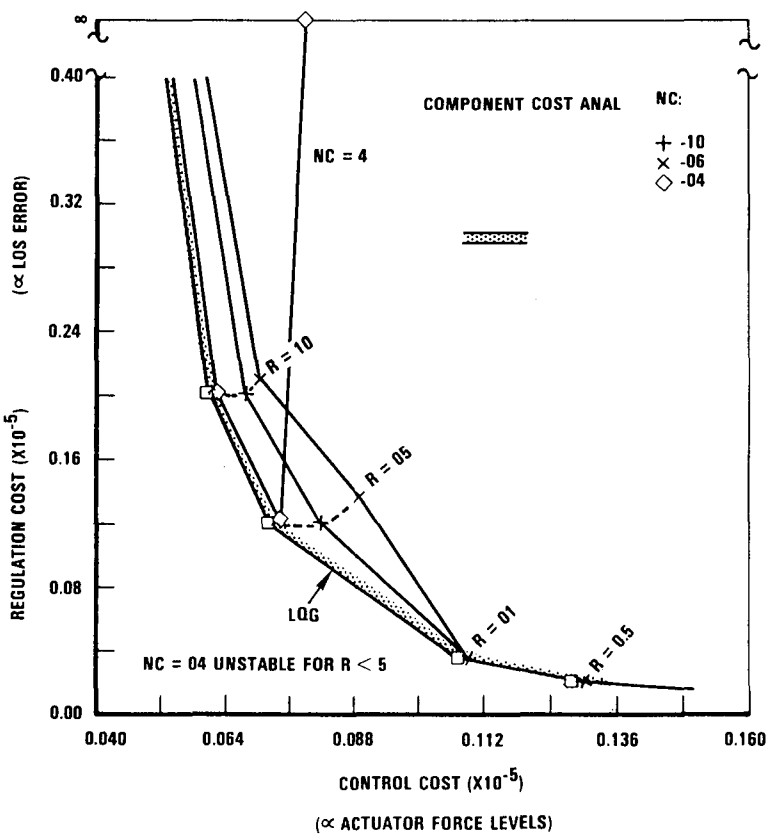

Figure 14

OPTIMAL PROJECTION RESULTS FOR PERFORMANCE/COMPLEXITY TRADEOFF

To provide a more detailed picture of the optimal projection results, Figure 15 shows the percent of total performance increase relative to the full-order, LQG designs as a function of 1/R (proportional to controller bandwidth and to actuator force levels) for the various compensator orders considered.

Even for the 4th order design, the optimal projection performance is only ~5 percent higher than the optimal full-order design. Furthermore, the performance index for the optimal projection designs increases monotonically with decreasing controller order - as it should. Such is not the case for suboptimal design methods.

These results reinforce our belief that the optimal projection approach is a powerful and highly reliable alternative to current reduced-order control design methods.

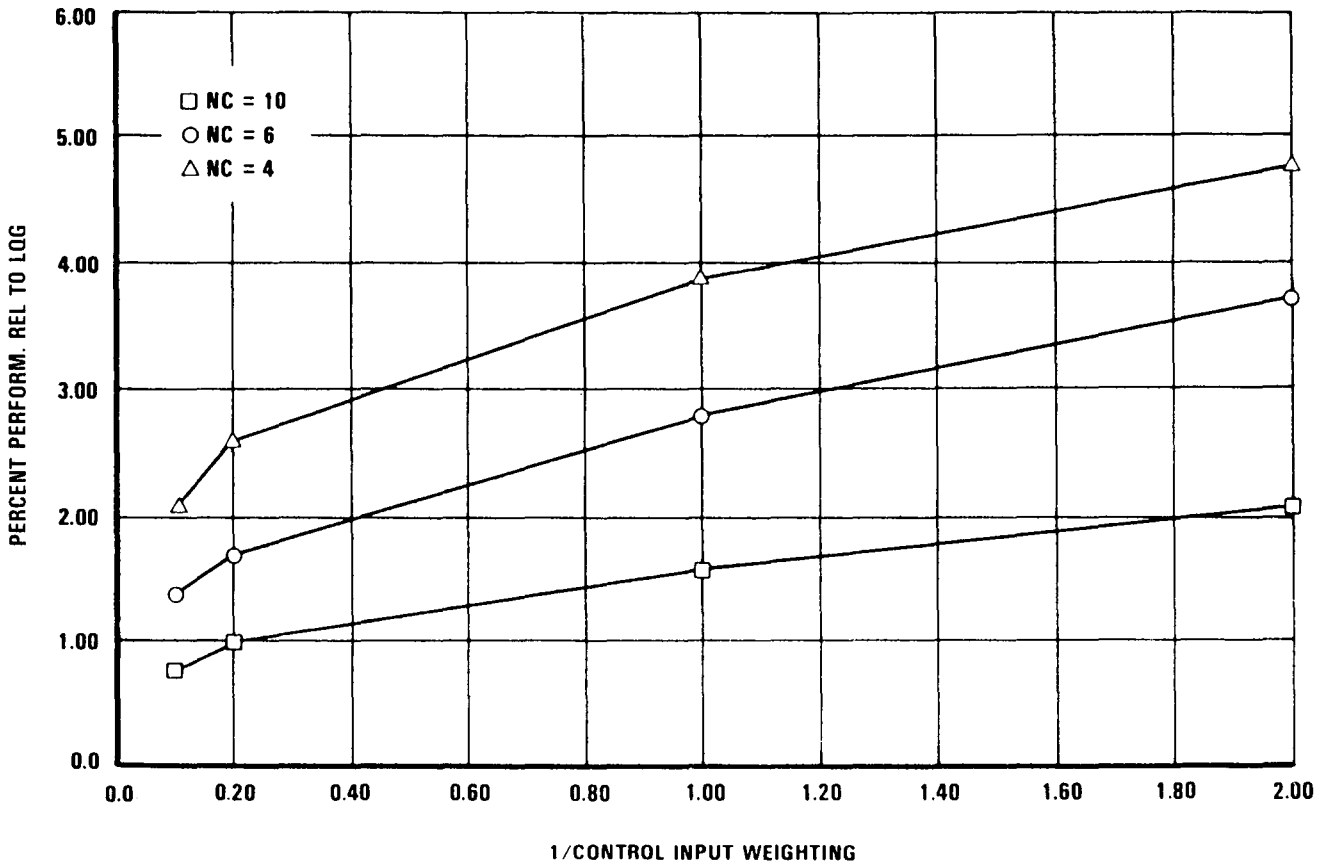

Figure 15

EXAMPLE 2: 15-M HOOP/COLUMN ANTENNA CONTROLS/DYNAMICS EXPERIMENT CONCEPT

The second example of the application of optimal projection involves significant interplay among controller design, experiment design, and control hardware selection.

To further the technology development goals of the planned Large Space Antenna Flight Experiment, Harris GASD has undertaken a preliminary study for design of a ground-based controls and dynamics experiment involving the 15-M Hoop/Column Antenna. This structure is a deployable mesh reflector design for space communications applications.

In designing the experimental apparatus, it was our goal to establish performance requirements, disturbance spectra, etc., to emulate (not simulate a flight test) the generic pathologies of large space systems. Care was also taken in selecting control hardware and software in such a way as to provide a good test-bed for a variety of system identification and control design approaches.

The basic experimental configuration motivated by the above considerations is depicted in Figure 16. As shown, the entire spacecraft is suspended by a cable secured to the ceiling of a radome. The point of attachment to the structure is inside the primary column segment approximately 1.5 inches above the center of mass. The resulting gravity moment arm provides some slight restoring stiffness and prevents the cable from resting against the column. Absence of an RF feed (replaced by equivalent weights) permits the suspending cable to run clear through the aperture of the upper column segment, thereby permitting approximately 5° of rotational motion along both horizontal axes.

Steady-state random disturbances are to be supplied by two-axis torquers located within the spacecraft bus. The selected location provides significant disturbability to the first hundred modes and a high degree of disturbance to ~50 modes.

15-METER H/C MODEL CABLE SUSPENDED CONFIGURATION FOR GROUND TESTING

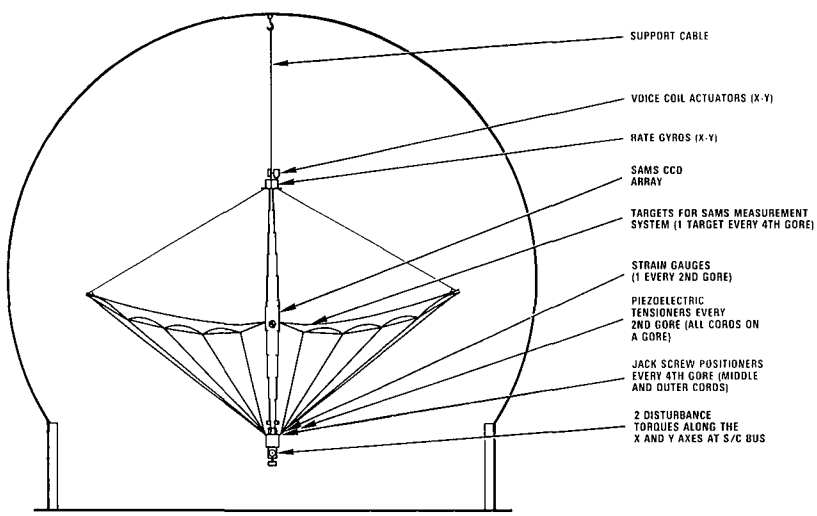

Figure 16

DISTRIBUTION OF MODAL FREQUENCIES FOR 15M CONTROLS/DYNAMICS EXPERIMENT CONCEPT

Detailed finite element analyses of this cable-suspended configuration have been carried out, and the overall distribution of modal frequencies can be summarized as in Figure 17. The figure shows the "mode-count" versus frequency; i.e., $N(\omega)$ denotes the number of modes below a given frequency, ω. As indicated, there is a collection of "quasi-rigid-body" nodes at low frequencies. Each of these modes involves a compound pendulum motion on the cable with the spacecraft undergoing essentially rigid-body rotations and translations. The quasi-rigid-body modes provide a rather accurate simulation of rigid body degrees of freedom. At ~7.5 Hz and above, there emerge the overall beam bending or "spacecraft" modes involving bending of the supporting hoop and central column. Finally, the rapid increase in mode count above ~11 Hz is accounted for by the very closely spaced "antenna surface" modes - involving motion primarily of the mesh surface and its underlying tensioning and control cords.

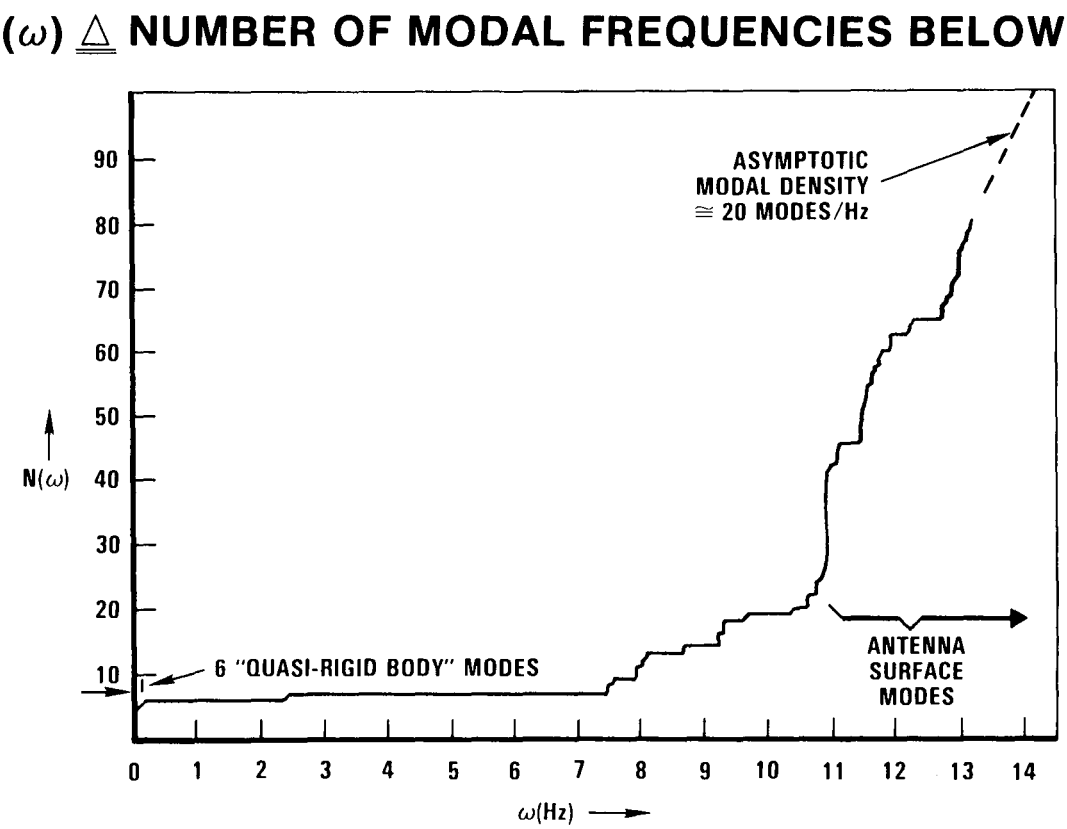

Figure 17

15-M EXPERIMENT - INSTRUMENTATION CONCEPT AND DESIGN RESULTS

Because there is a wide dispersion of disturbability for the selected disturbance source, it is possible to deliberately shape the disturbance spectrum to provide significant excitation of a desired number of modes. The selected spectrum is broad band with a half-power band limit of 15 Hz. As is evident from Figure 17, the 15 Hz bandwidth easily covers more than 100 modes.

Of course, significant disturbance on a large number of modes does not alone suffice to create a challenging control problem - selection and scaling of performance criteria are also necessary tasks in the experiment design. Refs. [92, 93] give details on the selected quadratic performance index. Basically, the state penalty consists of three main terms which impose performance penalties on (1) pointing errors, (2) misalignment and defocus errors, and (3) antenna surface shape errors.

With the control objectives thus defined, the control design and actuator/sensor selection methodologies were exercised iteratively to obtain a set of applicable, low-cost devices. The resulting instrumentation plan is depicted in Figure 18 a and detailed in [93].

Design results including dynamics models for the full complement of control hardware devices indicated in Figure 18 b are reported in [93]. For simplicity, we consider results on a subproblem involving only elastic mode vibration control using four jackscrew positioner devices and four strain gauges mounted on the control cords.

Despite a large number of modes included in the design model, optimal projection designs were successfully obtained and the effect of decreasing the control input penalty (progressively increasing the control authority) on closed-loop system poles is indicated in Figure 18 b. It is seen that while high order modes remain stable, significant increases in damping can be achieved for lower order modes within the limitations (force/bandwidth) of the actuators and sensors.

OVERALL EXPERIMENT HARDWARE CONCEPT

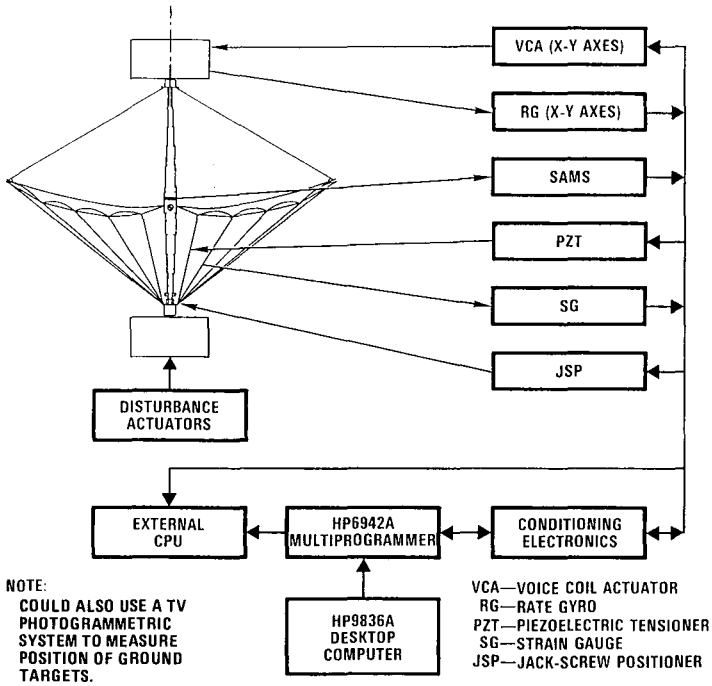

Figure 18 a

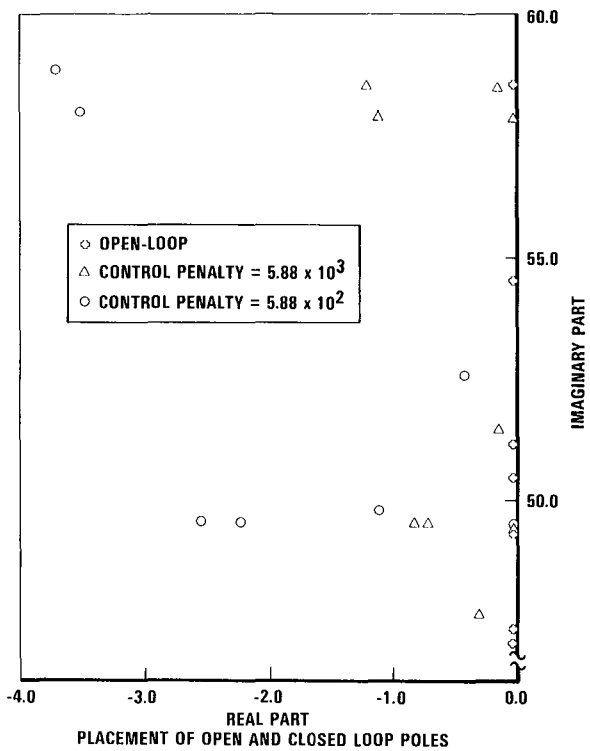

Figure 18 b

15-M EXPERIMENT: PERFORMANCE/COMPLEXITY TRADEOFF RESULTS

For the problem considered above, Figure 19 summarizes the tradeoffs of performance versus controller complexity (compensator dimension) and control authority (control input weighting in the performance index). Generally, it is seen that compensators of dimension > 10 yield negligible improvement in performance. This conclusion holds for the general problem including all hardware devices and rigid body modes. Thus, memory and throughput requirements for the processor needed to implement the control algorithm were sized on the assumption that $N_c \leq 10$. These estimates were then used to arrive at the processor selection indicated in Figure 18.a. Specifically, the control algorithm would be implemented on the HP 9836A Desktop Computer. This is a Motorola MC68000 microprocessor-based (16-bit) machine. Also, the HP-6942A Multiprogrammer can be utilized to perform all a/d and d/a conversions as well as data handling. An external CPU is included to assist in data handling and route data to off-line storage. After completion of a given experimental sequence, stored data can be analyzed, parameter identification tests can be performed and results can be correlated with analytical predictions.

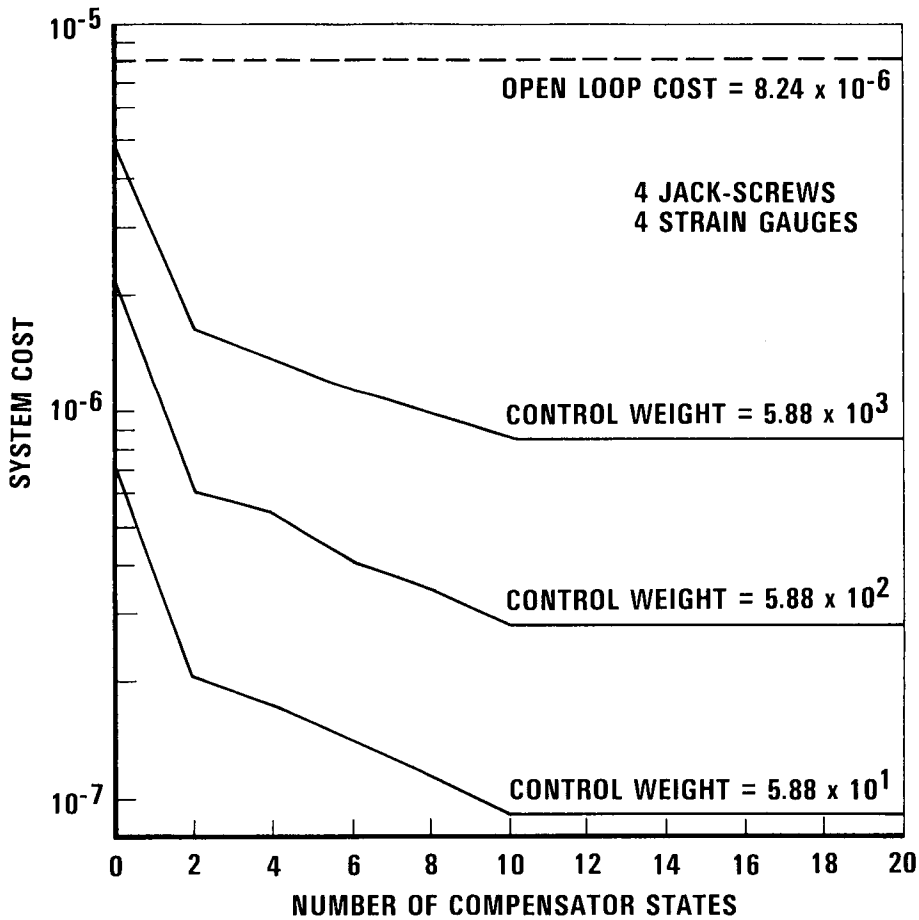

Figure 19

EXAMPLE 3: SPACECRAFT CONTROL LABORATORY EXPERIMENT (SCOLE)

Our third and last example is used primarily to illustrate application of the maximum entropy design-for-uncertainty approach. Harris GASD has just completed a NASA LaRC supported study on the Spacecraft Control Laboratory Experiment (SCOLE) configuration shown in Figure 20. This is the subject of the NASA/IEEE Design Challenge described in [94]. Since the study is specifically aimed at exploring the maximum entropy approach, its scope is restricted in other areas. Specifically, we consider the steady state pointing problem using linear, continuous-time models of all subsystems.

A high order finite element model was constructed for SCOLE, treating the Shuttle and reflectors as rigid bodies and the connecting mast as a classical beam with torsional stiffness. This model includes the Shuttle products-of-inertia and the offset between reflector center-of-mass and its attachment point on the mast. The quadratic performance penalty on the system state is simply the total mean square line of sight error (as defined in [94]). Full details of our model and design results are given in [95].

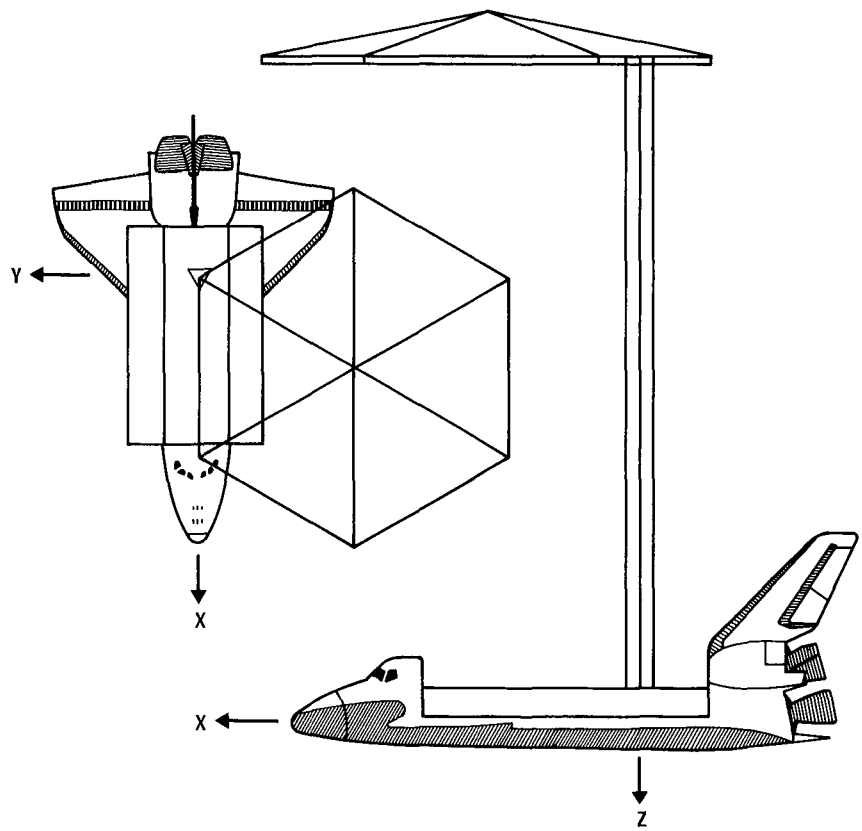

Figure 20

COMPARISON OF CLOSED-LOOP POLE SENSITIVITY FOR LQG AND MAXIMUM ENTROPY DESIGNS

As part of the SCOLE study, we considered a system model including the first eight modes and (1) performed LQG studies to select the control authority and establish a baseline and (2) designed full-order (16 state) compensators with a maximum entropy model of modal frequency uncertainties. The maximum entropy model assumed that all elastic mode frequencies were subjected to independent variations (due to modelling error) of $+\sigma$ to $-\sigma$ relative to their nominal values. Thus the positive number σ denotes the overall fractional uncertainty.

Although robust stability is obtained under these independent and simultaneous variations, the robustness properties of specific designs are simply illustrated here by looking at the variation of performance and closed-loop poles when all modal frequencies are varied by the same fractional change from the nominal values. In other words, we interconnect a given controller design (be it LQG or maximum entropy) with a perturbed plant model wherein all modal frequencies are changed by δ x (nominal values) and evaluate the closed-loop performance and pole locations. This is repeated for a range of values of δ.

Figure 21 a shows how the pole locations for an LQG design wander under a $\pm$5% variation of the modal frequencies. It is seen that two of the pole pairs are particularly sensitive and are nearly driven unstable by only this $\pm$5% variation. This happens because the associated structural modes contribute little to performance and the LQG design attempts a "cheap control" (small regulator and observer gains) by placing compensator poles very close to the open-loop plant poles. For nominal values, this scheme achieves significant shifts of open-loop poles with very small gains, but it is highly sensitive to off-nominal perturbations.

Figure 21 b shows closed-loop poles for the same conditions except that a maximum entropy compensator design with $\sigma = 0.1$ (10% variation modelled) was utilized. In contrast with Figure 21 a, the maximum entropy design makes the compensator poles "stand-off" deeper in the left half plane. (This is a direct consequence of the Stratonovich correction.) Consequently, the strong and sensitive interactions noted above are entirely eliminated. The poles associated with higher-order structural modes are seen to vary only along the imaginary axis and are not destabilized.

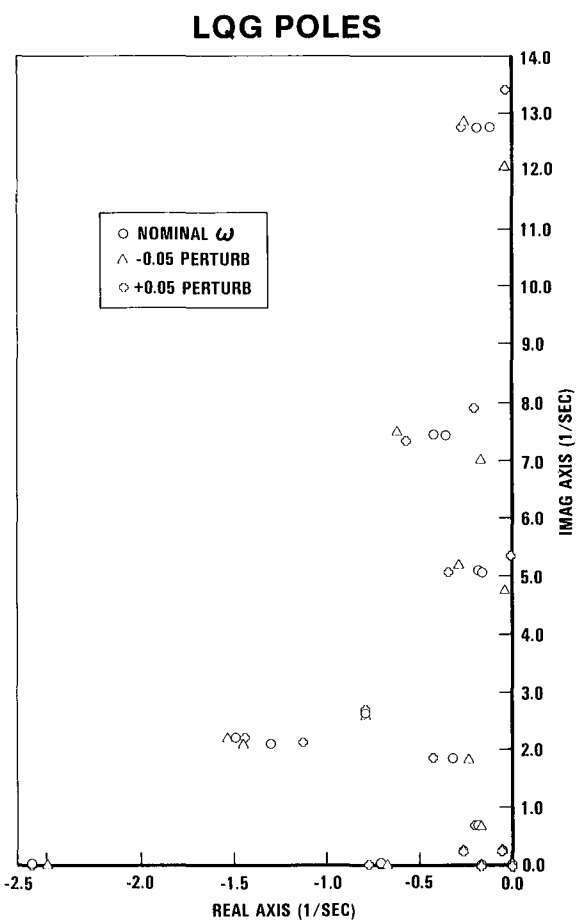

Figure 21 a

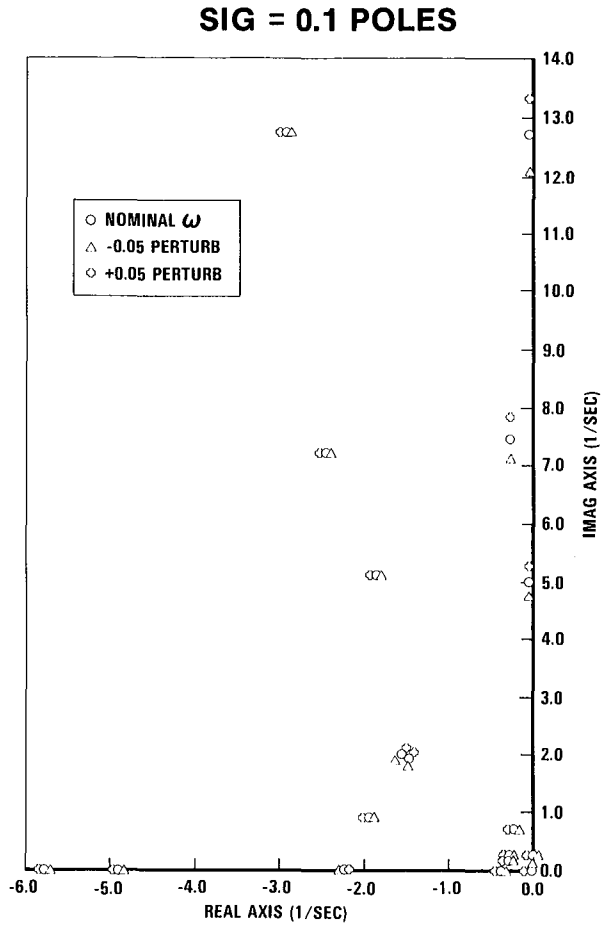

Figure 21 b

VARIATION OF PERFORMANCE WITH SYSTEM PARAMETER DEVIATIONS:
DETERMINISTIC MODELLING VERSUS MAXIMUM ENTROPY DESIGN

Figure 22 illustrates how the total performance index for given controller designs varies as the structural mode frequencies are perturbed relative to their nominal values. The LQG design (which is simply a maximum entropy design for $\sigma = 0$) becomes unstable for > 7% and < -14% variations. In contrast and even with a modest 10% level of modelled uncertainty, the maximum entropy designs completely eliminate the sensitivity. Note that within the parameter range for which LQG is stable, the $\sigma = 0.1$ maximum entropy design experiences only a ~12-15% degradation. Of course, over the regions for which LQG is unstable, the maximum entropy designs are qualitatively superior.

These results serve to illustrate a general fact: By incorporating parameter uncertainty as an intrinsic facet of the basic design model, the maximum entropy formulation is able to secure high levels of robustness with little degradation of nominal performance.

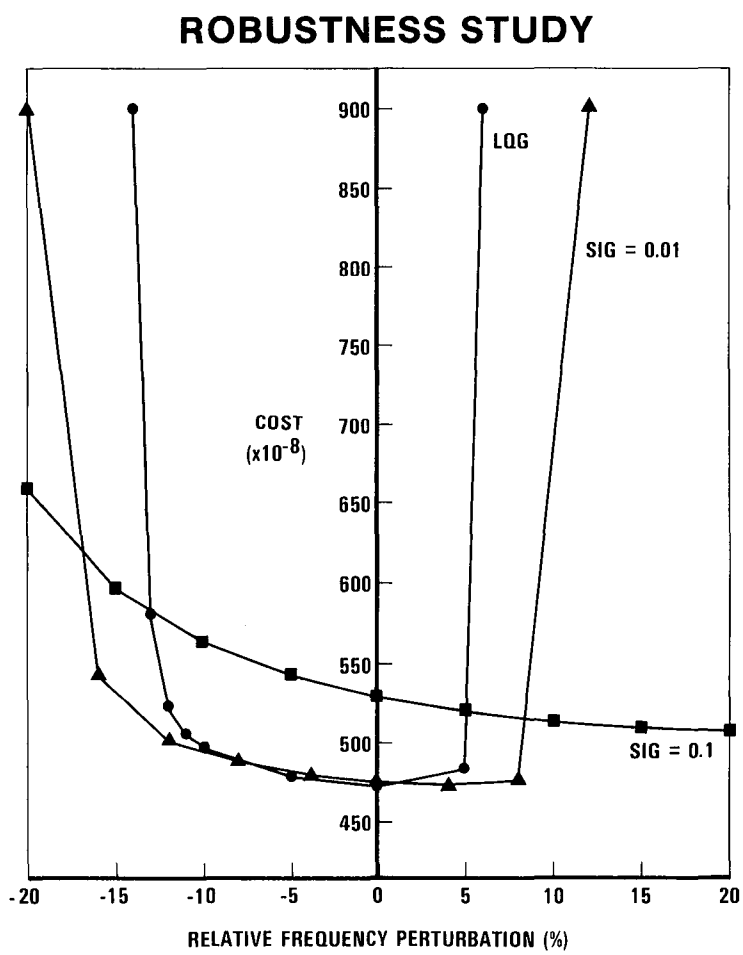

Figure 22

COMBINED OP/ME DESIGN: PERFORMANCE/COMPLEXITY TRADEOFF

Finally, the combined OP/ME design capability was exercised, taking the 16-state maximum entropy compensator design with $\sigma = 0.10$ frequency uncertainty level as the starting point. Reduced order compensator designs were constructed for compensators of order 14,12,10,8,6 and 5. Figure 23 shows the tradeoff between performance (total, closed-loop performance index evaluated for nominal values of modal frequencies) and controller dimension. The Figure clearly shows that performance degradation for compensator orders above 6 is negligible. The 6th order controller sacrifices only 3% of the performance of the full-order (16 state) controller. This would seem to be acceptable in view of the better than sixfold decrease in implementation costs (e.g., flops required in matrix multiplication) which results from order reduction.

In conclusion, these results, together with much additional material included in [95], demonstrate automated solution of the full OP/ME design equations (shown in Figure 12) and illustrate the performance and implementation benefits to be expected under this unified approach.

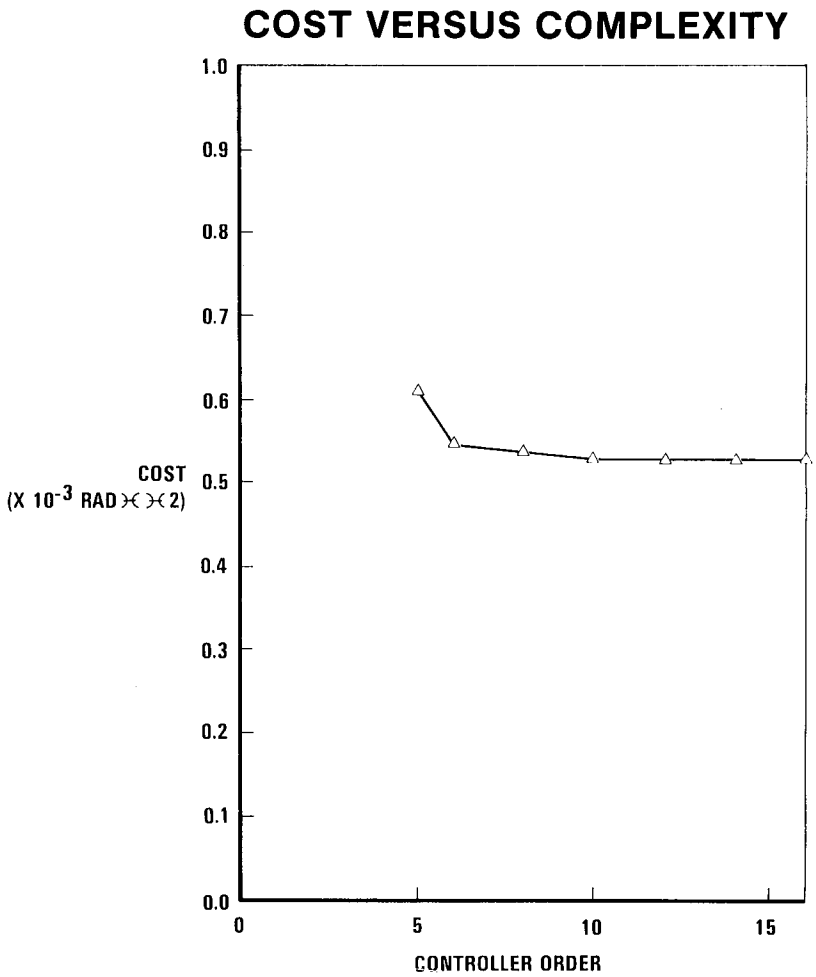

Figure 23

References

1. D. C. Hyland, "Optimal Regulation of Structural Systems With Uncertain Parameters," MIT, Lincoln Laboratory, TR-551, 2 February 1981, DDC# AD-A099111/7.

2. D. C. Hyland, "Active Control of Large Flexible Spacecraft: A New Design Approach Based on Minimum Information Modelling of Parameter Uncertainties," VPI&SU/AIAA Symposium, Blacksburg, VA, June 1981.

3. D. C. Hyland, "Optimal Regulator Design Using Minimum Information Modelling of Parameter Uncertainties: Ramifications of the New Design Approach," VPI&SU/AIAA Symposium, Blacksburg, VA, June 1981.

4. D. C. Hyland and A. N. Madiwale, "Minimum Information Approach to Regulator Design: Numerical Methods and Illustrative Results," VPI&SU/AIAA Symposium, Blacksburg, VA, June 1981.

5. D. C. Hyland and A. N. Madiwale, "A Stochastic Design Approach for Full-Order Compensation of Structural Systems with Uncertain Parameters," AIAA Guidance and Control Conference, Albuquerque, NM, August 1981.

6. D. C. Hyland, "Optimality Conditions for Fixed-Order Dynamic Compensation of Flexible Spacecraft with Uncertain Parameters," AIAA 20th Aerospace Sciences Meeting, Orlando, FL, January 1982.

7. D. C. Hyland, "Structural Modeling and Control Design Under Incomplete Parameter Information: The Maximum Entropy Approach," Modelling, Analysis and Optimization Issues for Large Space Structures, NASA CP-2258, 1983, pp. 73-96.

8. D. C. Hyland, "Maximum Entropy Stochastic Approach to Control Design for Uncertain Structural Systems," American Control Conference, Arlington, VA, June 1982.

9. D. C. Hyland, "Minimum Information Stochastic Modelling of Linear Systems with a Class of Parameter Uncertainties," American Control Conference, Arlington, VA, June 1982.

10. D. C. Hyland and A. N. Madiwale, "Fixed-Order Dynamic Compensation Through Optimal Projection," Proceedings of the Workshop on Applications of Distributed System Theory to the Control of Large Space Structures, JPL, Pasadena, CA, July 1982.

11. D. C. Hyland, "Minimum Information Modelling of Structural Systems with Uncertain Parameters," Proceedings of the Workshop on Applications of Distributed System Theory to the Control of Large Space Structures, JPL, Pasadena, CA, July 1982.

12. D. C. Hyland, "Mean-Square Optimal Fixed-Order Compensation - Beyond Spillover Suppression," AIAA Astrodynamics Conference, San Diego, CA, August 1982.

13. D. C. Hyland, "Robust Spacecraft Control Design in the Presence of Sensor/Actuator Placement Errors," AIAA Astrodynamics Conference, San Diego, CA, August 1982.

14. D. C. Hyland, "The Optimal Projection Approach to Fixed-Order Compensation: Numerical Methods and Illustrative Results," AIAA 21st Aerospace Sciences Meeting, Reno, NV, January 1983.

15. D. C. Hyland, "Mean-Square Optimal, Full-Order Compensation of Structural Systems with Uncertain Parameters," MIT, Lincoln Laboratory TR-626, 1 June 1983.

16. D. C. Hyland and D. S. Bernstein, "Explicit Optimality Conditions for Fixed-Order Dynamic Compensation," Proc. 22nd IEEE Conference on Decision and Control, San Antonio, TX, December 1983.

17. D. C. Hyland, "Comparison of Various Controller-Reduction Methods: Suboptimal Versus Optimal Projection," Proc. AIAA Dynamics Specialists Conference, Palm Springs, CA, May 1984.

18. D. S. Bernstein and D. C. Hyland, "The Optimal Projection Equations for Fixed-Order Dynamic Compensation of Distributed Parameter Systems," Proc. AIAA Dynamics Specialists Conference, Palm Springs, CA, May 1984.

19. D. S. Bernstein and D. C. Hyland, "Numerical Solution of the Optimal Model Reduction Equations," AIAA Guidance and Control Conference, Seattle, WA, August 1984.

20. D. C. Hyland and D. S. Bernstein, "The Optimal Projection Approach to Model Reduction and the Relationship Between the Methods of Wilson and Moore," 23rd IEEE Conference on Decision and Control, Las Vegas, NV, December 1984.

21. D. S. Bernstein and D. C. Hyland, "The Optimal Projection Approach to Designing Optimal Finite-Dimensional Controllers for Distributed-Parameter Systems," 23rd IEEE Conference on Decision and Control, Las Vegas, NV, December 1984.

22. D. C. Hyland and D. S. Bernstein, "The Optimal Projection Equations for Fixed-Order Dynamic Compensation," IEEE Trans. Autom. Contr., Vol. AC-29, No. 11, pp. 1034-1037, 1984.

23. D. S. Bernstein and D. C. Hyland, "The Optimal Projection Equations for Finite-Dimensional Fixed-Order Dynamic Compensation of Infinite-Dimensional Systems," SIAM J., accepted for publication, 1984. (Also presented at 1983 SIAM fall meeting, Norfolk, VA, November 1983, as "Explicit Optimality Conditions for Fixed-Order Dynamic Compensation of Infinite-Dimensional Systems.")

24. D. C. Hyland and D. S. Bernstein, "The Optimal Projection Equations for Model Reduction and the Relationships Among the Methods of Wilson, Skelton and Moore," IEEE J., accepted for publication, 1984.

25. D. S. Bernstein and D. C. Hyland, "The Optimal Projection Equations for Reduced-Order State Estimation," submitted to IEEE J., 1984.

26. E. T. Jaynes, "New Engineering Applications of Information Theory," Proceedings of the First Symposium on Engineering Applications of Random Function Theory and Probability, J. L. Bogdanoff and F. Kozin, pp. 163-203, Wiley, New York, 1963.

27. E. T. Jaynes, "Prior Probabilities," IEEE Trans. Sys. Sci. Cybern., Vol. SSC-4, pp. 227-241, 1968.

28. E. T. Jaynes, "Where Do We Stand on Maximum Entropy," The Maximum Entropy Formalism, D. Levine and M. Tribus, eds., The MIT Press, pp. 15-118, Cambridge, MA, 1979.

29. R. D. Rosenkrandtz, ed., "E. T. Jaynes: Papers on Probability, Statistics and Statistical Physics," Reidel, Boston, 1983.

30. K. Ito, On Stochastic Differential Equations, Amer. Math. Soc., Providence, RI, 1951.

31. E. Wong and M. Zakai, "On the Relation Between Ordinary and Stochastic Differential Equations," Int. J. Engrg. Sci., Vol. 3, pp. 213-229, 1965.

32. R. L. Stratonovich, "A New Representation for Stochastic Integrals," SIAM J. Contr., Vol. 4, pp. 362-371, 1966.

33. R. L. Stratonovich, Conditional Markov Process and Their Application to the Theory of Optimal Control, Elsevier, NY, 1968.

34. A. H. Jazwinski, Stochastic Processes and Filtering Theory, Academic Press, New York, 1970.

35. E. Wong, Stochastic Processes in Information and Dynamical Systems, McGraw-Hill, New York, 1971.

36. E. J. McShane, Stochastic Calculus and Stochastic Models, Academic Press, Press, New York, 1974.

37. L. Arnold, Stochastic Differential Equations: Theory and Applications, Wiley, New York, 1974.

38. W. H. Fleming and R. W. Rishel, Deterministic and Stochastic Optimal Control, Springer-Verlag, New York, 1975.

39. H. J. Sussmann, "On the Gap Between Deterministic and Stochastic Ordinary Differential Equations," The Annals of Probability, Vol. 6, pp. 19-41, 1978.

40. W. M. Wonham, "Optimal Stationary Control of Linear Systems with State-Dependent Noise," SIAM J Contr., Vol. 5, pp. 486-500, 1967.

41. M. Metivier and J. Pellaumail, Stochastic Integration, Academic Press, New York, 1980.

42. W. M. Wonham, "On a Matrix Riccati Equation of Stochastic Control," SIAM J. Contr., Vol. 6, pp. 681-697, 1968.

43. W. M. Wonham, "Random Differential Equations in Control Theory," in Probabilistic Analysis in Applied Mathematics, A. T. Bharucha-Reid, ed., Vol. 2, pp. 131-212, Academic Press, New York, 1970.

44. D. Kleinman, "Optimal Stationary Control of Linear Systems with Control-Dependent Noise," IEEE Trans. Autom. Contr., Vol. AC-14, pp. 673-677, 1969.

45. P. J. McLane, "Optimal Linear Filtering for Linear Systems with State-Dependent Noise," Int. J. Contr., Vol. 10, pp. 41-51, 1969.

46. P. McLane, "Optimal Stochastic Control of Linear Systems with State- and Control-Dependent Disturbances," IEEE Trans. Autom. Contr., Vol. AC-16, pp. 793-798, 1971.

47. D. Kleinman, "Numerical Solution of the State Dependent Noise Problem," IEEE Trans. Autom. Contr., Vol. AC-21, pp. 419-420, 1976.

48. U. Haussmann, "Optimal Stationary Control with State and Control Dependent Noise," SIAM J. Contr., Vol. 9, pp. 184-198, 1971.

49. J. Bismut, "Linear-Quadratic Optimal Stochastic Control with Random Coefficients," SIAM J. Contr., Vol. 14, pp. 419-444, 1976.

50. A. Ichikawa, "Optimal Control of a Linear Stochastic Evolution Equation with State and Control Dependent Noise," Proc. IMA Conference on Recent Theoretical Development in Control, Leicester, England, Academic Press, New York, 1976.

51. A. Ichikawa, "Dynamic Programming Approach to Stochastic Evolution Equations," SIAM J. Contr. Optim., Vol 17, pp. 152-174, 1979.

52. N. U. Ahmed, "Stochastic Control on Hilbert Space for Linear Evolution Equations with Random Operator-Valued Coefficients," SIAM J. Contr. Optim., Vol. 19, pp. 401-430.

53. C. W. Merriam III, Automated Design of Control Systems, Gordon and Breach, New York, 1974.

54. M. Aoki, "Control of Linear Discrete-Time Stochastic Dynamic Systems with Multiplicative Disturbances," IEEE Trans. Autom. Contr., Vol. AC-20, pp. 388-392, 1975.

55. D. E. Gustafson and J. L. Speyer, "Design of Linear Regulators for Nonlinear Systems," J. Spacecraft and Rockets, Vol. 12, pp. 351-358, 1975.

56. D. E. Gustafson and J. L. Speyer, "Linear Minimum Variance Filters Applied to Carrier Tracking," IEEE Trans. Autom. Contr., Vol. AC-21, pp. 65-73, 1976.

57. G. N. Milshtein, "Design of Stabilizing Controller With Incomplete State Data for Linear Stochastic System with Multiplicative Noise," Autom. and Remote Contr., Vol. 43, pp. 653-659, 1982.

58. M. Athans, R. T. Ku and S. B. Gershwin, "The Uncertainty Threshold Principle: Some Fundamental Limitations of Optimal Decision Making Under Dynamic Uncertainty," IEEE Trans. Autom. Contr., Vol. AC-22, pp. 491-495, 1977.

59. R. J. Ku and M. Athans, "Further Results on the Uncertainty Threshold Principle," IEEE Trans. Autom. Contr., Vol. AC-22, pp. 866-868, 1977.

60. T. L. Johnson and M. Athans, "On the Design of Optimal Constrained Dynamic Compensators for Linear Constant Systems," IEEE Trans. Autom. Contr., Vol. AC-15, pp. 658-660, 1970.

61. W. S. Levine, T. L. Johnson and M. Athans, "Optimal Limited State Variable Feedback Controllers for Linear Systems," IEEE Trans. Autom. Contr., Vol. AC-16, pp. 785-793, 1971.

62. K. Kwakernaak and R. Sivan, Linear Optimal Control Systems, Wiley-Interscience, New York, 1972.

63. D. B. Rom and P. E. Sarachik, "The Design of Optimal Compensators for Linear Constant Systems with Inaccessible States," IEEE Trans. Autom. Contr., Vol. AC-18, pp. 509-512, 1973.

64. M. Sidar and B.-Z. Kurtaran, "Optimal Low-Order Controllers for Linear Stochastic Systems, "Int. J. Contr., Vol. 22, pp. 377-387, 1975.

65. J. M. Mendel and J. Feather, "On the Design of Optimal Time-Invariant Compensators for Linear Stochastic Time-Invariant Systems, "IEEE Trans. Autom. Contr., Vol. AC-20, pp. 653-657, 1975.

66. S. Basuthakur and C. H. Knapp, "Optimal Constant Controllers for Stochastic Linear Systems, "IEEE Trans. Autom. Contr., AC-20, pp. 664-666, 1975.

67. R. B. Asher and J. C. Durrett, "Linear Discrete Stochastic Control with a Reduced-Order Dynamic Compensator, "IEEE Trans. Autom. Contr., Vol. AC-21, pp. 626-627, 1976.

68. W. J. Naeije and O. H. Bosgra, "The Design of Dynamic Compensators for Linear Multivariable Systems," 1977 IFAC, Fredricton, NB, Canada, pp. 205-212.

69. H. R. Sirisena and S. S. Choi, "Design of Optimal Constrained Dynamic Compensators for Non-Stationary Linear Stochastic Systems, "Int. J. Contr., Vol. 25, pp. 513-524, 1977.

70. P. J. Blanvillain and T. L. Johnson, "Invariants of Optimal Minimal-Order Observer Based Compensators, "IEEE Trans. Autom. Contr., Vol. AC-23, pp. 473-474, 1978.

71. C. J. Wenk and C. H. Knapp, "Parameter Optimization in Linear Systems with Arbitrarily Constrained Controller Structure, "IEEE Trans. Autom. Contr., Vol. AC-25, pp. 496-500, 1980.

72. J. O'Reilly, "Optimal Low-Order Feedback Controllers for Linear Discrete-Time Systems," in Control and Dynamic Systems, Vol. 16, edited C. T. Leondes, ed., Academic Press, 1980.

73. D. P. Looze and N. R. Sandell, Jr., "Gradient Calculations for Linear Quadratic Fixed Control Structure Problems," IEEE Trans. Autom. Contr., Vol. AC-25, pp. 285-8, 1980.

74. M. Aoki, "Control of Large-Scale Dynamic Systems by Aggregation," IEEE Trans. Auto. Contr., Vol. AC-13, pp. 246-253, 1968.

75. R. E. Skelton, "Cost Decomposition of Linear Systems with Application to Model Reduction," Int. J. Contr., Vol. 32, pp. 1031-1055, 1980.

76. B. C. Moore, "Principal Component Analysis in Linear Systems: Controllability, Observability, and Model Reduction," IEEE Trans. Autom. Contr., Vol. AC-26, pp. 17-32, 1981.

77. L. Pernebo and L. M. Silverman, "Model Reduction via Balanced State Space Representations," IEEE Trans. Autom. Contr., Vol. AC-27, pp. 382-387, 1982.

78. K. V. Fernando and H. Nicholson, "On the Structure of Balanced and Other Principal Representations of SISO Systems," IEEE Trans. Autom. Contr., Vol. AC-28, pp. 228-231, 1983.

79. S. Shokoohi, L. M. Silverman, and P. M. Van Dooren, "Linear Time-Variable Systems: Balancing and Model Reduction," IEEE Trans. Autom. Contr., Vol. AC-28, pp. 810-822, 1983.

80. E. I. Verriest and T. Kailath, "On Generalized Balanced Realization," IEEE Trans. Autom. Contr., Vol. AC-28, pp. 833-844, 1983.

81. E. A. Jonckheere and L. M. Silverman, "A New Set of Invariants for Linear Systems - Application to Reduced-Order Compensator Design," IEEE Trans. Autom. Contr., Vol. AC-28, pp. 953-964, 1983.

82. R. E. Skelton and A. Yousuff, "Component Cost Analysis of Large Scale Systems," Int. J. Contr., Vol. 37, pp. 285-304, 1983.

83. A. Yousuff and R. E. Skelton, "Controller Reduction by Component Cost Analysis," IEEE Trans. Autom. Contr., Vol. AC-29, pp. 520-530, 1984.

84. J. S. Gibson, "An Analysis of Optimal Modal Regulation: Convergence and Stability," SIAM J. Contr. Optim., 19(1981), pp. 686-707.

85. J. S. Gibson, "Linear-Quadratic Optimal Control of Hereditary Differential Systems: Infinite Dimensional Riccati Equations and Numerical Approximations, SIAM J. Contr. Optim., 21(1983), pp. 95-139.

86. H. T. Banks and K. Kunisch, "The Linear Regulator Problem for Parabolic Systems," SIAM J. Contr. Optim., 22(1984), pp. 684-698.

87. H. T. Banks, K. Ito and I. G. Rosen, "A Spline Based Technique for Computing Riccati Operators and Feedback Controls in Regulator Problems for Delay Equations," ICASE Report 82-31, Institute for Computer Applications in Science and Engineering, Hampton, VA, 1982; SIAM J. Sci. Stat. Comput., 5(1984).

88. T. L. Johnson, "Optimization of Low Order Compensators for Infinite Dimensional Systems," Proc. of 9th IFIP Symp. on Optimization Techniques, Warsaw, Poland, September 1979.

89. R. K. Pearson, "Optimal Fixed-Form Compensators for Large Space Structures," in ACOSS SIX (Active Control of Space Structures), RADC-TR-81-289, Final Technical Report, Rome Air Development Center, Griffiss AFB, New York, 1981.

90. R. K. Pearson, "Optimal Velocity Feedback Control of Flexible Structures, Ph.D. Dis., MIT. Dept. Elec. Eng. Comp. Sci., 1982.

91. R. E. Skelton and P. C. Hughes, "Modal Cost Analysis for Linear Matrix Second-Order Systems," J. Dyn. Syst. Meas. and Contr., Vol. 102, pp. 151-180, September 1980.

92. F. M. Ham, J. Shipley and D. C. Hyland, "Design of a Large Space Structure Vibration Control Experiment," 2nd IMAC, Orlando, FL, February 1984.

93. F. M. Ham and D. C. Hyland, "Vibration Control Experiment Design for the 15-M Hoop/Column Antenna," JPL Workshop on Identification and Control of Flexible Space Structures, San Diego, CA, June 1984.

94. L. W. Taylor and A. V. Balakrishnan, "A Mathematical Problem and a Spacecraft Control Laboratory Experiment (SCOLE) Used to Evaluate Control Laws for Flexible Spacecraft ... NASA/IEEE Design Challenge," NASA/IEEE Report, June, 1984.

95. D. C. Hyland and L. Davis, "Application of the Maximum Entropy Design Approach to the Spacecraft Control Laboratory Experiment (SCOLE)," presented at SCOLE Workshop, December 6-7, 1984, NASA Langley Research Center.

ELECTROMAGNETIC ANALYSIS FOR SURFACE TOLERANCE EFFECTS ON LARGE SPACE ANTENNAS

C. R. Cockrell
NASA Langley Research Center
Hampton, Virginia

R. C. Rudduck
Ohio State University
Columbus, Ohio

Large Space Antenna Systems Technology - 1984
December 4-6, 1984

TYPES OF DISTORTIONS

The types of distortions which can occur in reflector surfaces are shown in figure 1. Only the periodic-deterministic type is addressed in some detail in this paper. The radiation pattern for periodic surface distortions exhibits a phenomenon which doesn't occur in the other type distortions. The periodic surface distortion causes higher side lobe radiation levels (grating lobes) in isolated regions of the radiation pattern than levels one would normally expect. One can treat the random type distortion by using the method of Ruze (Ref. 1) or others (Refs. 2 & 3).

- **RANDOM**
- **DETERMINISTIC**
  - **Aperiodic**
  - **Periodic**

Figure 1

SMOOTH REFLECTOR GEOMETRY

The technique of aperture integration is used in computing radiation patterns of reflector antennas. Fields in an aperture plane which is located in front of the reflector are determined by ray tracing from the feed to the reflector surface then to the aperture plane. These fields are then integrated to determine the radiation pattern. As noted in figure 2, the rays leave the reflector surface parallel if they emanate in phase from the focal point of the parabolic reflector. The fields in the aperture plane are determined by applying the appropriate boundary conditions. For the smooth reflector (perfect) as shown, determination of the fields is straightforward.

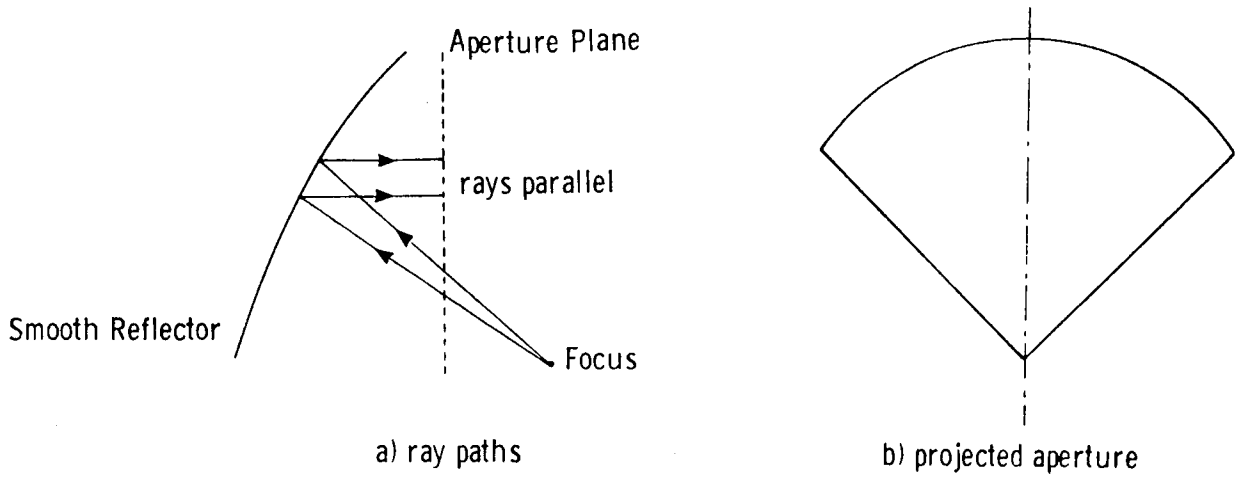

Figure 2

DISTORTED REFLECTOR GEOMETRY

Figure 3 shows the ray paths for a focus fed offset distorted parabolic reflector. The true ray paths are shown in figure 3a. Rays that emanate from the focus are reflected in a direction depending on the normal to the distorted reflector, and thus no longer leave the reflector surface parallel. Figure 3b shows the approximate ray paths used in the phase perturbation technique in which the reflected rays are assumed to leave the reflector surface parallel. The phase perturbation is the difference between the path length from the focus to the aperture plane via the smooth reflector and the path length from the focus to the aperture plane via the distorted reflector.

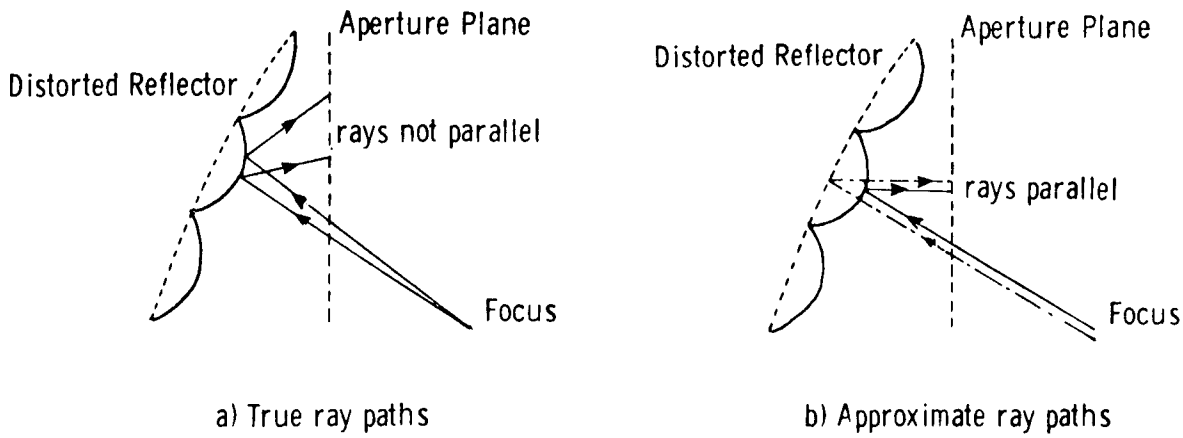

a) True ray paths

b) Approximate ray paths

Figure 3

PHOTOGRAPH OF SUB-SCALE MODELS

Two of the three models built for testing are shown in figure 4. Radiation patterns of these models at 35 GHz are used to compare with computed radiation patterns.

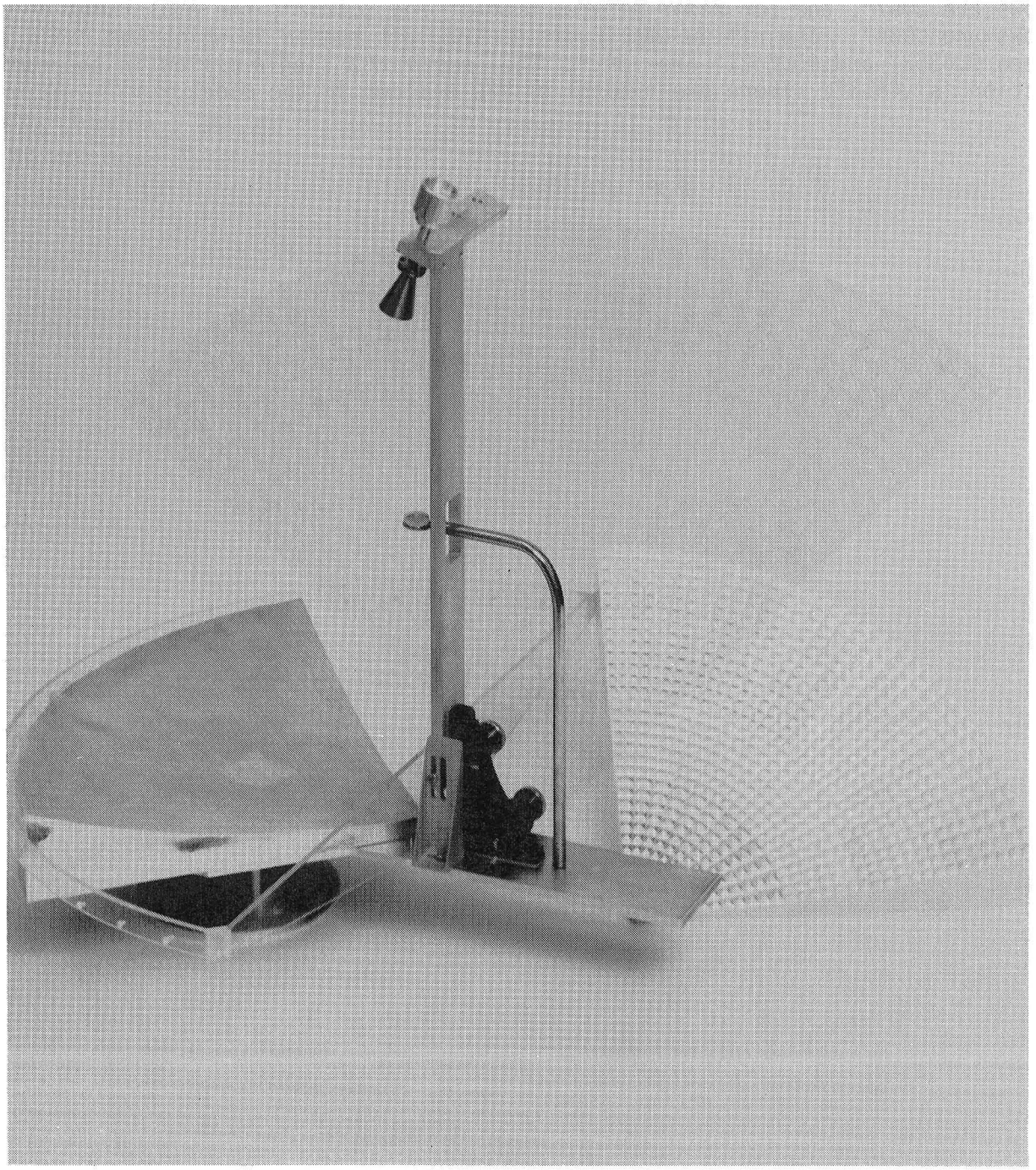

Figure 4

PHASE PERTURBATION DISTRIBUTION FOR 35 GHz MODEL

The phase perturbation distribution model for the 35 GHz test model is shown in figure 5. The distribution is a rectified sine wave both radially and circumferentially. There are three bands or regions in which the amplitudes of the pillows are different. For radii between 2.687" and 6.0561", the amplitudes of the pillows are .067", and for radii between 6.0561" and 9.4252", the amplitudes of the pillows are .034". The pillow amplitudes in the last region in which the radii are between 9.4353" and 15.6821" are .042". The length of a single pillow in the radial direction is .4813". There are a total of 720 pillows in the model.

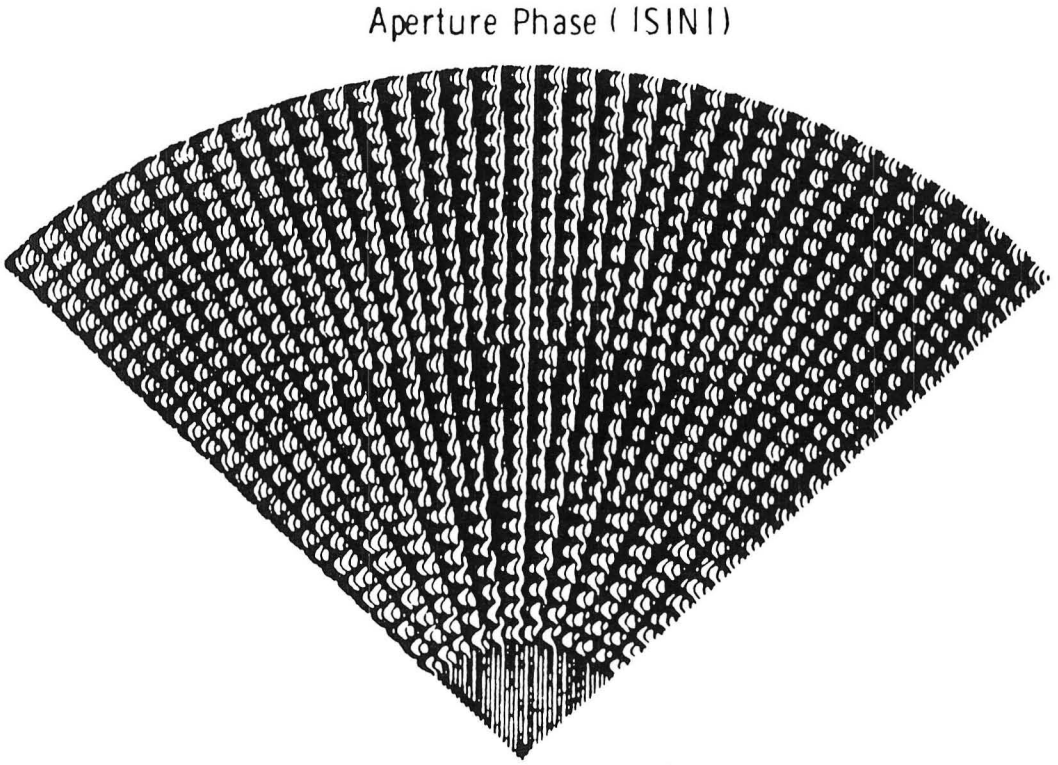

Figure 5

SUB-SCALE MODEL VERIFICATION (F = 35 GHz) OF PILLOWED REFLECTOR SURFACE

Figure 6 is a composite figure which shows the verification model and its measured pattern, and the predicted pattern which is calculated by using the phase perturbation technique. Grating lobes are clearly shown for both measured and predicted results. The locations of the grating lobe are predicted quite well; however, the predicted levels of intensity for the grating lobes are higher than the measured levels. These discrepancies are caused by the failure of the phase perturbation technique to accurately model the reflector surface, i.e., the reflector surface varies too rapidly for the parallel ray assumption to be applicable. In the next paper, Rudduck (ref. 4) discusses a modification to aperture integration technique that produces better grating lobe level agreement. It is also shown in his paper that the unmodified version of aperture integration is sufficient for slowly varying reflector surface distortions. The unmodified version of the aperture integration with phase perturbation, therefore, is used in computing radiation patterns for the 15 meter quad aperture antenna.

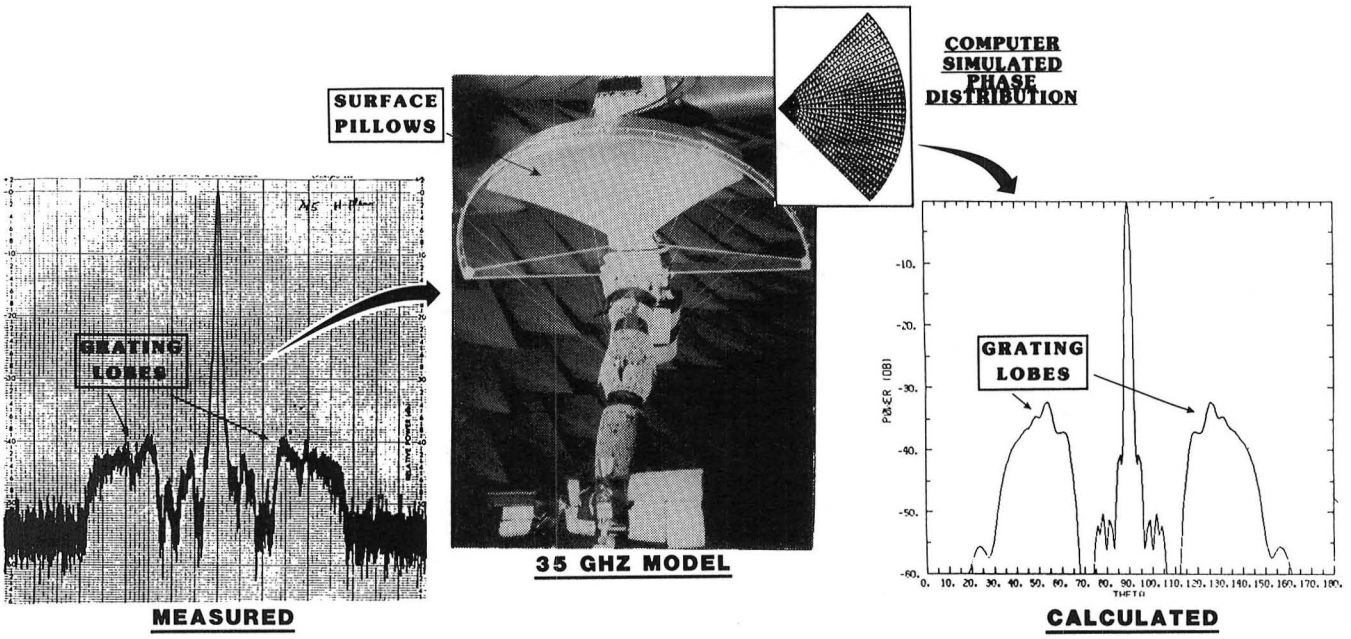

Figure 6

15 METER QUAD APERTURE ANTENNA

Figure 7 shows an artist's conception of the 15 meter quad aperture antenna. The mesh antenna is made up of four individual offset paraboloidal reflectors, each of which is illuminated from its own feed panel as shown. The focal point of each paraboloidal reflectors lie in its respective feed panel. Feeds at the focal point produce boresight patterns whereas feeds at other positions in the feed panel generate scanned patterns.

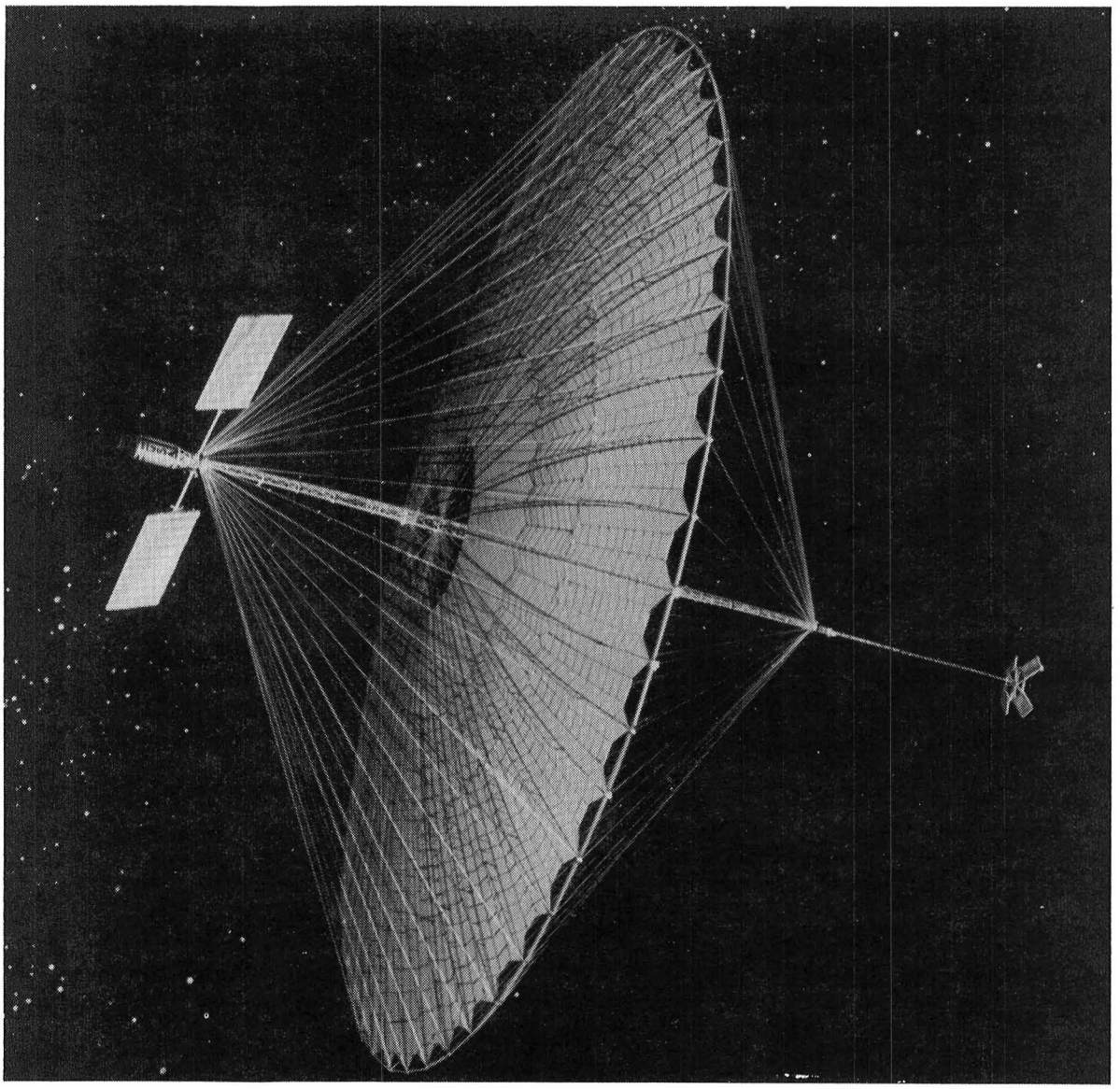

Figure 7

QUAD APERTURE SURFACE

A sketch of the 15 meter quad aperture antenna in which a single quad is emphasized is shown in figure 8. The EM analysis in this paper concentrates on a single quad aperture which is illuminated from its focal point.

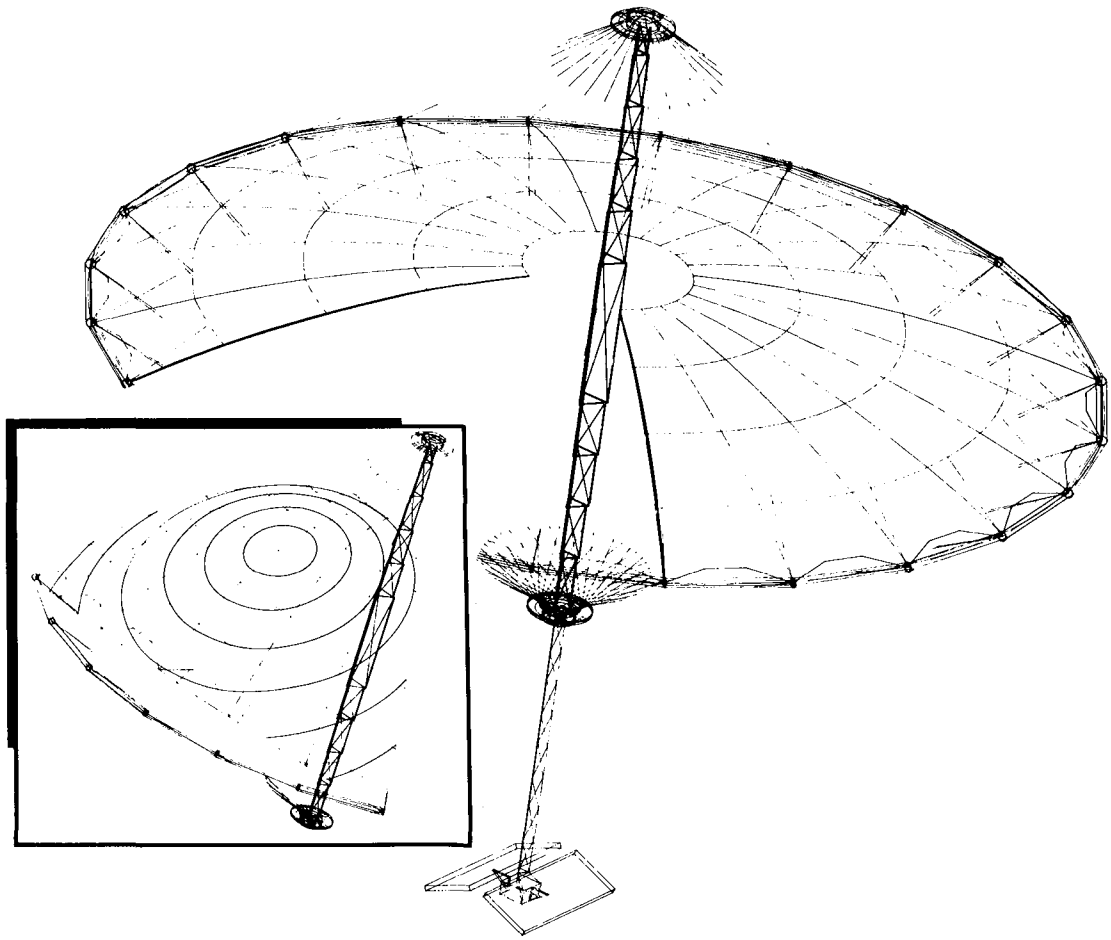

Figure 8

PHASE PERTURBATION DISTIBUTION FOR 15 METER QUAD APERTURE

The phase perturbation distribution model for the 15 meter quad aperture antenna is shown in figure 9. Because of the tie-cord configuration for the mesh antenna, pillowing of the surface occurs. This pillowing is represented in the phase perturbation model as sine squared, both radially and circumferentially.

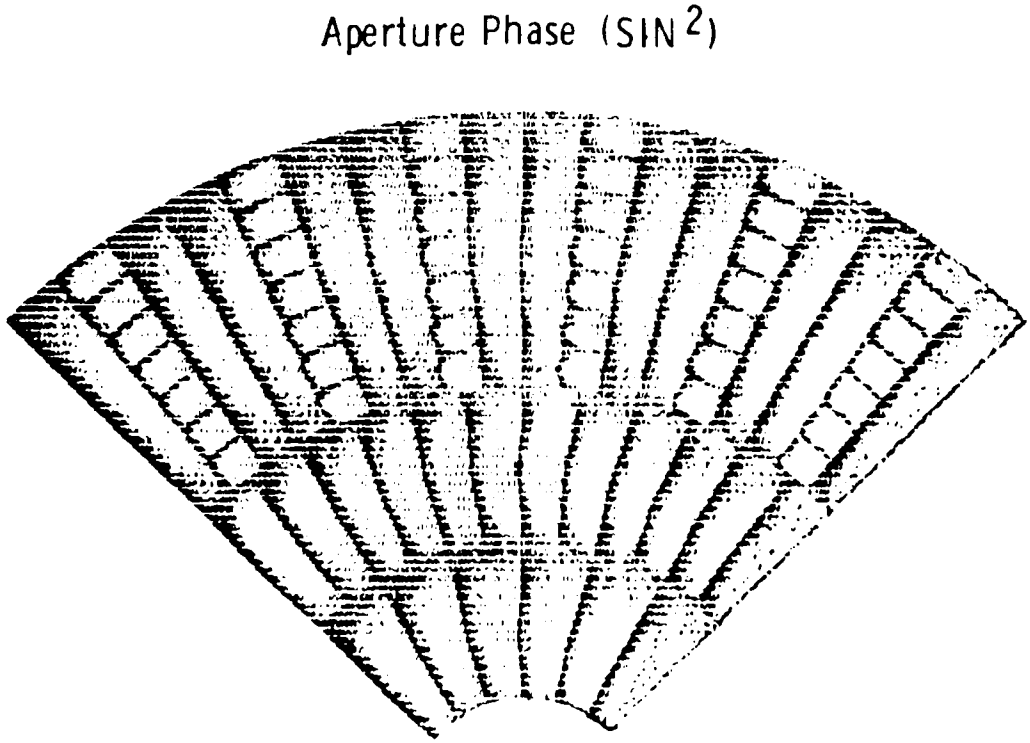

Figure 9

FEED PATTERN

Figure 10 shows the principal plane radiation patterns for the feed used in the analysis of the single quad 15 meter antenna.

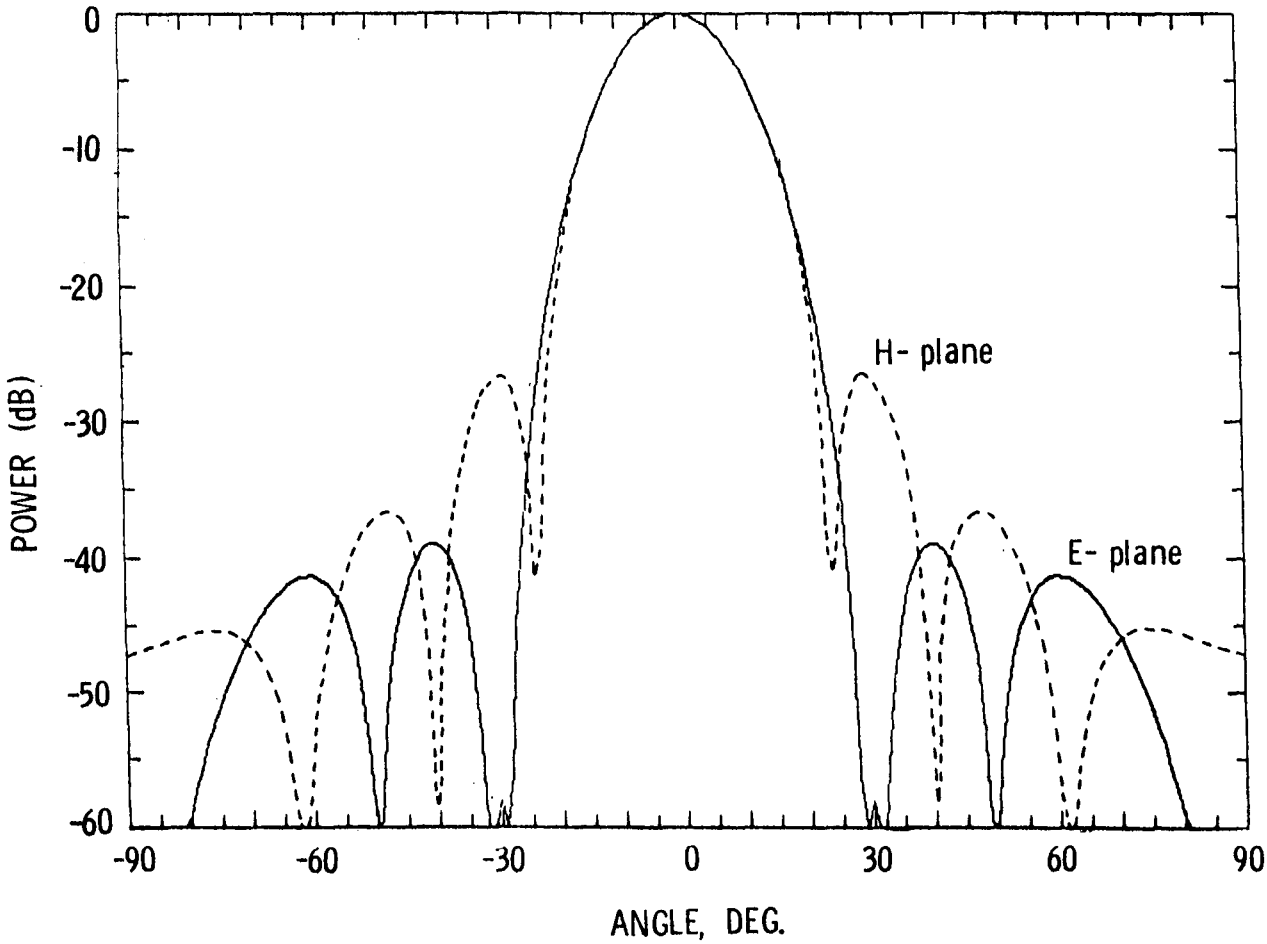

Figure 10

COMPUTED PATTERNS FOR SMOOTH, .008", AND .02" SURFACES AT 2.3 GHz

For the periodic distortion assumed in figure 9, computed H-plane and E-plane radiation patterns are shown in figures 11a and 11b, respectively. The grating lobes due to the periodic distribution are shown clearly for the different rms surface distortions.

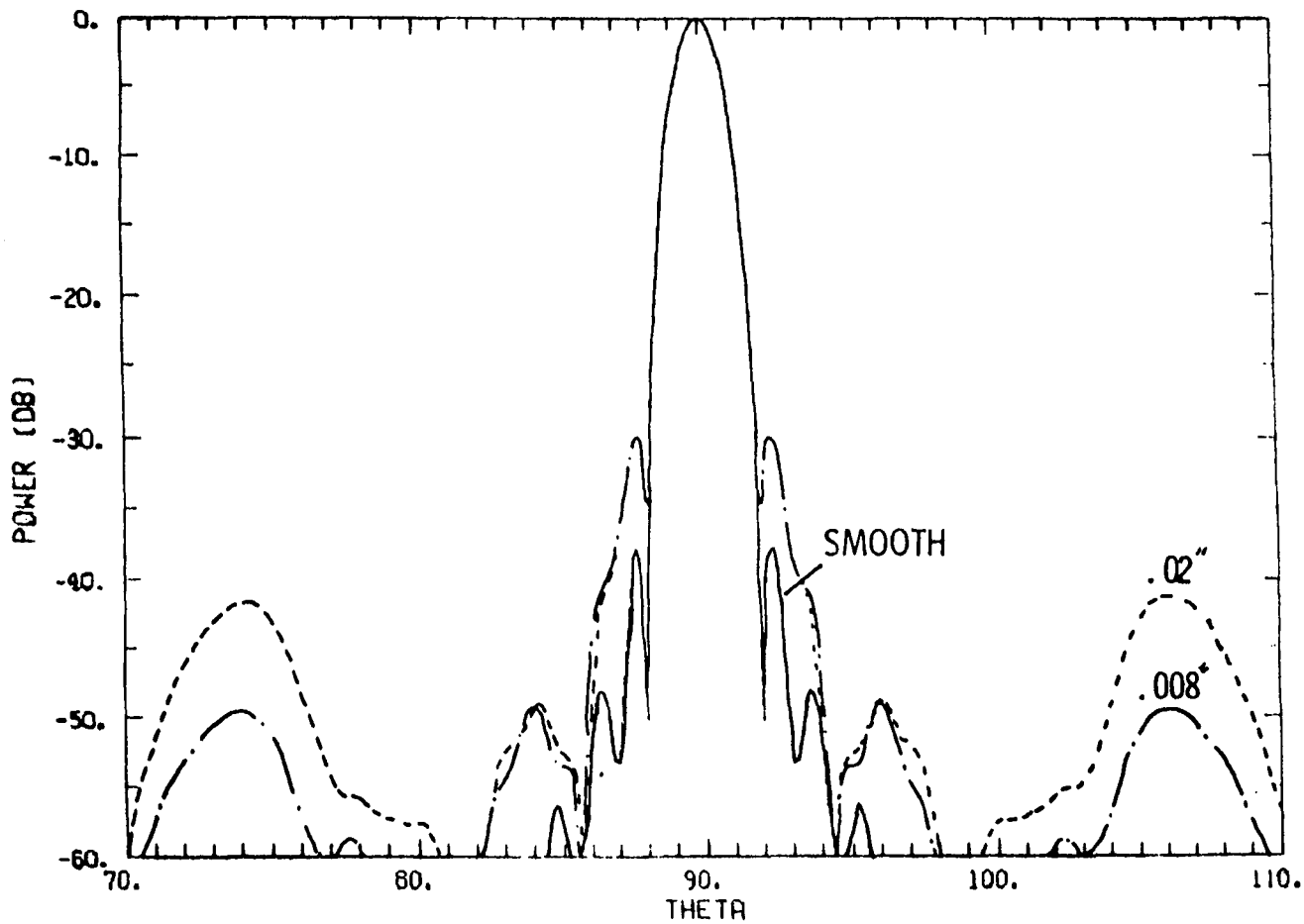

H- PLANE PATTERNS FOR SMOOTH, .008" and .02" RMS SURFACES AT 2.3 GHz.

Figure 11a

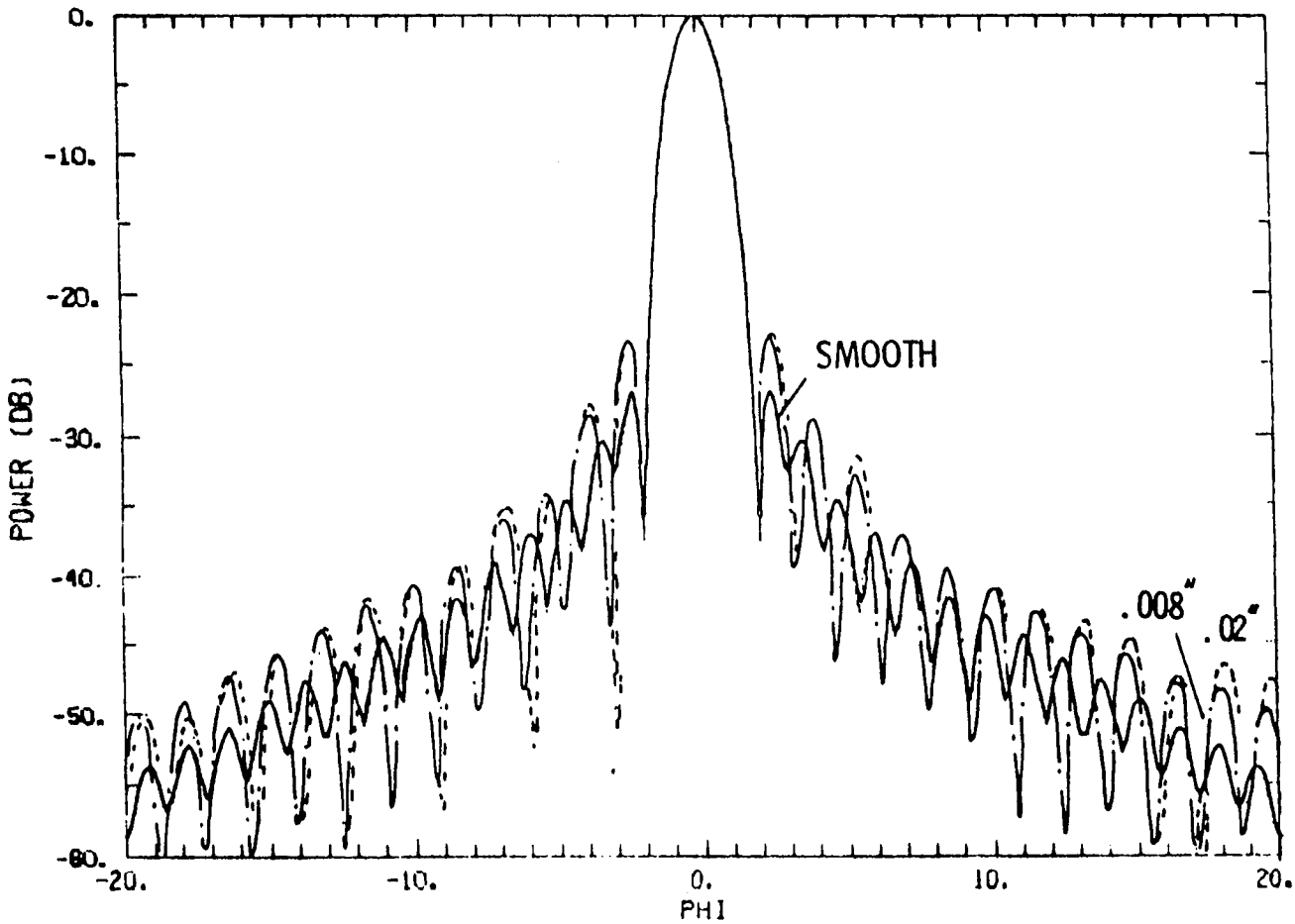

E- PLANE PATTERNS FOR SMOOTH, .008" and .02" RMS SURFACES AT 2.3 GHz.

Figure 11b

COMPUTED PATTERNS FOR SMOOTH, .008", and .02" RMS SURFACES AT 12.0 GHz

For the periodic distortion assumed in figure 9, computed H-plane and E-plane radiation patterns are shown in figures 12a and 12b, respectively. The grating lobes for the same two rms surface distortions are even higher in level and occur closer to the main beam than the grating lobes in the previous figure. The level of intensity and the angular position of the grating lobes depend on the frequency of operation.

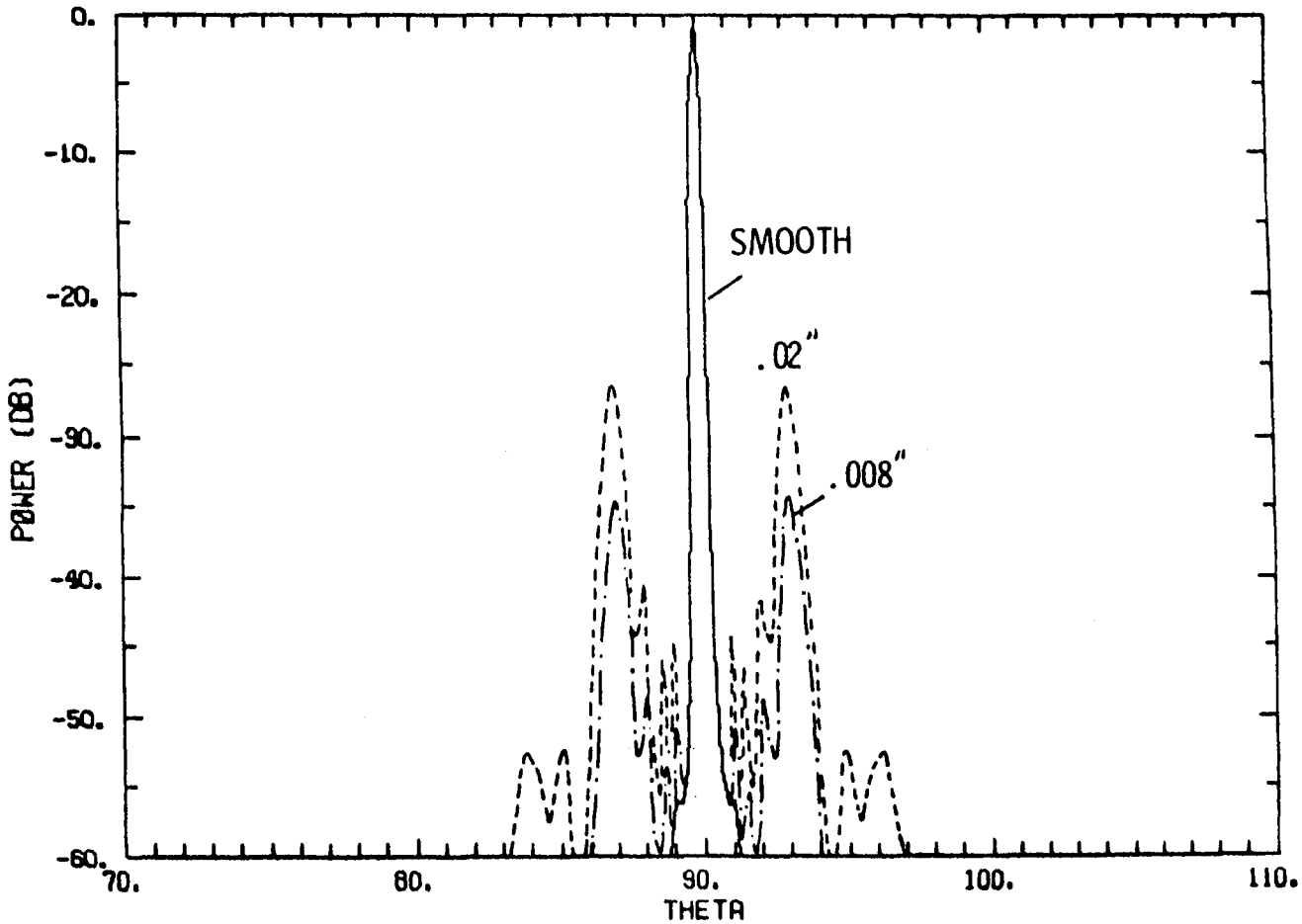

H- PLANE PATTERNS FOR SMOOTH, .008" and .02" RMS SURFACES AT 12.0 GHz.

Figure 12a

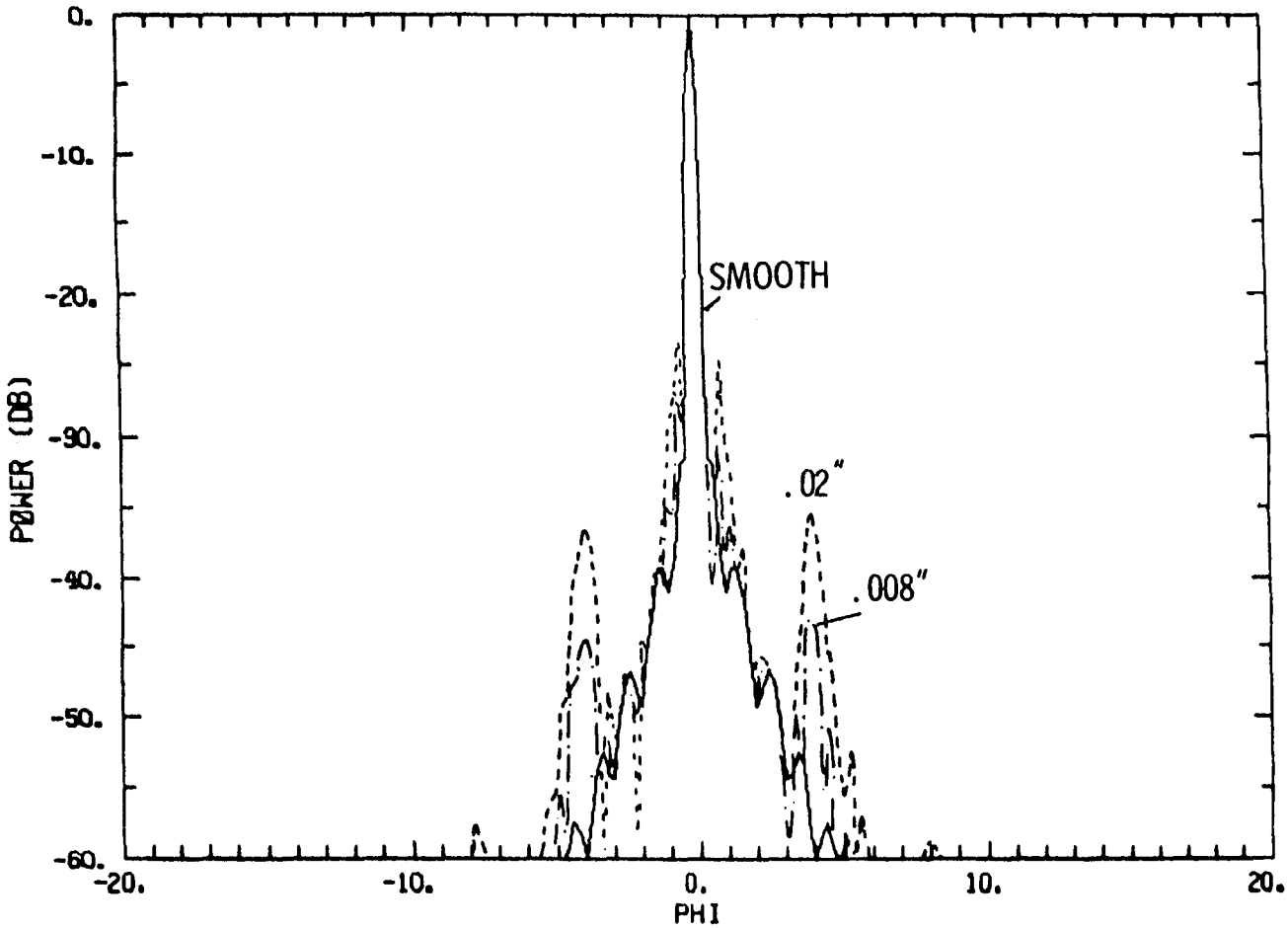

E- PLANE PATTERNS FOR SMOOTH, .008" and .02" RMS SURFACES AT 12.0 GHz.

Figure 12b

COMPUTED H-PLANE PATTERNS FOR PERIODIC SURFACE AT 2.3, 4.3, 8.0, AND 12.0 GHz

For the periodic surface distortion in figure 9, computed H-plane radiation patterns for a single quad of the 15 meter antenna are given in figure 13. Figure 13a gives the patterns for .008" rms surface distortion whereas the patterns for .02" rms surface distortion are shown in figure 13b. These figures clearly show how the grating lobe level increases as the frequency increases. Movement of the grating lobes closer to the main beam as the frequency increases is also shown. Since the level of intensity and angular position of the grating lobes can be a problem in many applications, one must be cognizant of what level of periodic surface distortion can be tolerated.

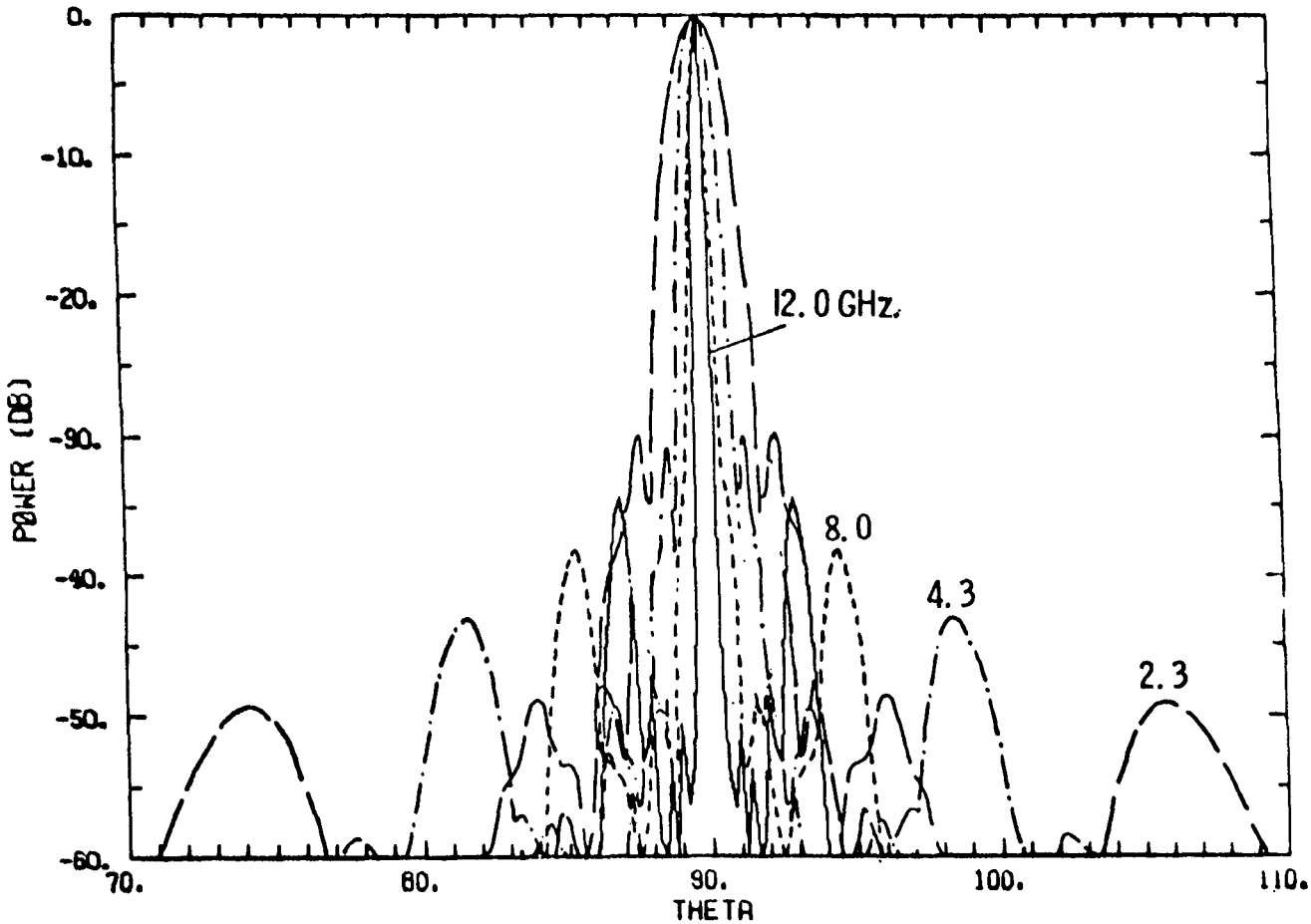

H- PLANE PATTERNS FOR .008" RMS SURFACE AT 2.3, 4.3, 8.0, and 12.0 GHz.

Figure 13a

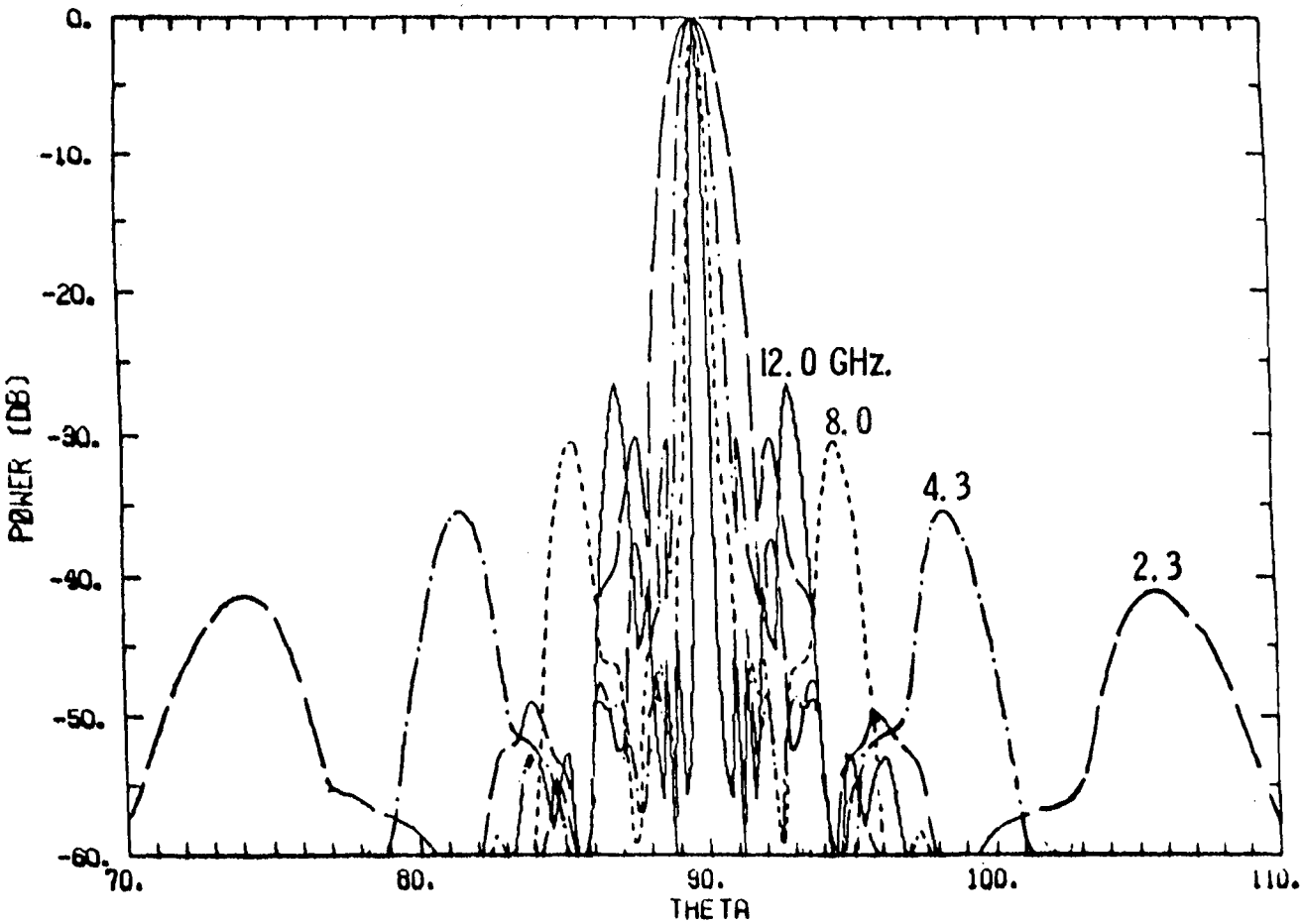

H- PLANE PATTERNS FOR .02" RMS SURFACE AT 2.3, 4.3, 8.0, and 12.0 GHz.

Figure 13b

RADIATION PATTERN PREDICTIONS FOR 15-METER QUAD REFLECTOR-PILLOWED SURFACE

A summary composite for the 15-meter quad reflector-pillowed antenna is shown in figure 14. For the 15-meter model, the phase distribution and a typical radiation pattern showing grating lobes are included.

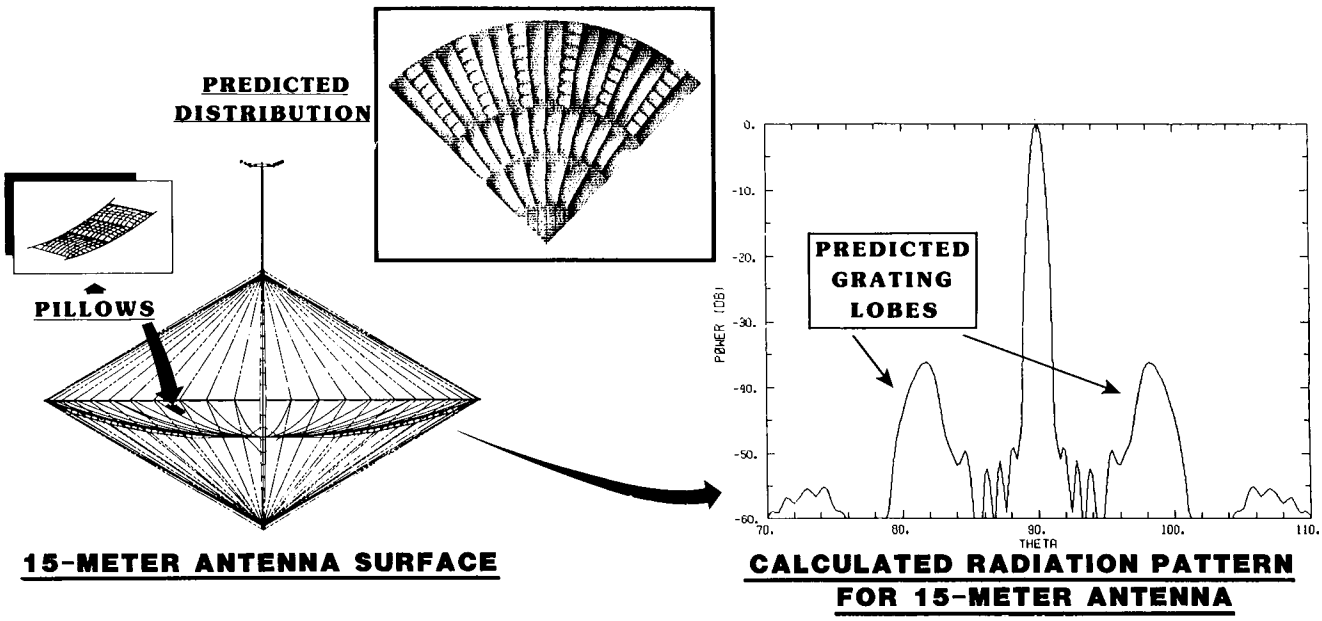

Figure 14

REFERENCES

1. Ruze, John: Antenna Tolerance Theory - A Review. Proc. IEEE, Vol. 54, pp. 633-640, April 1966

2. Shifrin, Ya. S.: The Statistics of the Field of a Linear Antenna. Radio Engineering and Electronic Physics, No. 3, March 1963.

3. Bao, V. T.: Influence of Correlation Interval and Illumination Taper in Antenna Tolerance Theory. Proc. IEE (London) Vol. 116, No. 2, pp. 195-202, 1969.

4. Rudduck, Roger C.: Application of Modern Aperture Integration (AI) and Geometrical Theory of Diffraction (GTD) Techniques for Analysis of Large Reflector Antennas. Large Space Antenna Systems Technology - 1984, NASA NASA CP-2368, Part 2, 1985, pp. 675-691.

Page intentionally left blank

Application of Modern Aperture Integration (AI) and Geometrical Theory of Diffraction (GTD) Techniques for Analysis of Large Reflector Antennas

Roger C. Rudduck

Ohio State University

Columbus, Ohio

Large Space Antenna Systems Technology-1984

December 4-6,1984

COMPUTER MODELING FOR REFLECTOR ANTENNAS

The calculation of patterns for large spaceborne antenna systems is very challenging. One of the reasons is that very large amounts of data need to be calculated and processed. For example, on the order of 50,000 samples are often required for the aperture field or surface current data even for small scale versions of future spaceborne antennas. Several efficient techniques have been developed for the aperture integration part of the OSU Reflector Antenna Code which significantly reduce the required time. One is the large subaperture method, with which the subapertures can be electrically large, thus minimizing the computer storage and also the amount of numerical integration required. An even more significant technique, which can be used for far field computations, is the rotated grid method as shown in Figure 1. The major feature of the rotated grid method is that the y-integrations are carried out for each column of the aperture and each one-dimensional integration result is stored. The stored values for the y-integrations are then used for each pattern angle in the plane perpendicular to the rotated y-axis, thus the efficiency approaches that of a one-dimensional integration. Computational advantages for the OSU Reflector Code on the order of 30 to 100 in computer time over other reflector codes are frequently encountered.

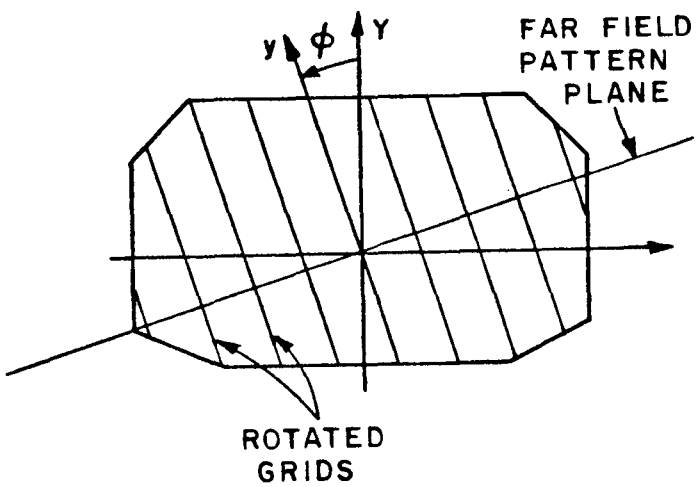

Figure 1. Rotated grid method for high efficiency of aperture integration.

VALIDATION OF ANALYSES AND COMPUTER CODES

A major aspect in the development of computer analyses and their associated codes is their reliability. Numerous validations need to be made with measured patterns and other methods of analysis. Furthermore, as new capabilities are added to a code, countless checks need to be made during the development process. This process requires much diligence and patience on the part of the developers.

The validation of the OSU code with measured patterns of the RF Verification Model is of special interest here. This model was fabricated and tested by Harris Corporation (Melbourne, Florida) under contract to NASA Langley Research Center. This prototype for the 15 meter hoop/column reflector antenna consists of a two-quadrant parabolic surface, with a small separation between the vertices of each quadrant. The radiation patterns calculated by the computer code were obtained separately for each quadrant and the superimposed patterns are shown in Figure 2(a). The parasitic lobe produced by the second quadrant has a peak value of 19 dB below the main beam peak. The measured pattern furnished by Harris Corp., as shown in Figure 2(b), provides a good validation of the computer model for this type of antenna. The envelopes of the calculated and measured patterns are in excellent agreement; the ripple in the measured pattern is caused by the interference between these two quadrants.

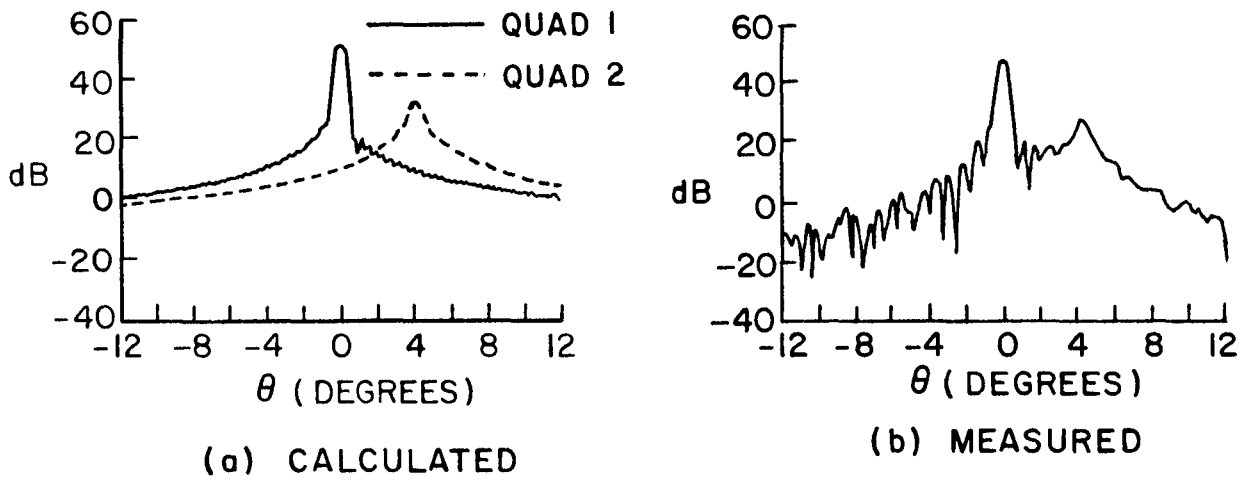

Figure 2. Patterns of RF Verification Model with ordinary horn feed.

COMPUTER-AIDED DESIGN MODIFICATIONS

Use of the efficient techniques described above has provided the capability to generate large amounts of pattern data in a reasonable time. This capability has been used to determine the feasibility of improving the antenna design of Figure 2. Several types of feed designs have been tested with the computer code: ordinary horns, corrugated horns, an array feed and a multimode horn. The 19 element array feed designed by M.C. Bailey of NASA Langley has been predicted to provide significant improvement over ordinary and corrugated horn feeds. This array feed should provide performance comparable to a multimode horn, yet it requires less space than multimode horn designs. The calculated pattern for the RF Verification Model with an early version of the 19 element array feed is shown in Figure 3a, where the parasitic lobe level has been reduced to -26.5 dB below the peak. This is a 7.5 dB improvement over that achieved with the ordinary horn feed used in Figure 2. This array feed design is being further improved to provide even lower levels.

Another approach for reducing the parasitic lobe was also studied. It was shown that the parasitic lobe could be reduced by increasing the separation between quadrants. A typical result is shown in Figure 3b, where a level of -29.5 dB is predicted for a quadrant separation of 15 inches (a separation of 7.8 inches is used in Figures 2 and 3(a)).

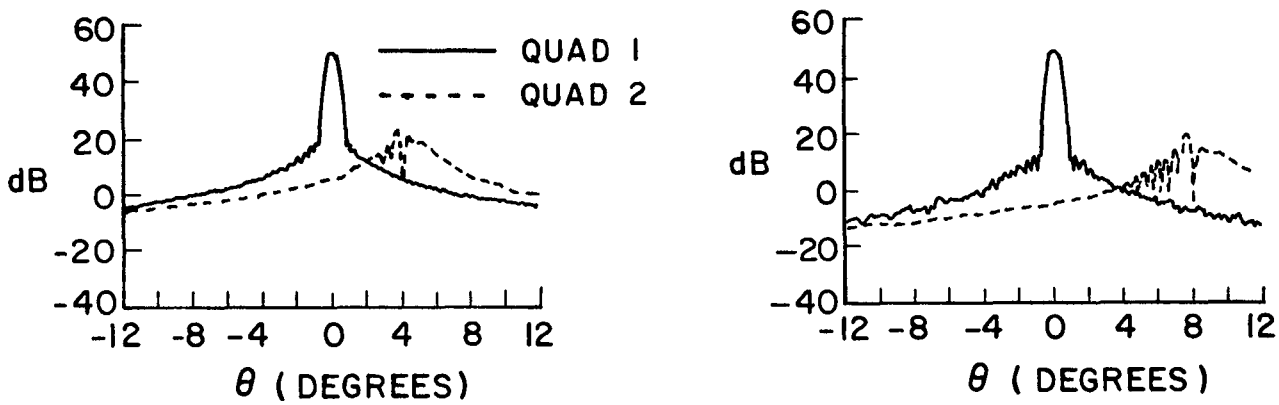

(a) Quadrant separation= 7.8"

(b) Quadrant separation= 15"

Figure 3. Patterns of RF Verification Model with 19 element array feed.

LIMITATION ON THE CONVENTIONAL APERTURE INTEGRATION (AIC) METHOD

The conventional AIC approach in which the Geometrical Optics fields are integrated over the reflector aperture has some limitations, even in the close-in sidelobe region, especially for small offset reflectors. The major reason for this limitation is that only the G.O. fields are included in the aperture fields, as shown in Figure 4(a). The GTD diffracted fields are not included. The pattern shown in Figure 4(b) for an 18.8 wavelength diameter offset reflector illustrates the deficiency of the conventional AIC. In this case, the conventional AIC approach gives the wrong pattern lobe structure as compared to the GTD pattern in Figure 4(b). Note that GTD is not valid in the main beam, i.e. theta less than five degrees.

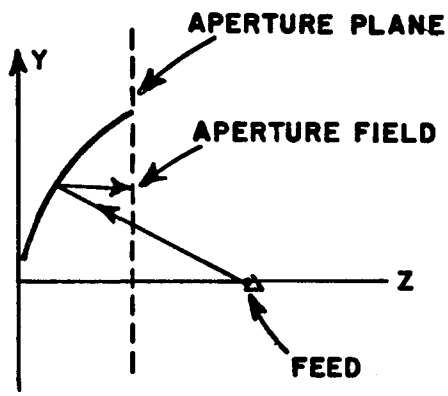

(a) Only G.O. field in aperture

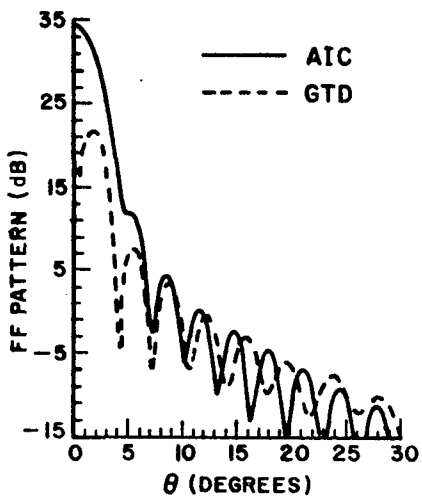

(b) AIC(——) compared to GTD(- - -)

Figure 4. Conventional AI approach (AIC).

EXTENDED APERTURE INTEGRATION (AIE) METHOD

The AIE method adds the uniform GTD (UTD) diffracted fields from the reflector rim to the original G.O. aperture fields as shown in Figure 5(a). In addition, the aperture needs to be extended to include the GTD diffracted fields outside the original G.O. aperture as shown in Figure 5(b). The addition of the GTD fields in the aperture provides a more accurate representation of the aperture fields than the conventional G.O. approximation. Although AIE is more accurate than the conventional AIC, it is more expensive because of the numerous computations required for adding the GTD fields to the aperture fields.

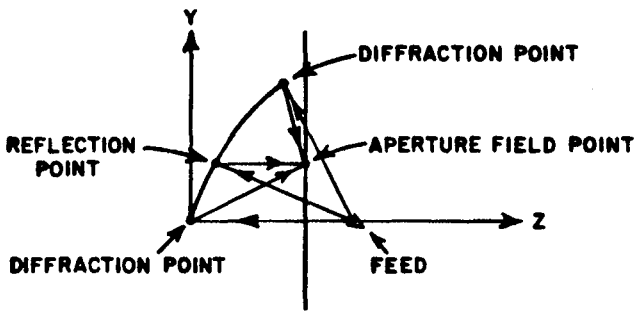

(a) The addition of the diffracted fields to the original G.O. aperture field.

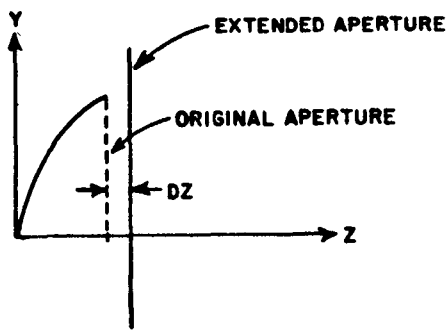

(b) The aperture needs to be extended.

Figure 5. The features in the AIE.

IMPROVED RESULTS FROM THE AIE METHOD

Figure 6 shows the improvement that the AIE method provides for the reflector pattern of Figure 4(b). Note that the GTD fails for the main beam as expected and that the AIE still has some errors for the wide angle sidelobes because the new aperture is not extended far enough. Those differences in the sidelobes will be reduced if the aperture is extended further and a finer grid is used. This, however, is not necessary because GTD can be directly used beyond the second sidelobe.

It should also be noted that GTD is not usually accurate for the first sidelobe or two, as happens to be the case for this example. Furthermore, since GTD ordinarily is used to calculate the effect of the reflector rim, it does not provide the pattern distortion effects of reflector surface inaccuracies.

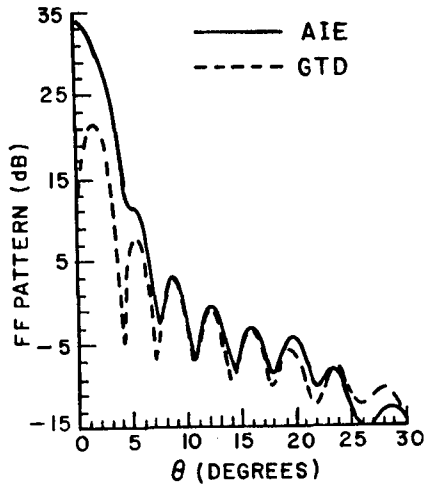

Figure 6. AIE(——) patterns compared to GTD(- - -) patterns.

AIE METHOD FOR FEED SCATTERING CALCULATIONS

Another reason that reflector analysis is challenging is that these are numerous scattering mechanisms which need to be modeled. One example of this is the scattering from feed structures located outside the direct geometrical optics (G.O.) region of the reflector, but which may still degrade the pattern. The 35 GHz offset reflector model reported by T.G. Campbell [ref.1] has its feed structure located outside the G.O. region as depicted in Figure 7(a).

In this approach the AIE method discussed above is used to calculate the forward scattering from the feed scattering apertures as shown in Figure 7(b). The total fields of the reflector are then obtained by subtracting these forward scattered fields from the unblocked reflector fields.

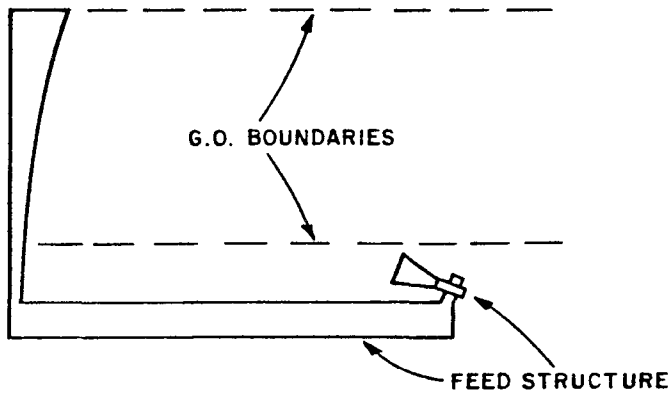

(a) OFFSET FEED STRUCTURE

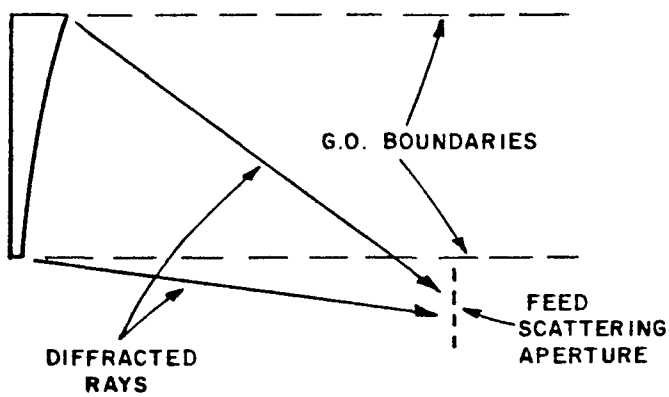

(b) FEED SCATTERING APERTURE

Figure 7. AIE method for Feed Scattering Model.

FEED SCATTERING RESULTS FOR 35 GHZ REFLECTOR MODEL

The measured E-plane pattern of the 35 GHz reflector is reproduced from reference 1 in Figure 8(a). The pattern calculated by using the AIE method for the feed scattering contribution is shown in Figure 8(b). The comparison demonstrates the capability of this feed scattering analysis to provide good engineering predictions for offset feeds.

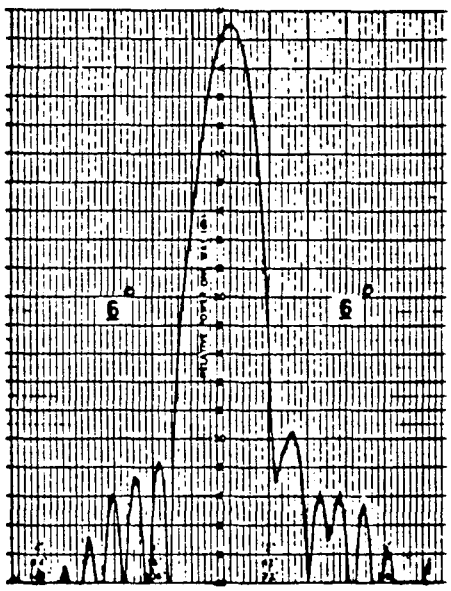

(a) Measured

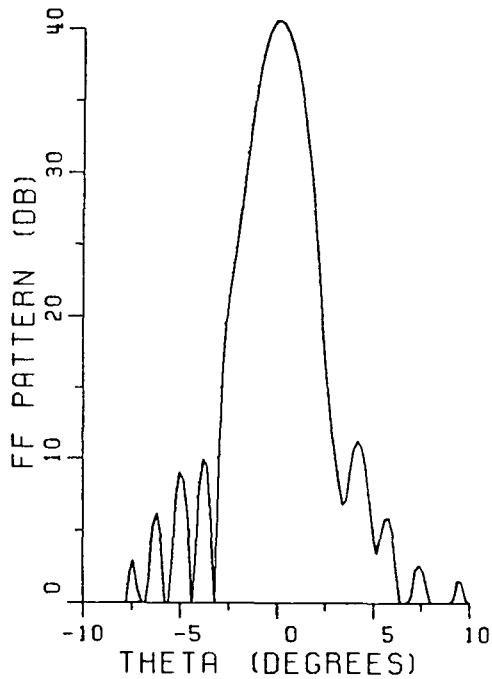

(b) Calculated

Figure 8. Patterns of 35 GHZ Reflector Model.

NEAR FIELD PROBING PREDICTIONS FOR 15 METER MODEL

The capability to calculate GTD diffracted fields in the aperture of a reflector antenna is also being used to predict results for the 15 meter hoop-column reflector antenna model. This model is to be shipped to Martin Marietta's near field probing facility at Denver. The OSU Reflector Antenna Code is currently being modified to calculate the near field probing data for this four-quadrant reflector. A preliminary result is given in Figure 9 where the predicted near field data is shown across the middle of one quadrant. After the code modification is completed, it is planned to use the AIE method to calculate the far field patterns which correspond to the simulated near field data.

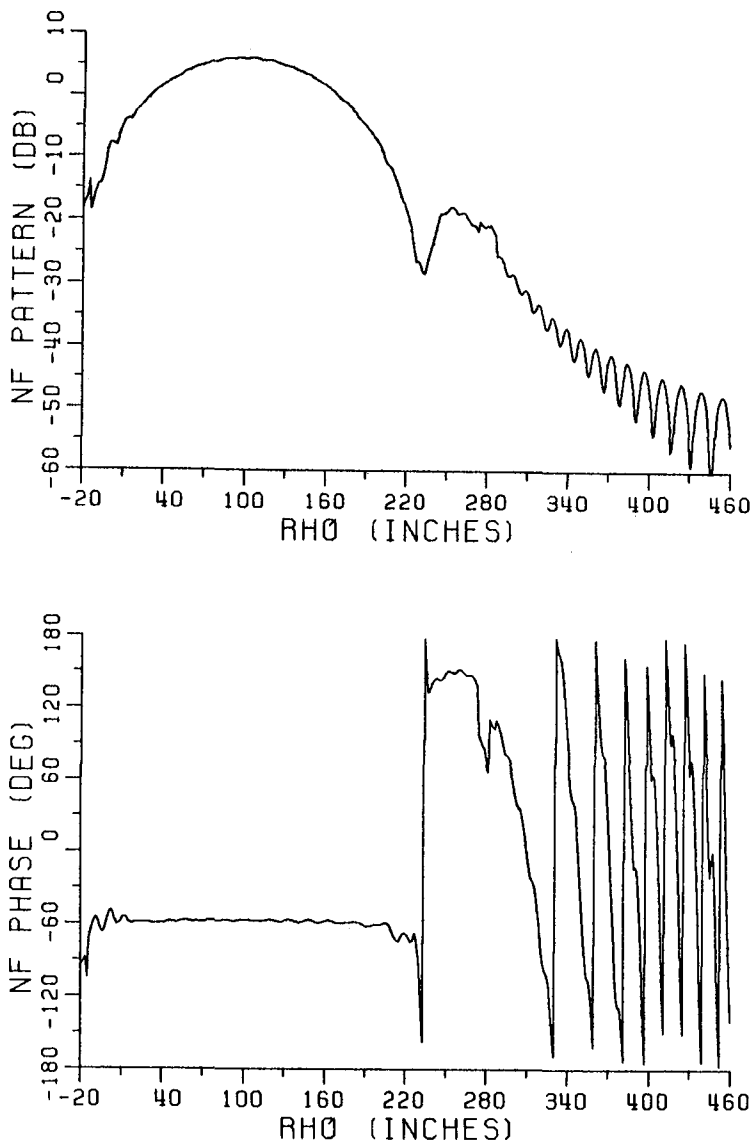

Figure 9. Predicted Near Field Probing data for the 15 meter hoop/column reflector antenna for the 19 element array feed at 2.3 GHz.

LIMITATION ON AIC FOR SURFACE TOLERANCE EFFECTS

Another limitation on the AIC method concerns the analysis of surface tolerance effects. These effects are currently being analyzed by a surface perturbation method (See ref.2) which assumes that the reflector surface normals are not greatly distorted. If the surface normals are significantly distorted from the ideal reflector surface, as shown in Figure 10(a), the AIC method is not accurate because the direction of the undistorted ray is used. The 35 GHz offset reflector model (with 0.2 wavelength surface distortion) discussed in reference 2) cannot be accurately analyzed by the AIC method because the normals for this case are distorted by as much as 20 degrees.

The generic curves given in Figure 10(b) for center-fed reflectors show the effect of distortions of the surface normals on the phase error in the aperture field, when the AIC method is used. For example, if the surface normal is distorted by 10 degrees for F/D= 0.3, the pathlength error/diameter is 0.01. This means that a one wavelength path error or 360 degrees phase error occurs for a D=100 wavelength diameter antenna. On the other hand, a normal distortion of 1 degree will cause only a 3.6 degree phase error for D= 100 wavelengths. Consequently, the AIC method can accurately analyze reflectors with reasonably smooth surface distortions.

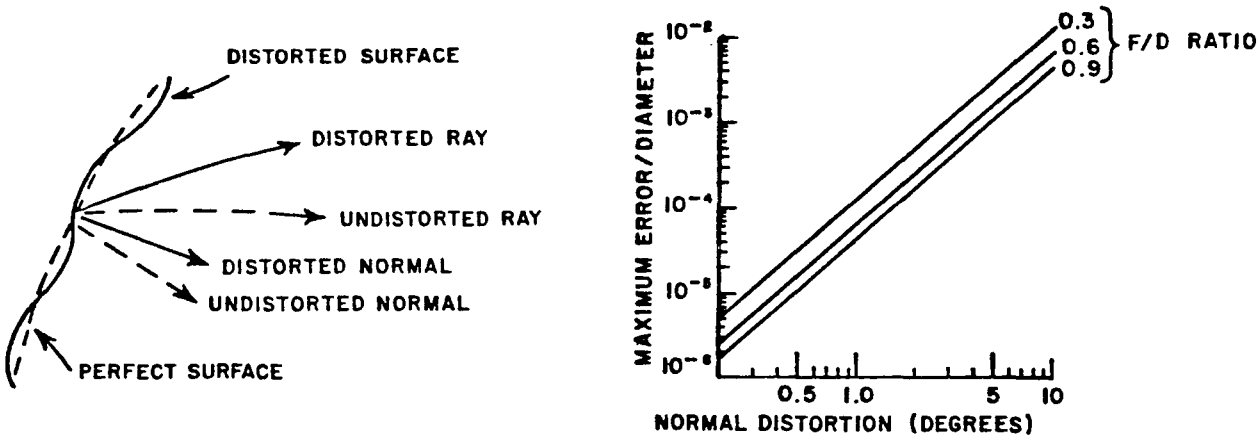

(a) Distorted surface normal and rays (b) Errors caused by distortion

Figure 10. Limitation of the AIC method for distorted reflector surfaces.

APERTURE INTEGRATION ON THE SURFACE (AIS) METHOD

The previously discussed limitation for the conventional AIC method is caused by the distortions of the surface normals and their associated rays. This limitation could possibly be overcome by using the true surface normals to trace rays to the aperture plane. However, a more accurate ray tracing for the aperture fields is not always adequate because of diffractions from surface discontinuities, e.g. the cusps in the "rectified cosine" surface used for the 35 GHz model. The surface current approach as shown in Figure 11(a) is often used for reflector antennas. It appears that this type of approach could overcome the most serious limitation of the AIC method. Consequently, a modified surface integration approach was implemented in the OSU Reflector Code in order to overcome the limitations of the AIC method. The modified approach, called Aperture Integration on the Surface (AIS), uses a "stair step" aperture as shown in Figure 11(b). Therefore, the aperture field is calculated at the reflector surface, instead of a planar aperture, by using the same basic computer software as that used for the aperture field calculation in the AIC method. The most significant difference between the AIS and AIC methods is that a 2-D integration is required for each pattern angle in the AIS method, whereas only a 1-D integration is used with the AIC method through the rotated grid approach. As a result, the AIS calculations are much more expensive than AIC calculations.

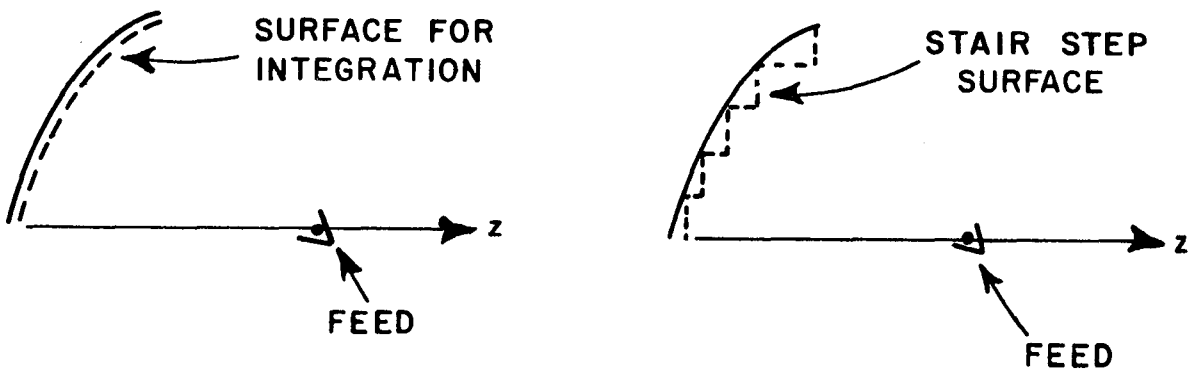

(a) Surface current integration

(b) Stair step surface for AIS integration

Figure 11. Surface Integration Methods.

VALIDATION OF THE AIS METHOD

The AIS method can be validated by comparing the results with the AIE method for a smooth reflector surface. The reflector antenna shown in Figure 12 is a good example for comparison. This reflector which has a 7.5 foot radius is the basic design currently proposed for the next generation of compact range reflectors. In the final design of this reflector, curved surface edges (rolled edges) will be added to the semi-circular rim shown in Figure 12(b). The near zone fields were calculated along the vertical line shown in Figure 12 for the reflector with sharp edges. The results from both methods demonstrate the validity of the AIS method as shown in Figure 12(b).

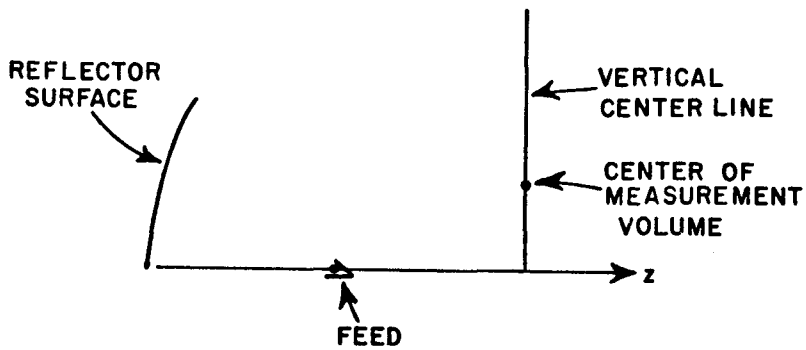

(a) Reflector geometry

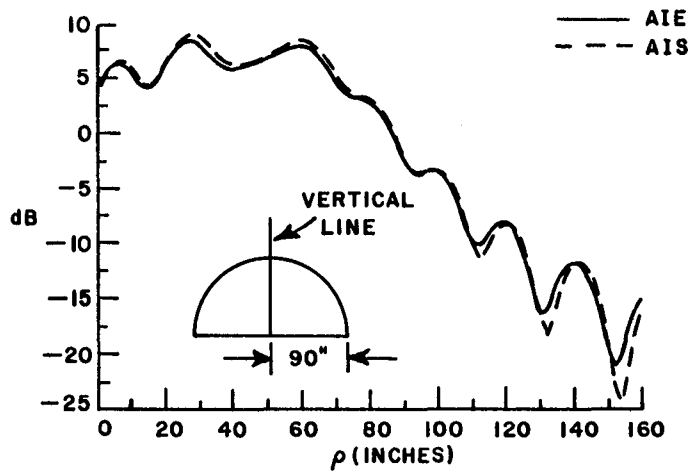

(b) Comparison between AIS and AIE methods

Figure 12. Validation of the AIS method with a compact range reflector example.

AIC AND GTD CALCULATIONS FOR THE COMPACT RANGE REFLECTOR

The results of the AIC and GTD methods have also been calculated for the same case, as shown in Figure 13. It turns out that the AIE and GTD methods are in excellent agreement and appear to be the most accurate of the four methods. As can be seen from these results, this example provides further validation of the AIS method because it differs only slightly from both the AIE and GTD methods. On the other hand, the conventional AIC method gives significant errors as can be seen from Figure 13.

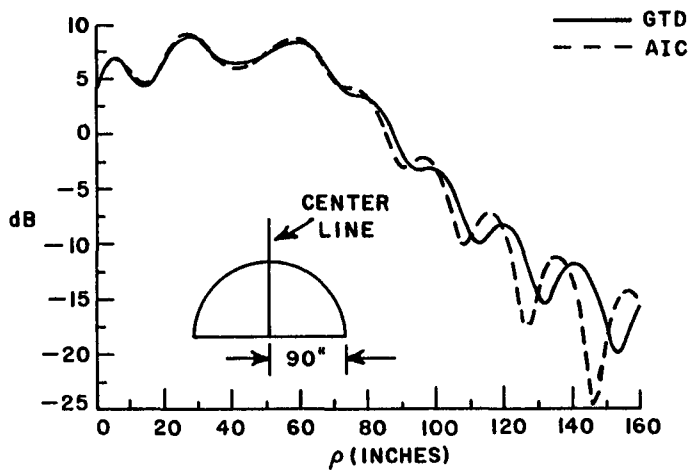

Figure 13. Limitation of the AIC method for near zone calculations.

IMPROVED SURFACE TOLERANCE CALCULATIONS FOR THE 35 GHZ MODEL

As previously discussed the conventional AIC method does not provide very accurate results for the 35 GHz model; it predicts grating lobes which are about 8 dB higher than the measurement data with the 0.2 wavelength surface. The AIS method provides an improved comparison with the pattern measured at NASA Langley as shown in Figure 14. Although the pattern shapes do not agree as well as desired, the AIS method does provide a good estimate of the grating lobe level for the 35 GHz model.

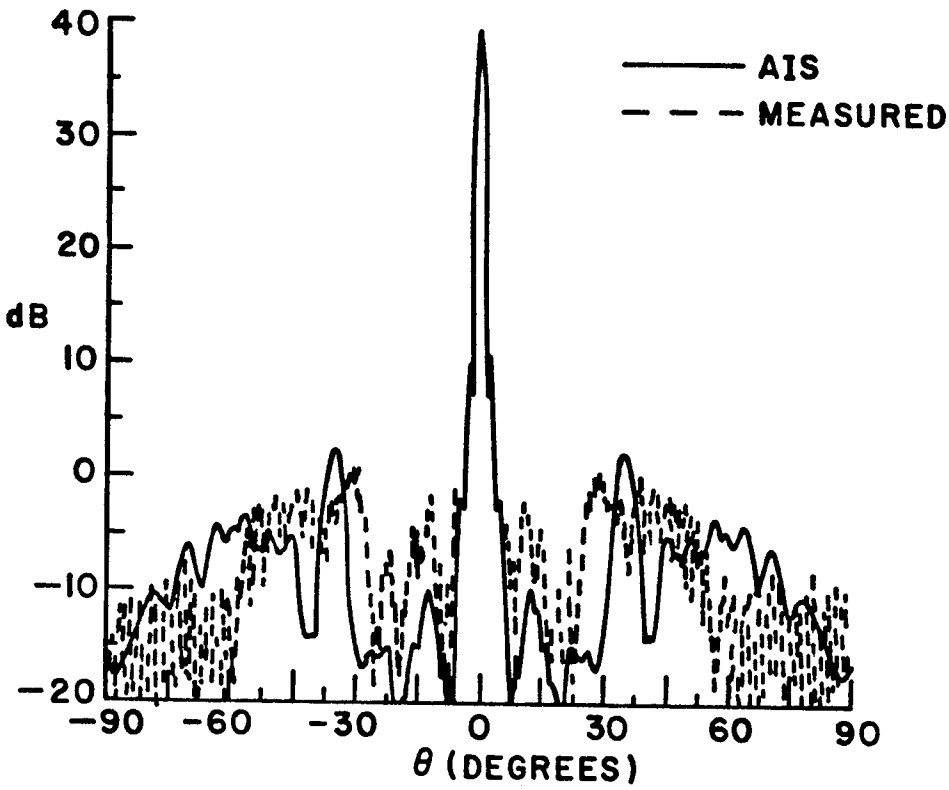

Figure 14. Comparison between the AIS calculated pattern and the measured pattern for the 35 GHz model with 0.2 wavelength surface.

SURFACE TOLERANCE CALCULATIONS FOR THE 15 METER ANTENNA

It is expected that the AIC method can analyze reflectors with reasonably smooth surface distortions. The 15 meter hoop/column reflector antenna model falls into this category. Both the AIC and AIS methods were used to calculate the patterns for the 15 meter model with a periodic sine squared surface distortion and a 0.05 inch amplitude. The patterns, as shown in Figure 15, were calculated for a frequency of 13.9 GHz. It should be noted that this is somewhat a "worst case" example for this antenna because a 0.05 inch surface error and a 13.9 GHz frequency are assumed. As can be seen from Figure 15, both methods agree well for levels as low as 50 dB below the peak. This example demonstrates the validity of the more efficient AIC method for reflectors with reasonably smooth surfaces. The accuracy of the AIC method will improve for smaller surface distortions and/or lower frequencies.

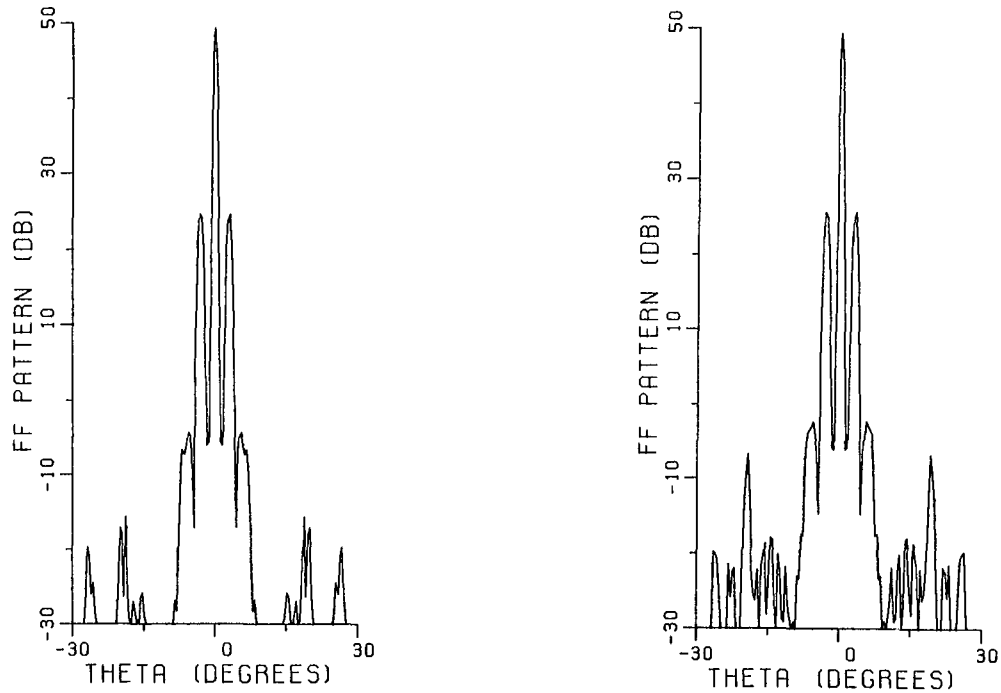

(a) AIS

(b) AIC

Figure 15. Surface tolerance calculations for a smooth reflector surface.

REFERENCES

1. Campbell, T. G., and W. R. Young, Preliminary experimental test results using 35 GHz offset fed reflector simulating surface pillows and aperture cables, Large Space Systems Technology - 1981, NASA CP-2215, Part 2, 1982, pp. 557-581.

2. Cockrell, C. R., and R. C. Rudduck, Electromagnetic analysis for surface tolerance effects on large space antennas. Large Space Antenna Systems Technology - 1984, NASA CP-2368, Part 2, 1985, pp. 655-673.

Page intentionally left blank

FEED SYSTEM DESIGN CONSIDERATIONS FOR LARGE SPACE ANTENNA SYSTEMS

PART I - MULTIPLE APERTURES WITH NON-OVERLAPPING FEEDS

M. C. Bailey
NASA Langley Research Center
Hampton, Virginia

Large Space Antenna Systems Technology - 1984
December 4-6, 1984

COMPARISON OF CIRCULAR AND QUADRANT APERTURE REFLECTOR RADIATION PATTERNS

One consideration in the design of feeds for multiple apertures, such as the quadrant apertures as presently configured for the 15-meter hoop/column antenna, is the effect of the aperture shape upon the beam quality of the antenna. The contour pattern calculations in figure 1 indicate that the main beam of the antenna is very nearly the same for a quadrant aperture and a circular aperture whose diameter can be inscribed within the quadrant. The major difference between the two patterns occurs in the side lobe region since the corners of the quadrant aperture are illuminated at a lower level and also an aperture with corners naturally produces lower side lobes in those directions. The feed used to calculate the pattern in figure 1 was the same for both reflector apertures and was designed to produce a -15 dB illumination at the edge of the circular aperture.

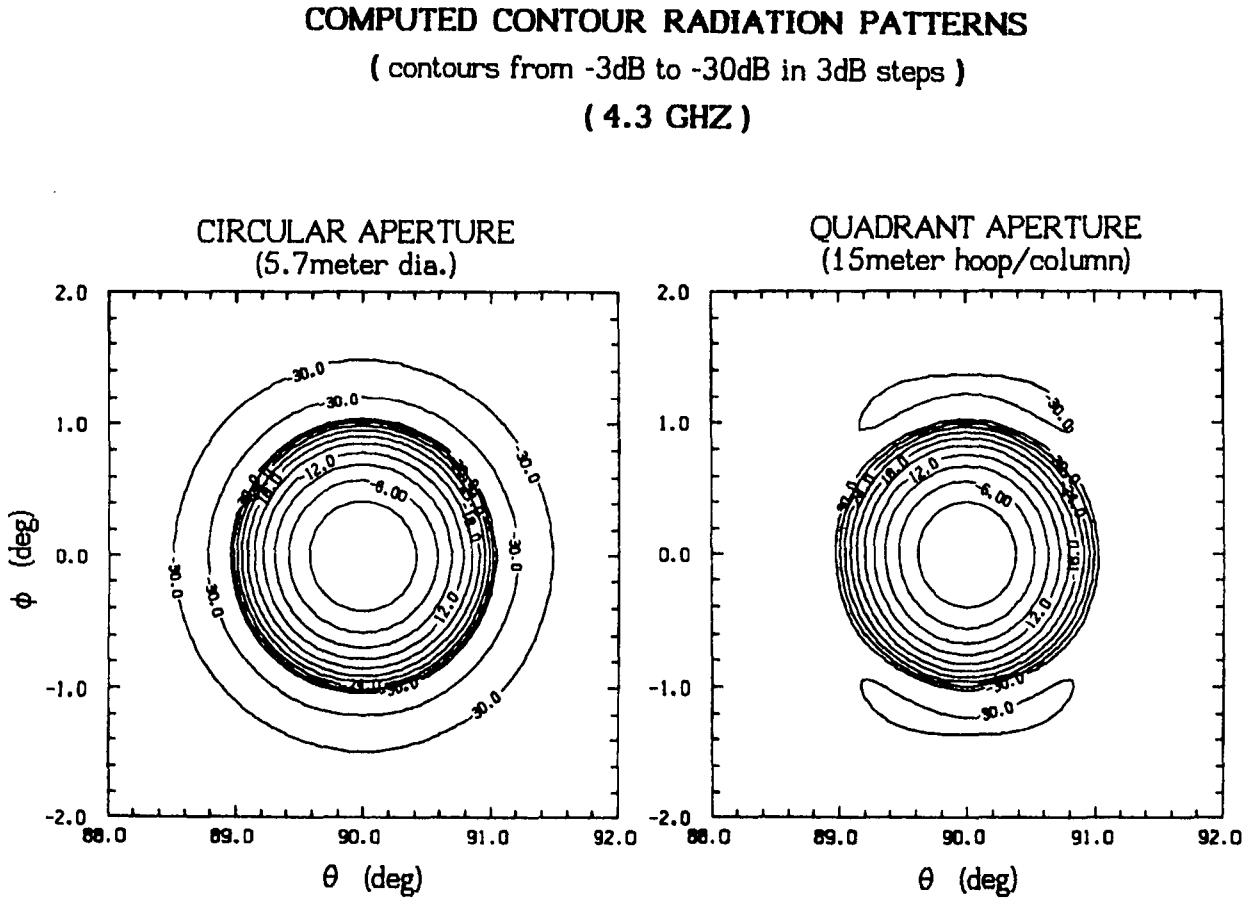

Figure 1

EFFECT OF ADJACENT APERTURE UPON RADIATION PATTERN
OF MULTIPLE-APERTURE REFLECTOR ANTENNA

The measured radiation pattern in figure 2 illustrates another consideration in the design of feeds for multiple-aperture reflector antennas. The data was obtained by illuminating one quadrant of a two-quadrant reflector with a pyramidal horn feed. The effect of the adjacent reflector can be observed as a significant side lobe (approximately -19 dB) due to the spillover of the feed onto the adjacent reflector. This lobe appears as a side lobe although actually it is the result of the adjacent reflector focusing the spillover from the feed, and since the feed is located away from the focal point of the adjacent reflector, this lobe is scanned away from boresight.

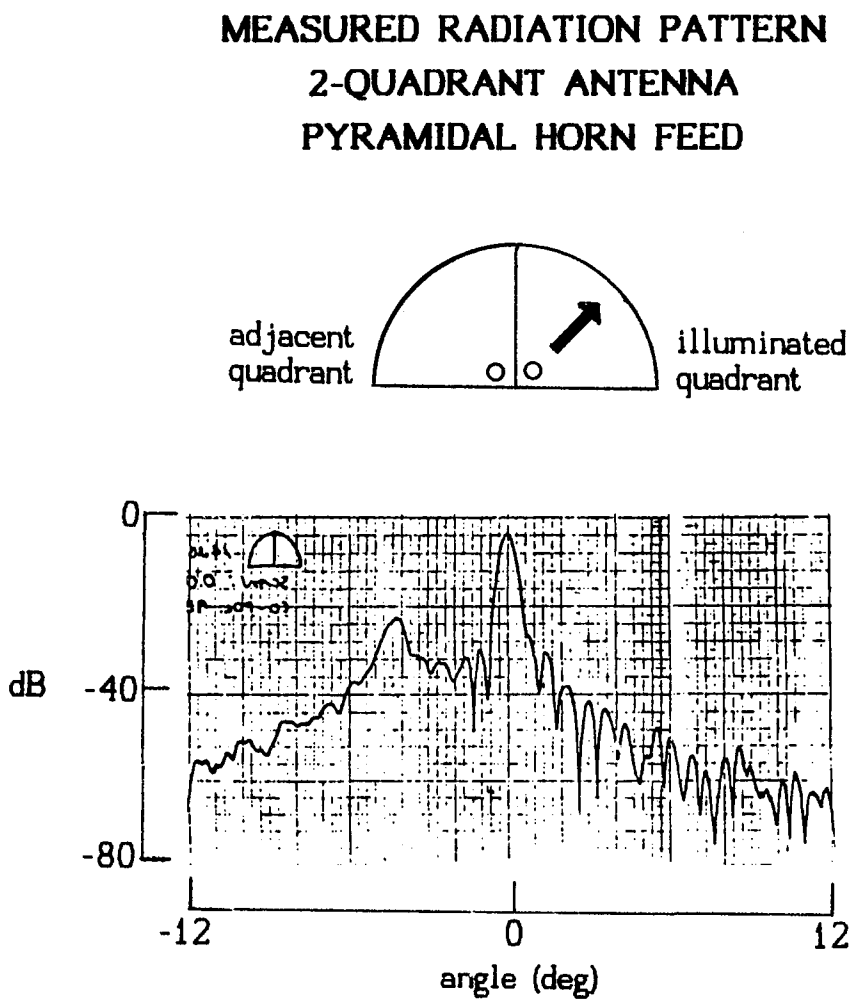

Figure 2

Figure 3 shows the aperture illumination of the primary quadrant of the 15-meter hoop/column reflector and the illumination of the other quadrants of the reflector due to feed spillover. This illumination was computed for a feed optimized for a four-quadrant reflector. The feed is a 19-element array of circular microstrip patch radiators in an equilateral triangular grid with an interelement spacing of 0.95 wavelengths. The element excitation coefficients were adjusted to minimize the spillover onto adjacent quadrants while maintaining a -dB illumination at the edges of the primary quadrant.

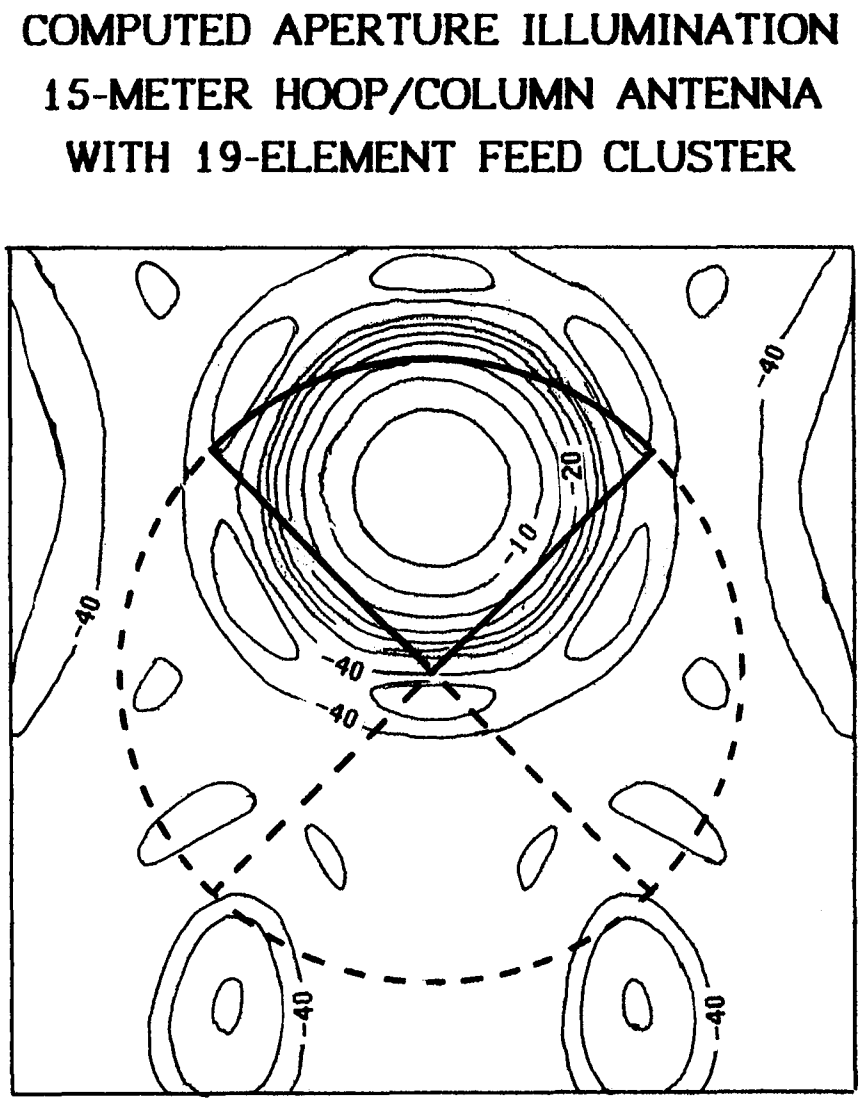

Figure 3

RADIATION PATTERN FOR 2-QUADRANT REFLECTOR WITH OPTIMIZED FEED DESIGN

Figure 4 shows the composite radiation pattern computed for two quadrants of the 15-meter hoop/column reflector antenna with the 19-element feed described in figure 3. This calculation shows that, when the adjacent aperture illumination is considered in the feed design, the lobe due to spillover onto the adjacent aperture can be reduced to an acceptable level (-32 dB for the 19-element feed versus -19 dB for a pyramidal horn feed). If more space is allowed for the feed array design, the spillover onto the adjacent apertures could be reduced further since more elements in the array would provide more control over the feed radiation pattern. The present feed design was limited to 19 elements since several feed arrays were to be placed side-by-side in a conceptual multiple-beam feed design where the spacing between feeds was limited to between 4 and 4.5 wavelengths in order to produce beam crossovers of -3 dB.

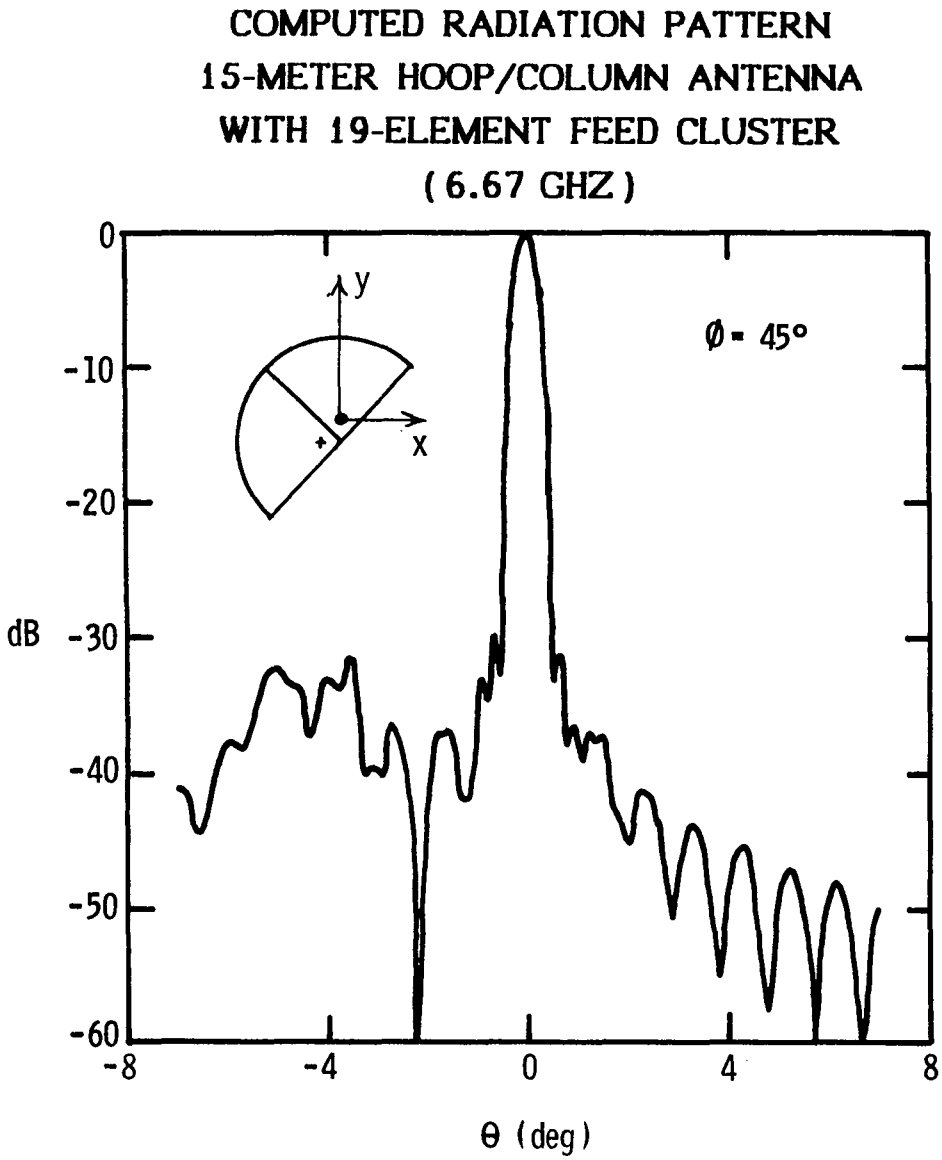

Figure 4

MULTIPLE-BEAM CONCEPT UTILIZING MULTIPLE APERTURES AND NON-OVERLAPPING FEEDS

Figure 5 shows a conceptual feed panel layout and beam topology for coverage of the contiguous United States using the hoop/column antenna configured as four quadrant apertures. The four feed panels illuminate the four separate apertures. Each feed panel consists of either 22 or 24 hexagonal feeds which are envisioned as 19-element arrays as discussed in figure 4. The beam topology is obtained by interleaving the beams from all four quadrant apertures (the circles represent -3 dB contours) resulting in 92 contiguous beams.

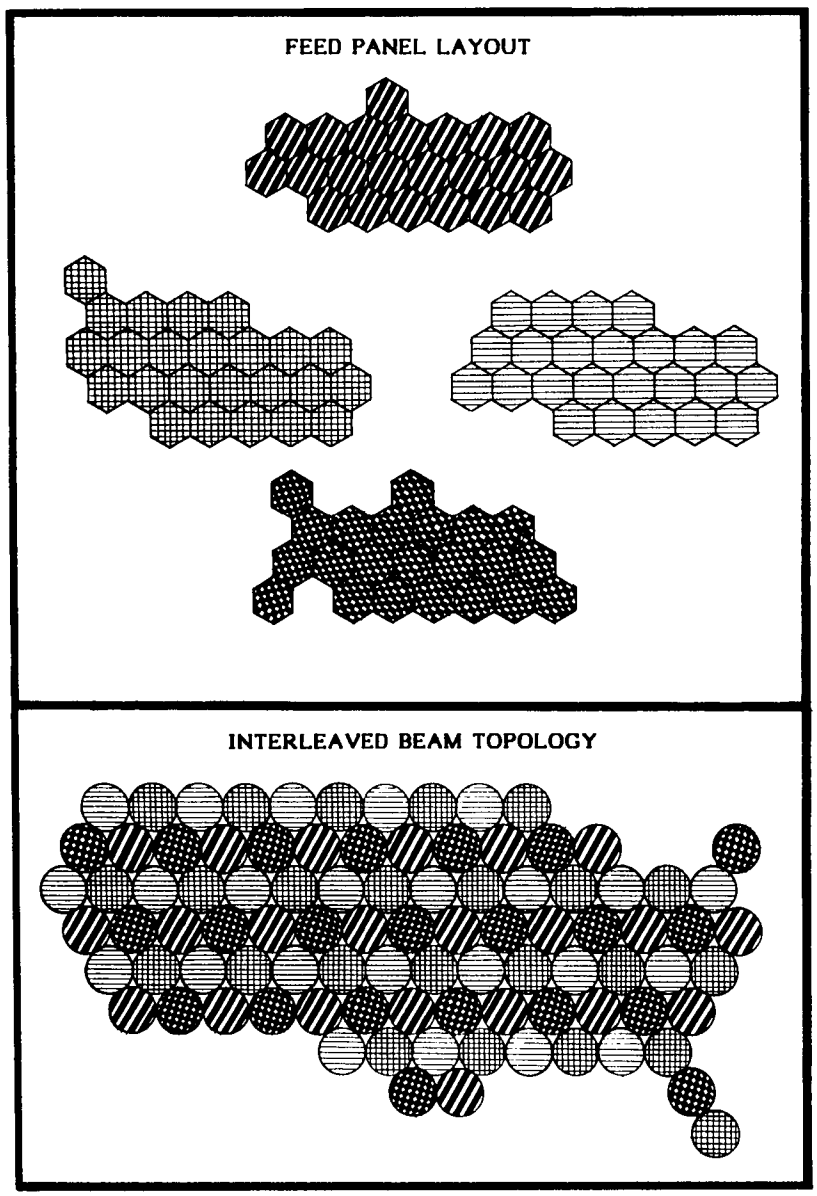

Figure 5

BEAM CONTOURS FOR TWO QUADRANTS OF MULTIPLE-BEAM MULTIPLE-APERTURE CONCEPT

The -3 dB contour radiation patterns were computed for eight beams from each of two quadrants in order to determine the effect upon the beam interleaving due to scanning the quadrant apertures. Figure 6 shows the individual beam contours for these two quadrants. The solid dot on the graphs is the boresight direction of the hoop/column antenna.

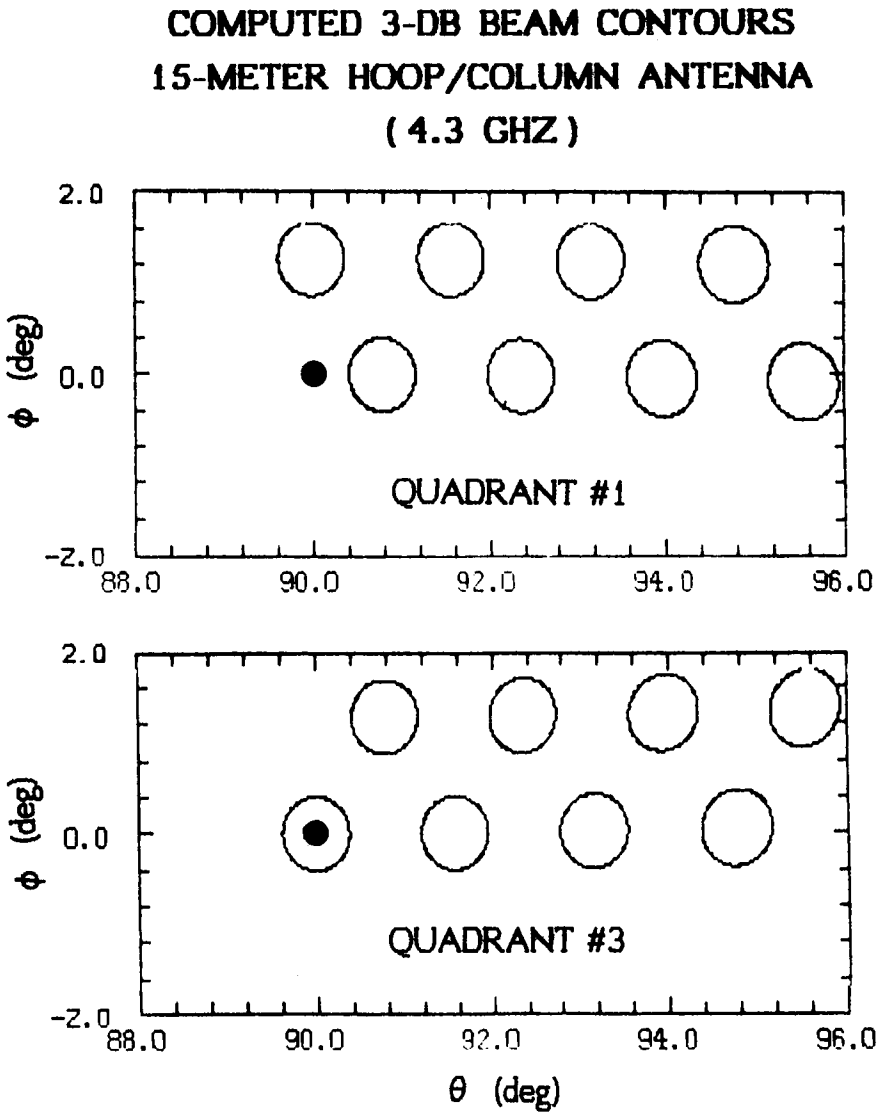

Figure 6

SUPERPOSITION OF BEAMS FROM TWO QUADRANTS OF MULTIPLE-BEAM MULTIPLE-APERTURE CONCEPT

Figure 7 shows the superposition of the computed beams from figure 6. One readily notices that the beams are not quite aligned as in the conceptual beam layout. This misalignment is the result of a slight beam scan in the plane orthogonal to the plane of feed displacement. This slight orthogonal beam scan is characteristic of offset reflectors and is enhanced further by the non-circular reflector aperture. Interleaving beams from two oppositely offset reflectors (as demonstrated here) results in a staggered beam effect.

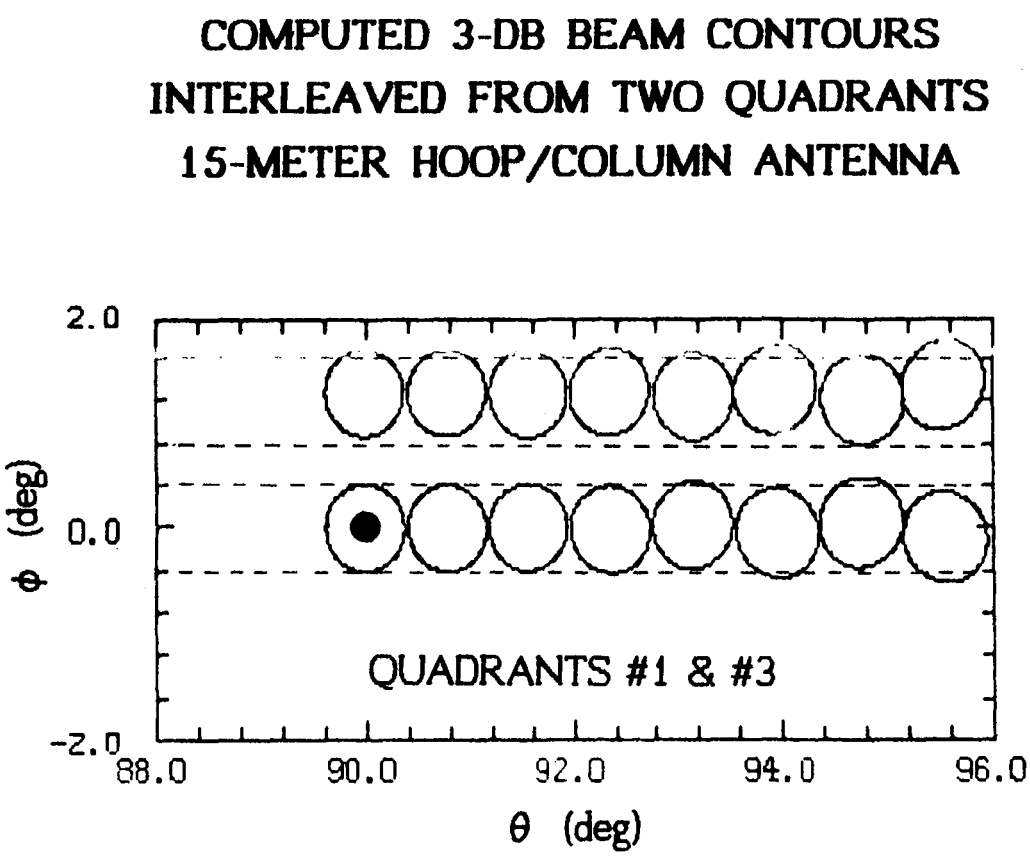

Figure 7

COMPENSATION FOR MISALIGNMENT OF INTERLEAVED BEAMS FROM TWO QUADRANTS

One method of compensating for the orthogonal beam scan (discussed in figure 7) is to tilt each feed array such that the peak of the feed pattern points to the center of the offset aperture. This could also be accomplished by leaving the feed array in the same plane as the panel and phasing the feed distribution network so as to scan the feed pattern to point to the center of the offset aperture. The -3 dB reflector beam contours shown in figure 8 are the result of interleaving beams from two quadrants of the hoop/column antenna with each feed array physically tilted to point to the center of the illuminated quadrant.

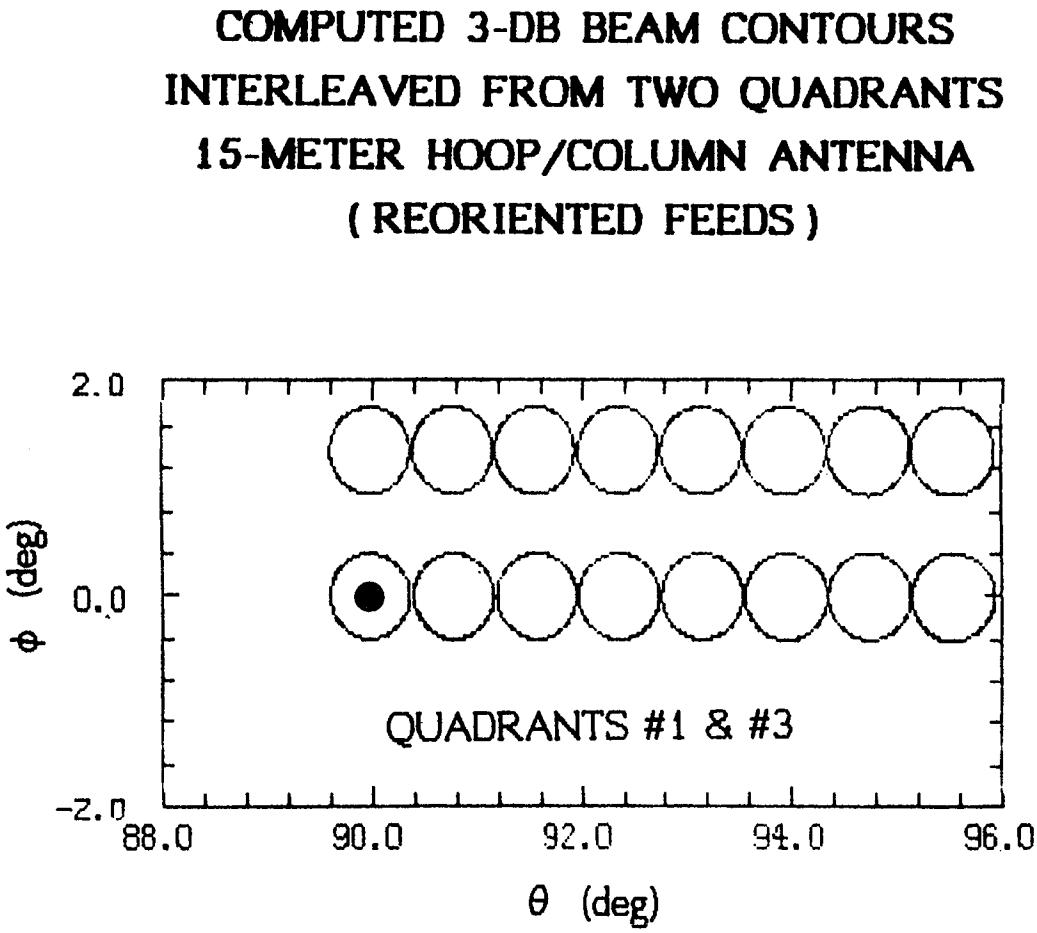

Figure 8

BEAM QUALITY IMPROVEMENT DUE TO REORIENTING FEED FOR OFFSET REFLECTOR

Figure 9 shows the improvement in beam quality due to reorienting the feed array to point to the center of the offset reflector quadrant. Without reorienting the feed array, a ridge of side lobes extends away from the main beam and could cause unacceptable interference with other beams in a multiple-beam application. By repointing the feed, the -30 dB or higher side lobes are contained around the main beam and possibly only the adjacent beams in a multiple-beam application would need to utilize polarization diversity techniques or frequency channel isolation.

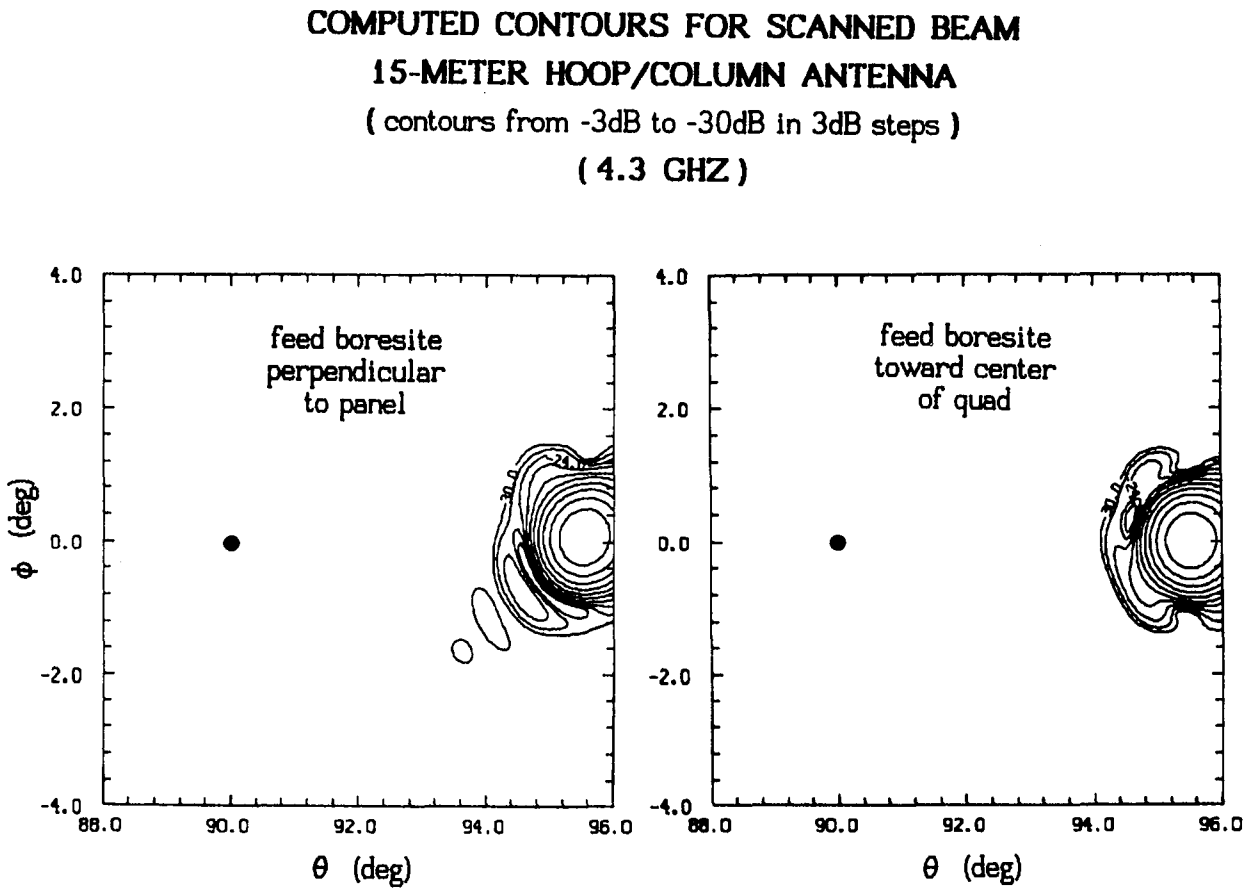

Figure 9

FEED SYSTEM DESIGN CONSIDERATIONS FOR LARGE SPACE ANTENNA SYSTEMS

PART II - SINGLE APERTURE WITH OVERLAPPING FEEDS

V. Jamnejad
Jet Propulsion Laboratory
Pasadena, California

Large Space Antenna Systems Technology - 1984
December 4-6, 1984

INTRODUCTION

Although extensive efforts have been devoted to the design of multibeam antenna systems in the past few years, many problem areas still remain. One general problem area is the weight of the large antenna systems, which tends to rule out the use of phased arrays and lens structures for the spaceborne systems. The use of symmetric reflector systems is also unacceptable due to the high blockage introduced by the large multifeed array of the multibeam system. If, however, one reverts to offset-fed reflector antenna systems which are relatively light, there still remains the problem of feed packing for contiguous multibeam operations. Simply stated, contiguous multiple beams are used in order to make use of the same set of frequency bands at different beams at different geographical locations (frequency reuse by spatial diversity) and hence achieve the most efficient use of precious frequency allocation. This is feasible only if the interference among cochannel beams (beams operating at the same frequencies) is below some acceptable level, usually indicated in terms of C/I (carrier/interference) ratio. This typically requires individual beam patterns of very low sidelobes, which in turn necessitates narrow feed patterns (see Fig. 1). This can be achieved at the expense of larger feed aperture sizes, which will be significantly larger than the area available for a single feed. A physically realizable solution to this problem entails either more than one reflector (twin or quad reflectors), more complicated optics (shaped reflectors), or breaking of each feed into a cluster of smaller elements, some of which would then be shared by adjacent beams (see Fig. 2). The latter, however, would require a rather complicated beam-forming network (BFN) for the proper feeding of the elements. It should be recognized that the feedpacking problem is not unique to reflector antennas and exists in lens type antennas as well. Furthermore, the BFN and associated problems are already present in the phased array antennas and on a much larger scale.

Another problem associated with reflector systems is poor scan capabilities. The scan properties of offset-fed reflector systems can be improved by choosing a very large F/Dp (focal length to parent reflector diameter) ratio, which of course requires a longer boom to support the feed. In the case of reflectors with cluster feed arrangements (so-called hybrid systems), the scan capability for smaller F/Dp ratios can be improved by proper adjustment of cluster element excitations. In general, such a system seems to be appropriate for up to 10 beamwidths scan (a few hundred beams in total). For a larger number of beams, systems with wider scan capabilities, such as phased arrays or phased-array/reflector combinations, become more appealing.

EIGHT-BEAM OVERLAPPING FEED ARRAY.

An example of the application of the multibeam systems is a proposed land mobile satellite system using a 55-meter offset-fed reflector antenna studied by JPL [1]. This system uses the seven-element overlapping concept with a single-aperture reflector antenna in order to produce 87 beams at high UHF frequencies, as shown in Fig. 3. In order to experimentally verify this feed concept, an eight-beam overlapping feed array has been designed and fabricated. This feed is designed for operation at the center frequency of 2.24 GHz and is intended for experiments with a single 6-meter diameter aperture of the Langley-Harris quad-aperture hoop/column antenna [2,3]. Fig. 4 shows the schematic diagram of the eight beams. Each beam is produced by seven elements, some of which are shared by adjacent beams. The six peripheral elements of each cluster will operate at a level approximately 13 dB below the center element. This arrangement has been made to provide a near optimum illumination of the reflector so that sidelobe levels of lower than 30 dB are achieved while minimizing the gain loss. Each element itself is composed of four circularly polarized

microstrip patches. Thus, a total of 28 patches contribute to the formation of one beam. The theoretical co-pol patterns of a single patch, a 4-patch element and a cluster of seven such elements are shown in Fig. 5. Mutual coupling and ground plane edge diffraction effects are not included. A typical theoretical pattern of the expected secondary far-field pattern of the Harris-Langley antenna, whose nominal parameters are given in Fig. 6, is shown in Figs. 7 (a, b). Sidelobes of equal to or better than 35 dB are observed. The effects of reflector surface irregularities, however, are not included and are bound to increase the final achievable sidelobe levels.

A complete integrated beam-forming network is an integral part of the overlapping cluster-feed array. An schematic of the network for the eight beam array is shown in Fig. 8. This network produces upwards of 10 dB loss in an actual operational system. Since power in the space environment is at a premium, in addition to the complexities of disposing of large amounts of heat dissipation, the position of the multibeam forming network should be selected at least behind the final amplification stage and not immediately behind the radiating elements (see Fig. 9). Such a beamforming network for the 8 beam array has been designed and constructed by the Ford Aerospace Development Laboratories under contract with the Jet Propulsion Laboratory. The total network is composed of two layers of stripline (barline) networks. One layer divides the power coming from eight input signals while the second layer combines the signals into 21 outgoing ports which will connect to the 21 elements of the feed array.

This network can be used in either a transmit or a receive mode. Two such networks will be needed in an actual flight system in which receive and transmit operations are performed by the same feed array and single-reflector antenna. JPL intends to explore the possibility of designing and fabricating compact seven-way divider/combiner elements which would allow the interleaving and integration of the receive and transmit multibeam-forming networks into a single unit.

REFERENCES

1. Naderi, F. (Ed.): Land Mobile Satellite Service (LMSS): A Conceptual System Design and Identification of Critical Technologies, Jet Propulsion Laboratory Publication, February 1982.

2. Sullivan, Marvin R.: LSST (Hoop/Column) Maypole Antenna Development Program. NASA CR-3558, Parts 1 and 2, 1982.

3. Woo, K. E., Y. Rahmat-Samii, and W. Imbriale: Large Space Antenna Communications Systems - Integrated LaRC/JPL Technology Development Activities: III. JPL Activities. Large Space Antenna Systems Technology - 1982, NASA CP-2269, Part 2, 1983, pp. 833-852.

BEAM SEPARATION DICTATES FEED SEPARATION

$$d_f/\lambda \cong (F/D)\sqrt{BET/3}$$

BET: BEAM CROSS OVER LEVEL IN DB

* CONFLICT ? *

GAIN OPTIMIZATION AND/OR SIDELOBE LEVELS DICTATE FEED SIZE AND CONFIGURATION

$$d/\lambda \cong (F/D)\sqrt{FET/3}$$

FET: FEED TAPER AT REFLECTOR EDGE IN DB

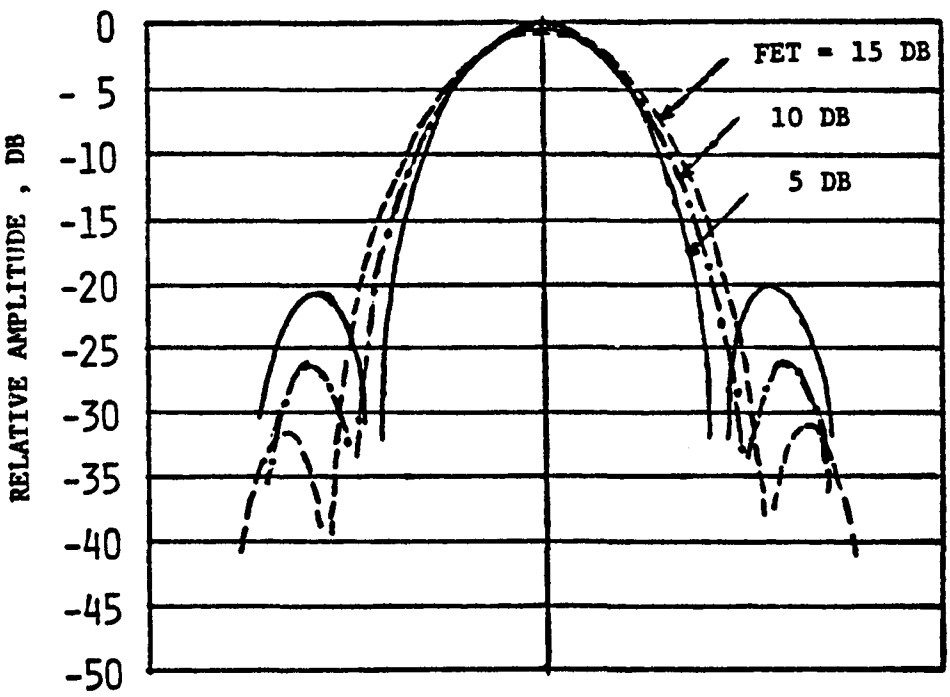

Figure 1. RF performance vs feed size and configuration.

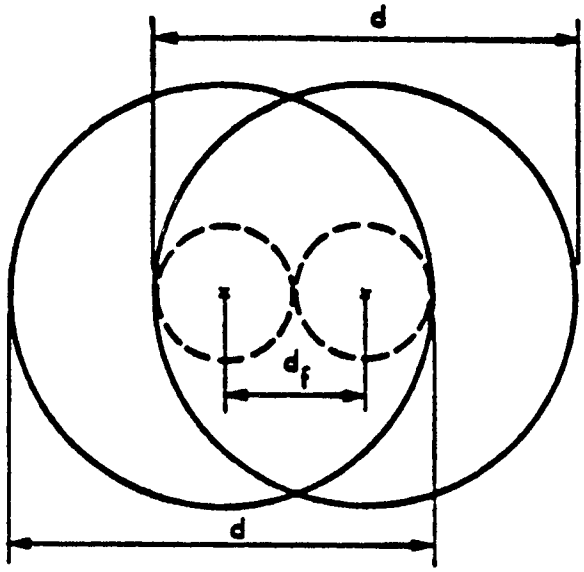

TWO OVERLAPPING SINGLE FEEDS (PHYSICALLY IMPOSSIBLE)
(THE DASHED CIRCLES REPRESENT THE LARGEST PHYSICALLY ACCEPTABLE SINGLE APERTURE SIZES)

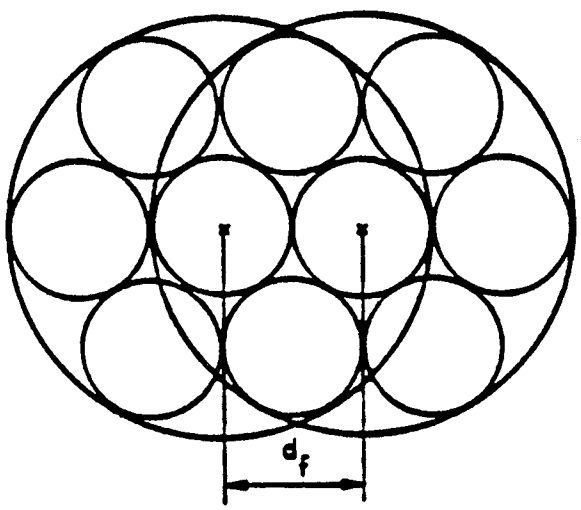

TWO OVERLAPPING 7-ELEMENT CLUSTER FEEDS (FOUR COMMON ELEMENTS)

Figure 2. Overlapping cluster feed concept.

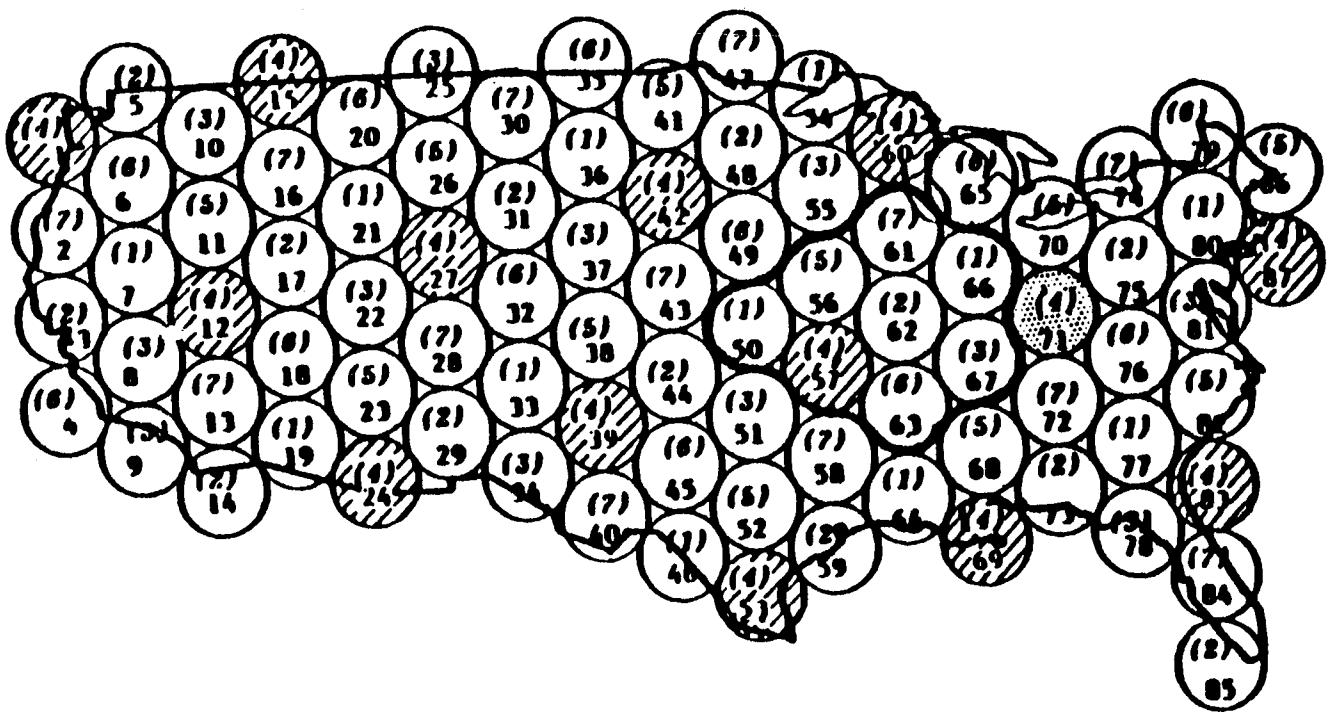

Figure 3. Layout of 87 beams covering CONUS with 7-frequency reuse arrangement, proposed for a future Land Mobile Satellite System (1). (Numbers in parentheses designate frequency assignments.)

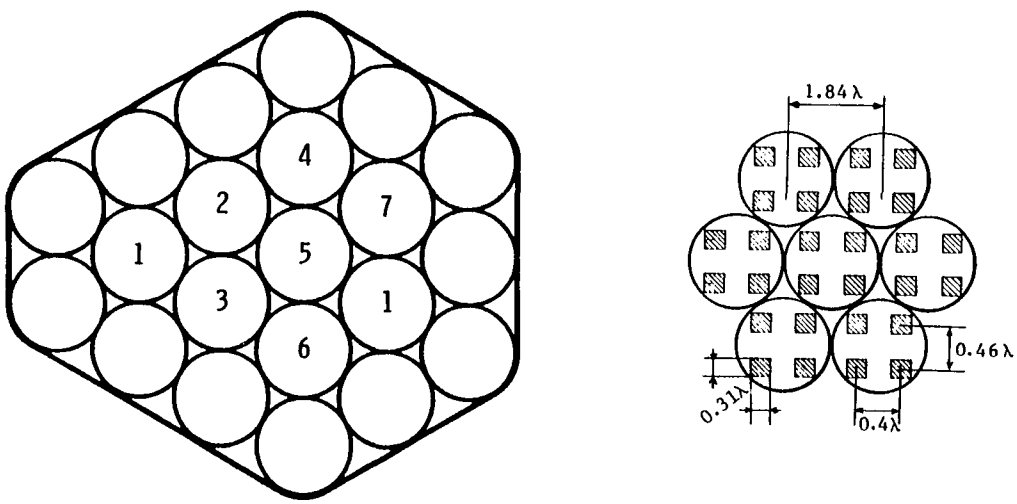

21 ELEMENTS

8 BEAMS

SIMULATING 7-FREQUENCY REUSE CASE OF LMSS

A CLUSTER OF 7 ELEMENTS PRODUCES ONE BEAM

EACH ELEMENT IS COMPOSED OF 4 MICROSTRIP PATCHES

Figure 4. Overlapping cluster feed design.

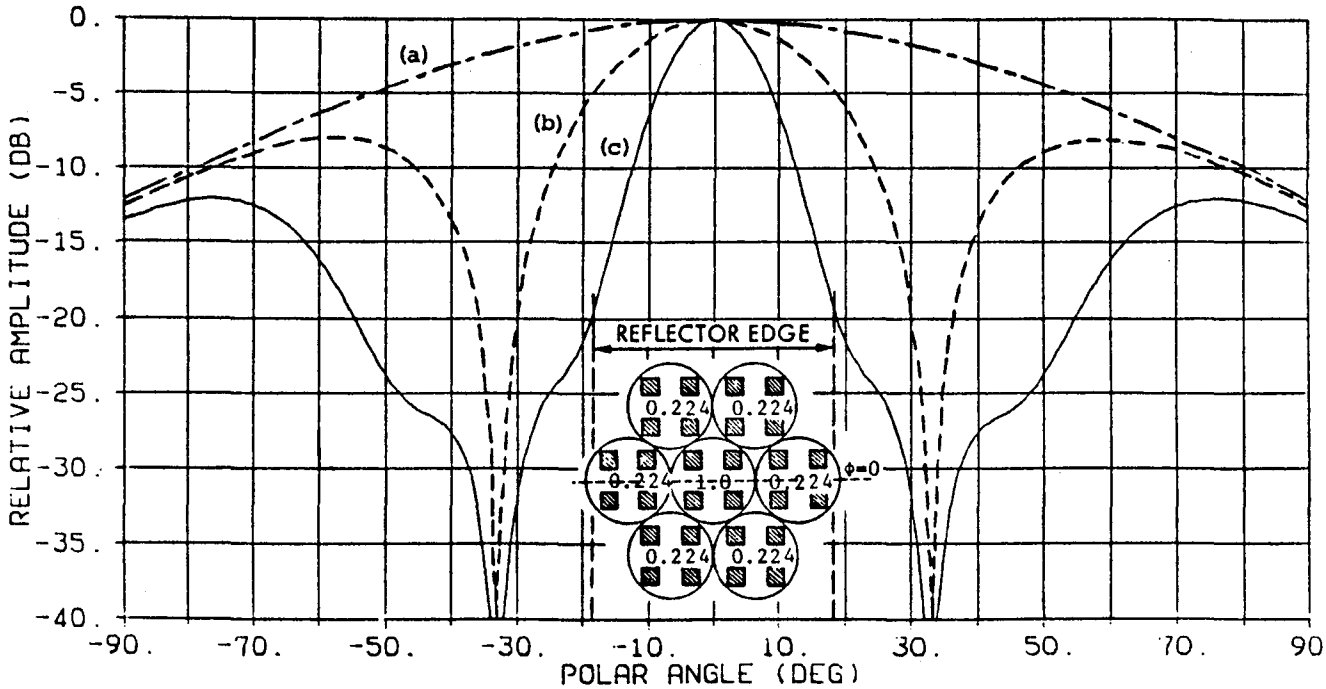

I-PATTERN (IN ϕ = 0° PLANE) OF SQUARE PATCH FEED ELEMENTS
(a) ONE PATCH (b) 4 PATCHES (ONE ELEMENT) (c) A CLUSTER OF 7 ELEMENTS

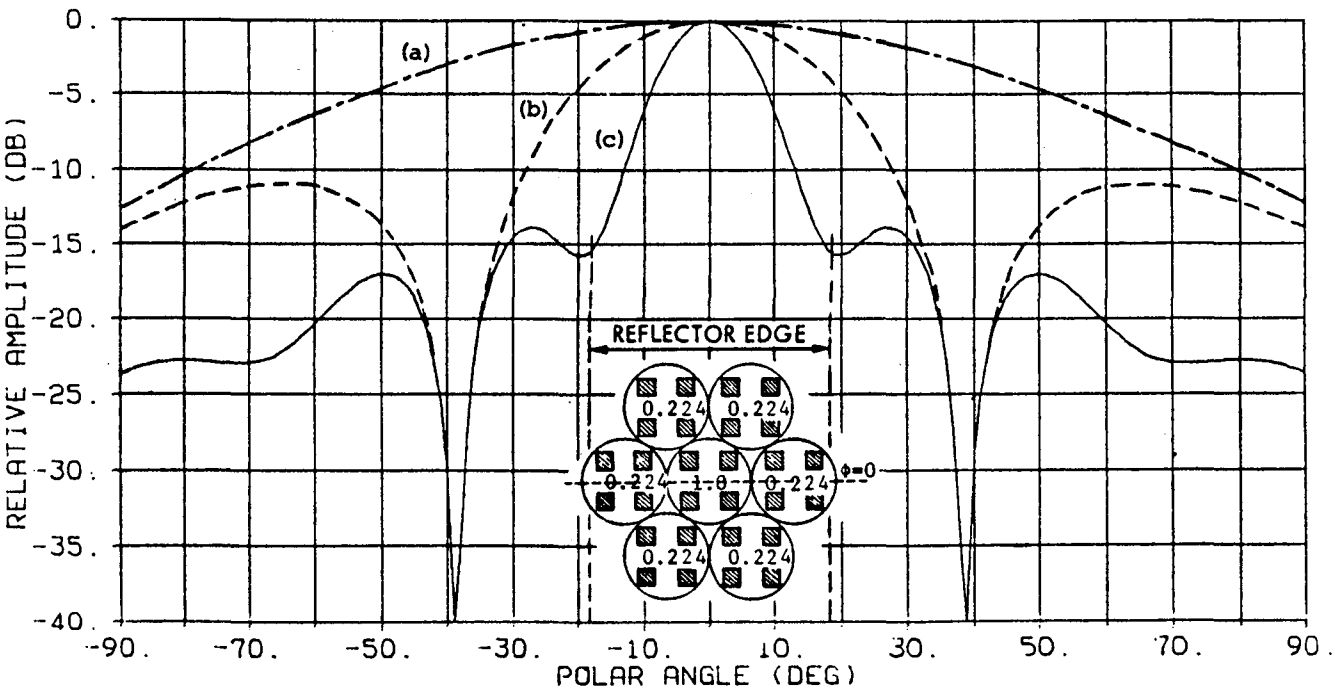

II-PATTERN (IN ϕ =90° PLANE) OF SQUARE PATCH FEED ELEMENTS
(a) ONE PATCH (b) 4 PATCHES (ONE ELEMENT) (c) A CLUSTER OF 7 ELEMENTS

Figure 5. Theoretical co-pol patterns of one patch, a four-patch element, and a cluster of seven elements.

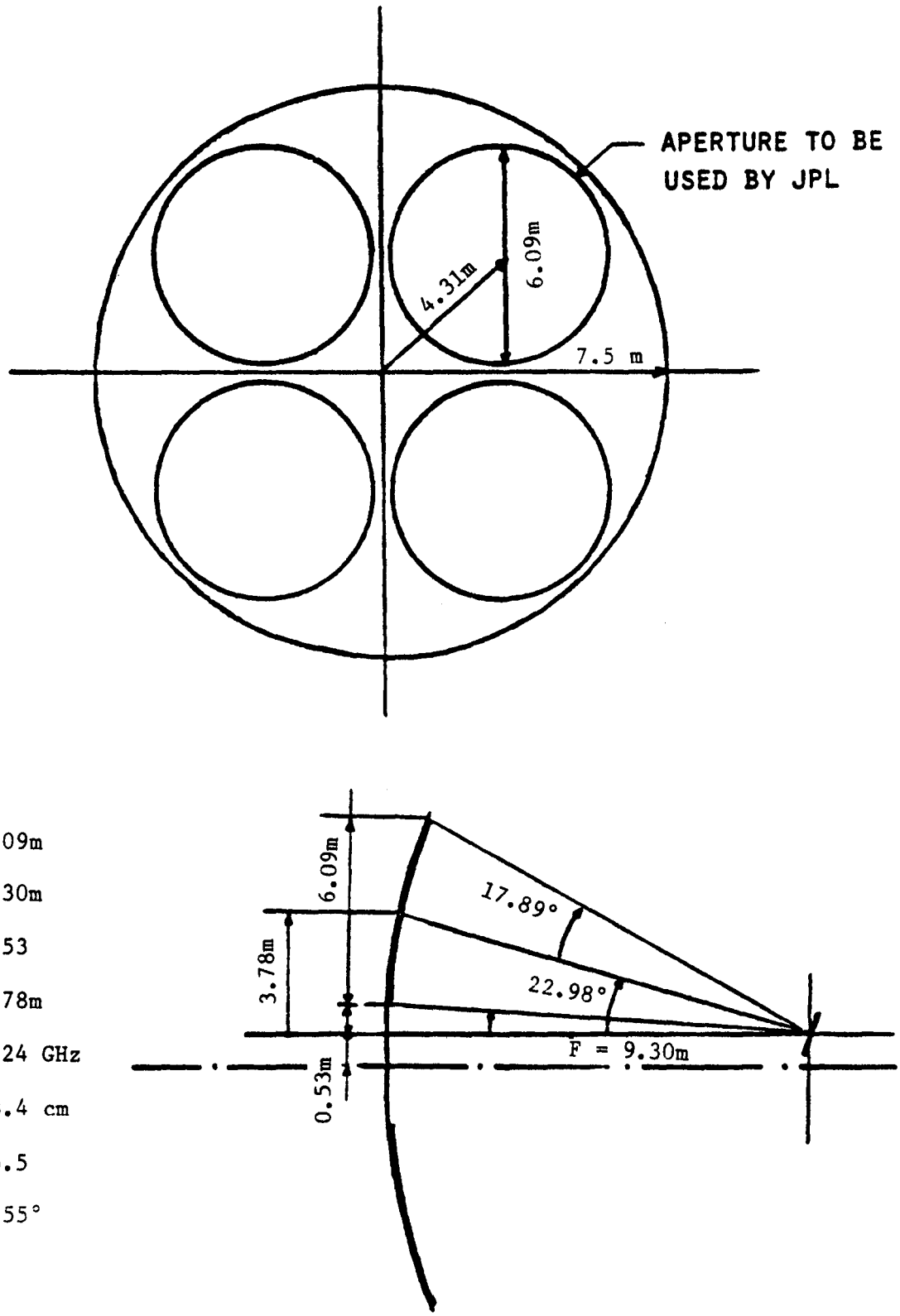

Figure 6. Langley-Harris 15-meter antenna.

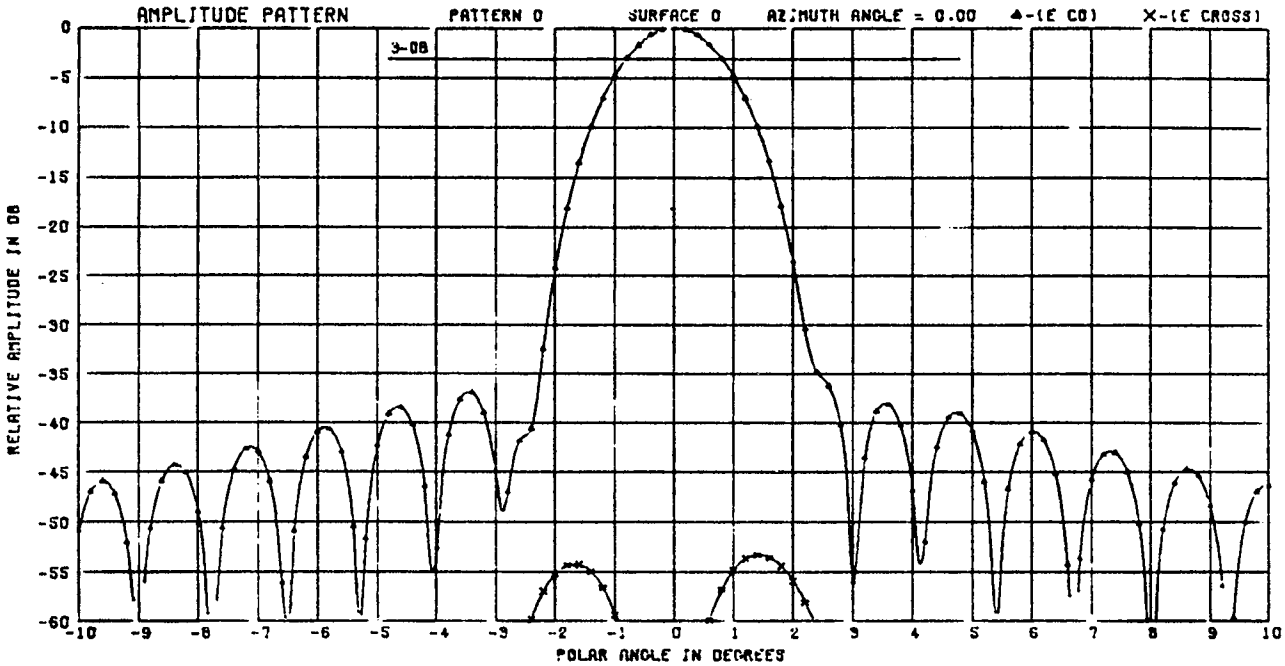

(a) Pattern in offset plane.

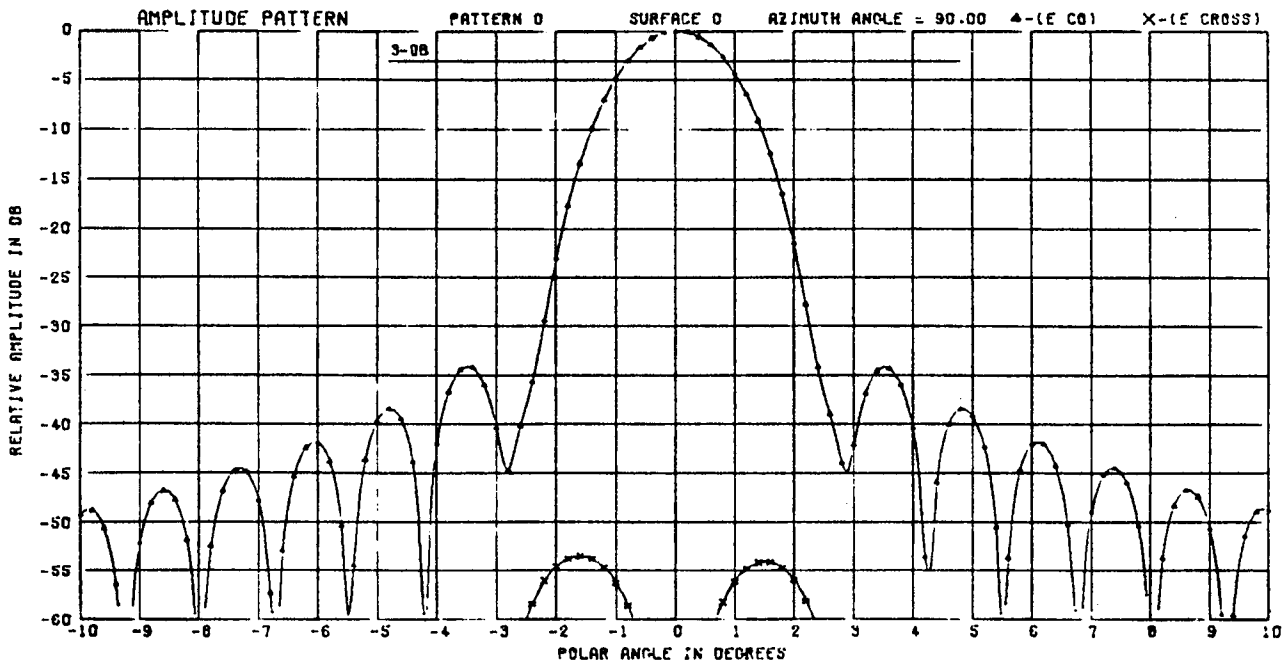

(b) Pattern normal to offset plane.

Figure 7. Theoretical patterns of 6-meter sub-aperture of Langley-Harris antenna with seven-element cluster feed.

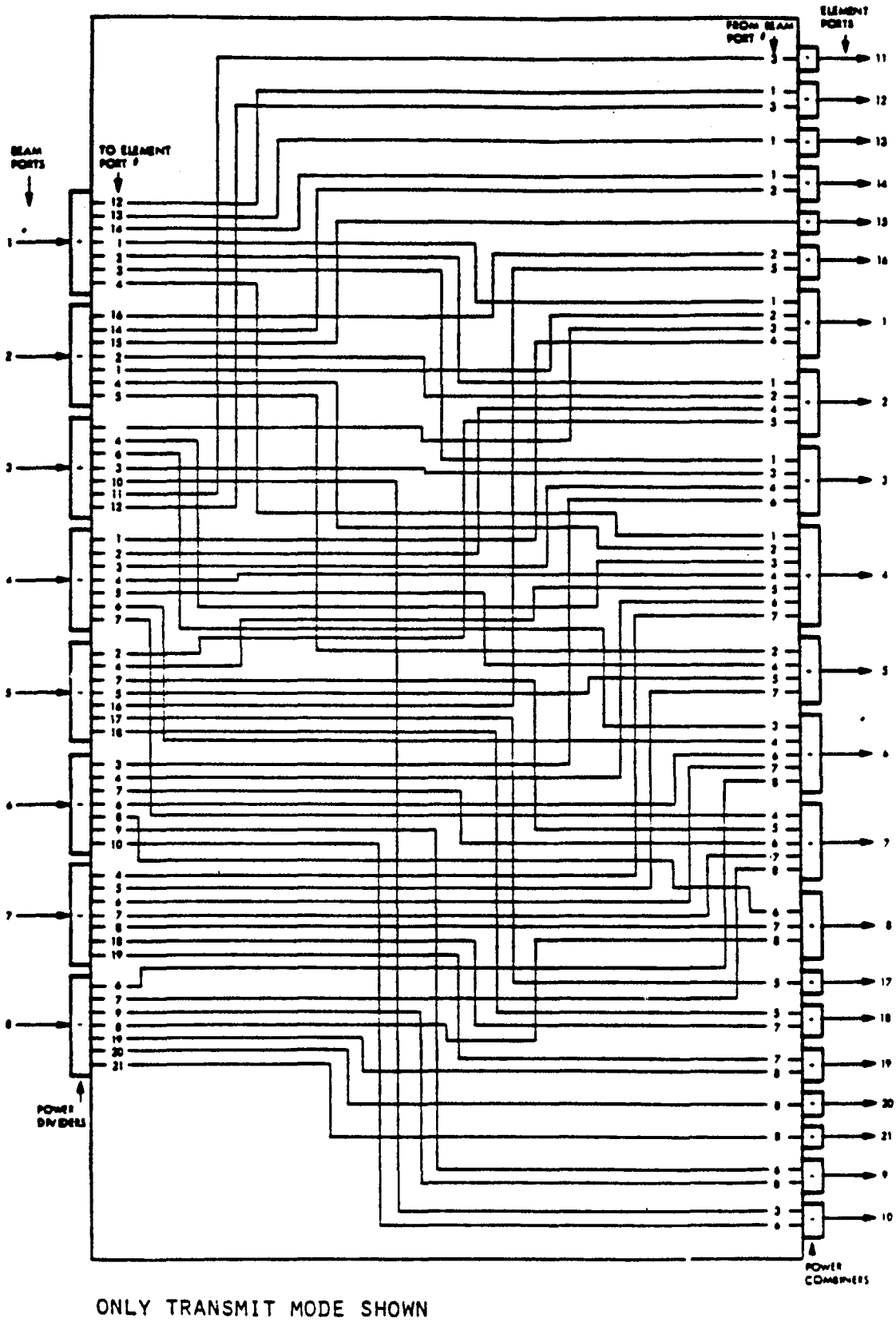

Figure 8. Beam-forming network schematic.

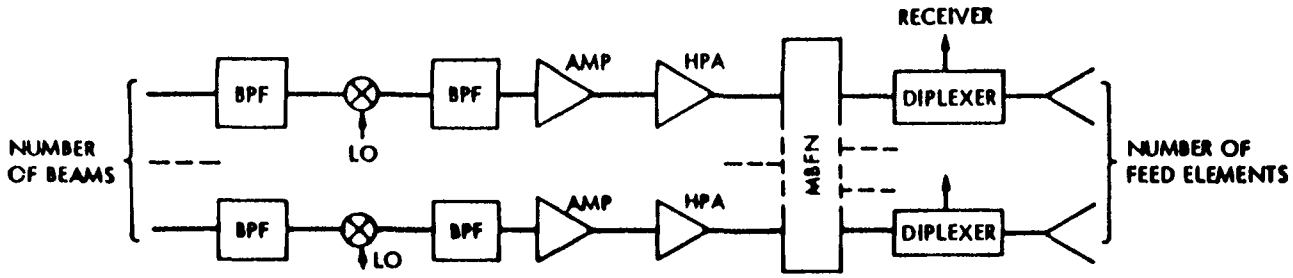

(a) MBFN at the RF stage, after high power amplifier (HPA), bulky with high loss.

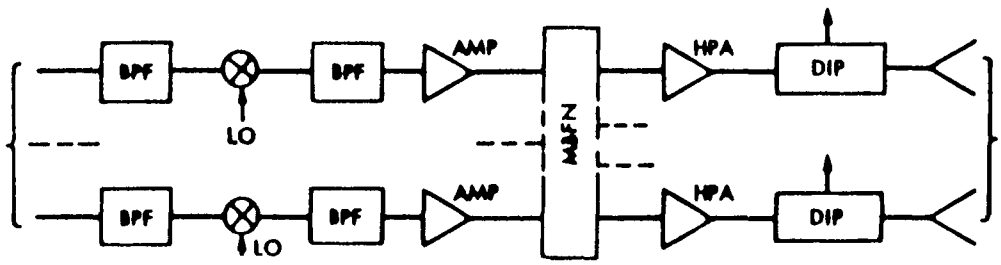

(b) MBFN at the RF stage, before HPA. Bulky, but low loss. Might require phase tracking.

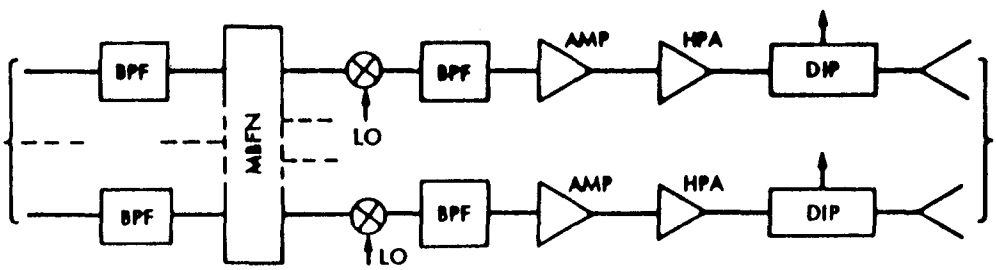

(c) Multibeam forming network at the IF stage. Small size and low loss. Will require phase tracking.

Figure 9. Position of Multibeam Forming Network (MBFN) in transmitter.

Page intentionally left blank

DIFFRACTION ANALYSIS OF MESH DEPLOYABLE REFLECTOR ANTENNAS

Y. Rahmat-Samii
Jet Propulsion Laboratory
California Institute of Technology
Pasadena, California

Large Space Antenna Systems Technology - 1984
December 4-6, 1984

INTRODUCTION

Accurate performance analysis of mesh deployable satellite communications antennas for multiple and contour beam applications demands that the effect of the mesh be properly accounted for in the vector diffraction analysis. This is particularly important when determining the boresight gain and the cross-polarized patterns. It is the purpose of this paper to present a general formulation and many representative numerical results for mesh reflector antennas. This is done first by determining the reflection (transmission) coefficient matrix for the prescribed mesh configuration and then by properly accounting for the local coordinate system of the mesh cells at each point on the curved reflector surface. A novel strip aperture model has been used to formulate the transmission coefficient matrix for a variety of mesh cell configurations. Numerical data are tailored to the dimensions of a conceptually designed land mobile satellite system (LMSS) which employs a large mesh-deployable offset parabolic antenna, as depicted in Figs. 1 and 2. Results are also shown for an offset parabolic reflector having mesh surfaces similar to the mesh surface of TDRSS (tracking and data relay satellite system) antenna.

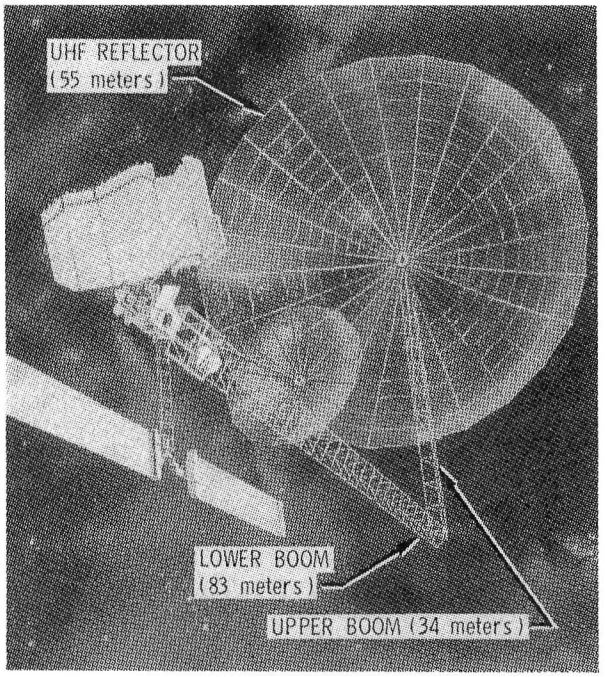

Figure 1

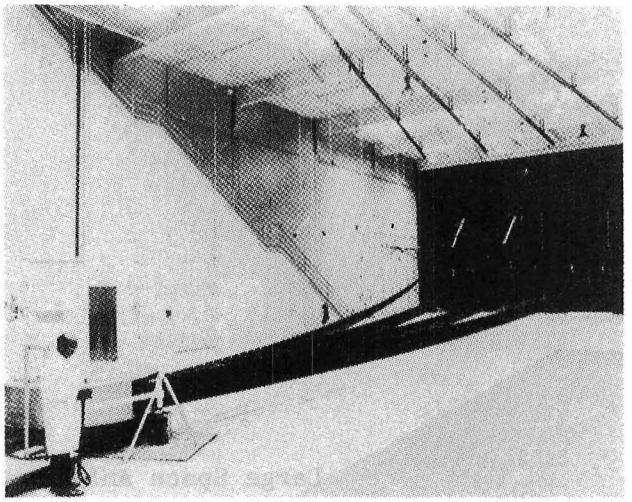

Figure 2

MOTIVATIONS AND FEATURES

The motivations for using mesh reflector antennas and their features for both space and ground applications are listed in Fig. 3.

MOTIVATION:

- DEPLOYABLE REFLECTORS ARE MADE OF MESHES
- LARGE GROUND ANTENNAS ARE PERFORATED
- LINEARLY LOW CROSS-POLARIZED REFLECTORS USE UNI-DIRECTIONAL MESHES
- ⋮

FEATURES:

- UNFURLABLE
- LOW WEIGHT
- REDUCED WIND EFFECTS
- ⋮

Figure 3

In order to properly incorporate the effects of meshes, the physical-optics-induced current on the solid reflector surface needs to be modified. This is done first by determining the reflection (transmission) coefficient matrix for the prescribed mesh configuration and then by properly accounting for the local coordinate system of the mesh cells at each point on the curved reflector surface. The reflection coefficient matrix is obtained by using (i) measured data, (ii) the wire grid formulation, or (iii) the strip aperture formulation. Although measured data should be used for the cases where the data is available, in many parametric studies it is necessary to employ an analytical/numerical formulation which allows more versatility than measurement. Fig. 4 shows the flow diagram for the steps involved in performing vector diffraction analysis for mesh reflector antennas.

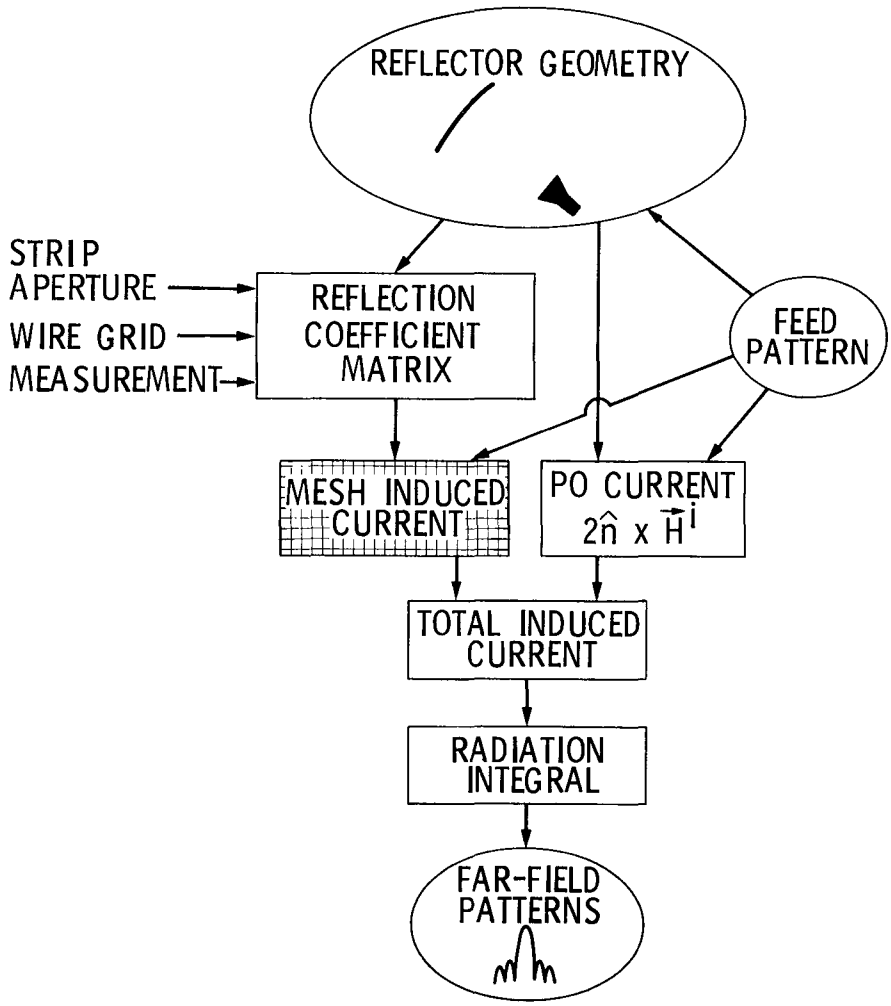

Figure 4

INDUCED SURFACE CURRENTS

The construction of the reflector far-field pattern is based on the application of the total induced surface currents. Some researchers have used both the electric and magnetic surface currents to construct the far fields. However, it has been found that the application of the total induced electric current, which is based on the fields on both sides of the reflector surface, should be sufficient. Fig. 5 represents the basis of the diffraction integral obtained from both the total induced electric current and the electric and magnetic currents. These are designated by paths "a" and "b". It has been found that path "a" is a more realistic model of the mesh surface than is path "b" because it incorporates the existence of the transmitted field behind the reflector. It is also worth mentioning that the incorporation of the path "a" formulation into an existing solid surface physical optics computer program is very readily achieved.

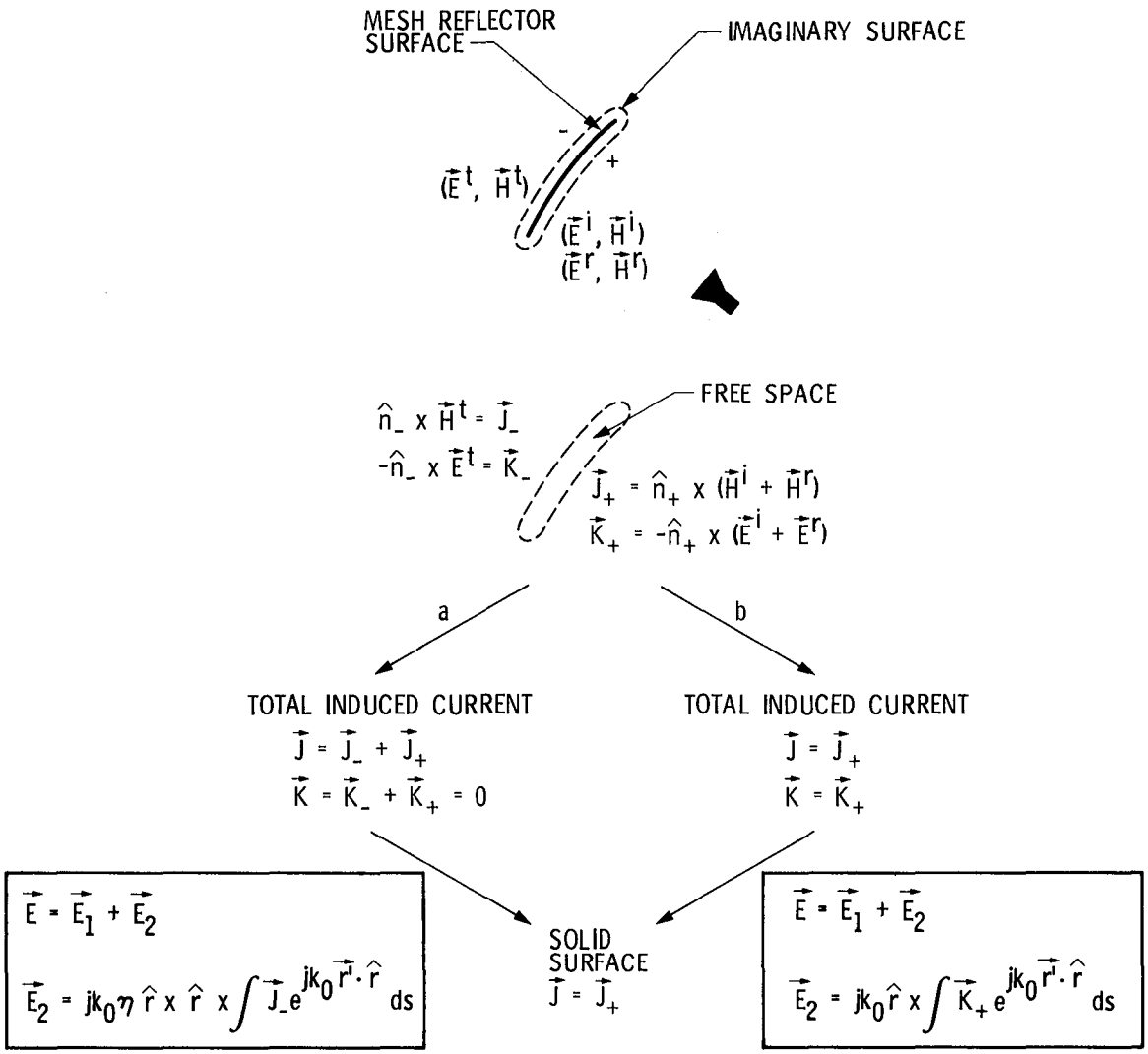

Figure 5

THE CONSTRUCTION OF MESH-INDUCED CURRENT

The geometry of a mesh reflector is shown in Fig. 6. According to the physical optics approximation, the induced surface current at P is the same as when the surface is replaced by its tangent plane at this point. Fig. 6 also depicts this tangent plane of the planar mesh with periodic cells in the mesh rectangular coordinates (x_m, y_m, z_m). The total induced current may be written in terms of $\vec{J}_{po}$ and $\vec{J}_m$ as shown in the Figure. The first term is the solid-surface physical optics current and the latter term is due to the non-zero transmission through the mesh. This current may be expressed in terms of the mesh transmission coefficient as described in the Figure. In this Figure, (I, $\bar{I}$) defines the components of the E-field radiated from the feed at P and the 2 x 2 matrix is the transmission matrix at point P. The construction of this transmission matrix is discussed next.

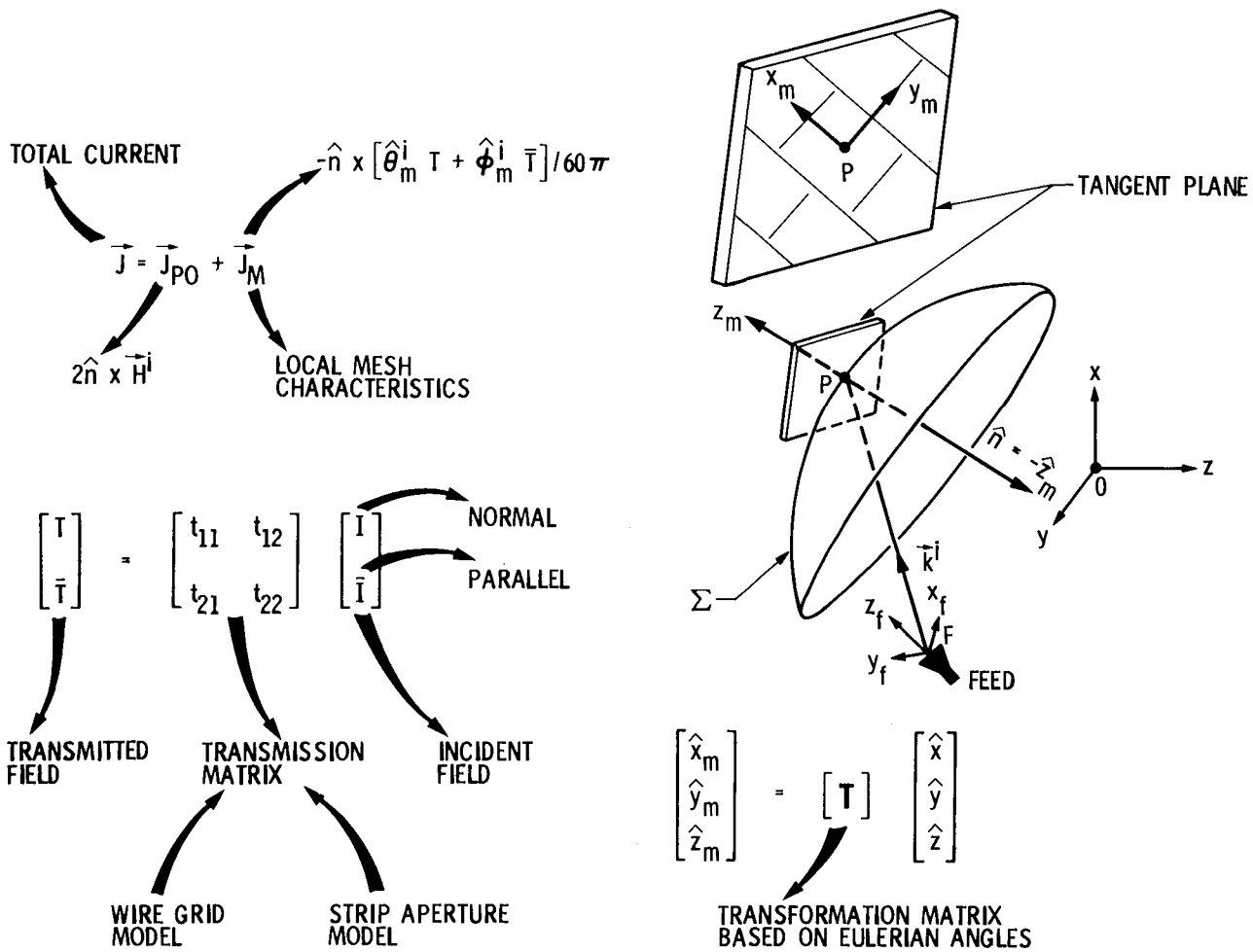

Figure 6

COORDINATE TRANSFORMATIONS BASED ON EULERIAN ANGLES

To construct $\vec{J}_m$, it is very important to properly account for the local mesh coordinates at point P with respect to the reflector coordinate system. It has been found that transformation between the mesh coordinates (x_m, y_m, z_m) in the reflector coordinates (x, y, z) can be formulated by using the Eulerian angle construction such that the transformation matrix elements can be obtained from the three Eulerian angles at point P, as shown in Fig. 7. Two of these Eulerian angles, namely α and β, can be uniquely defined using the fact that $\hat{z} = -\hat{n}$, where $\hat{n}$ is the unit normal to the reflector surface, as shown in the Figure. The third Eulerian angle, γ, defines the orientation of the mesh tangent plane and can be properly selected to match the mesh configuration.

$$\begin{cases} \sin\alpha_m = \hat{x}\cdot\hat{z}_m/\Delta \\ \cos\alpha_m = -\hat{y}\cdot\hat{z}_m/\Delta \end{cases}$$

$$\begin{cases} \sin\beta_m = \Delta \\ \cos\beta_m = \hat{z}\cdot\hat{z}_m \end{cases}$$

$$\begin{cases} \sin\gamma_m = \hat{z}\cdot\hat{x}_m/\Delta \\ \cos\gamma_m = \hat{z}\cdot\hat{y}_m/\Delta \end{cases}$$

$$\Delta = |\hat{z}_m - (\hat{z}\cdot\hat{z}_m)\hat{z}|$$

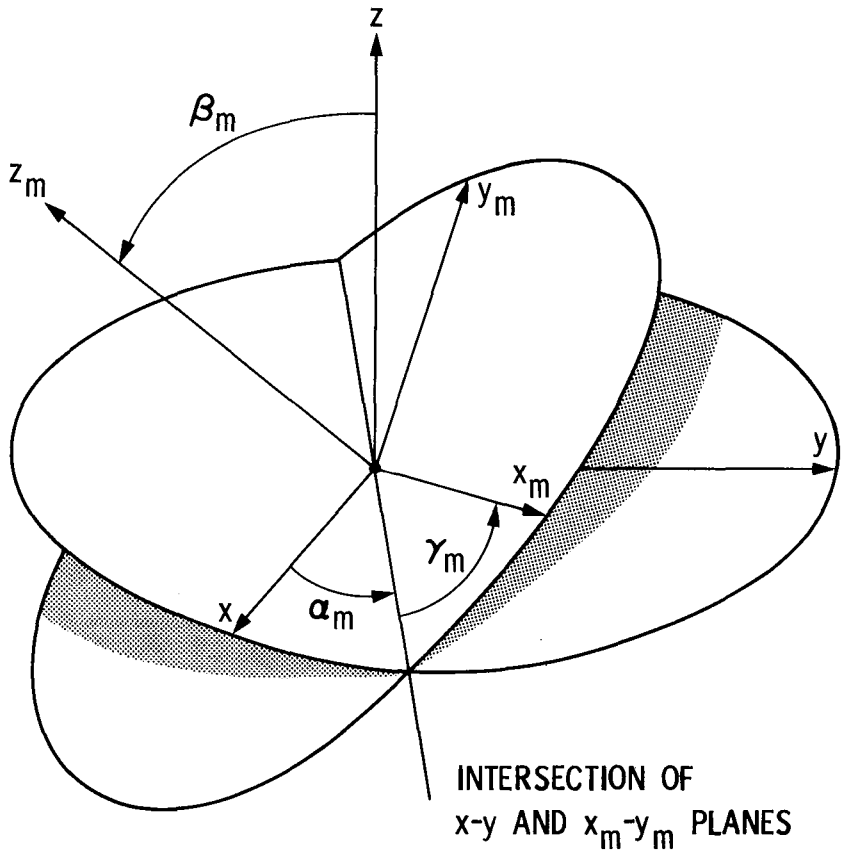

Figure 7

TRANSMISSION COEFFICIENT MATRIX BASED ON WIRE GRID MODEL

The details of the mesh for the wire grid case are shown in Fig. 8, where parameters a, b and r_0 are used to characterize it. Application of an analytic model based on an "average boundary condition" allows one to derive the transmission coefficient matrix in a closed form, as shown in Fig. 9.

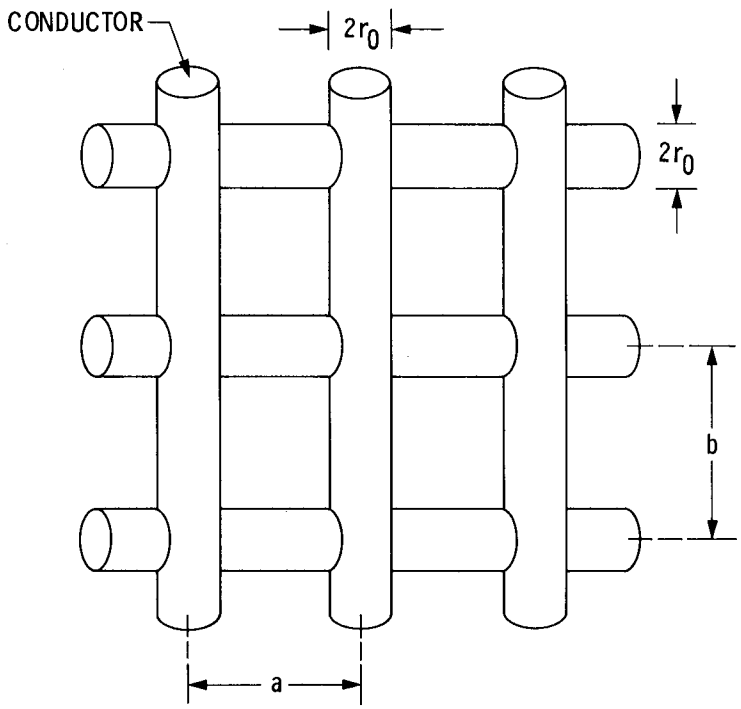

Figure 8

$$\begin{bmatrix} T \\ \bar{T} \end{bmatrix} = \begin{bmatrix} t_{11} & t_{12} \\ t_{21} & t_{22} \end{bmatrix} \begin{bmatrix} I \\ \bar{I} \end{bmatrix}$$

$$t_{11} = 1 - k I_0^{-1} \left\{ \cos\theta_m^i + k\left[\gamma_1 \cos^2 \phi_m^i + (\delta_2 - \delta_1) \sin \phi_m^i \cos \phi_m^i - \gamma_2 \sin^2 \phi_m^i \right] \right\}$$

$$\vdots$$

$I_0, \gamma_1, \delta_2, \delta_1, \gamma_2$ ARE FUNCTIONS OF $b\ell n \frac{b}{2\pi r_0}$, $\frac{a/b}{1 + a/b}$, θ_m^i, ϕ_m^i ...

- THICKNESS AND WIDTH ARE THE SAME
- RESTRICTED CELL SHAPES

Figure 9

TRANSMISSION COEFFICIENT MATRIX BASED ON STRIP APERTURE MODEL

The details of the mesh for a strip aperture case are shown in Fig. 10, described by lattice parameters (a, b, Ω_1) and by the aperture parameters (c, d, Ω_2). Several typical aperture shapes are also sketched in this Figure. It is clear that application of the strip aperture model allows more versatility in describing the mesh geometry; in particular, it allows staggered lattice configurations.

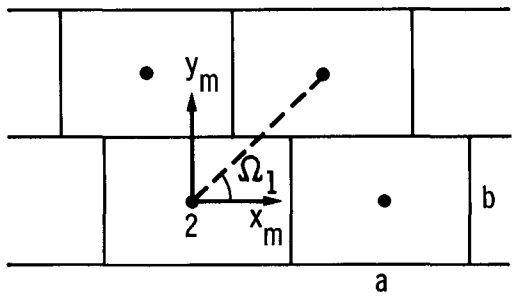

(a) LATTICE

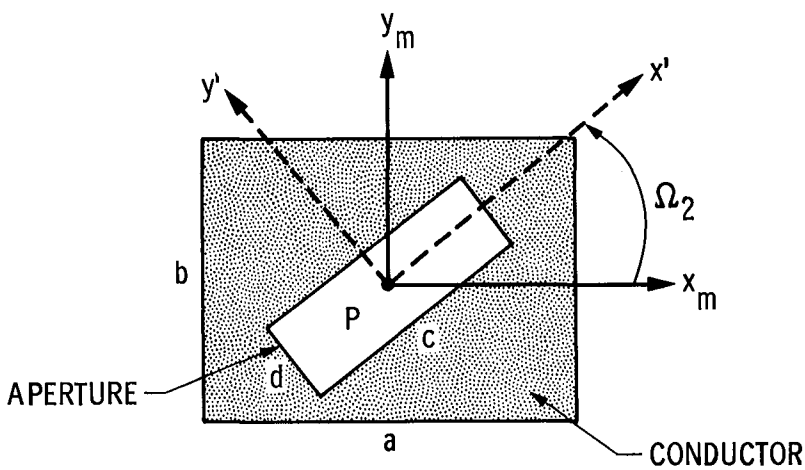

(b) A UNIT CELL

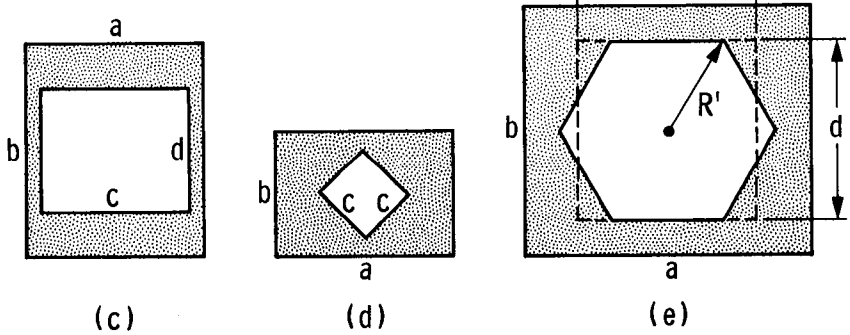

(c) (d) (e)

Figure 10

TRANSMISSION COEFFICIENT MATRIX BASED ON STRIP APERTURE MODEL (CONTINUED)

For the strip aperture model, the reflection coefficient matrix can be derived using a Floquet modal expansion, as shown in Fig. 11. This solution, in general, depends on all the geometrical parameters which define the mesh configuration. After lengthy manipulations and proper application of the continuity conditions, one is then able to obtain the transmission coefficient matrix, as summarized in Fig. 12.

- FLOQUET SPACE HARMONICS EXPANSION
- TWO-MODE APPROXIMATION

$$\vec{E} \approx jab \sum_{n=1}^{2} C_n \vec{g}_n (x', y')$$

TO BE DETERMINED IN THE APERTURE

$$\vec{g}_1 = \sqrt{2/cd}\, \hat{x}' \cos(\pi y'/d); \quad \vec{g}_2 = \sqrt{2/cd}\, \hat{y}' \cos(\pi x'/c)$$

- CONTINUITY CONDITIONS

Figure 11

AFTER LENGTHY MANIPULATIONS

$$\begin{bmatrix} C_1 \\ C_2 \end{bmatrix} = k \sin\theta_m^i \bar{\bar{Q}}^{-1} \begin{bmatrix} \sigma_{00}^{11*} \cos\theta_m^i & \sigma_{00}^{21*} \\ \sigma_{00}^{12*} \cos\theta_m^i & \sigma_{00}^{22*} \end{bmatrix} \begin{bmatrix} I \\ \bar{I} \end{bmatrix}$$

$$Q_{mn} = \sum_p \sum_q \left[\gamma_{pq} \cdots \sigma_{pq} \cdots \right]$$

WHERE γ_{pq} AND σ_{pq} ARE FUNCTIONS OF a, b, c, d, Ω_1, Ω_2, θ_m^i, ϕ_m^i

FINALLY:

$$\begin{bmatrix} T \\ \bar{T} \end{bmatrix} = \frac{1}{k \sin\theta_m^i} \begin{bmatrix} \sigma_{00}^{11} & \sigma_{00}^{12} \\ \sigma_{00}^{21} \sec\theta_m^i & \sigma_{00}^{22} \sec\theta_m^i \end{bmatrix} \begin{bmatrix} C_1 \\ C_2 \end{bmatrix}$$

Figure 12

COMPARISON WITH THE EXACT NUMERICAL SOLUTION

For the strip aperture mesh configuration, sketched in Fig. 13, the transmission coefficients can be exactly formulated in an infinitely large matrix equation by the mode-matching techniques. After truncating the matrix at a sufficiently large rank and inverting it numerically with the aid of a computer, the solution can be considered as an "exact" numerical solution. In Fig. 13, the present approximate solution is compared with the exact numerical solution. It is found that they are in good agreement for a/λ up to the appearance of the first grating lobe. For mesh reflectors, a/λ is usually on the order of 0.1; therefore, the present solution is sufficiently accurate.

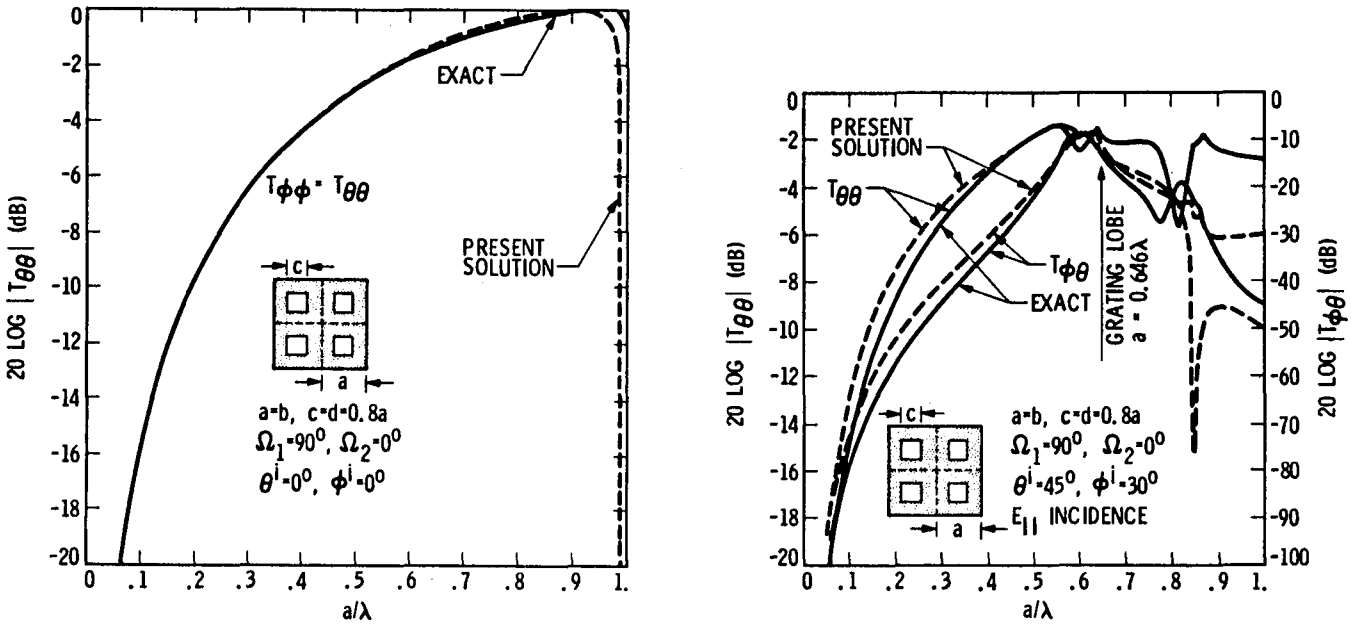

- AGREEMENT IS VERY GOOD BEFORE THE OCCURRENCE OF THE FIRST GRATING LOBE

Figure 13

EVALUATION OF DIFFRACTION INTEGRAL USING JACOBI-BESSEL SERIES

Once the total induced current is constructed, the physical optics radiation integral can be evaluated to determine the far-field pattern. The evaluation of this integral may be performed in a variety of ways; however, here the Jacobi-Bessel expansion is used, as shown in Fig. 14.

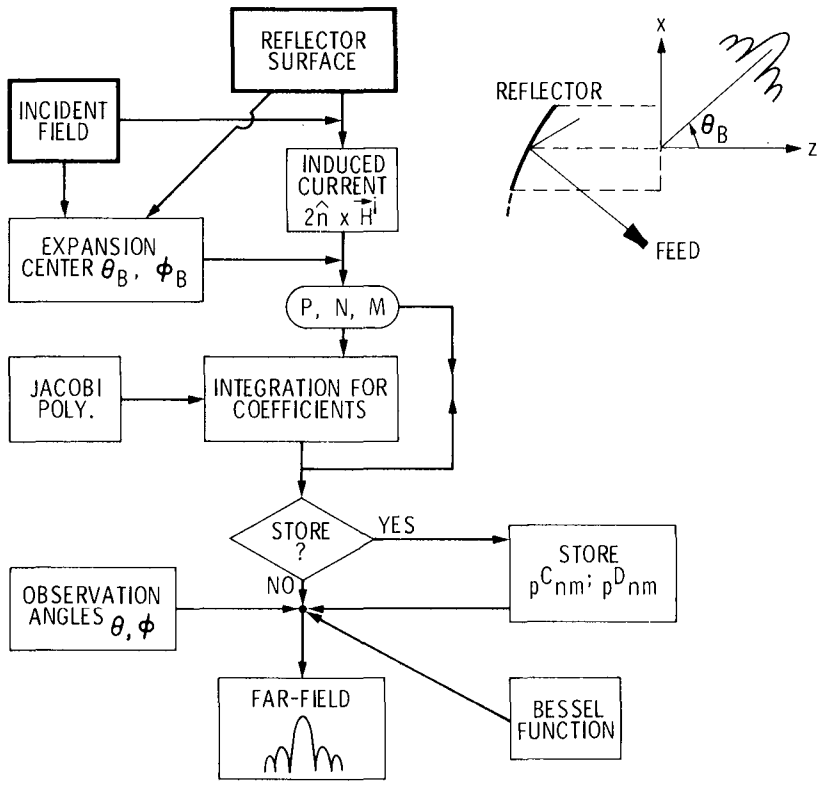

Figure 14

AN OFFSET PARABOLIC REFLECTOR WITH TDRSS MESH SURFACE CHARACTERISTICS

As an example, an offset parabolic reflector with dimensions as shown in Fig. 15 is considered. It is assumed that this reflector is constructed from a mesh surface similar to the Harris-built TDRSS (tracking and data relay satellite system) antenna with dimensions as shown in Fig. 16. Also shown in this Figure are the equivalent strip aperture model dimensions.

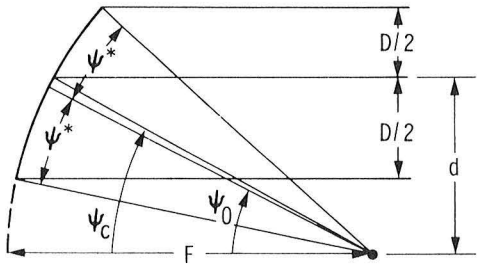

$D/\lambda = 120$ ET = -15 dB
$F/\lambda = 117$ $\psi^* = 27°$
$d/\lambda = 70$

Figure 15

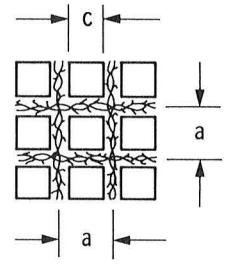

a = 10 mil
a-c = 11 mil
r = 1.2 mil

1 mil = 1/1000 inch
1 inch = 2.54 cm

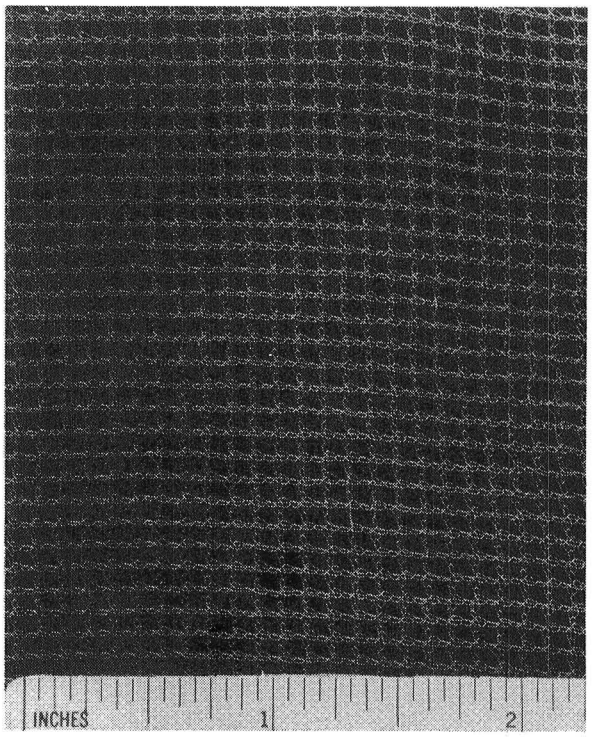

Figure 16

TDRSS MESH REFLECTIVITY LOSS VERSUS FREQUENCY

Reflectivity loss versus the incident angle is shown in Fig. 17 for different frequencies and for both the TE and TM polarizations. It is interesting to note that, for small values of the incident angle, the reflectivity loss is almost independent of the polarization. These results are compared versus the available measured data and good agreement is observed. It should be mentioned that, in all these cases, it is assumed that the mesh surface is lossless.

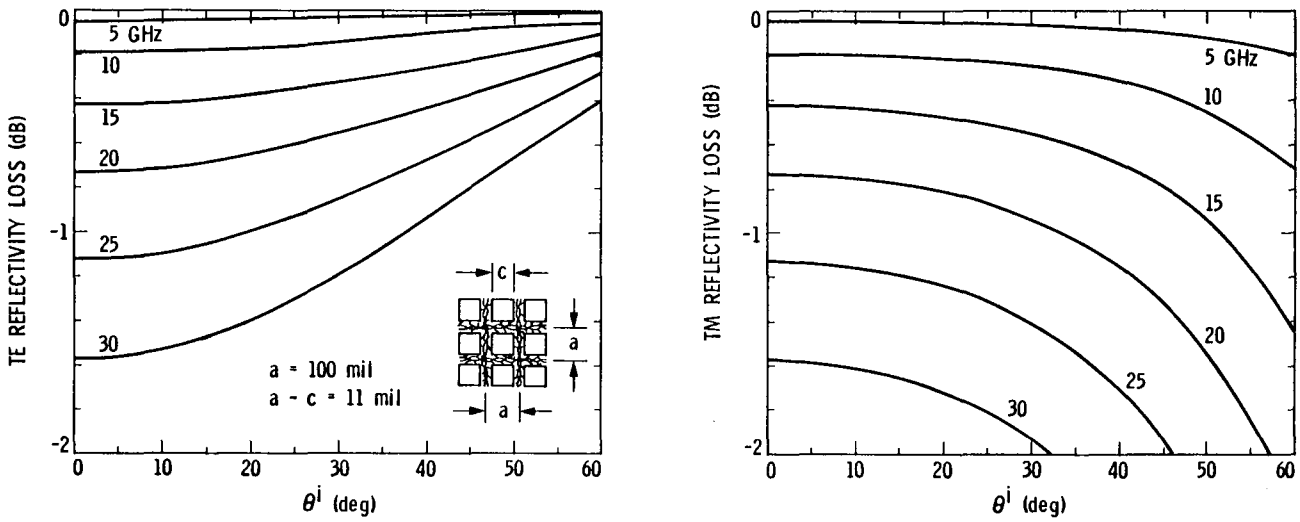

Figure 17

TDRSS MESH REFLECTIVITY LOSS VERSUS MESH CELL THICKNESS AT 15 GHz

TE and TM reflectivity losses are plotted versus the incident angle in Fig. 18. In this Figure, the mesh thickness is varied to demonstrate how the reflectivity loss changes. It is clear that, as the mesh thickness increases (smaller mesh openings), the reflectivity loss becomes smaller and less dependent on the incident angle and polarization.

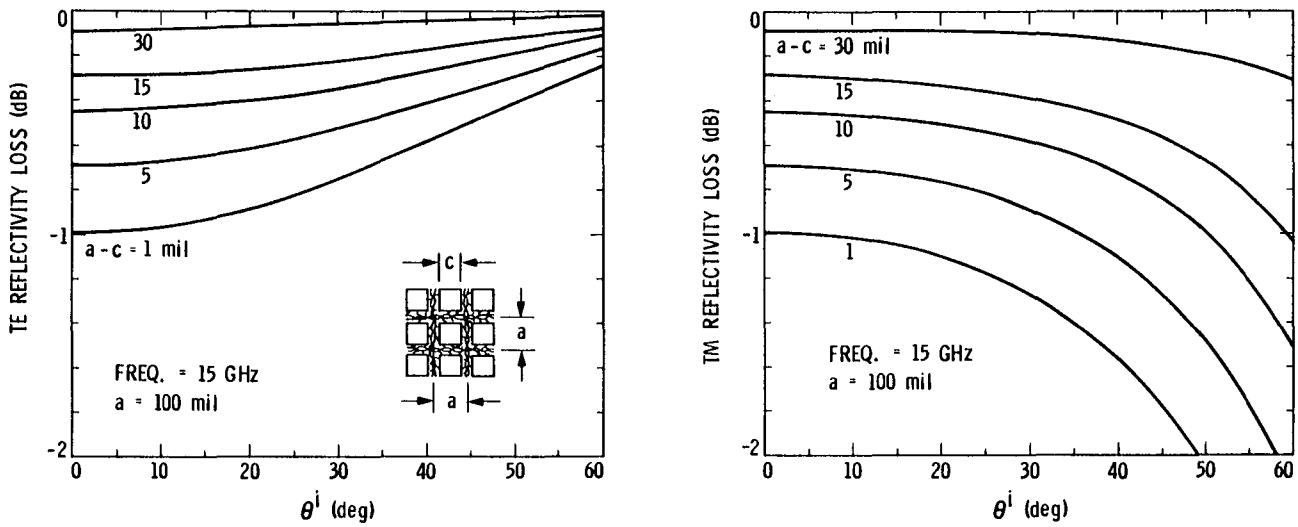

Figure 18

GAIN LOSS OF AN OFFSET REFLECTOR ANTENNA WITH
TDRSS MESH VERSUS FREQUENCY

For an offset parabolic reflector antenna with dimensions as shown in Fig. 19, and illuminated by a feed radiating a symmetric pattern with an edge taper of -15 dB, the gain loss has been computed for a reflector mesh surface similar to the TDRSS mesh. The gain loss, as a function of frequency, is depicted in the same Figure. It is seen that, at 15 GHz where the mesh opening is about $\lambda/9$, the gain loss is approximately 0.5 dB. It has also been found that this gain loss is directly related to the mesh reflectivity loss for the cases of small incident angles.

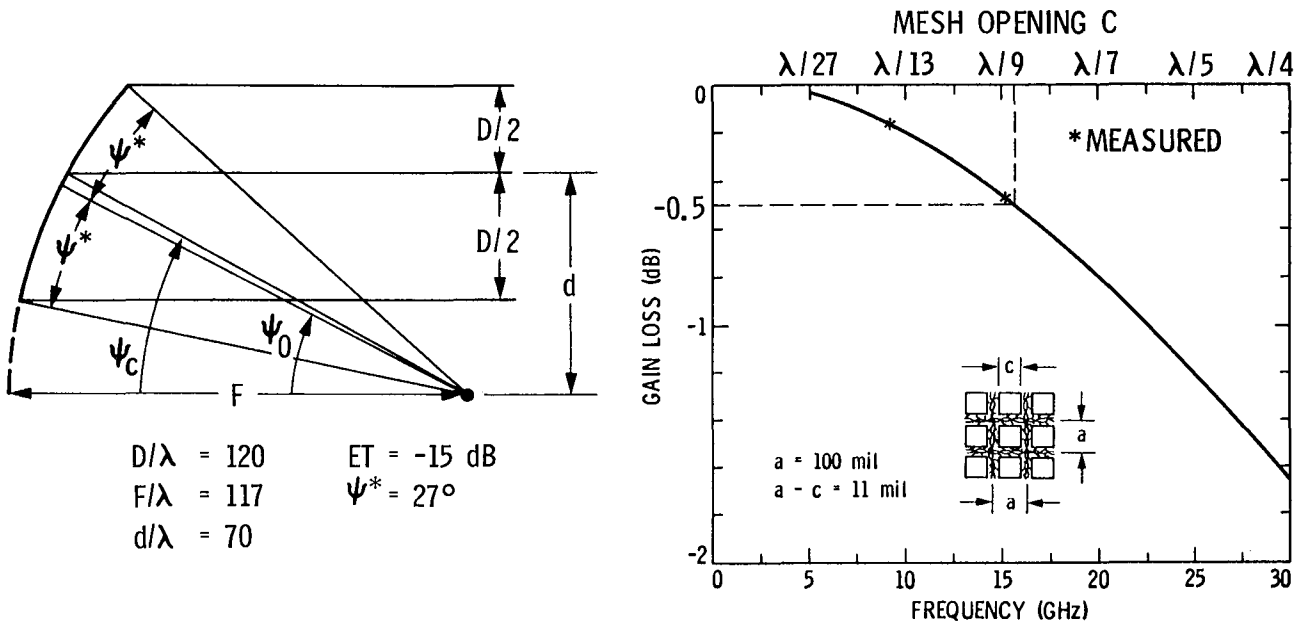

- REFLECTOR GAIN LOSS IS DIRECTLY RELATED TO THE MESH REFLECTIVITY LOSS

Figure 19

CROSS-POLAR PATTERNS VERSUS MESH CELL ELONGATION

For the offset reflector with dimensions as given in Fig. 19, the far-field patterns have been determined for the circularly polarized illumination and for the mesh surface with different cell elongations. Results are shown in Fig. 20 for both the co-polar (RCP) and cross-polar (LCP) patterns. It is observed that the co-polar pattern does not change appreciably for the mesh cell dimensions shown in this Figure, whereas the cross-polar pattern changes drastically as the mesh cell becomes more elongated. This is, in particular, pronounced for the circularly polarized illumination where the cross-polar level is always low for balanced feed illuminations on offset parabolic reflector antennas.

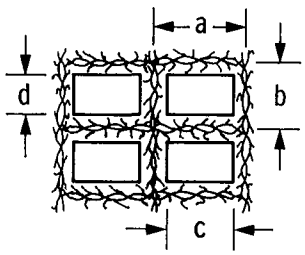

b = 10 mil
a-c = b-d = 11 mil
FREQ = 15 GHz

a: SOLID SURFACE
b: a = 2b
c: a = 1.5b
d: a = 1.1b

CIRCULARLY POLARIZED

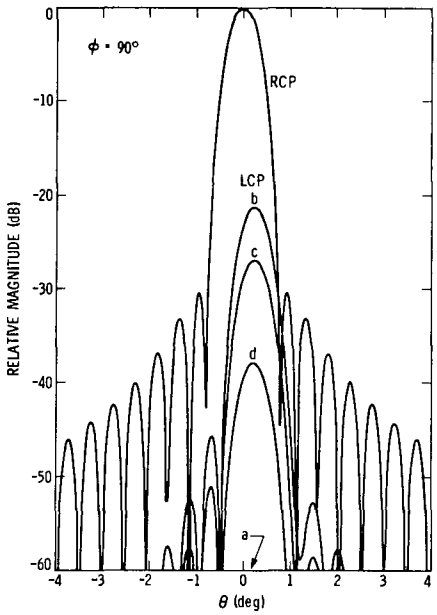

- CO-POLAR PATTERN DOES NOT CHANGE APPRECIABLY
- CROSS-POLAR PATTERN CHANGES DRASTICALLY

Figure 20

OFFSET REFLECTOR OF LMSS

For the mesh deployable offset wrap-rib reflector antenna of the conceptually designed Land Mobile Satellite System (LMSS), the effects of different mesh configurations on the far-field patterns are studied. The dimensions of this reflector antenna are:

freq. = 871.5 MHz (λ = 34.42 cm)
F = focal length = 82.5 m = 239.69λ
D = diameter = 55 m = 159.79λ
d = offset height = 34 m = 98.78λ

The strip aperture mesh parameters are:

a = 0.53 cm = 0.0155λ, b = 0.53 cm = 0.0155λ
c = 0.38 cm = 0.0111λ, d = 0.38 cm = 0.0111λ
Ω_1 = 90 deg, Ω_2 = 0 deg

Some of the above mesh parameters are changed to allow parametric studies. A schematic of this mesh reflector antenna is shown in Fig. 21.

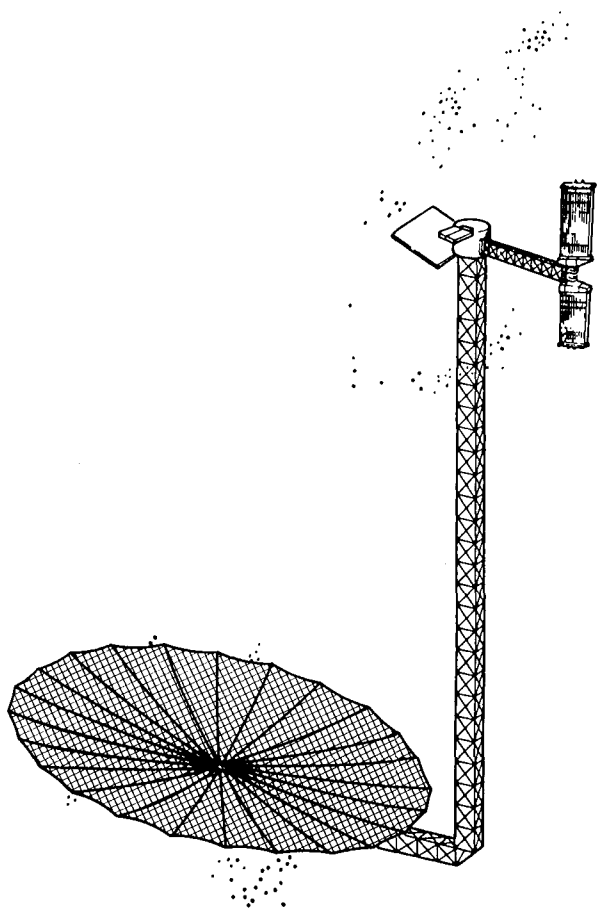

Figure 21

EFFECTS OF LARGE CELLS

In order to observe the amount of boresight gain loss, larger mesh cells with different openings are studied. Results are shown in Fig. 22, which clearly demonstrates that, as the mesh aperture (mesh opening) becomes larger (from 0.15λ to 0.29λ), the boresight gain drops due to the transmission through the mesh. It is also observed that the cross-polar pattern increases for this particular configuration, which is illuminated by a circularly polarized feed.

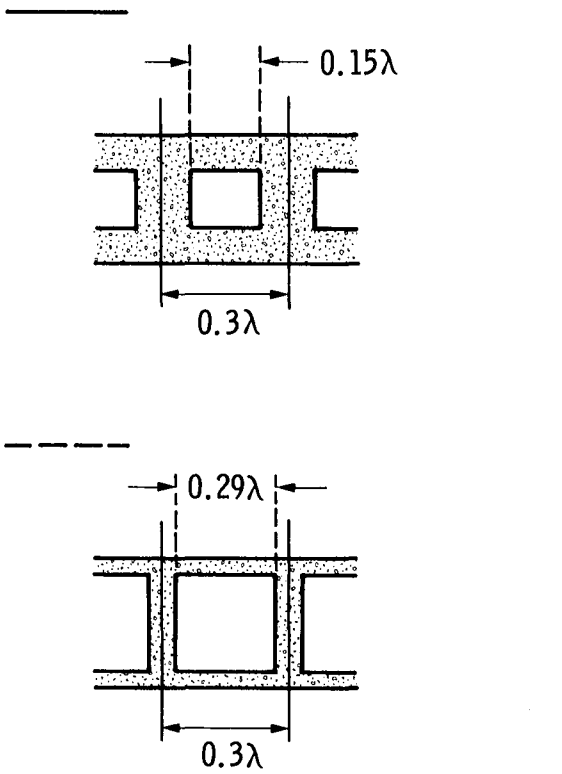

- GAIN LOSS DUE TO TRANSMISSION
- INCREASED CROSS-POL LEVEL

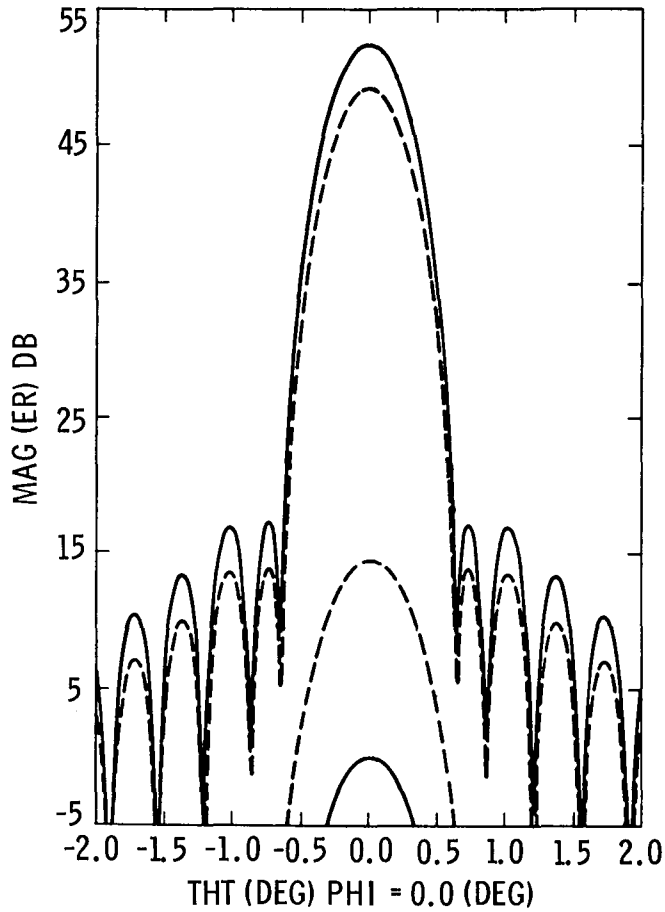

Figure 22

LMSS PATTERNS VERSUS MESH CELL ELONGATION FOR FEED AT FOCAL POINT

For the LMSS reflector illuminated by a circularly polarized feed, the effects of square and rectangular meshes are studied with results as shown in Fig. 23. The square mesh with dimensions given previously in Fig. 21 has a cross-polar level of -60 dB below the co-polar peak; however, for the rectangular mesh configurations, the level of cross-polar patterns increases considerably. It is worthwhile to mention that, in all cases, the co-polar pattern does not change appreciably. In particular, for the square mesh, the difference between the mesh reflector and the solid reflector is very small for the parameters used.

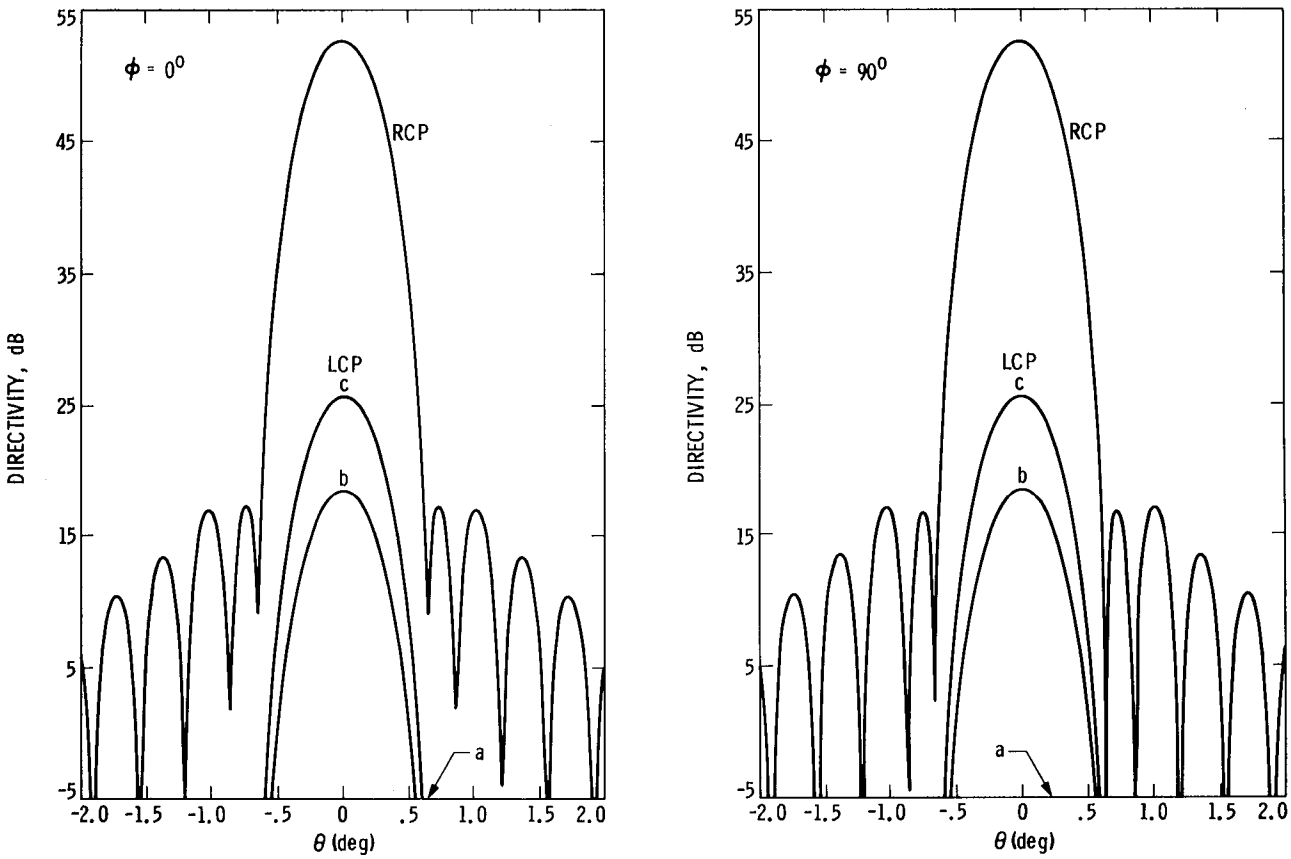

(a) a=b=0.0155λ, c=d=0.0111λ (b) a=2b (c) a=3b

Figure 23

LMSS PATTERNS VERSUS MESH CELL ELONGATION FOR FEED OFF FOCAL POINT

Similar observations are also made for the cases when the feed is displaced from the focal point. For example, Fig. 24 shows the far-field patterns of the LMSS reflector illuminated by a feed displaced away from the focal point such that the beam is scanned 3 degrees off the reflector axis in the plane of offset. The peak directivity is reduced from 52.65 to 51.67 dB. Furthermore, it is noticed that the co-polar pattern has not changed appreciably for different mesh cells, whereas the cross-polar pattern has changed noticeably.

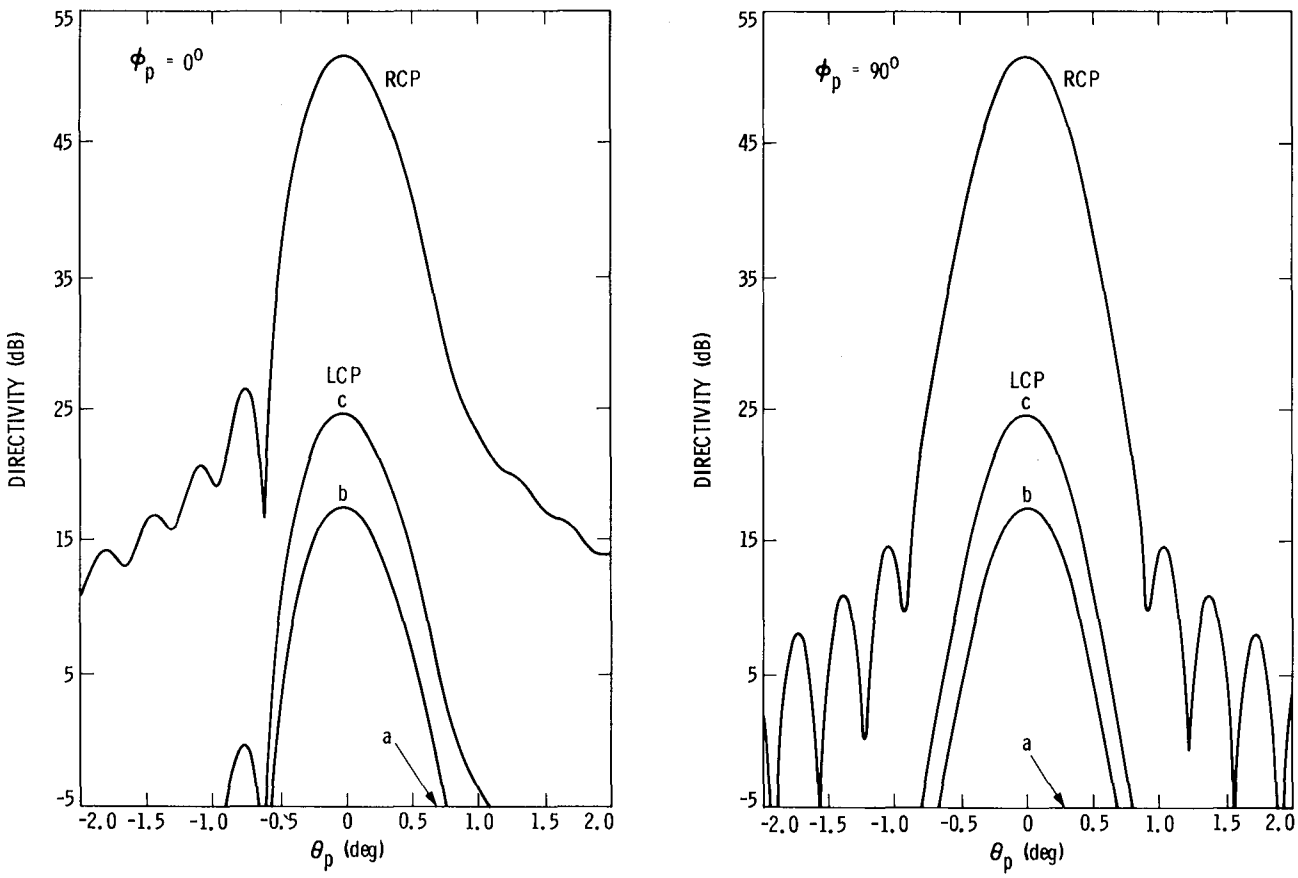

(a) a=b=0.0155λ, c=d=0.0111λ (b) a=2b (c) a=3b

Figure 24

CONCLUSIONS

Based on many numerical simulations, useful observations are made, as depicted in Fig. 25. Attempts are being made to perform measurements in order to further validate the accuracy of the results obtained. This would also allow one to choose the effective mesh cell dimensions from a few representative measured data and then use these dimensions in the strip aperture model in order to run the computer program.

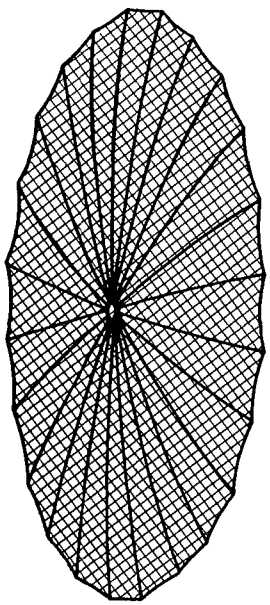

- A VERSATILE MESH REFLECTOR VECTOR-DIFFRACTION ANALYSIS HAS BEEN DEVELOPED
- IMPROVEMENTS OVER THE STANDARD WIRE GRID MODELS HAVE BEEN OBTAINED
- FOR UNIFORM MESH CELLS THE NORMALIZED CO- AND CROSS-POLAR PATTERNS HAVE BEEN FOUND TO BE VERY SIMILAR TO THE SOLID SURFACE PATTERNS
- FOR LARGE MESH CELL OPENINGS ($\sim\lambda/8$) GAIN LOSSES OF THE ORDER OF 0.5 dB CAN BE OBSERVED
- FOR ELONGATED MESH CELLS THE LEVEL OF THE CROSS-POLAR PATTERNS CAN BE DRASTICALLY INCREASED
- THE DEVELOPED COMPUTER CODE CAN BE EASILY INTEGRATED WITH ANY EXISTING PO COMPUTER PROGRAMS

Figure 25

DETERMINATION OF ELECTROMAGNETIC PROPERTIES OF MESH MATERIAL USING ADVANCED RADIOMETER TECHNIQUES

R. F. Harrington and
H-J. C. Blume
NASA Langley Research Center
Hampton, Virginia

Large Space Antenna Systems Technology - 1984
December 4-6, 1984

122-METER HOOP/COLUMN SOIL MOISTURE RADIOMETER ON THE EARTH OBSERVATION SYSTEM SPACE STATION

The requirement for a large-diameter deployable antenna to map soil moisture with a 10-kilometer or better resolution using a microwave radiometer was presented in a paper by Shiue and Lawrence of the Goddard Space Flight Center (Ref 1). The requirement for a 6-meter deployable antenna to map sea surface temperature on the Navy Remote Ocean Sensor System (NROSS) was also presented in a previous paper by Hollinger and Lo of the Naval Research Laboratory (Ref 2). Both of these deployable antennas require a mesh membrane material as the reflecting surface. The determination of the electromagnetic properties of mesh materials is a difficult problem. The Antenna and Microwave Research Branch (AMRB) of Langley Research Center was asked to measure the material to be used on NROSS by NRL. A cooperative program was initiated to measure this mesh material using two advanced radiometer techniques developed by the authors.

Figure 1 presents an artist's illustration of a candidate Soil Moisture Radiometer employing a 122-meter Hoop/Column antenna system to achieve the required 10-kilometer resolution. A pushbroom array of beams (Ref 1) could achieve both spatial resolution and wide swaths while viewing the Earth on a global basis.

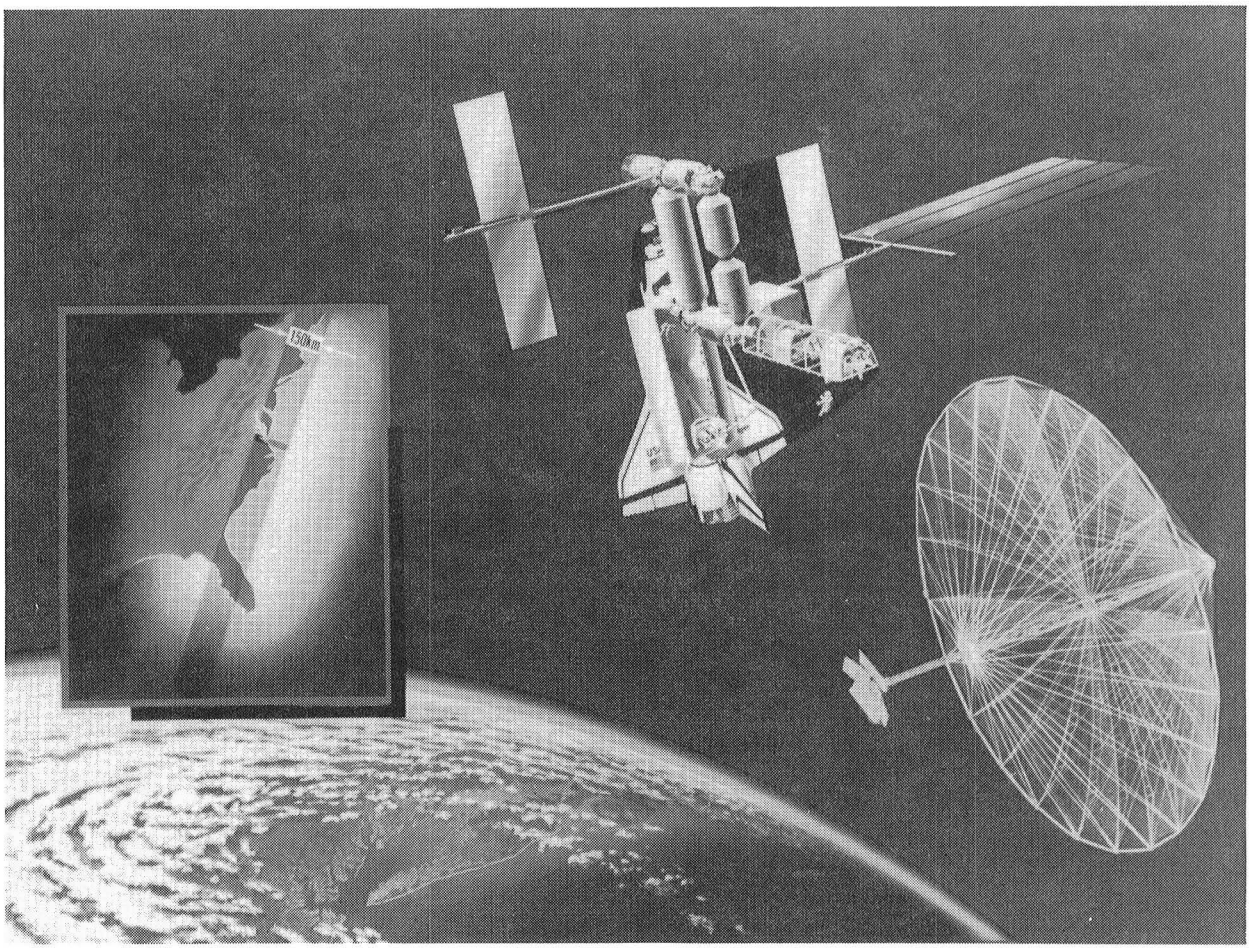

Figure 1

The next two photographs show the two techniques using advanced design precision microwave radiometers. The outdoor system (fig 2(a)) is a radiometric "bucket" method. This system uses the Stepped-Frequency Microwave Radiometer (SFMR) operating at 5.2 GHz. The large plywood structure next to the equipment trailer is lined with aluminum. The SFMR is located in the plywood housing and looks through the bucket wall toward a 45° reflecting plate. The cold sky (7 K) is used as the measurement source.

The indoor system (fig 2(b)) uses the S-Band Microwave Radiometer (S-band) operating at 2.65 GHz. The radiometer is mounted on a hoist next to the equipment rack with its antenna horizontal pointing to a liquid nitrogen cold load. There is a 90° bend using a 45° heated reflection plate in the S-band antenna. The liquid nitrogen load (77 K) is used as the measurement source in the indoor system.

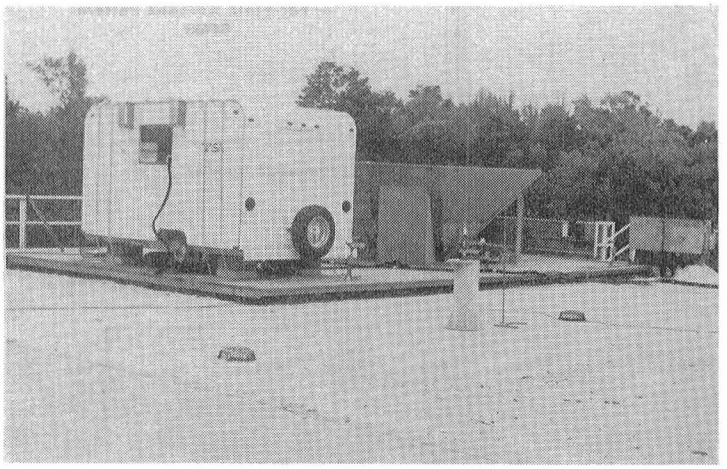

(a)

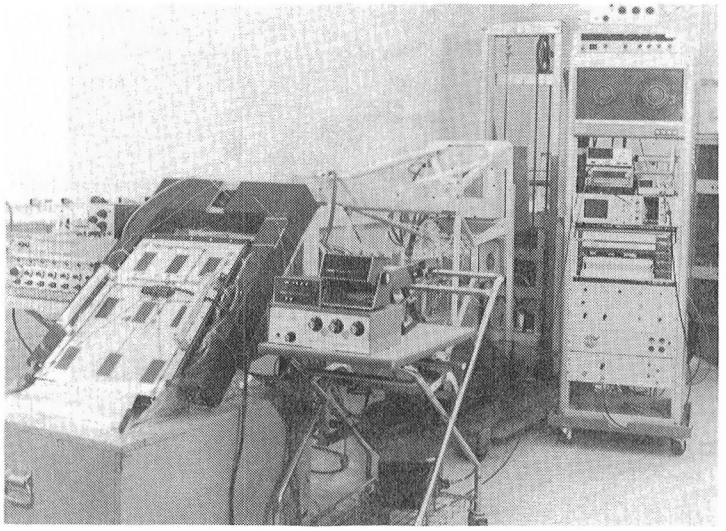

(b)

Figure 2

5.2-GHz RADIOMETER BUCKET TECHNIQUE

A sketch of the radiometric bucket is presented in fig 3(a). The SFMR, fig 3(b), is positioned such that it looks through the bucket wall, and in fig 3(c), towards a 45° reflecting plate. The 308 K self radiation from the SFMR is reflected to deep space. The known incoming radiation, 7 K, is received by the SFMR. The electromagnetic properties of the mesh are determined by using four different test configurations at the reflection plate. These include a reflecting surface only, fig 3(c), an absorber in an aluminum box, fig 3(d), mesh in a frame placed over the reflecting surface, fig 3(e), and mesh placed over the absorber box, fig 3(a). With the four configurations and the stability of the extraterrestrial radiation, the four unknowns can be determined from the four independent measurements.

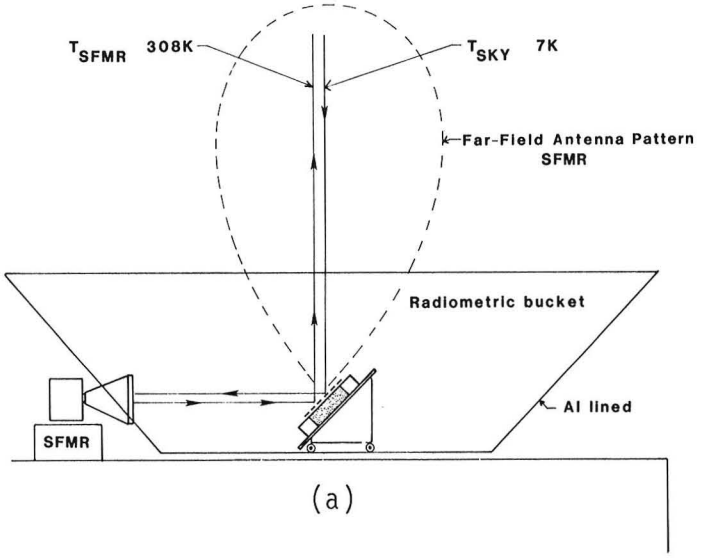

(a)

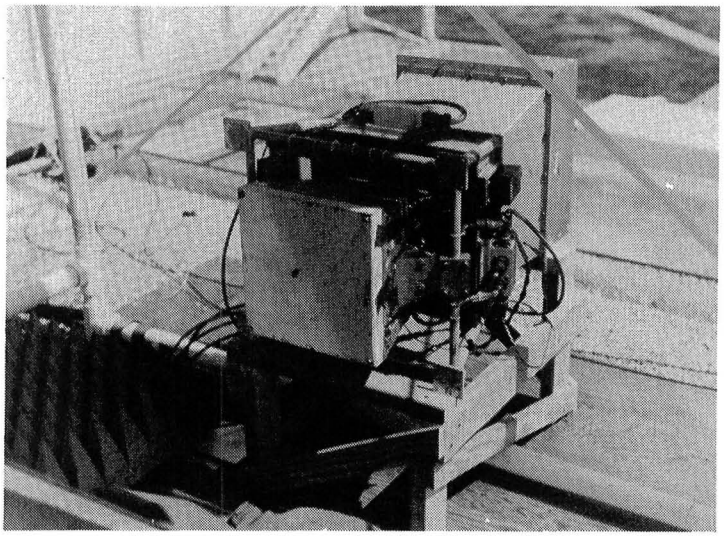

(b)

Figure 3

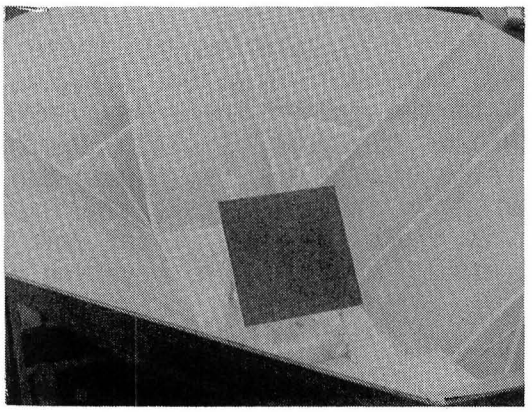

(c)

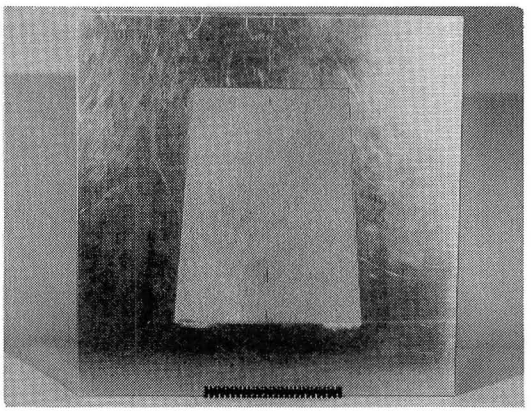

(d)

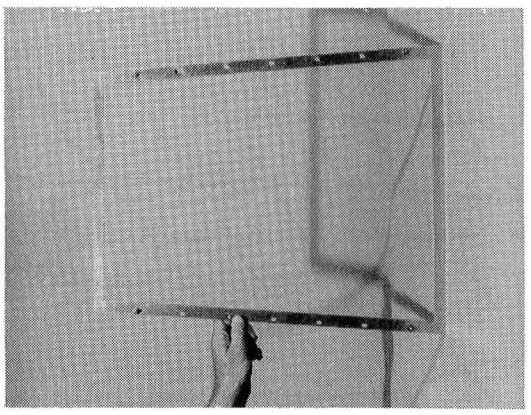

(e)

Figure 3 (Concluded)

ELECTROMAGNETIC PROPERTIES OF MESH MEMBRANE MATERIAL

The electromagnetic properties of the mesh include reflection, transmission, emission and scattering. Figure 4 illustrates how these factors are related in the radiometric bucket method. The sky radiation, T_{sky}, is reflected by the mesh reflection coefficient, r_x, to the radiometer. Any radiation behind the mesh, $T_{backgrd}$, is transmitted through the mesh by the transmission coefficient, t_x: The self emission or emissivity of the mesh, e_x, times the physical temperature, T_{phy}, determines the self radiation from the mesh. During these measurements it is assumed that scattering is a second-order effect and is neglected. Testing has shown this to be a good assumption. The conservation of energy requires that

$$r_x + e_x + t_x = 1$$

and ideally a perfect mesh would have the following characteristics

$$e_x = 0 \quad r_x = 1 \quad t_x = 0 \quad s_x = 0$$

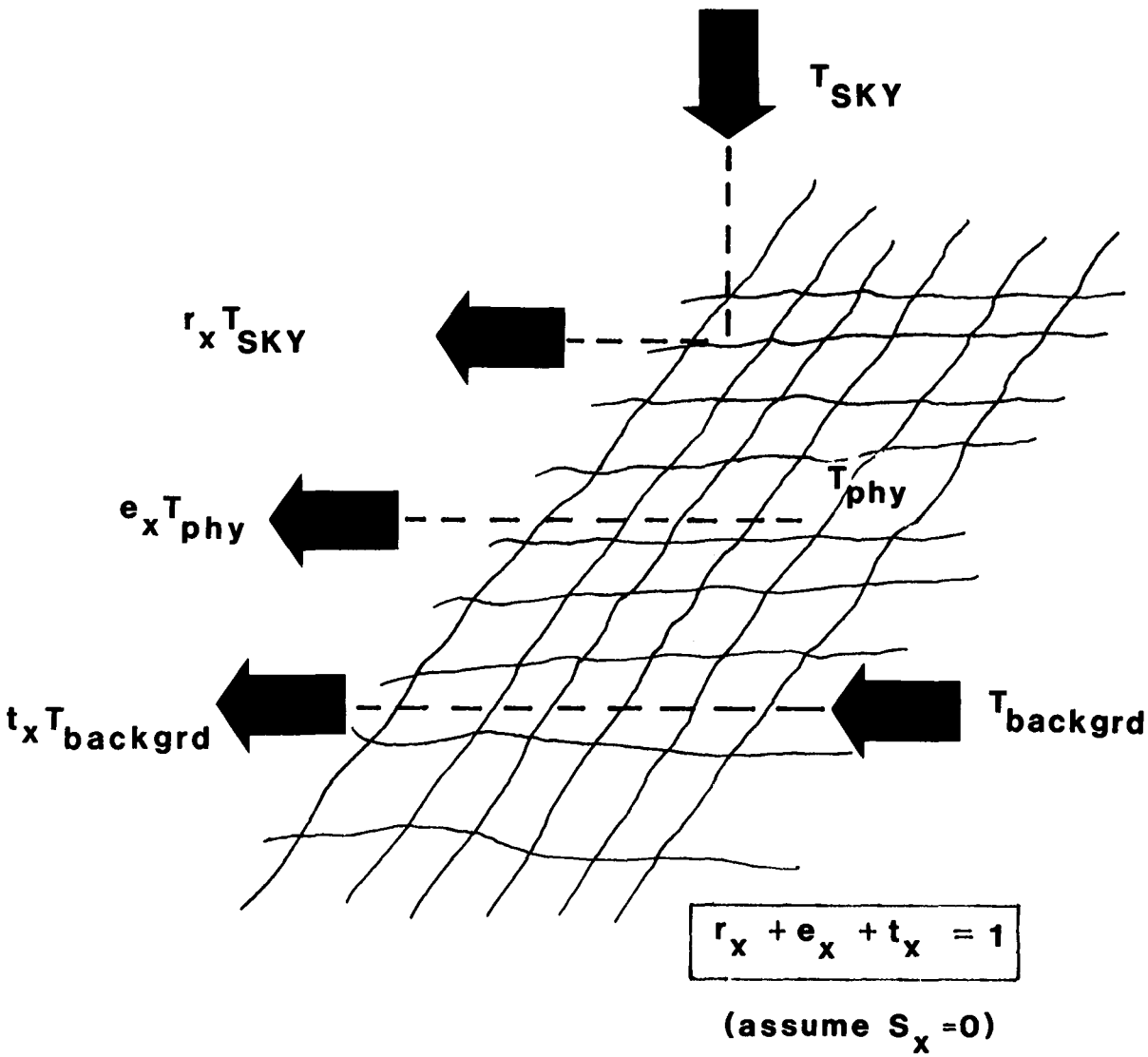

Figure 4

TEST CONFIGURATIONS IN THE RADIOMETER BUCKET

The four independent test configurations are shown in figs 5(a) and 5(b). These include measurements of the splash plate (reflecting surface) only, T_{spo}; the mesh over the splash plate, T_{msp}; the mesh over the absorber, T_{mas}, and the absorber only, T_{asp}. The individual sources for each configuration and the equation are given in figs 5(a) and 5(b).

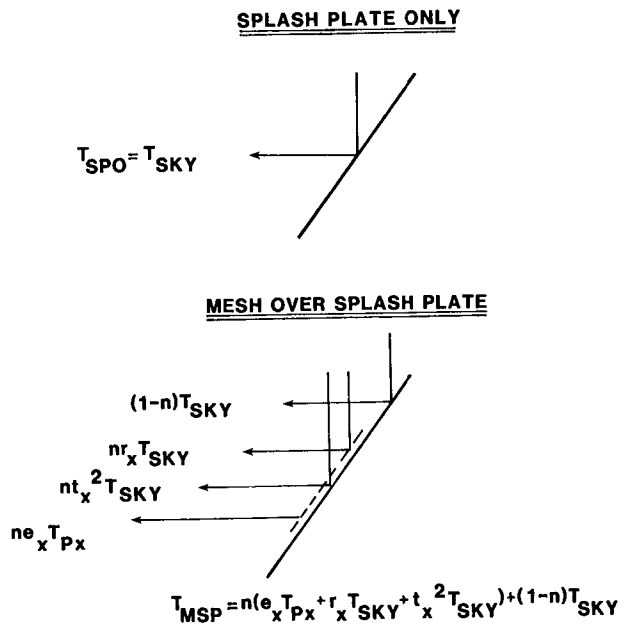

(a)

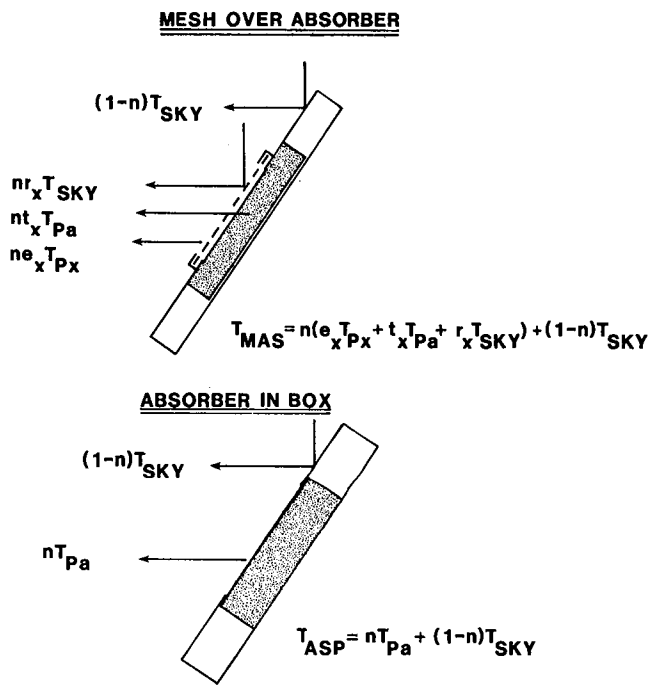

(b)

Figure 5

FILL FACTOR AND TRANSMISSION THROUGH MESH

The equation for the fill factor is given in fig 6(a). The fill factor determines the percentage of the beam pattern of the SFMR that the mesh sample occupies. The equation for the transmission through the mesh is given in fig 6(b).

FILL FACTOR

$$n = \frac{T_{ASP} - T_{SKY}}{T_{Pa} - T_{SKY}}$$

T_{SKY} = Sky radiation (zenith)

T_{Pa} = Physical temperature of absorber

(a)

TRANSMISSON THROUGH MESH

$$t_x = \frac{T_{MAS} - T_{MSP}}{n(T_{Pa} - t_x\ T_{SKY})}$$

n = Fill factor

T_{SKY} = Sky radiation (zenith)

T_{Pa} = Physical temperature of absorber

(b)

Figure 6

The equation for reflectivity is given in fig 7(a) and for emissivity in fig 7(b).

REFLECTIVITY

$$r_x = \frac{T_{ASP} - T_{MSP}}{n\left[T_{Pa} - T_{SKY}\right]} - \frac{S_x \; T_{Pa}}{\left[T_{Pa} - T_{SKY}\right]}$$

S_x = Scattering by the mesh

n = Fill factor

T_{SKY} = Sky radiation (zenith)

T_{Pa} = Physical temperature of absorber

(a)

EMISSIVITY

$$e_x = \frac{T_{MSP} - T_{SPO}}{n(T_{Px} - T_{SKY})} + \frac{(t_x - t_x^2)\,T_{SKY}}{(T_{Px} - T_{SKY})} + \frac{S_x \; T_{SKY}}{(T_{Px} - T_{SKY})}$$

t_x = Transmission through mesh

S_x = Scattering by the mesh

n = Fill factor

T_{SKY} = Sky radiation (zenith)

T_{Px} = Physical temperature of mesh

(b)

Figure 7

RADIOMETER SYSTEM FOR ELECTROMAGNETIC MEASUREMENT OF SURFACES

The system shown in figures 8(a) and 8(b) consists of the 2.65-GHz radiometer with the horn antenna, the cryoload cooled with liquid N_2 and the test section. The radiometer is of the Dicke-type with pulsed noise injection feedback which has proven to be stable over long periods of time (years). With an integration time of 22 sec the brightness temperature resolution was better than 0.02 K. The cryoload is a matched load filled with liquid nitrogen.

The test section has two extension walls to the horn antenna which support the heat convection space. It consists of an oxygen-free copperplate silverplated and gold flashed for consistent high reflectivity. With 1-inch separation from plate surface another Ecco-foam sheet is installed to build the lower wall of the heat correction chamber. Inside the correction chamber the surface under test, in this case the mesh membrane, is placed with a holding frame.

The space between the Ecco-foam cover of the cryoload and the Ecco-foam wall of the convection chamber is purged with dry air to prevent water condensation at the Ecco-foam surfaces. This photograph (fig 8(a)) shows the electronics and the recording equipment mounted in a relay rack. The constant temperature heating supplies are located on both sides of the test section.

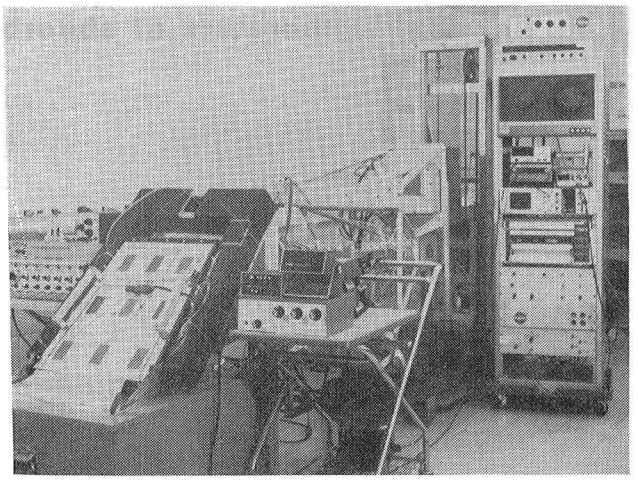

(a)

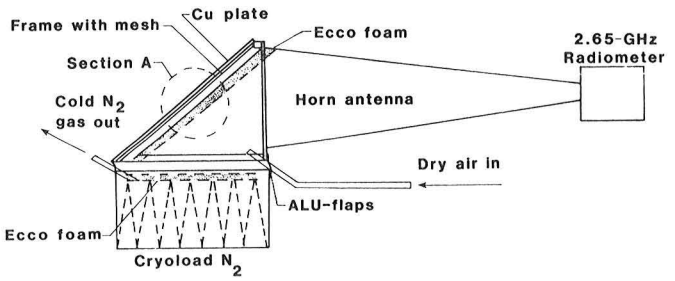

RADIOMETER SYSTEM FOR E-M MEASUREMENTS OF SURFACES

(b)

Figure 8

EXPANDED SECTION A

The heater elements are bonded to the upper surface of the copperplate. The mesh membrane is mounted in a support frame which is located underneath the plate. The heat convection space is enclosed by the low-loss Ecco foam. The spacing strips containing the airflow openings are goldplated stainless steel metal pieces pressed over bakelite to provide a low heat conductivity path from the copperplate to the aluminum horn antenna.

The photograph (fig 9) shows the same in a perspective view.

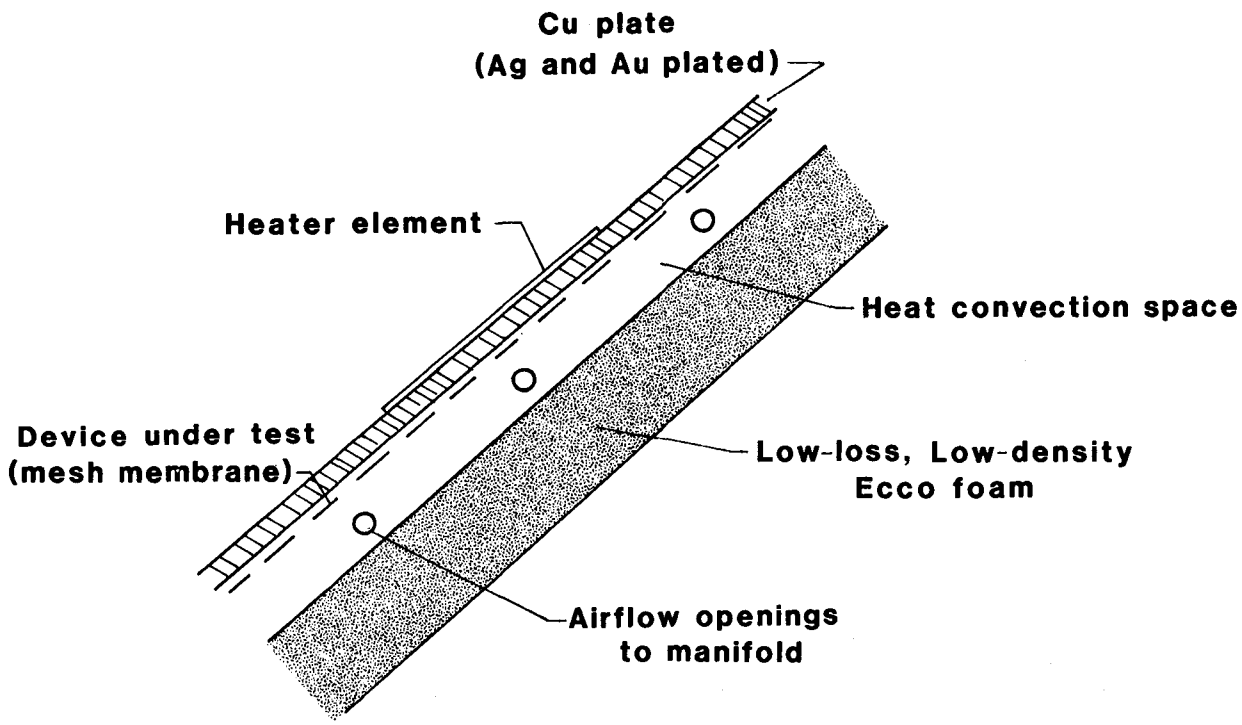

EXPANDED SECTION A

Figure 9

REFLECTION PLATE

The plate in fig. 10 is provided with heating elements with a power consumption up to 2 kW. The temperature is measured at five locations to monitor the temperature distribution of the reflection plate.

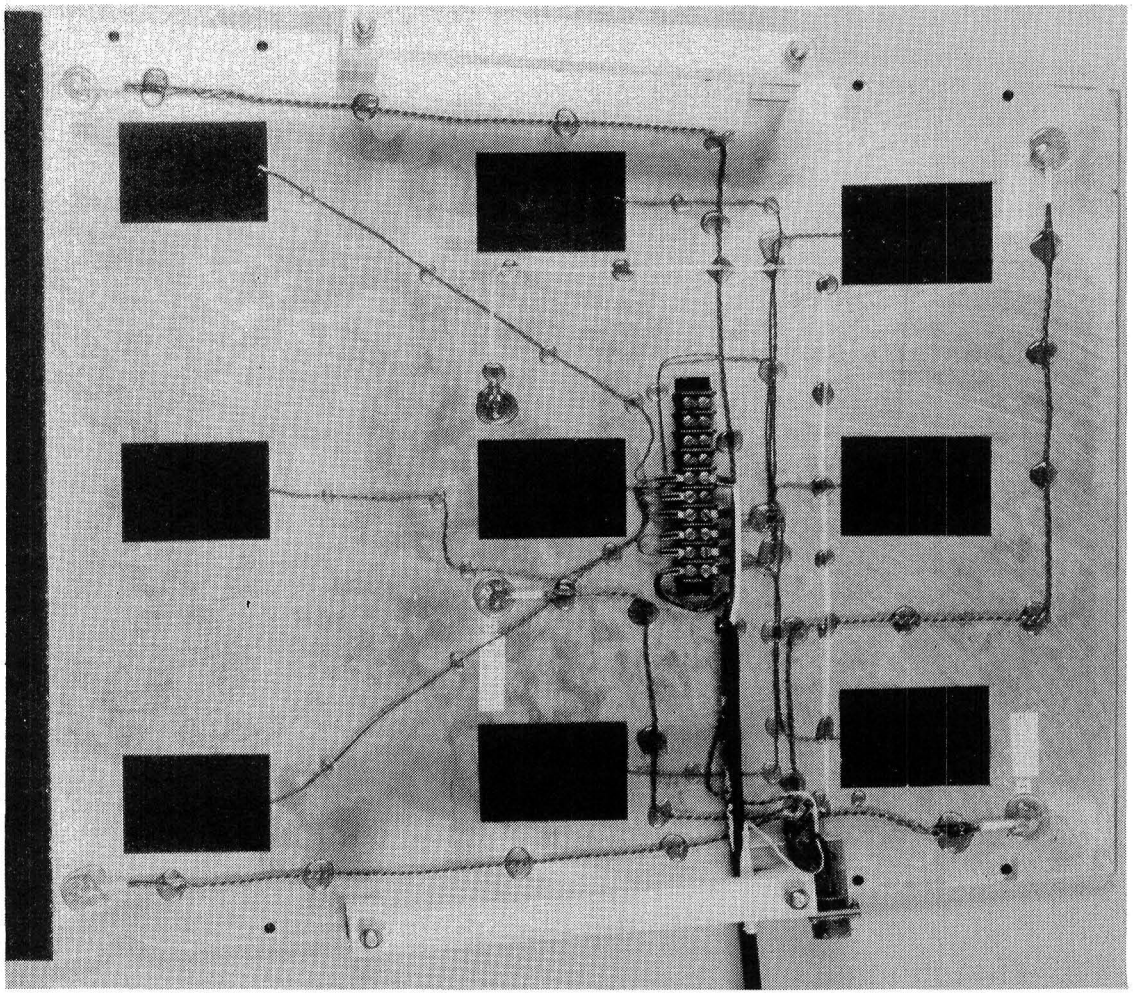

Figure 10

CRYOLOAD AND ECCO-FOAM COVER

The cold N_2 gases that are outgased from the LN_2 are prevented from entering the test section by the Ecco-foam cover. These gases escape through the built-in exhaust tubings. This is shown in the figures 11(a) and 11(b).

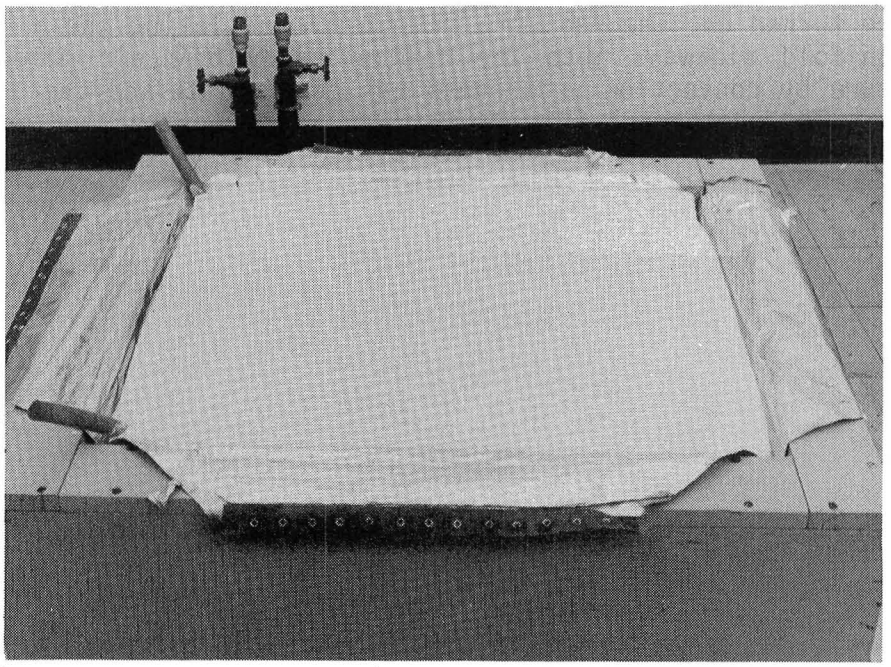

(a)

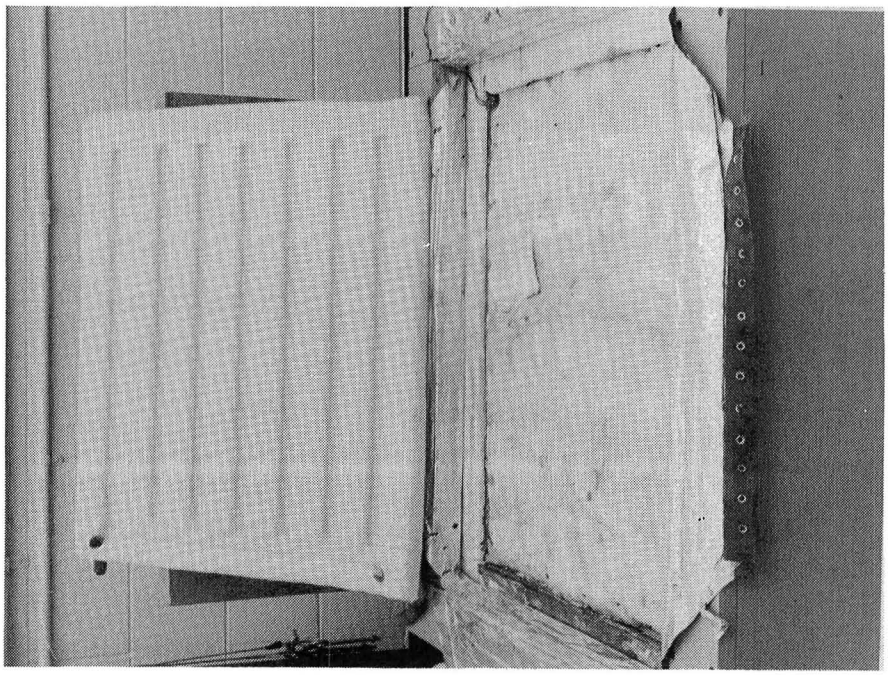

(b)

Figure 11

AIRFLOW DIAGRAM OF HEATED DRY AIR

It is very important to keep the test space free of humidity. Before the start-up phase i.e., starting from room temperature to heating up, the test space must be thoroughly purged with dry air. After the brightness temperature indicated by the radiometer reaches a minimum the preheater and the heaters on two of the copperplates are turned on. The fan (fig 12(b)) is circulating the air as indicated through the manifold sideways into the chamber where the air molecules take on higher temperature by convection underneath the copperplate and thereby heat up the mesh under test. The photograph (fig 12(a)) shows the construction and location of the airflow elements.

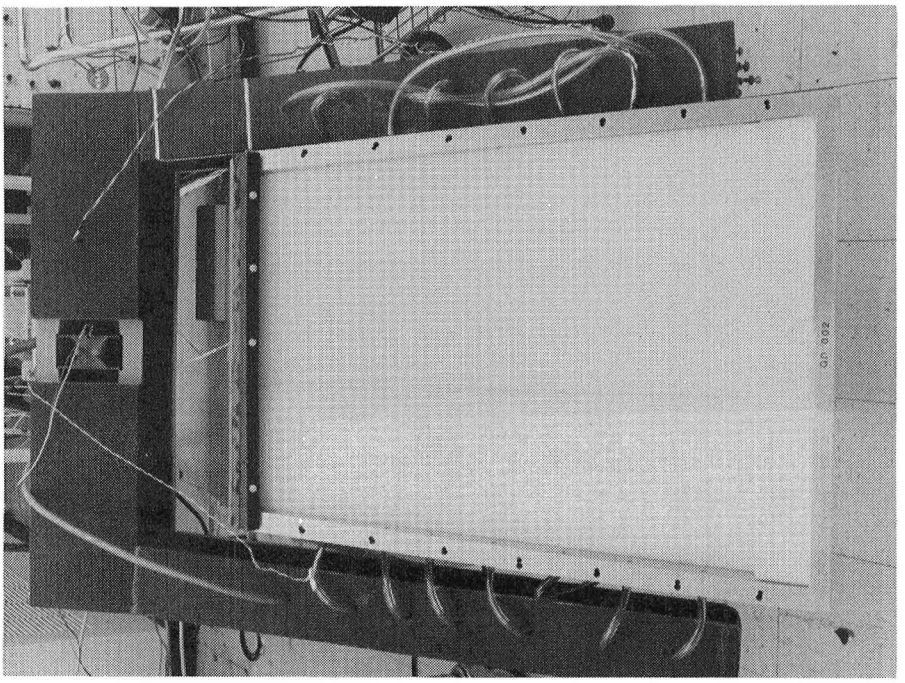

(a)

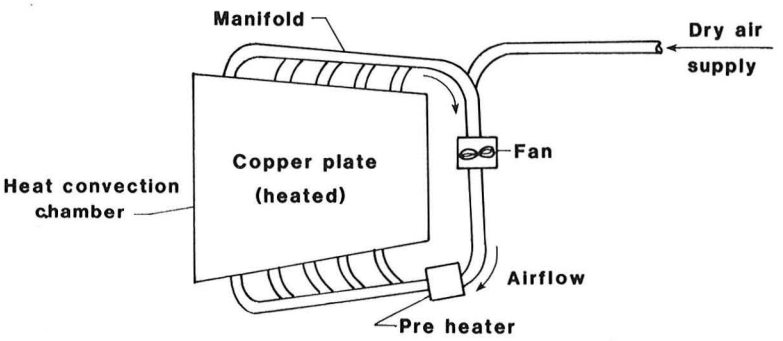

AIRFLOW DIAGRAM OF HEATED DRY AIR

(b)

Figure 12

BRIGHTNESS TEMPERATURE AS A FUNCTION OF DISTANCE (d) BETWEEN CRYOLOAD AND REFLECTING SURFACE UNDER TEST

It can be shown mathematically that there is partial correlation between the reflected and incident waves at the surface. This results in either an addition or partial cancellation depending on the relative phase between the two waves. The predominant factors of this behavior are the small bandwidth (100 MHz) and the relative high center frequency (2.65 GHz). The reflection back into cryoload would be negligible if the test surface is in the form of a paraboloid. The focal point of the paraboloid must be the feedpoint of the horn antenna in order to have some freedom from small changes of the distance (d). The operating point was shown to be at the minimum as shown in fig. 13. A distance change of less than 1 cm over more than 90 min is achieved by letting the cryoload come to an isothermal state of the boiling point of N_2 gas with a minimum of N_2 gas boiling off.

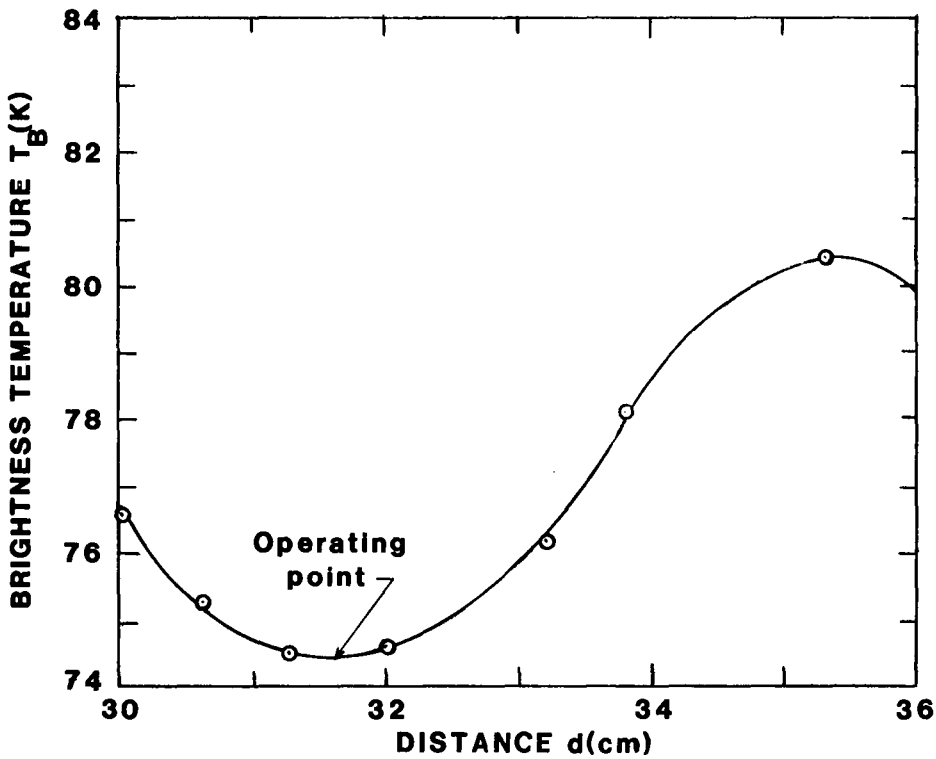

Brightness temperature dependence on distance(d) between cryoload and reflecting surface under test

Figure 13

RADIOMETER BRIGHTNESS TEMPERATURE T_b VARIATION AS A FUNCTION OF THE PHYSICAL TEMPERATURE T_m OF THE MESH MEMBRANE MATERIAL

The diagram in fig. 14 is the dependence of T_b as a function of T_m. The time "Heaters on" is condition (1) of T_b and T_m and time "Heaters off" is condition (2).

The ratio of the differences of both temperatures T_b and T_m gives the emissivity of the mesh surface. All other effects of reflections (distortion of equal phase front) and their partial correlation of incident and refected waves remain constant and cancel in the difference operation.

The proof of cancellation was demonstrated by heating-up the empty test chamber by 30°C and a variation of T_b of 0.08 K was measured under this condition.

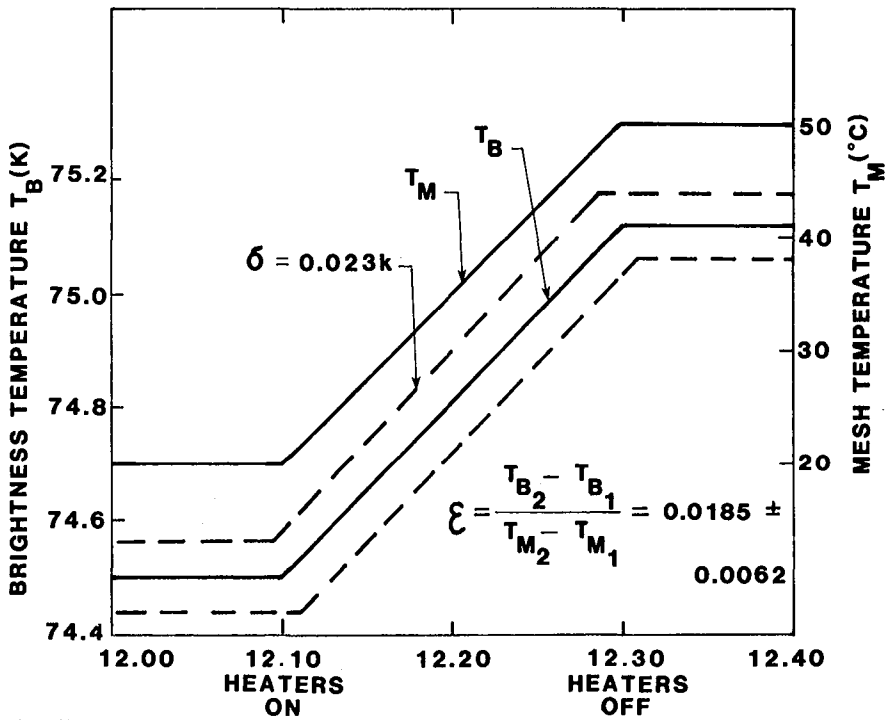

Radiometer brightness temperature variation in dependence of the physical temperature of the losses of the mesh membrane material

Figure 14

MESH MEMBRANE MATERIAL SPECIFICATIONS

The mesh material used in the testing presented during this presentation was provided to the authors by the General Dynamics Corp. A photograph of the mesh is shown in fig 15(a). The specifications of the mesh membrane material are given in fig 15(b).

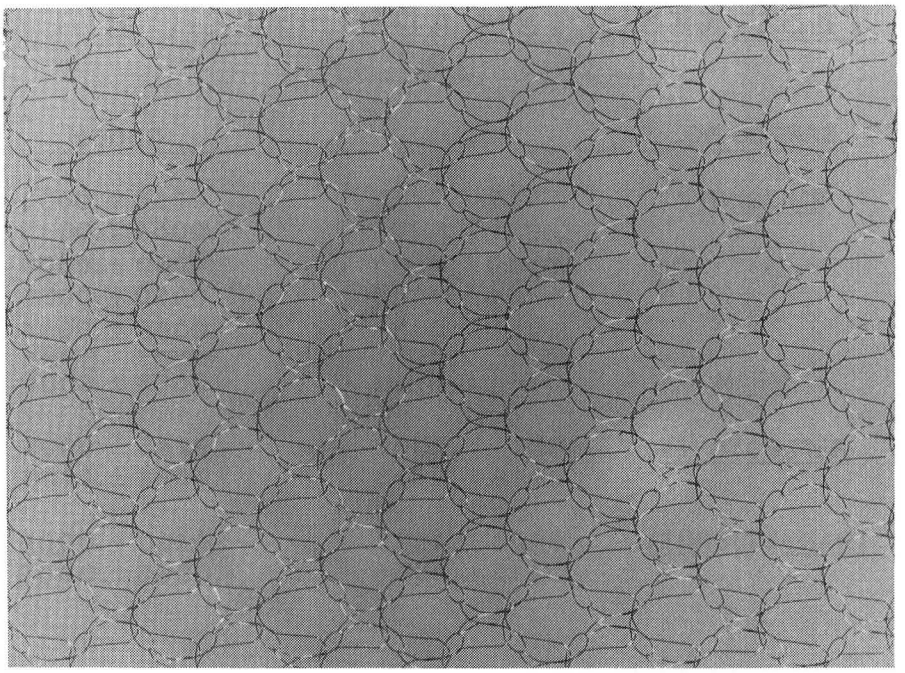

(a)

SPECIFICATIONS OF THE MESH MEMBRANE MATERIAL TESTED

- MOLYBDENUM WIRE DIAMETER - 0.0304mm (1.2 mil.)
- GOLD PLATING - 1μm (6-8% of Mo.-weight)
- TENSIONS IN BOTH DIRECTIONS - 8.9g/cm (0.05 lbs/inch)
- NUMBER OF OPENINGS (diagonally) - 11 per cm (28 per inch)

(b)

Figure 15

The measurement results on two samples of the General Dynamics mesh using the 5.2-GHz radiometric bucket are given in fig 16(a). The measurement results for emissivity of the same two General Dynamics mesh samples using the 2.65-GHz indoor system are given in fig 16(b).

TEST RESULTS-RADIOMETRIC BUCKET (5.2 GHz)

SAMPLE NO.	GD001	GD002
EMISSIVITY	.0048 ± .0002	.0050 ± .0003
	.0041 ± .0003	.0054 ± .0012
	.0049 ± .0003	.0050 ± .0003
	.0051 ± .0003	.0050 ± .0003
	.0046 ± .0004	.0059 ± .0004
MEAN:	.0047 ± .0004	.0053 ± .0004
REFLECTIVITY	.9724 ± .0005	.9743 ± .0005
	.9716 ± .0008	.9693 ± .0006
TRANSMISSIVITY	.0266 ± .0006	.0190 ± .0006
	.0213 ± .0008	.0233 ± .0003

(a)

TEST RESULTS-CLOSED SYSTEM (2.65 GHz)

SAMPLE NO.	GD001	GD002
EMISSIVITY	0.0185	0.0156
	0.0287	0.0167
	0.0134	0.0255
	0.0129	0.0183
	0.0137	0.0168
	0.0130	
MEAN:	0.0167 0.0062	0.0186 0.004

(b)

Figure 16

CONCLUSIONS

The conclusions from the two techniques of measuring mesh membrane materials are given in fig 17.

A COOPERATIVE LaRC/NRL PROGRAM HAS DEVELOPED TWO DIFFERENT METHODS FOR MEASUREMENT OF THE ELECTROMAGNETIC PROPERTIES OF MESH MATERIAL.

(1) Radiometric bucket method

Measures reflectivity, emissivity and transmission
Problems: RFI, solar interference, weather, multiple measurements

(2) Closed system

Measures emissivity directly
Problems: Limited intergration time, heating/cooling rate limitations

Figure 17

REFERENCES

1. Shiue, J. C., and Lawrence, R. W.: Orbiting Multi-Beam Microwave Radiometer for Soil Moisture Sensing. Large Space Antenna Systems Technology - 1984, NASA CP-2368, Part 1, 1985, pp. 73-85.

2. Hollinger, J. P., and Lo, R. C.: Low-Frequency Microwave Radiometer for N-ROSS. Large Space Antenna Systems Technology - 1984, NASA CP-2368, Part 1, 1985, pp. 87-95.

THE SPACE STATION AS A CONSTRUCTION BASE FOR LARGE SPACE STRUCTURES

R. M. Gates
Boeing Aerospace Company
Seattle, Washington

Large Space Antenna Systems Technology - 1984
December 4-6, 1984

INTRODUCTION

The development and implementation of the Space Shuttle to provide transportation to low Earth orbit has provided an important step in the development of large space systems. Now, with the approval of funds to develop a Space Station, we are beginning to take the next step: that of creating a place to construct these systems. The costs involved in larger, more precise instruments are too great to accept an "all-or-nothing" philosophy of launching an automatically deployable satellite system which cannot be fully tested and checked out on Earth.

The use of the Space Station as a construction site for large space structures (LSS) will not only reduce the risks involved by providing on-the-spot test and checkout but also allow the design to be less complicated through the use of assemblable structures instead of the more complex automated systems. Advancements in space suit technology will make human involvement in the construction of large space systems more routine. The Space Station crew will be able to react to contingencies and make adjustments before the spacecraft is released to perform its assigned mission.

In this paper I will present an overview of the results of a program entitled "Definition of Technology Development Missions for Early Space Stations - Large Space Structures" performed by the Boeing Aerospace Company under contract to the NASA Marshall Space Flight Center. First, I will describe the rationale use to select the LSS technology development missions (TDM's). Then I will describe three TDM's which were designed to demonstrate these objectives and identify some of the potential problems and concerns which they create. Finally, I will identify the resources and accommodations which the Space Station must provide to support LSS construction.

TECHNOLOGY DEVELOPMENT MISSION SELECTION

The definition of LSS technology development missions must be responsive to the needs of future space missions which require large space structures. Long range plans for space were assembled by reviewing Space System Technology Models (SSTM) and other published sources. Those missions which will use large space structures were reviewed to determine the objectives which must be demonstrated by technology development missions.

In addition to these objectives, three other criteria were used in the selection of technology development missions. First, the missions should not be "dead ended" after their use as TDM's, but should provide long term benefits as scientific instruments, as testbeds for the development of other technologies, or as permanent Space Station facilities. Second, they should emphasize the need for a Space Station and its unique resources and accommodations. And third, they should be accomplished at a reasonable cost. (See Figure 1.)

- **Demonstrate technology development mission objectives**
  - **Deployment and assembly of LSS**
  - **Installation and checkout of subsystems**
  - **Installation of reflector surfaces**
  - **Precision control of LSS (pointing and figure)**
  - **Demonstrate human capabilities**
  - **Develop materials for LSS**
- **Provide long term benefits**
- **Emphasize the need for a Space Station**
- **Accomplish TDM's at a reasonable cost**

Figure 1

LSS TECHNOLOGY DEVELOPMENT MISSIONS

The three TDM's defined during this study and shown in Figure 2 are: 1) a Construction/Storage/Hangar Facility, 2) a Passive Microwave Radiometer, and 3) a Precision Optical System.

The Construction/Storage/Hangar Facility is a 18 x 28 meter truss platform and demonstrates the deployment of a planar truss and can serve as a permanent Space Station facility following its use as a large space structures technology development mission.

The Passive Microwave Radiometer is 100 meters in diameter and demonstrates the elemental assembly of a large space structure, the assembly of deployable structural components, and the installation of a membrane reflector system. Following its use as a LSS TDM, it has the potential of being used either as a testbed for the development of other technologies or as a scientific instrument.

The Precision Optical System has an aperture of approximately 10 meters and demonstrates the construction of high precision structure and the use and control of segmented optics. It can also be used for other technology development or as a working scientific instrument following its use as a LSS TDM.

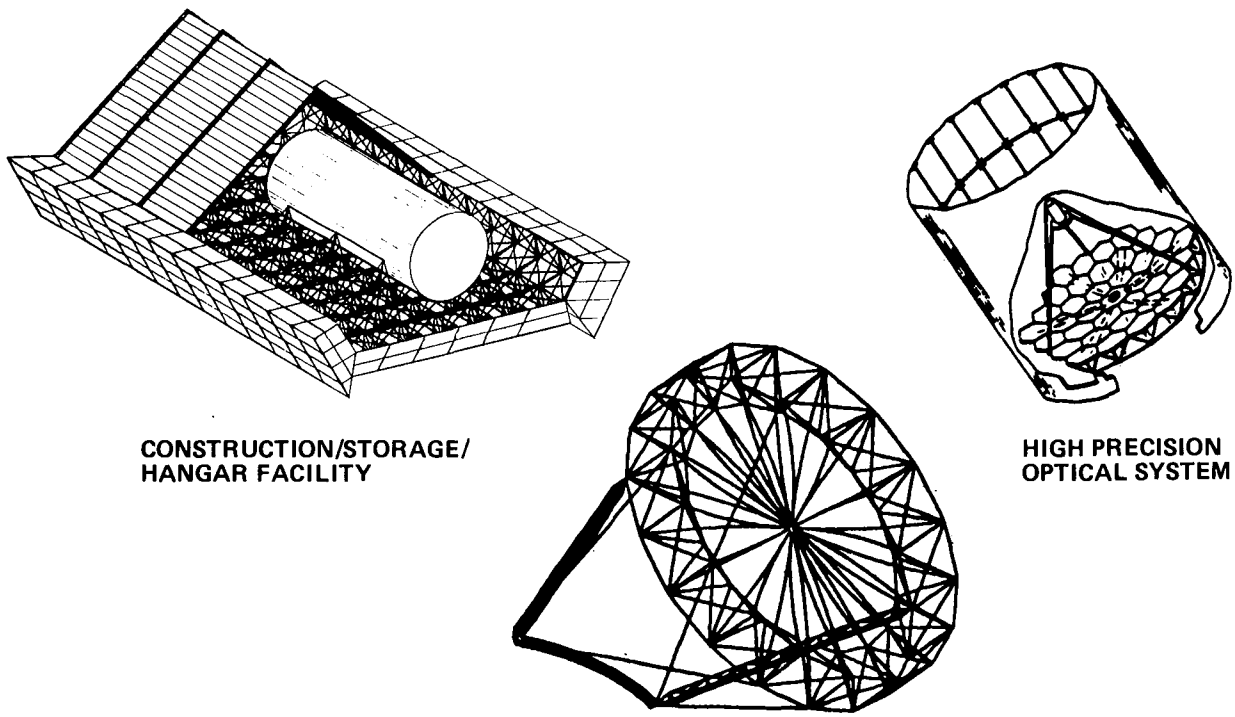

Figure 2

CONSTRUCTION/STORAGE/HANGAR FACILITY

The Construction/Storage/Hangar Facility is an 18 x 28 meter deployable pentahedral truss platform with raised edges as shown in Figure 3. It is connected at its center to a transfer tunnel which is attached to a Space Station berthing port. Although other attachment methods are possible, the early stage of Space Station design caused this "universal" attachment to be used. A pair of rails are attached to the truss using quadripod supports which mimic the Orbiter payload bay longerons so that large modules can be taken directly from the Orbiter and stored or serviced. Sections of the platform surface can be fitted with floor panels to serve as tie-down locations for smaller modules and equipment. A tracked manipulator or work station can be attached to the platform to aid in construction and servicing tasks.

The hangar consists of fixed, lightweight panels attached to the bottom and sides of the truss and deployable "roof" panels which serve to protect the EVA crew from solar heat and glaring sunlight. The hangar also acts as a containment facility which allows the crew to work untethered, and keeps small objects from drifting away.

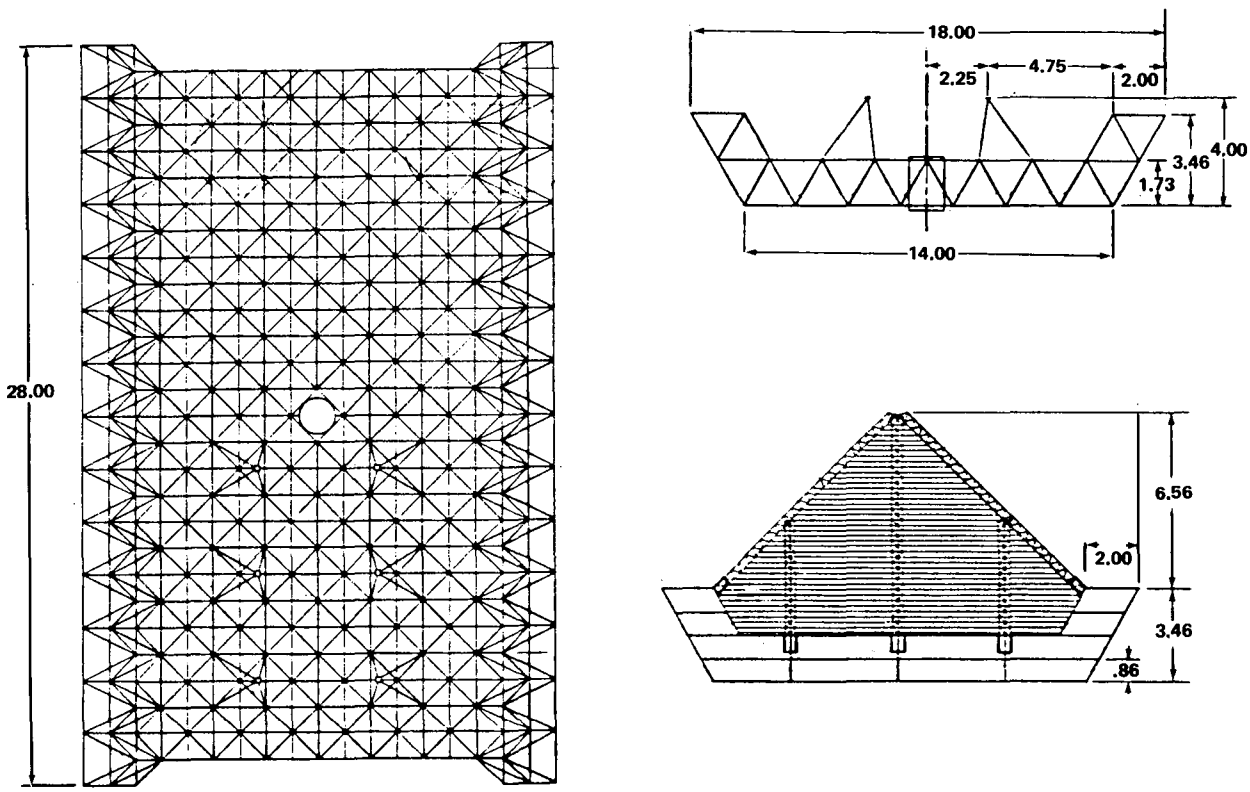

Figure 3

PLATFORM CONSTRUCTION SCENARIO

The construction scenario shown in Figure 4 begins with the attachment of the transfer tunnel to a berthing port. The truss, which is delivered in a 2.72 x 1.75 x 2.24 meter package, is then deployed and connected to the transfer tunnel. The payload support rails, floor panels, utilities, fixed and deployable hangar panels, etc. are then installed. Included in the 85 hours required to construct the platform are tests conducted to determine the dynamic characteristics, structural accuracy and thermal deformations of the platform at various stages of construction. These tests will broaden our knowledge of the behavior of deployable trusses in the space environment.

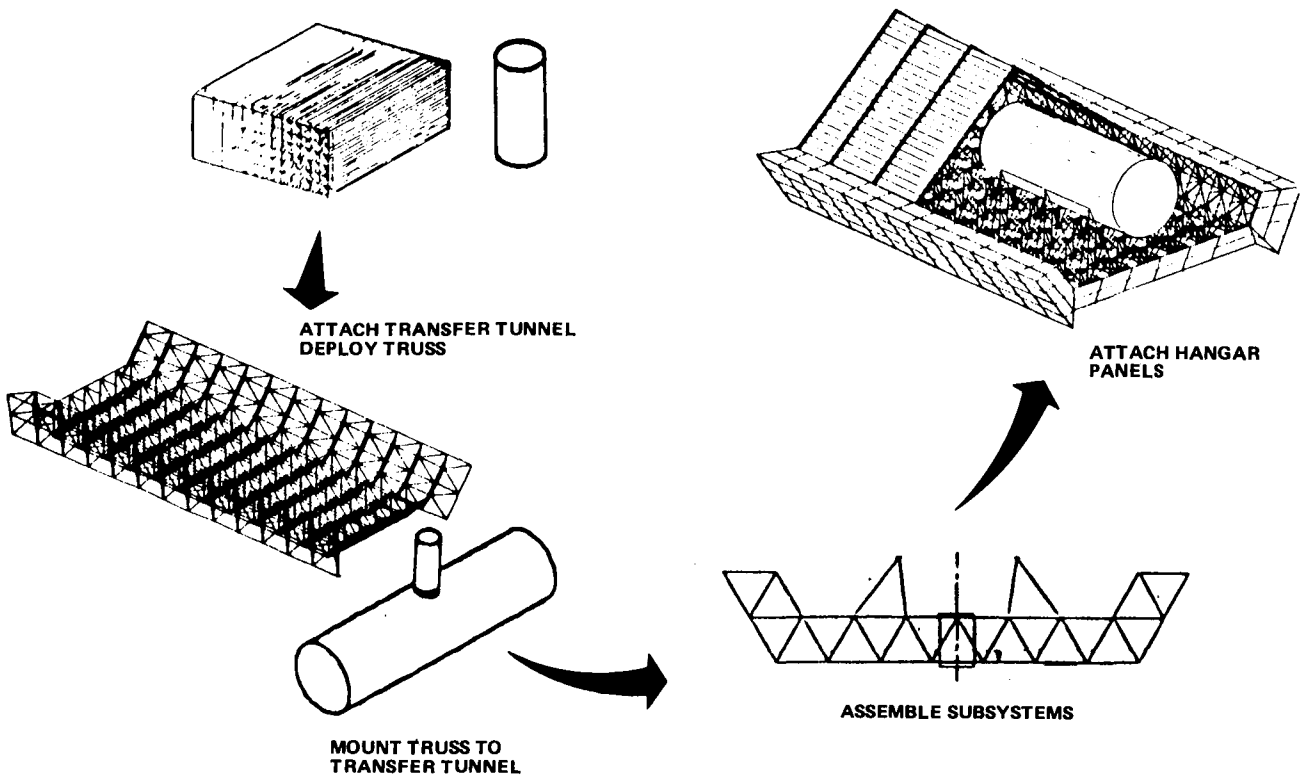

Figure 4

PASSIVE MICROWAVE RADIOMETER

The Passive Microwave Radiometer shown in Figure 5 is a 100 meter diameter antenna system which will demonstrate several LSS mission objectives. To provide maximum benefit, the antenna structure can be equipped with microwave sensors, electronics, power supply, propulsion and attitude control following its use as a technology development mission and used as an Earth sensing instrument. Or it can be used to develop reflector membrane technology and radiometry while attached to the Space Station.

The basic reflector support structure is an assemblable ring truss of pentahedral elements as shown. The structural members are tapered, nestable, graphite/epoxy struts 18 meters in length. Figure 5 also shows the strut configuration along with the center and end joints used in the construction. They are designed to eliminate all "slop" in the joints to insure high structural stiffness. The curved feed array structure and its supports are deployable truss beams which are braced using four graphite cables. A knitted, gold-plated molybdenum wire mesh reflector is stretched within the upper edge of the ring and is controlled by a network of actively controlled cables connecting the mesh with a series of radial cables attached to the bottom edge of the truss ring.

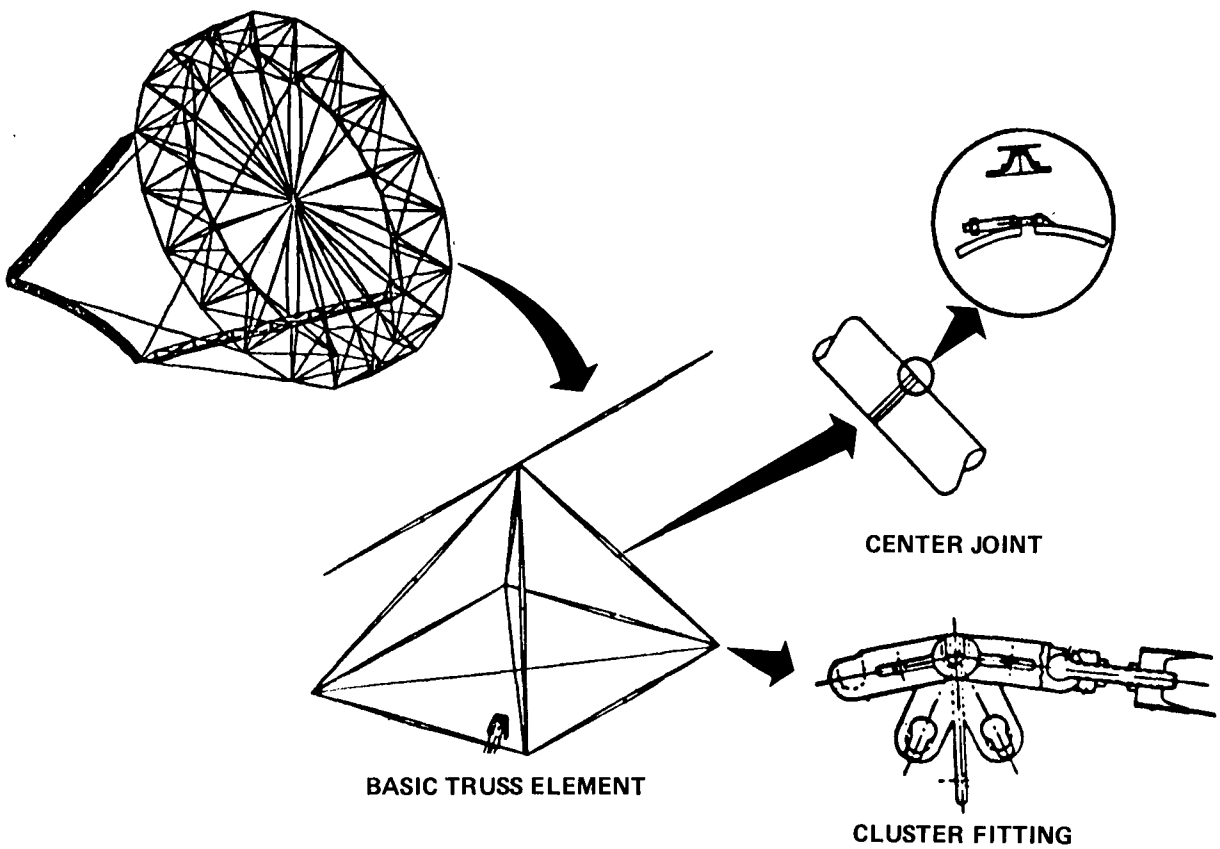

Figure 5

RADIOMETER CONSTRUCTION SCENARIO

The assembly of the radiometer structure is supported by the special construction fixture shown in Figure 6. It is a pair of curved rails attached by a series of tripods to the edges of the construction platform discussed earlier. The truss ring cluster fittings are attached to carriages on these rails and the ring is assembled, one module at a time. As each pentahedral module is completed, the truss assembly is indexed along the track so that the next module can be assembled. After the truss ring is completed, the feed array beam, its support beams and bracing cables are deployed and attached. The reflector mesh and its control cables are then installed. The construction of this structure requires 195 hours, which includes several tests to determine the structural accuracy, dynamic characteristics and thermal deflections at various stages of construction. These measurements will add to the knowledge needed for the construction of very large space systems at the Space Station.

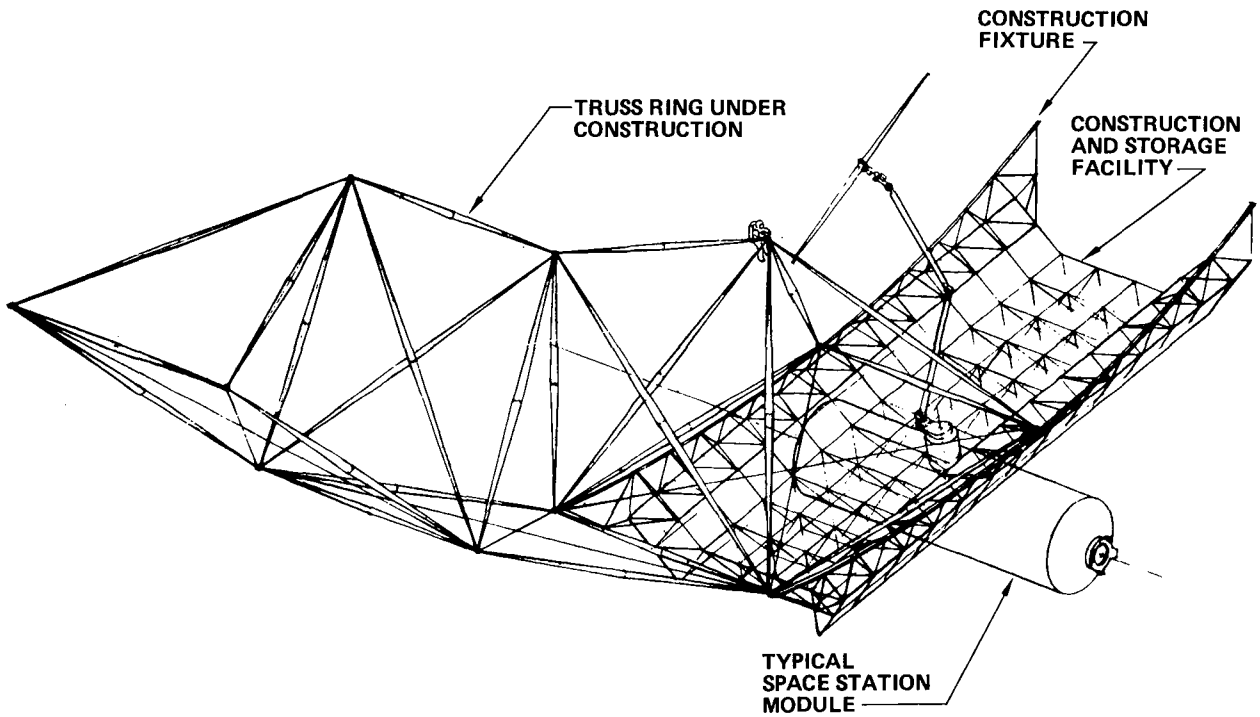

Figure 6

PRECISION OPTICAL SYSTEM

An optical spacecraft such as the one shown previously can be used to demonstrate the on-orbit construction of a large space structure which requires high precision and the use of segmented optics. The primary mirror assembly shown in Figure 7 consists of seven structural modules, each with seven hexagonal mirror segments. Each of the structural modules is a tetrahedral truss constructed using a combination of deployable and assemblable techniques. The upper surface of each module is a rigid framework manufactured to high precision, with the seven mirror segments attached on the ground. The lower surface is also a rigidly fabricated frame with the deployable diagonal struts attached to it. This allows the upper and lower components of each module, which are sized to fit within the 4.5 meter Orbiter bay diameter, to be packaged efficiently and still be made stiff. A trade study comparing the costs (including DDT&E, manufacture, transportation and on-orbit construction) of this modular construction method compared with deployable and assemblable concepts showed this to be a more economical construction method.

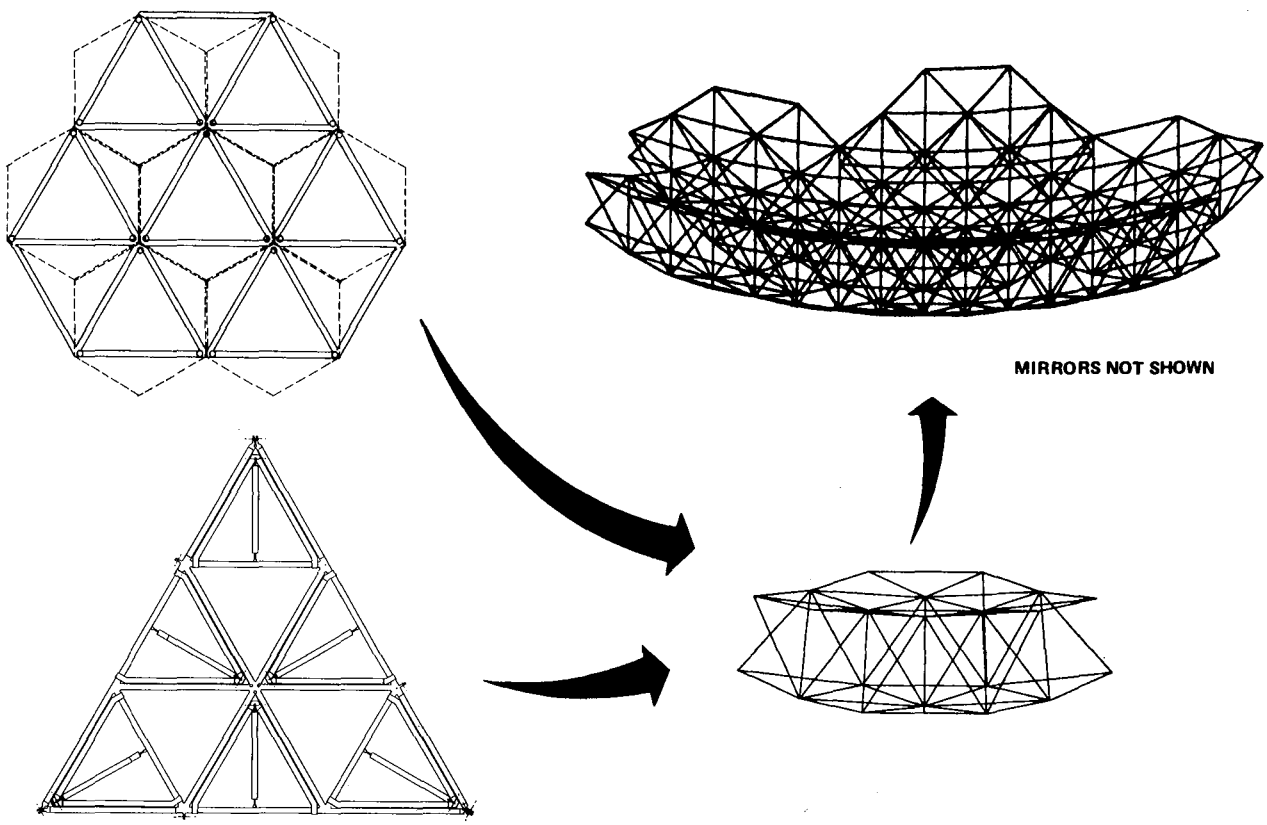

Figure 7

OPTICAL SYSTEM CONSTRUCTION SCENARIO

At the Space Station, each module is assembled by first deploying the diagonal members from the lower truss frame and then attaching the upper truss frame (with mirrors) to it. The modules are then attached together, as shown in Figure 8, to form the primary mirror assembly. The secondary mirror and supports are then attached followed by the light shield. Dynamic tests and accuracy measurements during the 200 hours of construction will be used to verify the characteristics of the structure and construction methods.

Following its use as a large space structures technology development mission, the assembly can be equipped with optical (or IR) sensors and mounted on a gimballed pointing system to be used while attached to the Space Station, or it could be completed as a free-flying optical system and separated from the Space Station.

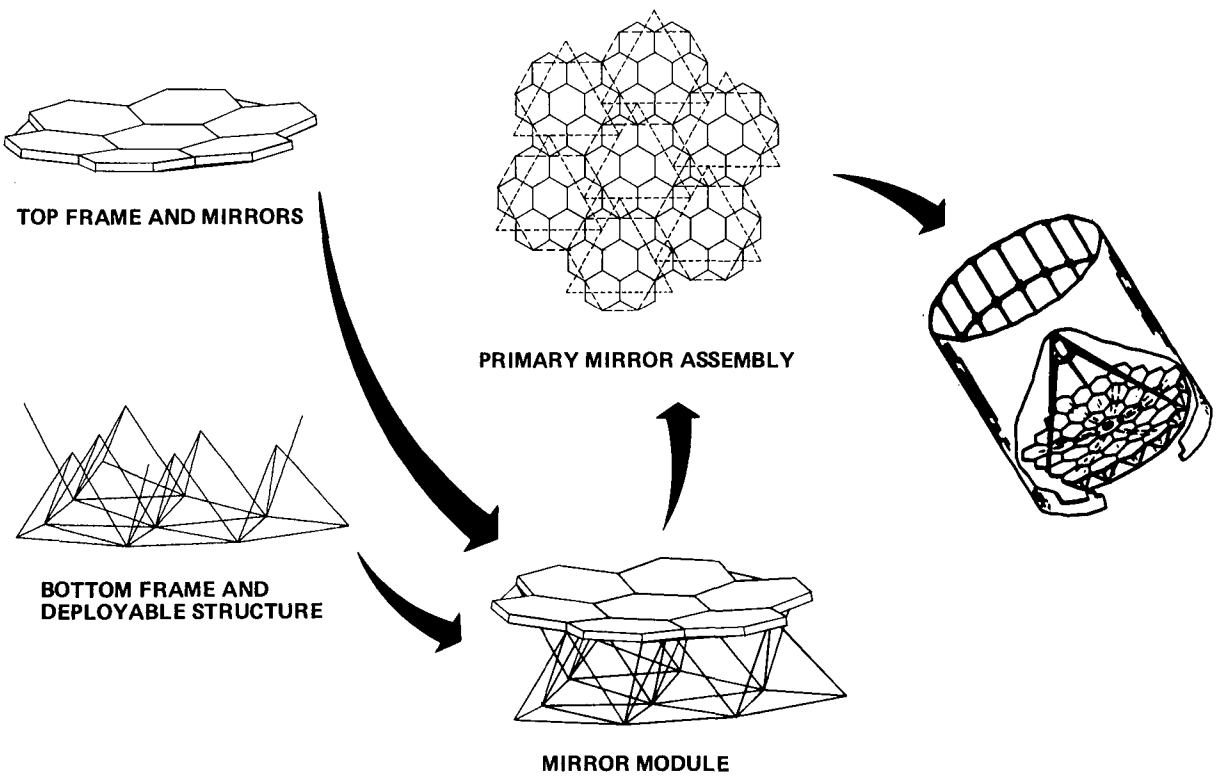

Figure 8

POTENTIAL PROBLEMS AND CONCERNS

These missions have helped to identify areas of concern which must be considered when constructing large space structures on the Space Station. In all cases, the mass and inertias of the projects as well as their structural dynamic characteristics must be accommodated by the Space Station control system. During the assembly of the radiometer truss ring, for example, the structural frequencies become lower and lower as more of the ring is constructed (Figure 9). When all but the last segment is completed, the first mode frequency drops to 0.1 Hz. Upon completion of the ring, the frequency increases to 0.25 Hz. The dynamic loads resulting from the additional mass must also be accounted for.

Another concern created by LSS construction is the increased frontal area which increases the rate of orbital decay due to drag. The orientation of the structure can have a pronounced effect on the drag. For instance, if the radiometer reflector is a continuous membrane and is oriented perpendicular to the flight path, the frontal area of the Space Station will be increased by more than 450 percent. The large size of the structures may also influence the thermal balance of the Space Staiton and interfere with communication paths.

These and other concerns raised by the construction of large space structures affect a wide range of technologies and subsystems and need to be carefully considered in the design of the Space Station as well as in the design of the construction project.

- **MASS PROPERTIES**
- **DRAG**
- **LOADS AND DEFLECTIONS**
- **STRUCTURAL DYNAMICS**

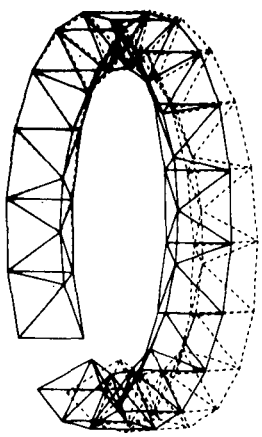

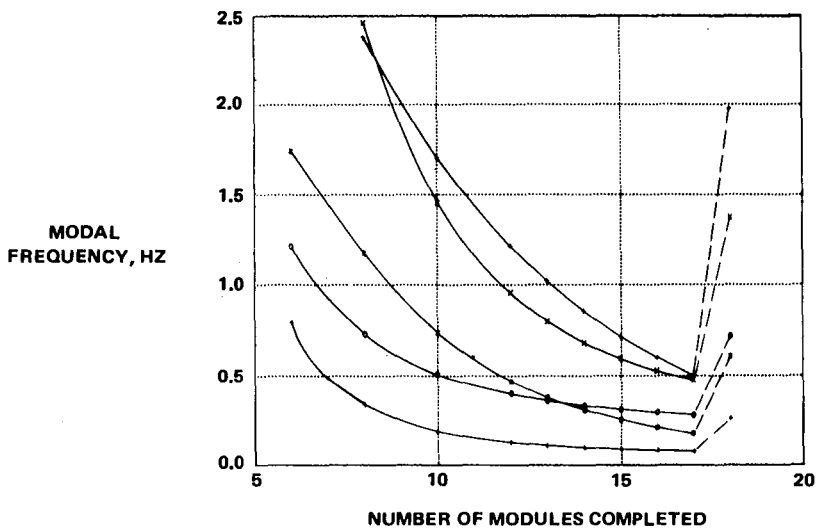

Figure 9

SPACE STATION ACCOMMODATIONS

These technology development missions were used to identify the accommodations that the Space Station must provide to support the construction of large space structures. First, it must have a large construction platform or other attachment provisions with an adequate volume to support the project. It must also provide adequate storage areas for parts, tools, components and other equipment needed. The construction area must be easily accessible for EVA support, and it must provide utilities such as power, lighting, data lines, TV, communications, etc. Certain test equipment such as laser ranging equipment and dynamic test equipment should be included in the collection of standard Space Station equipment so that it can be used for a variety of projects. A remote manipulator (either fixed, mobile or tracked) is necessary to move and position structural components, equipment and personnel during construction. And, as previously mentioned, the Space Station must be able to accommodate the increased mass, inertias and dynamics resulting from LSS construction. (See Figure 10.)

- **Construction platform or attachment provisions**
- **Large clearances**
- **Airlock near construction area**
- **Utilities (power, lighting, etc.)**
- **RMS or MRMS capability**
- **Capability to accommodate additional mass, area & flexibility**
- **Support equipment (fixtures, aids, etc.)**
- **Instrumentation (alignment, loads, dynamics, thermal)**
- **Data Systems (recording, storage, manipulation, downlink)**
- **Small tools**

Figure 10

CONCLUSIONS

Future space systems will require the development of the facilities and techniques needed for the on-orbit construction of large space structures. The logical place for this task is the Space Station which can supply the needed human and physical resources. We need to start now to design into the Space Station the facilities and accommodations required for these projects. Space system designs must also reflect the availability of a construction site in low Earth orbit and the valuable human resource which can reduce the complexity and expense of future systems. (See Figure 11.)

The large space structures technology development missions described can serve to advance the design and operational techniques for LSS construction at the Space Station. These missions provide a logical progression from ground tests and Orbiter flight tests. They can also be used as testbeds to support the technology advancement of other disciplines.

- **LSS construction at the Space Station can reduce costs and risks**
- **TDMs provide logical progression from ground and orbiter flight tests**
- **Provision for LSS construction must be designed into the Space Station**

Figure 11

Page intentionally left blank

UTILIZATION OF SPACE STATION BY THE LARGE DEPLOYMENT REFLECTOR

L. W. Bandermann and W. H. Alff

Lockheed Missiles & Space Company, Inc.
Research and Development Division
Palo Alto, California

Large Space Antenna Systems Technology - 1984
December 4-6, 1984

INTRODUCTION

The Large Deployable Reflector (LDR) is a NASA concept of a very large, orbiting, far-infrared to sub-millimeter telescope (diffraction limited at 50 μm). To be launched in the 1990s, LDR has a projected life of 10 years and is to be serviced every 2 to 3 years. Lockheed is currently conducting a System Concept and Technology Definition Study of LDR for NASA Ames. Of particular interest is the utilization of Space Station (SS) by LDR.

Study results indicate that launch of a 20-m LDR, operating in a 700- to 800-km orbit, requires two shuttle loads. The components of LDR are assembled in a lower parking orbit, and the system is checked out and then transferred to the operational orbit. Furthermore, for servicing, LDR may have to be retrieved to the same lower orbit (and later returned to operational altitude) by an orbit transfer vehicle.

These requirements bring up the question of a suitable assembly, checkout, and servicing platform. The deployment process is time consuming and may require special equipment not necessarily available from the orbiter itself. The SS is an attractive choice for that platform.

ADVANTAGES OF USING SPACE STATION

Several advantages derive from utilization of the SS by LDR:

1. Use of SS by LDR lessens constraints on LDR weight and volume and permits a more flexible schedule for launch and deployment. Various components of LDR - major ones being the telescope plus spacecraft and the sunshade - can be brought to SS on several STS trips. This activity can be coordinated with the deployment of other payloads to SS in order to minimize LDR launch costs.

2. SS provides a convenient and protected storage environment for the LDR components from which the components can be retrieved at a convenient time for checkout and assembly of the system.

3. Because of the severe time and work constraints of orbiter crews, it is presently difficult to see how a 20-m LDR could be assembled cost effectively and with minimum risk using only orbiter facilities. LDR is a very large and complex system for which the initial alignment and checkout could be quite tedious. The primary mirror, for example, consists of a minimum of 30 segments which are positioned on a metering truss by actuators. The sunshade, whose dimensions are typically 30 m by 30 m, must be deployed and attached to the telescope itself. Finally, there are eight separate science instruments with a variety of service requirements including cryogenics. It seems likely that any time constraints would interfere with the safe, precise, and efficient execution of any of these activities.

4. If cryogens and propellants are available at SS, it may be possible to transfer these to LDR at SS rather than on the ground, and the total cryogen and propellant requirements of LDR will be limited by the two to three reservicing intervals rather than the total 10-year lifetime, thereby reducing the total LDR on-orbit weight, volume, and inertia.

5. During assembly, checkout and servicing, the technical crews will have at their disposal greater communications facilities and equipment than those of the orbiter, as well as the electrical power of SS.

CONCEPTUAL DEPLOYMENT SCENARIO USING THE SPACE STATION

Presently, we envision the transport of the telescope and spacecraft in one payload to SS, and the sunshade in a second load. A possible method of transferring the components to SS is by unloading and tethering them at a distance (200 to 300 ft) from the SS and then pulling them to the storage or assembly station. Assembly is likely to be at a turntable attached to the SS spline (Figure 1), so that assembly can proceed with a minimum of operational constraints, e.g., LDR can be rotated such that placement of components and work on subsystems can proceed with maximum convenience and at minimum risk to the working crew.

Upon assembly, the LDR can be transferred to a neighboring orbit (or tethered from the SS) for final checkout. During this interval, the system is allowed to cool down to operational temperatures, and some initial measurements with the various instruments can be made. Upon satisfactory completion of the measurements, the

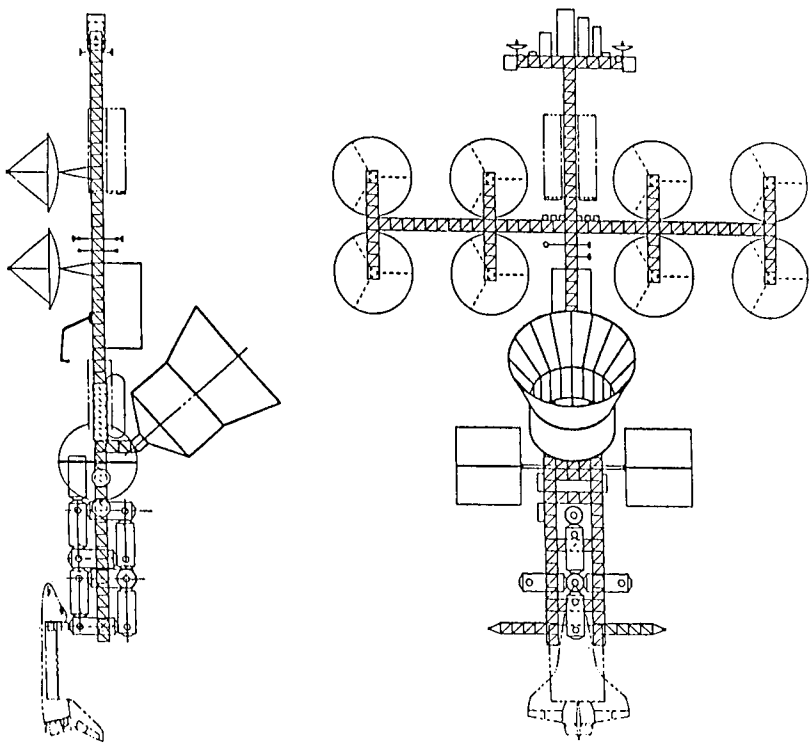

Figure 1

system is then transferred to the operational orbit using a vehicle such as the upper Centaur stage as Orbit Transfer Vehicle (OTV). The exact requirements for the transfer are not yet definite, since neither the orbital altitude of SS or LDR nor LDR weight has been finalized. LDR internal propulsion will probably be limited to station keeping and will use a cold gas to minimize contamination of optics.

POSSIBLE PROBLEM AREAS

There are two possible problem areas in the utilization of SS by LDR. First, contamination of LDR optics and other critical surfaces by the SS environment is of concern because the assembly area for LDR is likely to be near and above the STS docking area and SS habitation module. Contamination rises with each arrival and departure of the shuttle, and it falls in the intervening intervals. Quantitative assessment of these effects with respect to LDR is very difficult to make at this point, since the contamination level at SS as a function of time is not precisely known, but the issue must be kept in mind. Contamination threats will be minimized if special contamination-free compartments are available on SS.

Second, since LDR is a very heavy payload - possibly 10 to 15 percent of the weight of the Final Operational Configuration (FOC) of SS - there will be a dynamic interaction of LDR and SS which needs to be controlled and kept to a minimum. Particularly, there may be a problem during the alignment and checkout of LDR at SS. This is a reason that final checkout at a distance from the SS (possible on a tether) has been suggested. We are examining these and other issues in further detail in the present and future studies.

ACKNOWLEDGMENT

This work was carried out as part of contract NAS2-11682 for NASA Ames.

LARGE DEPLOYABLE REFLECTOR (LDR) REQUIREMENTS FOR SPACE STATION ACCOMMODATIONS

David A. Crowe
Michael J. Clayton
Eastman Kodak Company
Rochester, New York

Fritz C. Runge
McDonnell Douglas Astronautics Company
Huntington Beach, California

Large Space Antenna Systems Technology - 1984
December 4-6, 1984

(Produced under NASA-Ames Contract NAS2-11861)
(Technical Monitor: Bruce Pittman)

ession on
Systems and Space Station

NASA/Langley Research Ce.
December 6, 1984

LARGE DEPLOYABLE REFLECTOR OBSERVATORY

The objectives of this presentation are to develop top level requirements for assembly and integration of the LDR Observatory at the Space Station.

Concepts are currently under study for LDR which will provide a sequel to the Infrared Astronomy Satellite and the Space Infrared Telescope Facility. LDR will provide a spectacular capability over a very broad spectral range.

The Space Station will provide an essential facility for the initial assembly and check-out of LDR, as well as a necessary base for refurbishment, repair and modification.

By providing a manned platform, the Space Station will remove the time constraint on assembly associated with use of the Shuttle alone. Personnel safety during necessary EVA is enhanced by the presence of the manned facility.

OBJECTIVE:

PROVIDE TOP LEVEL REQUIREMENTS FOR ASSEMBLY AND INTEGRATION OF THE LDR OBSERVATORY ON THE SPACE STATION

KEY ASSUMPTIONS:

- **20 METER SEGMENTED PRIMARY MIRROR**
- **MULTIPLE SHUTTLE LAUNCHES**
- **EVA ASSEMBLY**
- **PERIODIC REFURBISHMENT**

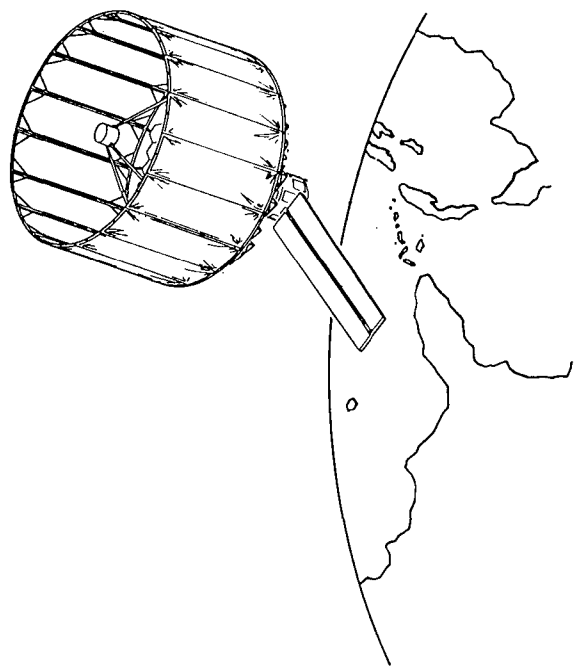

CRITICAL SPACE STATION ISSUES

At this point in time, it appears as though four critical issues related to the LDR Observatory/Space Station exist.

Personnel safety is an issue because of the amount of EVA that will be required to assemble and test LDR. A corollary to personnel safety is the issue of hardware integrity. The concern here is to prevent damage and contamination of the optics, structure and instrument package during assembly.

Contamination is a serious concern because of the need for LDR to function as an optical system with fairly stringent requirements on the blur circle size, dictating that control over surface contamination be maintained. In addition, because the focal plane instruments will be cooled, care must be taken to prevent contamination by gaseous and particulate materials.

Alignment and testing of the optical system will require a great deal of attention to assure that system performance goals will be met. The key alignments are listed. Methods and metrology must be developed.

Cryogenics is critical because of the required operating temperatures and lifetimes. These impact required technology development and consumables that must be stored onboard the Space Station.

- **SAFETY**
  - **PERSONAL**
  - **HARDWARE**
- **CONTAMINATION**
  - **OPTICS**
  - **FOCAL PLANE**
- **ALIGNMENT/VERIFICATION**
  - **SYSTEM TO SYSTEM**
  - **PRIMARY MIRROR TO SECONDARY MIRROR**
  - **INSTRUMENTS/SYSTEMS**
  - **SPACECRAFT**
- **CRYOGENICS**
  - **VOLUME**
  - **INITIAL COOL DOWN**
  - **REFURBISHMENT**

SPACE STATION REQUIREMENTS

Of the requirements listed here, perhaps the most controversial and uncertain is the contamination requirement. A class 100,000 environment is commonly used for optical systems of the LDR category. However, specific data on the nature and magnitude of contamination as well as its effects is required.

LDR must be provided with adequate electrical power, support equipment, cryogenics, and telemetry for data transmission. In addition, optical test and alignment will require an isothermal, vibration isolated environment.

• POWER	6500 WATTS
• MASS	PRIME 50,000 KG
	SSE 25,000 KG
• VOLUME	
ASSEMBLY	$\approx$ 30,000 M^3
STORAGE	$\approx$ 2,500 M^3
• ENVIRONMENT	
VIBRATION ISOLATION	DECOUPLED/CONSTRAINED
ILLUMINATION	SOLAR/LOCAL
TEMPERATURE	ISOTHERMAL 200° $\pm$ 5° K
PRESSURE	SMALL POSITIVE PRESSURE
• CONTAMINATION CONTROL	EQUIVALENT CLASS 100,000
• SUPPORT EQUIPMENT MAINTENANCE AND CONTROL	TBD
• DATA TRANSMISSION	TBD (TDRS LIMITATION)
• CRYOGENICS	STORAGE/HANDLING

OBSERVATORY ASSEMBLY

The assembly flow sequence shown schematically here is intended to reflect a basic philosophy: As much manufacturing and assembly will be accomplished on the ground as possible; assembly will be accomplished inside a contamination controlled environment; final performance verification will be obtained only after deployment.

GROUND FACILITY

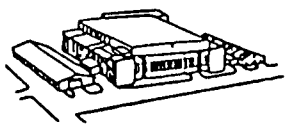

- Mirror Module Manuf.
- Test
- Manuf. Primary Reaction Structure
- Fabricate Instr. Module & Spacecraft

LAUNCH

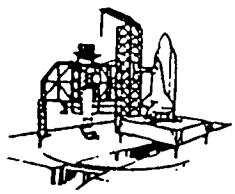

SPACE STATION

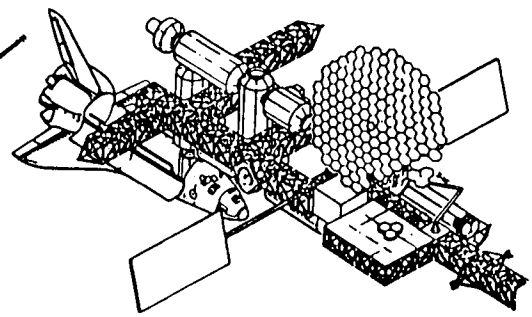

- Assemble Shroud
- Assemble/Align Primary
- Assemble Secondary & Structure
- Align Primary/Secondary
- Sun Shield
- Align/Test, Integrate, Functional Test

ORBITAL DEPLOYMENT

- Orbit Insertion
- Final Functional Test
- Performance Ver.

In summary, we would point out that utilization of the Space Station for LDR assembly and checkout eliminates the need for construction of an unmanned platform to accommodate the construction of LDR.

The presence of the Space Station eliminates time on station constraints associated with the use of the Shuttle and an unmanned platform for assembly. An LDR assembly crew can be in continuous residence on station.

Refurbishment, repair, and modification of the LDR Observatory will be greatly simplified with the presence of the Space Station.

Personnel safety is enhanced by having a habitable, manned station for use while assembly takes place.

- **EXISTING INTEGRATION PLATFORM**
- **INTEGRATION TIME CONSTRAINT RELIEVED**
- **REFURBISHMENT**
- **SAFETY**

LDR ON SPACE STATION

The LDR flight system will be assembled at a particular position on the back of the lower keel of the Space Station. This exterior position is assigned for large structure assembly in general and suits the LDR in particular.

LDR specialists as well as assembly control and checkout equipment will be located in one of the LAB modules at the lower portion of the Space Station.

Two LAB modules and two HAB, or habitation modules, make up the IOC pressurized modules. In addition to Astrophysics activities in the LAB modules, there will be Life Science, Earth Science, Materials Processing, Spacecraft Servicing, Vehicle Launching, Technology Development Test and a variety of other activities in a constantly changing customer scenario throughout the life of the Space Station. Shuttle visits to the Station are planned to be every 90 days.

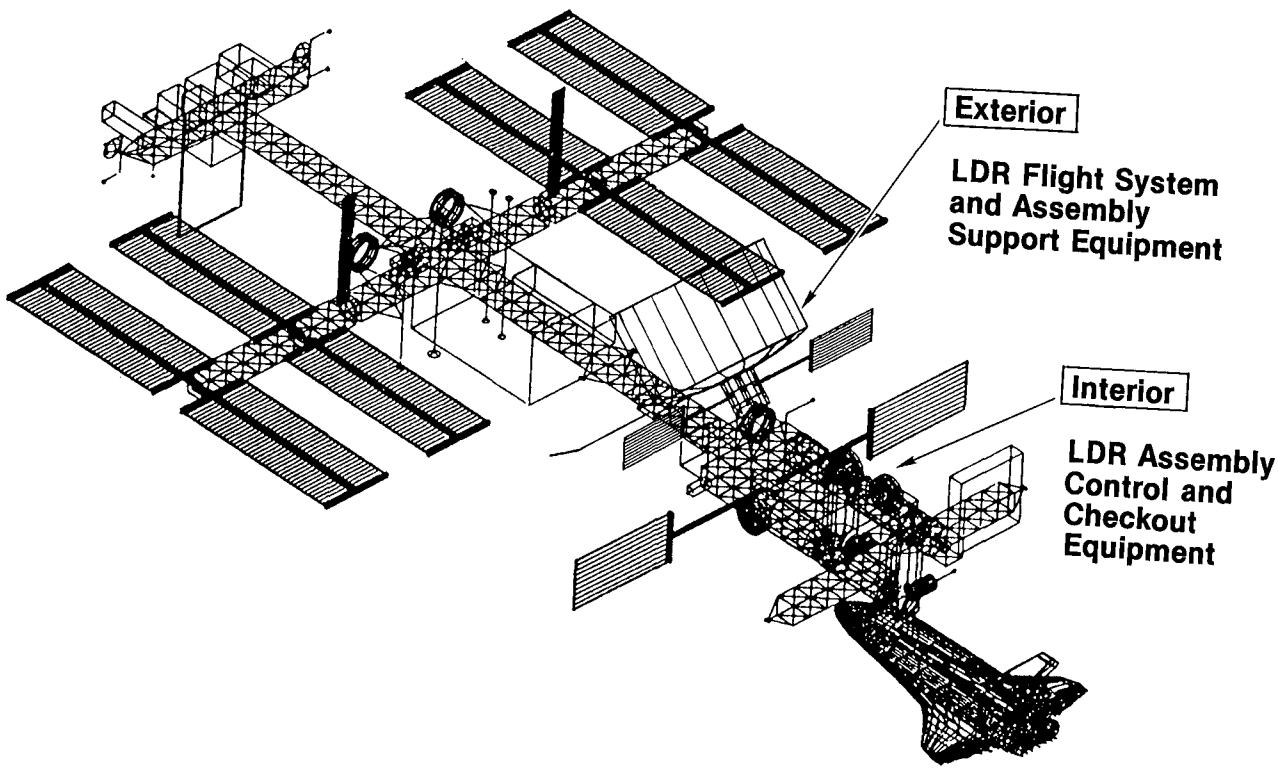

LDR SPACE STATION CONFIGURATION

LDR elements will be delivered by the Shuttle and integrated with Space Station in a variety of ways. LDR flight system elements will be packaged (and in some cases, protected against contamination) in the Shuttle cargo bay and removed and stowed on the Station by the combined use of the Shuttle and Station remote manipulators. LDR equipment which ends up installed in the LAB module is delivered in the Space Station logistics module and crew-transferred through one end of the Habitat module to its destination in LAB #1. Construction viewing is provided by a combination of Station TV coverage, EVA astronaut on-site witnessing and LAB #1 window utilization. Logistics of the entire LDR operation, covering all parts and procedures, will utilize the Space Station logistics system which begins with pre-launch ground preparations, tracks all orbit transfer/stowage/disposition and ends with return to earth of any LDR elements.

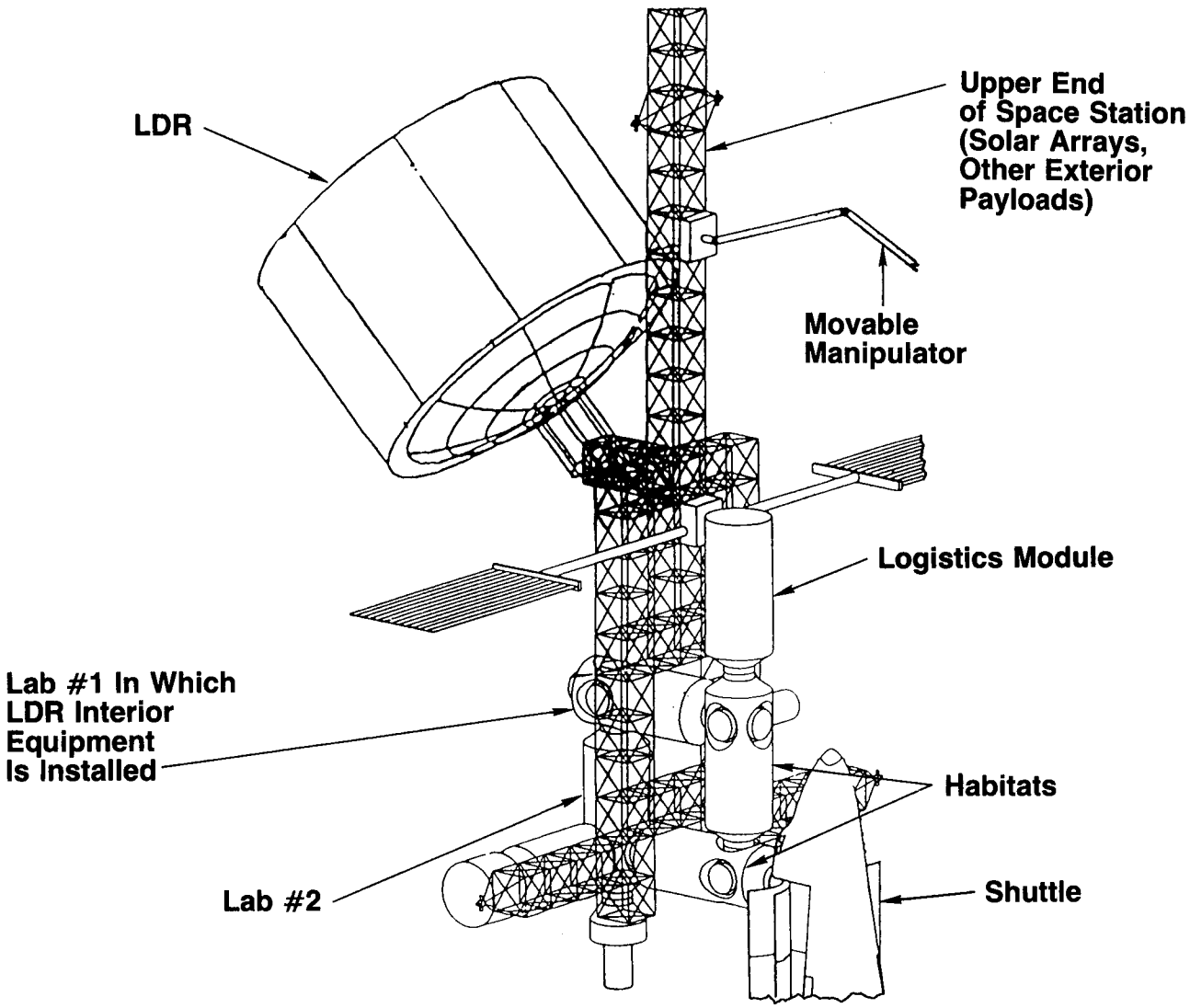

FIRST LDR ELEMENTS DELIVERED
BY SHUTTLE

The LDR flight system elements will be delivered to the Space Station for assembly in three to four Shuttle cargo loads. The first load will consist of the LDR spacecraft, the science instrument unit and the core mirror segments pre-assembled as a set into their flight configuration. This pre-assembled set will be extracted from the Shuttle cargo bay and moved along the Space Station keel structure (9 foot x 9 foot truss work) with a movable remote manipulator and installed on a two-tier cube truss which features a rotating tilt-table head, specifically for large structures.

The LDR assembly control and checkout equipment will delivered inside the Space Station logistics module (which is delivered/replaced every 90 days). That interior LDR equipment will be transferred by the crew through the Space Station hatch at one end of the habitation module and finally installed in the vertical racks of Lab Module #1 where Astrophysics activities are broadly assigned.

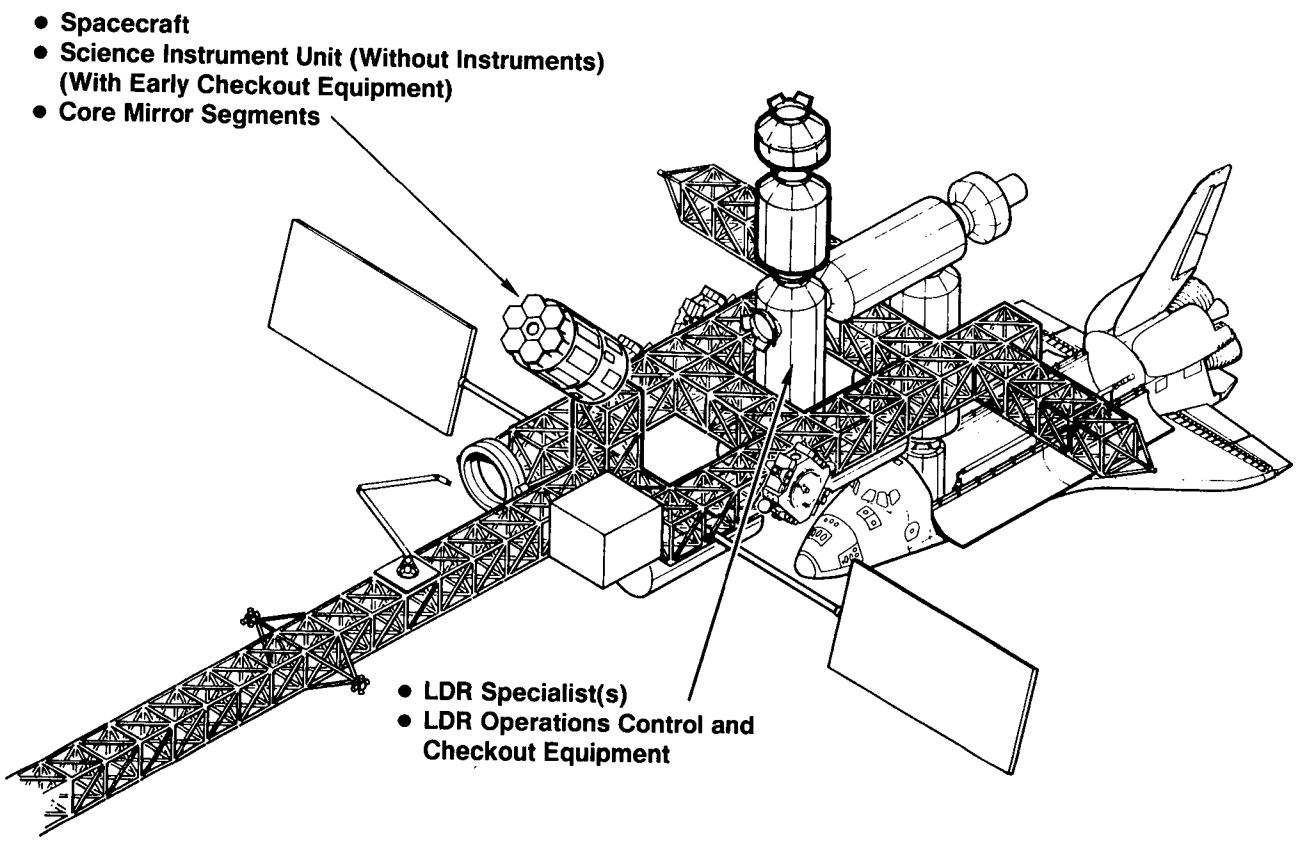

LDR MIRROR SET ASSEMBLY

Individual mirror segments will be transported to orbit in a special stowage rack in the orbiter cargo bay, and shrouded in some way to prevent contamination.

At the Station the rack of mirrors will be removed from the cargo bay, transferred to and installed in a position near the assembly location accessible to the assembly manipulator. Here, the contamination shroud will be removed and the mirrors extracted and assembled edge-to-edge at their support frames. Each mirror is actually mounted on three "piston and tilt positioning actuators" which are mounted on the support frame.

The movable remote manipulator is controlled by one EVA astronaut, while another assists in the actual latching or perhaps even bolting together of the mirror support frames.

Portable, temporary fixtures are used to support progressive checks and adjustments of the mirror positions and inter-mirror relationships.

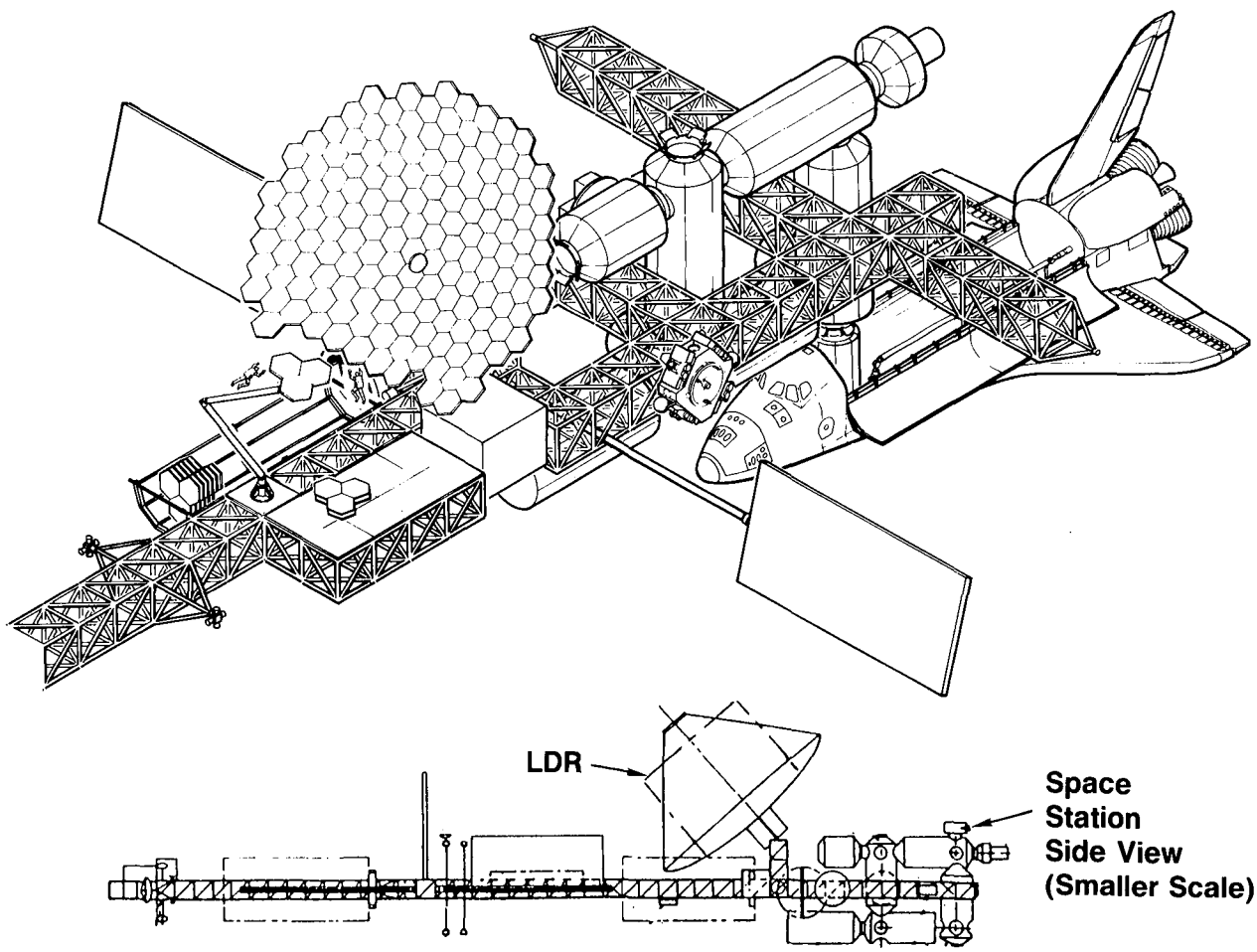

LDR MIRROR-SET BACK-UP
STRUCTURE ASSEMBLY

A complex trusswork provides the reaction structure for the mirror assemblage. This 20 meter diameter structure is divided into numerous orbit-assemblable segments for compaction and delivery in the Shuttle cargo bay. Its struts (which number in the hundreds) are graphite-epoxy tubes connected by a variety of a simple and complex joints.

The trusswork segments are "bundled" and stored in a carrier-cradle during Shuttle transport, and on orbit, the cradle is transferred to a location accessible to the assembly area/manipulator. Here it may be necessary to provide an auxiliary platform or fixture for intermediate truss deployment/rigidization prior to attaching each truss segment to the back of the mirror sets.

EVA support will probably be required for (1) the interim truss deployment/rigidization function as well as (2) the truss-to-mirror-set attachment, which may be a simple bolting function for optimum high-load/low-cost joining. Structural dynamics requirements call for high-load joints which are difficult to achieve with reasonable-cost, automated latch mechanisms.

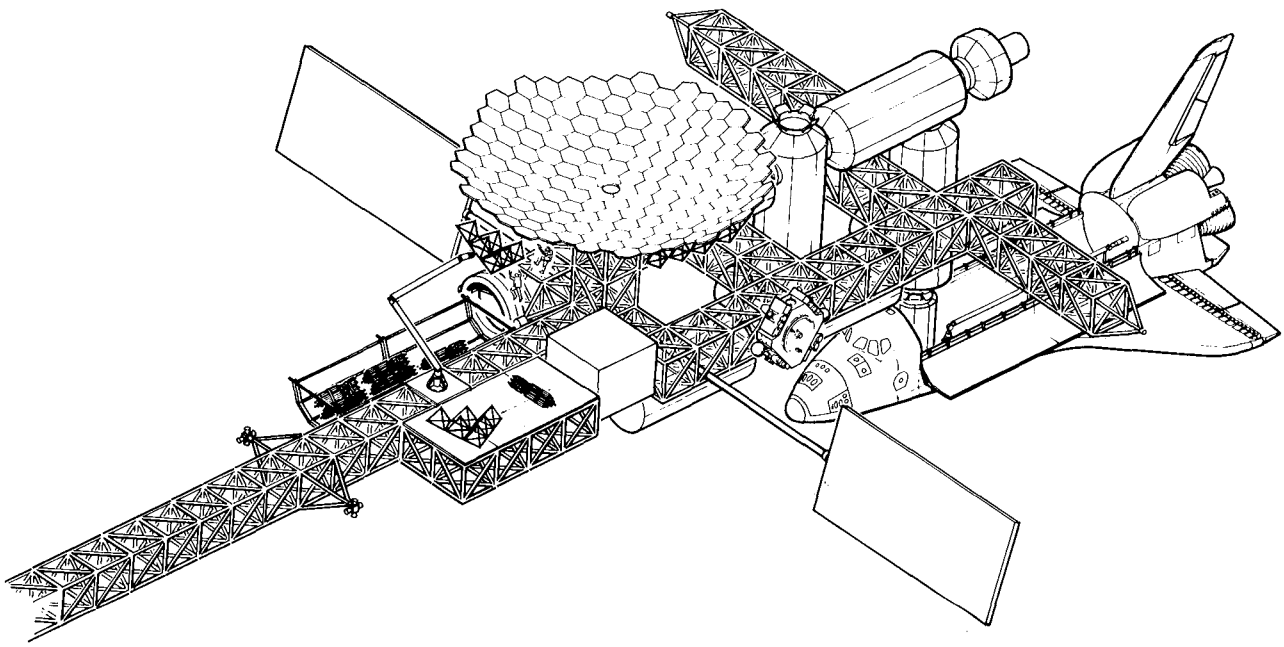

LSD SUNSHIELD AND SECONDARY MIRROR ASSEMBLY

Once the primary mirror segments are all assembled and a peripheral structural ring is added, assembly/erection of the sunshield and secondary mirror can begin.

The sunshield will probably consist of around 20 vertical sections of multi-layer insulation stretched between solid or deployable verticals, each erected individually. Also, there is a high likelihood that large radiators will be attached over two of the diametrically opposed sunshield panels. These radiators will be "plumbed" into a thermal control pump system located in the spacecraft using EVA. Another peripheral stiffening ring may have to be installed at the forward end (opening) of sunshield to suppress dynamics. This ring, as well as the lower one, would be brought to orbit in sections, in an orbiter bay cradle.

The secondary mirror unit and its supporting tripod would be assembled before or during the sunshield assembly. This unit is a complex assemblage of moveable optics, a cryogenic dewar, electronics and thermal control. The tripod would be delivered folded or disassembled. The complexity of LDR and other large assembly jobs may call for an operations monitoring cab as shown for various on-site support functions.

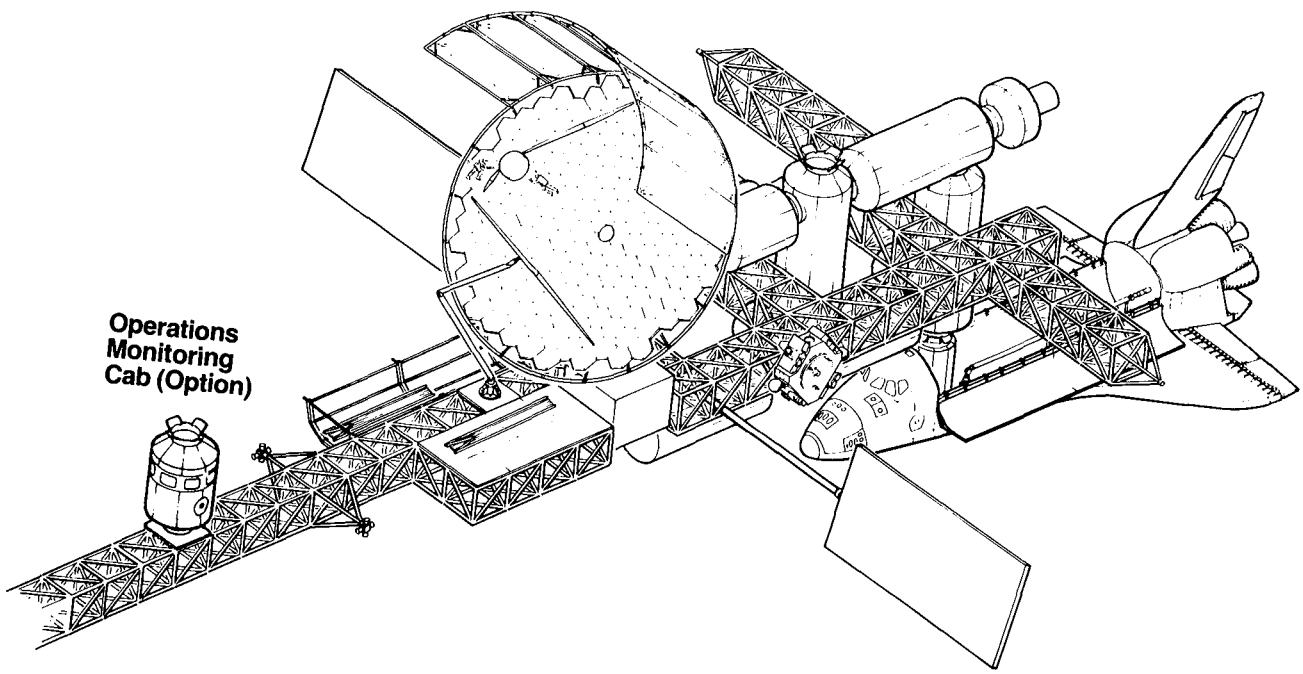

CONTAMINATION AVOIDANCE SHROUD

The LDR mirrors are sensitive to particulate and gas-film deposition; therefore, some LDR protection will be required against the environment around the Space Station due to visiting Shuttle reaction control system effluents, Station atmosphere leakage and a variety of other contaminants from Space Station and payloads.

Also, the incidence of sunlight on the LDR mirrors and structures during construction may counter the high-accuracy optical figure and element position measurements envisioned.

Therefore, there may be a requirement for some sort of environmental shielding, either fully or fractionally enclosing the LSD. This can be provided with a lightweight covered structure as shown below. In view of the expense involved in such a unique accessory, a study of the needs of other environmentally sensitive payloads or payload servicing functions should be analyzed before a design is selected.

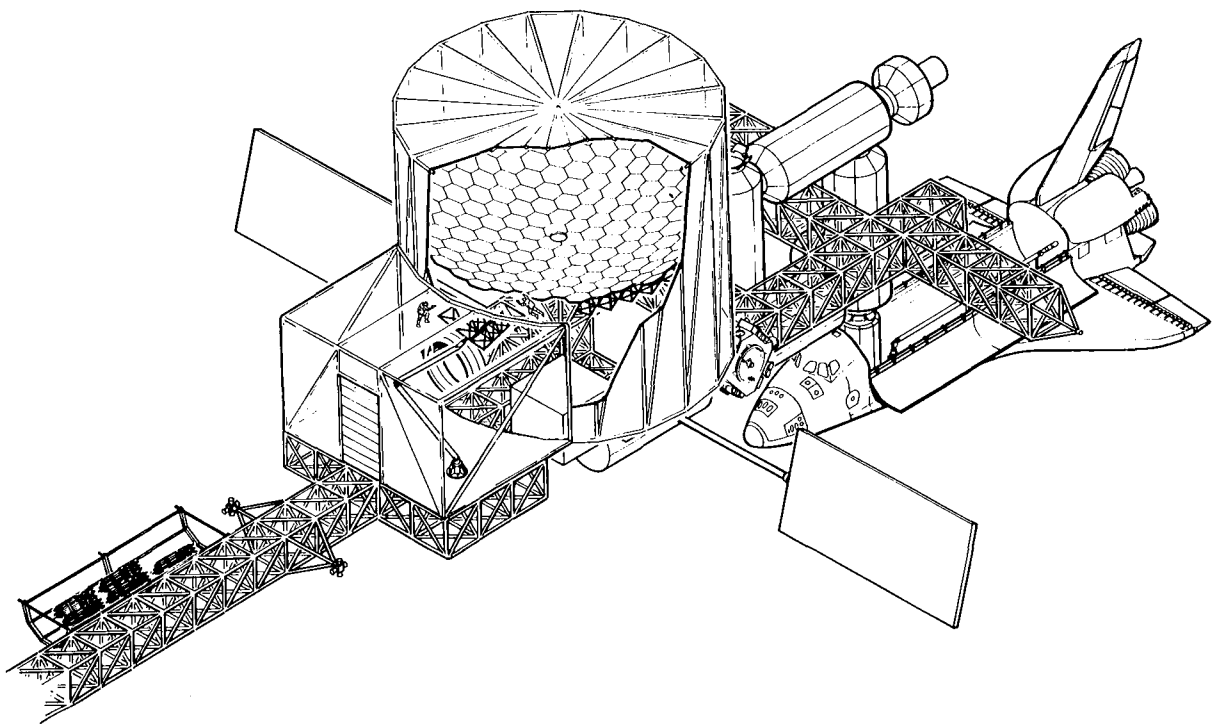

LDR INTERIOR EQUIPMENT INSTALLATION

Assembly, checkout and launch of the LDR on Space Station will be complex and perhaps long in duration (weeks, maybe months). The on-site control, monitoring, diagnosis and corrective action (when required) will be concentrated in LDR specialists and equipment located inside LAB #1 on the Space Station.

The LDR specialists and equipment will have been involved in LDR pre-flight testing on earth as will certain of the Space Station crew members who are assigned and trained specifically to support LDR activities.

The interior equipment (delivered in the Space Station Logistics module) is used to activate, control, record and diagnose data related to the entire LDR activity on Space Station.

Since the LDR will be brought up in "pieces," the checkout functions will involve a long series of progressively integrated steps. Some will involve temporarily "rigged" checkout fixtures, some fraction of subsystems, and finally an "all-up" integrated test, countdown and launch. This spectrum of activities is envisioned to require approximately the family of interior support equipment shown below.

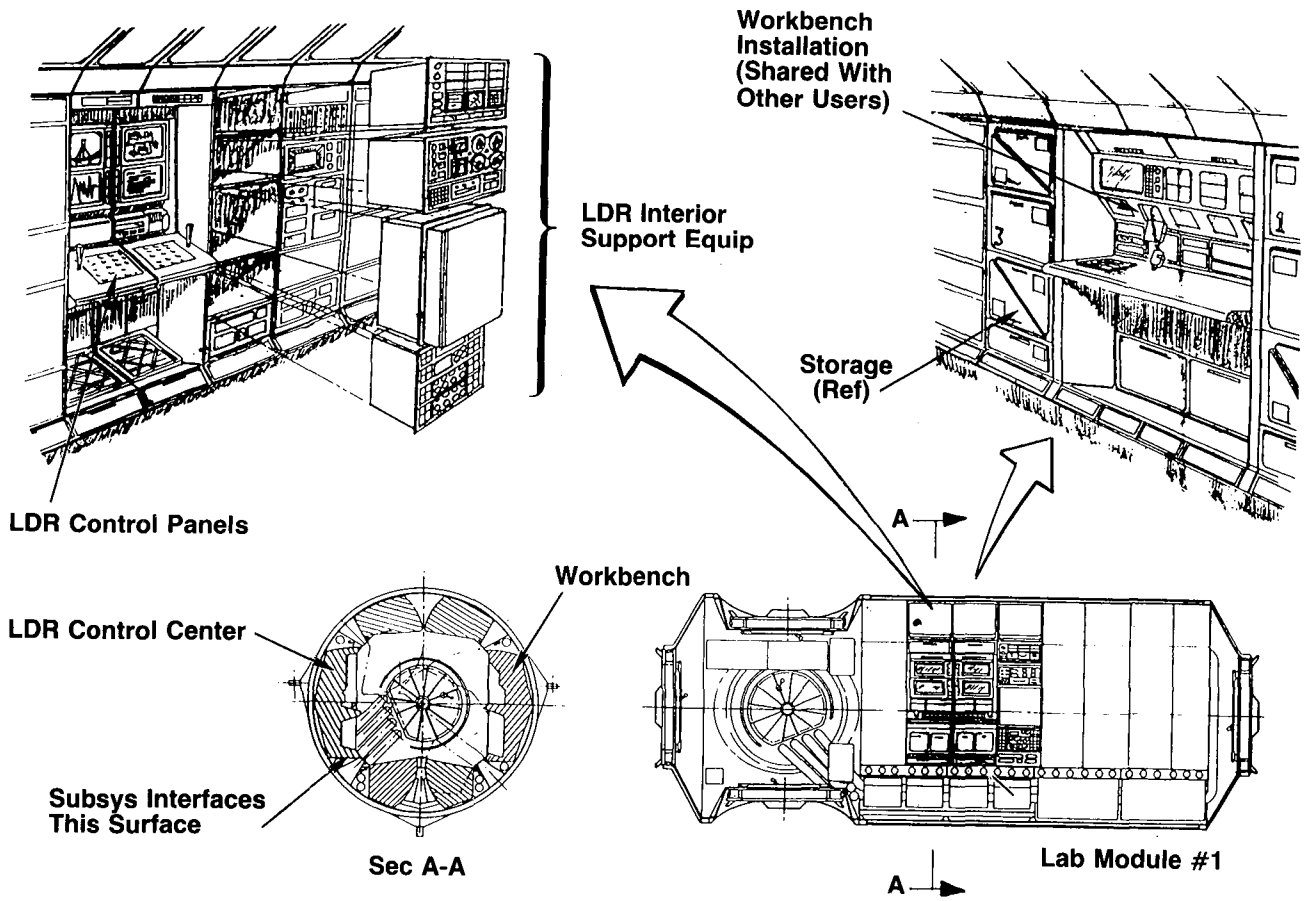

ORU EXCHANGE LOGISTICS MODULE
(OMV-BASED)

After being launched from the Space Station, the LDR will transfer to a higher altitude for sustained operations, propelling itself or being transferred by the OMV (Orbit Maneuvering Vehicle). LDR will operate on a self-sustaining basis, under ground mission control, for about two years, at which time some sort of servicing is anticipated; at least cryogens will have to be replenished. In the interim, some malfunctions may require earlier servicing. If the servicing can be provided by a "smart kit" on the front of an OMV, i.e., module exchanger as manipulator for other purposes, then on-orbit refurbishment will be possible, therefore not requiring the return of the LDR observatory to the Space Station.

The LDR subsystems and science instruments will be designed for on-orbit replacement, either remotely via OMV or under a major service need situation, back at the Space Station. The latter return to Space Station is only planned for a six-year cycle for major refurbishment/overhaul/update and also replenishment. In that cycle length, it is anticipated that the technology of detectors and science interests will be advanced to a degree which merits science instrument replacement.

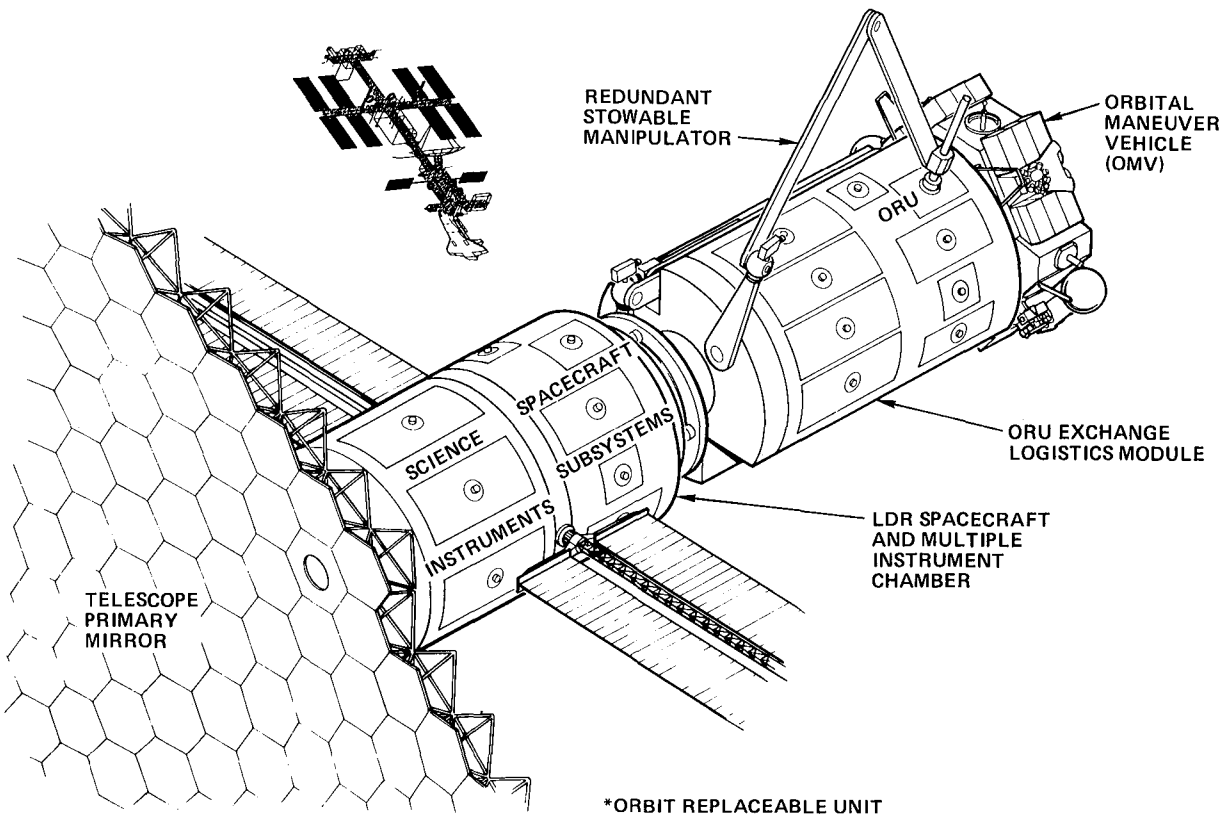

SPACE STATION TECHNOLOGY MISSIONS (FOR LDR)
(1993)

Well in advance of LDR assembly and launch at the Space Station, certain critical technologies, integrated subsystems and procedures will be tested on the Space Station.

Envisioning this need, the NASA Office of Aeronautics and Space Technology (OAST) is planning generic and system-oriented Technology Development Missions on Space Station, utilizing its unique capabilities for zero-g and other environment provision plus a crew-training base for real-situation exercises.

The Space Station Mission Model contains the two missions shown below which have definite LDR contributor potential. There are others for Figure Control, Structural Dynamics, etc. which apply to or may be focused on LDR technology advancement needs.

Beyond such technology testing there may well be a need for practicing certain critical LDR assembly and checkout operations in advance on Space Station for procedural and design certification and crew training.

Missions

- Telepresence Advanced EVA Technology TDM2460 (MRWG 2464)
- Assembly of Structures Using Teleoperation TDM2460 (MRWG 2461)

Objectives

- In Situ Simulation/Training
- Capability/Environment Establishment
- Performance Envelope Procedural Development

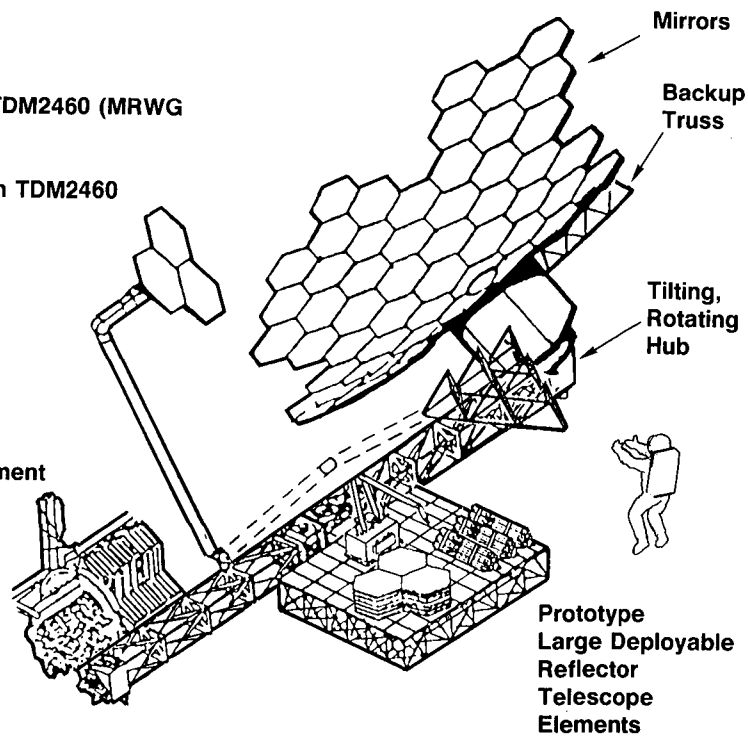

THE ORBITAL ASSEMBLY OF A LARGE ANTENNA*

D. Waltz
TRW
Redondo Beach, California

Large Space Antenna Systems Technology - 1984
December 4-6, 1984

*Paper unavailable at time of publication.

Page intentionally left blank

A CONCEPT FOR A MOBILE REMOTE MANIPULATOR SYSTEM

Martin M. Mikulas, Jr., Harold G. Bush,
Richard E. Wallsom, and J. Kermit Jensen
NASA Langley Research Center
Hampton, Virginia

Large Space Antenna Systems Technology - 1984
December 4-6, 1984

REFERENCE SPACE STATION CONFIGURATION

NASA has selected a gravity gradient stabilized space station concept as a reference configuration for further study. A drawing of the reference configuration selected is shown in Figure 1 with typical payloads attached. A major challenge with such a configuration is achieving access to all parts of the station. A movable platform with a Shuttle remote manipulator system (RMS) attached is shown attached to the "keel" truss structure, directly above the cylindrical modules. Such a platform could provide the necessary access to all parts of the station.

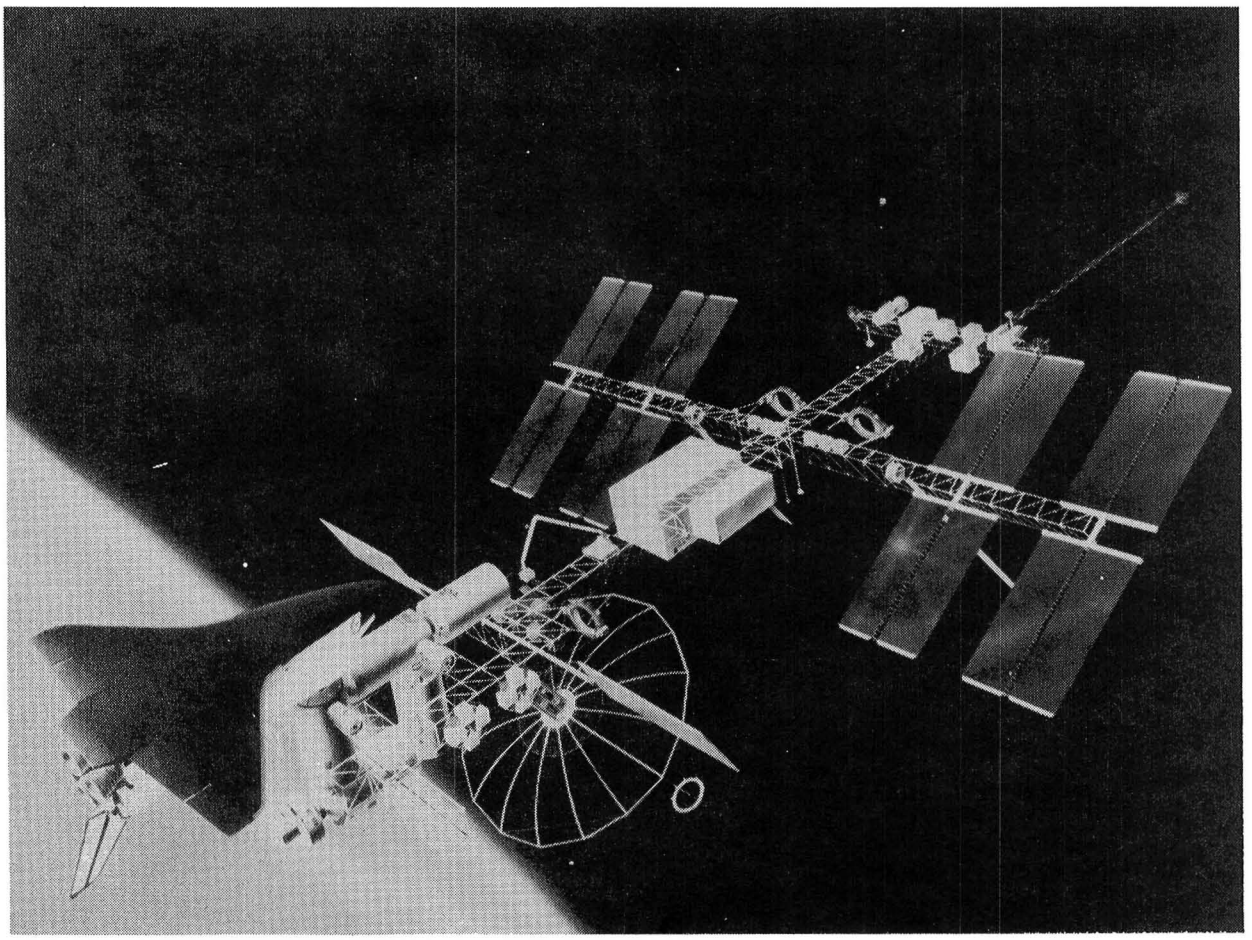

Figure 1

APPLICATIONS OF A MOBILE REMOTE MANIPULATOR SYSTEM (MRMS) ON SPACE STATION

Space station studies have identified the need for a mobile remote manipulator system (MRMS). Such a logistics or utility device is envisioned to be outfitted with a spacecrane capability (i.e., Shuttle RMS), and probably astronaut foot restraint positioning arms. The system is required during initial station construction activities to position astronauts for EVA functions, transport modules and/or payloads from the Shuttle cargo bay and position them for attachment to the truss structure. Subsequent to the initial space station construction activities, a mobile remote manipulator system is considered necessary for maintenance or repair activities, and to provide a construction capability for future station growth or large spacecraft assembly and servicing. The mobile platform which possesses the capabilities described above will be referred to as an MRMS in subsequent paragraphs. (See fig. 2.)

- INITIAL STATION CONSTRUCTION
- TRANSPORTATION AND ATTACHMENT OF PAYLOADS
- STATION MAINTENANCE
- SPACECRAFT ASSEMBLY
- SPACECRAFT SERVICING

Figure 2

MRMS MOBILITY REQUIREMENTS

The square bay truss structure of the reference space station configuration suggests the need for an MRMS which can move in two orthogonal directions. This capability permits movement (1) along the space station keel structure between the modules and the solar array support structure, and (2) perpendicularly along the solar array support booms. An MRMS with only unidirectional mobility theoretically could be rail mounted to accomplish this function but would probably need to be detached and reattached to additional orthogonal rails to move in a perpendicular direction--an operational drawback which probably should be avoided. Mounting rails onto the space station truss structure introduces additional mass and significant design complexity which also must be considered.

The lower mass alternative of positioning rails on the MRMS (instead of the truss) which "ride" on the truss hard points is possible. However, endless tracks (chains or belts) which provide mobility in this case must completely span two (2) truss bays to ensure stability of the MRMS during motion. Such an arrangement avoids the increased mass and complexity of rails attached to the truss structure and provides for a "smooth," continuous unidirectional motion capability. However, movement in a perpendicular direction is not enhanced, and the undesirable feature of an MRMS which must be two (2) bays in length is introduced. A two-bay-long MRMS presents Shuttle packaging problems and degrades maneuverabilty and, therefore, usefulness of maintenance and construction activities, particularly in close proximity to the modular habitats or surface attachment equipment. A conceptual design for a bidirectional MRMS which is only one bay square and avoids a truss mounted rail system is illustrated in figure 3.

A robotic walker ("spider") conceptually could serve as an MRMS and accomplish the necessary functions, but would require extensive development of a device which is not considered state of the art.

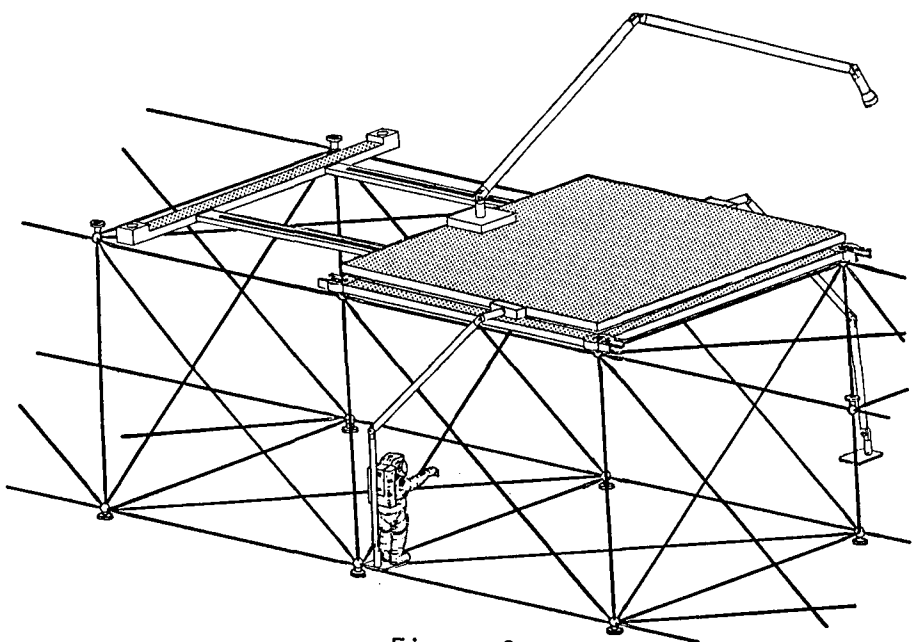

Figure 3

MOBILE REMOTE MANIPULATOR SYSTEM ELEMENTS (EXPLODED VIEW)

This design, which is a modification of a two bay long device described in reference 1, consists of three basic elements or layers such as shown in figure 4, each layer of which will be discussed in subsequent figures.

The MRMS could have a self contained, rechargeable power supply which does not require umbilicals or power rails. Control of all features of the MRMS could reside with the EVA astronaut(s) to avoid hardline or RF control links to a central station. Transport cradles or similar devices must be provided to support payloads being moved above the space station surface by the MRMS. The research which led to the development of the MRMS discussed herein is presented in references 1, 2, and 3.

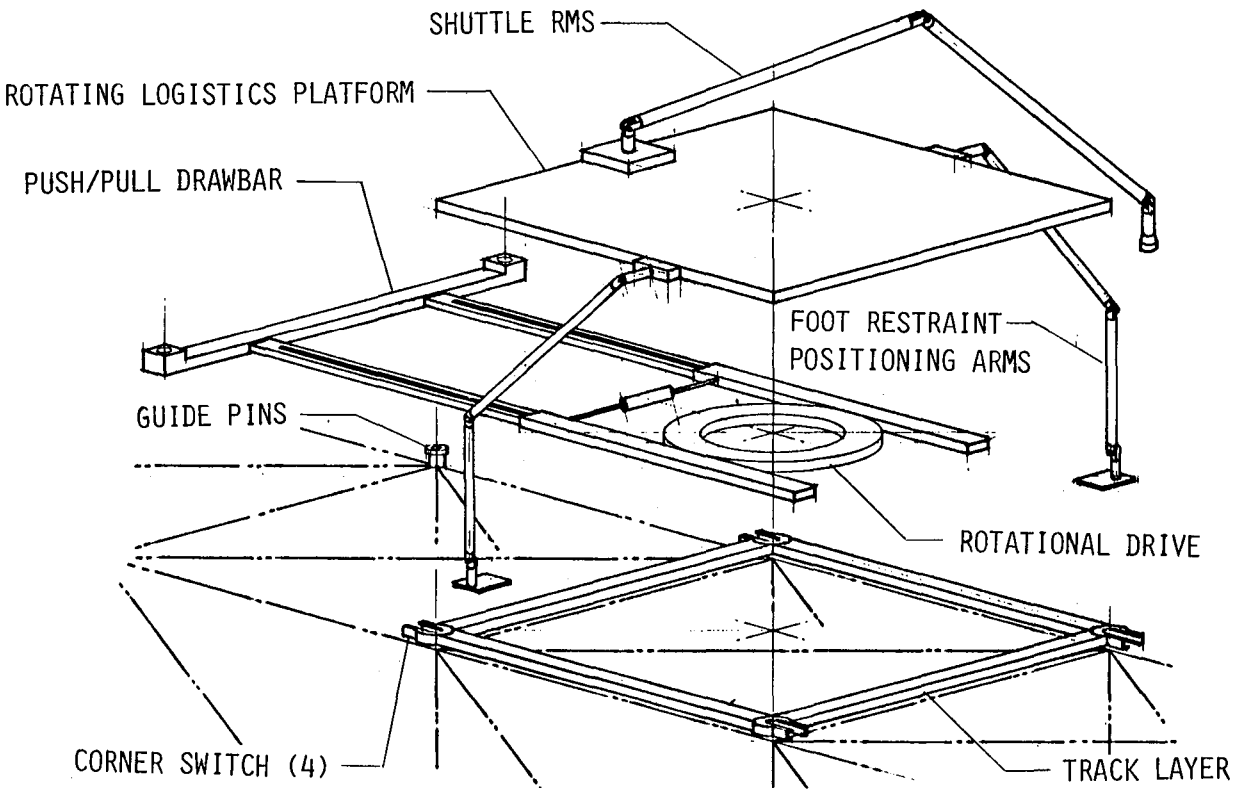

Figure 4

REMOTE MANIPULATOR AND MOBILE FOOT RESTRAINT (MFR)
POSITIONING ARM ARRANGEMENT

The top element of the MRMS is the logistics platform which is envisioned to rotate with respect to either the track or drive elements. This platform would serve to transport payloads and cargo over the space station surface. A central feature of this element would be the capability to operate a transposed Shuttle RMS, which is shown in figure 5 mounted on a moving carriage. Also shown in figure 5 are mobile foot restraints (MFR) positioning arms. Pressure suited astronauts attached to the MFR's are positioned within their work envelope by the movable positioning arms in a manner similar to that described in reference 2. The MFR arms should not be considered to be miniature versions of the Shuttle RMS, with its precedent setting precision control requirements. Rather, each MFR arm should be controllable by the astronaut who can adjust its position in a manner similar to a utility serviceman operating a "cherry picker" bucket. The degrees of freedom required by the MFR arms are determined by the extent to which EVA is utilized to perform various future space station functions.

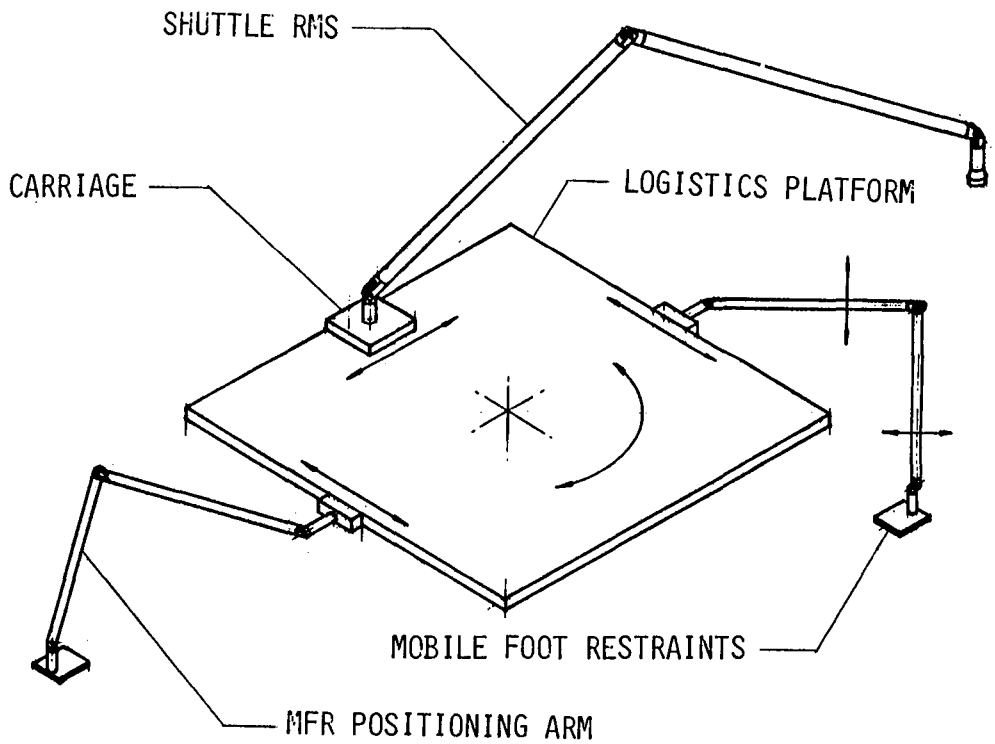

Figure 5

PUSH/PULL DRIVE SYSTEM ARRANGEMENT

The central element consists of a push/pull drive mechanism which also has 360° rotation capability (see figure 6). This feature permits platform movement in four directions by either a push or pull operation and greatly enhances maneuverability without requiring additional structure for translation. It also permits changing movement direction without rotating the logistics platform (e.g., attached payloads). The push/pull motion is envisioned to be powered by an electric stepper motor through a rack and pinion drive. Mounted on the drawbar ends are "drive" rods which are aligned with and electrically inserted into the nodal guide pins and locked. The switches are aligned appropriately and the drawbar is actuated to push or pull the MRMS in the desired direction. The drawbar extends to span a complete bay, such that four point support of the MRMS is maintained at all times. Thus, translation of the MRMS is accomplished by operation of the push/pull drive mechanism to move the platform longitudinally in an "inch-worm" fashion.

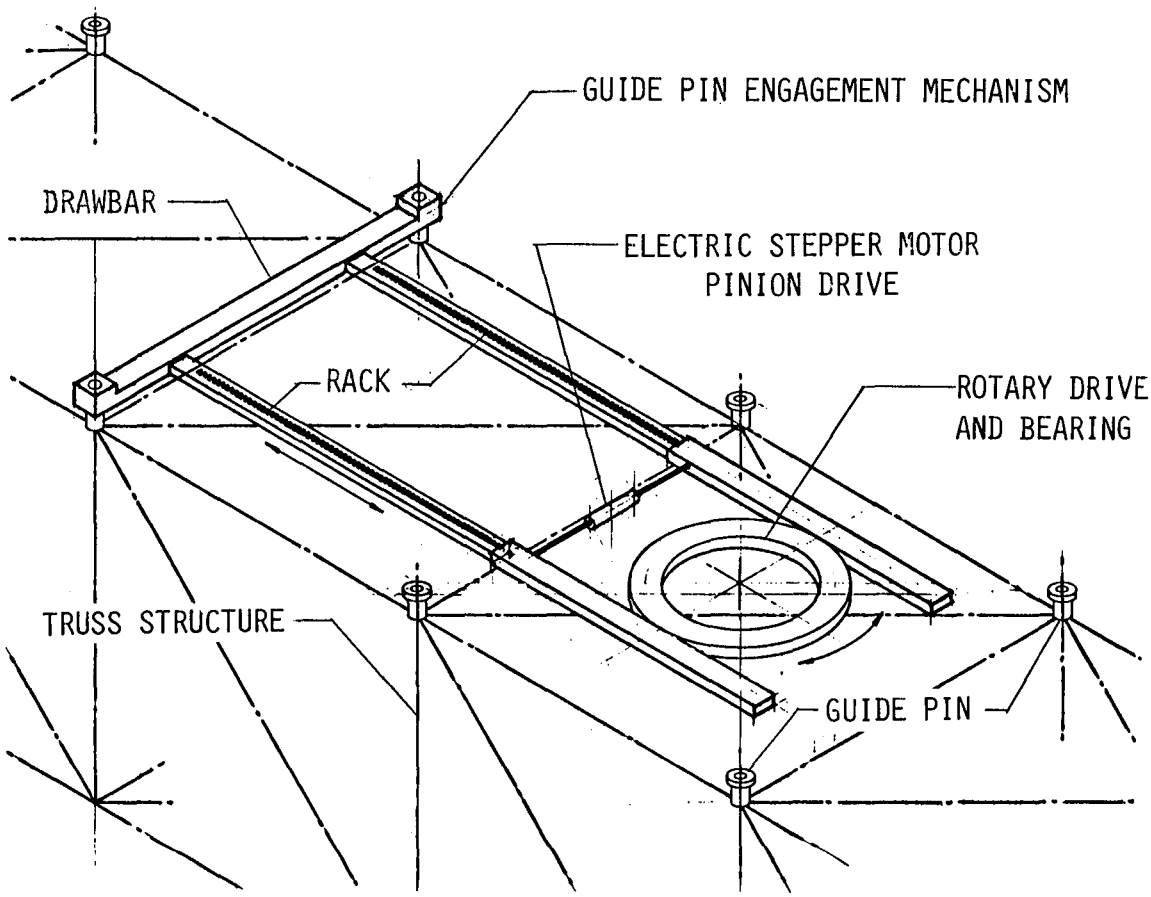

Figure 6

TRACK AND CORNER SWITCH ARRANGEMENT

The bottom or track layer consists of a square track arrangement which rides on structural guide pins attached to the truss nodes. The four (4) tracks are arranged in a single plane and connected at the corners by "switches" which can be aligned to permit motion over the guide pins in either of two orthogonal directions (see figure 7). The track layer does not rotate relative to the truss structure. The four corner switches rotate 90° but only when centered over the guide pins.

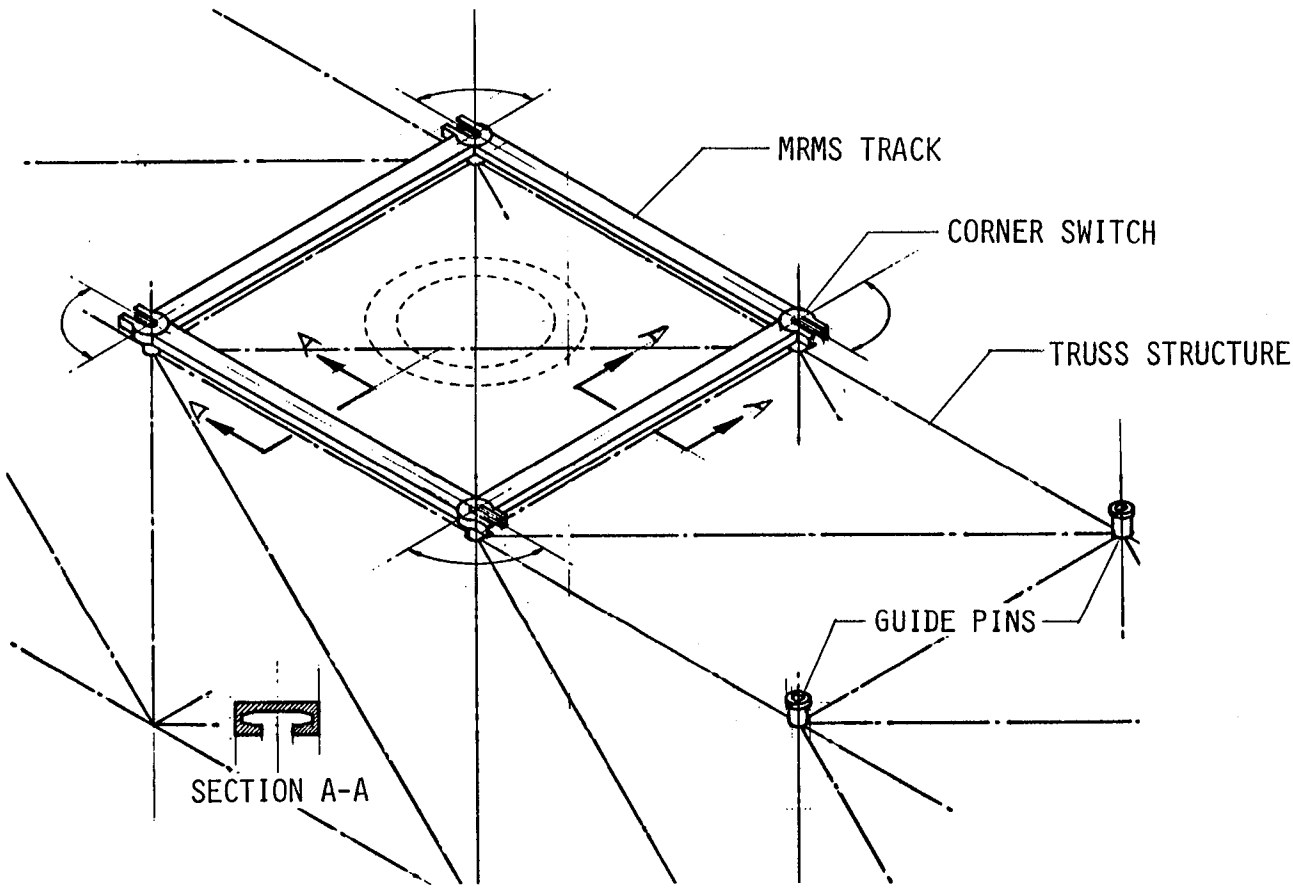

Figure 7

MOBILE REMOTE MANIPULATION SYSTEM TRANSLATION

Longitudinal translation of the MRMS is accomplished as shown by the sequence of events illustrated in the upper half of figure 8. Transverse translation involves use of the pivoting, as well as the push/pull feature of the mechanism, and is illustrated in the lower half of figure 8. Sketch (A) shows the MRMS pivoting 90° from the direction of travel. Sketch (B) shows a translation to construct an adjacent truss cell which is in the next row. Sketch (C) shows the MRMS sliding onto the cell just constructed. Sketch (D) shows a 90° rotation into a position parallel to the original but on an adjacent row. Sketches (E) and (F) show longitudinal motion and construction of added cells to complete a platform. The corner switch illustrated in figure 7 permits the drawbar to lock onto a guide pin which is also occupied by a track switch.

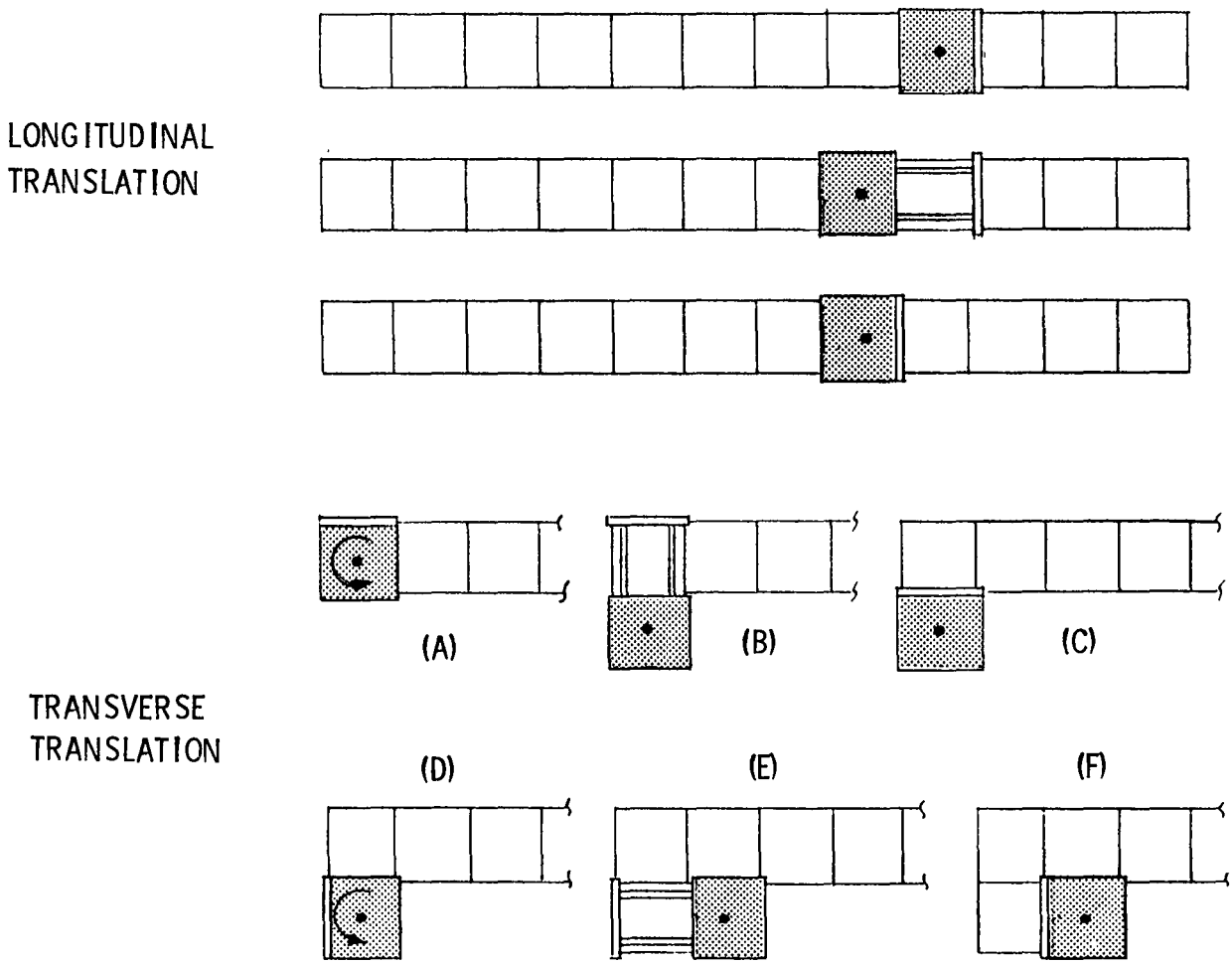

Figure 8

MRMS OPERATIONAL PLANE CHANGE CONCEPT

The proposed MRMS can operate over both the "top" and "bottom" surfaces of the reference configuration, if required, using the rotary joints and solar array boom rotation as a turntable to translate between the two parallel surfaces. For generality and versatility, however, it is desired to operate the MRMS in a plane which is perpendicular to these parallel surfaces. Two (2) concepts for rotating the operational plane of the MRMS 90° from its original position are shown in Figures 9 and 10. The concept shown in Figure 9 uses a tilting frame approach to rotate the MRMS 90° and enable translation to and operation on a perpendicular plane. The tilting mechanism is envisioned to be self-contained and installed as a truss cell unit into a beam or along a platform edge. This unit should be capable of rotating 90° in both the "left" and "right" hand directions.

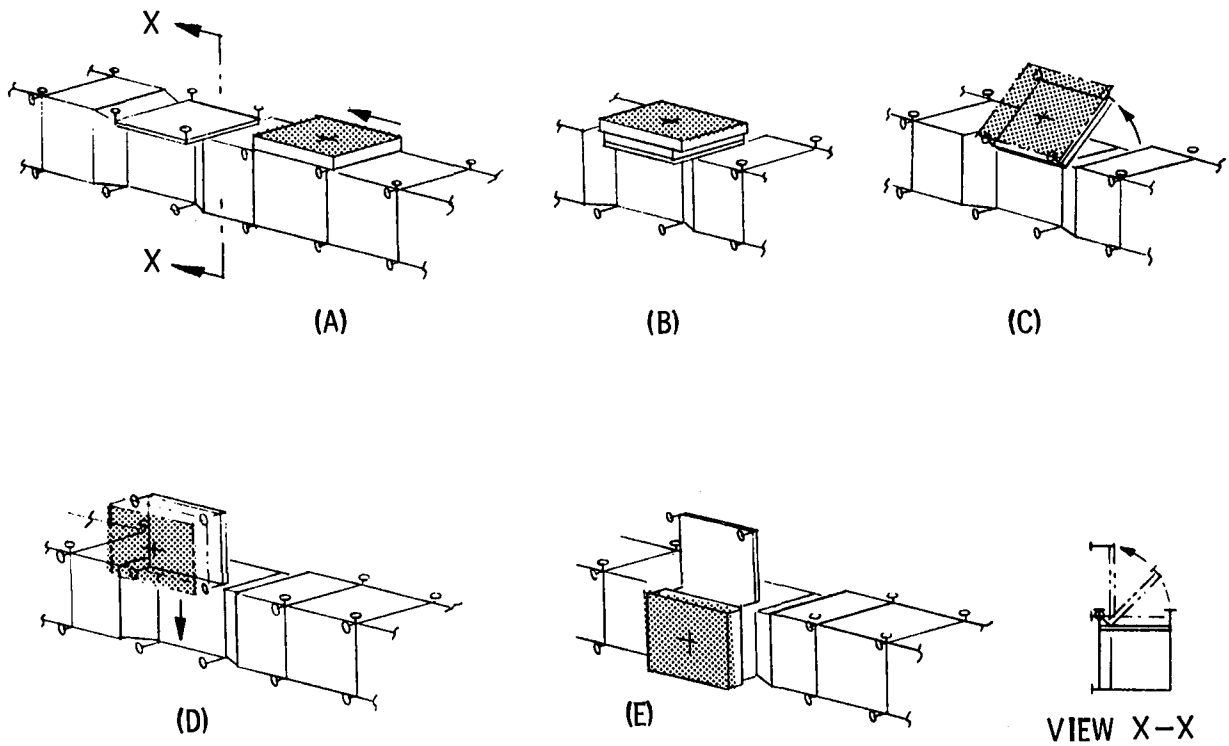

Figure 9

ALTERNATE MRMS OPERATIONAL PLANE CHANGE CONCEPT

A second approach is illustrated in figure 10 which is operationally more complex but mechanically simpler and probably more comapct than that of figure 9. This concept consists of a planar guide pin frame which is attached to the original structure at the center of an element which replaces a truss strut. A center section of this element contains a "T" fitting which has two perpendicular rotational degrees of freedom. Operationally, the MRMS translates laterally onto the attached guide pin frame. The MRMS and frame are then rotated 180° around the frame centerline attachment as shown in figure 10 into an "upside down position." The MRMS and frame are then rotated 90° around the strut which is perpendicular to its original operational plane.

Two devices, such as those just discussed or another appropriate design, placed on opposite faces of the truss structure would permit more rapid and convenient translation of the MRMS between "top" and "bottom" surfaces of the station rather than interrupting the rotation of the solar wing for this purpose.

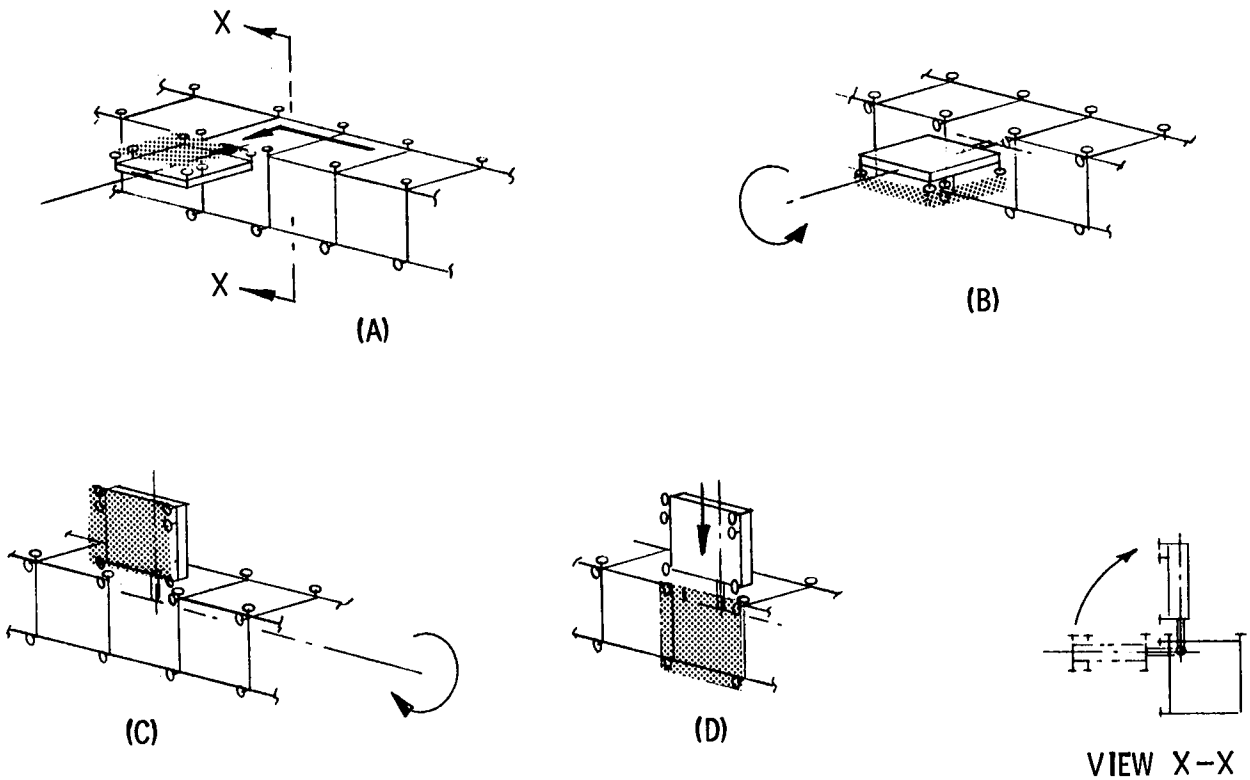

Figure 10

LARGE SUBMILLIMETER ASTRONOMICAL OBSERVATORY
(ARTIST SKETCH OF PROPOSED OBSERVATORY)

In addition to assembling a space station platform and solar arrays shown in the preceding illustration, the MRMS can be used to assemble other space structures such as large antennas and astronomical observatories. Several studies have been conducted to define the technical requirements for an orbiting submillimeter astronomical observatory. An artist sketch illustrating the proposed observatory is shown in figure 11. This proposed observatory would require a parabolic primary mirror with a diameter of up to 30m having diffraction limited optical quality. The mirror must be shaded from stray light and passively maintained at a constant temperature in the range of 150-200 K. Primary mirrors with an f/D from 0.5 to 1.0 are of interest, and to maintain the desired thermal conditions, the mirror must have a circumferential sunshade with a length approximately equal to the mirror diameter.

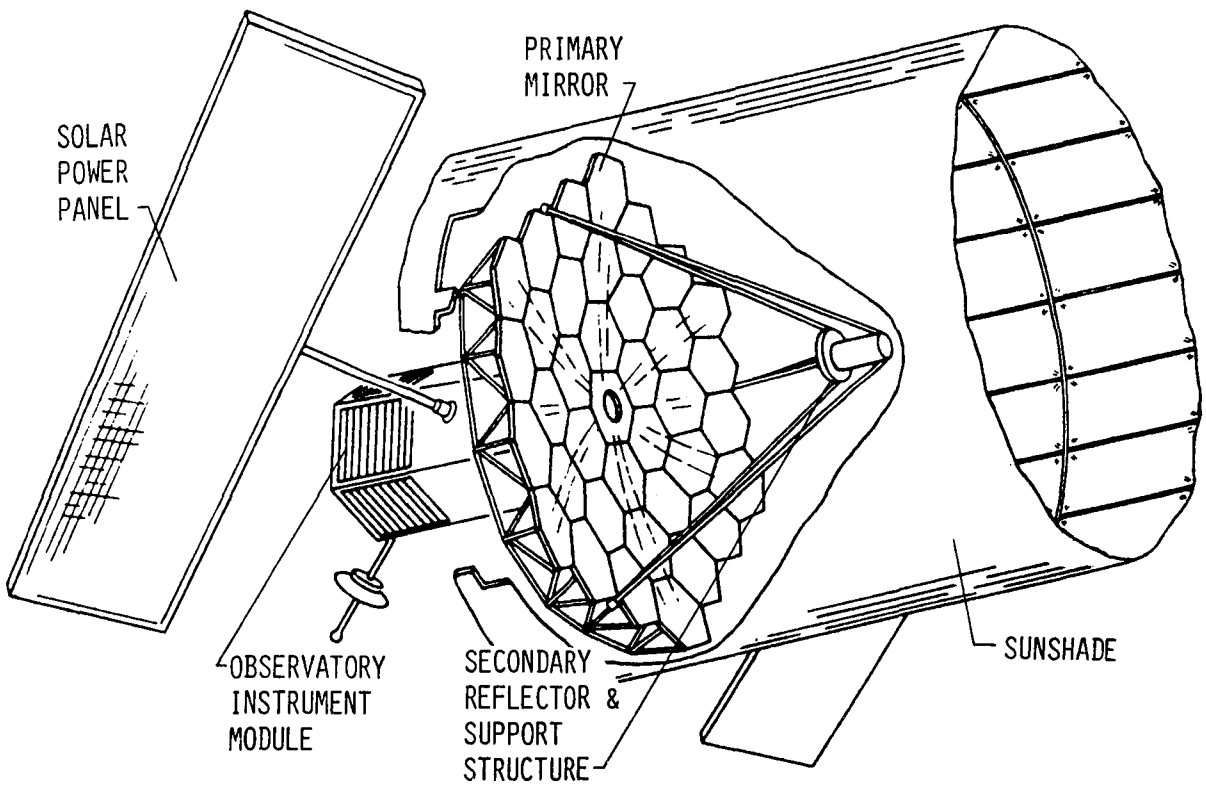

Figure 11

LARGE SUBMILLIMETER ASTRONOMICAL OBSERVATORY ASSEMBLY CONCEPT USING THE MRMS

Construction scenarios for this observatory have been built around the use of deployable modules or tetrahedral substructures on which hexagonal mirror facets are located using a special remote manipulator. An alternative to these approaches is to use the MRMS to assemble the truss support structure and attach the mirror facets. Figures 12 and 13 illustrate this alternate scenario. The construction would be initiated by attaching a module containing the focal plane and various other observatory instruments to the space station truss platform using a "temporary" support cradle. This cradle would permit the instrument module to rotate about its centerline. The centerline is canted to the plane of the station platform approximately 7° (f/D = 1, D = 30m). The proposed assembly sequence for the primary mirror is shown in the next figure.

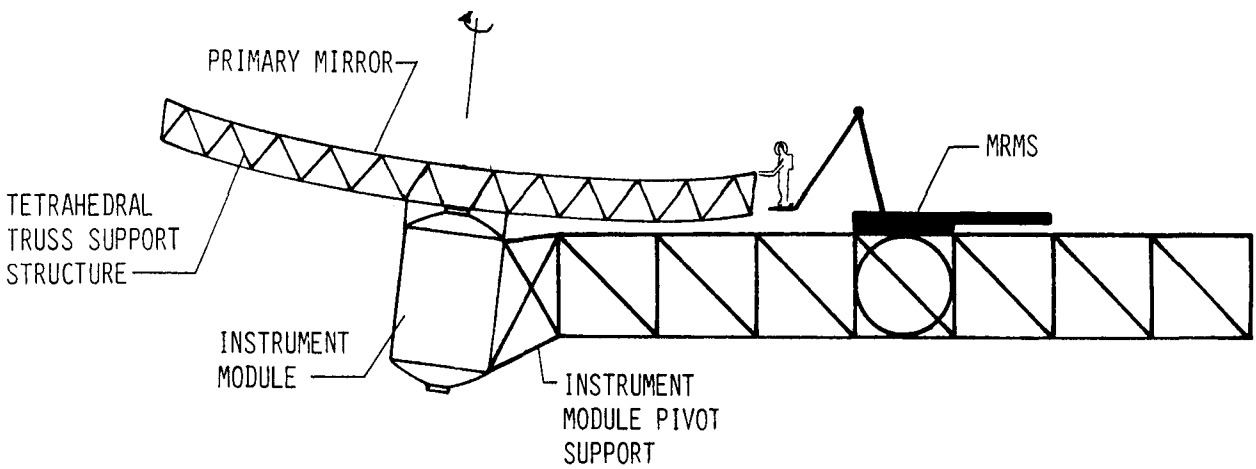

Figure 12

LARGE SUBMILLIMETER ASTRONOMICAL OBSERVATORY
PRIMARY MIRROR ASSEMBLY

Construction of the primary mirror would be initiated by astronauts assembling rings of tetrahedral truss support structure with the interior rings attached to the instrument module. As sections of the support structure are completed, hexagonal mirror facets are moved from the MRMS and secured at three attachment points. Control actuators would be installed and connected as each facet is secured. The instrument module rotates about the mirror axis thus permitting the astronauts to assemble the mirror with moderate motion of the workstations to which they are attached and only linear translation of the MRMS. The canted axis of the instrument module permits the entire mirror to be assembled with changes in elevation of the astronauts of less than 1m. For this configuration, the size of the truss elements and the distance between parallel sides of the facets are considered to be about 2 meters. One or two rings could be assembled during each revolution of the module. The dark circle in the center of the mirror represents a hole which is required for the Cassegrainian system. (See fig. 13.)

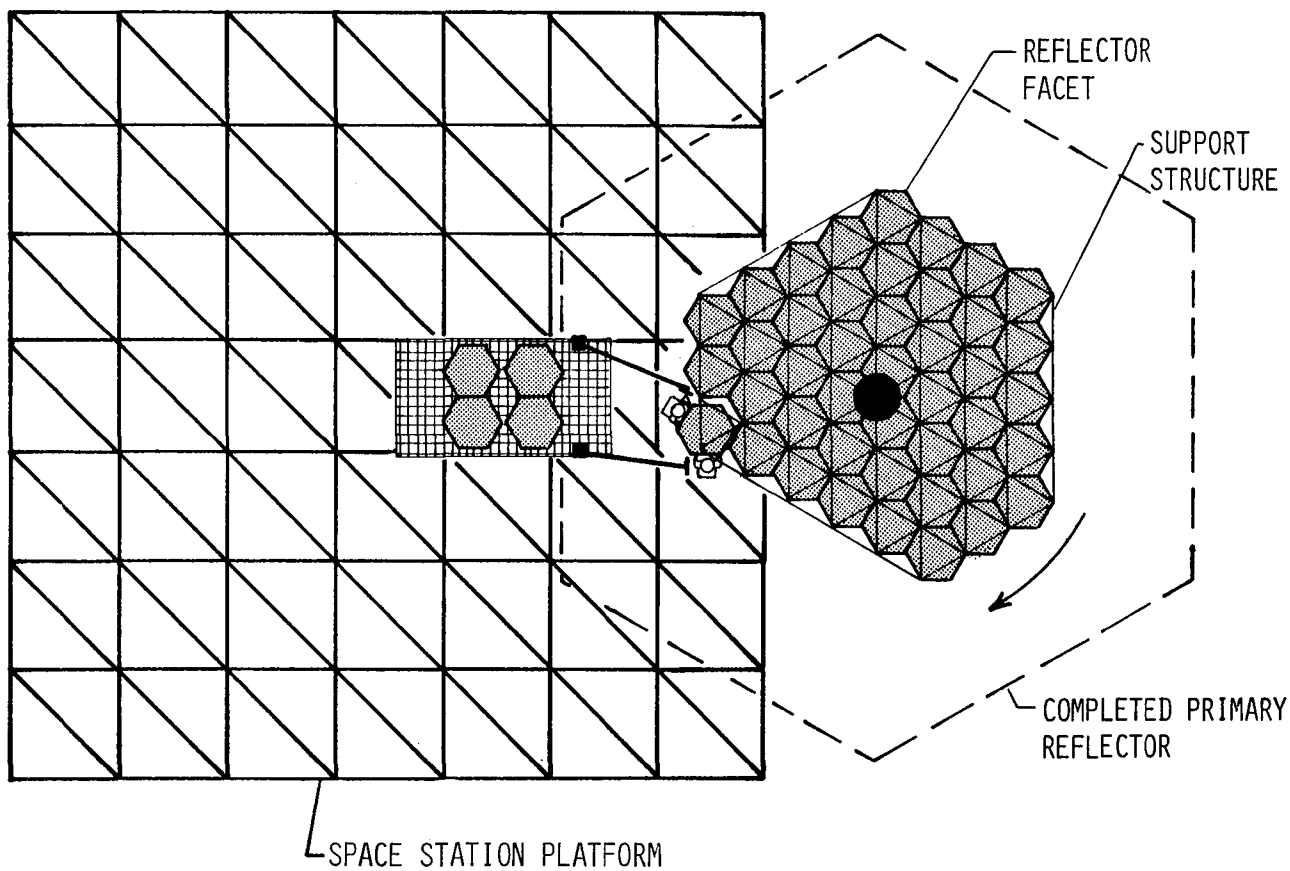

Figure 13

CONCLUDING REMARKS

A conceptual design for a mobile remote manipulator system has been presented. This concept does not require continuous rails for mobility (only guide pins at truss hardpoints) and is very compact, being only one bay square. The MRMS proposed is highly maneuverable and is able to move in any direction along the orthogonal guide pin array under complete control at all times. The proposed concept would greatly enhance the safety and operational capabilities of astronauts performing EVA functions such as structural assembly, payload transport and attachment, space station maintenance, repair or modification, and future spacecraft construction or servicing. (See fig. 14.)

The MRMS drive system conceptual design presented is a reasonably simple mechanical device which can be designed to exhibit high reliability. The Shuttle RMS is a developed system, which only needs minor modification to permit its installation and operation from a mobile base. The MFR positioning arms are not envisioned to need the precision control capability of the RMS. Developmentally, all components of the proposed MRMS either exist or are considered to be completely state-of-the-art designs requiring minimal development--features which should enhance reliability and minimize costs.

- MRMS IS A HIGHLY VERSATILE LOGISTICS AND UTILITY VEHICLE FOR THE SPACE STATION
- MECHANICAL SYSTEMS STATE OF THE ART
- MOBILE WORK STATION DEMONSTRATED PRACTICALITY
- MRMS PROVIDES CAPABILITY FOR ASSEMBLY OF LARGE SPACECRAFT

Figure 14

REFERENCES

1. Mikulas, Martin M., Jr.; Bush, Harold G.; Wallsom, Richard E.; Dorsey, John T.; and Rhodes, Marvin D.: A Manned-Machine Space Station Construction Concept. NAS TM 85762, February 1984.

2. Heard, Walter L., Jr.; Bush, Harold G.; Wallsom, Richard E.; and Jensen, J. Kermit: A Mobile Work Station Concept for Mechanically Aided Astronaut Assembly of Large Space Trusses. NASA TP 2108, March 1983.

3. Bush, Harold G.; Mikulas, Martin M., Jr.; Wallsom, Richard E.; and Jensen, J. Kermit: Conceptual Design of a Mobile Remote Manipulator System. NASA TM 86262, July 1984.

SPACE-BASED ANTENNA MEASUREMENT SYSTEM CONCEPTS FOR SPACE STATION OPERATION

C. Louis Cuccia
NASA Office of Space Science
and Applications

Thomas G. Campbell
NASA Langley Research Center

W. L. Pritchard
Satellite Systems Engineering, Inc.
Bethesda, Maryland

Jud Lyon
The Howland Company, Inc.
Atlanta, Georgia

Large Space Antenna Systems Technology - 1984
December 4-6, 1984

INTRODUCTION

The rapid growth of radio frequency systems in space indicates a future requirement for the capability to conduct space-based antenna measurements. This capability would allow functional checks of communications satellites in low Earth orbit before boost to geosynchronous orbit as well as other near-term radio frequency applications. The growth in satellite communications and in the demonstrated Shuttle deployment and retrieval capability indicates the time for such on-orbit RF testing is rapidly approaching. Future space station operations will also require an on-orbit measurement capability for the multitude of antennas and microwave systems proposed for that system. The continued development of large space antennas could become dependent upon the development of a space-based measurement system. Examples of future system requirements for on-orbit measurement capability are presented below.

- **Growth in satellite communications and in Shuttle deploy/retrieval capability**
- **Development of advanced satellite communications**
  - **Multibeam and shaped beam antennas**
  - **Intersatellite communication links**
  - **Millimeter wave transmission**
  - **Mobile satellite communications**
  - **Direct broadcast**
- **Spacecraft space station communications systems**
  - **IOC**
  - **Evolutionary space station**
- **Geostationary platform era**
- **Development of large space antenna technology**

COMMUNICATIONS REQUIREMENTS IN THE SPACE STATION SYSTEM

The growth in the space segment for communications systems is presented in the figure below. The expected activity during the support of the space station era alone justifies the development of technology for space-based antenna measurement systems. This technology, in particular, this capability, will be required in the assembly, testing and operation of large space structures.

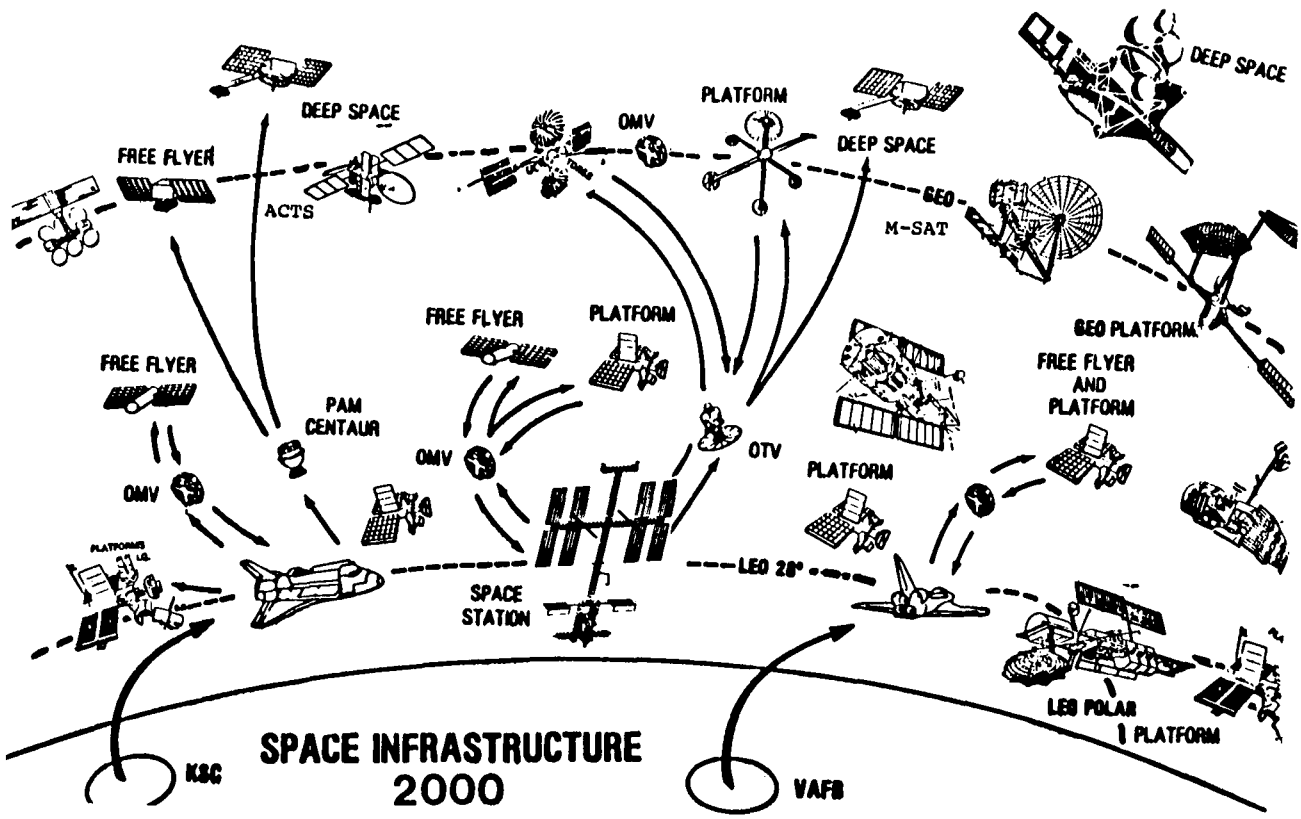

GROWTH OF COMMUNICATIONS SYSTEMS IN SPACE -
THE TRACKING AND DATA RELAY SATELLITE (TDRS) SYSTEM

The operational status of the TDRS satellite system is a significant milestone in the advancement of space communications systems. The booster problems encountered during the deployment of the first TDRS from Shuttle and the successful method implemented to achieve orbital transfer were indeed remarkable. The boost to GEO with antennas in the deployed condition essentially displayed that a large aperture system could be deployed and tested in LEO and then boosted to GEO in the deployed state for on-orbit operation.

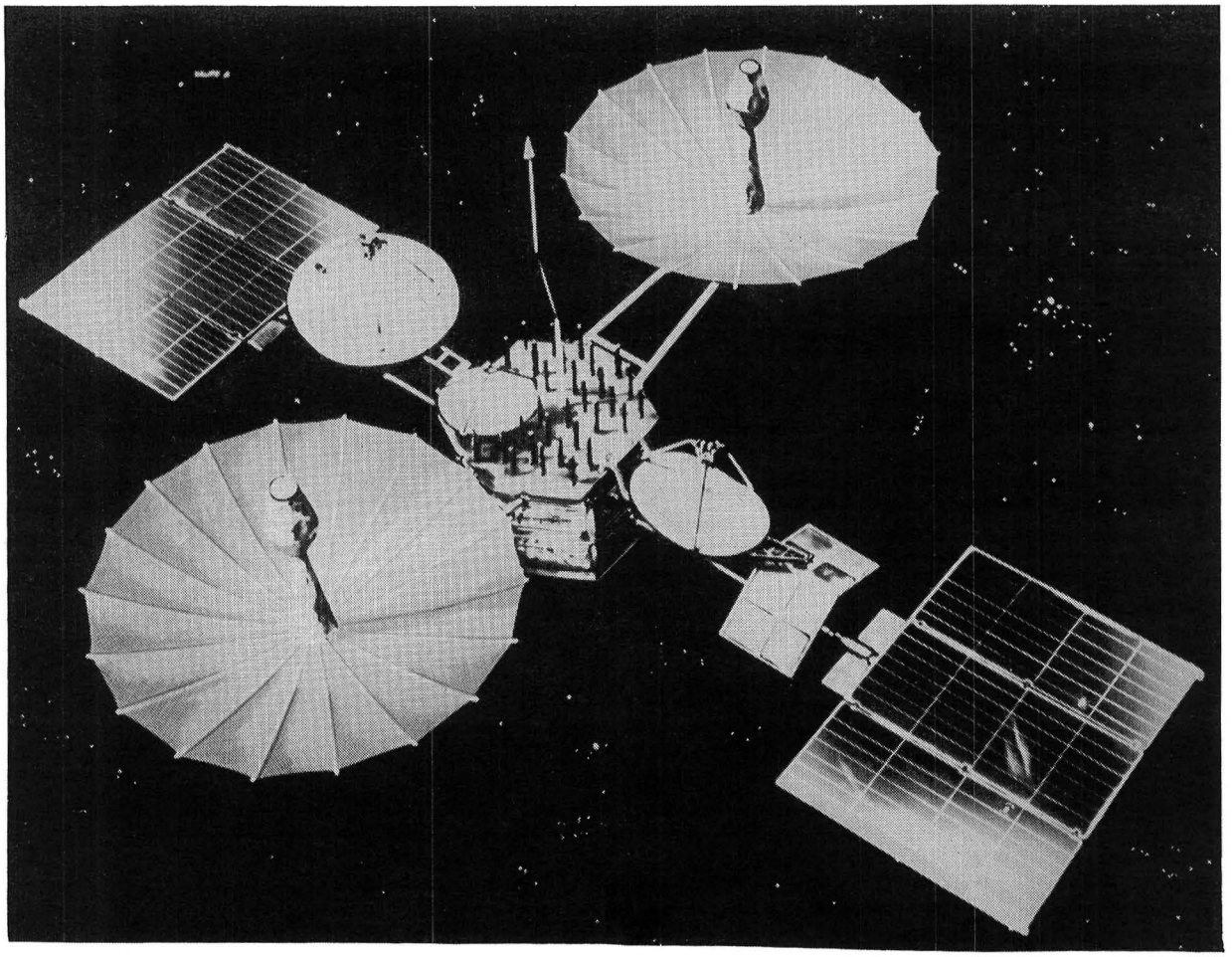

TDRS SATELLITE IN THE STOWED CONFIGURATION

A photograph of the TDRS satellite in the stowed condition is shown below. The rigid-rib deployable antennas are located at the top of the spacecraft.

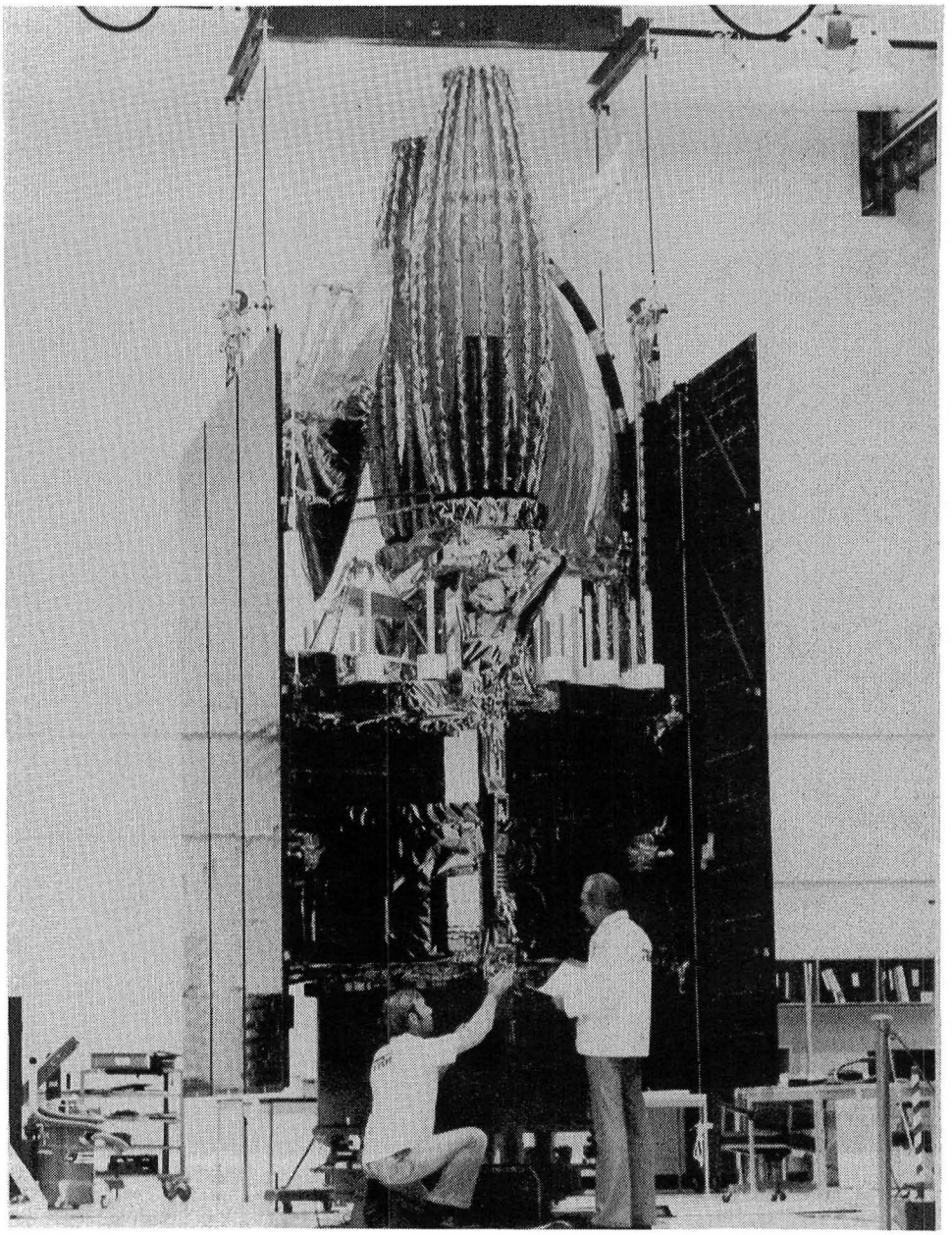

SPACE STATION OPERATIONS - USING THE
EARLY CONCEPT DEVELOPMENT GROUP (CDG) CONFIGURATION

Several of the communication systems requiring simultaneous multiple beams are depicted in the figure below. Methods and apparatus for evaluating antenna performance on space stations will be required.

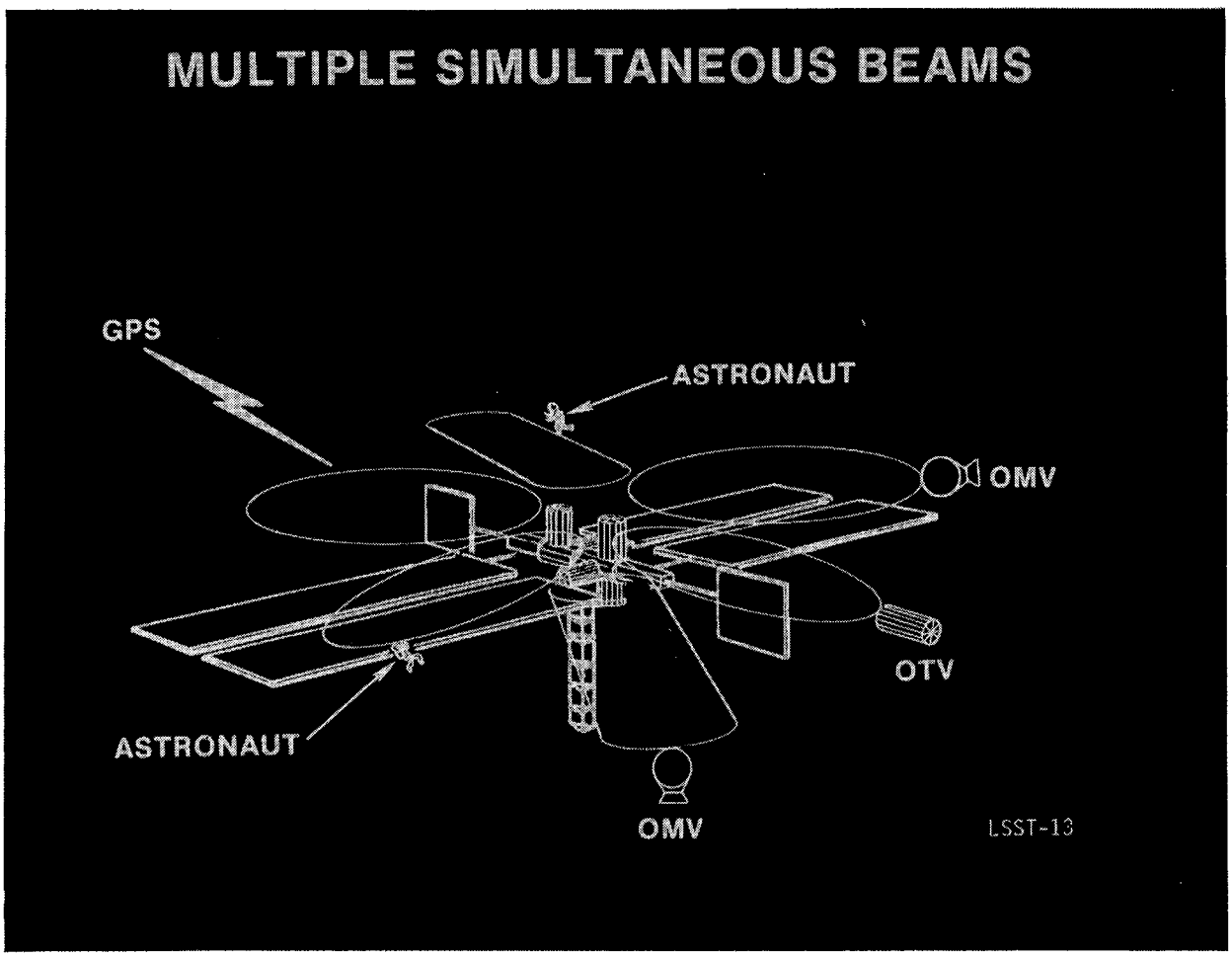

GEOSTATIONARY PLATFORMS IN THE SPACE STATION ERA

As the space station becomes a reality, the growth in the commercial communication satellite system is increasing at a phenomenal rate. As a result of the growth in commercial systems, the slots in GEO are being depleted. Therefore, the utilization of a geostationary platform will be a logical addition to the space station family in the 1990's to augment operations as well as to conserve the orbital arc. Several points concerning geostationary platforms are listed below.

- **Geostationary platform logical addition to space station family in 1990's**
- **Optimize utilization of orbital arc**
- **Enable effective aggregate of payloads to enhance arc/spectrum resource**
- **European and Japanese advocate geostationary platforms**

ON-ORBIT ASSEMBLY OF LARGE SPACE ANTENNA (LSA) SYSTEM

The deployment and assembly of a large space antenna are depicted in the figure below. After completing the assembly and deployment task in low Earth orbit, it would be necessary to conduct antenna functional checks before boosting to the prescribed orbit. These radio frequency checks could then be made without the involvement of an Earth-based system and, thereby, expedite the evaluation process.

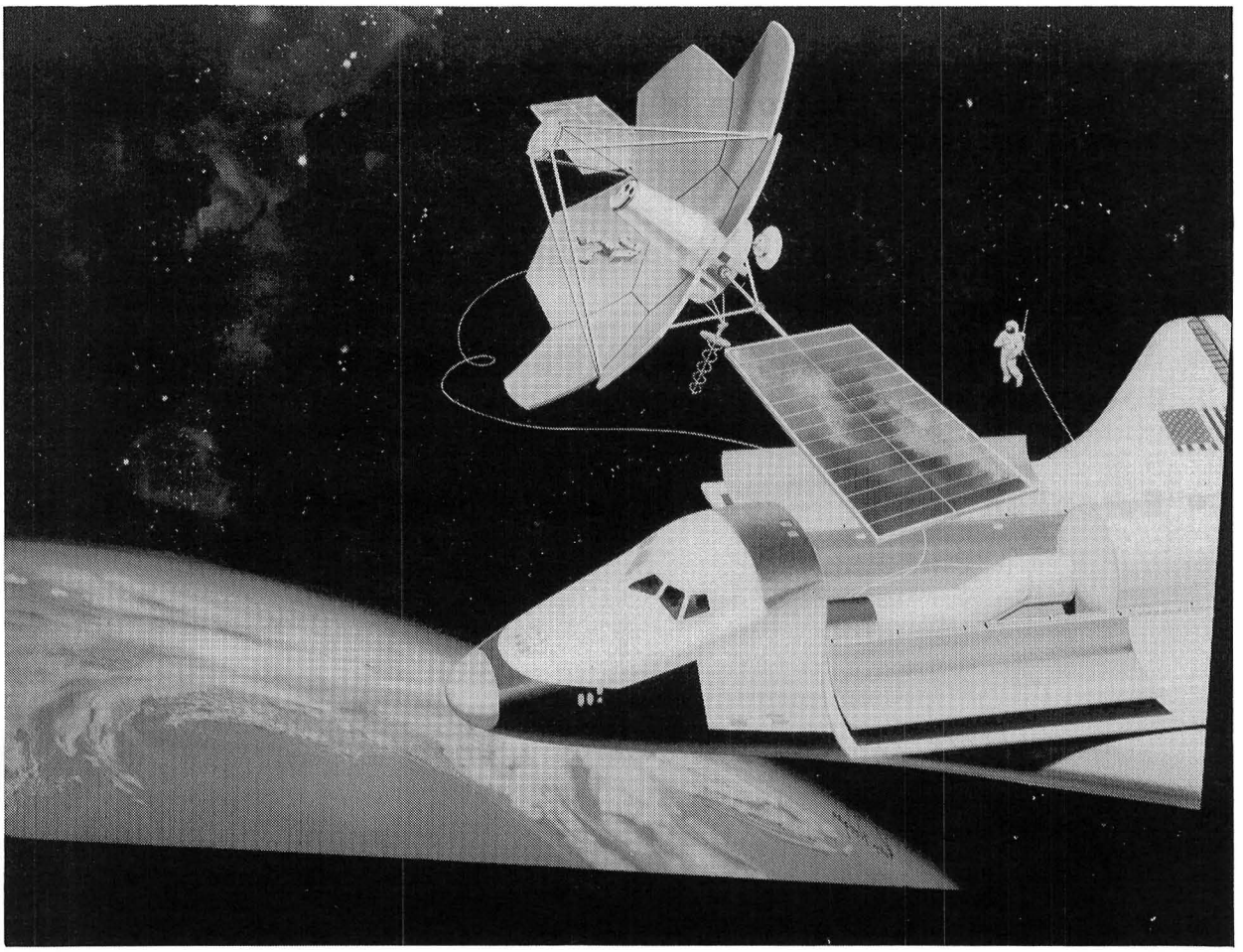

EARTH-BASED NEAR-FIELD ANTENNA TEST FACILITY

The ability to test large aperture antennas on Earth is limited by the size and availability of the Near-Field Test Facilities. Presently, only one major Near Field Test Facility exists which is suitable for testing LSA's (on the order of 15 meters in diameter). Even assuming gravity effects on large flexible structures could be minimized using counter-balancing systems, no facility presently exists which would allow testing prior to launch. Shown in the figure below is the Near Field Test Facility, proposed by NASA Lewis Research Center, which is critically needed by the Agency to support the future need for testing antennas up to 20 meters.

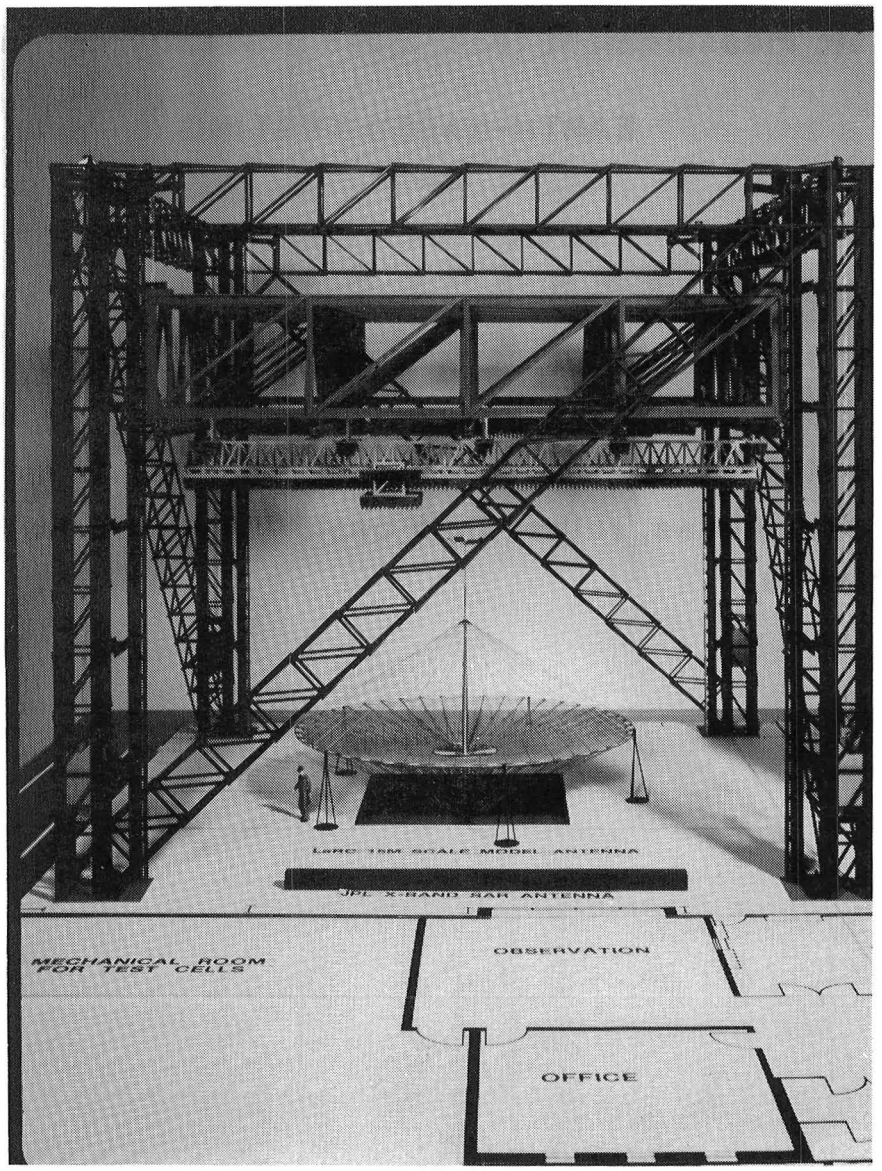

CANDIDATE SYSTEMS FOR SPACE-BASED TESTING OF LARGE ANTENNAS

All basic measurement techniques presently employed in Earth-based and Earth-link testing are candidate techniques for space-based testing. Practical difficulties and economic constraints may prevent the application of some of these techniques, rather than basic "laws of physics" constraints.

- **All basic measurement techniques presently employed in**

  EARTH-BASED TESTING
  and
  EARTH-LINK TESTING

  are candidate techniques for space-based testing.

- **Practical difficulties and economic constraints may preclude some techniques, rather than basic "LAWS OF PHYSICS" constraints.**

BASIC TECHNIQUES FOR SPACE-BASED ANTENNA MEASUREMENTS

Basic techniques open to consideration for space-based antenna measurements include:

- Far-Field Direct
- Far-Field Indirect
- Aperture Plane

A brief review of the major defining parameters of these techniques follows.

- **Far-field ranges** :$R \geq ND^2/\lambda$
  - **R=range length**
  - **D=aperture dimension**
  - **λ=wavelength**
  - **N=varies from 2 to $\geq$10**

OR • **COMPACT RANGES**

- **"R"= a few 10's of feet**
- **"N"=simulated as $\geq$2**

In either case the typical scenario involves a fixed "sampling" antenna and an exercise of the test antenna through angular segments of a spherical coordinate system.

- **Further examples :**
  - **Earth-link tests of orbiting and geosynchronous satellites**
  - **Radio star source testing of Earth station antennas**

EXTENDED-RANGE MEASUREMENT REQUIREMENTS FOR LOW SIDE LOBE, LARGE APERTURE ANTENNAS

The far-field range requirement is extended when extreme low sidelobe antennas are measured. The requirement to extend the range on Earth-based measurements for low side lobe antennas further justifies the need to consider space-based systems.

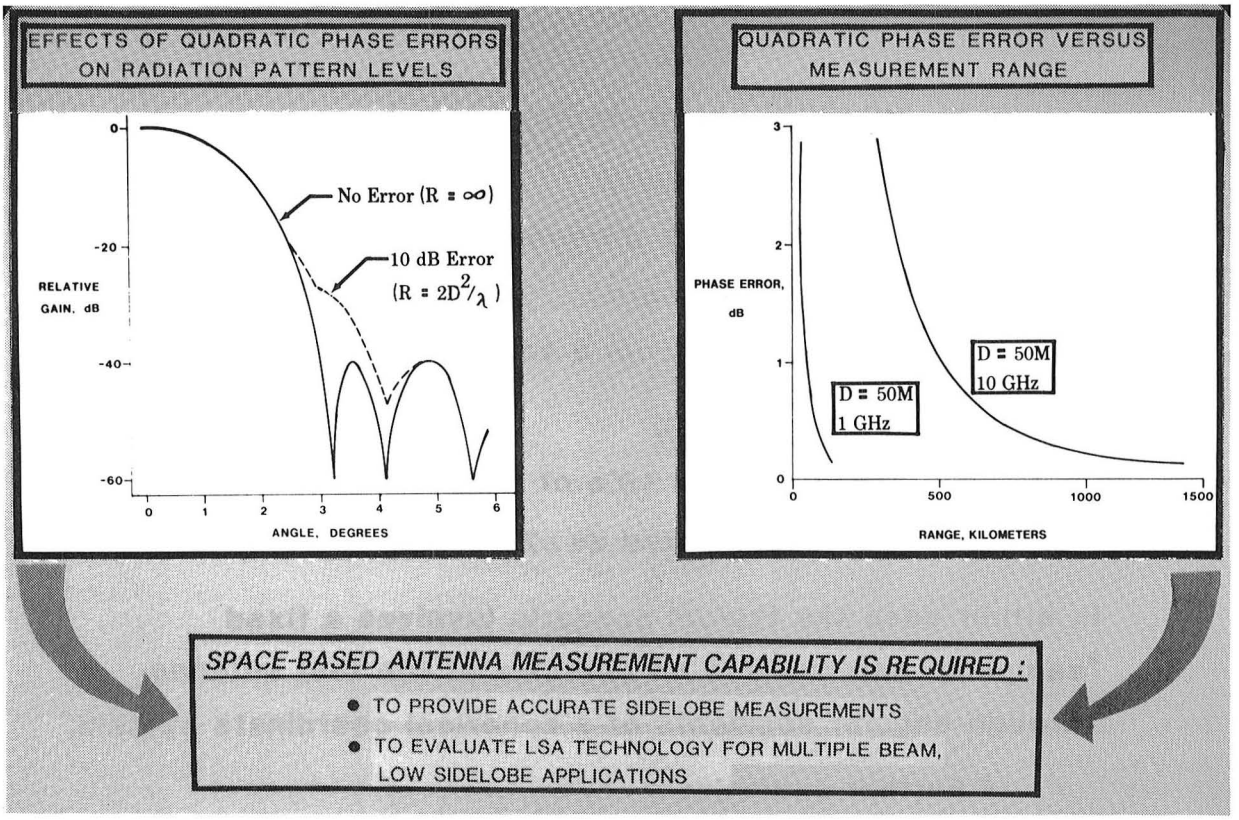

COMPACT RANGE ANTENNA MEASUREMENT SYSTEMS

A relatively new approach in antenna measurement systems involves the use of compact reflectors which drastically reduce the range requirement in testing high frequency antennas. Compact reflectors have proven to reduce the phase error in the aperture plane in the vicinity of the antenna test zone which allows larger aperture antennas to be tested at a reduced range - usually in an indoor anechoic chamber. The components of a compact reflector system are shown in the figure below. This technology must be reviewed for potential space-based applications as well.

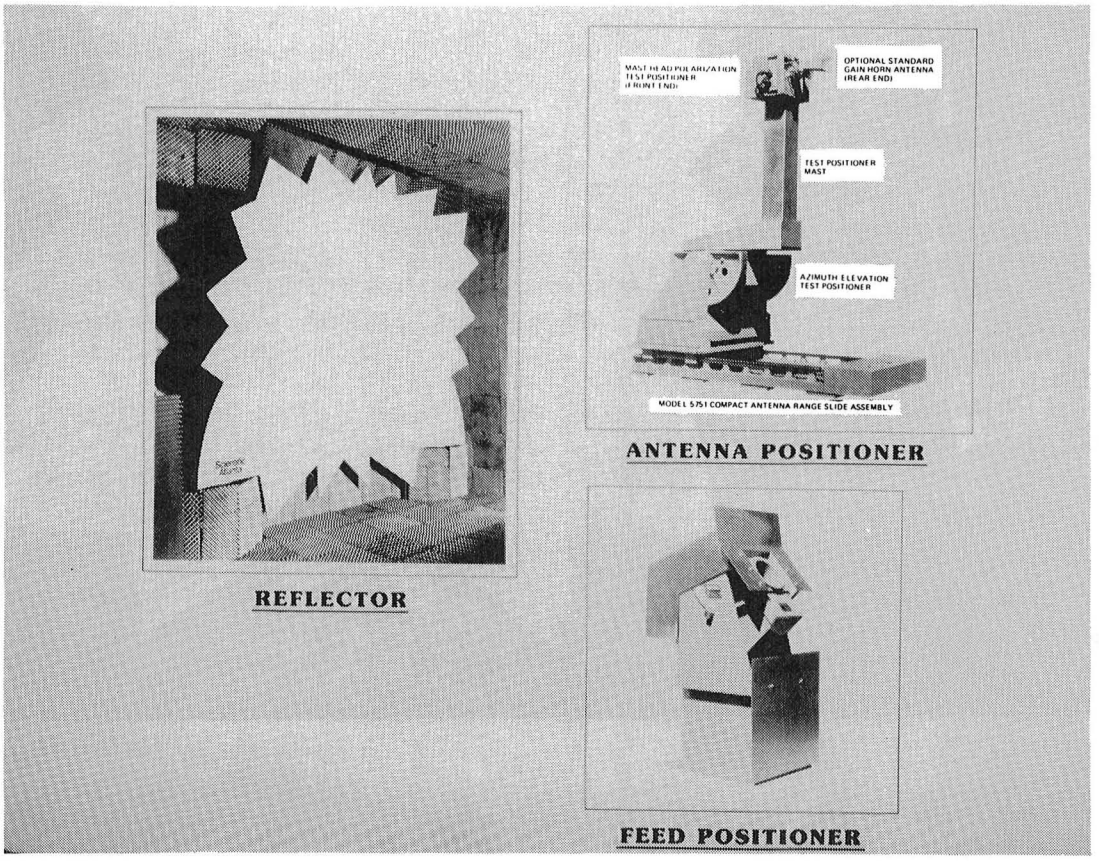

STANDARD COMPACT RANGE REFLECTOR CONFIGURATION

The standard compact range reflector configuration is shown below. The reflector was designed to have serrated edge treatment to reduce scattering back into the aperture plane and test zone for antenna measurements.

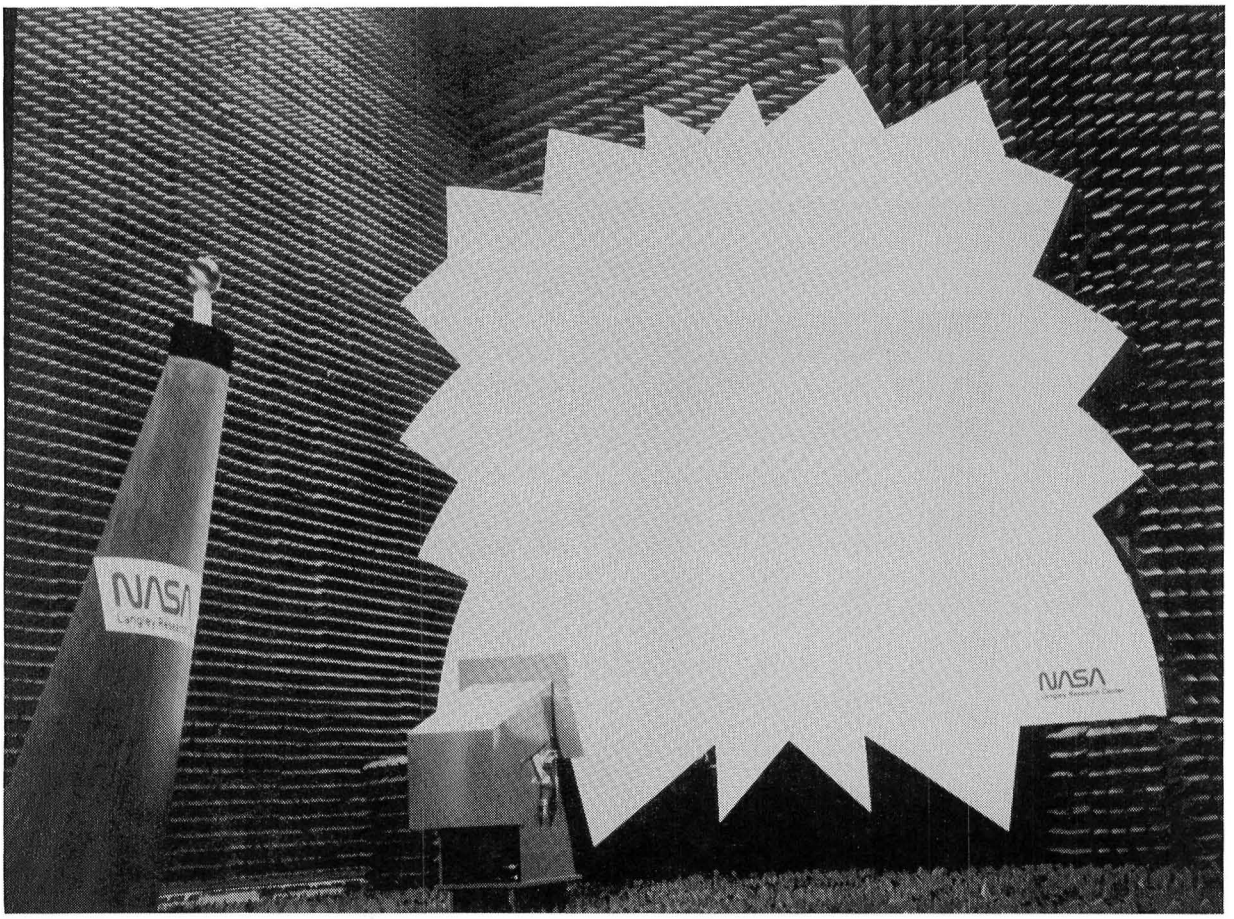

MODIFIED COMPACT RANGE REFLECTOR CONFIGURATION

Through research activities at Ohio State University and the Langley Research Center, a modified compact range reflector configuration has been designed which provides a significant improvement in radio frequency performance over the standard configuration. A rolled-edge modification has been developed which can be integrated with the serrated edge design of the standard reflector configuration. The rolled-edge reflector configuration is shown in the figure below.

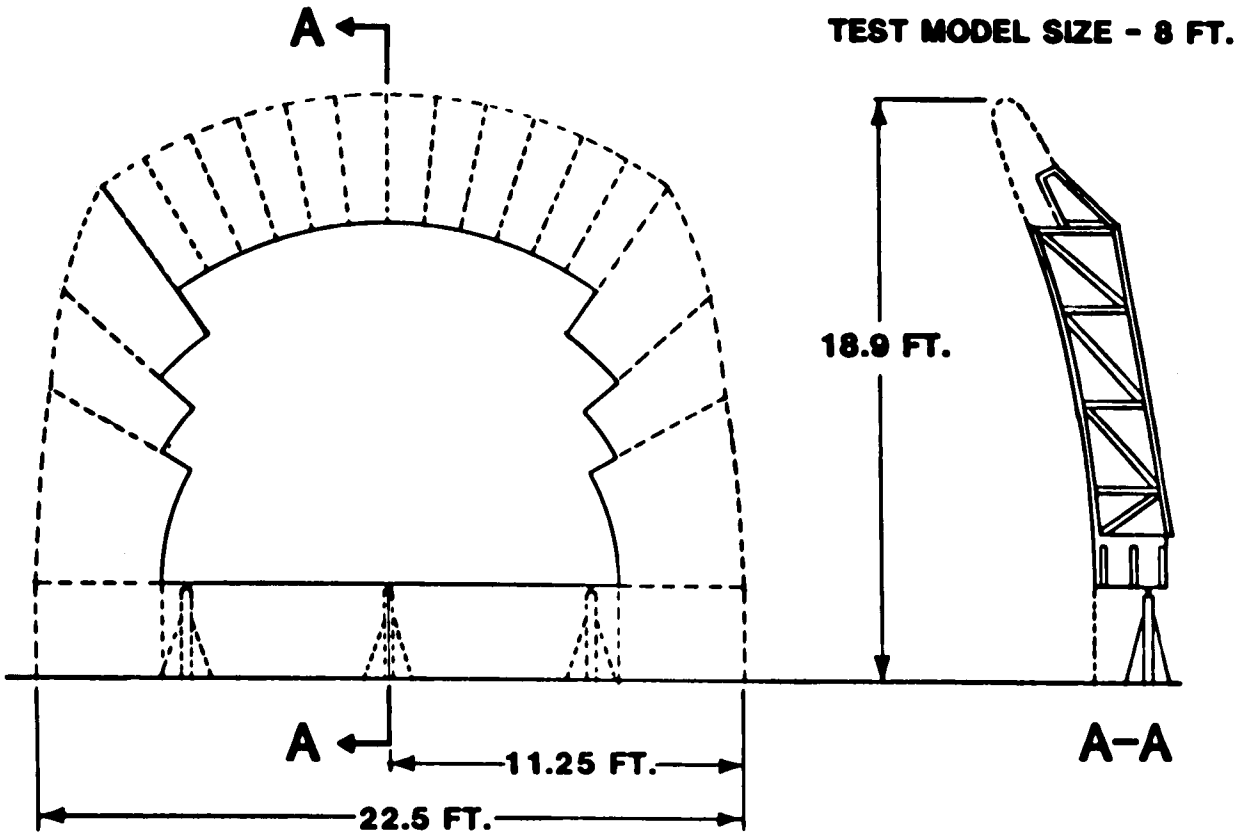

INSTALLATION OF THE ROLLED-EDGE SEGMENTS ON THE COMPACT REFLECTOR AT THE LANGLEY RSEARCH CENTER

A recent research activity at the Langley Research Center has been the design, development and installation of rolled-edge segments to a standard compact reflector configuration. Essentially, this research effort, initiated through a joint program between NASA Langley and Ohio State University, has provided the first installation of a rolled-edge reflector and measured performance data. The photograph below shows the installation process of the rolled-edge segments on the compact reflector at Langley Research Center.

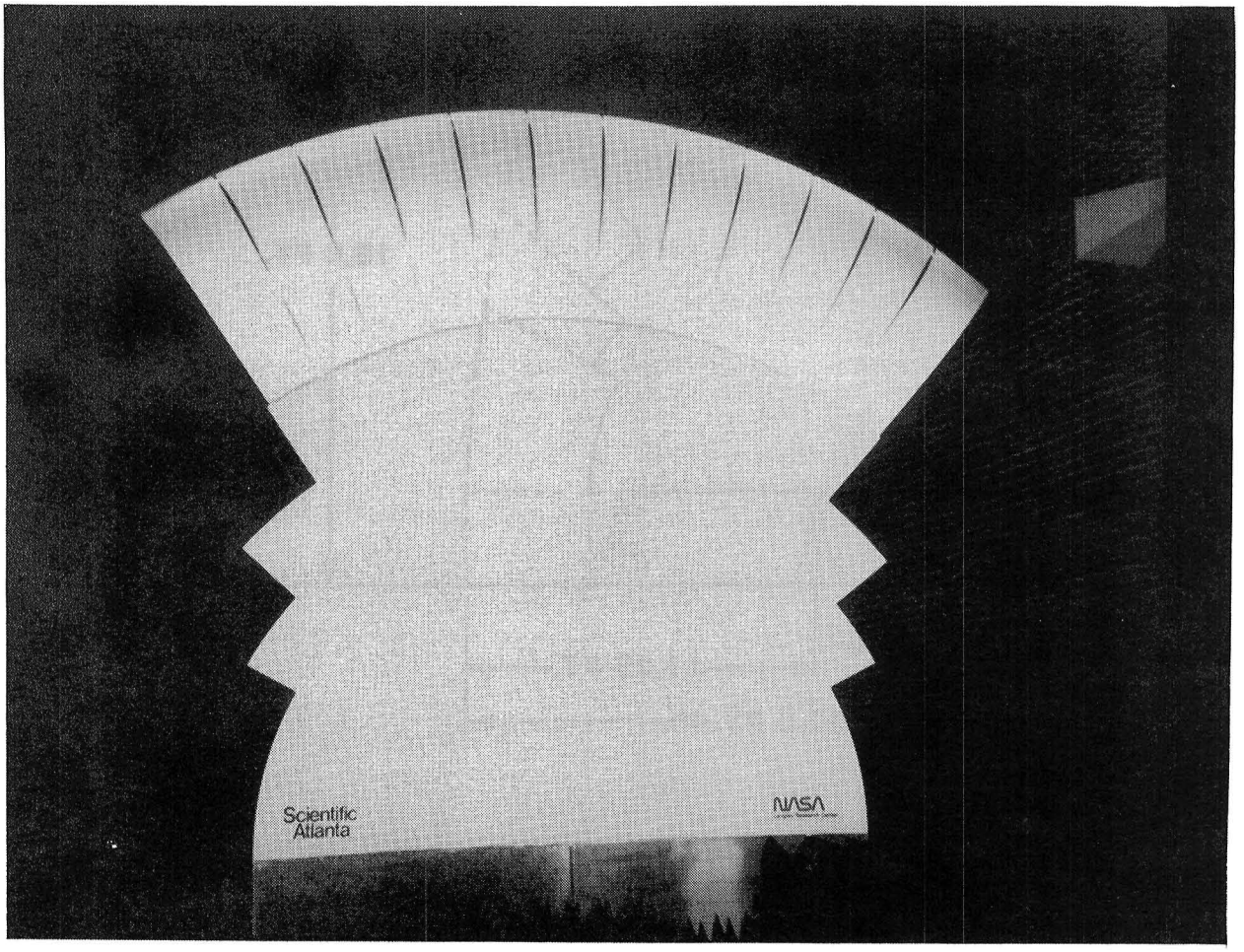

MEASURED AMPLITUDE DATA FOR THE COMPACT REFLECTOR WITH ROLLED-EDGE MODIFICATION

The initial measurement results obtained by scanning vertically the aperture plane of the compact reflector without and with the rolled-edge segments are presented. The improvement in amplitude tape which increases the size of the test zone can be noted.

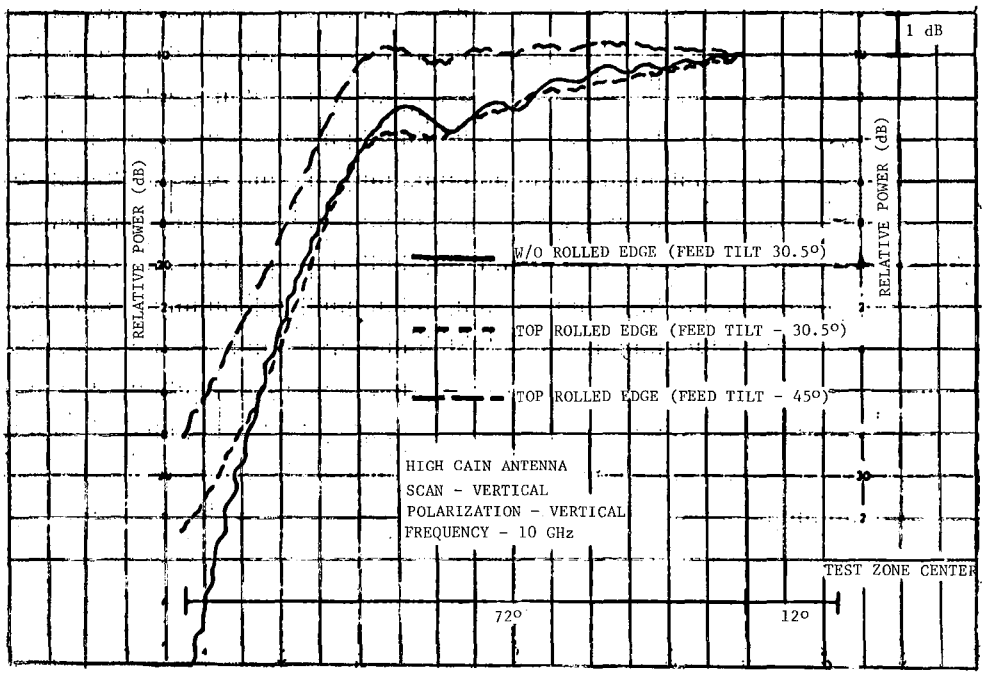

EARTH-LINK TESTS OF ORBITING SATELLITES
(FAR-FIELD DIRECT TESTING)

After a communications satellite has been placed in orbit, it is necessary to conduct functional performance tests to verify performance prior to certification. The use of an Earth-link test with the satellite has proven effective and elements of the same procedure may be required in space-based measurement systems. Comments concerning the Earth-link tests for evaluating communications satellites are listed below.

An extremely valuable satellite system test approach

INTELSAT systems have utilized on-going test program on the Fucino,Italy Earth station complex

For pattern tests , satellite may be taken out of normal communications operation, and despun or reoriented relative to Earth-axis coordinates

- **Data are taken point by point**
- **Coverage is limited to a few degrees in Az and El, or longitude and latitude.**

TESTING OF EARTH-BASED ANTENNAS USING RADIO STAR SOURCES (FAR-FIELD DIRECT TESTING)

In testing large aperture antennas on Earth, such as radio astronomy reflector antennas, it is necessary to use radio star sources. This testing approach is very effective when cross correlation techniques are used with precision reference antennas near the antenna under test. Several limitations associated with measuring large space antennas are listed below.

RADIO STAR SOURCES are also employed in direct far-field tests of large Earth station and radio astronomy antennas

Measurements include:

- G/T
- BORESIGHTING
- TRUE FOCUSING
- GAIN/EFFICIENCY
- POLARIZATION
- PATTERN PARAMETERS

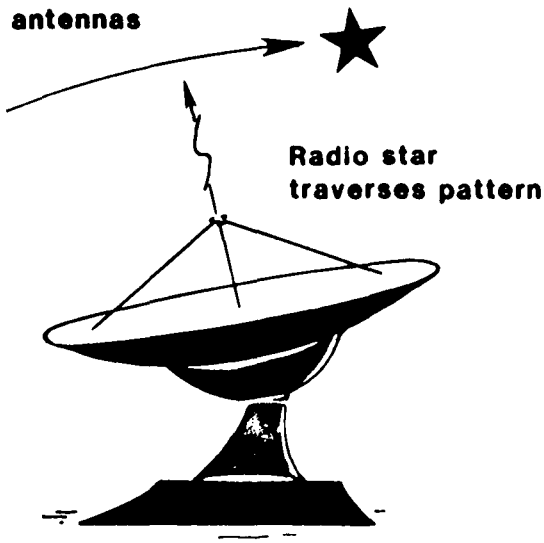

L,S, and C band systems have been enhanced with tracking interferometer auxiliary antennas

LIMITATIONS:

- Atmospheric effects above 10 GHz
- Lowering flux densities with increasing frequencies
- Gravity effects for deployable antennas
- Background thermal effects

FAR-FIELD INDIRECT MEASUREMENT TECHNIQUES
FOR LARGE APERTURE ANTENNA SYSTEM

Several techniques have been developed for measuring the far-field characteristics of a large aperture antenna indirectly and then transforming the data for direct far-field characteristics. Reducing the phase error encountered by testing the antenna in the near field (but using a far-field measurement approach) can be achieved by defocussing the feed system illuminating the reflector. The more common approach, however, is to use near-field scanning techniques, and the various types of near-field methods are listed below.

FAR-FIELD INDIRECT techniques include, in the order of complexity:

ON-AXIS "GAIN" in the near field at approximately

$$D/2 < R < 2D$$

DE-FOCUSED PATTERNS at $R < 2D^2/\lambda$

NEAR-FIELD TECHNIQUES, involving

- **NEAR-FIELD PROBING**
  - **Spherical**
  - **Cylindrical**
  - **Planar**
- **PROBE POSITION AND PATTERN CORRECTIONS**
- **COORDINATE CONVERSIONS**
- **FFT TRANSFORMS TO FAR FIELD**

TEST CONFIGURATION FOR THE SPHERICAL
NEAR-FIELD MEASUREMENT SYSTEM

The test configuration for the Spherical Near-Field Measurement System is shown below. The advantage of this approach is that the antenna under test is positioned in a similar manner as in a standard antenna pattern test and thereby does not require the complexity of scanning probes as in the case of planar near-field systems.

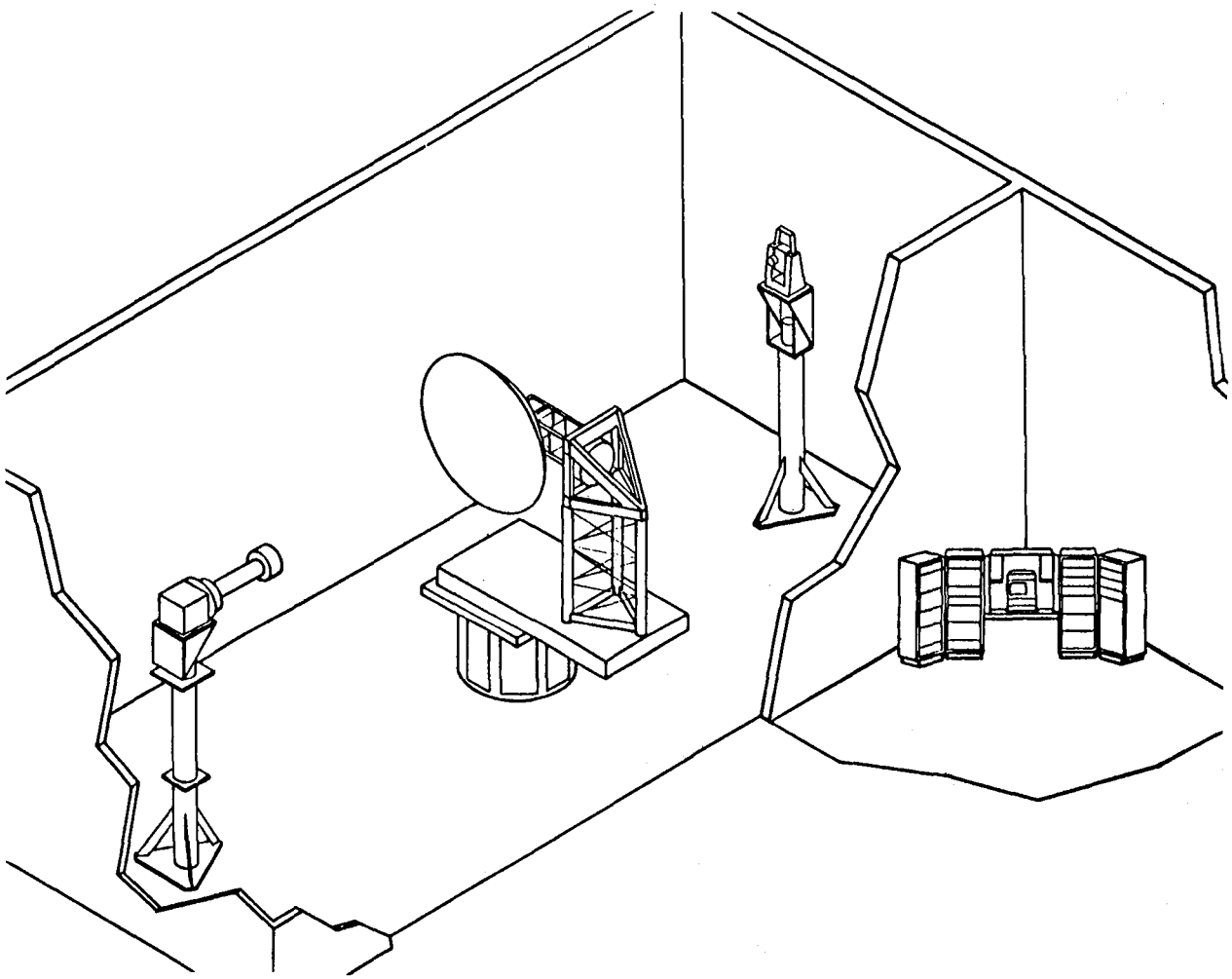

NEAR-FIELD TEST FACILITY
AT MARTIN MARIETTA AEROSPACE

The Near-Field Test Facility at Martin Marietta Aerospace in Denver, Colorado, is a planar scanning system and represents the type of investment required to achieve precision near-field measurements of large aperture antennas. This facility is shown in the photograph below.

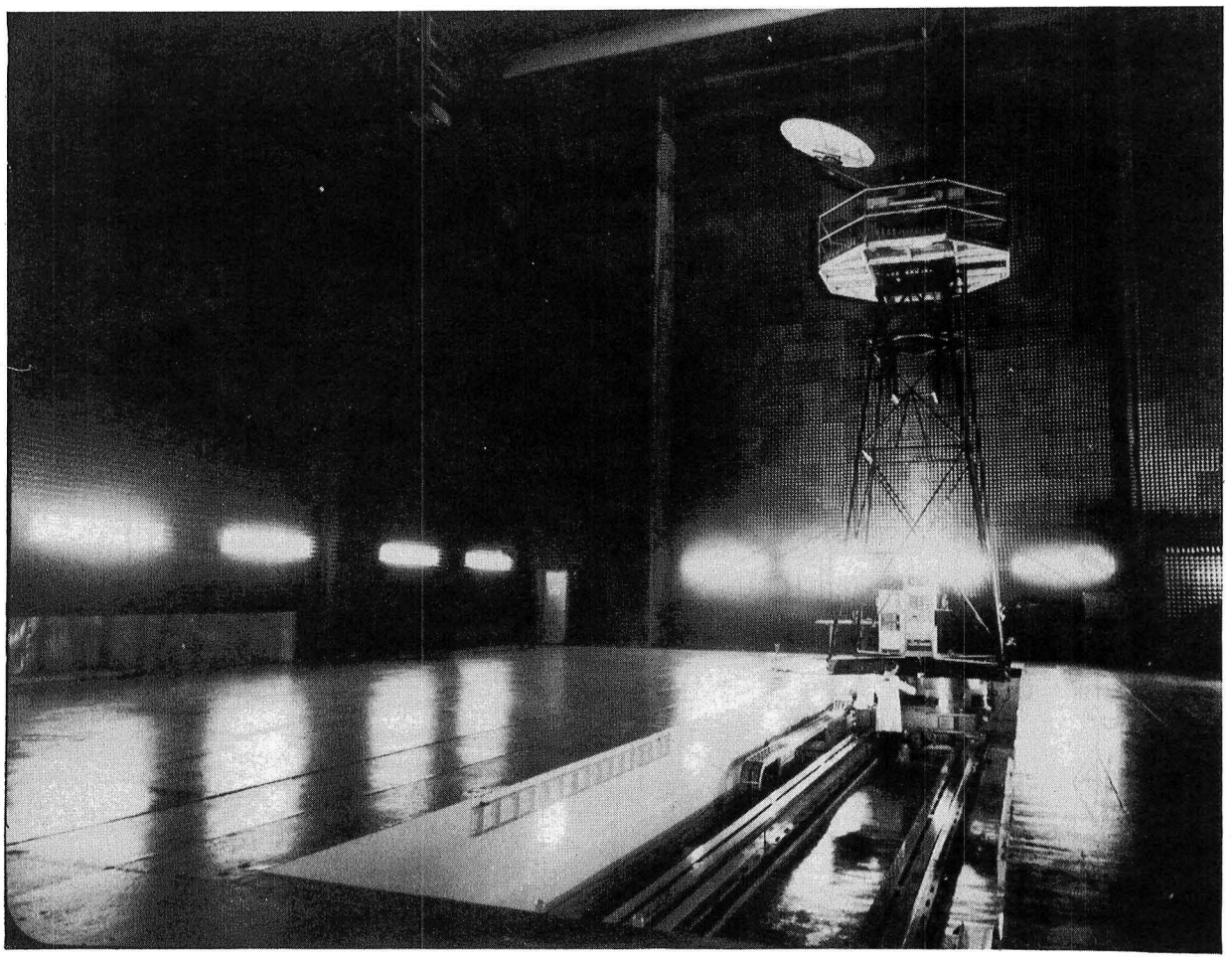

CONSIDERATION FOR SPACE-BASED ANTENNA MEASUREMENTS

In considering space-based antenna measurement systems, the following comments were made.

SPACE-BASED APPLICATIONS Would have some

- **Evident advantages**

  and

- **Significant problems**

Obviously the 1G distortion problem would be solved, with any candidate technique. To illustrate some other factors, we assume the following test requirement:

Assure within local space station environs, prior to injection into synchronous orbit, proper deployment and functional performance of an antenna with

- **D = 15 Meters**
- **f = 15 GHz**

SPACE-BASED FAR-FIELD DIRECT
MEASUREMENT SYSTEM CONCEPT

The advantage and concerns for applying a far-field direct measurement system approach for space-based application are listed below.

- $2D^2/\lambda \leq R \leq 10D^2/\lambda$

  $23Km \leq R \leq 115Km$

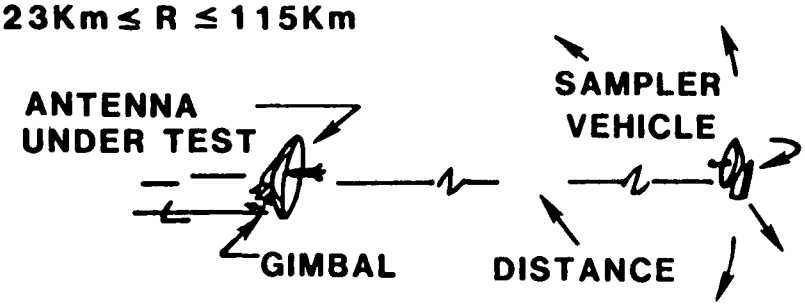

ADVANTAGES

- Virtually unlimited "REAL ESTATE"
- Direct access to test article
- With computational capacity and phase data, would provide basis for holographic aperture plane technique

CONCERNS

- Station-keeping for remote sampler
- Power levels for acceptable RFI vs. desired dynamic range
- Fuel requirements for sampler with fixed test antenna
- Gimbal requirements for test antenna with fixed sampler

UTILIZATION OF A SPARTAN CARRIER CONCEPT FOR FAR-FIELD DIRECT TESTING IN SPACE

NASA has developed the capability to place sounding rocket-type of experiments into Earth orbit using the Space Shuttle. The Space Shuttle has proven itself to be a successful and adaptive tool. One unique and new capability is the deployment and retrieval of satellites by the Shuttle crew. Spartan is a small experiment carrier developed by NASA to make use of the capability demonstrated by Shuttle. The Spartan carrier has been configured to conduct astrophysics experiments and, possibly, such a carrier could be instrumental for space-based antenna measurement. A conceptual far-field measurement using the Spartan carrier is shown below.

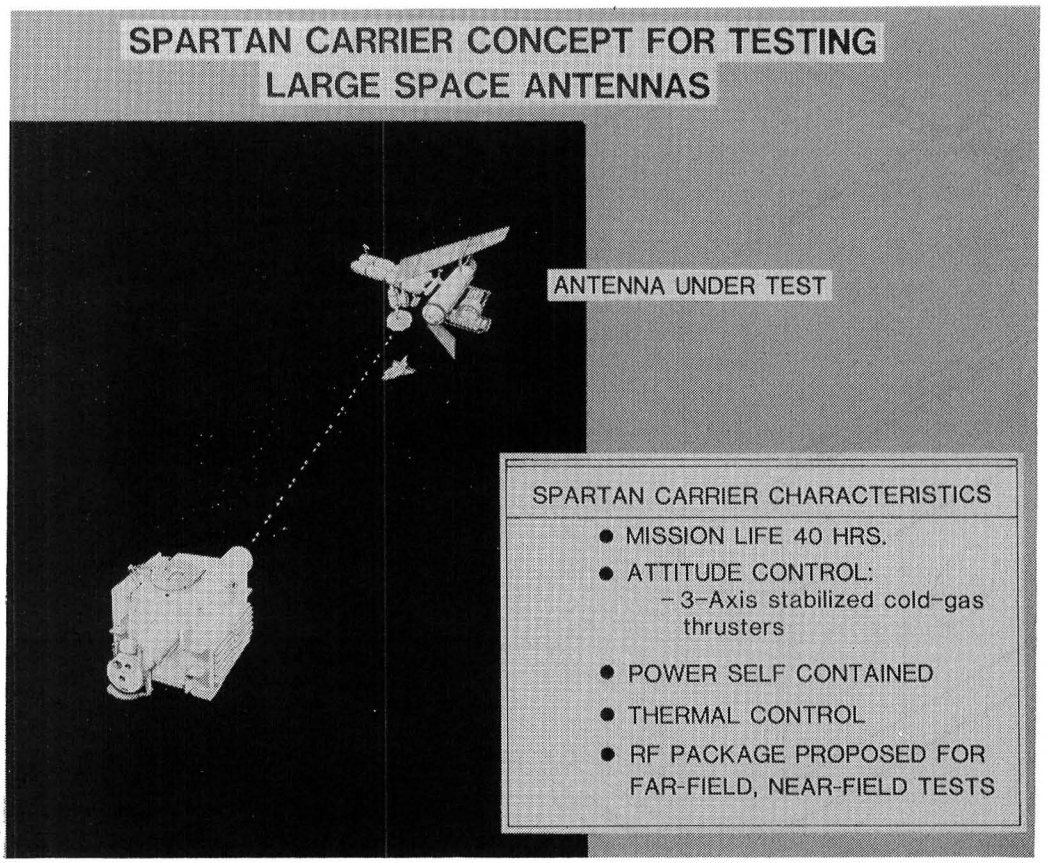

SPARTAN MODULE CONFIGURATION

The Spartan module configuration is shown in the figure below. The envelope available for RF instrumentation is indicated. A task would be to design RF components for conducting space-based antenna measurements without violating Spartan carrier envelope requirements if possible.

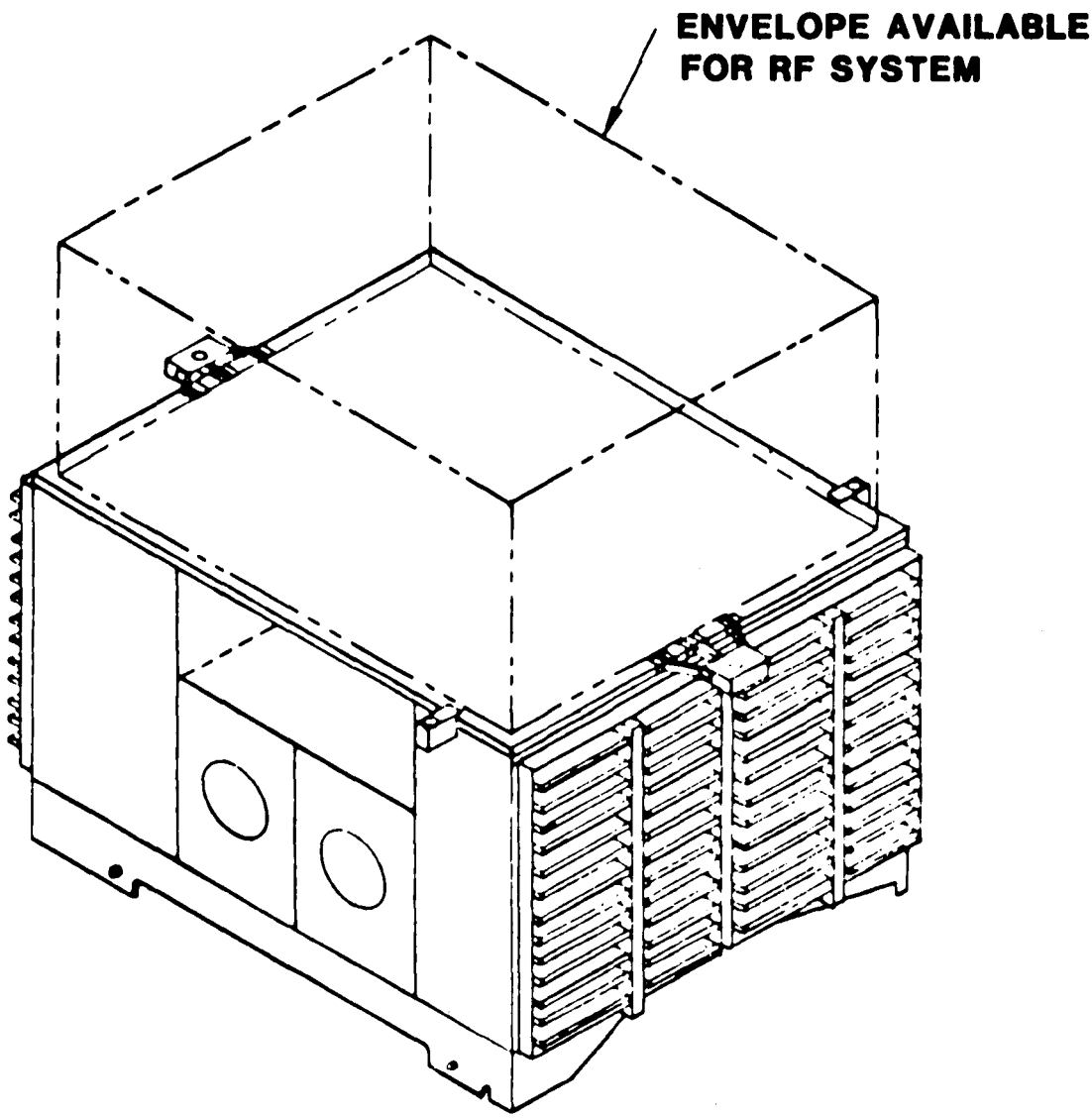

SPARTAN CARRIER - AN AUTONOMOUS SUBSATELLITE SYSTEM

The Spartan carriers and Shuttle deployment sequences are shown in the figure below.

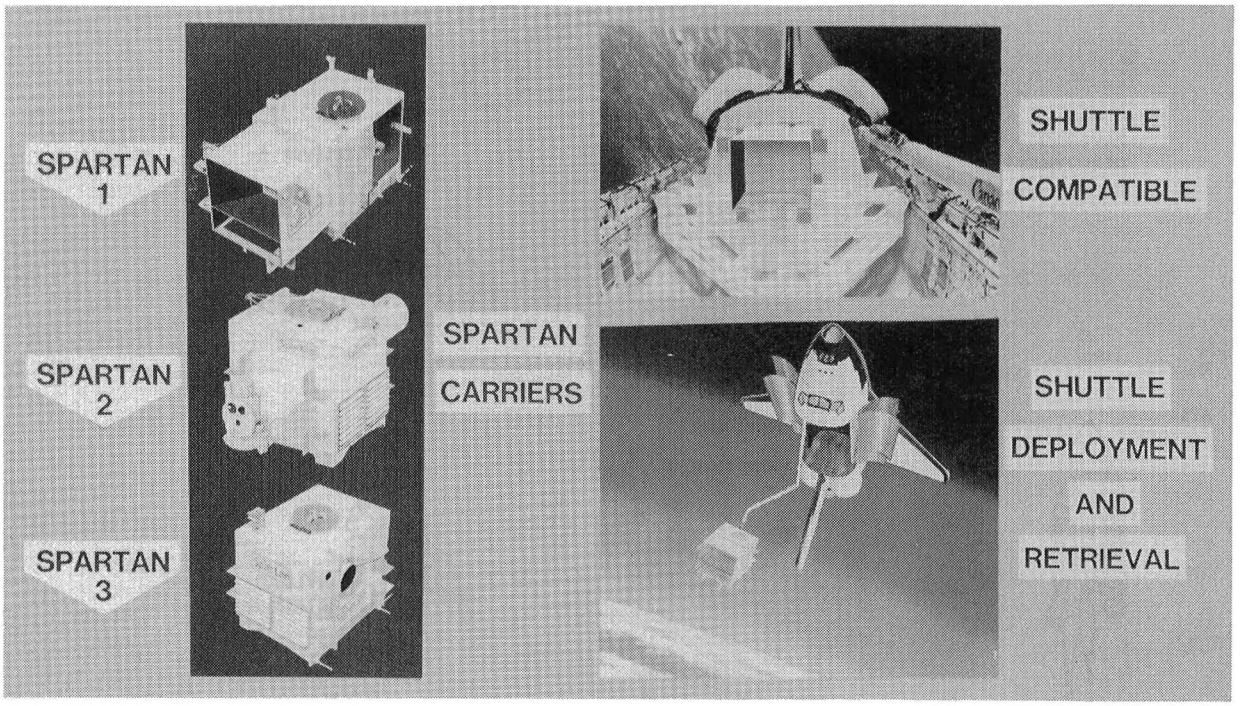

SPARTAN MISSION PROFILE

The Spartan mission profile is presented below.

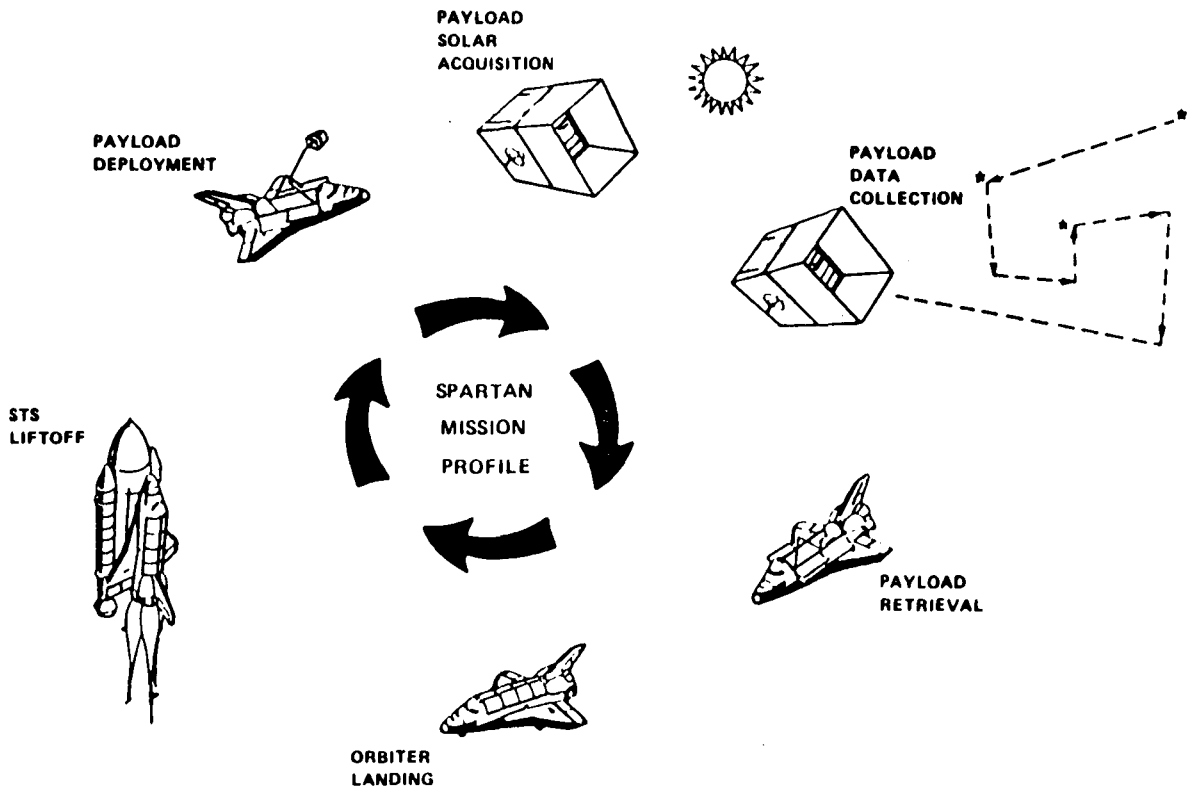

SPACE-BASED FAR-FIELD MEASUREMENTS USING RADIO STAR SOURCES

As described earlier in Earth-link tests using radio star sources, similar measurements could be conducted in space. A concept for using the radio star method in measuring a large antenna attached to a space station is depicted in the figure below. The advantages and concerns are listed as well.

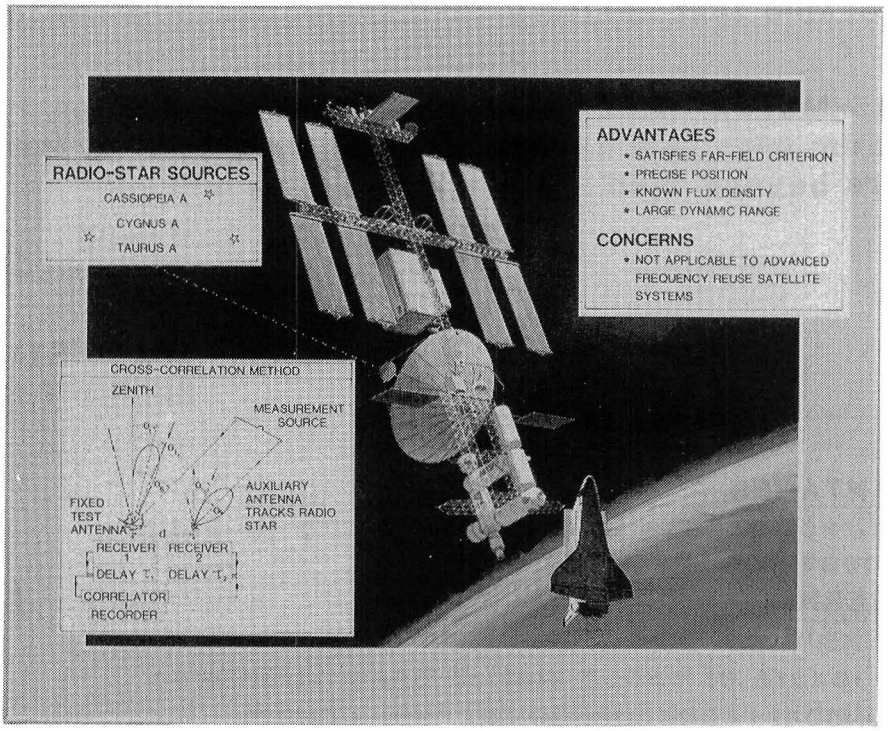

SPACE-BASED MEASUREMENTS USING COMPACT REFLECTOR TECHNOLOGY

The advances in compact reflector technology in Earth-based measurement systems were discussed earlier in this presentation and this technology may be applicable to space-based measurement systems as well. The possible advantage of using compact reflector systems is that it could allow measurements to be conducted directly on the space station platform. The advantages and concerns for such an application in space are listed in the figure below.

Reasonable test-aperture-to-range-reflector-diameter ratio is 1 : 4

For 15-METER TEST example: Compact reflector 30m high and 60m wide/test system mounted on gimbal at least 15 meters beyond feed

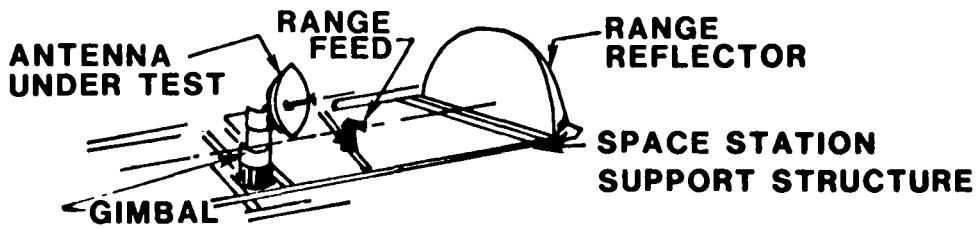

ADVANTAGES

- **Direct access to test article and to entire measurement system**

CONCERNS

- **Significant on-board volume**
- **Flexure of space station beam structures**
- **Gimbal requirements for test system**
- **Control of local RFI and reflections**
- **Thermal gradient effects on station supports and particularly on range reflector geometry**

COMPACT REFLECTOR SYSTEM CONCEPT FOR SPACE STATION

In an effort to stimulate discussion on possible uses of compact reflector systems for space station operations, a concept for including a compact reflector on the space station (side view) is shown in the figure below.

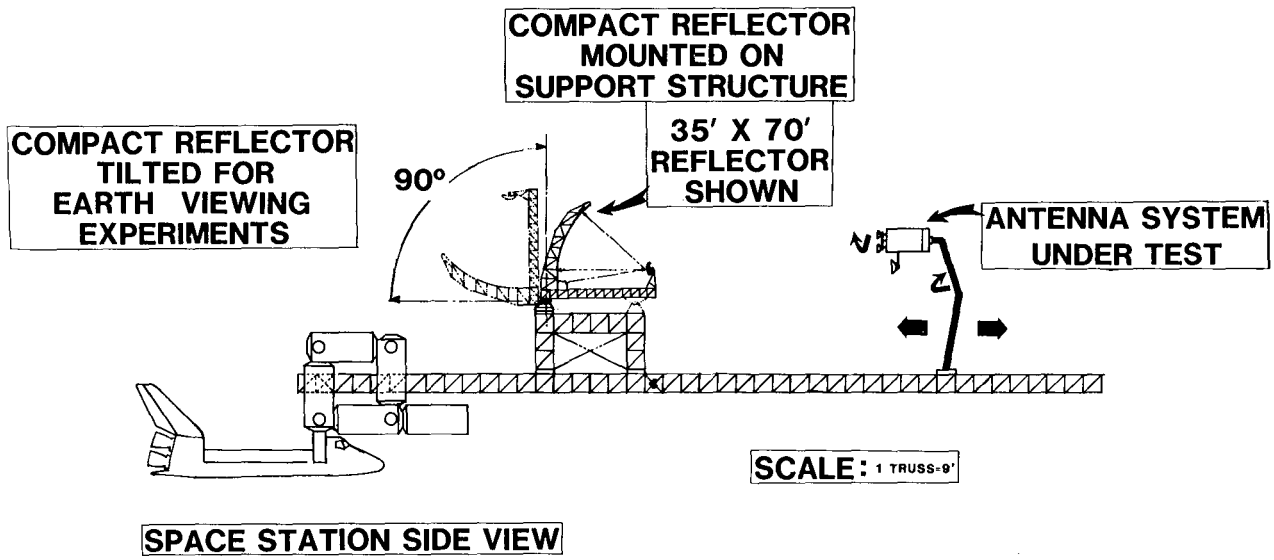

COMPACT REFLECTOR SYSTEM CONCEPT FOR SPACE STATION

The top view of the compact reflector system attached to space station is presented in the figure below.

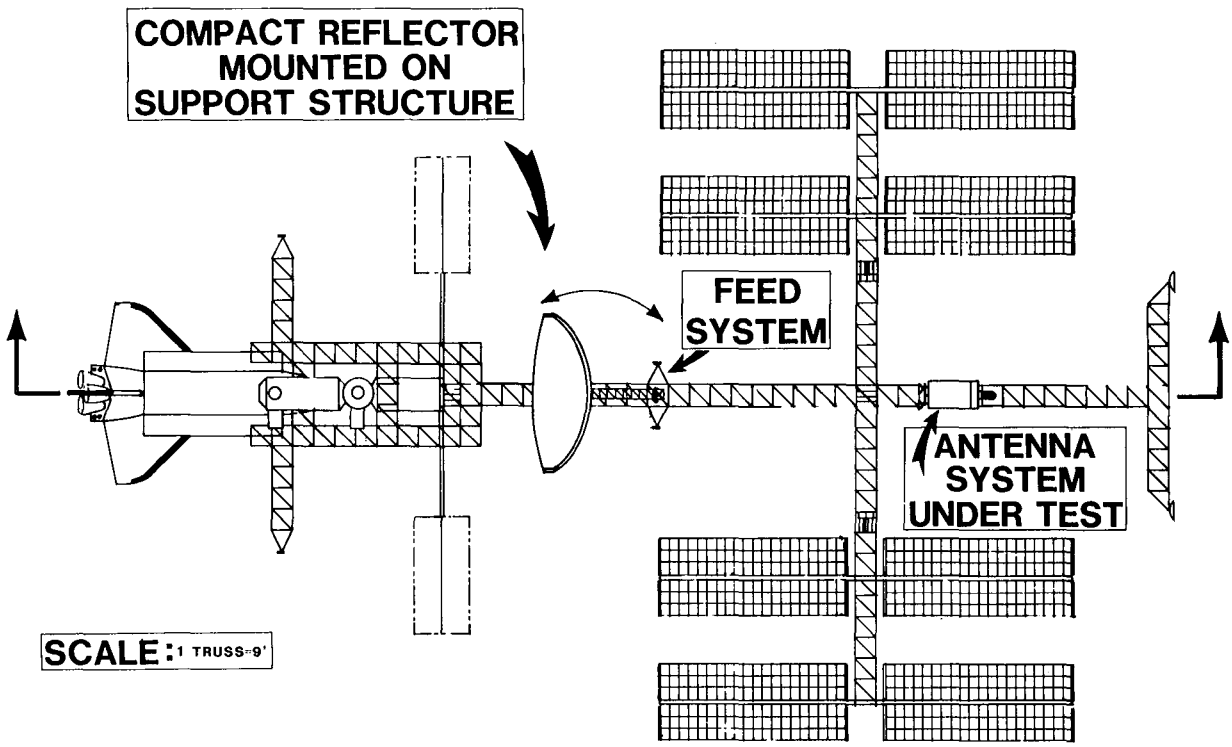

SPACE STATION TOP VIEW

SPACE-BASED NEAR-FIELD MEASUREMENT
CONCEPT USING SPARTAN CARRIER

Due to the expressed difficulty in achieving spherical and planar near-field measurements in space, another approach must be investigated which would rely upon advances being made in near-field algorithms and data collection techniques. If this can be done, then the utilization of a Spartan-type carrier for collecting near-field data would become feasible. The use of a Spartan carrier in a near-field data collection experiment over the Shuttle-attached 15-meter hoop/column antenna is shown in the figure below.

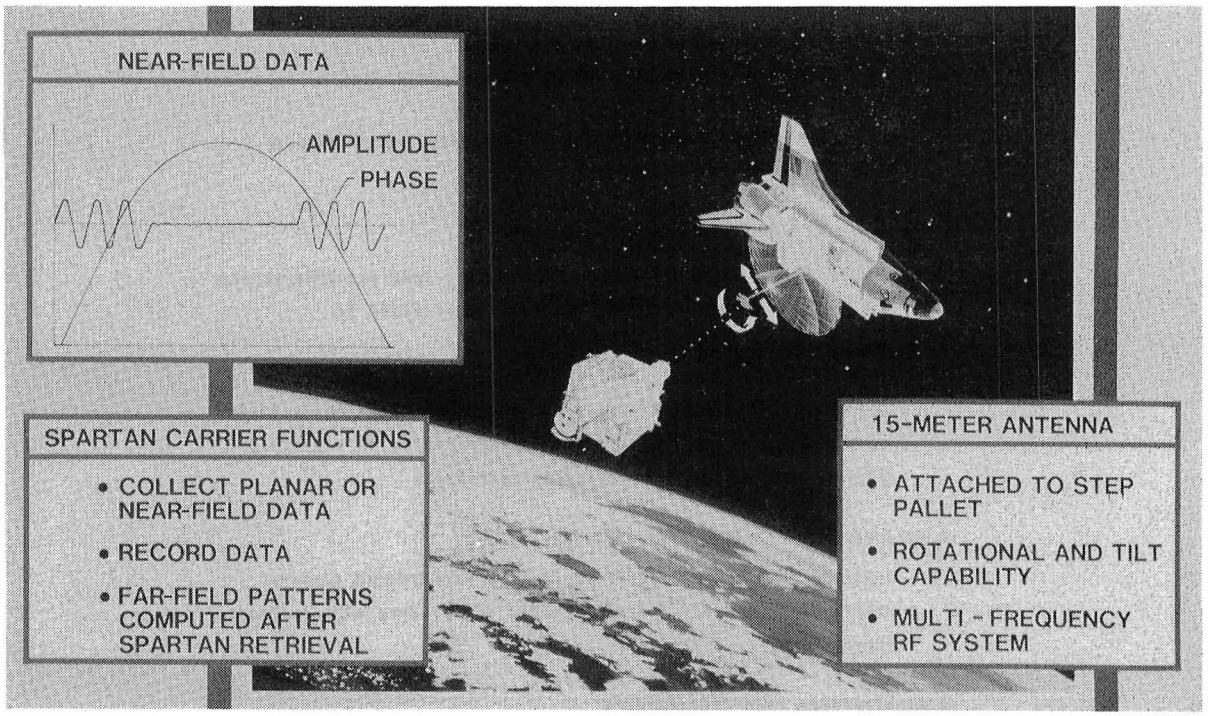

PROPOSED TASKS FOR THE DEVELOPMENT OF A SPACE-BASED ANTENNA MEASUREMENT SYSTEM

In an effort to initiate the technology development in support of a space-based antenna measurement system, the following tasks are proposed. In the immediate future, the Langley Research Center shall propose such a development program to the Office of Space Sciences and Application for consideration.

- **REQUIREMENTS DEFINITION**
  - **Update current assessment of on-orbit test requirements currently used in testing/certifying satellite systems (using Earth links)**
  - **Project requirements for future satellite systems (Multiple beams, multiple apertures, etc.)**
  - **Develop requirements for initial space-based measurement system**
- **ANALYSIS AND DATA PROCESSING**
  - **Investigate data thinning techniques and modifications to FFT to speed conversion of near-field to far-field**
  - **Investigate candidate data collection and processing techniques - including added complexity of multiple beams and shaped beam test problems**
- **MEASUREMENT SYSTEM DESIGN**
  - **Initiate "BRASSBOARD" design of homodyne and/or other instrumentation and radio frequency subsystem concepts**
- **SPACE SYSTEM CONCEPTS**
  - **Develop mission scenario using Spartan carrier in either near-field of far-field test configurations**
  - **Develop a list of supporting hardware and capabilities to support Spartan carrier approach**
  - **Establish advocacy for measurement system on space station (IOC/evolutionary)**
  - **Develop candidate concepts for space station measurement**

IN-SPACE PERFORMANCE OF THE TDRSS ANTENNA SYSTEM*

B. C. Tankersley
Harris Corporation
Melbourne, Florida

Large Space Antenna Systems Technology - 1984
December 4-6, 1984

*Paper unavailable at time of publication.

Page intentionally left blank

SOLAR ARRAY EXPERIMENT (SAE)
FLIGHT EXPERIENCE

Henry C. Hill and Leighton E. Young
National Aeronautics and Space Administration
George C. Marshall Space Flight Center
Marshall Space Flight Center, Alabama

Gary F. Turner
Lockheed Missiles &
Space Company Incorporation
Sunnyvale, California

Large Space Antenna Systems Technology - 1984
December 4-6, 1984

BACKGROUND

In 1975, a ground demonstration version of a large, flat flexible panel solar array was developed for NASA's Marshall Space Flight Center by Lockheed Missiles and Space Company. Even though ground demonstration was successful, final proof of some important operational characteristics resulting from its light weight could only be proven through space flight testing.

In 1978, NASA's Office of Aeronautics and Space Technology (OAST) gave approval to refurbish the ground demonstration unit and fly it as an experiment in space.

The experiment was designed to accomplish several objectives:

- Demonstration of functional operation of the wing deployment and packaging system
  - Survival of launch loads
  - 70% and 100% multiple extensions and retractions
  - Complete retraction with automatic reapplication of preload
  - Survival of landing loads
- Electrical Performance
  - Measure on-orbit performance of the solar cell panels
- Thermal Performance
  - Obtain electrical and mechanical performance data during stable operation, deployment and retraction under various sun angles
- Dynamic Performance
  - Obtain mode shapes and frequencies of the array wing when excited with the orbiter Vernier Control System
  - Measure dynamics using three independant instrumentation techniques - accelerometers, video photography, and optical displacement measurement

EXPERIMENT DESCRIPTION

The general features of the solar array wing are shown in Figure 1. The blanket is composed of 84 panels in a flat-fold configuration which make up, when deployed, a 32 x 4 meter array. The size of the array can be appreciated when viewed as an astronaut will see it from the cargo bay of the Space Shuttle. Stretching over 10 stories high, the Solar Array Experiment is the largest deployable space structure ever placed in orbit by mankind. The wing is of flight design; however, due to the high cost of solar cells, only one of the panels, the third from the outboard end, is a full electrical module. Half of the panel is composed of 2 x 4 x .02 cm cells with the other half composed of 5.9 x 5.9 x .02 cm cells. The remaining panels are covered with aluminum plates which simulate the mass of solar cells. A fully populated array would be capable of producing approximately 13,000 watts of electricity. The array is mounted on a government-furnished support structure which includes support brackets, MLI blankets, electrical cables, a Flexible Multiplexer/Demultiplexer, and a power control box. It is secured to the orbiter with four standard pallet trunnion fittings and one keel fitting.

The solar array portion of the experiment is composed of two major elements in addition to the Solar Array Wing itself. These are the Wing Support Structure, and the Data Acquisition System. These elements accommodate the array to the Space Shuttle and provide and control the external services necessary to meet the experiment goals.

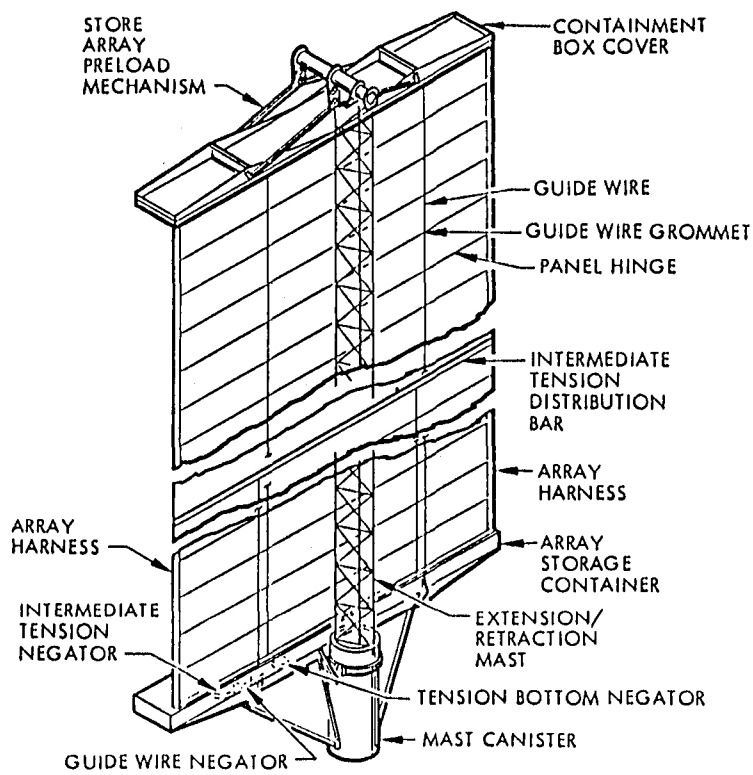

Figure 1. Solar array design description.

The support structure holds the experiment in a fixed position for launch and landing and interfaces with the NASA structure. It contains both pyroinitiated and manual release capability so that a Remote Manipulator System (RMS) - assisted jettison function could be performed in case an experiment failure prevents proper stowage of the array for reentry.

The Data Acquisition System is designed to monitor, process, and record experiment data during experiment operations. It includes a tape recorder for data storage, signal conditioning for dynamic and thermal instrumentation, power control functions, and pyrotechnic circuits for emergency jettison.

The following instrumentation was employed:

Accelerometers (6)-	3 Top of Mast
($1x10^{-6}$ g resolution)	2 Mast Canister
	1 Containment Box
Temperature Sensors (10)-	Solar Panels - 5
I 300°F	Other Locations - 5
Solar Panel Output	Open Circuit Voltage
	Short Circuit Current
	8 Intermediate Points
Motor Voltage (1)	
Motor Current (1)	
Dynamic Mode Shapes	
Photographic Measurement	63 Targets on Blanket
Optical Measurement	16 Targets on Blanket
	3 at Tip of Array
	4 on Mast

In addition, two dynamics measurement systems were employed, a photogrammetry system developed by the Langley Research Center and the Dynamic Augmentation Experiment (DAE) developed by MSFC. These are the subjects of other papers at this conference.

The Photogrammetry System uses the white circles on the array blanket (Figure 2) as targets for the orbiter TV cameras, to detect motion of the array during programmed firings of the vehicle control system. Also located on the array (Figure 3) is a series of pop-up targets to be used for the dynamic augmentation experiment.

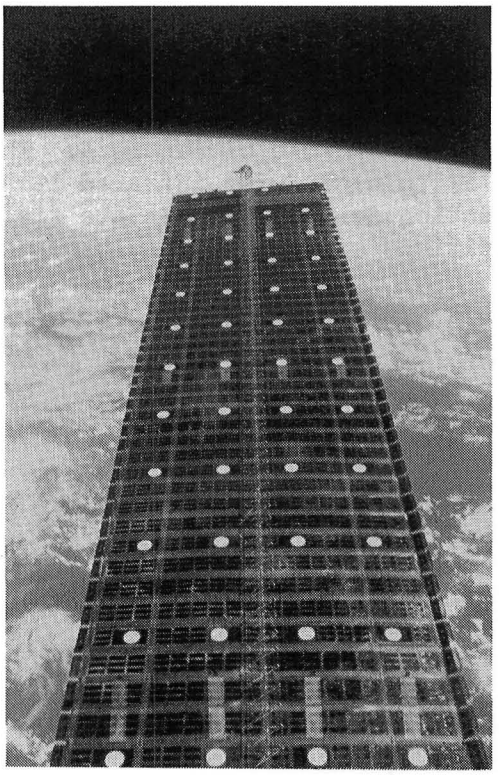

Figure 2. Illuminated solar array.

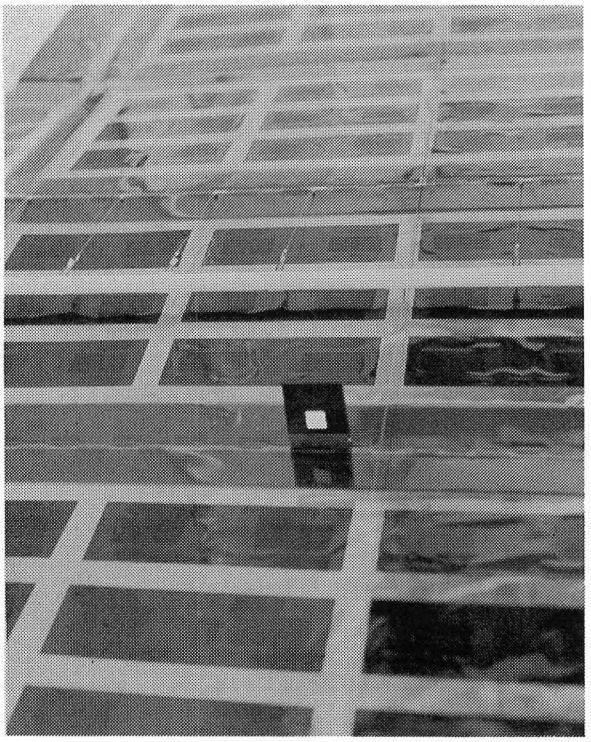

Figure 3. DAE target.

The emitter/sensor for this experiment is the first of its kind to be used for space application by NASA. It is a small white cannister mounted on its support stand shown in the far right side of Figure 4. The emitter section contains laser diodes which illuminate, with infrared light, the pop-up targets on the array. A charge-injection-device solid-state field tracker measures the array target motion during firings of the orbiters thrusters.

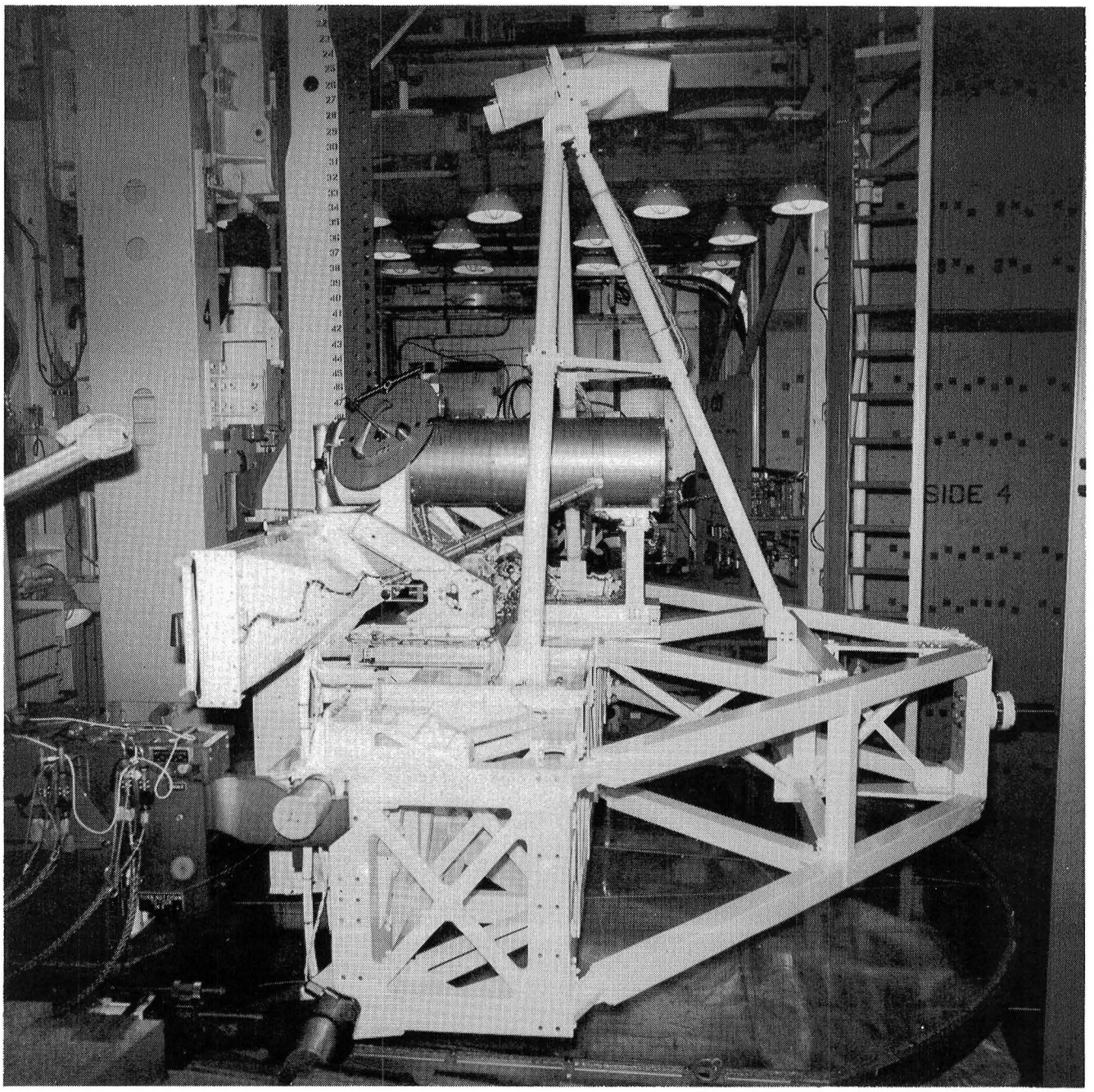

Figure 4. DAE emitter/sensor.

FLIGHT OPERATIONS

After sucessfully completing extensive ground testing, the experiment was delivered to KSC in February 1984, where pre-flight integration and checkout activities were initiated in preparation for flight on STS 41-D. After a number of delays, the Orbiter Discovery successfully carried its payloads into a circular orbit 174 nautical miles above the earth on August 30, 1984. After the deployment of three commercial communications satellites, SAE operations were initiated. Flight testing was sequenced into six basic test elements:

A. Extension/Retraction

B. Initial low level dynamics

C. Initial solar cell performance

D. Dynamics - 70% Extension

E. Dynamics - 100%

F. Final solar cell performance

A more detailed description of the actual events is shown in Figure 5.

ORBIT NUMBER*	EVENT DESCRIPTION
	INITIAL MAST NUT UNLOCK AND 12 INCH MAST EXTENSION.
36	FIRST EXTENSION TEST TO 70% POSITION.
36	FIRST RETRACTION TEST TO SOFT STOP POSITION.
	EXTEND TO 70%
37	FIRST PHOTOGRAMMETRY DYNAMICS TEST AT 70%, OUT-OF-PLANE.
37-38	FIRST DAE DYNAMICS TEST AT 70%, OUT-OF-PLANE.
	RETRACT TO SOFT STOP POSITION.
	EXTEND TO 70%.
47-48	SOLAR CELL PERFORMANCE TEST AT 70%.
49	PHOTOGRAMMETRY DYNAMICS TEST AT 70%, MULTI-MODAL.
49-50	DAE DYNAMICS TEST AT 70%, MULTI-MODAL.
50	PHOTOGRAMMETRY DYNAMICS TEST AT 70%, OUT-OF-PLANE.
50-51	DAE DYNAMICS TEST AT 70%, IN-PLANE.
51	PHOTOGRAMMETRY DYNAMICS TEST AT 70%, MULTI-MODAL.
51-52	DAE DYNAMICS AT 70%, MULTI-MODAL.
	EXTENSION TO 100%.
52	PHOTOGRAMMETRY DYNAMICS TEST AT 100%, OUT-OF-PLANE.
	RETRACT TO 70%.
	EXTEND TO 100%.
53	PHOTOGRAMMETRY DYNAMICS TEST AT 100%, MULTI-MODAL.
	RETRACT TO SOFT STOP POSITION.
	EXTEND TO 70% POSITION.
66	MINI SOLAR CELL PERFORMANCE TEST AT 70%.
66-67	DAE DYNAMICS TEST AT 70%, 1.5 DAP LOADING, MULTI-MODAL.
67	PHOTOGRAMMETRY DYNAMICS TEST AT 70%, 1.5 DAP LOADING, MULTI-MODAL.
67-68	DAE DYNAMICS TEST AT 70%, 1.5 DAP LOADING, IN-PLANE.
68	PHOTOGRAMMETRY DYNAMICS TEST AT 70%, 1.5 DAP LOADING, IN-PLANE.
	RETRACT TO FULLY STOWED POSITION.

*WHERE KNOWN. FLIGHT DATA/LOGS STILL BEING REDUCED.

Figure 5. Solar array flight experiment sequence of events/tests.

FLIGHT RESULTS

The operation of the system was trouble-free and was considered a 100% success as a demonstration of light weight solar array technology. Although review of the detailed data has not yet been completed, video tapes and crew logs have been reviewed and several phenomena were observed and are being evaluated.

During the first deployment, some minor panel-to-panel sticking was observed. This had also been observed during a ground test performed after a prolonged period of storage under full preload conditions. Early hypotheses tend to attribute this to very minute residual deposits of adhesive on the aluminum mass simulators causing bonding of the panels which were under local pressure over a long period. Because of the small areas involved and the fact that these adhesives are employed extensively only in the non-operational solar cell mass simulators, no change appears necessary for future panels using solar cells. As expected, subsequent deployments exhibited no sticking.

An out-of-plane mast motion was observed on all deployments when the array was approximately 50% deployed. This is attributed to a resonance between the first mast bending frequency and the rate of bay deployment on the mast that was predicted analytically and observed during ground tests. The motion was minor in nature and no future design changes should be required.

Damping of the mast motion was much higher than the 0.5% assumed for dynamic analysis. This resulted in shorter "wait" periods to reach quiescence between dynamics tests and allowed twice the minimum planned tests to be run. These new damping values, believed to be 4-5%, will be factored into future dynamics models.

During the last ten feet of retraction, panel motion seemed to increase, although never enough to cause any concern or impede retraction in any way. This has not yet been completely analyzed. However, it may be caused by a torsional correction in the mast correcting a $3\text{-}5^{o}$ twist known to be present in the first ten feet. For operational flights, this twist should be corrected. This was not done in this case, since the twist was considered acceptable for experiment purposes. Further evaluation will be performed during post flight ground test.

One solar panel temperature looked erratic, which indicates the possibility of a debonded thermistor. This well be checked during post-flight inspection.

During the dark portion of the orbit, there was a distince curvature to the panels (Figure 6) which corrected itself during the light portion of the orbit (Figure 2). Several possibile causes are being evaluated:

1. Kapton hinge loops not sliding on the S-glass epoxy hinge pins

2. Differential thermal growth between the aluminum panel frames and the Kapton substrate

3. Hydroscopic contraction of the Kapton panels

4. Thermal gradients in the aluminum frame members

5. Discrete torsion springs at the panel hinge lines

During fabrication, Kapton hinge loops were formed very tight around the hinge pins. If the hinge pins were unable to slide in the hinge loops, they would merely have a tension load under hot temperatures and have no deflection, whereas under cold temperatures, they would buckle under compressive loads. If this turns out to be the case, the fix would be to open up the tolerances in the hinge loops. The other possible causes listed are used in the experiment-peculiar mass simulator panels only, and no change for operational flights would be necessary. Although the phenomenon did no harm and had no effect on performance, some post flight ground tests are under consideration to try to understand and pinpoint the cause.

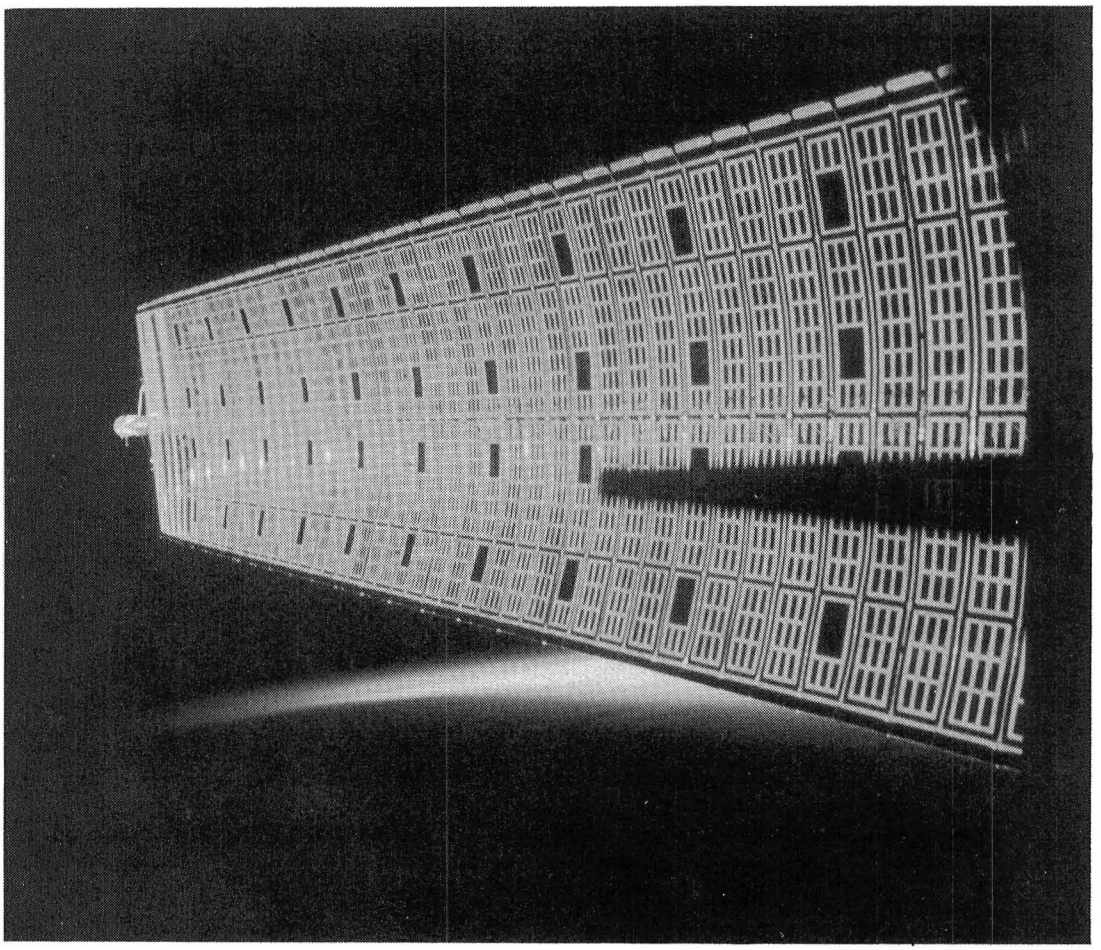

Figure 6. Panel curvature, dark side.

CONCLUSIONS/REMAINING WORK

Based on results evaluated to date, the Solar Array Experiment was 100% successful in meeting its goals. Reduction of tape recorder data is nearing completion at MSFC for evaluation by all participants. Videotapes of array motion are now being evaluated, and the dynamic model will be employed to correlate predictions with DAE and photogrammetric measurements using input acceleration and reduced mode shape data. The external hardware was inspected at KSC after flight and no damage of any kind was evident. The hardware was then shipped to Lockheed, where a post-flight ground deployment test will be conducted in early January at which time the blanket will be inspected for any signs of flight degradation. In addition, the array will be deployed to assure proper operation after exposure to Shuttle landing environments.

The flight of the Solar Array Experiment aboard mission 41-D demonstrated a technology which can reduce the weight and volume of space arrays to approximately 1/8 of that flown on Skylab. Future solar arrays which use this technology can be developed at approximately 50 percent of the cost for previous arrays, while at the same time having longer lifetime capabilities. In addition, the Dynamic Augmentation Experiment validated the concept of on-orbit test to define structural dynamic characteristics and greatly enhances future large space structural systems on-orbit control capability.

ASSEMBLY CONCEPT FOR CONSTRUCTION OF ERECTABLE SPACE STRUCTURE (ACCESS) NEUTRAL BUOYANCY TESTING RESULTS

Walter L. Heard, Jr.
NASA Langley Research Center
Hampton, VA 23665

Large Space Antenna Systems Technology - 1984
December 4-6, 1984

INTRODUCTION

To support space missions that will require large structures, orbital construction methods using astronauts in extravehicular activity (EVA) are being investigated. Ground test programs (e.g., refs. 1, 2, 3, and 4) have been conducted that show astronaut EVA assembly of an erectable truss structure is well within human capabilities. References 3 and 4 show that high assembly rates are achievable using a work station/assembly line approach. ACCESS, which is an acronym for Assembly Concept for Construction of Erectable Space Structure, is a planned Shuttle flight experiment to assess the potential of a manual on-orbit construction concept and generate assembly data for correlation of ground test data. The individual parts (struts and nodal joints used to interconnect the struts) of the beam truss shown attached to the Shuttle in the figure will be unpackaged and assembled by two astronauts working from fixed foot restraints (work stations). In this paper, the planned flight experiment is described and results of the baseline neutral buoyancy simulation of the flight test are presented.

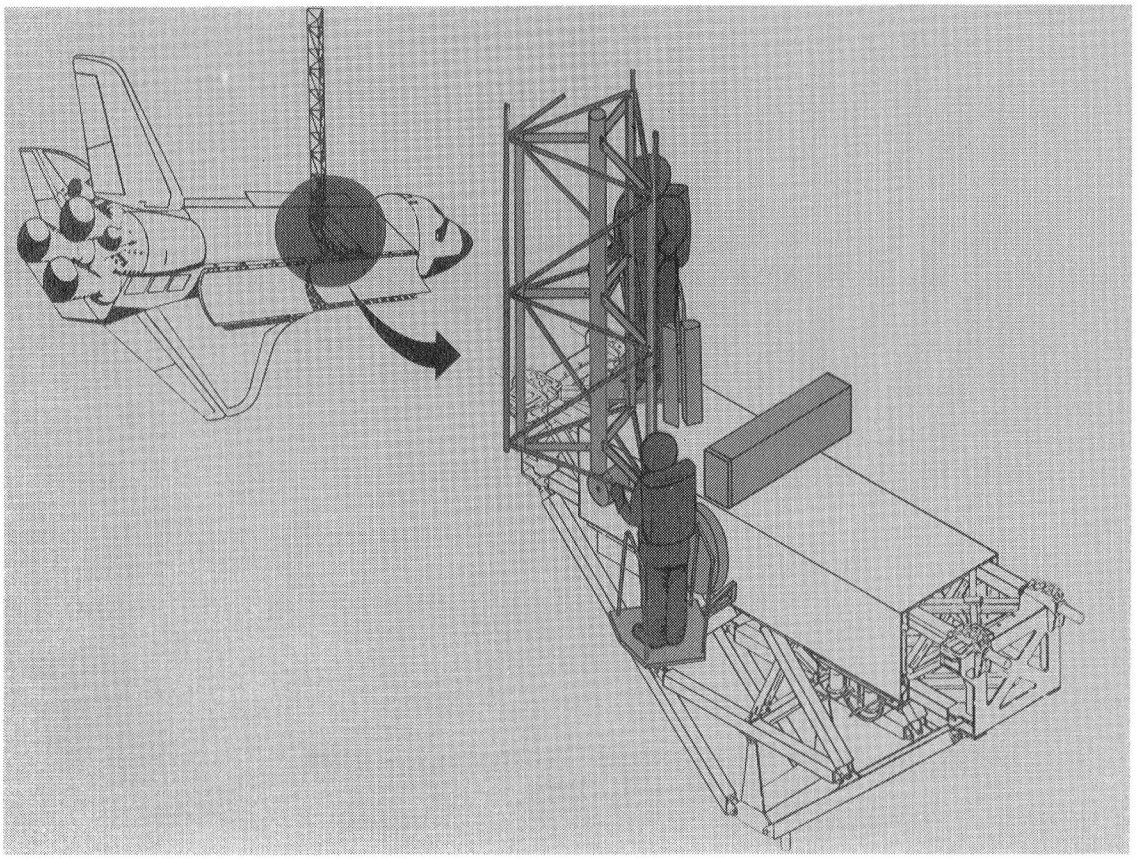

TYPICAL SPACE STRUCTURE

This figure shows the Space Station Reference Configuration (ref. 5). It is shown to illustrate the extensive use of beam trusses typical of those that could be constructed with relatively simple EVA methods similar to ACCESS.

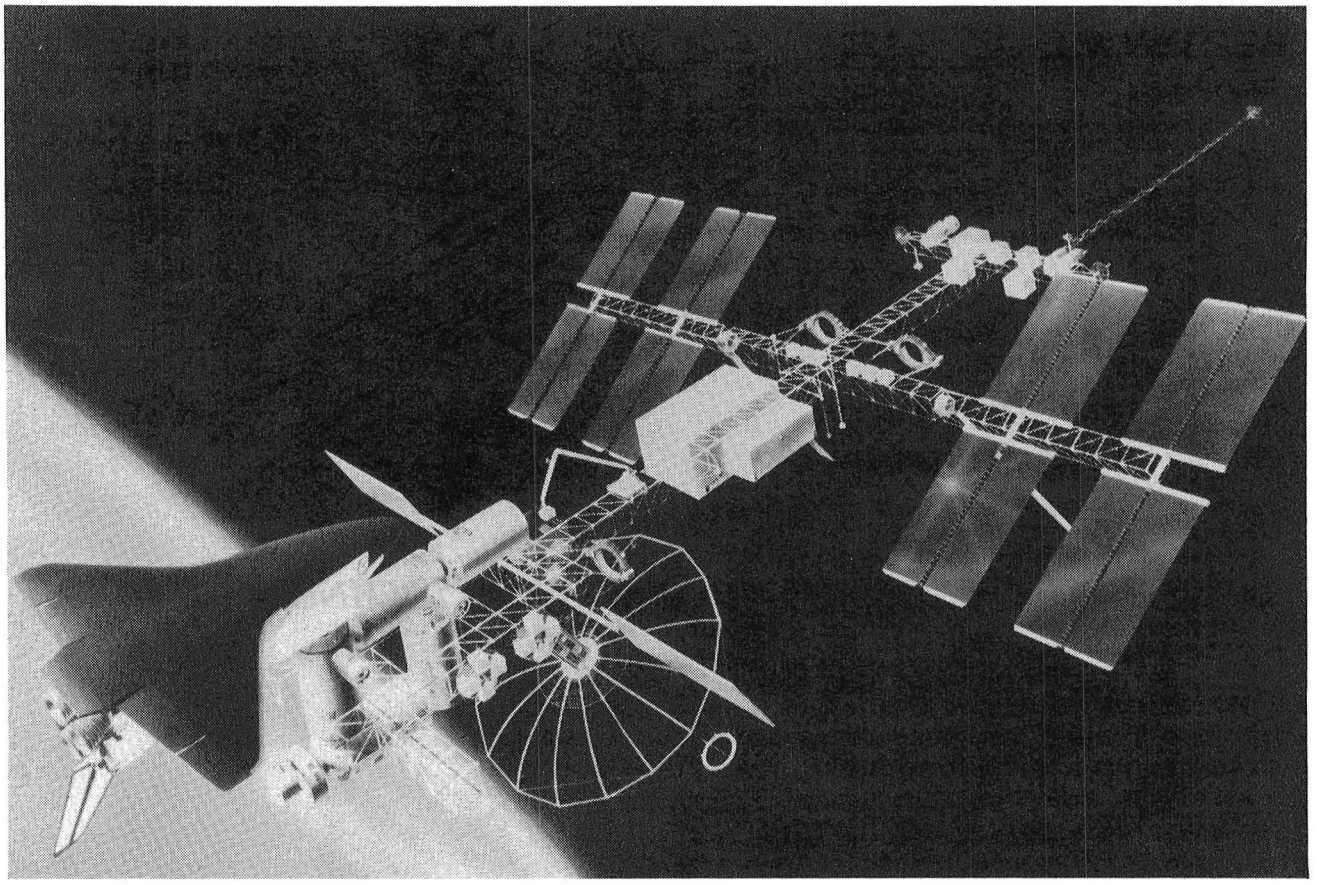

ACCESS SPONSORS

ACCESS is a planned NASA space construction experiment that is jointly sponsored by the Office of Space Flight (OSF) through its Flight Demonstrations Program and by the Office of Aeronautics and Space Technology (OAST) through base funding for research and development. ACCESS is classified as a Payload of Opportunity. This classification means that the experiment is not a primary payload, but an add-on experiment for a Shuttle mission when space is available. Thus, manifesting flexibility must be retained. Because of this Payload of Opportunity classification, ACCESS was designed to be relatively simple with no significant accommodations requirements, inexpensive, lightweight, and capable of being compactly packaged to eliminate interference with primary payloads.

NASA SHUTTLE FLIGHT TEST

- ***OFFICE OF SPACE FLIGHT (OSF)***
  - ***FLIGHT DEMONSTRATIONS PROGRAM (PAYLOAD OF OPPORTUNITY)***
- ***OFFICE OF AERONAUTICS AND SPACE TECHNOLOGY (OAST)***
  - ***SUPPORTED THROUGH BASE R & D***

ACCESS FLIGHT TEST OBJECTIVES

The objectives of the flight test are shown in this figure. The experiment is intended to provide data for correlation of assembly rates and techniques obtained from simulated zero-gravity (neutral buoyancy in water) ground test data. The ACCESS flight experiment will duplicate the ground test and thus will provide a direct comparison of data for the work station/assembly line space construction approach. Secondly, ACCESS will provide valuable and unique on-orbit construction experience using a concept designed specifically for efficient EVA construction. And, finally, ACCESS will be used to identify elements of the work station/assembly line construction procedure that will improve erectable structures productivity, reliability, and safety in the real space environment.

- *PROVIDE DATA FOR CORRELATION OF ORBITAL ASSEMBLY RATES AND TECHNIQUES WITH SIMULATED 0-G GROUND TEST DATA*
- *GAIN ON-ORBIT CONSTRUCTION EXPERIENCE*
- *IDENTIFY CONSTRUCTION PROCEDURE ELEMENTS WHICH WILL IMPROVE ERECTABLE STRUCTURES PRODUCTIVITY, RELIABILITY, AND SAFETY*

ACCESS HARDWARE
(STOWED CONFIGURATION)

This figure shows the ACCESS hardware in its stowed configuration. It consists of three fixed foot restraints, two strut canisters, a node canister, and an assembly fixture. The assembly fixture has a central tube with three guide rails (shown folded along the central tube). The assembly fixture pivots on a bearing to an upright position with respect to the Mission Peculiar Equipment Support Structure (MPESS). The pivot axis is perpendicular to the aft face of the MPESS, and is located near the left-hand end of the assembly fixture shown in the figure. When orbit is achieved, two astronauts pivot the assembly fixture to its upright position and deploy the guide rails.

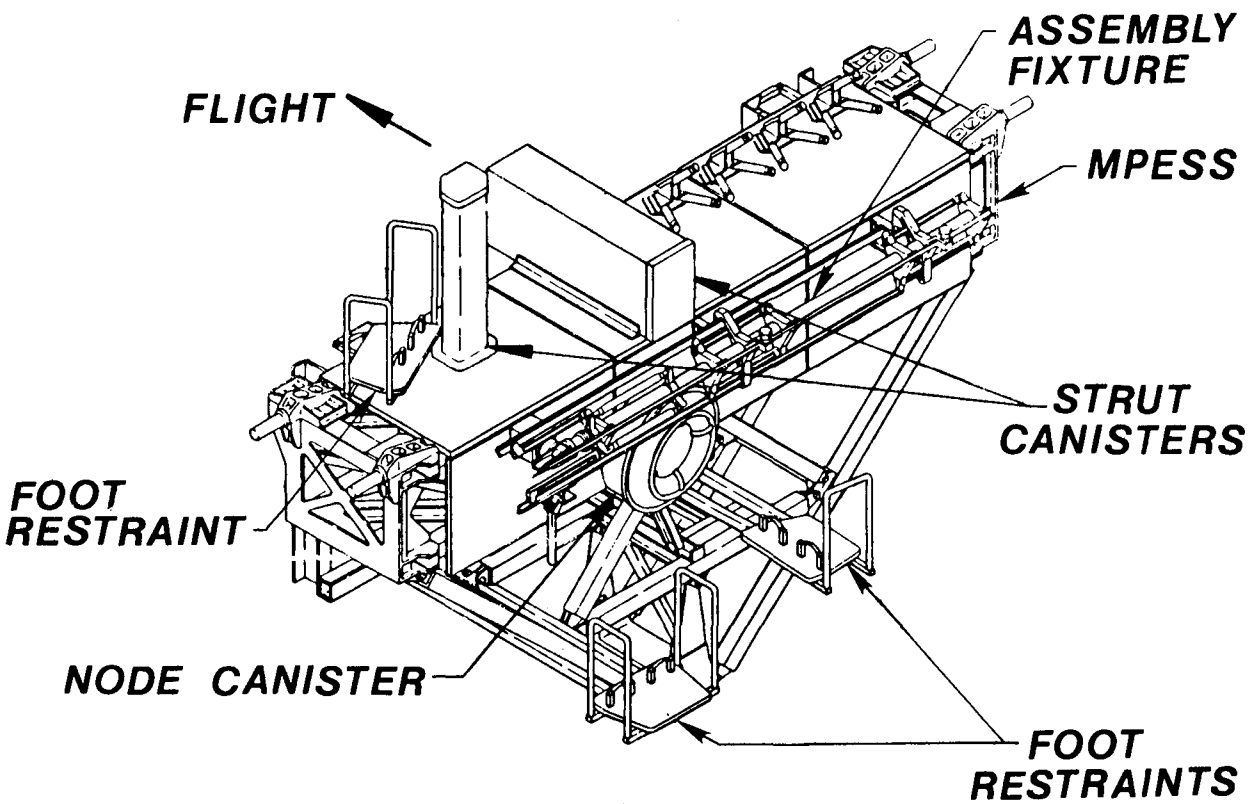

ACCESS HARDWARE
(DEPLOYED CONFIGURATION)

This figure shows the assembly fixture deployed and the two astronauts ready to assemble the truss. The inset shows the truss partially assembled and the approximate location of the experiment in the Shuttle cargo bay. The truss is made up of: (1) longerons--main vertical struts, (2) diagonals--bracing struts for the square bays of the truss, and (3) battens--horizontal struts that maintain the triangular cross section of the truss. The battens and longerons are each 4.5 feet long. The diagonals are 6.36 feet long. The assembly fixture can accommodate two bays of the truss at any one time. The truss is built strut by strut, one bay at a time on the lower half of the assembly fixture. The astronaut on the left works with the upper joints and the one on the right works with the lower joints. The assembly fixture is rotated about its longitudinal axis during assembly to provide the astronauts with access to all the joints. When a bay is completed, it is manually pushed up the assembly fixture to clear the lower portion for assembly of the next bay. The process is repeated until a truss of the desired length is attained. A 45-foot long, ten-bay truss will be assembled from 93 struts and 33 nodal joints. After the truss is assembled it will then be disassembled and restowed.

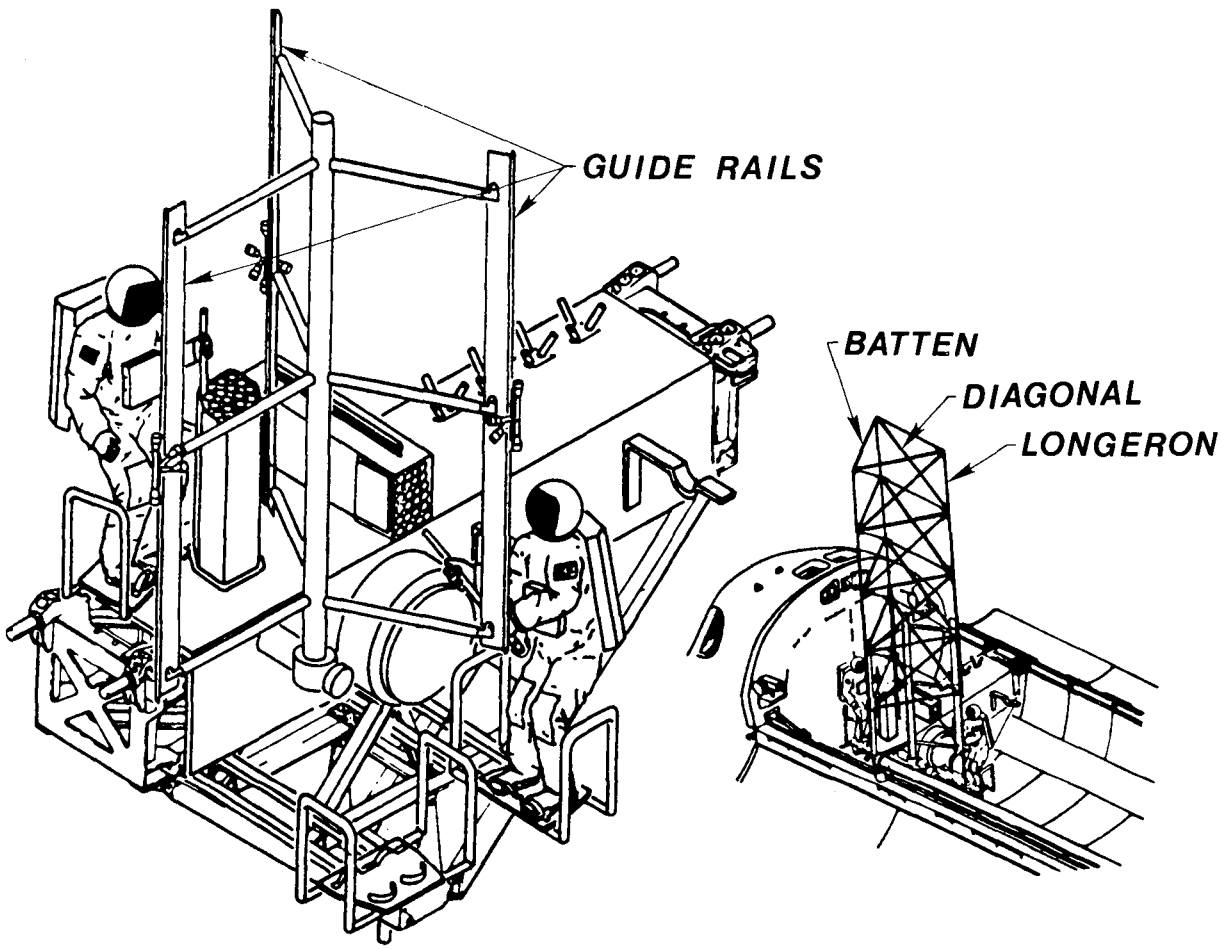

DATA

The data collected for ACCESS will consist of: audio and video recordings with time display of the complete experiment; still photographs and motion pictures for documentary purposes; some biomedical data such as crew heart rates and blood pressures for assessment of work load; and crew comments for qualitative assessment of assembly tasks. The data will be used to calculate orbital assembly rate in terms of struts per minute. The assembly rate will be correlated with the results from the simulated zero-gravity ground tests. The biomedical data and crew comments will be studied to identify tasks that may require modification to eliminate excessive physical exertion or otherwise degrade the efficiency of the assembly procedure.

- ***AUDIO-VIDEO COVERAGE***
- ***STILL PHOTOGRAPHS & MOTION PICTURES***
- ***BIOMEDICAL***
- ***CREW COMMENTS***

SCHEDULE REQUIREMENTS

In order to carry out the ACCESS experiment it was decided early in the program that two sets of hardware would be required and that they would be fabricated in-house at the Langley Research Center. One set would be used for develomental testing and training, and the other for flight. The primary material used would be aluminum. The training hardware is of high fidelity and was subjected to rigorous vibration and thermal tests as well as the corrosive environment associated with the underwater neutral buoyancy tests. The figure shows the major milestones of the program. When the schedule was planned, ACCESS was manifested on Shuttle flight 51-G scheduled for launch in May 1985. Subsequently, however, the orbiter Challenger was grounded for heat-shield repairs and complications developed with the scheduling of other flight assignments. As a result, ACCESS was removed from flight 51-G. The current status is that the flight hardware will be delivered to Kennedy Space Center in April 1985; the experiment will be ready to fly thereafter when the opportunity arises.

▶ *CONCEPT DEFINITION*	*JUN 1983*
▶ *PDR*	*JAN 1984*
▶ *TRAINING HARDWARE DELIVERY*	*MAY 1984*
▶ *NBS DEVELOPMENT TESTS*	*JUN 1984*
▶ *VIBRATION & THERMAL VACUUM TESTS*	*AUG 1984*
▶ *CDR*	*AUG 1984*
▶ *NBS BASELINE ASSEMBLY TESTS*	*OCT 1984*
▶ *FLIGHT HARDWARE DELIVERY*	*APR 1985*

NEUTRAL BUOYANCY TEST OBJECTIVES

The ACCESS training hardware was installed in the Neutral Buoyancy Simulator (NBS) at the Marshall Space Flight Center in October 1984 for zero-gravity simulations of the baseline flight experiment. The NBS is a cylindrical water tank 75 feet in diameter and 40 feet deep. Astronaut mission specialists as well as engineer test subjects working in space suits were used to perform all anticipated procedures (leave airlock, translate to work site, deploy assembly fixture, assemble a ten-bay truss, disassemble and stow truss, stow assembly fixture, and translate to airlock). Because of the limited depth of the water in the NBS, only six bays of the truss could be assembled and still maintain submersion of the structure for neutral buoyancy. Thus, the procedure was modified to perform assembly of six bays, disassembly and stowage of four bays, reassembly of the four bays, and finally, disassembly and stowage of six bays. In addition to generating data needed for correlation with orbital assembly data, hardware modifications arising from the ACCESS Critical Design Review were exercised and evaluated.

- ***DUPLICATE FLIGHT TEST TO PROVIDE CORRELATION DATA***
- ***EXERCISE AND EVALUATE CDR HARDWARE MODS***

TRANSLATE TO WORK SITE

This photograph shows the hardware installed on the MPESS, which is mounted in a mockup of the Shuttle cargo bay in the Neutral Buoyancy Simulator. The test subjects have translated from the airlock (hole in bulkhead in the upper center of this photograph) to their respective work sites and are preparing to deploy the assembly fixture.

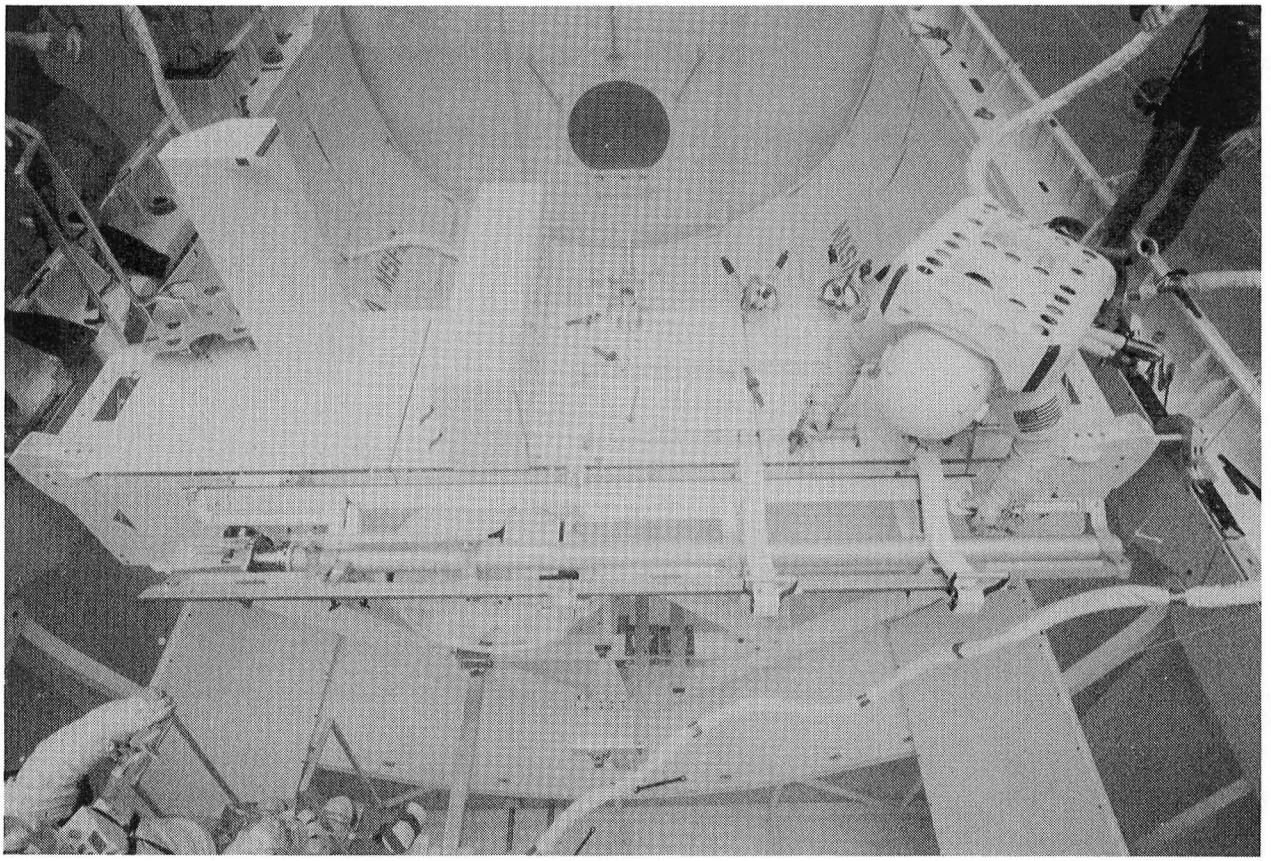

RELEASE OF ASSEMBLY FIXTURE CLAMPS

This photograph shows a test subject releasing one of the two redundant clamps used for securing the assembly fixture in the launch (stowed) configuration. After both clamps are released and secured in the fully open position, the assembly fixture is ready for deployment.

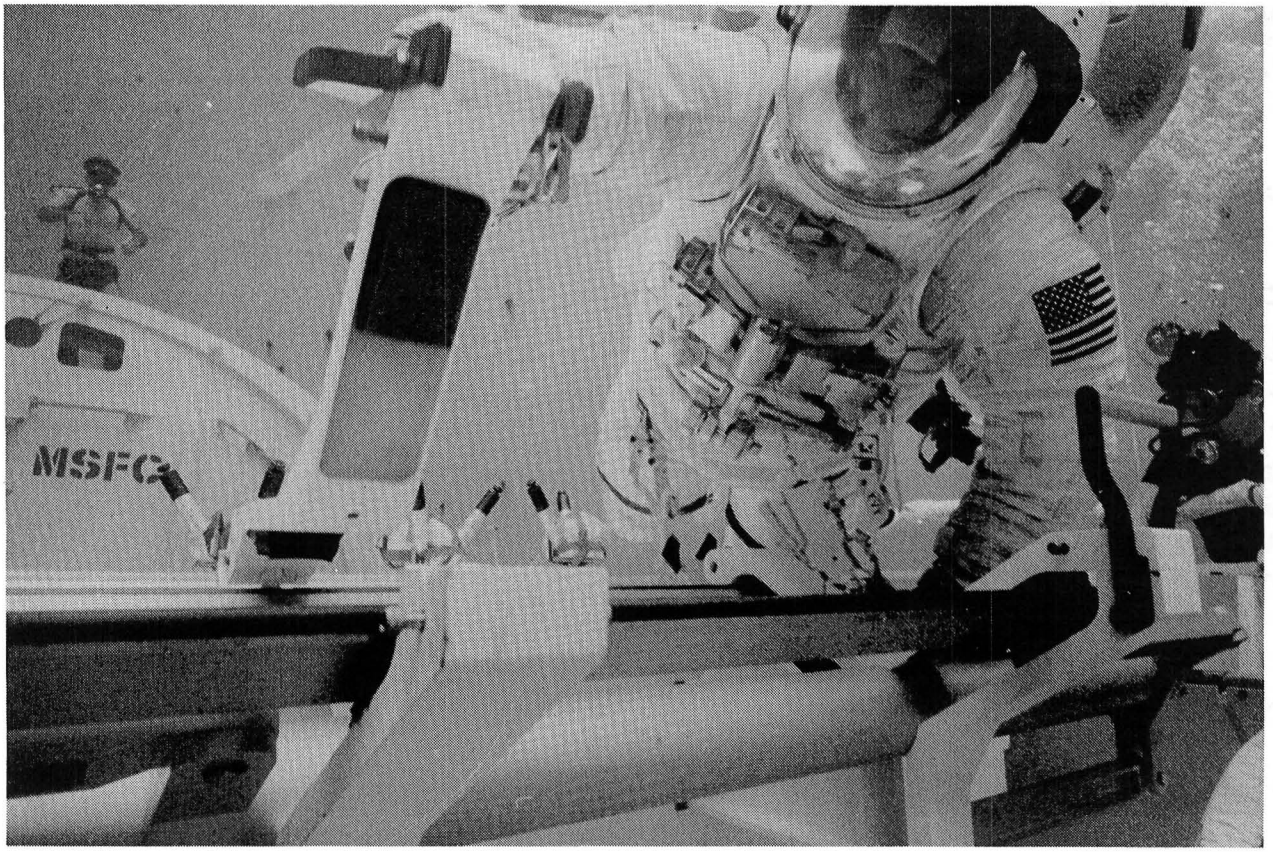

DEPLOYMENT OF ASSEMBLY FIXTURE

This photograph shows the assembly fixture being erected to its upright position where it will be secured before the three guide rails are deployed. The test subject in the left-hand side of the photograph is attached to foot restraints. The one in the right-hand side aids in initiating the rotation of the assembly fixture before translating to the upper work station where he will attach to foot restraints.

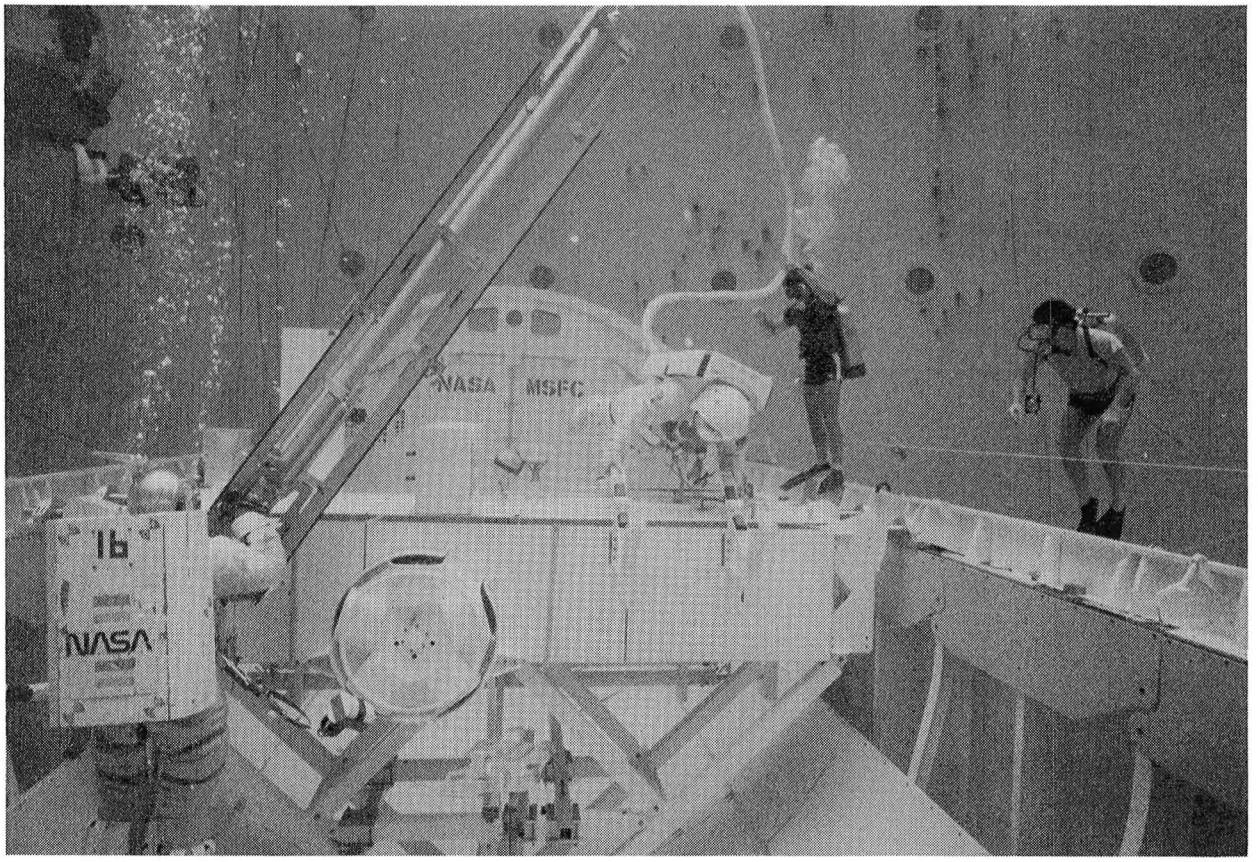

DEPLOYED ASSEMBLY FIXTURE

This photograph shows the assembly fixture fully deployed. The test subjects are positioned in their respective foot restraints and assembly of the truss has been initiated by the installation of the first nodal joint and diagonal strut. All nodal joints are installed on the guide rails by the lower test subject (shown in the right-hand side of the photograph). The longeron and batten struts are located in the horizontal strut canister and are accessible to the lower test subject. The vertical strut canister contains the diagonal struts and is accessible to the higher test subject.

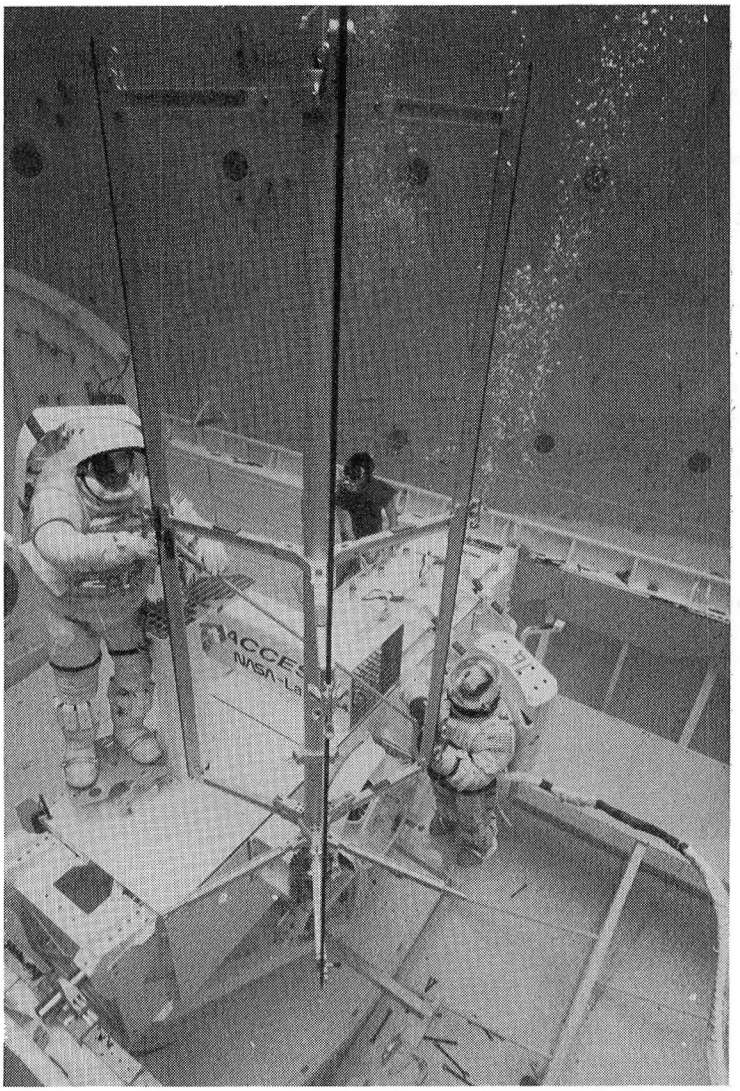

REMOVAL OF NODAL JOINT FROM CANISTER

This photograph shows the lower test subject removing a nodal joint from the compartment in the node canister. Each compartment accommodates six nodal joints and there are five compartments. Thus thirty nodes are stowed in the canister. The remaining three nodes are stowed in their proper locations on the assembly fixture guide rails prior to launch. When a compartment of the canister is emptied, the canister is rotated so that a full compartment becomes accessible to the test subject.

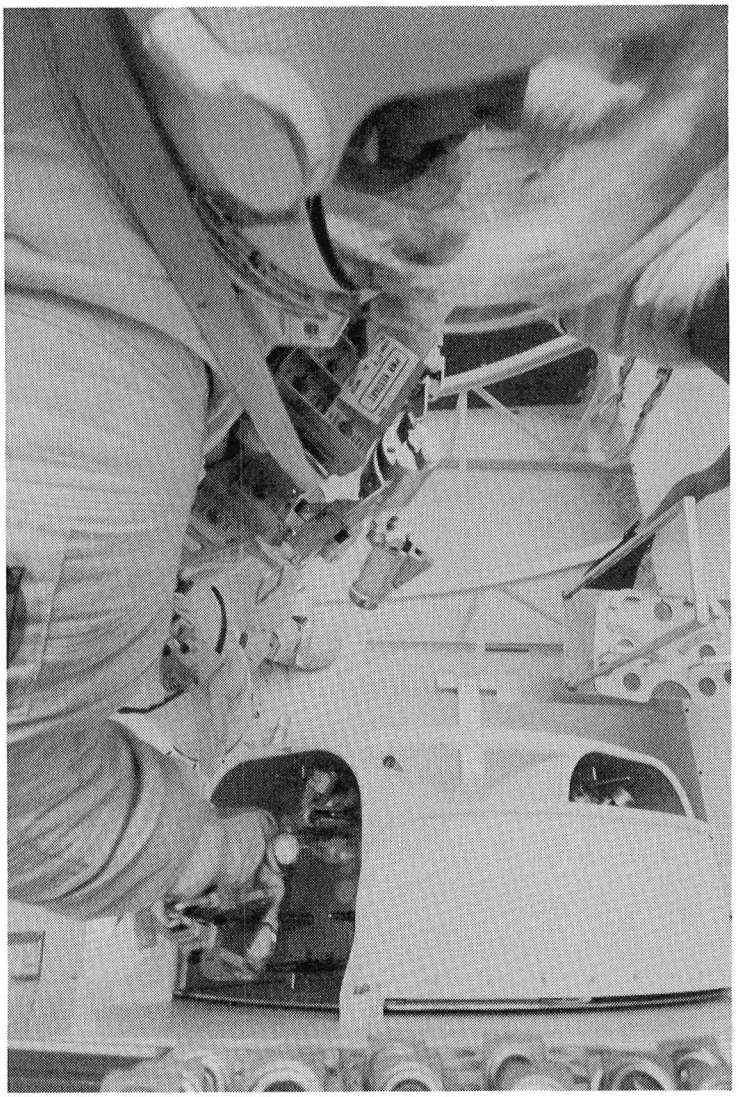

INSTALLATION OF NODAL JOINT ON GUIDE RAIL

This photograph shows the lower test subject installing a nodal joint on one of the guide rails of the assembly fixture. The joint has a slot that is slid onto the tapered end of the teflon-coated stainless steel rod shown just above the test subject's right hand. Both the rod and slot in the joint are coated in order to reduce frictional forces. No special orientation of the joint is required as long as the slot and rod are aligned. The joints are secured in the proper positions for assembly by latches and/or detents.

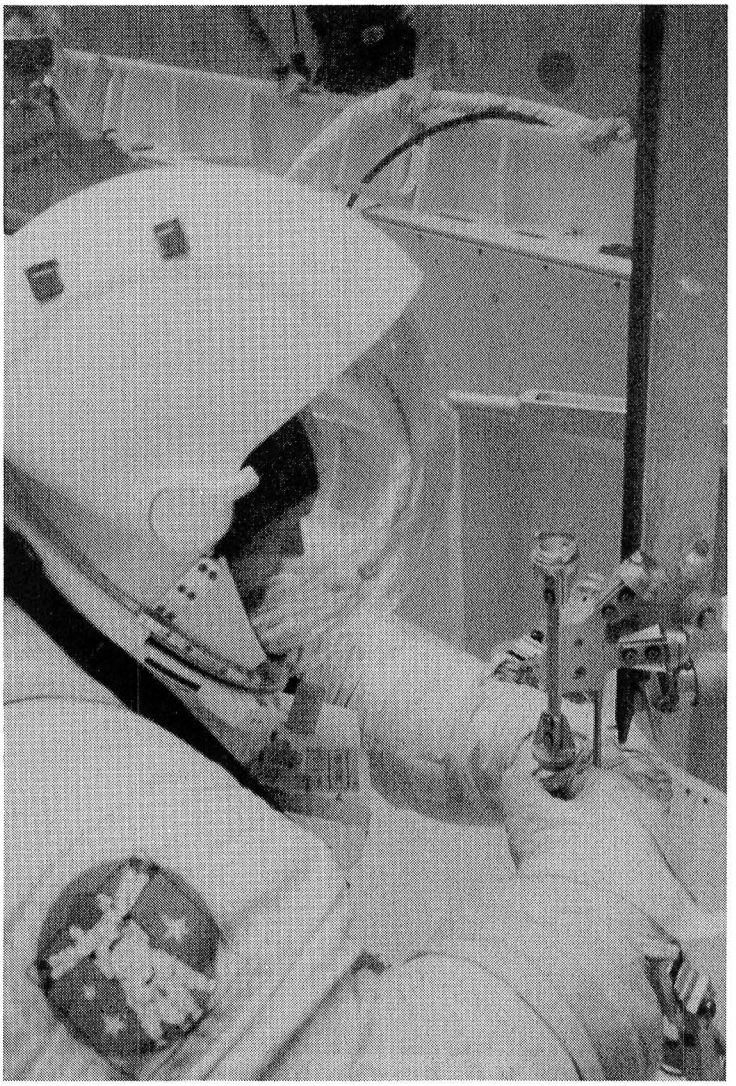

TRUSS ASSEMBLY

This photograph shows the truss assembly under way. The assembled portion of the truss has been slid up the guide rails to the upper half of the assembly fixture and an additional bay is being assembled below. Each test subject attaches struts to the nodal joint nearest his work station. The assembly fixture is then rotated 120 degrees about its axis so that the opposite ends of the struts can be connected.

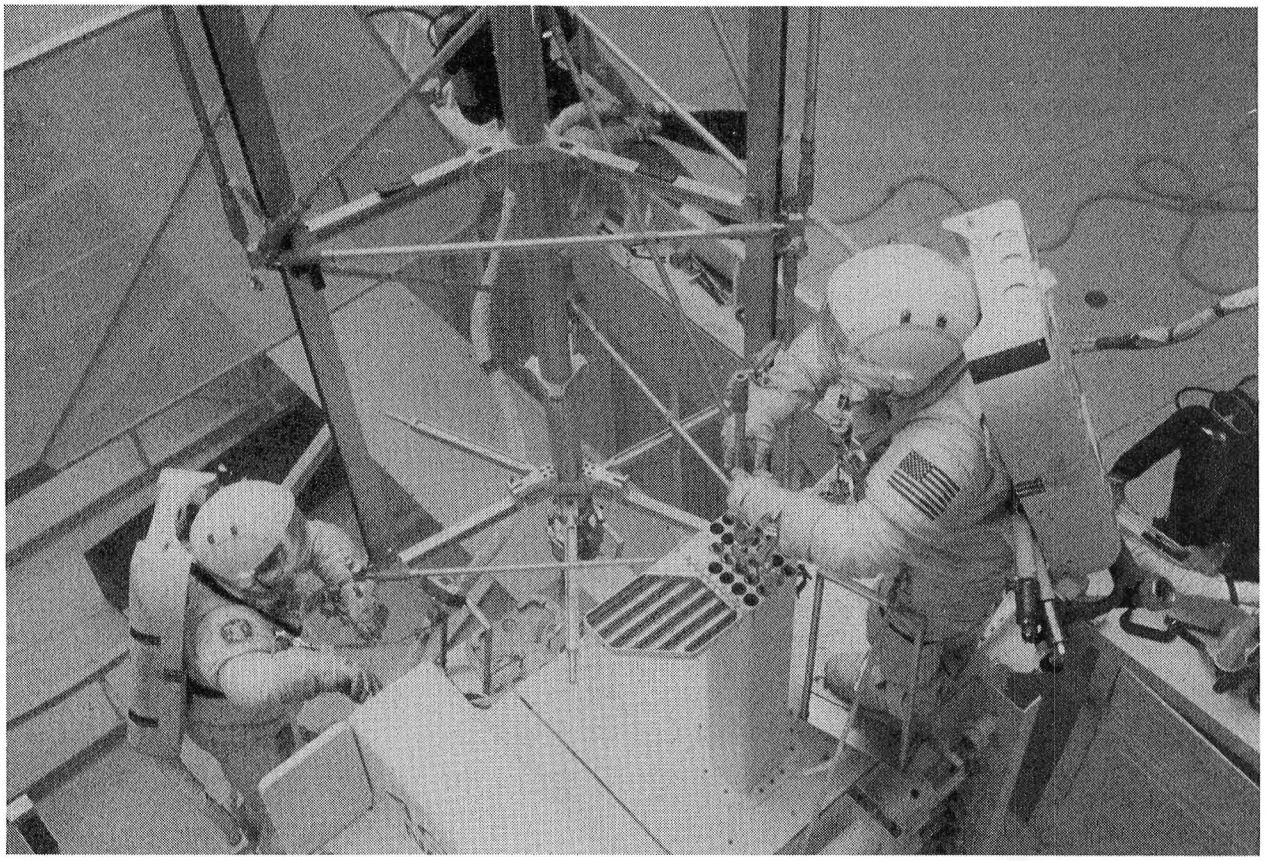

RESULTS OF NEUTRAL BUOYANCY TESTS

The baseline flight experiment procedures were performed by astronaut and engineer test subjects in simulated zero-gravity conditions. A complete baseline test was performed in one hour and nine minutes and the data showed no reduction in productivity due to astronaut fatigue. Translation to work sites, deployment of assembly fixture, disassembly and stowage for reentry took a large portion of this time. The actual assembly of ten bays was accomplished in 34 minutes and 40 seconds for an assembly rate of 2.7 struts/minute. Assembly tests were also performed on ACCESS in an Earth gravity and air environment with the test subjects in SCUBA. A comparison of results indicates that water viscosity has only a small effect on assembly time for the ACCESS hardware. In addition to acquiring the data needed for comparison with the flight data, the CDR hardware modifications and assembly procedures were evaluated by astronaut test subjects and found to be acceptable for flight.

BASELINE *ACCESS* SHUTTLE FLIGHT EXPERIMENT SIMULATED IN UNDERWATER NEUTRAL BUOYANCY TESTS

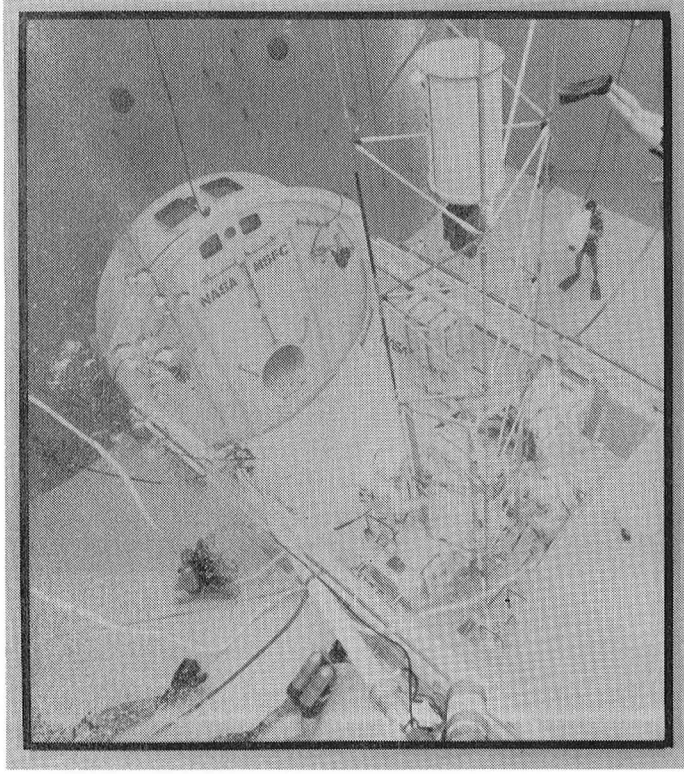

SIMULATED FLIGHT EXPERIMENT PERFORMED IN 1 HR. 9 MIN.

GROUND TEST DATA REQUIRED FOR CORRELATION WITH FLIGHT DATA OBTAINED

ASTRONAUT EVALUATED PROCEDURES AND HARDWARE FOUND ACCEPTABLE FOR FLIGHT

REFERENCES

1. Bement, Laurence, J.; Bush, Harold G.; Heard, Walter L., Jr., and Stokes, Jack W. Jr.: EVA Assembly of a Large Space Structure Element. NASA TP-1872, June 1981.

2. Akin, David; Bowden, Mary; and Mar, James: Manned Assembly of Space Structures. NASA CR-2269, Part 1, 1983.

3. Heard, Walter L., Jr.; Bush, Harold G.; Wallsom, Richard E.; and Jensen, J. Kermit: A Mobile Work Station Concept for Mechanically Aided Astronaut Assembly of Large Space Trusses. NASA TP-2108, March 1983.

4. Watson, Judith J.; Heard, Walter L., Jr.; and Jensen, J. Kermit: Swing-Arm Beam Erector (SABER) Concept for Single Astronaut Assembly of Space Structure. NASA TP-2379, January 1985.

5. Mikulas, Martin M., Jr.; Croomes, Scott D.; Schneider, William; Bush, Harold G.; Nagy, Kornell, Pelischek, Timothy; Lake, Mark S.; and Wesselski, Clarence: Space Station Truss Structures and Construction Considerations. NASA TM-86338, July 1984.

Page intentionally left blank

EXPERIMENTAL ASSEMBLY OF STRUCTURES IN EVA (EASE) NEUTRAL BUOYANCY TESTING RESULTS*

D. L. Akin
Massachusetts Institute of Technology
Cambridge, Massachusetts

Large Space Antenna Systems Technology - 1984
December 4-6, 1984

*Paper unavailable at time of publication.

Page intentionally left blank

SPACE TECHNOLOGY EXPERIMENTS PLATFORM (STEP) STATUS - AN IN-SPACE TEST FACILITY

Jack E. Harris
NASA Langley Research Center
Hampton, Virginia

Large Space Antenna Systems Technology-1984
December 4-6, 1984

INTRODUCTION

The NASA Office of Aeronautics and Space Technology (OAST) is actively involved with utilization of the Space Transportation System (STS) for technology experiments in space. STEP is the acronym for the Space Technology Experiment Platform, a Shuttle-borne experiment support facility for use primarily by structures, structural dynamics, and control of flexible structures technology flight experiments. The STEP in-space facility is undergoing development for OAST by the Langley Research Center.

This paper discusses the STEP concept, shows its relationship to broad NASA goals and objectives, presents the development chronology, describes the current system capability in block diagram format, and concludes with the presentation of the STEP development schedule.

STEP CONCEPT

Figure 1 identifies the STEP concept. This chart is the same one used during the 1982 Large Space Antenna Systems Technology Conference (ref. 1). At that time the concept's mechanization was under study. Now I am pleased to report that the concept's mechanization has moved into the hardware development stage. While the specific implementation has varied during the development process, the concept itself has not. The objective was, and still is, to provide a cost effective method of utilizing the Space Transportation System (STS) to provide routine access to the zero-gravity laboratory of space for a vigorous large space structures technology flight experiment program--an experiment program that involves a research community consisting of NASA, other governmental agencies, universities, and industry.

The approach to fulfilling this objective has also remained unchanged. It continues to be to develop and operate a reusable Shuttle-borne payload interfacing system configured to accommodate flight experiments primarily in the structures, structural dynamics, and control of flexible structures research disciplines. The guidelines serving as policy direction to the approach mechanization also have remained firm and include the requirements to provide experiment mounting, command, data handling and storage, and power distribution support; utilize standardized hardware and management interfaces with the STS to the maximum extent possible consistent with experiment requirements; operate as a research facility providing the flexibility to be responsive to evolving research opportunities; be reusable to provide cost effective multiple flight capability; and though not listed, nevertheless a key requirement, to minimize reliance on Orbiter services that involve complex or lengthy integration.

Those of us that, in the past, have been associated with the advocacy of in-space test facilities, recently were gratified by the fact that this concept is now reflected in the NASA Goals and Objectives Statement. Figure 2 presents the related goal and objective extracted from the September 1984 NASA Goals and Objectives Statement released by the Administrator.

OAST's STEP CONCEPT

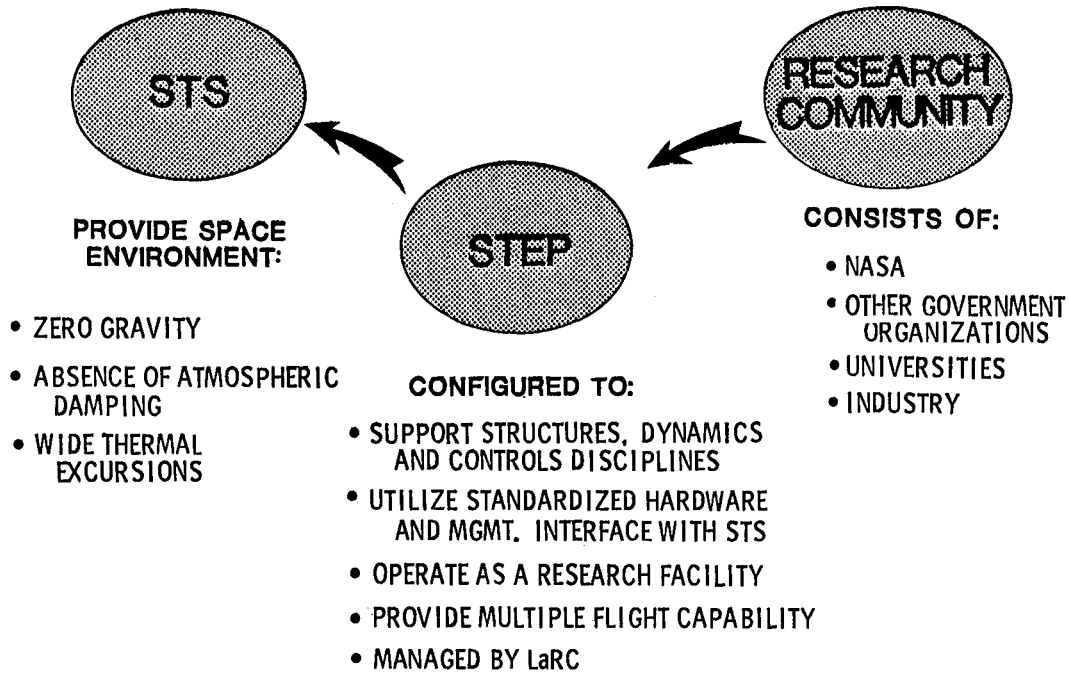

Figure 1

RELATED NASA GOALS/OBJECTIVES

GOAL 6

"CONDUCT EFFECTIVE AND PRODUCTIVE SPACE APPLICATIONS AND TECHNOLOGY PROGRAMS WHICH CONTRIBUTE MATERIALLY TOWARD U.S. LEADERSHIP AND SECURITY."

OBJECTIVES

6.2 - "PROVIDE ENGINEERING TEST AND TECHNOLOGY FACILITIES FOR CONDUCTING IN-SPACE RESEARCH AND OPERATE SUCH FACILITIES, UTILIZING SHUTTLE AND EVENTUALLY SPACE STATION, FOR NASA, UNIVERSITY, AND INDUSTRY RESEARCHERS CONDUCTING COOPERATIVE PROGRAMS."

EXTRACTED FROM SEPTEMBER 1984 NASA GOALS AND OBJECTIVES STATEMENT

Figure 2

STEP CHRONOLOGY

Now that everyone is acquainted with the STEP concept, let us review how we arrived at where we are today. Figure 3 provides a chronological list of key STEP milestones. The activity was initiated by the Langley Research Center Director in March 1982. A small in-house team conducted a feasibility study and in June the results of that study were presented to the Office of Aeronautics and Space Technology (OAST) Associate Administrator. Following that review, he authorized Langley to proceed further into the planning. The feasibility study team was augmented and a system definition activity was initiated. This definition activity was underway during the last conference and preliminary study results were presented at that meeting (ref 1). The study was completed in March 1983. A statement of STEP capabilities resulting from the definition study was included in a letter sent to the STEP target research community soliciting potential experiment requirements. A workshop was then held at Langley Research Center in June 1983 to refine the definition of STEP capabilities based on detailed review of potential experiment requirements received from the solicitation and direct interaction with potential users (ref. 2). A Project Initiation Agreement was mutually signed by the OAST Associate Administrator and the Langley Research Center Director in June 1983 and the project proceeded into the formal development phase. In November 1983, the Director of the Spacelab Program Office within the Office of Space Flight (OSF) at NASA Headquarters indicated to OAST management that he was interested in initiating an upgrade activity for the multiplexer, demultiplexer (MDM) pallet (a system that had been initially considered by STEP but rejected), and wanted to use the STEP requirements as the driving set of design requirements. OAST expressed an interest and Jim Harrington, Spacelab Program Office Director, assigned the responsibility for defining the potential MDM upgrade to the Marshall Space Flight Center (MSFC). STEP Project Office personnel at Langley worked with MSFC personnel to ensure that they understood the STEP requirements and participated in various trade studies. The activity culminated in a meeting of the Associate Administrators of OAST and OSF. At that meeting the two Associate Administrators agreed to mutually advocate the MDM upgrade. OSF would develop the hardware, to be called the Enhanced MDM Pallet (EMP) for STEP, and OAST would utilize it as a key element of STEP. The upgrade activity has been authorized and is underway at MSFC.

STEP CHRONOLOGY

- ACTIVITY INITIATED MARCH 1982
- FEASIBILITY STUDY RESULTS PRESENTED TO OAST ASSOCIATE ADMINISTRATOR JUNE 1982
- IN-HOUSE SYSTEM DEFINITION ACTIVITY COMPLETED IN MARCH 1983
- STEP/USER WORKSHOP HELD JUNE 1983
- STEP PROJECT INITIATION AGREEMENT SIGNED JUNE 1983
- MDM AVIONICS UPGRADE SUITABILITY STUDY INITIATED NOVEMBER 1983
- OAST/OSF AGREEMENT ON USE OF UPGRADED MDM AVIONICS FOR STEP JUNE 1984

Figure 3

STEP SYSTEM CONFIGURATION

The STEP system configuration is shown in Figure 4. This configuration consists of three major hardware elements: A Spacelab Pallet element, a pallet-mounted electronics element, and modular interface hardware element.

The Spacelab Pallet element consists of a standard pallet and an active thermal control subsystem. The standard pallet is a U-shaped support structure measuring 3 meters long by 4 meters wide, is attached to the Shuttle Orbiter through trunnions and keel fittings, and provides a standardized structural interface with the Orbiter. The active thermal control subsystem consists of a freon pump, liquid cooling loop, and cold plate support structures for pallet-mounted subsystem and experiment equipment.

The pallet-mounted electronics provide command, data management, and power distribution services for use by experiments. These subsystems are being developed by the Marshall Space Flight Center as part of the Enhanced MDM Pallet for STEP activity mentioned previously.

The modular interface element, which we call Payload Integration Equipment (PIE), consists of the set of mechanical and electromechanical hardware items from which a STEP user can select to facilitate integration of an experiment to the STEP carrier. It includes modular mounting platforms, a single degree-of-freedom rotation unit, emergency release mechanisms, and various special cables and brackets. Three platform modules are being developed. Two are approximately equal in length to one quarter of the total pallet length and the third is approximately equal to one half the pallet length. They may be used in five possible configurations ranging from one one-quarter module to all three modules covering the full pallet length. These hardware items are under design at Langley and will be built at Langley.

STEP SYSTEM CONFIGURATION

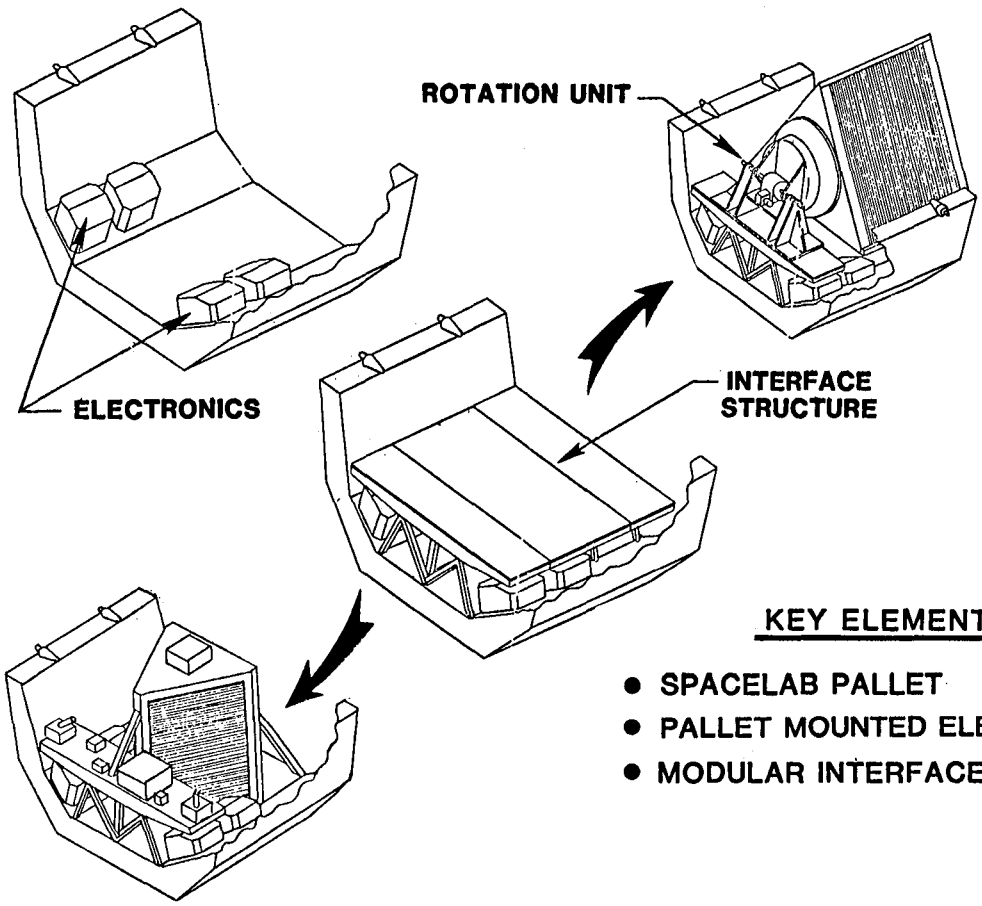

KEY ELEMENTS

- SPACELAB PALLET
- PALLET MOUNTED ELECTRONICS
- MODULAR INTERFACE STRUCTURE

Figure 4

ELECTRONIC FUNCTIONAL REQUIREMENTS

Next let us look at STEP at a slightly more detailed level. Figure 5 lists the command and control, data handling and storage, and electric power distribution subsystem functional requirements developed during the definition process and refined during the STEP workshop. Figures 6 and 7 illustrate via block diagram format how those requirements have been implemented.

The key STEP assemblies used to implement the command and control requirements are the Dual Wide Smart Flexible Multiplexer Demultiplexer (SFMDM) mounted on the pallet and the Data Display and Control Unit (DDCU) mounted on the aft flight deck of the Orbiter. Preprogrammed command sequences are executed in the SFMDM and commands are issued to the user experiments either as coded commands in a serial bit stream, or as low level (5 V) or high level (28 V) discrete commands. Mass storage for the command program library is provided via bubble memory located in the DDCU. The SFMDM can perform limit checking on selected data received from the user experiment and depending upon the response algorithm used, initiate a command response back to the user or merely cause the information to be displayed at the DDCU, and wait for a response to be initiated from that work station. The DDCU is the main STEP man/machine interface where real-time onboard control is exercised. The standard switch panel (SSP) also located on the Orbiter aft flight deck is an Orbiter service that can be used to provide additional real-time onboard control via hardwire commands. Some limited modification of preprogrammed sequence parameters can be accomplished via Orbiter uplink. Two uplink paths are available. A high rate path (128 K) when the TDRSS link (and hence the Ku-band) is available and a low rate path (2 K) via the S-band and Payload Signal Processor (PSP) feed into the SFMDM.

The STEP assemblies used to implement the data handling and storage requirements are the High Rate Multiplexer (HRM) and the High Data Rate Recorder (HDRR). These two units are pallet mounted versions of Spacelab module equipment. High rate science data is collected and formatted by the HRM and then is either transmitted directly to the ground via the Orbiter Ku-band downlink or recorded on the HDRR for replay at a later time. Low rate data input to the SFMDM is also channeled to the HRM for multiplexing into the high rate data stream. In addition to the Ku-band downlink, a low rate output from the SFMDM is downlinked via a 16 K S-band downlink. Its Orbiter input port is the Payload Data Interleaver (PDI). As mentioned previously the DDCU is used to display selected user data.

The STEP assembly used to implement the power requirements is the Power Control Box (PCB). Switched AC and DC are available to the user from the PCB under control from the SFMDM. Auxiliary DC power is also provided to the user via a direct path.

ELECTRONICS FUNCTIONAL REQUIREMENTS

COMMAND AND CONTROL

- PRE-PROGRAMMED COMMAND SEQUENCING
- MASS STORAGE ... COMMAND SEQUENCE PROGRAM LIBRARY
- INTERACTIVE EXPERIMENT CONTROL ... STATUS AND LIMIT CHECKING
- REAL-TIME ON-BOARD CONTROL ... AFD KEYBOARD AND DISPLAY
- PRE-PROGRAMMED PARAMETER MODIFICATION ... ORBITER UPLINK

DATA HANDLING AND STORAGE

- COLLECTION, FORMATTING, AND RECORDING OF DATA
- DOWNLINK OF DATA ... ORBITER Ku AND S BAND LINKS
- REAL-TIME DISPLAY ... AFD KEYBOARD AND DISPLAY

POWER

- SWITCHING AND DISTRIBUTION
- 28 V DC
- AUX 28 V DC
- 110 V AC, 400 Hz, 3 PHASE

Figure 5

FUNCTIONAL BLOCK DIAGRAM STEP CDMS

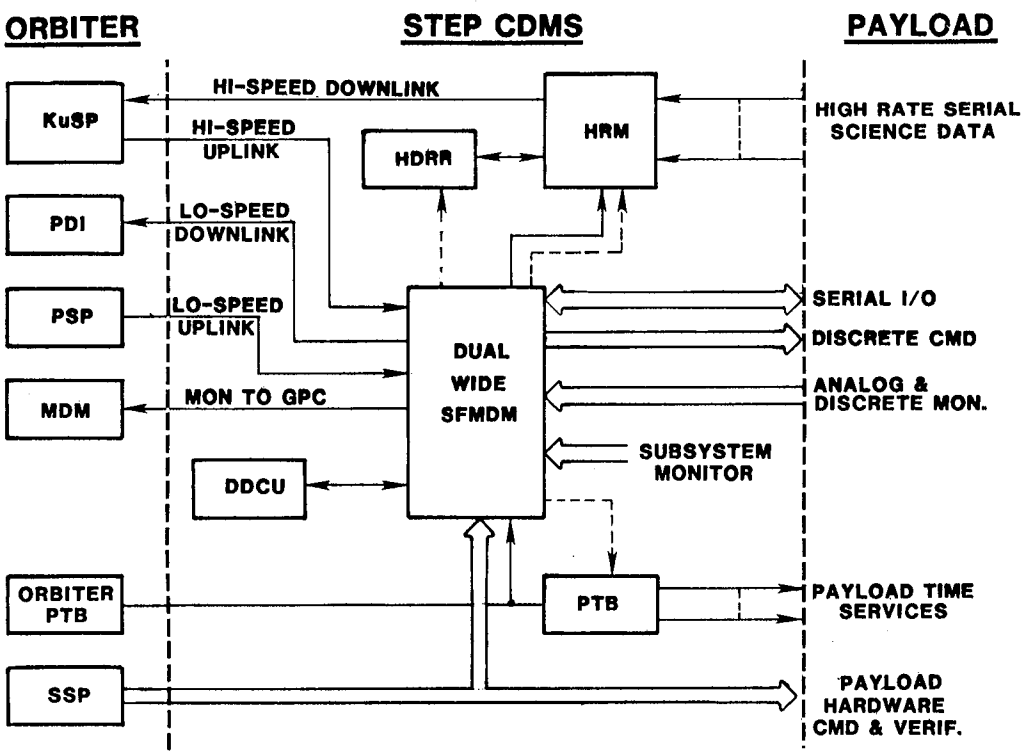

Figure 6

FUNCTIONAL BLOCK DIAGRAM STEP EPDS

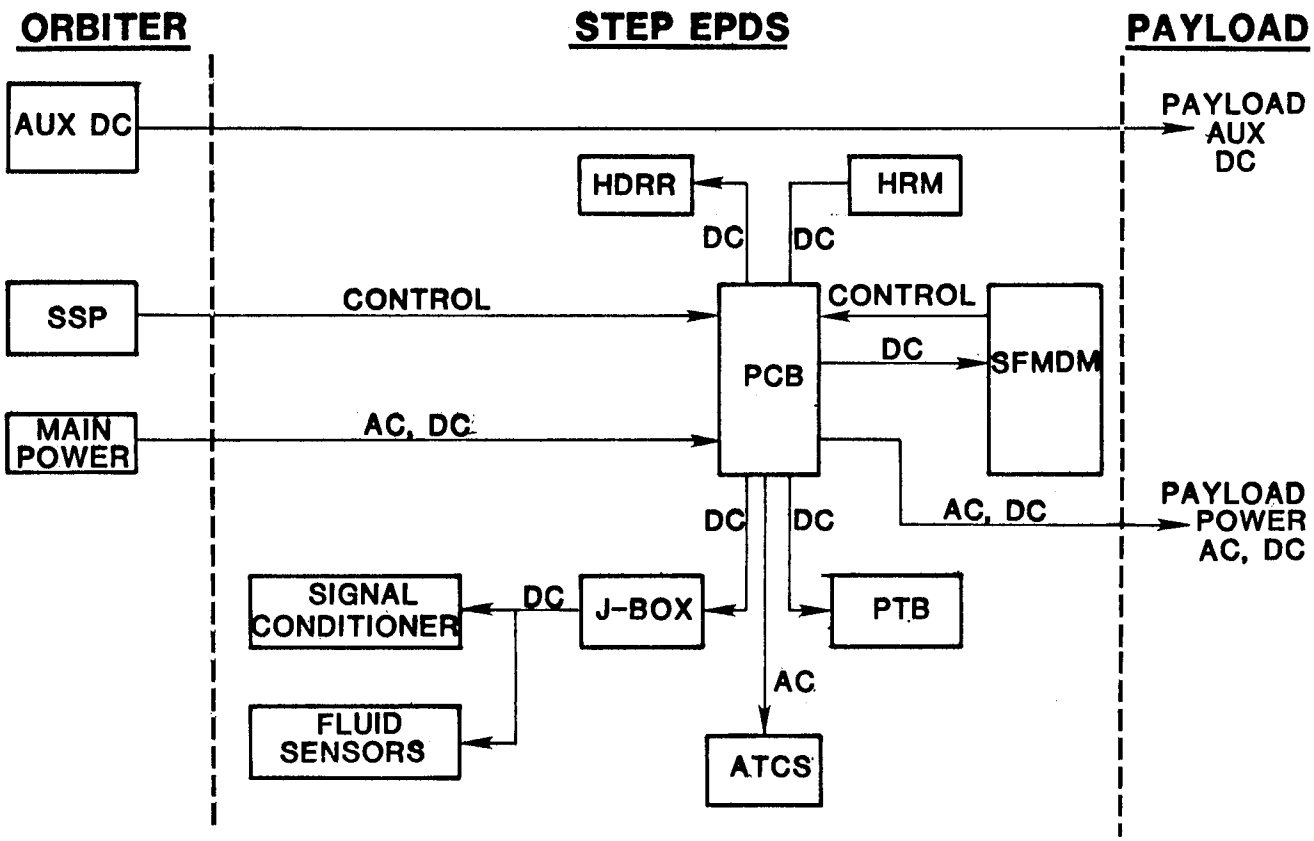

Figure 7

MECHANICAL FUNCTIONAL REQUIREMENTS

Following a similar format as employed with the electronics, Figure 8 lists the STEP mechanical functional requirements and Figure 9 illustrates the mechanization used to meet these requirements.

As previously mentioned during the STEP system configuration description, the Spacelab Pallet provides the necessary mechanical support and alignment for the STEP and user electronics and the Payload Integration Equipment. The Active Thermal Control Subsystem (ATCS) provides the cooling for STEP electronics and for any pallet-mounted experiment electronics. Use of a standard Spacelab pallet provides a standardized mechanical interface with the Shuttle orbiter.

The Payload Integration Equipment includes modular platforms for experiment mounting, a single-degree of freedom rotation unit, separation system hardware and miscellaneous cables, brackets, connectors.

The modular platforms are designed to accommodate experiments weighing up to 2000 kg.

SPACELAB PALLET

- MECHANICAL SUPPORT AND ALIGNMENT FOR STEP ELECTRONICS AND INTERFACE STRUCTURE
- THERMAL COOLING FOR STEP ELECTRONICS AND FOR PALLET MOUNTED EXPERIMENT ELECTRONICS
- STANDARDIZED MECHANICAL INTERFACE WITH SHUTTLE ORBITER

INTERFACE STRUCTURE AND MECHANISMS

- EXPERIMENT MOUNTING, LATCH AND RELEASE, CONTROLLED ROTATION AND SEPARATION
- EXPERIMENT WEIGHTS UP TO 2,000 kg
- PACKAGED EXPERIMENTS UP TO 3 METERS IN DIAMETER AND VARIABLE LENGTH UP TO 12 METERS

Figure 8

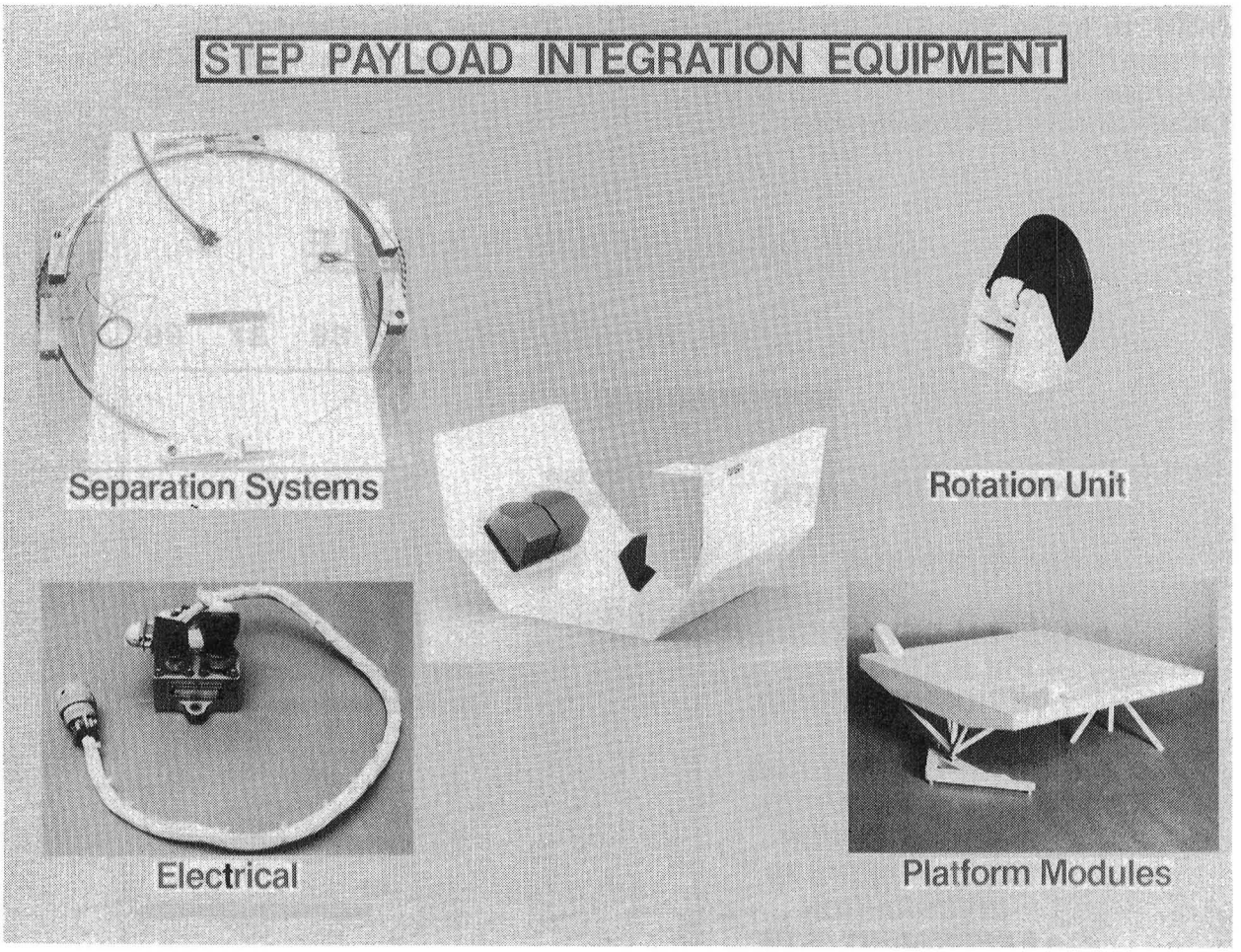
STEP PAYLOAD INTEGRATION EQUIPMENT
Separation Systems
Rotation Unit
Electrical
Platform Modules

Figure 9

STEP DEVELOPMENT SCHEDULE

The STEP development schedule is shown in figure 10. The feasibility, system definition, and update activities have been previously discussed. The Payload Integration Equipment is being designed and will be fabricated by the Langley Research Center. The avionics for STEP are being designed and procured by the Marshall Space Flight Center. Both the PIE and the avionics will be staged onto a Spacelab Pallet at the Kennedy Space Center (KSC) to bring the STEP Facility on-line. Typical experiments/STS integration time spans are also shown. The activity is initiated with the development of a Payload Integration Plan (PIP) and progresses through launch and flight operations.

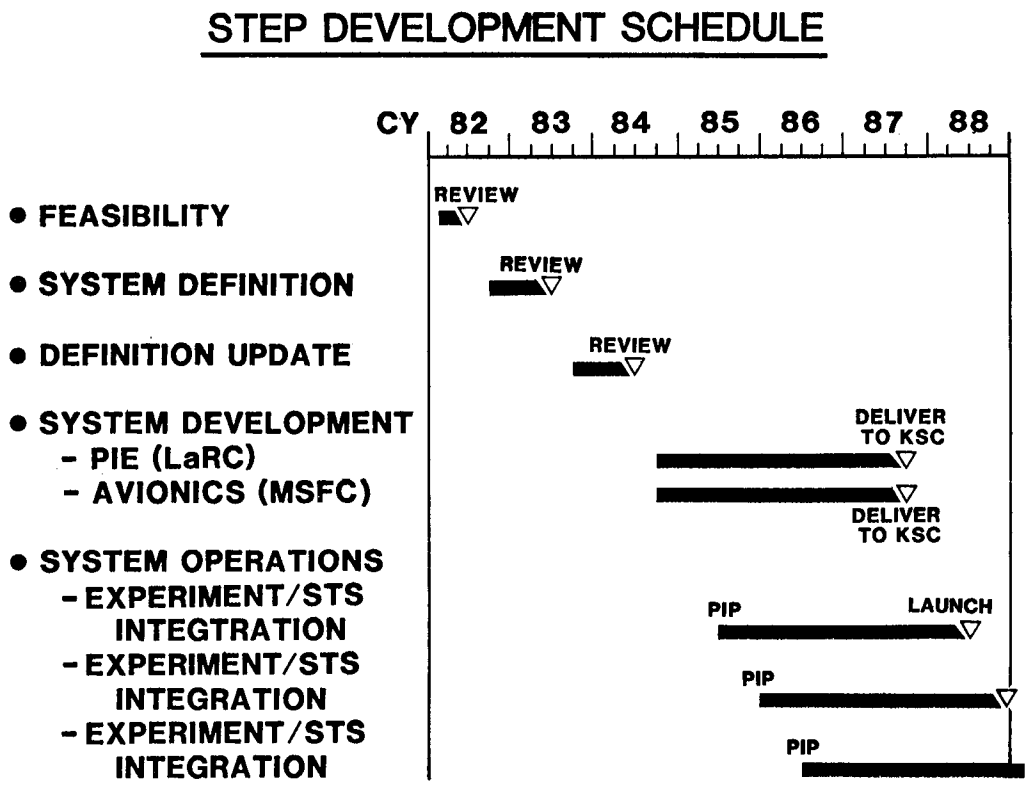

Figure 10

REFERENCES

1. Harris, Jack E.; and Pinson, Larry D.: Space Technology Experiment Platform (STEP). A Shuttle-Borne Support Facility for Structures, Structural Dynamics, and Control Technology Flight Experiments. Large Space Antenna Systems Technology - 1982, NASA CP-2269, Part 2, 1983, pp. 969-980.

2. STEP Experiment Requirements. NASA CP-2294, 1984.

Page intentionally left blank

CONTROL OF FLEXIBLE STRUCTURES (COFS) FLIGHT EXPERIMENT BACKGROUND AND DESCRIPTION

Brantley R. Hanks
NASA Langley Research Center
Hampton, Virginia

Large Space Antenna Systems Technology - 1984
December 4-6, 1984

INTRODUCTION

Next-generation space systems such as large antennas or a space station may have dimensions on the order of 30 m to 200 m, yet their basic structures may be relatively lightweight and flexible, making ground tests for loads, controls analyses, and design verification questionable if not impossible. Abandoning the extensive ground test and analysis verification program that led to the success of previous spacecraft is not a sensible option; making it meaningful using current technology will require inefficient, ultraconservative structure and control designs. The alternative is to improve the test and prediction technology.

This paper presents some of the background and rationale for a research study in structures, structural dynamics, and controls using a relatively large, flexible beam as a focus. This experiment would address fundamental problems applicable to large, flexible space structures in general and would involve a combination of ground tests, flight behavior prediction, and instrumented orbital tests. The experiment is intended to be multidisciplinary but basic within each discipline. It is expected to provide improved understanding and confidence in making design trades between structural conservatism and control system sophistication for meeting static shape and dynamic response/stability requirements. Also, it will result in quantitative results for use in improving the validity of ground tests for verifying flight performance analyses.

A fundamental problem in designing and delivering large space structures to orbit is to provide sufficient structural stiffness and static configuration precision to meet performance requirements. These requirements are directly related to control requirements and the degree of control system sophistication available to supplement the as-built structure.

RIGID-BODY APPENDAGE EFFECTS ON SPACECRAFT ROTATIONAL INERTIA

The usual method to reduce flexible structural motions is to increase the stiffness of the structure. However, this increases control force requirements due to rigid-body inertia. A significant increase in control force requirements for excess distributed mass on large space structures is illustrated in figure 1. Here the normalized rotational inertia for a hollow cylindrical spacecraft with two rigid appendages is shown as a function of the ratio of the appendage mass to the spacecraft core mass for three appendage lengths. A heavy rotational inertia (and, hence, control torque) penalty is paid for excess mass, particularly for large dimensions. The cost of this penalty in terms of control energy could be large over a period of ten years or more. Where such maneuvers are necessary, lightweight construction often comes at the expense of structural stiffness and, hence, the control system must deal with flexible motion as well as the rigid motion of the figure.

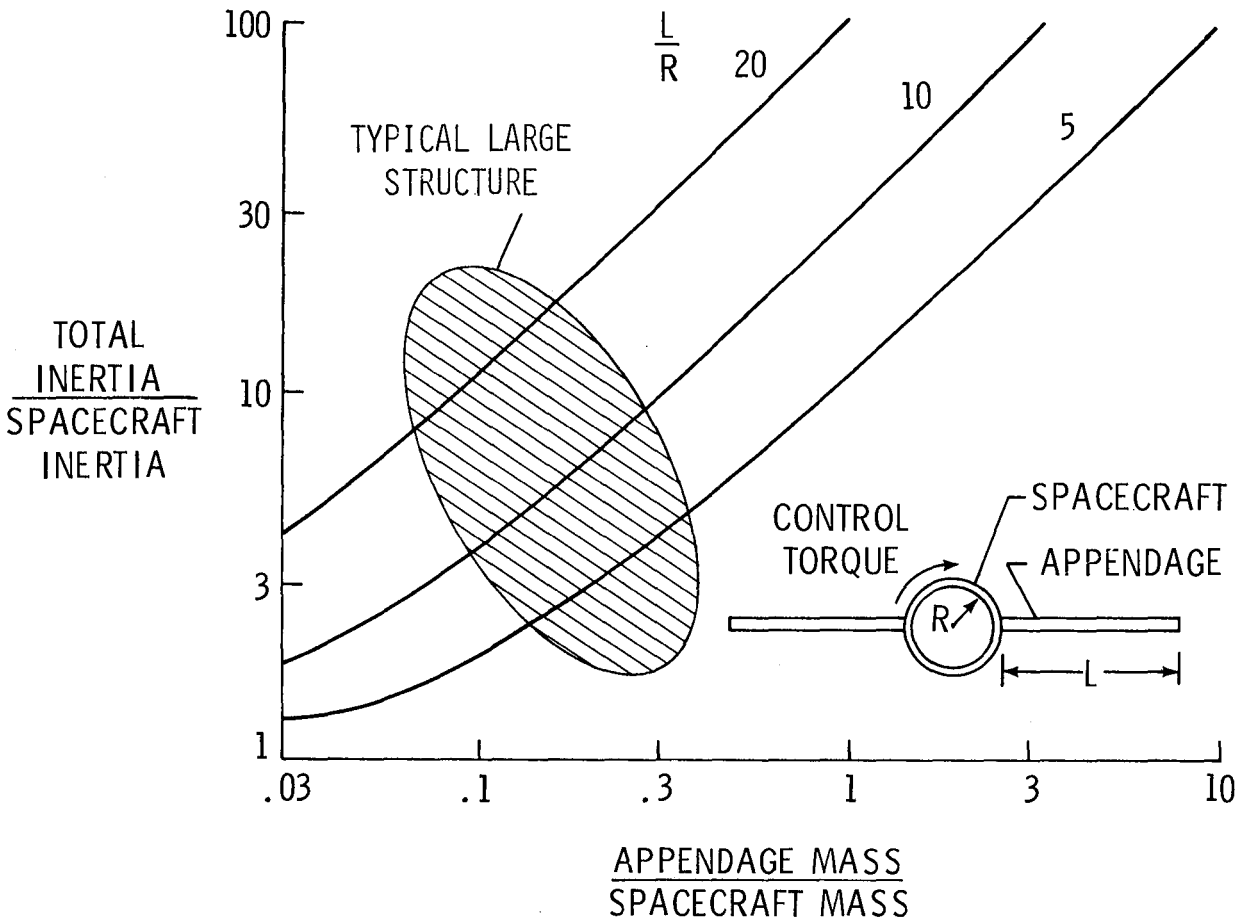

Figure 1

CONTROL OF HIGHLY FLEXIBLE STRUCTURES

Controlling the motions and configuration of highly flexible structures using active systems offers potential relief to requirements for very stiff precision structures in future applications. The control of flight systems using advanced methods often involves a mathematical model of the system built into the control loop (figure 2). This model is used to determine the motion occurring over the system based upon measurements of some subset of the total number of motions of interest. Then, control forces are computed based on both the measured and the calculated system motions. If flexible motion is present, an accurate structural dynamics model is necessary in addition to the usual need for accurate rigid-body mass, center-of-gravity, and moment-of-inertia and control hardware dynamics information. Even without an analytical model in the control loop the design of efficient control systems and sizing of control components for flexible structures requires accurate structural dynamics analyses. Such accurate models usually are available only after an extensive ground test and modeling iteration effort.

An alternative is in-flight, possibly on-line, identification of the system dynamic properties. However, system identification is extremely difficult if the proper form (i.e. correct nonlinearity treatment, sufficient degrees of freedom, etc.) of the analytical model is unknown. Furthermore, the higher the modeling uncertainty, the higher is the need for conservatism or robustness in control design. The necessity for better flight response prediction techniques cannot be avoided.

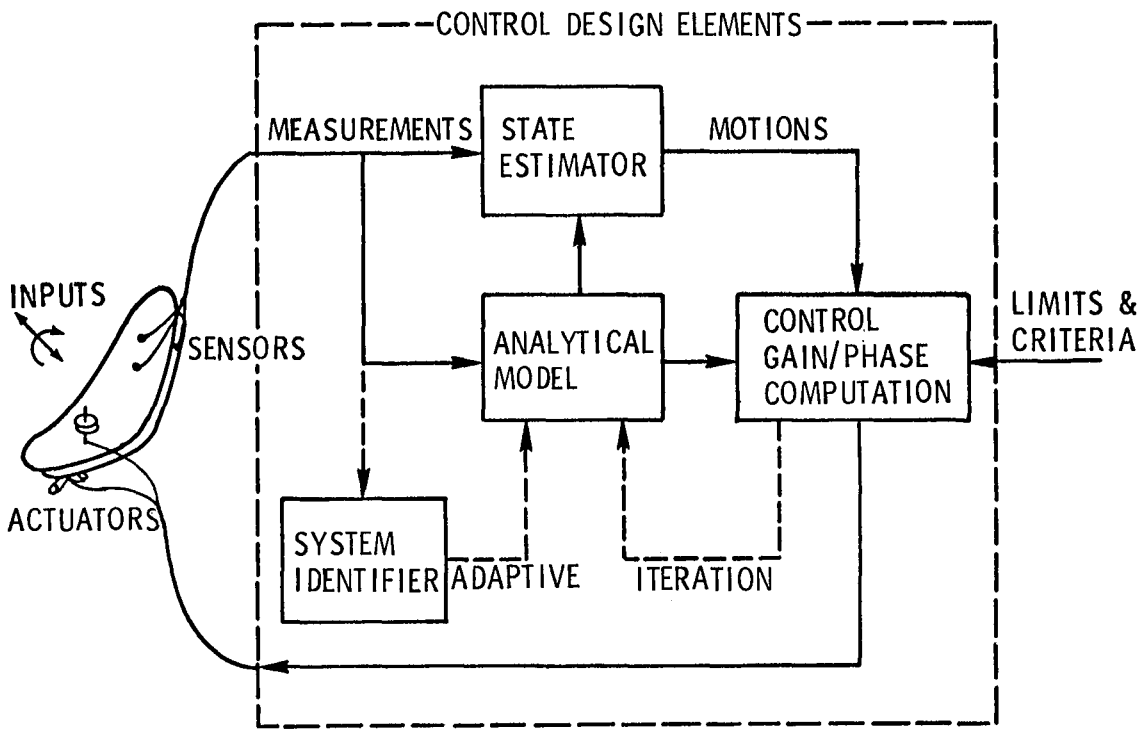

Figure 2

GROUND TEST DIFFICULTIES FOR FLEXIBLE BEAMS

The usual approach to reducing mathematical modeling uncertainty is to conduct a ground test program to validate the analytical results and to correct the model if agreement with test results is poor. Unfortunately, for very large space structures, the effects of differences in ground and orbital environments may be greatly magnified over those observed in past experiences. As a result, the ground test and analysis process may tend to be less rather than more accurate.

Of all potential large space structural components, beams are among the simplest to ground test. This by no means assures that a simple valid test can be conducted for any size beam. As beams become long, frequencies become low, and gravity effects in dynamic tests become difficult to remove. Three approaches to tests on a long uniform beam are shown in figure 3: vertical suspension by one end, horizontal suspension on lightweight cables, and tests on segments which are then mathematically joined to predict the full-beam behavior. In the vertical test, tension along the beam varies with height producing a large stiffening effect at the top. (The opposite approach, base support, produces equally detrimental compression loads.) In the horizontal tests, cables must be long enough to prevent interference between the first beam-bending mode and the pendulum mode of the beam on the cables. For very low-frequency beams ($f_1 < 1$ Hz), this results in cables having lateral vibration frequencies which interfere with higher beam modes. The third approach, tests on substructures (pieces) with mathematical extrapolation, leads to questionable treatment of connection behavior and very poor understanding of overall beam damping.

The validity of dynamic ground tests on low-frequency, lightweight beams (particularly where joints are present) is questionable; on other structures, it is even more questionable. A test program that compares various ground test methods with flight results on a large beam is believed to be a sensible starting place.

Figure 3

OVERCOMING GRAVITY IN GROUND TESTS

In the previous figure, all significant motion of the test articles was parallel to the ground plane and not opposed directly by gravity. For three-dimensional motion, as for the antenna dish shown below (left), motion in the vertical direction must be permitted by mounting on a soft suspension system. However, if the structure being tested has a very low first natural frequency, prevention of interference of the springs (and possibly the supporting structure to which they are attached) can require impractically soft springs. This is illustrated in figure 4 (right) where the static deflection of the suspended test article is shown as a function of test article first natural frequency, requiring the bounce frequency of the structure on the springs to be one-fourth the first structural resonance. To evaluate this type of situation the addition of non-planar cross-axis coupling to the beam experiment is desired.

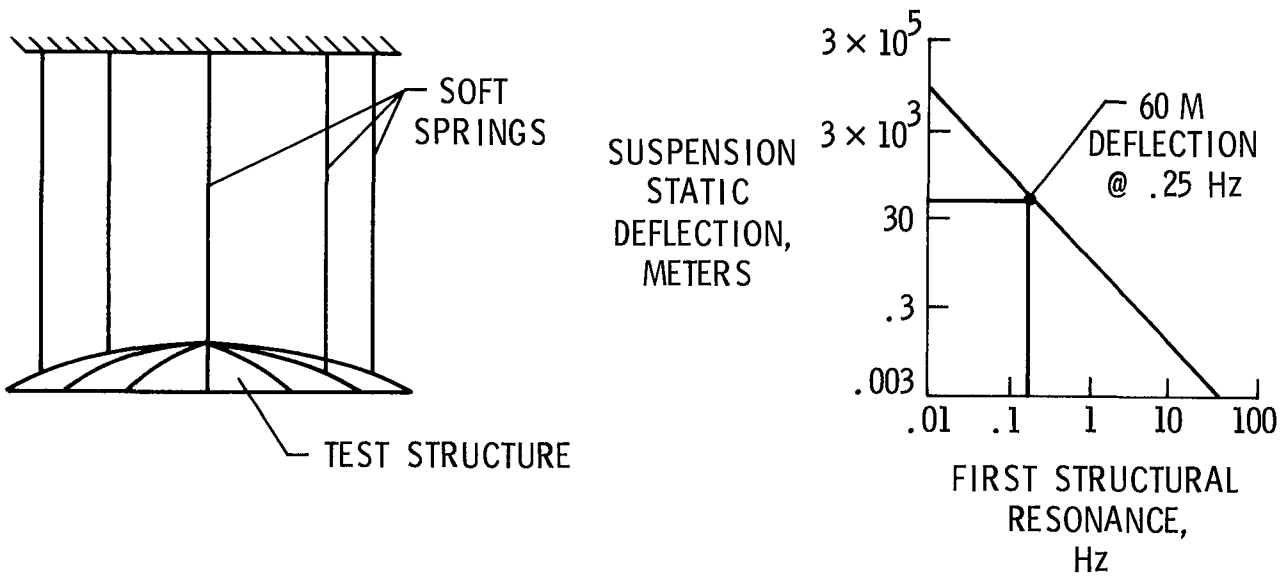

Figure 4

GRAVITY AFFECTS NONLINEAR JOINTS

Another effect of gravity on large structures is illustrated in figure 5. Here a truss beam hanging vertically has different joints carrying different static loads due to the weight of the structure beneath. However, as shown on the right side of the figure, pinned joints, the type most suitable for space trusses, behave nonlinearly under large load changes. Hence loaded joints are much stiffer than unloaded ones. Also, joints in compression often exhibit different stiffnesses from those in tension. In zero gravity, loading is light and structural stiffness may be considerably lower than in ground tests. Other ground test configurations give similar behavior and different joint types exhibit variations in nonlinear behavior. Not shown here is the effect of gravity loads on joint hysteresis which provides the very important damping (energy dissipation) forces which reduce structural vibration. In fact, the effect of the orbital environment on joint damping in real, low-frequency structures is uncertain since only sparse measured data exists for comparing characteristics.

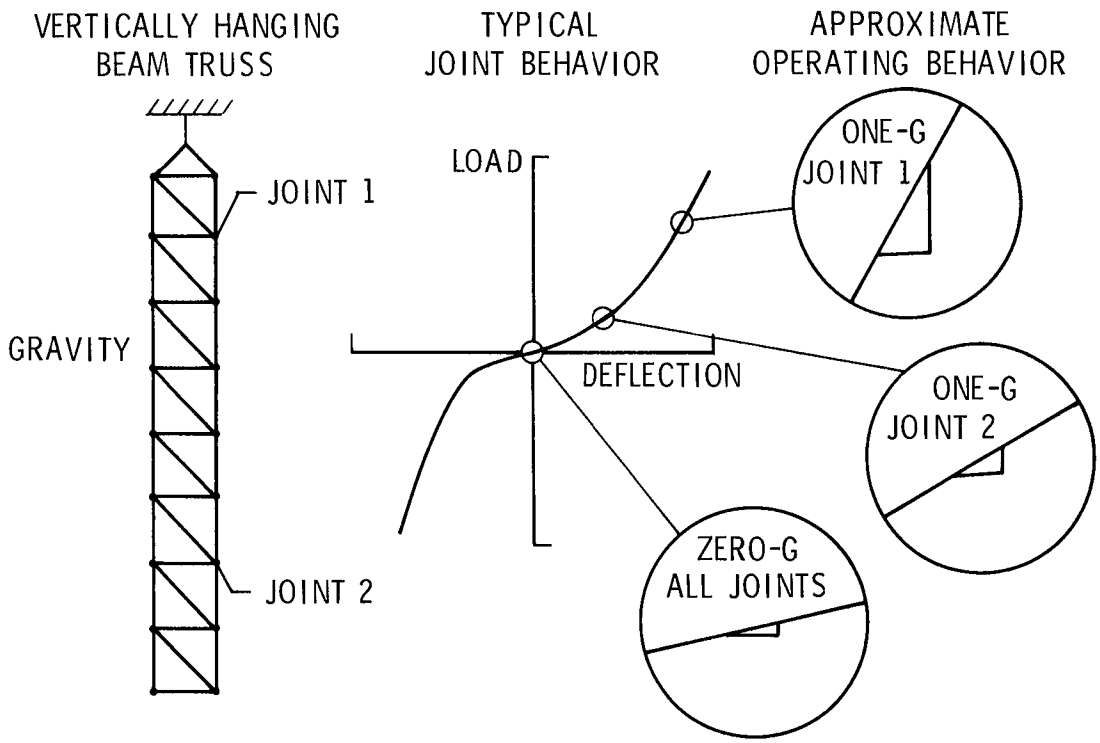

Figure 5

GRAVITY AFFECTS DEPLOYMENT MOTIONS

Consider the deploying truss of figure 6. Such a mechanism may be integrated into booms for antenna masts and space station substructures or in two-dimensional trusses such as platforms and dish antennas. In ground tests, gravity tends to resist the upward motion of the top members while it assists the downward motion of the bottom members. Members moving parallel to the ground (not shown) would receive an out-of-plane bending torque causing joint performance changes. Compensating for these effects directly requires precise motion control of each joint either by the test fixture or by compensating devices built into the truss itself. Joint motion control by floating deploying devices on water or air bearings is useful for quasi-static mechanism tests in a single plane but does not allow correct dynamic motions or out-of-plane motions which may occur, and must be controlled, in orbit. Underwater tests using neutrally bouyant members, joints, and fixtures remove the planar motion requirement at the expense of modifying the structure purely for the test. However, drag and inertia loading seriously compromise this technique for all but ultraslow deployment. Zero-gravity tests using drops and parabolic trajectory aircraft flight overcome these problems but available space is limited and test times are never more than thirty seconds. The structures of the future are likely to be more complicated to deploy than the simple truss of figure 6. Assuming that deployment is a desirable option for future large space structures, at least one well-instrumented, on-orbit, deployment control test is needed simply to evaluate the usefulness of ground tests for realistic large structures. Such a test obviously should be preceded by a comprehensive component/subassembly ground test program.

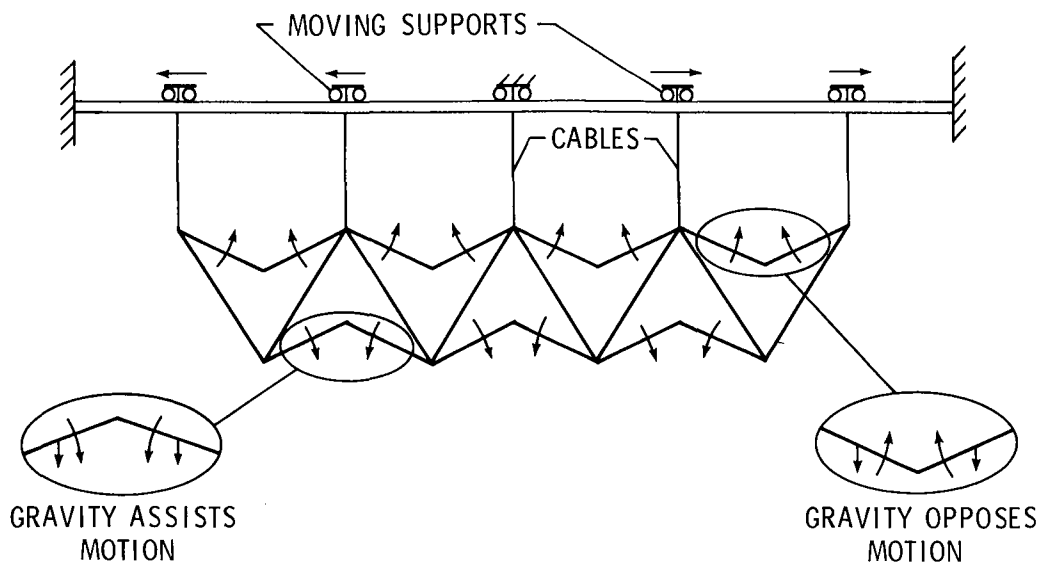

Figure 6

AN ORBITAL TEST PROGRAM IS NEEDED

The reasons listed here are strong incentives to conduct orbital "laboratory experiments" in order to assure adequate understanding of technical problems before committing expensive major large space systems to orbit. A coordinated program of ground tests, analyses, and flight tests on a practical structure that is reasonably well understood is needed to study phenomena and to calibrate the design/test process (figure 7).

STRUCTURES

- NEED DATA ON BASIC "JIG SHAPE" OF DEPLOYED PRECISION GRAPHITE STRUCTURE IN ORBITAL ENVIRONMENT

STRUCTURAL DYNAMICS

- VERY LARGE MASTS CANNOT BE DYNAMICALLY GROUND TESTED BECAUSE OF GRAVITY EFFECTS
- DATA ARE NEEDED TO CONFIRM OUR ABILITY TO
    1. PREDICT THE DYNAMICS OF JOINT-DOMINATED STRUCTURES
    2. EXTRAPOLATE GROUND DATA FROM SUBELEMENT TESTS
- PREDICTION OF DAMPING IN 0-G IS MOST DIFFICULT

CONTROLS

- DATA NEEDED TO CONFIRM ABILITY TO DEVELOP RELIABLE CONTROL MODELS BY SYSTEM IDENTIFICATION/REDUCED-ORDER MODELING
- BECAUSE OF FLEXIBILITIES IN STRUCTURE, ACTUATOR/SENSOR PERFORMANCE IS DIFFICULT TO CONFIRM IN GROUND TESTS
- ON-ORBIT VALIDATION OF DISTRIBUTED CONTROL STRATEGIES IS REQUIRED FOR FLEXIBLE BODY CONTROL

Figure 7

A SHUTTLE-ORBITER-ATTACHED DEPLOYABLE TRUSS BEAM FOR ORBITAL SPACE TESTS

A relatively simple cantilevered truss beam, deployed from the Shuttle orbiter payload bay, is an excellent candidate for the needed studies. Such an experiment, proposed to be flown as a part of the the Space Technology Experiments Program (STEP), is shown in figure 8. Electronic and power support to the experiment, in addition to mechanical attachment interfaces, would be provided by the STEP Dedicated Support System (SDSS). The experiment would provide hardware, sensors, signal conditioning, and operational devices for conducting a variety of tests including deployment, static shape, dynamic response and control performance measurements.

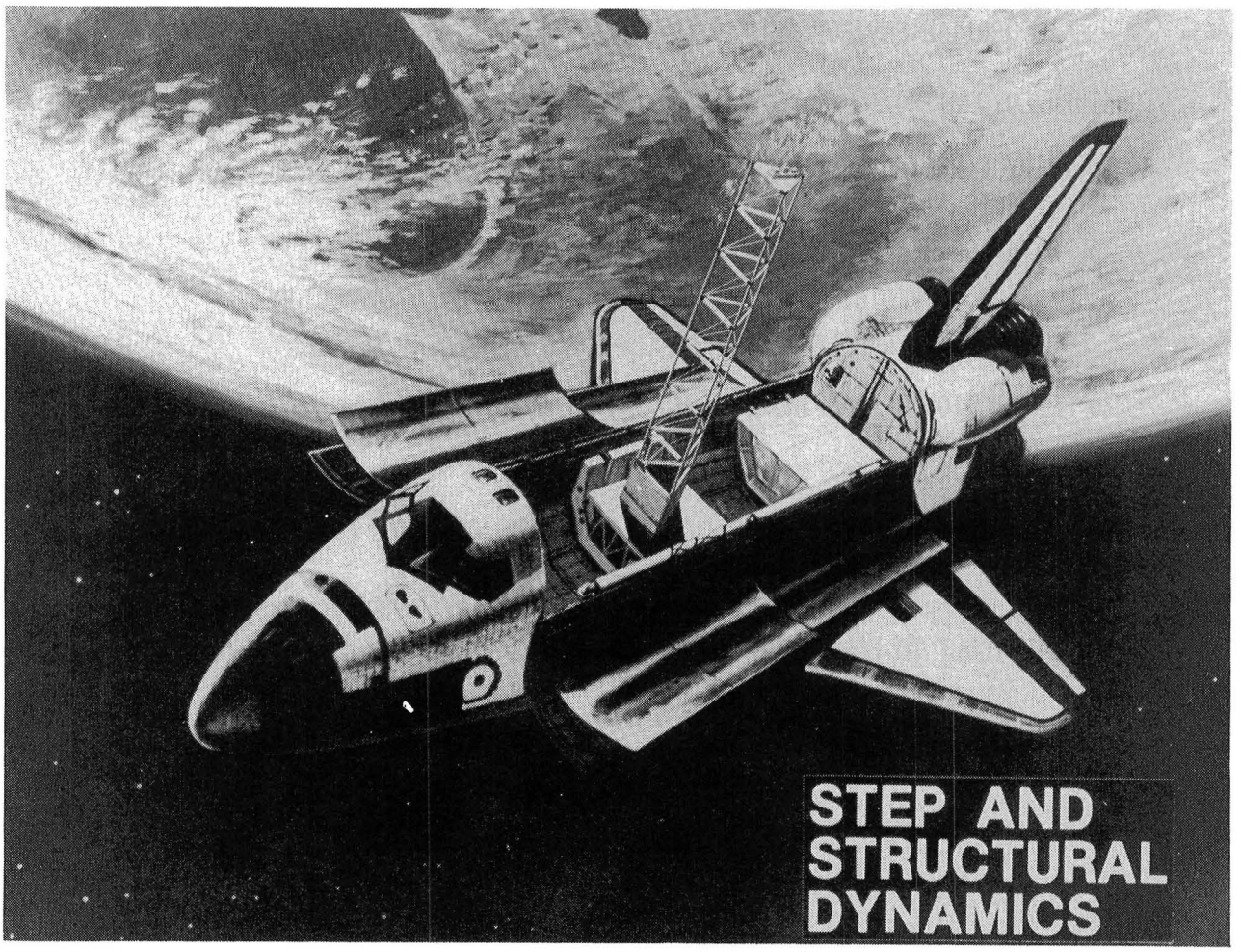

Figure 8

PRELIMINARY BEAM DESIGN

The preliminary dimensions and requirements of a beam planned for such an experiment (the COFS 1 or Mast experiment) are shown in figure 9. The beam outline relative to that of an astronaut demonstrates the size planned. The properties and features listed at the right in the figure are included to meet the previously described research needs. The listed options are desirable if suitable cost-effective candidates can be identified.

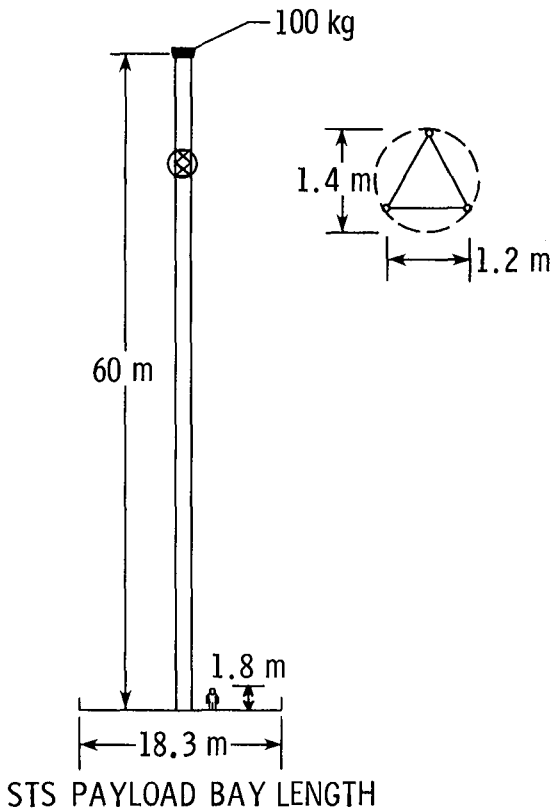

- o STATICALLY DETERMINATE
- o NEAR-ZERO THERMAL EXPANSION
- o ACCURATE CONFIGURATION
- o TRUSS-BEAM CONSTRUCTION
- o DEPLOYABLE/RESTOWABLE
- o CANTILEVER ATTACHED TO STEP
- o ACTIVE EXCITATION/CONTROL

- o OPTIONS:
  - PARAMETER MODIFICATION
  - ADDITIONAL ACTUATORS

Figure 9

EXAMPLE FLIGHT TEST SEQUENCE

The orbital test sequence shown here allows verification of safety by checking predictions at partial deployment (i.e., at higher frequencies there is less potential for Shuttle control interaction) before extending to full length. Such a test sequence may require more than one deployment on the same flight to allow time for analysis verification. Test times could thus be kept to reasonable lengths (see figure 10).

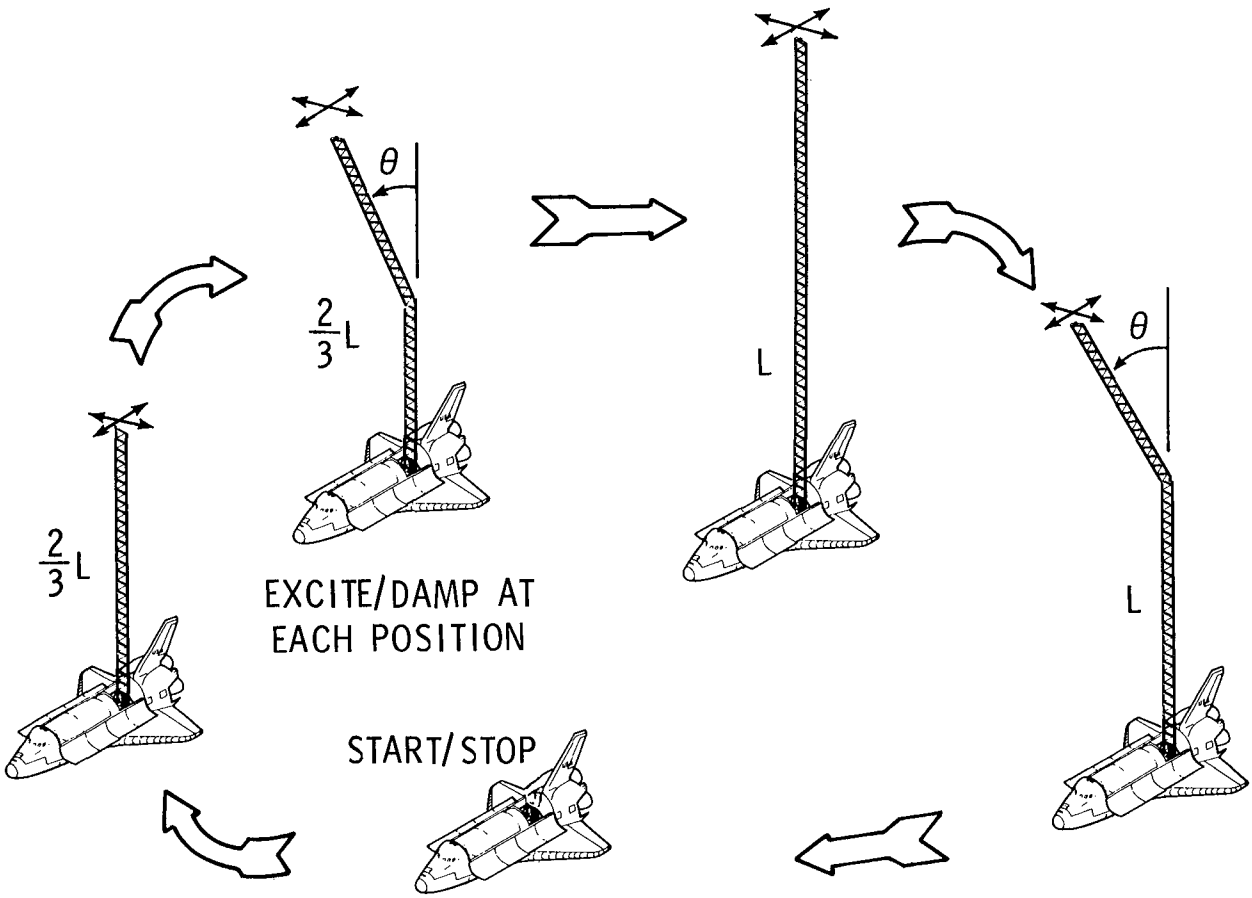

Figure 10

DEPLOYABLE BEAM EXPERIMENT TEST ARTICLES

Figure 11 overviews the progression of test articles to be used in the deployable beam experiment program. The primary test structure is the 60m flight article shown in the center of the figure. It is expected to be about 1.2 - 2.0 meters in diameter, of lightweight construction, and sequentially deployable from a small package while maintaining cantilever end conditions. To determine its static, dynamic, and thermal performance, it will be tested in Earth-based test facilities and in orbit (extended from the Shuttle orbiter payload bay as shown in the right of the figure). The beam will include a capability for changing its physical properties, such as the ability to tilt one end as shown in the figure, in order to change the frequency spacing and cross-axis coupling between modes.

Because of the combination of large size, lightweight construction, and expected low natural frequencies (beginning well below one Hz), the validity of ground test data on the 60m beam is questionable. This situation was deliberately created to simulate the problems of developing future large space structures such as the space station or large antennas. The remainder of the test articles shown are intended to develop accurate analyses for the large beam using smaller articles on which valid ground test data may be obtained. They include a 20m laboratory "prototype" test beam which has similar physical characteristics to the flight article although it isn't of the same design, construction, and component dimensions. The purpose of this model is to develop test and analysis methods applicable to the flight beam but in advance of its construction. In addition, segments, joints, and structural members identical to those of the flight article will be tested to determine stiffness, hysteresis, deployment, and thermal behavior for evaluating and calibrating analytical predictions. Analyses for predicting the behavior of the full flight article will then be developed and evaluated using the ground and flight data on the complete beam.

A final research objective, represented by the 1/4-and 1/2-scale beam models shown in the figure, is not a part of the initial plan but may be implemented at a later date. These would be constructed and tested on the ground to develop accurate analytical models once a flight design is available. The analytical models would then be used to predict full-scale ground and flight behavior. The degree to which sub-scale models can be used for developing analyses applicable to large, joint-dominated space structures can thus be determined and, hopefully, increased.

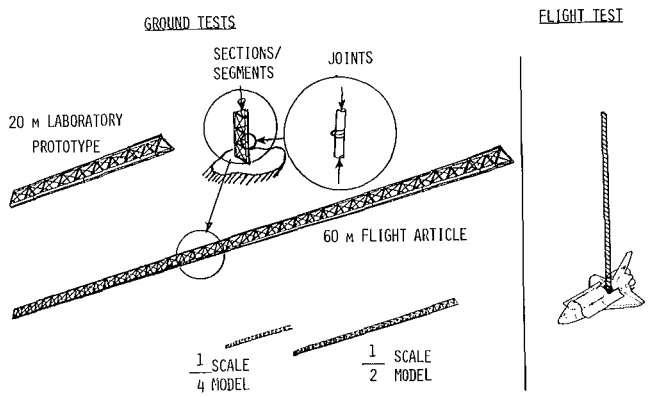

Figure 11

RESEARCH ON FLEXIBLE STRUCTURE CONTROL

The deployable truss beam experiment is initially planned for structural configuration accuracy, deployment, structural dynamics, and collocated actuator/sensor active control studies. However, follow-on flights would include studies of more advanced flexible structure control methods. Control experiments that emphasize algorithm performance with realistic physical structure, actuator, and sensor characteristics should provide considerable information about advanced control methods. Such information is needed to remove doubt as to the degree to which advanced algorithms can be practically relied on for future spacecraft design.

A parameter modification capability, illustrated in the right of figure 12 as a tilt of the upper portion of the beam, adds particular versatility to the experiment by allowing varying degrees of frequency spacing and cross-axis coupling. Other methods of accomplishing similar results include deployable tip extensions at skew angles, tensionable cables for compressing parts or all of the beam, moveable masses such as a pendulum or dumbbell with an axis which rotates relative to the beam axis and, to a limited extent, by "fooling" the control system using sensors mounted such that uncoupled modes of similar frequencies appear coupled.

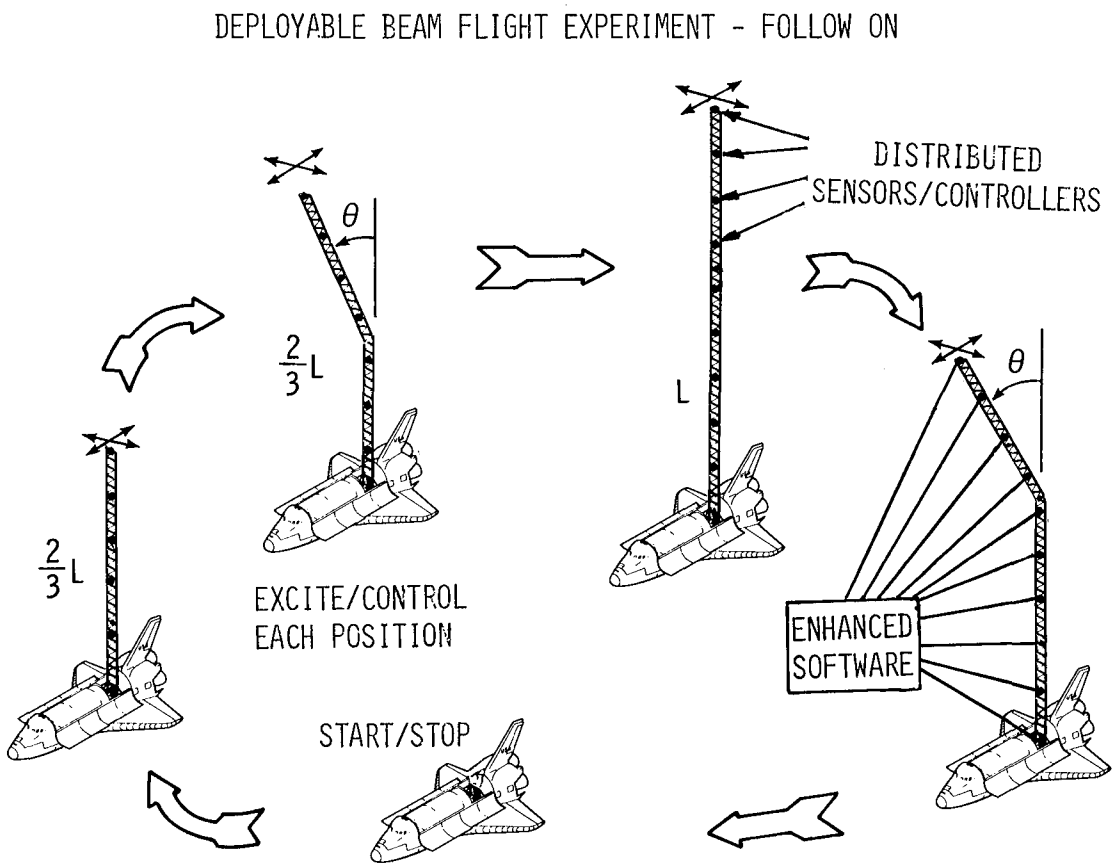

Figure 12

EXPERIMENT DESIGN CONSIDERATIONS

The design of a deployable-beam experiment to conduct the described research involves a number of multidisciplinary trade-offs. Packaging requirements must be met and yet an acceptable design which can be deployed with parameter modification devices, control, actuators, sensors, and related hardware attached must be generated. Manufacturing and assembly precision affects static shape deployment kinematics, and joint structural behavior. Bandwidths and dynamic range requirements of data acquisition equipment are directly affected by beam response characteristics. Responses must be sufficient that they can be measured but not so large as to cause experiment hardware failures or endanger the Shuttle orbiter. Control actuator weight and force requirements directly affect the structural design. Safety, reliability, and redundancy requirements must be satisfied. The complete system design must strike a careful balance between many technical factors to be acceptable (see figure 13).

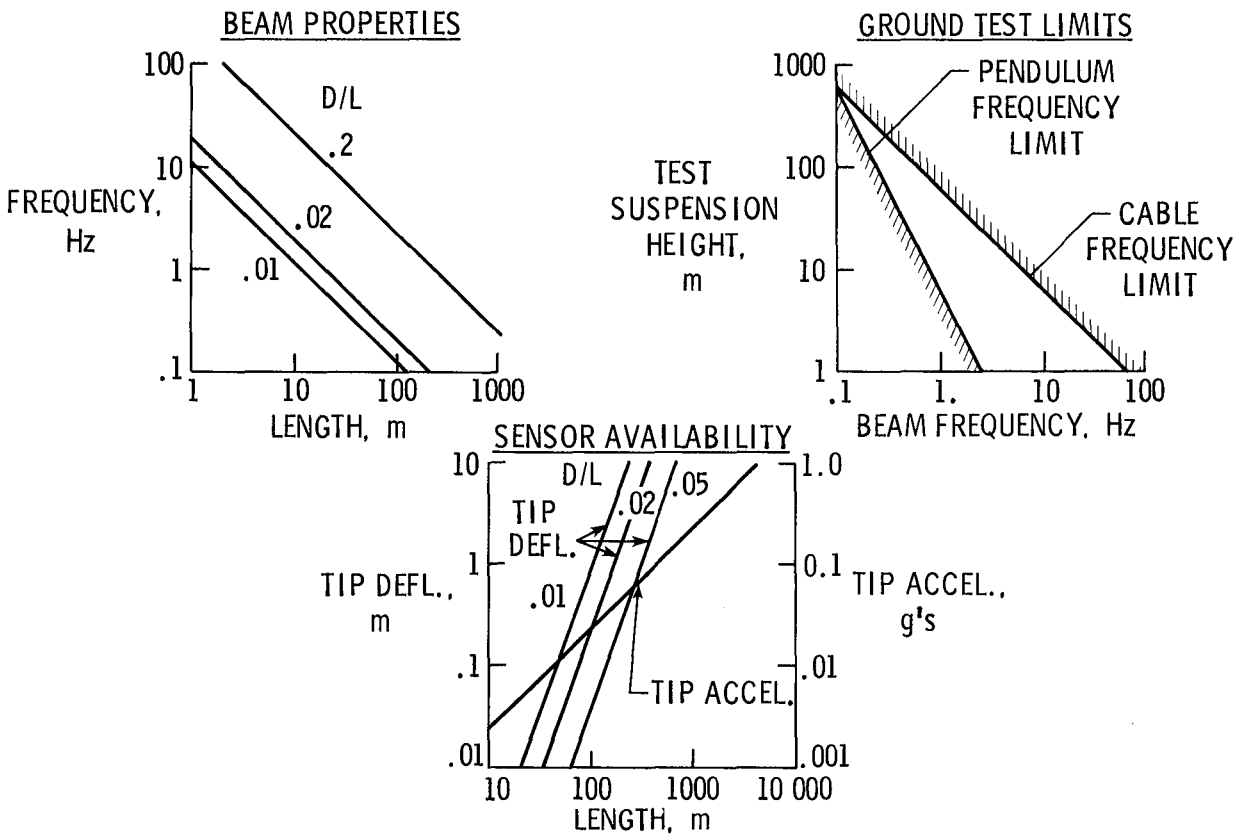

Figure 13

SUMMARY

As space structures grow larger, having critical dimensions of 30m or more, the possibility of increased flexibility creates the potential for problems heretofore of little concern. In particular, obtaining accurate static configurations may require extreme care in manufacturing. Also obtaining sufficient stiffness to allow control systems to deal with only rigid-body motion may be difficult or, at least, costly. Given this situation, confidence in designing and qualifying flight hardware with precision shape requirements and with control systems which control both rigid and flexible motions must be established. This in large part requires accurate mathematical models verified by test. However, ground test technology becomes questionable at frequencies below about one Hertz and gravity effects make tests of very large joint-dominated components difficult at even higher frequencies. Hence, a flight test program on candidate structures is needed to study the problems involved and to calibrate the ground test/analysis effort.

To study these problems, a research test program is proposed which focuses on a deployable beam of practical applications size. This program would consist of system ground tests, flight tests and analyses and would be supplemented by component, subsystem and scale-model ground tests. The flight system will be developed under contract and flown by NASA as a laboratory research test in the Shuttle orbiter. A multiflight program growing in complexity from structures and structural dynamics with simple controls to advanced distributed, adaptive control is envisioned. A critical part of the program is proper instrumentation of the flight hardware and design of the hardware to maximize information obtained. Options for modifying the physical parameters of the beam and for providing multiple actuator inputs are desirable. Design of the flight system requires a multidisciplinary trade-off effort which considers the research needs of the experiment tempered by the practicalities of orbiter-attached flight safety.

SHUTTLE-ATTACHED ANTENNA FLIGHT EXPERIMENT DEFINITION STUDY (FEDS)

G. J. Hannan
Lockheed Missiles and Space Co.
Sunnyvale, CA

SELECTED CONFIGURATION/KEY SUBEXPERIMENTS

Since the early 1970's numerous theoretical developments involving the identification and control of large space structures have appeared within technical literature. More recently, some development and test has been carried out on simplified, scaled laboratory articles. Now, as the Space Transportation System (STS) has achieved operational status, a first LSS flight experiment, SAFE (Solar Array Flight Experiment), has flown. Substantially more ambitious large space structure (LSS) control flight experiments are being discussed within the technical community. The overall purpose of the FEDS was to provide a "Phase A level" feasibility analysis of an LSS control flight experiment. This feasibility study was addressed from the control system technologists's reference. Our primary interest was to assess the control algorithms, techniques, and hardware which would be required to support such an experiment, and to determine whether these items were within the current state of the art. Althought it was necessary to select a strawman flight configuration relative to which control algorithms could be developed and performance assessed, the study results are largely "configuration transparent". We believe that performance requirements and capabilities, timelines, hardware, and algorithms will remain essentially independent of the particular flight experiment configuration selected.

- 55 METER DIAMETER LMSC WRAP-RIB REFLECTOR
- THREE DEGREE-OF-FREEDOM GIMBAL
- KEY SUBEXPERIMENT
  - GEOMETERY ID
  - MASS PROPERTIES ID
  - SYSTEM ID
  - DISTRIBUTED CONTROL
  - SLEWING
- ALGORITHM TRANSPARENCY
  - 50 M TO 100 M CLASS REFLECTOR
  - 100 M TOWER(S)
  - SURFACE ACCURACY f(n)
  - SIMILAR INERTIA CHARACTERISTICS

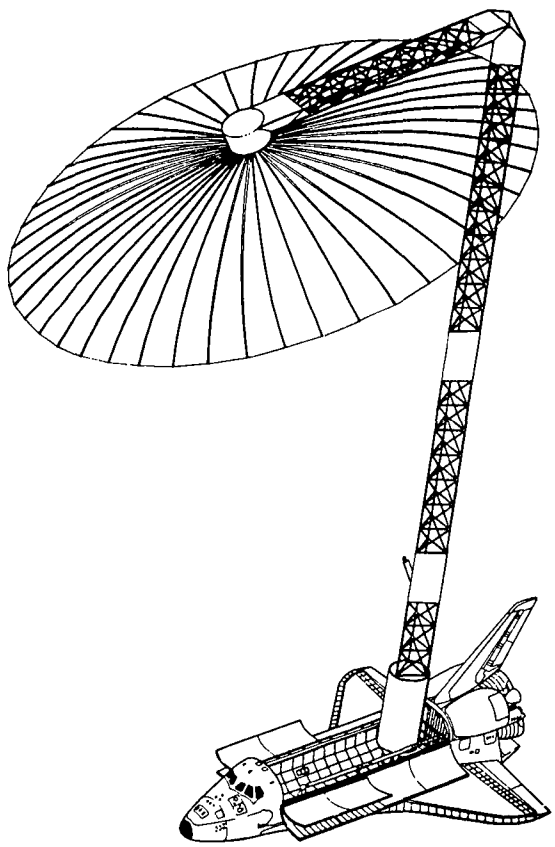

SUBEXPERIMENT PERFORMANCE REQUIREMENTS

The requirements imposed on the subexperiments are of the form of measurement system sensitivity or resolution requirements. In order to quantify these in a meaningful way it is useful to postulate a complementary mission with realistic performance requirements. Such a set of strawman requirements was recently defined as part of a study conducted under the direction of NASA LaRC.

GEOMETRY IDENTIFICATION

The requirements associated with these quantities are all specified in terms of the RF wavelength λ. We specify the measurement capability to be one order of magnitude more accurate than the associated performance requirement.

MASS PROPERTY IDENTIFICATION

Based on previous experience with flight hardware, typical prediction accuracies are 0.2% for mass, 1% for mass center location, and 5% for inertias. To verify this capability, the measurement requirements have been set at 10% of these values.

ELASTIC MODE IDENTIFICATION

The identification requirements for this S/E will be assumed to be consistent with the accuracies obtained in conventional ground based modal test procedures.

CONTROL

Because the inherent structural damping is expected to be very low (<0.5%), the time constant associated with the lowest frequency bending mode (0.094Hz) will be at least 340 sec. The requirement for controlled settling has been set at 10% of this value.

SLEWING

The induced vibrations must be of sufficient magnitude to be readily measurable with the available sensing system.

SUBEXPERIMENT	QUANTITY	REQUIREMENT
GEOMETRY ID	DEFOCUS LATERAL DISPLACEMENT SURFACE QUALITY	0.3 cm (λ/10) 0.03 cm (λ/100) 0.004 cm (λ/800)
MASS PROPERTY ID	MASS C.G. LOCATION INERTIAS	0.02 % 0.1 % 0.5 %
MODAL ID	NO. OF MODES FREQUENCY DAMPING MODE SHAPE	10 0.001 Hz 15% 15-25%
CONTROL	SETTLING TIME POINTING ACCURACY	30 SEC 0.007 DEG (TBR)
SLEWING	LOS JITTER SURFACE QUALITY SLEW RATE SLEW ACCELERATION	0.0007-0.07 DEG 0.0004-0.04 cm 1 DEG/MIN 2 DEG/MIN^2

MOUNT LOCATION EFFECTS UPON JITTER

A five body simulation of the shuttle and test article was built with the ALLFLEX computer program. The dish was modelled with distributed flexibility derived from a 6000 node finite element model, and joint flexibililty was included at interfaces between the various rigid bodies.

In order to assess the impact on subexperiment performance with a three DOF mount we could execute the ALLFLEX simulation of the antenna/shuttle two-body dynamics and analyze antenna jitter as system parameters are varied. This would require many runs of the complex and expensive ALLFLEX simulation.

However, we recognized that antenna jitter is due to reaction forces acting at the antenna/shuttle attachment point. Therefore the analysis approach was to use a simple parameter variation computer program to characterize the reaction forces at the attachment point as system parameters are varied. The ALLFLEX simulation was used to generate antenna jitter for just a few cases. A linear relationship between reaction forces and antenna jitter was derived by matching the limited ALLFLEX generated jitter data to the corresponding reaction forces. This relationship was then used to translate reaction forces output from the parameter variation computer program into antenna jitter. We can therefore establish antenna jitter characteristics as system parameters are varied without running the ALLFLEX simulation for every individual combination of system parameters.

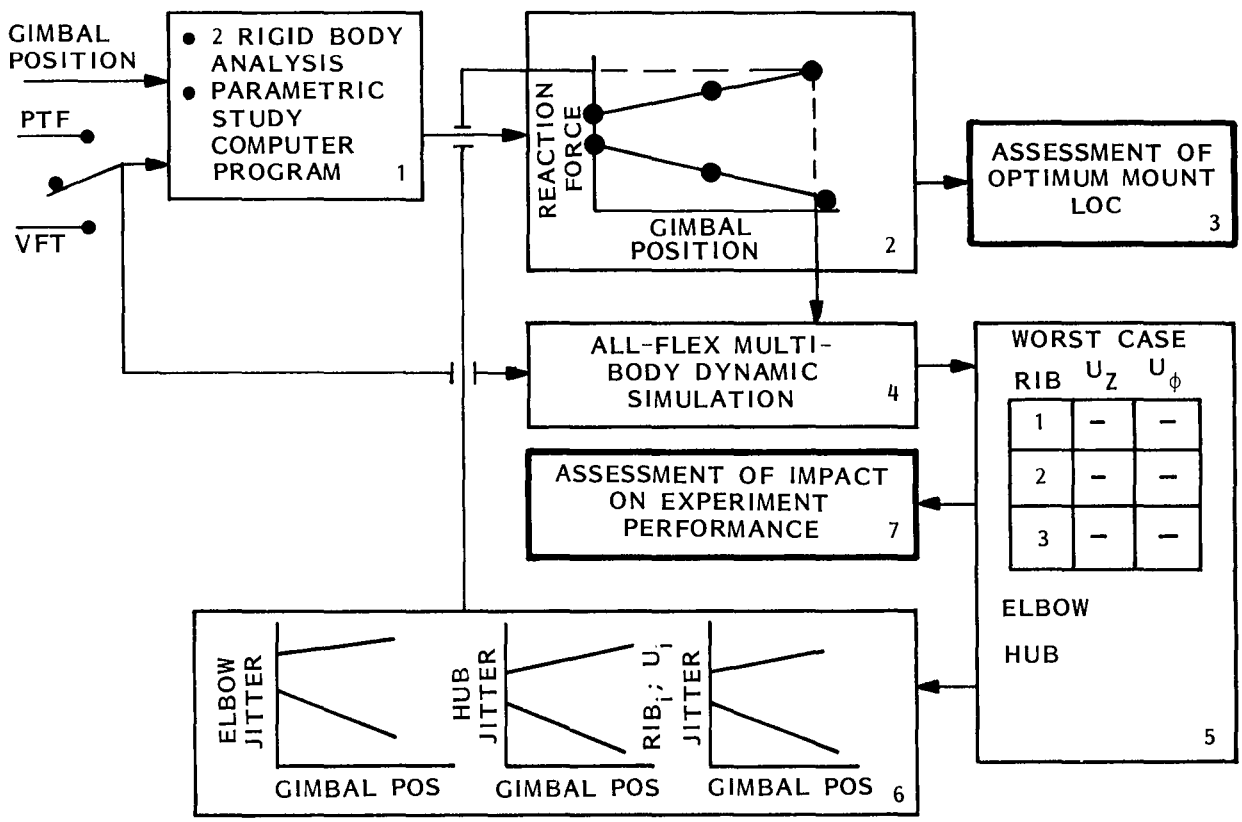

WORST CASE JITTER SUMMARY

The surface quality requirement was used to draw conclusions regarding the impact of the three DOF mount on subexperiment performance. The average reflector plunging motion U_Z due to vernier firing for stations 41, 42 and 43 is 0.115 inches, or 0.29 cm. The surface quality requirement is $\lambda/80$, which translates into 0.0375 cm for a 10 GHz antenna and .375 cm for a 1 GHz antenna.

Selection of the three-axis or six-axis gimbal depends upon the antenna quality and performance specified. These preliminary flexible body analyses indicate that the system jitter induced by vernier thruster firings is approximately 100% of the jitter allowable with a 10 GHz RF system.

Hence, we conclude that a 10 GHz system should consider a six DOF gimbal. A three DOF gimbal should adequately accommodate vernier thrust for a 1 GHz level flight experiment.

If the flight experiment is not in an operational mode, performing a subexperiment, a vernier thruster firing will not be a problem. However, during this nonoperational mode the gimbals may be locked and a primary thruster firing could potentially lead to structural damage of the mount or the antenna. What is required to accurately assess this structural damage situation is a stress analysis; however, the jitter results do provide some insight into this situation. The 40 foot deflection of the elbow with respect to the bus indicates structural damage is a clear possibility and further analysis is required.

VERNIER THRUSTERS
FREE GIMBAL

DISH STATION	U_θ	U_Z
41	0 IN.	0.014 IN.
42	0.2 IN.	0.012 IN.
43	0.26 IN.	0.01 IN.
44	0.2 IN.	0.007 IN.
45	0 IN.	0.006 IN.

ELBOW	0.09 IN.	WRT BUS
HUB	0.08 IN.	WRT ELBOW

PRIMARY THRUSTERS
LOCKED GIMBAL

STATION	U_θ	U_Z
41	0.0002 IN.	0.5 IN.
42	10 IN.	0.5 IN.
43	20 IN.	0.5 IN.
44	10 IN.	0.5 IN.
45	0.0002 IN.	0.5 IN.

ELBOW	40 FT	WRT BUS
HUB	4 IN.	WRT ELBOW

STATIC GEOMETRY IDENTIFICATION

The purpose of the geometry identification subexperiment (S/E) is to estimate the shape, orientation, and surface quality of the flight experiment's antenna assembly.

This S/E uses 48 retroreflectors (RRs) dispersed along the ribs of the antenna reflector surface, four RRs placed upon the lower surface of the hub, three RRs placed on each of the long and short booms, a laser measurement device (LMD), and a Kalman filter to estimate reflector shape and surface quality, hub orientation, and boom orientation.

The estimation process assumes the antenna can be described as a paraboloid of revolution, the hub as a planar surface, and the booms as straight lines. Based upon these models, the reflector surface shape ID S/E uses a nine state extended Kalman filter; the hub ID S/E uses a three state Kalman filter; and the boom ID S/Es use a six state Kalman filter. The estimated parameters define a spatial model of the reflector surface, hub, and booms, and an estimate of a reflector surface quality. From the geometric description of the surface, the position of any point can be estimated as $\hat{P}_j$. The RMS difference between the estimated $\hat{P}_j$ and the measured $\hat{P}_m$ for the complete RR set then provides an indication of the degree to which the measure points do not fit the best fit parabola, hence a measure of the reflector surface quality.

- KEY PARAMETERS FOR ESTIMATION
  - SHAPE
  - ORIENTATION
  - SURFACE QUALITY
- TASKS
  - BOOM GEOMETRY
  - HUB LOCATION AND ORIENTATION
  - REFLECTOR SURFACE QUALITY
- HARDWARE
  - LASER SOURCE AND DETECTOR
  - 58 RETROREFLECTORS
  - FLIGHT COMPUTER

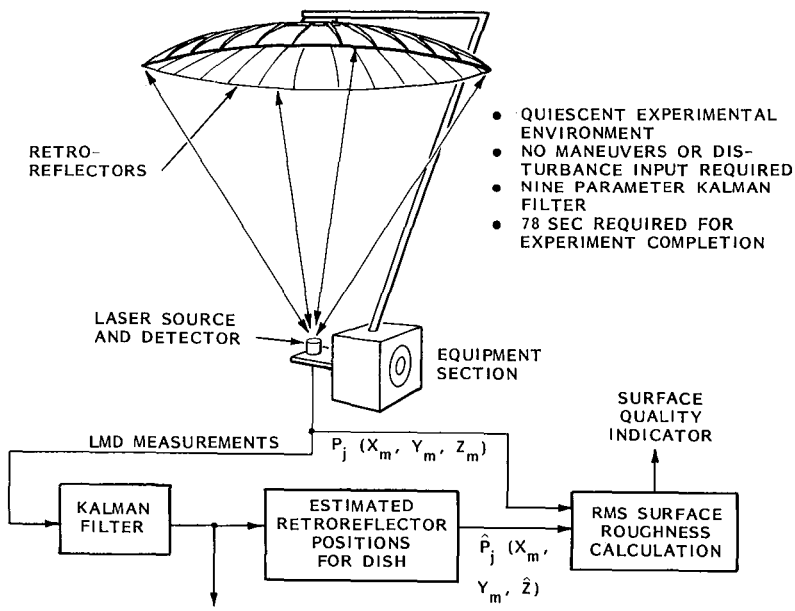

- QUIESCENT EXPERIMENTAL ENVIRONMENT
- NO MANEUVERS OR DISTURBANCE INPUT REQUIRED
- NINE PARAMETER KALMAN FILTER
- 78 SEC REQUIRED FOR EXPERIMENT COMPLETION

GEOMETRY ID PERFORMANCE/REQUIREMENTS

The RMS value represents the accuracy with which the subexperiments can be expected to predict the deployed experiment geometry. This index also represents the point at which actual structural deformations can no longer be distinguished from estimation errors.

The table shows the attainable RMS system performance measure for the hub, boom, and dish ID subexperiments. Three rows exist for each of the three ID subexperiments. Each row corresponds to the expected RMS system performance achievable with the SHAPES sensor, a sensor of ten times lower quality than SHAPES, or a sensor of 100 times lower quality than SHAPES. The last column contains the RF frequency (10 GHz, 1 GHz, or <1 GHz) for which the corresponding ID subexperiment meets the requirements.

The most stringent requirement is on surface accuracy. If we assume no structural vibration, the SHAPES LMD is capable of a surface accuracy of .014 mm. A LMD of ten times larger measurement errors than SHAPES is capable of a surface accuracy of .096 mm. Thus, in the absence of structural vibration, SHAPES sensor will meet the requirements for 10 GHz.

A sensor of ten times less accuracy will meet the requirements for 1 GHz. If structural ringing is included, SHAPES will meet the 1 GHz requirement. Thus, to meet the 10 GHz requirements the antenna structure must be settled before the ID subexperiments can be attempted.

ID S/E AND LMD COMBINATION	REQUIRED RMS SYSTEM PERFORMANCE FOR 10 GHz	REQUIRED RMS SYSTEM PERFORMANCE FOR 1 GHz	ATTAINABLE RMS SYSTEM PERFORMANCE	RF CAPABILITY
DISH ID S/E USING THE JPL SHAPES LMD	0.0375 mm	0.375 mm	0.014 mm	10 GHz
DISH ID S/E USING A LMD 10 TIMES WORSE THAN SHAPES	0.0375 mm	0.375 mm	0.096 mm	1 GHz
DISH ID S/E USING A SMD 100 TIMES WORSE THAN SHAPES	0.0375 mm	0.375 mm	1.0 mm	<1 GHz
DISH ID S/E USING SHAPES LMD INCLUDING RINGING	0.0375 mm	0.375 mm	0.363 mm	1 GHz
HUB ID S/E USING THE JPL SHAPES LMD	0.02 mm	0.2 mm	0.016 mm	10 GHz
HUB ID S/E USING A LMD 10 TIMES WORSE THAN SHAPES	0.02 mm	0.2 mm	0.17 mm	1 GHz
HUB ID S/E USING A LMD 100 TIMES WORSE THAN SHAPES	0.02 mm	0.2 mm	0.11 mm	1 GHz
BOOM ID S/E USING THE JPL SHAPES LMD	0.2 mm	2.0 mm	0.030 mm	10 GHz
BOOM ID S/E USING A LMD 10 TIMES WORSE THAN SHAPES	0.2 mm	2.0 mm	0.15 mm	10 GHz
BOOM ID S/D USING A LMD 100 TIMES WORSE THAN SHAPES	0.2 mm	2.0 mm	1.4 mm	1 GHz

MASS PROPERTIES IDENTIFICATION

The mass properties identification subexperiment is intended to provide estimates of the mass, center of mass, and moment of inertia of the flight experiment test article. These quantities all appear in the two-body equations of motion describing the coupled STS test article dynamics and kinematics. An extended Kalman filter has been formulated with both the dynamic states (angles and rates) and the mass property parameters of interest appearing in the state vector. All of the mass properties are rendered observable by commanding large relative angle motion between the two bodies.

Subexperiment performance evaluation is performed by simulation of a simplified planar two-body case. The gimbal angle histories used for performance evaluation with the planar model are then generalized to the three dimensional case to establish an experiment timeline.

The performance of the subexperiment is taken to be the accuracy or resolution with which the parameters may be determined. An evaluation of this measurement accuracy is not a product of the flight experiment, but is rather the product of detailed preflight analysis.

- KEY PARAMETERS FOR ESTIMATION
  - $I_{ANTENNA\ ASSY}$
  - $CM_{ANTENNA\ ASSY}$
  - $M_{ANTENNA\ ASSY}$
  - STS PROPERTIES
- APPROACH
  - EXPERIMENT ASSEMBLY MANEUVERS
  - GIMBAL AND CMG TORQUES
  - SUBSTANTIAL CONFIGURATION VARIATIONS
  - KALMAN FILTER
- HARDWARE
  - ARS
  - CMG
  - GIMBAL TORQUES
  - FLIGHT COMPUTER
  - GIMBAL ENCODER

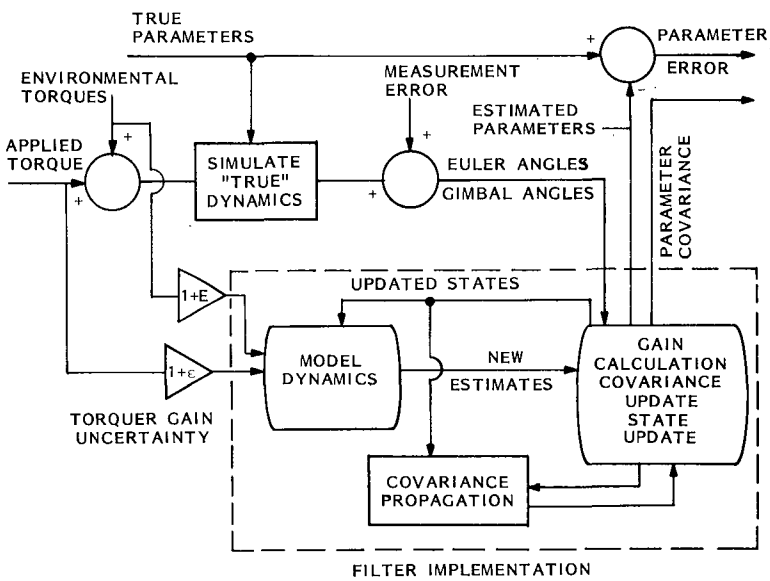

MASS PROPERTIES ID PERFORMANCE/REQUIREMENTS

Results obtained to date indicate that while the parameters are observable, some of them are only weakly observable. The estimator performance level obtained to date has not met the baseline requirements.

The estimator process is complicated by the fact that the postulated three degree of freedom gimbal results in a system with coupled two-body dynamics. Some of the parameters of interest do not significantly affect the system dynamics, and consequently are not accurately estimated. A further difficulty is that time-consuming three axis large angle motion is needed to enhance parameter observability to achieve even the modest results obtained.

Although it has not been analyzed, it is felt that a free-flying or six DOF mounted experiment will allow for much improved mass property identification. Time-consuming large angle maneuvers would not be required. Inertia estimate quality would presumably be as good as control torque knowledge. Center of mass location could be determined by comparison of accelerometer measurements taken on the test article periphery. Mass estimation will remain difficult since translational actuators (thrusters) typically have relatively uncertain force levels. Additional instrumentation, such as pressure transducers for cold gas thrusters, could solve this problem.

	QUANTITY	PERFORMANCE REQUIREMENT	ACTUAL PERFORMANCE
MASS PROPERTY ID	MASS	0.02%	4.076%
	C.G. LOCATION	0.1%	3.88%
	INERTIAS	0.5%	1.1%

SYSTEM MODE IDENTIFICATION

Since the number of parameters whose values are to be estimated is large, any of the well-known identification approaches (such as maximum likelihood, extended Kalman filter, instrumental variables) is likely to be ill-conditioned, and to require substantial amounts of off-line data processing. Simple techniques to improve the conditioning of the identification problem are exercised first, followed by a relatively few iterations of one of the general purpose identification algorithms mentioned above.

To this end, the following simple algorithms are used:

- Fast Fourier transforms (FFT) to obtain improved modal frequency information
- Eigenvalue-eigenvector perturbation (EEP) techniques to obtain first order corrections to mode frequency and mode shape data
- Narrow-band excitation of the antenna system near the predicted modal frequencies, to maximize the information content of the sensed signal.

After improved initial parameter estimates are obtained, the maximum likelihood estimation (MLE) procedure is invoked. The MLE procedure begins with initial estimates of system parameter values. This set of parameters consists of natural frequencies, damping ratios, mode shapes, masses, inertias, stiffnesses, etc. MLE is the process by which a performance measure, J, is minimized with respect to the parameters while maintaining consistency with the system dynamics.

- PARAMETERS FOR ESTIMATION
  - FREQUENCY
  - DAMPING
  - MODE SHAPE
- APPROACH
  - STRUCTURAL EXCITATION
  - ESTIMATION ALGORITMS
    - FET
    - MLE
- HARDWARE
  - IRU (BUS, HUB, AND STS)
  - STAR SENSORS (BUS, HUB, AND STS)
  - GIMBAL ANGLE ENCODERS
  - CMG
  - GIMBAL TORQUERS
  - VERNIER STS THRUSTERS

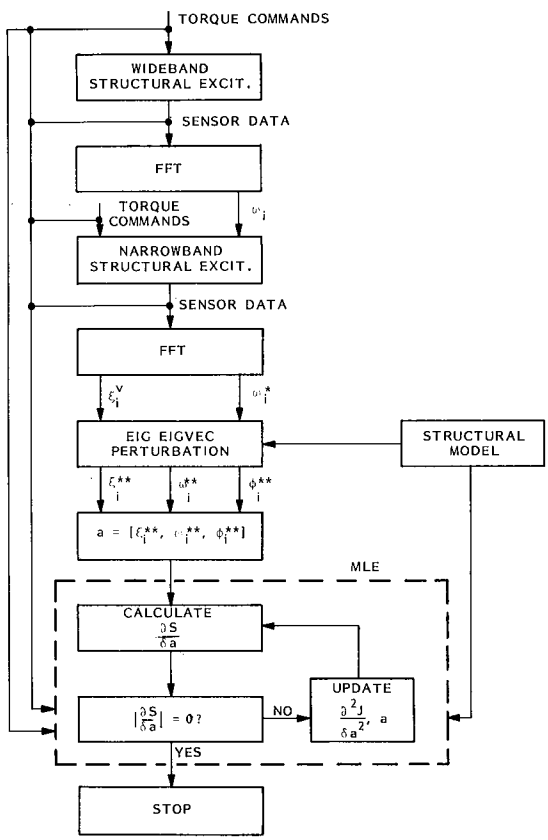

MLE EXAMPLE PERFORMANCE

A typical Maximum Likelihood Estimator (MLE) case for FEDS is summarized below. The parameter vector consists of three modal frequencies, two damping ratios, two mode shapes associated with actuation, and two mode shapes associated with sensing.

This identification procedure begins with a 1 sec step applied to all the actuators. During this one second and for an additional nine seconds, all of the sensors are sampled at a 10 Hz rate. The total of 100 samples of data from each of 18 sensors is processed off-line with MLE.

It should be pointed out that for this simulation, all 16 of the mode shape values in the model have been perturbed by 5%, but that only a few selected mode shape parameters are allowed to be varied in MLE. The MLE procedure does its best to account for these unmodeled parameter errors by adjusting the relatively few parameters that have been freed. This explanation accounts for the convergence of the parameter vector to a value that is biased away from the true value.

START	ITERATION NO. 1	ITERATION NO. 2	ITERATION NO. 3	ITERATION NO. 4	ITERATION NO. 5	ITERATION NO. 6	TRUE
2.0	1.9416	1.9200	1.9164	1.9205	1.9186	1.9160	1.940
6.0	6.0	6.0	6.0	6.0001	6.0001	6.0002	6.0530
10.0	9.9981	9.9971	9.9940	9.9741	9.9655	9.9362	9.7620
0.0	0.0	0.0	-0.0001	-0.0001	-0.0001	-0.0001	-0.0050
0.0	-0.0022	-0.0031	-0.0038	-0.0071	-0.0083	-0.0101	-0.0050
0.0600	0.0692	0.0789	0.0764	0.0793	0.0787	0.0776	0.0826
0.0600	0.0685	0.0576	0.0551	0.0405	0.0359	0.0285	0.0642
-240.0	-240.0001	-240.0001	-240.0003	-240.0013	-240.0017	-240.0062	-243.4728

SYSTEM ID DATA PROCESSING REQUIREMENTS

The sample rate and data processing requirements for FFT, eigenvalue-eigenvector perturbation, and the Maximum Likelihood Estimator are given in the table.

For the most detailed shuttle/antenna system model considered, the appropriate values for the previous table are:

N = 32 states
M = 9 actuators
S = 18 sensors
P = 9 parameters
T = 100 samples at 10 Hz rate

In this case, the 10 Hz sample rate was chosen to be five times the maximum modal frequency of interest (2 Hz). Consequently, the frequency resolution using FFT alone is 0.1 Hz. The computation storage and time requirements for FFT are virtually nil (time - 5 s, storage - 100 words).

The most demanding algorithm in terms of processing requirements is the Maximum Likelihood Estimator. In this example, two hours of computation time (time shared VAX 1170 in demand mode using MATRIX$_X$ interpreter) and 30,000 words of storage were needed. The major storage requirements are dictated by the need of storing the partial derivatives of the system matrices (32 x 32) with respect to the parameters (9 x 1) which itself requires almost 10,000 storage locations.

	FFT	EEP	MLE
SAMPLE RATE	THE FREQUENCY RESOLUTION OF FFT IS INVERSELY PROPORTIONAL TO THE SAMPLE RATE	-	4 TO 5 TIMES THE HIGHEST FREQUENCY COMPONENT OF INTEREST
DATA PROCESSING TIME	ST LOG_2 T	N^2 PER PERTURBATION	N^2 P (MTS) T
DATA PROCESSING STORAGE	T	N^2	$(N^2 + NM + NS)$ P

WHERE:

N = NUMBER OF STATES
M = NUMBER OF ACTUATORS
S = NUMBER OF SENSORS
P = NUMBER OF PARAMETERS, AND
T = NUMBER OF SAMPLES

FEDS EXAMPLE

N = 32 STATES
M = 9 ACTUATORS
S = 18 SENSORS
P = 9 PARAMETERS
T = 100 SAMPLES AT 10 Hz RATE

- FEDS EXAMPLE REQUIRED 32K WORDS VAX STORAGE
- NOT REALTIME
- GROUND COMPUTER CALCULATIONS

CONTROL SYSTEM SUBEXPERIMENT

The overall objective of this control subexperiment is on-orbit demonstration of distributed control for large space structures. While completing this demonstration, the subexperiment will also study the control capability of currently available actuators for Damping Augmentation Control, Hub/Feed Orientation Control, and Line-of-Sight Pointing Control of the 55m antenna structure by means of:

1. Control effort provided only by torquers at the bus,
2. Control effort provided by torquers at the bus and the hub,
3. Control effort provided by torquers at the bus and the hub, and by force actuators at the hub.

Nine different controllers will be designed and evaluated on the ground and verified during this control subexperiment.

The antenna will be deployed with the gimbals locked. When the antenna is fully deployed and the gimbals unlocked, small disturbances are applied to the antenna. Controllability will be demonstrated for each of the controller configurations described above. Feedback control gains should be low and gradually increased during the experiment. These gains are computed on the ground and stored in the flight computer.

- CONTROLLER CONFIGURATIONS
  1. BUS TORQUE
  2. BUS TORQUE, HUB TORQUE
  3. BUS TORQUE, HUB TORQUE, HUB FORCE
- CONTROL PHILOSOPHIES
  - MODAL
  - HUB/FEED
  - LINE-OF-SIGHT
- APPROACH
  - STRUCTURAL EXCITATION
  - CONTROL USING DIFFERENT CONFIGURATIONS
  - SETTLING TIME FOR PERFORMANCE INDICATOR
- HARDWARE
  - ACTUATORS AS SHOWN IN FIGURE
  - BUS AND HUB IRUs AND STAR SENSORS
  - TRANSLATIONAL DISPLACEMENT SENSOR (ELBOW)

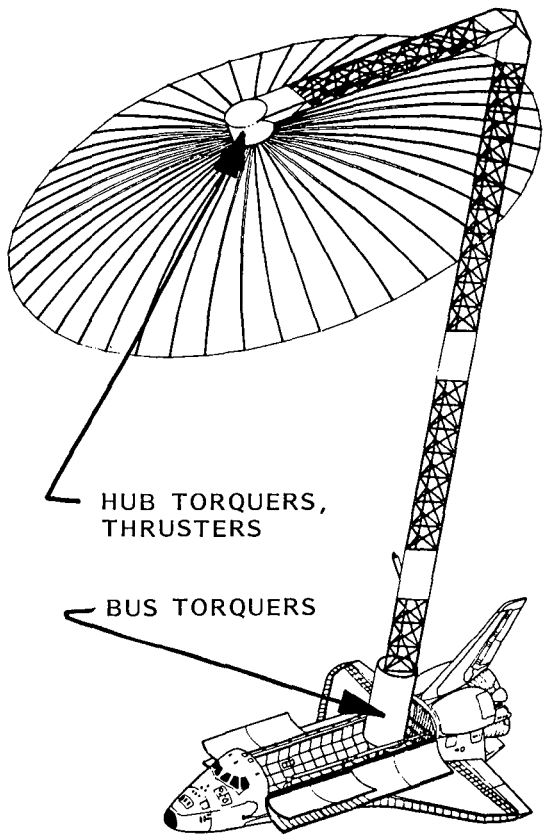

CONTROL SUBEXPERIMENT ACTUATOR REQUIREMENTS

The actuator and sensor requirements from each of the subexperiments were determined to support the preliminary hardware selection. This chart shows how some of the actuator requirements for the control subexperiment varied with the controller configuration. The requirements addressed here are actuator bandwidth and to peak force and torque. The values shown are from simulation results with a level of excitation consistent with an associated set of sensor requirements. Note the insensitivity of actuator bandwidth to controller configuration. Note also the reduction in control effort of the actuators as other actuators are brought into the system when system performance is held nearly constant.

Other actuator and sensor requirements derived from this and the other subexperiments included maximum sensed rates and displacements, minimum sensor and actuator resolution, scale factor accuracy, etc.

		REQUIRED FORCE AMPLITUDE (LB)	REQUIRED TORQUE AMPLITUDE (FT-LB)	REQUIRED FORCE BANDWIDTH (Hz)	REQUIRED TORQUE BANDWIDTH (Hz)
DAMPING AUGMENTATION CONTROL	CONTROLLER CONFIG				
	1	N/A	34.0	N/A	3.5
	2	N/A	16.0	N/A	3.0
	3	0.6	2.6	3.0	3.0
HUB/FEED ORIENTATION CONTROL	CONTROLLER CONFIG				
	1	N/A	30.0	N/A	3.0
	2	N/A	11.0	N/A	3.0
	3	0.15	1.15	3.5	3.0
LINE-OF-SIGHT POINTING CONTROL	CONTROLLER CONFIG				
	1	N/A	100.0	N/A	3.0
	2	N/A	14.0	N/A	3.5
	3	0.16	6.0	3.5	3.0

CONTROL SUBEXPERIMENT DATA PROCESSING REQUIREMENTS

Steady state filter and control gains are calculated prior to the actual experiment using the a priori plant model or that derived from the identification subexperiments. Dimensions of the various vectors and matrices are as indicated for the different controller configurations. The 4 MBYTE data storage requirement indicated is for a single 50 sec test with a 64 Hz sample rate as is the 200 KOPS throughput. These storage and throughput requirements are consistent with existing flight computer and tape recorder performance.

	CONTROLLER CONFIGURATION 1	CONTROLLER CONFIGURATION 2	CONTROLLER CONFIGURATION 3
CONTROL VECTOR U	3 x 1	6 x 1	9 x 1
STATE VECTOR X	22 x 1	22 x 1	22 x 1
MEASUREMENT VECTOR Y	15 x 1	15 x 1	15 x 1
Φ	22 x 22	22 x 22	22 x 22
Γ	22 x 3	22 x 6	22 x 9
H	15 x 22	15 x 22	15 x 22
K	22 x 15	22 x 15	22 x 15
C	3 x 22	6 x 22	9 x 22

- TOTAL STORAGE 4.0 MBYTES
- THROUGHPUT 200K FLOPS ASSUMING 64 Hz SAMPLE FREQUENCY

SLEWING SUBEXPERIMENT

This subexperiment will compare the performance capabilities and operational constraints of three command generators - Versine, Gauss Filter, and Optimal. For purposes of this study we have concentrated on the versine slew. We anticipate that the versine slew will exercise the command and sensing systems associated with this subexperiment to a degree representative of all three command generators. Equipment, computation, and timeline requirements which accommodate the versine slew should accommodate the alternate slew techniques.

The versine slew subexperiment consists of two basic steps - applying a slew command to the antenna structure, and measuring the resulting vibration. Antenna rib and line-of sight (LOS) vibration are used as the performance measures of slew quality. An ideal slew induces no structural vibration. The command will be computed in real time by the on-board computer, according to parameters either loaded before the flight, or input during flight. A CMG cluster mounted on the equipment section and/or the hub will apply the commanded torque profile. The dish distortion and LOS vibration will be measured with the array of retroreflectors and the laser measurement device.

The CMG array as sized by its momentum requirement can provide torques greater than those corresponding to the required accelerations. Increased acceleration were found necessary to excite bending sufficiently for easy measurement.

- OBJECTIVE
  - ASSESS VARIOUS TECHNIQUES FOR MANEUVERING EXPERIMENT ASSEMBLY
  - VERIFY ANALYTICALLY GENERATED JITTER PREDICTIONS
  - COMPARE JITTER INDUCED BY VARIOUS COMMAND GENERATORS

- HARDWARE REQUIREMENTS

	H FT-LB-SEC	τ FT-LB	RESOLUTION/ SENSITIVITY	BANDWIDTH	DYNAMIC RANGE
TORQUER SENSOR	820	70	2 IN.-LB 1 μRAD 0.00005 IN. (0.001 IN.)	1 Hz 3 Hz IN.	-10 -10 0.5-100 μRAD 0.00005-0.001 IN.

- PERFORMANCE

NO.	AXIS	Tp (SEC)	τ (FT-LB)	MIDSLEW		POSTSLEW	
				Ax(y) (μRAD)	u (IN.) ($\times 10^{-2}$)	Ax(y) (μRAD)	u (IN.) ($\times 10^{-2}$)
1	PITCH	15.17	54.6	24.6	0.00822	25.0	0.026
2	PITCH	13.67	48.9	17.7	0.00472	18.0	0.0094
3	ROLL	15.17	49.2 (R) 11.4 (Y)	54.6	0.0238	22.0	0.033

FLIGHT EXPERIMENT HARDWARE SUMMARY

Hardware requirements for each of the subexperiments have been determined, not only qualitatively but also to reflect maximum and minimum commandable or measureable levels, bandwidths, etc. An aggregate of these subexperiment requirements was formed, and a set of hardware which appears to meet the resulting flight experiment requirements was assembled. Selected hardware items at this point reflect "typical" devices which provide adequate capability and can be used for cost estimates. A "phase B" level study would require substantially more trades and performance analyses, especially for computers, star sensor, and gyros for which many options exist.

ITEM	VENDOR	LOCATION	NO. REQUIRED	UNIT WEIGHT (LB)	UNIT VOLUME (IN^3)	AVG UNIT POWER (WATTS)	COMMENTS
CONTROL MOMENT GYRO ASSEMBLY	SPERRY	EQUIPMENT SECTION	3	260	43, 33, 70	48	1300 FPS; PEAK POWER ≈ 700 W
STAR SENSOR	BALL	EQUIPMENT SECTION	2	20.3	6.5, 8.2, 12	23.1	
INERTIAL REF PKG	BENDIX	EQUIPMENT SECTION	1	12	6, 8, 5.1	11/ CHANNEL	
SHAPES	–	EQUIPMENT SECTION	1	33		20	IN DEVELOPMENT AT JPL
EXP COMPUTER ASSEMBLY	ROCKWELL	EQUIPMENT SECTION	1	110	18, 19, 13	100	24 BIT WORD
FLIGHT RECORDER							
CONTROL MOMENT GYRO ASSEMBLY	SPERRY	HUB	3	115	35, 23,	48	225 FPS; PEAK POWER 250 W
STAR SENSOR	BALL	HUB	2	20.3	6.5, 8.2, 12	23.1	
INERTIAL REF PKG	BENDIX	HUB	1	12	6, 8, 5.1	11/ CHANNEL	
THRUSTER COMPLEX	–	HUB	6	2.7	7, 5, 2	10	
TORQUE MOTOR ASSEMBLY	LMSC	GIMBAL	3	200	24 x 20d	–	280 W PEAK POWER
TORQUE MOTOR ELECT	LMSC	GIMBAL	1	20	5, 9, 12		
DIGITAL ENCODER	BEC	GIMBAL	3				

FLIGHT EXPERIMENT TIMELINE

Execution time requirements for each of the separate subexperiments have been estimated and are indicated in the table. Under nominal conditions only one iteration of each subexperiment has been shown except for the Static Geometry Identification subexperiment. The approximately 10 second data collection time for this subexperiment makes such repetition easily accommodated.

The single largest block of time is reserved for the mass properties identification. The experiment time reserved is this long due to the need to move the large experiment test article through combinations of large angles in three gimbal axes in order to render the mass properties observable. The maneuver history assumed was based on extrapolation of planar simulation results and may be subject to significant revision in any further study of this concept.

The primary conclusion is that performance at all the subexperiments within a single shuttle flight appears feasible.

EXPERIMENT	SINGLE ITERATION	NO. OF ITERATIONS	TOTAL PROG TIME	CONTINGENCY	TOTAL SUBEXP TIME	CUMULATIVE ON-ORBIT TIME
1. STATIC GEOM	15 SEC	3	45 SEC	30 MIN	31 MIN	24.5
2. MODE ID	24 HR	1	24 HR	18 HR	42 HR	66.5
3. CONTROLS	3.5 HR	1	3.5 HR	7 HR	10.5 HR	77.0
4. SLEW	8 HR	1	8 HR	4 HR	12 HR	89.0
5. MASS PROP ID	73 HR	1	73 HR	24 HR	97 HR	186.0
TOTAL	108.5 HR	–	108.5 HR	53.5 HR	162 HR	186.0

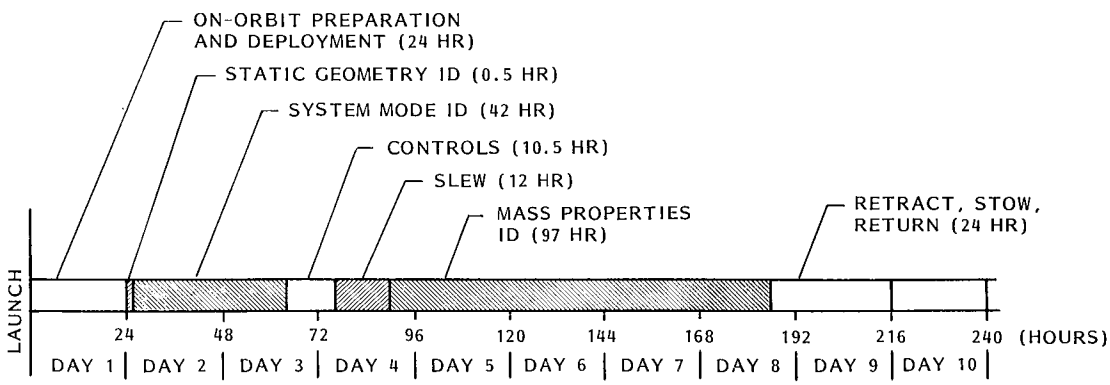

LSS CONTROL DEVELOPMENT TEST PLAN

Laboratory development tests must be designed and executed to verify separate portions of the LSS control theory. The purpose of this statement is to emphasize the need to execute such experiments with the specific intent of theory verification, rather than concept verification or simple agreement between analysis and experiment after repeated interations of the same test using the same test article. The objective is to develop the theory to a level where hardware system performance can reliably be expected to match analytical and simulation predictions without modification to the analytical model. This is the role of development testing.

The figure presents a development test program loop designed to emphasize theoretical verification. The plan calls for initial testing with simple test articles, these test articles designed for modification from level 1 through level 3 testing. The level 1 structure should be geometrically simple and easily analyzed, to aid physical interpretation of analysis and test results. The article nominally increases in size and complexity as testing passes through level 2 and level 3 testing. The corroboration (independent) test, initiated following successful level 2 testing, should employ a test article substantially different in geometry and other key physical characteristics from the original specimen.

The program format outline is similar to that which was followed during the ACOSS and VCOSS programs, although more extensive.

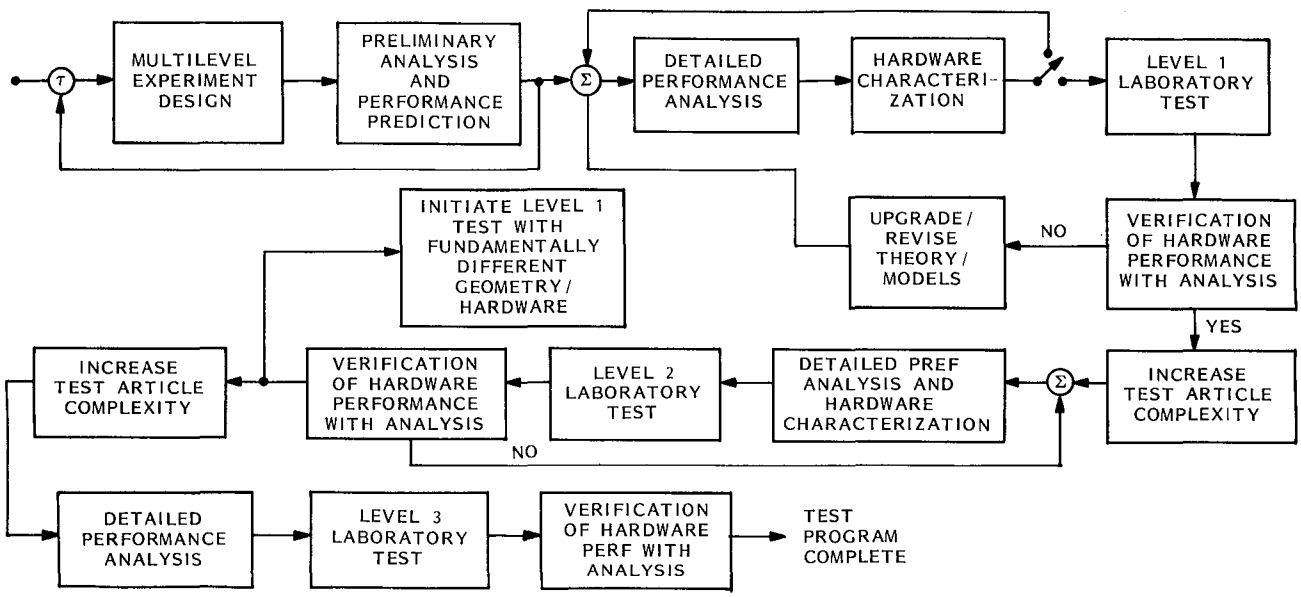

CONCLUSIONS

This study has provided a first assessment of some of the problems associated with, and our ability to pursue, a large space structure controls flight experiment.

Based upon this study we conclude that a shuttle attached flight experiment is feasible with respect to control system technology. The control and identification algorithms are reasonably well understood and can be adapted to current flight computers, when necessary. The required control/identification hardware is available with the exception of the SHAPES sensor, used for GEOMETRY IDENTIFICATION, and the control system RCS. The technology for SHAPES, in our opinion, is available, but a development program is required. The RCS will also require development. However, this RCS development should be a relatively low cost item which, in fact, is not mandatory to the experiment. Additional significant conclusions reached during this study are as indicated.

- OPERATIONAL LSS SYSTEMS ARE LIKELY TO REQUIRE AT LEAST ONE ADDITIONAL DESIGN ITERATION
- A 10 GHz SYSTEM WILL PROBABLY REQUIRE SIX DOF GIMBAL
- THE PROPOSED SUBEXPERIMENTS ARE FEASIBLE BUT BETTER APPROACHES MAY EXIST
- A FLIGHT EXPERIMENT SIMILAR TO THAT CONSIDERED WITHIN THIS STUDY CAN BE ACCOMPLISHED WITHIN THE CONSTRAINTS OF A NINE DAY STS MISSION
- THE FLIGHT EXPERIMENT SHOULD PROVOKE AN EXTENSIVE GROUND TEST PROGRAM

ELECTRO-SCIENCE REQUIREMENTS FOR SHUTTLE-ATTACHED ANTENNA FLIGHT EXPERIMENTS

William L. Grantham
Emedio M. Bracalente
Lyle C. Schroeder
Langley Research Center
Hampton, Virginia

Large Space Antenna Systems Technology - 1984
December 4-6, 1984

INTRODUCTION

With the considerable progress indicated by the papers at this conference, it is very clear that the time is right for a flight experiment of a large space antenna. The antenna system most suited by size and technical maturity for the first flight experiment is the 15 Meter Hoop/Column Antenna. This antenna is being developed under contract for LaRC by the Harris Corp. of Melbourne, Florida. Structural tests and modal surveys have already begun on the antenna as well as multiple deployment testing. Electromagnetic testing will begin in the spring of 1985 and refurbishment of this antenna to flight status is under consideration at this time.

Seven electro-science flight experiments are being studied to develop a manifest of experiments for shuttle-attached missions using this antenna. Papers in this conference (Ref. 1-5) describe elements of five of these experiment concepts.

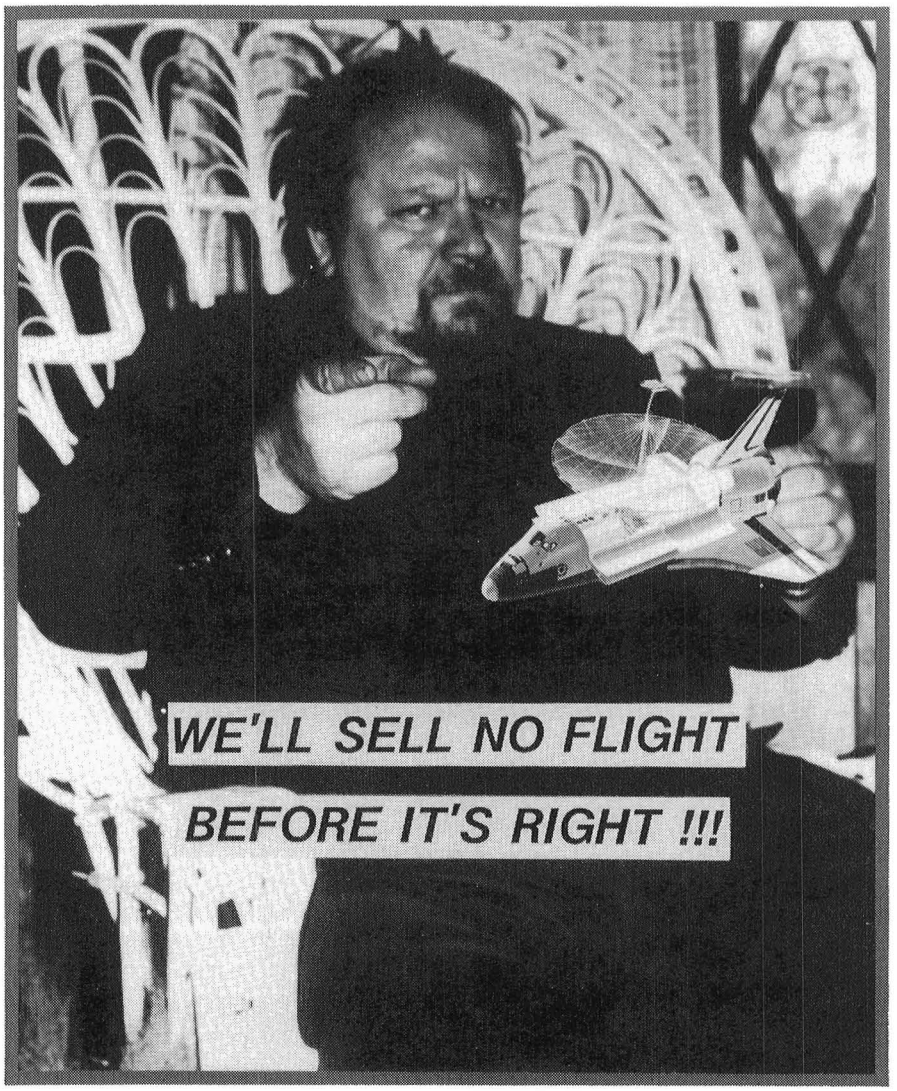

SUBJECTS TO BE DISCUSSED

This paper describes the activities of an in-house electro-science task group organized recently to conduct studies of shuttle-attached flight experiments using the 15 meter hoop-column antenna as a research tool for developing both improved sensor technology and LSA technology. Also, some experiments could provide significant amounts of scientific data such as radio star mapping and definition of ocean current eddies over limited geographic regions. The experiments originate from the microwave remote sensing community and other areas which require the inherently higher resolution and boresite gain of large space antennas.

Technology experiments are also being studied which would use the 15 meter antenna experiments as a stepping stone to 50-100 meter class reflector technology in the future. Details about an antenna technology experiment using the 15 meter antenna in a shuttle-attached mission are presented in this paper. Electromagnetic performance evaluation of a complete LSA system is essential to be sure the modeling is correct for each major subsystem and also to verify the interrelations of the subsystems.

- **PURPOSE**
- **ACTIVITIES**
- **LIST OF EXPERIMENTS**
- **SHUTTLE-STEP CONSTRAINTS**
- **ANTENNA REQUIREMENTS**
- **ANTENNA TECHNOLOGY EXPERIMENT**
- **SUMMARY**

TASK GROUP PURPOSE

The pre-phase-A task group studies will first address shuttle-attached experiments with possible later studies of free flyer missions.

ELECTRO-SCIENCE TASK GROUP

PURPOSE:

- **Conduct pre-phase-A study of potential flight experiments using the 15 meter hoop-column antenna**

- **Develop advocacy package for summer 85 budget considerations**

SHUTTLE ATTACHED FLIGHT EXPERIMENT

This sketch shows the 15 meter hoop-column antenna deployed in orbit and attached to shuttle thru the STEP pallet. A feed at the free end of the structure is shown for each of the four reflector sub-apertures. This reflector shape was chosen as a point design for an advanced communication mission since that design possessed the largest number of technology drivers which were realizable in the near future.

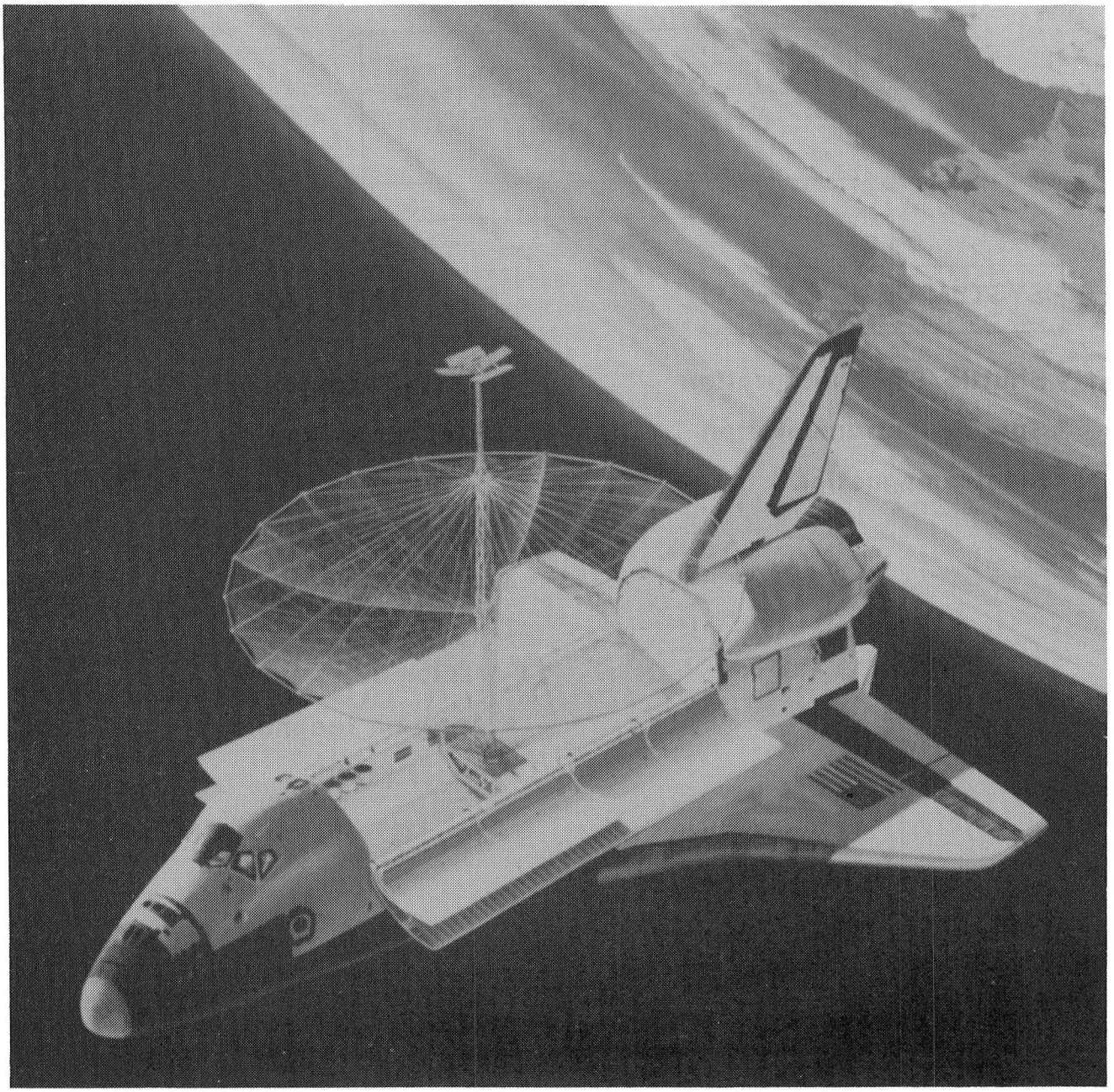

ORGANIZATION OF TASK GROUP

The task group is made up of a System Design Team and experiment advocates who will evaluate suitability of the electro-science experiments for shuttle attached implementation. The seven electro-science experiments shown are currently being studied and other experiments are being considered from the controls and structures technology areas.

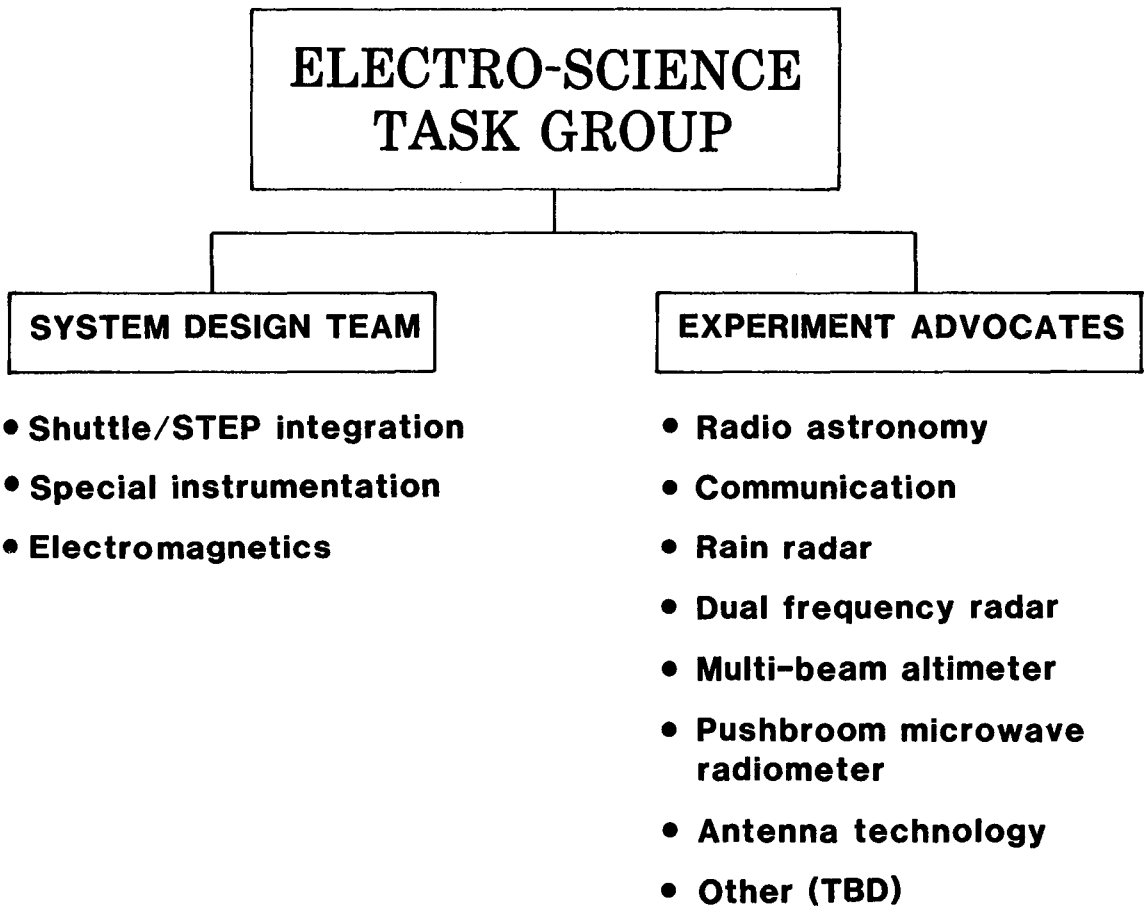

SEVEN ELECTRO-SCIENCE FLIGHT EXPERIMENTS

Electro-science experiments have been identified as mature candidates possibly suitable for experiments with a 15 meter antenna shuttle-attached mission. Five of these experiment concepts are discussed in papers at this conference (References 1 thru 5). In some cases, (radio astronomy, for example), free flying experiments are already being planned using a 15 meter class antenna and may not require an intermediate step such as a shuttle-attached experiment.

ELECTRO-SCIENCE FLIGHT EXPERIMENTS 15 METER ANTENNA

	EXPERIMENT CATEGORY	INFORMATION SOURCES	PURPOSE
*	Radio astronomy	JPL MIT MSFC	Map radio stars with .001 arc sec. resolution
*	Rain radar	U. of KANSAS	Develop advanced sensor and instrument technology
*	Dual frequency radar	HOFSTRA U. LaRC	
*	Multi-beam altimeter	WALLOPS	
*	Pushbroom microwave radiometer	GSFC LaRC	
	Communications	SSE Inc.	Evaluate system performance Develop enabling technology
	Antenna technology	LaRC JPL, HARRIS	

*DEC. 84 LSA CONFERENCE PAPER (REFERENCES 1-5)

TASK GROUP ACTIVITIES

The task group will develop experiment design concepts using experiment requirements (from electro-science, controls, and structures disciplines) and constraints of the shuttle, STEP and antenna capabilities. Configurations for launch and in-orbit will be developed to be sure the flight hardware can be packaged in the shuttle bay and to study in-orbit field-of-view and mission requirements.

After a preliminary definition of each experiment concept is developed and the commonality of flight hardware is clear, the possibility of combining several experiments on a single shuttle mission will be considered. Multiple missions with the same or different payloads may be also considered since the antenna can be restowed and returned to Earth.

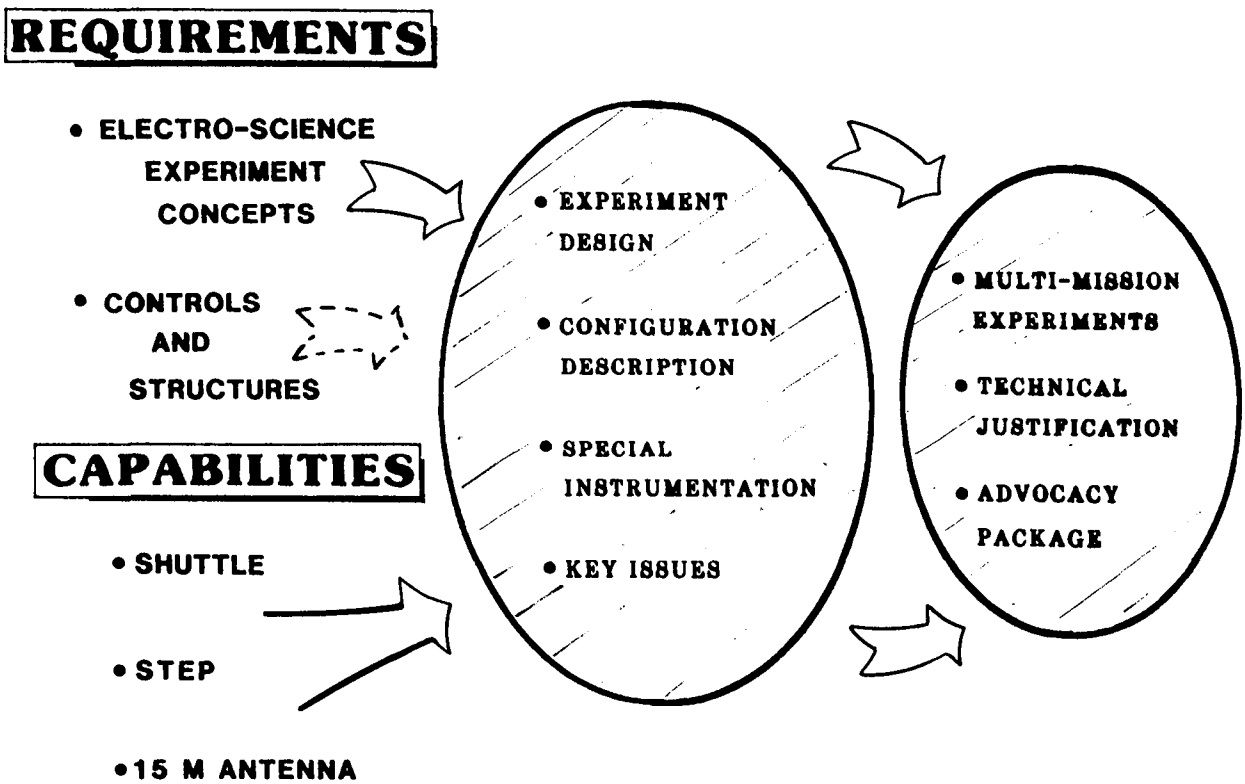

EXPERIMENT GUIDELINES

General guidelines being used for the study are listed on this chart. The precision gimbal (IPS) described later in this paper could be used if experiment pointing requirements exceed the 2.5 degrees accuracy provided by shuttle (at the payload interface) or if the VRCS usage disturbs the antenna during the tests.

One of the advantages of the hoop-column is that a wide range of reflector surface shapes can be used without changing the basic hoop-column structural members. For example, in one mission the reflector could use the current design (quad-aperture) and for later flights could be changed to a center fed parabolic, spherical, or even toroidal surface.

- **Shuttle attached antenna**
- **STEP usage planned**
- **Precision gimbal not excluded**
- **Reflector configuration - experiment option**
- **Mission scenario (Typical)**
  - **14 day mission (max)**
  - **Sequence**
    - **Launch**
    - **Orbiter C/O**
    - **Deploy other payloads**
    - **Antenna exp. systems check**
    - **Deploy antenna**
    - **Conduct experiments**
    - **Restow antenna**
    - **Deorbit and land**

TYPICAL DEPLOYMENT SEQUENCE

There are three catgories of mission interface constraints currently being considered. These constraints will be discussed next.

The 15 meter hoop-column antenna deployment out of the shuttle bay is depicted here. The exact distance of separation between the shuttle and the point of antenna attachment is not yet determined and probably will be influenced by the experiment objectives; for example, an experiment to study low side lobes would require antenna orientation to avoid spurious lobes from the shuttle; on the other hand, a controls or structural dynamics experiment would necessarily be designed to minimize shuttle-step effects on system ID tests, etc.

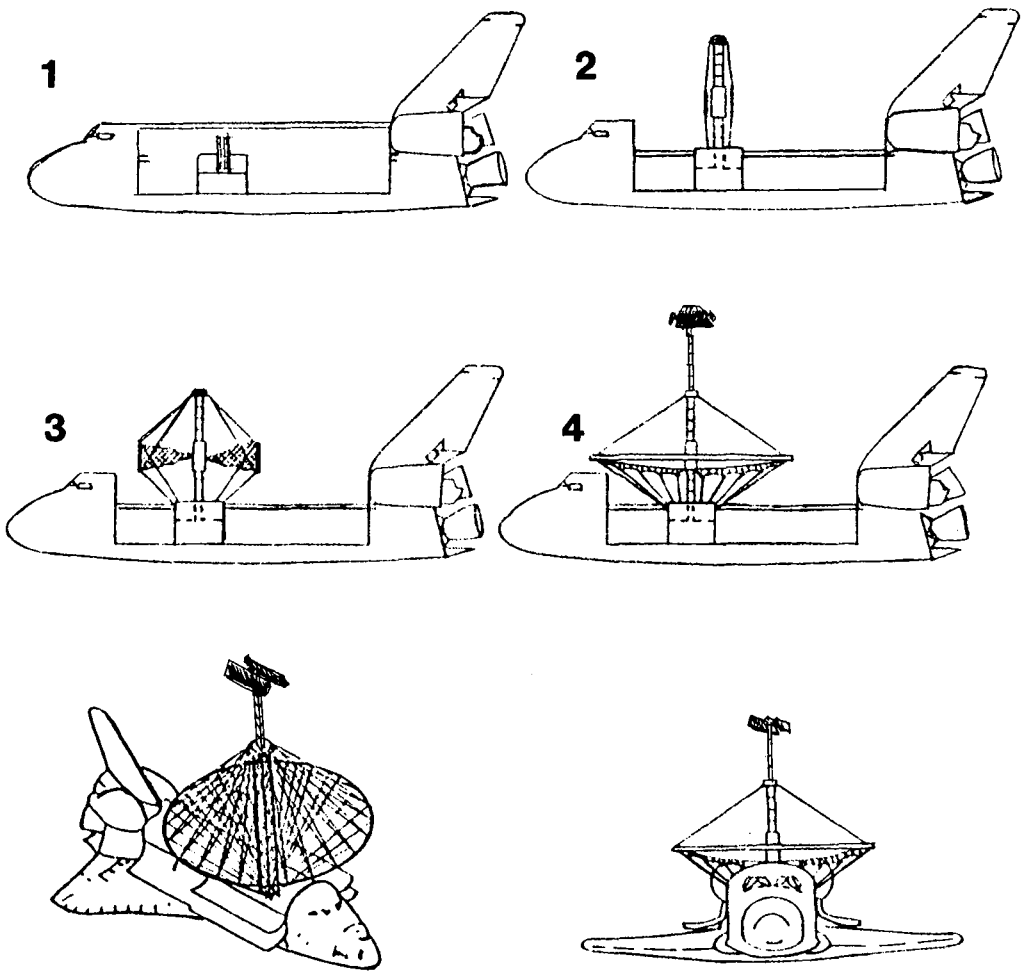

DEPLOYMENT CONFIGURATION

SHUTTLE CONSTRAINTS

A wide range of shuttle orbit inclinations is possible as shown here which generally satisfies currently defined experiment requirements. It is expected that all missions will use the KSC launch site, except the rain radar experiment which has some interest in polar ice mapping (requiring higher orbit inclination). The PBMR (pushbroom microwave radiometer, 57 degree inclination) requires CONUS coverage for soil moisture mapping of the United States during the 14 day mission. Also, the multi-beam altimeter prefers a 57 degree orbit inclination so that most ocean regions containing eddies can be measured during the 14 day mission.

The shuttle altitude and payload weight constraints are not considered restrictive relative to the lightweight flight hardware currently estimated for the experiments. The shuttle attitude control and knowledge (2.5 degrees), however, are generally not sufficient for most experiments. Therefore, the use of the IPS may be necessary in some cases. The IPS will be described in a later chart.

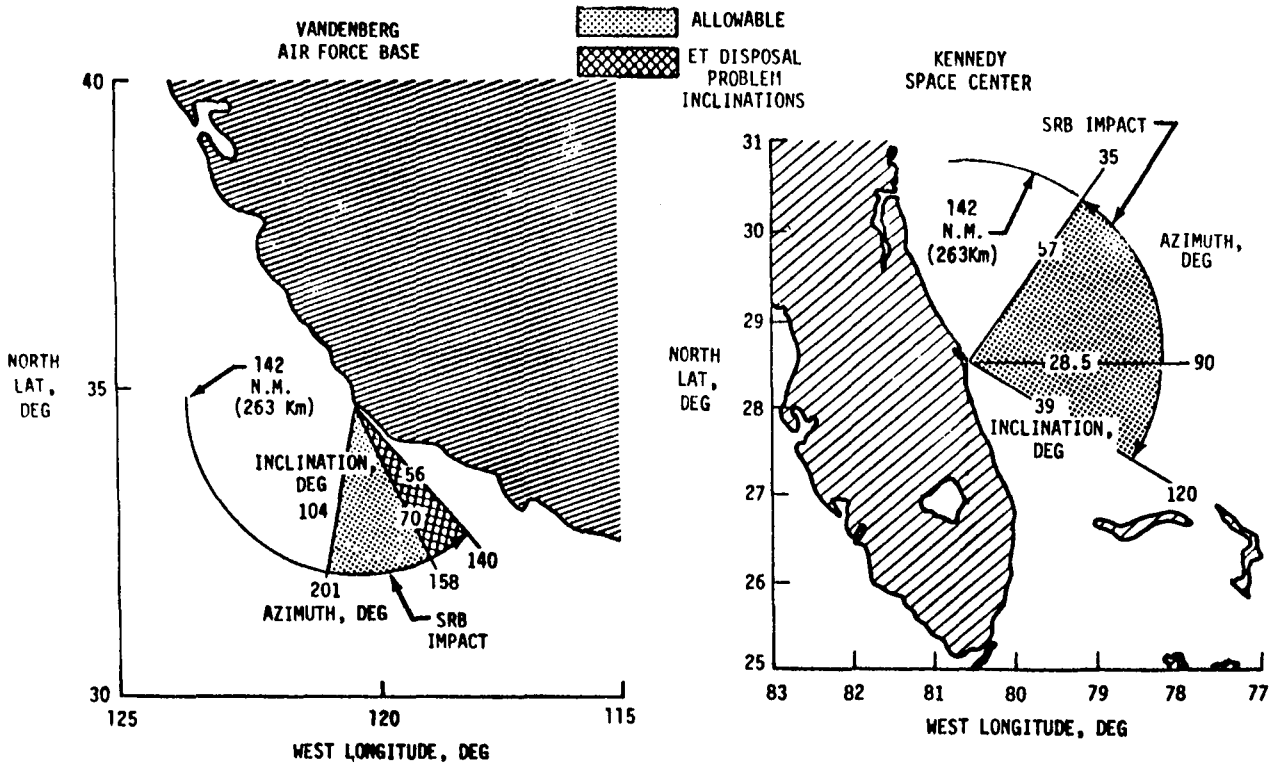

STEP FLIGHT HARDWARE

The STEP is planned to interface all experiments with the shuttle. There are several services provided by STEP which include mounting, command and sequencing, data processing, and power. Details are given in reference 6. This artist's concept shows different elements of the STEP flight hardware that fit in the shuttle bay. A rotation unit is available as part of STEP equipment to rotate the antenna out of the bay prior to deployment, if the IPS is not used. The STEP interface structure is very adaptable to experiment needs. It is expected that most of the electro-science experiments will have a common shuttle-STEP structural interface.

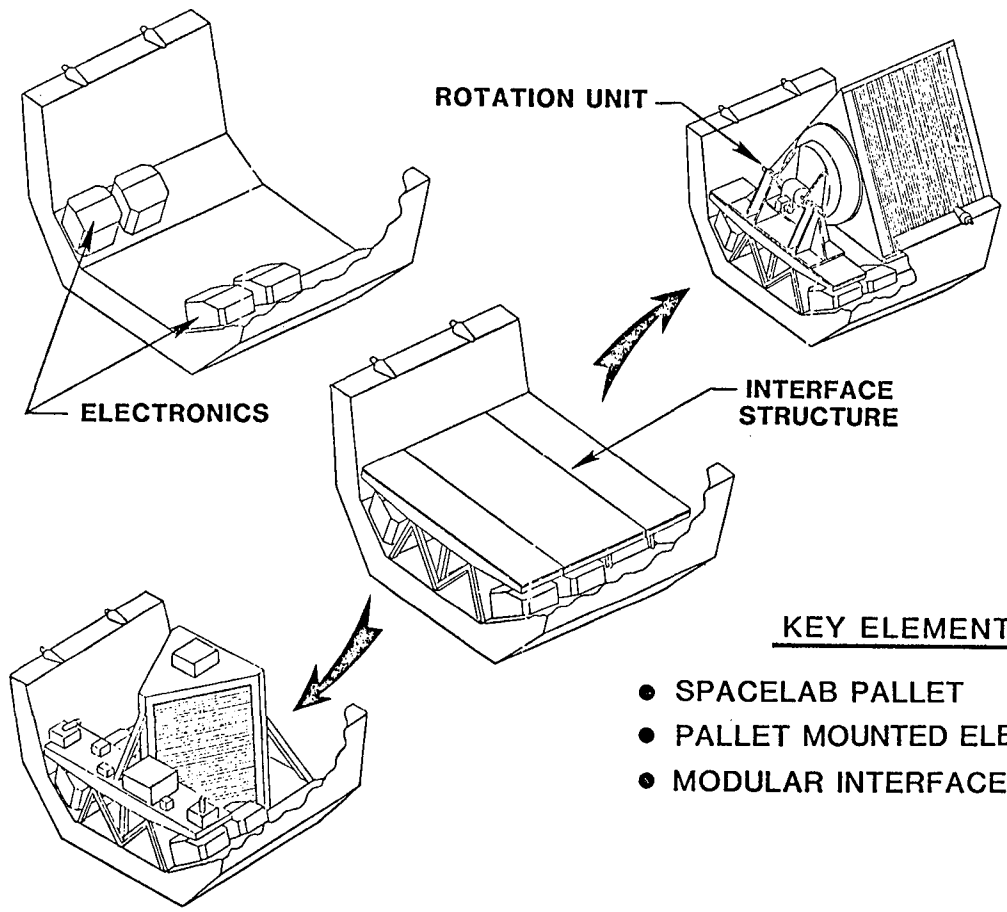

PRECISION GIMBAL

In cases where the shuttle pointing accuracy is not sufficient or dead-band requirements cause frequency VRCS firings, a precision three axis gimbal (IPS) is available with 3 arc sec (SPEC) pointing capability. The IPS has its own star tracker with field-of-view programmability to avoid blockage as might occur due to shuttle or the deployed mesh antenna. The IPS requires two STEP pallets (4000 lbs.) and weighs 1650 lbs. itself. These weights are within current shuttle launch capability without restricting the orbit inclination or altitudes currently envisioned for the electro-science experiments.

INSTRUMENT POINTING SYSTEM (IPS)

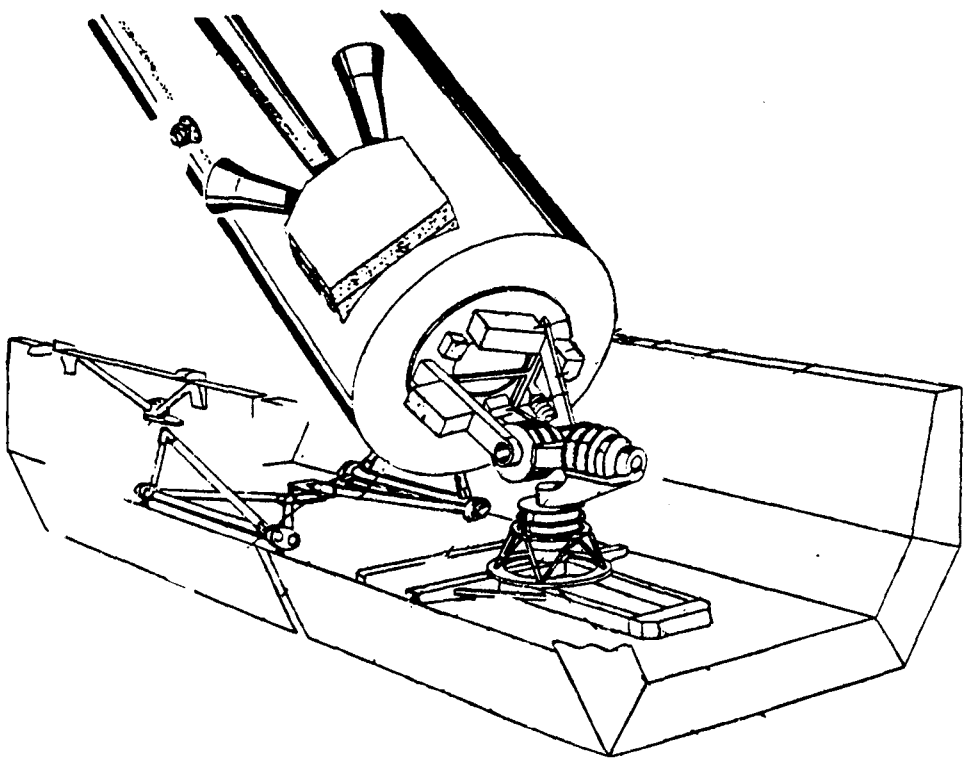

These preliminary antenna properties are still under study and are expected to change as the experiments become better defined. Several of the electro-science experiments have common requirements for reflector shape. Three different geometries are currently envisioned (see chart). Many of the experiments can be conducted with all three shapes. Program cost can be kept to a minimum by limiting the number of surface changes between missions. The frequency range for the experiments is L-band thru Ku-band and the PBMR requires the largest number of beams (to maximize swath width for rapid CONUS coverage).

15 METER ANTENNA CHARACTERISTICS (PRELIMINARY)

EXPERIMENT	REFLECTOR SURFACE*			BEAMS PER FREQ.	NO. OF FREQ.
	QUAD	BI-AP.	CENTER FED		
RADIO ASTRONOMY	—	—	√	1	TBD
RAIN RADAR	√	√	√	TBD	3
DUAL FREQUENCY RADAR	√	√	√	TBD	2
MULTI-BEAM ALTIMETER	√	√	√	10	1
PUSHBROOM MICROWAVE RADIOMETER	√	√	—	29	1
COMMUNICATION	√	√	TBD	TBD	TBD
ANTENNA TECHNOLOGY	√	√	—	5	4

*Heavy underline means preferred shape

ANTENNA TECHNOLOGY TESTS

A detailed study was conducted in 1983 at LaRC to define technology experiments for an LSA program. Although that particular study assumed a 50 meter antenna as the baseline space frame, the antenna technology experiment objectives and test requirements are similar for the 15 meter diameter hoop-column antenna listed on this chart.

Each test is designed to evaluate key antenna parameters in a variety of thermal and structural dynamic conditions. For example, the boresight transient test (test 2) would determine the antenna settle time after a slew and point maneuver. In this particular test, the boresight gain and angle would be the measured parameter rather than the conventional multiple "antenna pattern cuts."

For test 5, the upper electromagnetic frequency of operation would be chosen so that a measurable amount of boresight gain loss would occur due to reflector surface roughness; in this way the EM model predicts for rough surface reflectors could be compared with actual measurements on an LSA.

There are several measurement techniques which can be considered for these antenna tests. Some, however, require specific geometrical relations between the antenna, sun, and signal source used for the measurement which limit the type of measurement technique that can be used.

TEST		MEASURED PARAMETER[1]	TEST CONDITIONS
1	Pattern determination	Antenna pattern	• Full sun • Edge on sun • No sun
2	Boresight transient	Boresight gain and angle	
3	Thermal transient	Boresight gain and angle and ohmic loss[3]	• Near occultation • Edge on to full sun
4	Aperture illumination	Antenna pattern	• No sun • Variable illumination taper
5	Surface roughness effects		• No sun • D/λ= variable • Surface error 69 mils
6	Intermodulation[2]	Spurious frequencies	• No sun • Full sun

NOTES: [1]Optical measurement of antenna surface and feed required for all experiments
[2]Not part of base line
[3]Ohmic loss measurement is not part of baseline

METHODS FOR MEASURING ANTENNA PROPERTIES

One pattern measurement technique studied uses a co-orbiting precision sphere as a target. In this case, a one hundred watt signal would be transmitted by the Large Space Antenna to the sphere ($\geq 2\ D^2 / \lambda$ away) which would reflect a known amount of signal back to the antenna. By scanning the antenna and measuring the signal return as a function of azimuth and evaluation angles the full pattern could be determined including cross polarization.

The co-orbiting sphere method is more accurate for measuring absolute gain and cross polarization than any of the other techniques studied. The position of the sphere relative to the Large Space Antenna must be known precisely, however, which imposes rather stringent requirements on shuttle and sphere tracking during the test.

Similar pattern data can be obtained using a co-orbiting transmitter as a signal source such a SPARTAN (reference 7) and this technique has superior signal to noise conditions. Still another approach could use a ground based array of receivers which would give simultaneous multiple cuts through the pattern as was used to measure the pattern of the S-193 SKYLAB scatterometer in 1973.

Radio stars can be used as signal sources and there are a half-dozen or more sources bright enough. The celestial sources approach, however, does require special circuits and there are some unresolved technical questions not completely answered during the course of this short study. The boresight transient experiment (test 2) would use standard monopulse methods with the measurement range limited to about 1.5 beam widths.

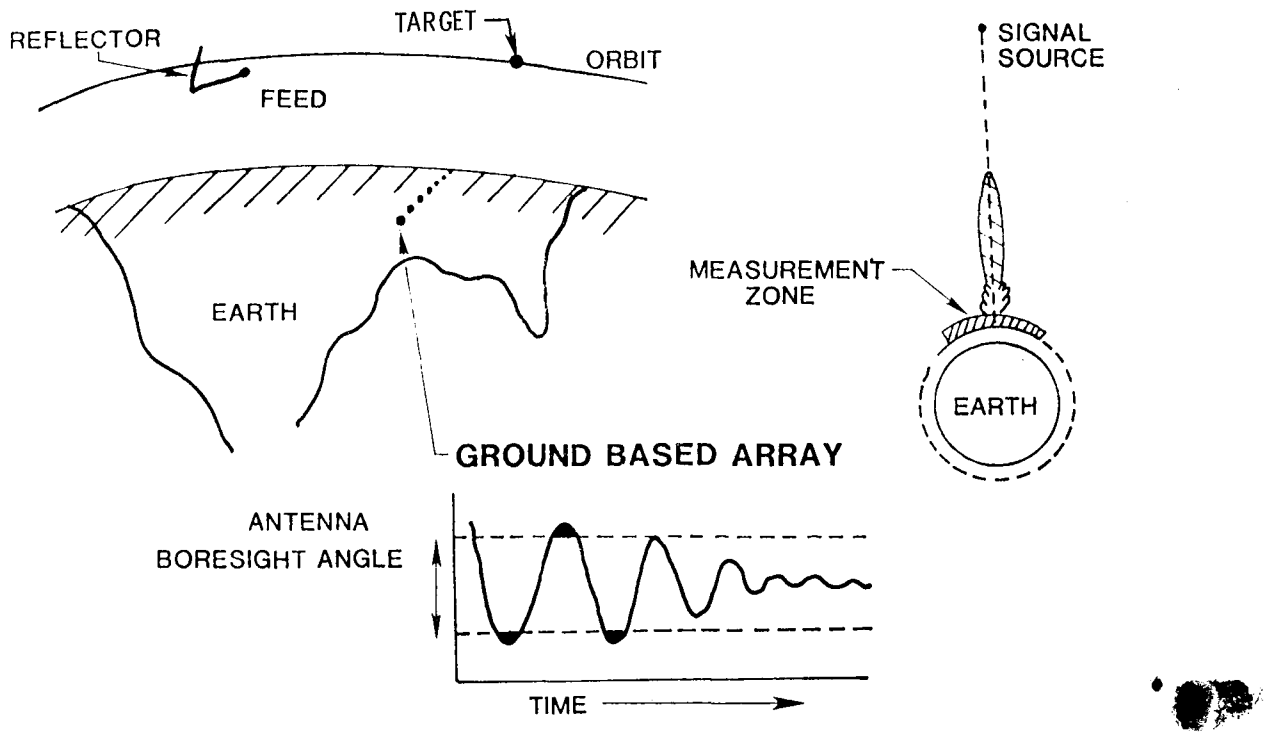

COMPARISON OF TECHNIQUES

Summarized here are the 1983 ad hoc committee findings which show the favored techniques for antenna parameter measurement. This chart is not all inclusive in that it does not consider the importance of geometry between the antenna, target, and sun for the thermal tests. For example, the ground-based array technique would not be satisfactory for that test.

There are several measurement techniques which have the potential of satisfying the antenna technology experiment requirements; each has features making it superior in one way or the other depending on the antenna parameter. For example, the LEO-sphere approach is inherently superior to the other techniques for measuring absolute gain and cross polarization because of the preciseness with which the target sphere radar cross section can be calculated (reference 8).

Both the LEO-xmit (SPARTAN, reference 7) and GEO-xmit (TDRSS) approach are rated excellent for boresight transient and hemispherical scan because of the inherently good signal to noise ratio. If the structure settling time is naturally short or if an active control system is used and works well enough to reduce the settle time to 15 seconds or less, then there would be time for the raster scan which would give many pattern cuts around the main beam. This would provide an excellent definition of near-in side lobes as well as boresight gain and angle.

The relative importance and accuracy requirements of each antenna parameter strongly depend on the eventual Large Space Antenna application or user. For that reason it is necessary, as a next step, to priortize each parameter according to its level of importance for the different users and to develop a measurement error budget for each technique, so that a final measurement method or combination of methods can be selected.

TECHNIQUE		ANTENNA PARAMETERS: BORESIGHT TRANSIENT	BORESIGHT STATIC	NEAR-IN SIDELOBES	HEMISPHERICAL SCAN	CROSS POLARIZATION	RASTER[3] SCAN	COMMENTS
CO-ORBITER	LEO-SPHERE	GOOD	EXCELLENT	POOR[1]	MARGINAL[1]	EXCELLENT	POOR[2]	RASTER SCAN IS LIMITED BY SETTLING TIME OF STRUCTURE
	LEO-XMIT	EXCELLENT	GOOD	GOOD	EXCELLENT	GOOD	POOR[2]	
	GEO-XMIT	EXCELLENT	GOOD	EXCELLENT	EXCELLENT	MARGINAL	POOR[2]	
CELESTIAL SOURCES	RADIO STARS	GOOD	MARGINAL	NEEDS STUDY	GOOD	MARGINAL	POOR[2]	•COMPLEX HARDWARE •TECHNICAL ISSUES
GROUND BASED SYSTEMS	ARRAY	POOR	MARGINAL	GOOD	GOOD	MARGINAL	EXCELLENT	•LIMITED TEST TIME •HIGH COST •NO FULL SUN
	SINGLE STATION	POOR	POOR	MARGINAL	MARGINAL	MARGINAL	POOR	•LIMITED TESTING TIME •NO FULL SUN

NOTES: [1]MAY BE IMPROVED WITH LARGER TARGET (INFLATABLE-TETHERED SPHERE)

[2]MAY BE IMPROVED IF SETTLE TIME IS SHORT

[3]ALSO PROVIDES MEASUREMENT OF REFLECTOR CONTOUR (HOLOGRAPHIC TECHNIQUE)

CROSS HATCH INDICATES SMALL LIKELYHOOD OF IMPROVEMENT

SUMMARY

- SEVEN CANDIDATE ELECTROSCIENCE EXPERIMENTS
- DIRECTOR'S REVIEW SPRING 1985
- ADVOCACY PACKAGE TO HEADQUARTERS SUMMER 1985
- STRUCTURES - CONTROLS EXPERIMENT DEFINITIONS NOW UNDERWAY

REFERENCES

1. Parsons, C. L.; McGoogan, J.; and Beck, F. B.: Application of Pushbroom Altimetry From Space Using Large Space Antennas. Large Space Antenna Systems Technology - 1984, NASA CP-2368, Part 1, 1985, pp. 63-71.

2. Shiue, J. C.; and Lawrence, R. W.: Orbiting Multi-Beam Microwave Radiometer for Soil Moisture Sensing. Large Space Antenna Systems Technology - 1984, NASA CP-2368, Part 1, 1985, pp. 73-85.

3. Moore, R. K.; and Gogineni, S. P.: Large Space Antenna Technology Applied to Radar-Imaging, Rain-Rate Measurements, and Ocean Wind Sensing. Large Space Antenna Systems Technology - 1984, NASA CP-2368, Part 1, 1985, pp. 97-108.

4. Weissman, D. E.; and Johnson, J. W.: Advanced Two-Frequency Ocean Sensing Radar Using High-Resolution Antenna Beams. Large Space Antenna Systems Technology - 1984, NASA CP-2368, Part 1, 1985, pp. 109-115.

5. Jordan, J. F.; Freeland, R. E.; Levy, G. S.; and Potts, D. E.: QUASAT - An Orbiting Very Long Baseline Interferometer Program Using Large Space Antenna Systems. NASA CP-2368, Part 1, 1985, pp. 117-125.

6. Harris, J. E.: Space Technology Experiments Program (STEP) Status - An In-Space Test Facility. Large Space Antenna Systems Technology - 1984, NASA CP-2368, Part 2, 1985, pp. 887-891.

7. Cuccia, C. Louis; Campbell, Thomas G.; Pritchard, W. L.; and Lyon, Jud: Space-Based Antenna Measurement System Concepts for Space Station Operation. Large Space Antenna Systems Technology - 1984, NASA CP-2368, Part 2, 1985, pp. 809-842.

8. Grantham, W. L.; and Schroeder, Lyle C.: Absolute Calibration of the RADSCAT Scatterometer Using Precision Spheres. NASA TN D-8259, 1976.

1. Report No.	2. Government Accession No.	3. Recipient's Catalog No.
NASA CP-2368, Part 2		

4. Title and Subtitle	5. Report Date
LARGE SPACE ANTENNA SYSTEMS TECHNOLOGY - 1984	April 1985
	6. Performing Organization Code: 506-62-23-01
7. Author(s): William J. Boyer, Compiler	8. Performing Organization Report No.: L-15950
	10. Work Unit No.
9. Performing Organization Name and Address: NASA Langley Research Center, Hampton, Virginia 23665	11. Contract or Grant No.
	13. Type of Report and Period Covered: Conference Publication
12. Sponsoring Agency Name and Address: National Aeronautics and Space Administration, Washington, DC 20546	14. Sponsoring Agency Code

15. Supplementary Notes

16. Abstract

This publication is a compilation of the papers presented at the NASA Conference on Large Space Antenna Systems Technology held at the NASA Langley Research Center, Hampton, Virginia, December 4-6, 1984. The conference, which was sponsored jointly by the NASA Office of Aeronautics and Space Technology (OAST) and the NASA Langley Research Center, was organized into seven sessions: Mission Applications for Large Space Antenna Systems, Large Space Antenna Structural Systems, Materials and Structures Technology, Structural Dynamics and Control Technology, Electromagnetics Technology, Large Space Antenna Systems and the Space Station, and Flight Test and Evaluation. All speakers and topics were selected by the session co-chairmen and included representation from industry, universities, and government. The program was organized to provide a comprehensive review of space missions requiring large antenna systems and of the status of key technologies required to enable these missions.

17. Key Words (Suggested by Author(s))

Large space antenna systems
Structures, materials, and analyses
Flight technology experiments
Structural dynamics and control

18. Distribution Statement

Unclassified - Unlimited

Subject Category 15

19. Security Classif. (of this report)	20. Security Classif. (of this page)	21. No. of Pages	22. Price
Unclassified	Unclassified	499	A21

For sale by the National Technical Information Service, Springfield, Virginia 22161 NASA Langley, 1984